U.PORTO

FEUP FACULDADE DE ENGENHARIA
UNIVERSIDADE DO PORTO

Variationally consistent mean-field homogenization models with applications to semi-crystalline polymers

Advisor:
Dr. Francisco Manuel Andrade Pires
Co-advisor:
Dr. Bernardo Proença Ferreira

Author:
José Luís Passos Vila-Chã

Document submitted in partial fulfillment of the requirements
for the degree of Doctor of Philosophy in
Mechanical Engineering

Porto, June 2026

Research group

CM2S | Computational Multi-Scale Modeling of Solids and Structures

Institutional support

U.PORTO FEUP FACULDADE DE ENGENHARIA UNIVERSIDADE DO PORTO

inegi driving science & innovation

Funding

fct Fundação para a Ciência e a Tecnologia

REPÚBLICA PORTUGUESA | EDUCAÇÃO, CIÊNCIA E INOVAÇÃO

Co-funding

PESSOAS 2030

PORTUGAL 2030

UNIÃO EUROPEIA

Fundo Social Europeu

Supported by the Portuguese Foundation for Science and Technology (FCT) under the scholarship 10.54499/2021.07345.BD.

Aos meus pais,
ao meu irmão
e à Helena.

Page intentionally left blank.

"If thou workest at that which is before thee, following right reason seriously, vigorously, calmly, without allowing anything else to distract thee, but keeping thy divine part pure, as if thou shouldst be bound to give it back immediately; if thou holdest to this, expecting nothing, fearing nothing, but satisfied with thy present activity according to nature, and with heroic truth in every word and sound which thou utterest, thou wilt live happy. And there is no man who is able to prevent this."

— *Marcus Aurelius,* Meditations*, III.12*

Page intentionally left blank.

Abstract

Variationally consistent mean-field homogenization models with applications to semi-crystalline polymers

Engineering design is inherently multiscale, requiring the simultaneous consideration of function, material, geometry, and manufacturing process. This interplay is particularly evident in heterogeneous materials, where microstructural features across multiple length scales decisively affect macroscopic thermomechanical behavior. Within this context, this thesis contributes to the development of computational tools for the multiscale modeling of heterogeneous materials, with a particular focus on semi-crystalline polymers.

Among computational homogenization techniques widely used in the modeling of heterogeneous materials, mean-field homogenization (MFH) methods are especially attractive due to their efficiency. A central contribution of this thesis is the formulation of mean-field homogenization within a rigorous and unified variational framework based on the Principle of Multiscale Virtual Power (PMVP) and its dual, the Principle of Multiscale Complementary Virtual Power (PMCVP). Together, these principles establish a physically consistent foundation for MFH modeling that guarantees mechanical power equivalence across scales and satisfaction of angular momentum conservation for non-dissipative materials.

Semi-crystalline polymers constitute a technologically and economically important class of thermoplastics, widely used in applications ranging from packaging and automotive components to biomedical devices. Structurally, these materials are characterized by the coexistence of crystalline and amorphous phases arranged in complex hierarchical morphologies, including lamellae, spherulites, shish-kebab structures, and fibrillar textures. Their mechanical response arises from the interaction of multiple deformation mechanisms, such that capturing this rich behavior within predictive and computationally efficient constitutive models remains a significant challenge.

A comprehensive review of existing modeling approaches is presented, covering the evolution from infinitesimal thermoviscoelasticity to finite-strain thermoviscoplastic formulations. Particular attention is given to models that distinguish between crystalline and amorphous phases and to the experimental evidence motivating such distinctions. The strengths, limitations, and implementation challenges of existing models are critically assessed, highlighting the need for approaches that balance physical fidelity, numerical robustness, and parameter identification feasibility. Based on the derived MFH formulations, two novel constitutive models for semi-crystalline polymers are proposed.

Overall, this work advances the theoretical foundations of mean-field homogenization, provides new tools for the constitutive modeling of semi-crystalline polymers, and contributes to the broader goal of predictive multiscale modeling of heterogeneous materials.

Keywords: computational mechanics, constitutive modeling, semi-crystalline polymers, computational homogenization, mean-field homogenization, Principle of Multiscale Virtual Power

Page intentionally left blank.

Resumo

Homogeneização de campo médio variacionalmente consistente com aplicações a polímeros semicristalinos

O design em engenharia é intrinsecamente multiescala e requer que se considere a função, o material, a geometria e o processo de fabrico, em simultâneo. Esta interdependência é particularmente evidente em materiais heterogéneos, onde as características microestruturais a diferentes escalas de comprimento afetam de forma decisiva o comportamento termomecânico à macroescala. Neste contexto, esta tese contribui para o desenvolvimento de ferramentas computacionais para a modelação multiescala de materiais heterogéneos, com especial ênfase em polímeros semicristalinos.

Entre as técnicas de homogeneização computacional, amplamente utilizadas na modelação de materiais heterogéneos, os métodos de homogeneização de campo médio (HCM) são particularmente atrativos dada a sua eficiência. Uma das principais contribuições desta tese é a formulação da homogeneização de campo médio no contexto de uma teoria variacional rigorosa e unificada, baseada no Princípio da Potência Virtual Multiescala (PPVM) e no seu dual, o Princípio da Potência Virtual Complementar Multiescala (PPVCM). Em conjunto, estes princípios estabelecem uma base fisicamente consistente para os modelos de HCM, que garante equivalência da potência mecânica entre escalas e a satisfação da conservação do momento angular para materiais não dissipativos.

Os polímeros semicristalinos constituem um grupo tecnológica e economicamente relevante de termoplásticos, amplamente utilizados em aplicações que vão desde embalagens e componentes automóveis a dispositivos biomédicos. Estruturalmente, estes materiais são caracterizados pela coexistência de fases cristalinas e amorfas organizadas em morfologias hierárquicas complexas. A sua resposta mecânica resulta da interação de múltiplos mecanismos de deformação, pelo que capturar este comportamento complexo em modelos constitutivos preditivos e computacionalmente eficientes continua a ser um desafio importante. Uma revisão bibliográfica abrangente das abordagens de modelação existentes é apresentada, cobrindo a evolução desde a termoviscoelasticidade infinitesimal até às formulações termoviscoplásticas de grandes deformações. Os aspetos positivos e negativos, bem como os desafios de implementação dos modelos existentes, são avaliados, destacando-se a necessidade de abordagens com um bom compromisso entre fidelidade física, robustez numérica e viabilidade na identificação de parâmetros. Com base nas formulações de HCM desenvolvidas, são propostos dois novos modelos constitutivos para polímeros semicristalinos.

Em suma, este trabalho contribui para os fundamentos teóricos da homogeneização de campo médio, disponibiliza novas ferramentas para a modelação constitutiva de polímeros semicristalinos e contribui para o objetivo mais amplo da modelação multiescala de materiais heterogéneos.

Palavras-chave: mecânica computacional, modelação constitutiva, polímeros semicristalinos, homogeneização computacional, homogeneização de campo médio, Princípio da Potência Virtual Multiescala

Page intentionally left blank.

Agradecimentos

Ao meu orientador, o Professor Francisco Pires, desejo expressar o meu sincero agradecimento pela orientação ao longo destes anos. Em particular, agradeço-lhe a oportunidade de desenvolver este trabalho, a confiança depositada, o rigor científico, a disponibilidade e o apoio nos momentos mais difíceis.

Ao meu coorientador, o Doutor Bernardo Proença Ferreira, agradeço o acompanhamento próximo do trabalho, as inúmeras discussões, a partilha de conhecimento, e a paciência e seriedade demonstradas ao longo de todo o percurso.

Fica também um agradecimento muito especial ao Doutor António Carneiro por ter colaborado comigo de uma maneira tão próxima, pelas palavras encorajadoras e pela disponibilidade constante.

Agradeço ainda aos restantes colegas que participaram no CM2S e que trabalharam na L301. Ao Rui, à Francisca, ao Tiago, ao Miguel, ao Rodrigo, ao Igor, ao Guilherme, ao Ricardo, ao Pedro e ao Denis. Pelo ambiente de trabalho, pelas discussões, pela camaradagem, pelo Tetris e pelo SuperTux (peço desculpa pelos queques!) que tornaram esta jornada muito mais agradável e memorável.

Por fim, mas não menos importante, à minha família. Em especial, aos meus pais, Cristina e José António, ao meu irmão Eduardo e à Helena, pelo apoio incondicional, pela paciência e por estarem sempre presentes ao longo de todos estes anos. Não conseguiria ter chegado ao fim sem vós.

Porto, junho de 2026

José Vila-Chã

Page intentionally left blank.

Contents

List of Figures

Page intentionally left blank.

List of Tables

Page intentionally left blank.

Notation

General abbreviations

BVP	**B**oundary **V**alue **P**roblem
DOF	**D**egrees **O**f **F**reedom
FEM	**F**inite **E**lement **M**ethod
MFH	**M**ean-**F**ield **H**omogenization
PCTFE	**P**oly**c**hloro**tri**fluoro**e**thylene
PE	**P**oly**e**thylene
PMCVP	**P**rinciple of **M**ultiscale **C**omplementary **V**irtual **P**ower
PMVP	**P**rinciple of **M**ultiscale **V**irtual **P**ower
RVE	**R**epresentative **V**olume **E**lement

Accents

$(\ddot{\bullet})$	Second-order time derivative
$(\dot{\bullet})$	First-order time derivative

Sets, domains and boundaries

$\mathsf{H}(\mathrm{curl}_0)$	Sobolev space of second-order tensor fields with square-integrable curl
$\boldsymbol{H}^1$	Sobolev space of vector-valued functions with square-integrable first derivatives
$\mathbb{S}^3$	Space of symmetric second-order tensors in three dimensions
$\mathbb{S}^3_+$	Space of symmetric positive-definite second-order tensors in three dimensions
$\mathscr{N}$	Constitutive manifold of the Biot stress, parameterized by the right stretch $\boldsymbol{U}$
$\mathscr{V}$	Tangent space to the constitutive manifold $\mathscr{N}$ at a given right stretch

$\mathfrak{so}(3)$ Lie algebra of SO(3), i.e. the space of skew-symmetric second-order tensors in three dimensions

SO(3) Special orthogonal group in three dimensions, representing all proper rotations

$\mathscr{B}$ Deformable body

$\mathscr{E}$ Euclidean space

$\mathscr{H}$ Space of virtual (statically admissible) stress-potential fields

$\mathscr{K}$ Space of kinematically admissible fields

$\mathscr{S}$ Space of statically admissible stress-potential fields

$\mathscr{V}$ Space of virtual (kinematically admissible) fields

Ω_0 Reference configuration of the body

$\partial\Omega_0$ Boundary of the reference configuration of the body

General notation

a Scalar

$\boldsymbol{a}$ First-order tensor

$\boldsymbol{A}$ Second-order tensor

$\mathscr{A}$ Body, space, or set

Operators and symbols

$(\bullet) : (\bullet)$ Double contraction between two second-order tensors

$\boldsymbol{A}_{\text{dev}}$ Deviatoric part of a second-order tensor

$\nabla_0(\bullet)$ Gradient operator with respect to the material coordinates

$\text{curl}_0(\bullet)$ Curl operator with respect to the material coordinates

A_m Mean normal component of a second-order tensor

Subscripts and superscripts

$(\bullet)_0$ Reference configuration

$(\bullet)_\mu$ Microscopic quantity

$(\bullet)_{\text{iso}}$ Isochoric part of a quantity

Variables

$\mathbf{0}$	Zero vector/tensor
$\boldsymbol{\alpha_F}$	Thermal expansion tensor
$\boldsymbol{\beta_P}$	Thermal stress tensor
$\boldsymbol{\Gamma}$	Lagrange multiplier tensor (PMCVP admissibility constraints)
$\boldsymbol{\sigma}$	Cauchy stress tensor
$\boldsymbol{\tau}$	Kirchhoff stress tensor
$\boldsymbol{\varepsilon}$	Infinitesimal strain tensor
$\boldsymbol{B}$	Left Cauchy-Green deformation tensor
$\boldsymbol{C}$	Right Cauchy-Green deformation tensor
$\boldsymbol{D}$	Rate of deformation tensor
$\boldsymbol{E}^{(m)}$	Seth-Hill generalized strain tensor
$\boldsymbol{F}^*$	Forcing macroscopic deformation gradient (single-inclusion problem)
$\boldsymbol{F}_{\text{iso}}$	Isochoric part of the deformation gradient
$\boldsymbol{g}_0$	Material gradient of temperature
$\boldsymbol{k}$	Heat-flux constitutive function
$\boldsymbol{L}$	Spatial velocity gradient tensor
$\boldsymbol{M}$	Mandel stress tensor
$\boldsymbol{N}$	Normal vector to a surface in the reference configuration
$\boldsymbol{n}$	Normal vector to a surface in the current configuration
$\boldsymbol{P}$	First Piola-Kirchhoff stress tensor
$\boldsymbol{P}^*$	Forcing macroscopic first Piola–Kirchhoff stress (single-inclusion problem)
$\boldsymbol{q}$	Heat flux vector
$\boldsymbol{R}$	Polar rotation tensor
$\boldsymbol{S}$	Second Piola-Kirchhoff stress tensor
$\boldsymbol{t}$	Cauchy traction vector
$\boldsymbol{t}_0$	First Piola-Kirchhoff traction vector
$\boldsymbol{T}_B$	Biot stress tensor
$\boldsymbol{U}$	Right stretch tensor
$\boldsymbol{V}$	Left stretch tensor
$\boldsymbol{W}$	Spin tensor
$\boldsymbol{x}$	Spatial coordinates in the deformed configuration
$\boldsymbol{Y}$	Microscopic material coordinates in the reference configuration
$\boldsymbol{Z}$	Beltrami-type stress potential tensor
A	Fourth-order strain localization (concentration) tensor
B	Fourth-order stress localization (concentration) tensor
D	Fourth-order isotropic elasticity tensor
G	Fourth-order relaxation modulus tensor

I	Fourth-order identity tensor
P_N	Fourth-order normal projection tensor (laminate interface)
P_T	Fourth-order tangential projection tensor (laminate interface)
$\boldsymbol{\varphi}$	Motion function
$\boldsymbol{b}$	Body forces
$\boldsymbol{F}$	Deformation gradient tensor
$\boldsymbol{u}$	Displacement vector
$\boldsymbol{X}$	Material coordinates in the reference configuration
$\boldsymbol{\varepsilon}^{(0)}$	Logarithmic or Hencky strain tensor
χ	Degree of crystallinity
λ_i	Principal stretches
ν	Poisson's ratio
ω	Angular frequency of the applied load
$\mathcal{A}_{\text{int}}$	Thermodynamic conjugate forces associated with the internal variables
$\mathcal{D}_{\text{int}}$	Internal dissipation
$\mathcal{H}^{\text{ep}}$	Thermomechanical coupling term (strain-driven form)
$\mathcal{K}^{\text{ep}}$	Thermomechanical coupling term (stress-driven form)
ψ	Helmholtz free energy density per unit mass
ρ	Density
$C_{\boldsymbol{F}}$	Specific heat at constant deformation
$C_{\boldsymbol{P}}$	Specific heat at constant stress
e	Specific internal energy
G	Shear modulus
J	Determinant of the deformation gradient
r	Specific heat supply
s	Specific entropy
T	Absolute temperature
t	Time

Chapter 1

Introduction

1.1 Context

Design permeates engineering. According to Ashby (1999), the main features of mechanical design are function, material, shape, and process. There is a profound interplay between all these facets of design when developing a mechanical component, as the component must meet functional criteria in terms of its thermomechanical behavior, with additional specifications of its electric, magnetic, or mass transfer characteristics also being possible. The aptitude of a component to satisfy these demands is determined by the material or materials that make it up, as well as by its shape. Some materials, however, cannot be manufactured into a particular shape or by using a specific manufacturing process. Weight, cost, and environmental impact reduction can all be included as goals, and their achievement is closely related to the material and method selected.

An even more intimate relationship between the final performance of the mechanical component and the process selected for its manufacturing may be uncovered by taking into account the hierarchical structure of engineering materials. Olson (2000) emphasizes the cause/effect relationship between the process, the material's structure at multiple scales ranging from the nanoscale to the macroscale, the material's properties, and its final performance. The reverse goals/means perspective can also be adopted where a given performance requirement drives the search for a material with a particular set of properties. These, in turn, may only be realized if the appropriate multiscale structure is obtained through a suitable process. Ashby (1999) highlights that first-order differences between the properties of materials, e.g., polymers and metals, are due to the mass of the atoms, the nature of the inter-atomic forces and the geometry of the atomic packing. The magnitude of the effect due to the microstructure on the properties of a material is generally an order of magnitude less than that of bonding and atomic structure.

There are several methodologies to systematically tackle the simultaneous design of materials, components, and processes. 'Integrated Computational Materials Engineering' (ICME) is one such approach proposed by Horstemeyer and Wang (2003) that includes the process-structure-property-performance relationships within a computational framework. Its goal is the simultaneous design of a component, the materials that it is composed of and the manufacturing process employed to produce it, taking into account the material's structure at different scales. To realize this vision, suitable models and numerical tools for simulating manufacturing processes and component life at a given time and length scale must be available. Experimental methods to probe the model's validity and acquire the corresponding material parameters are also crucial. To accurately capture the behavior of the material, the correct

boundary conditions, initial conditions, and material parameters must be established at each scale and time-frame. An adequate way to transfer information between the different scales must also be devised.

Taking into account the hierarchical nature of a material's structure, appropriate models may be set up at the structural (meters, centimeters), macro (millimeters), meso (hundreds to tens of micrometers), micro (micrometers), and atomic/nanoscale (angstrom). As an example, consider a polymer blend component. At the structural level, solutions obtained from the Finite Element Method (FEM) can be used to model the thermomechanical behavior both during manufacturing and the service life of a component or machine, with full-scale experiments being needed to gauge the accuracy of the predictions. To perform these simulations, an appropriate constitutive/rheological model must be devised at the macroscale. Its validation is performed through its use in suitable FEM simulations and comparison with simple mechanical experiments, e.g., uniaxial or torsion experiments. An even more faithful description of a polymer blend may be achieved by retaining the appropriate continuum constitutive models for each phase, and combining them with an accurate mesoscale representation employing, for example, computational homogenization.

1.2 Motivation

Within this context, this work aims to contribute to the development of computational tools for the multiscale modeling of heterogeneous materials, with a particular focus on semi-crystalline polymers. A brief introduction to computational homogenization and semi-crystalline polymers is provided next.

1.2.1 Computational Homogenization

The design, modeling, and optimization of advanced materials with tailored functionalities often yield nonlinear heterogeneous systems with complex microstructures. Within these intricate architectures, microscale mechanisms, such as phase transformations, plastic slip, damage, and interfacial debonding, interact in ways that decisively shape the macroscopic response. Despite decades of research, capturing the interplay between these internal mechanisms and effective material behavior remains a central and enduring challenge in the mechanics of materials community.

In settings where the continuum assumption holds, single-scale phenomenological constitutive models have traditionally served as the primary modeling approach, typically grounded in thermodynamics with internal variables (Maugin, 1999; de Souza Neto et al., 2008). These models, while effective for many applications, often fall short in accurately capturing the material's effective response due to the complex microstructural interactions that govern it. Alternatively, full-field direct numerical simulations, based on finite element (FE), fast Fourier transform (FFT), or boundary element methods, provide high-fidelity predictions by solving detailed boundary-value problems at the microscale. However, their applicability is severely constrained by the high computational demands and the difficulty of obtaining statistically representative microstructural data (Ortolano et al., 2013). Aiming to balance accuracy with computational feasibility, multiscale modeling techniques have thus emerged as a compelling middle ground. In particular, computational homogenization-based methods account for the material's response at different scales by solving nested boundary-value problems at each scale. Several modeling strategies that fall under the computational homogenization umbrella have been proposed in the literature. They span from the so-called FE^2 method based on the finite element method (Feyel, 1998; Feyel and Chaboche, 2000; Feyel, 2003), to asymptotic

homogenization (Sanchez-Palencia, 1974; Papanicolau et al., 1978; Guedes and Kikuchi, 1990), transformation field analysis (Aboudi, 1989; Paley and Aboudi, 1992; Dvorak, 1992), and fast Fourier transform methods (Moulinec and Suquet, 1998; Eyre and Milton, 1999; Michel et al., 2000).

The oldest of these methods is perhaps Mean-Field Homogenization (MFH). This approach bypasses the need for full microstructural spatial discretization while retaining essential features such as phase distribution, morphology, and volume fraction. What sets these methods apart is the simplified way they handle the interaction between different material phases by solving single-inclusion problems for simple geometries, such as simple laminates (Milton, 2004) or ellipsoidal inclusions (Eshelby, 1957).

Among the different interaction laws in the literature, we find the classical models by Voigt (1889) and Taylor (1938), as well as those by Sachs (1928) and Reuss (1929) based on uniform strain and stress assumptions, respectively, that provide upper and lower bounds on the effective properties. The dilute inclusion (Nemat-Nasser and Hori, 1993), Mori–Tanaka (Mori and Tanaka, 1973; Benveniste, 1987; Luo and Weng, 1987) and self-consistent methods (Kröner, 1958; Hill, 1965b; Walpole, 1969; Willis, 1977) are yet another set of approaches that offer more accurate estimates by considering interaction effects more rigorously. These are further refined in the generalized self-consistent method (Kerner, 1956; Christensen and Lo, 1979; Huang et al., 1994), the differential method (McLaughlin, 1977; Norris, 1985), and the double-inclusion model by Hori and Nemat-Nasser (1998). Over time, these techniques have been extended to tackle finite-strain nonlinearity (Ogden, 1974; Hill, 1997), polycrystalline aggregates (Hutchinson and Hill, 1997), and multiphysics problems such as thermomechanics and electromagnetism (Willis, 1986; Ponte Castañeda et al., 1997). A detailed overview is provided by Matouš et al. (2017).

Among computational homogenization methods, mean-field homogenization is one of the most computationally efficient and has the least stringent spatial discretization requirements. It displays acceptable performance in terms of macroscopic response accuracy, the inclusion of complex geometries, and nonlinear behavior. The limitations of such approaches include their inability to predict strain or stress distributions within the microgeometry accurately and to recover effects such as clustering, percolation, and size effects (Ortolano et al., 2013).

While computational homogenization methods, such as those discussed so far, can be formulated within various frameworks, the Method of Multiscale Virtual Power (MMVP), introduced by Blanco et al. (2016b), provides a variational and physically consistent foundation for multiscale modeling. Based on the Principle of Kinematical Admissibility (PKA), the Hypothesis of Multiscale Duality, and the Principle of Multiscale Virtual Power (PMVP), it generalizes the Hill–Mandel condition by requiring energetic consistency for all admissible virtual variations in a multiscale sense. This set of principles ensures a unified, systematic approach to multiscale modeling, grounded in sound physical principles, with clearly identified assumptions and downstream implications. The robustness of MMVP has been demonstrated across a broad spectrum of applications, including dynamic problems with inertia (de Souza Neto et al., 2015; Roca et al., 2019), FE^2 implementations (Tamsen and Balzani, 2021), fiber networks (Rocha et al., 2018), higher-order continua (Blanco et al., 2016a; Otero et al., 2018; Rodrigues Lopes and Andrade Pires, 2022), composite materials (Dalbosco et al., 2021), and porous media (Blanco et al., 2023; dos Santos et al., 2023, 2024). Its application to cohesive fracture (Toro et al., 2016b,a; Vieira de Carvalho et al., 2023), thermomechanics (Blanco and Giusti, 2014), poromechanics (Anonis et al., 2024; Thiesen et al., 2025), phase-field modeling (Storm et al., 2020, 2022), and fluid–structure interaction (Blanco et al., 2017; Shakoor and Park, 2023), along with its integration into advanced numerical methods like isogeometric analysis (Alberdi et al., 2018), underscores MMVP's potential as a general-purpose multiscale modeling tool.

1.2.2 Semi-crystalline polymers

According to a market study by Precedence Research (2022), the polymer market size in 2021 was 713 billion dollars, and is projected to reach 1078.5 billion by 2030. By type, the thermoplastics segment accounted for a 43% market share in 2021. Most semi-crystalline polymers are designated as thermoplastics, as they most often have linear structures and soften/harden when heated/cooled. Thermoplastics dominate the market due to their reduced production costs, energy efficiency, ability to replace metals with considerable weight savings, and ability to be produced in extremely high volumes with high precision at low cost.

By material, the polyethylene (PE) segment, a semi-crystalline polymer, captured a significant market share in 2021 and is growing. It is widely sought after for packaging items, tubing products, connections, bottles, and plastic surgery implants. Increased consumer spending and industrial operations across various industries, including the automobile, building, and packaging sectors, are the main drivers of this increase. Another widely used semi-crystalline polymer is polytetrafluoroethylene (PTFE), employed in many medical and industrial device applications, in particular, in rotary shaft seals, due to its tribological characteristics, chemical inertness and temperature stability (Kletschkowski et al., 2002). Polyamides (PA) are widely used materials due to their low cost, low density (approximately 12.5% the weight of bronze, 14.3% the weight of cast iron, and 50% the weight of aluminum), corrosion resistance, insulation qualities, and good load-bearing capacity. They are frequently used as a replacement for bronze, brass, aluminum and other metals (Khan and Farrokh, 2006). PA6 is used in conjunction with PE in polymer films for food packaging, due to its good mechanical strength and impermeability to gas (Zeng et al., 2010). Polyether ether ketone (PEEK) is yet another semi-crystalline polymer, which finds use in a variety of structural and insulation applications (Rae et al., 2007). Moreover, due to its excellent mechanical properties, PEEK is commonly used in seals and bearings, and, more recently, also in medical implants (e.g., spinal implants, screws, woven textiles) (Bergström, 2015), due to its biocompatibility, weight reduction, radiology advantage and 3D printing properties (Garcia-Gonzalez et al., 2015). Its exceptionally high melting temperature also makes it a good candidate for extreme service conditions (G'sell and Dahoun, 1994).

Semi-crystalline polymer structure

The majority of polymeric materials are made up of extremely long molecule chains with side groups composed of different elements, such as O, F, or Cl, or organic groups, like methyl, ethyl, or phenyl groups. These macromolecules comprise repeat units, which are smaller structural elements replicated along the chain. In turn, the polymer structure can range from a completely amorphous polymer, where the macromolecules are arranged randomly, to a highly crystalline polymer, where most polymer chains are tightly packed into a crystalline structure. In between, one finds semi-crystalline polymers where crystalline and amorphous zones coexist in a variety of complex and hierarchical heterogeneous morphologies that depend on the processing history, as well as mechanical and thermal histories, in addition to the polymer chemistry and conformation (Ward and Sweeney, 2004; Callister and Rethwisch, 2014).

Microstructure At the microscopic level, semi-crystalline polymers consist of at least two different phases: a crystalline phase and an amorphous phase (Khoury and Passaglia, 1976). The crystalline portion of a semi-crystalline polymer is formed by the constituent chains packing parallel to one another into lamellae in an orderly fashion, as shown in Figure 1.1.

There are at least two types of crystal lamellae found in semi-crystalline polymers, as detailed in Anderson (1964) for polyethylene (PE): the chain-folded lamellae and

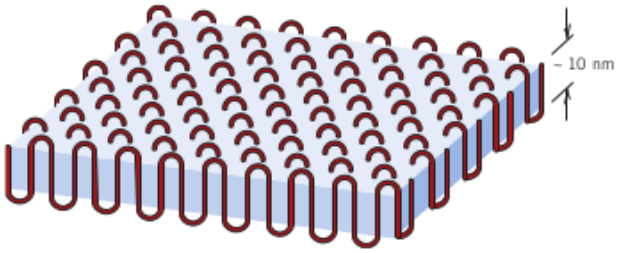

Figure 1.1: Arrangement of polymer chains into a lamella in the crystalline phase of a semi-crystalline polymer (Callister and Rethwisch, 2014).

extended-chain lamellae. In the former, the molecular chains within each platelet fold back and forth on themselves, with folds occurring at the faces. This picture is, in fact, an idealization, with reality more closely resembling a switchboard model, with the chains reentering through loose folds at non-adjacent sites or even forming tie-chains with neighboring lamellae (G'sell and Dahoun, 1994). The latter are more common at lower molecular weights, with the chains organized into lamellae in their extended conformation. The thickness of the lamellae in semi-crystalline polymers is of the order of nanometers, e.g., 10 nm to 15 nm for PE samples (Argon, 2013).

The crystalline structure depends on the particular polymer. PE often possesses orthorhombic symmetry, where the chain direction forms an angle with the normal vector to the crystalline lamella ranging between 17° and 40° (Nikolov and Doghri, 2000). On the other hand, the crystal structure found in polytetrafluoroethylene (PTFE) at temperatures above 19 °C is hexagonal, with individual molecules arranged in helical conformations (Bergström, 2015).

The crystallinity of a semi-crystalline polymer can be specified by the degree of crystallinity. It may range from completely amorphous to almost entirely crystalline. Ward and Sweeney (2004) mention values from 90% for polyethylene (PE) to about 30% for oriented poly(ethylene terephthalate) (PET). Commercially available semi-crystalline polymers range from 10% to 90% in the degree of crystallinity (van Dommelen et al., 2003). The degree of crystallinity by weight may be determined from accurate density measurements according to

$$\chi = \%\ \text{crystallinity} = \frac{\left(\rho_s - \rho_a\right)/\rho_s}{\left(\rho_c - \rho_a\right)/\rho_c} \times 100 \tag{1.1}$$

where ρ_s is the density of a specimen for which the percent crystallinity is to be determined, ρ_a is the density of the completely amorphous polymer, and ρ_c is the density of the perfect polymer crystallite. In addition to this method based on density, other experimental techniques employed to determine the crystallinity along with the lamellar thickness of the polymer crystallites include wide-angle (WAXS) and small-angle (SAXS) X-ray scattering (Schrauwen et al., 2004; Hobeika et al., 2000), differential scanning calorimetry (DSC) (Ayoub et al., 2011), and electron microscopy, e.g., transmission electron microscopy (TEM) (Bartczak et al., 1992).

The main parameters influencing the degree of crystallinity are the molecular structure, the molecular weight, the presence of plasticizers, and especially the thermomechanical history of the polymer (Khoury and Passaglia, 1976; Cangemi and Meimon, 2001). Because of the way polymer crystals form, polymer chains must have a linear structure; the more branches/pendant side groups, the lower the degree of crystallinity. However, even linear polymers must have sufficient regularity to crystallize (Khoury and Passaglia, 1976). A high molecular weight tends to suppress a high degree of crystallinity (Hoffman et al., 2007), as seen

when comparing high-density polyethylene (HDPE) and ultra-high molecular weight polyethylene (UHMWPE) (Brown et al., 2007). Since crystallization is a kinetic process, the crystallized fraction is a function of time, with the crystallization rate in polymers depending on the temperature difference relative to the melting temperature and the glass transition temperature (Callister and Rethwisch, 2014). As detailed later in this chapter, the mechanical loading of a polymer may also induce changes in crystallinity, e.g., through the phenomenon of strain-induced crystallization (Rao and Rajagopal, 2001). Accordingly, the most frequent approach to achieve different degrees of crystallinity is through the control of crystallization temperatures and crystallization times, be it when crystallizing from the melt or through annealing treatments (Fakirov and Krasteva, 2000; Schrauwen et al., 2004). However, preparing samples with different degrees of crystallinity is challenging for polymers such as HDPE since their crystallization rate is very high. It is possible to control the degree of crystallinity by taking PE samples differing in the degree of branching and introducing various amounts of defects in the main chain (Fakirov and Krasteva, 2000).

In what pertains to the amorphous portion of a semi-crystalline polymer, results reported by Zia et al. (2008) on isotactic polypropylene (iPP) point to the existence of two different amorphous phases—a mobile amorphous phase and a rigid amorphous phase—based on different glass transition temperatures. The results of Jolly (2000) concerning polyamide 11 (PA11), which were found employing WAXS at different axial deformation rates, also support the existence of a phase that is neither wholly amorphous nor wholly crystalline. According to Mandelkern (2006), the existence of a rigid amorphous phase is supported by experimental results obtained from density measurements, wide- and small-angle X-ray diffraction, thermal analyses, Raman spectroscopy, small-angle neutron scattering, dielectric relaxation and nuclear magnetic resonance involving different nuclei and techniques.

The reason for the increased rigidity in this part of the amorphous phase is the presence of polymer crystallites, which hinder the molecular mobility of the amorphous phase (Zia et al., 2008; Peacock, 2014). However, an increase in the degree of crystallinity will decrease the rigid amorphous fraction and the ratio between the rigid and mobile amorphous phases. This behavior is due to reduced covalent coupling between the polymer crystals and the amorphous phase in highly crystalline preparations (Zia et al., 2008). Furthermore, the presence of the crystallites also affects the properties of the mobile amorphous fraction, which is detected by a distinct decrease in its glass transition temperature, as shown for semi-crystalline iPP by Zia et al. (2008).

Mesostructure Depending on the processing, thermal, and mechanical history, as well as its degree of crystallinity, molecular weight, and polydispersity, a semi-crystalline polymer can display different mesoscopic structures (Cangemi and Meimon, 2001; Mandelkern, 2006). When the polymer crystallizes from a dilute solution, the structure is often lamellar and composed of multiple layers if the solution is quiescent, and of the shish-kebab variety[1] if the solution is subject to high shear (Khoury and Passaglia, 1976; Callister and Rethwisch, 2014; Peacock, 2014). When the polymer crystallizes from the melt, the two most commonly reported types of mesoscopic structures for semi-crystalline polymers are the spherulitic structure (Zeng et al., 2010) (see Figure 1.2(a)), obtained from quiescent crystallization, and the shish-kebab structure, obtained from crystallization under shear stress (Peacock, 2014) (see Figure 1.2(b)).

The spherulitic structure is composed of spherulites, aggregates of ribbon-like chain-folded crystallites that radiate outward from a single nucleation site in the center, their diameter approximately 10 µm and their lamellae approximately 10 to 20 nm thick for PE, and 2 to 6 nm

[1] The so-called shish-kebab structure consists of a long central fiber core (shish) surrounded by a lamellar crystalline structure (kebab) periodically attached along the shish (Na et al., 2006; Peacock, 2014).

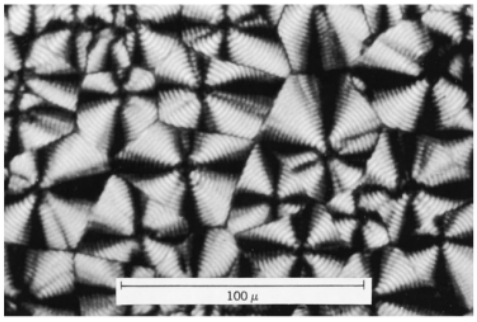

(a)

(b)

Figure 1.2: Mesostructures of polyethylene. (a) Transmission photomicrograph (using cross-polarized light) of a spherulitic structure (Callister and Rethwisch, 2014). (b) Electron micrograph of shish-kebab structure (Peacock, 2014).

for polyether ether ketone (PEEK), for example. Between them, there are amorphous regions, crossed by tie-chain molecules that act as connecting links between adjacent lamellae (Callister and Rethwisch, 2014; Khoury and Passaglia, 1976; Pouriayevali et al., 2013; G'sell and Dahoun, 1994). The lamellae are generally twisted about their long axis (Patlazhan and Remond, 2012). A sheave-like structure is also possible under suitable conditions (Peacock, 2014). Mandelkern (2006) warns, however, that spherulites, and other types of supermolecular structures, are not universally observed in homopolymers.

Mechanical loading will also lead to changes in the mesoscopic structure of the polymer. In higher crystallinity polymers such as HDPE, mechanical loading usually destroys the crystallites of the original morphology, followed by reordering to form new crystallites. The new lamellar morphology has a lamellar thickness independent of the original lamellar thickness, solely dependent upon the temperature at which the deformation occurred. In such morphologies, the unit cell axes are preferentially aligned in the stress direction, while the lateral planes of the lamellae lie approximately normal to the aligning force. These newly formed crystallites are themselves subject to disruption at higher deformation levels (draw ratios of approximately 10), being replaced by a fibrillar morphology, which consists of oriented crystallites arranged hierarchically into needle-like structures of various sizes. These macrofibrils are composed of microfibrils, in turn, made up of nanofibrils, stacks of crystallites separated by thin noncrystalline 'plates,' portions of which are spanned by 'intercrystalline bridges' (Peacock, 2014). A nearly perfect alignment of the crystallized chains along the fiber axis and the parallel arrangement of the crystal lamellae relative to the same axis define the final fiber structure (Peterlin, 1971). Moreover, plastically deformed HDPE develops three important types of texture, resembling that of a large quasi-single crystal (Argon, 2013):

1. crystallographic texture due to preferential orientation of crystallographic axes in the crystalline lamellae;

2. morphological texture due to preferential orientation of the normals to the broad faces of the crystalline lamellae;

3. macromolecular texture in the amorphous component, which is promoted by the alignment of molecules in the direction of maximum stretch.

For materials such as PET, in which the crystalline and amorphous components are intermixed, the most noticeable effect may be strain-induced crystallization due to

macromolecular texture, as described earlier (Ward and Sweeney, 2004). More specifically, temperatures above the glass transition temperature, a linear structure, and large deformations increase the crystallinity of the material (Ahzi et al., 2003). The crystalline structures produced in this way are oriented, which results in an anisotropic mechanical response. Experiments on polymer film also point to crystallization at lower strain when the strain rate is higher (Rao and Rajagopal, 2001). Most plastic products are manufactured by deforming the material at elevated temperatures to get it into the desired shape. Examples of these operations include film blowing, fiber spinning, and injection molding. In many of these applications, the formation of a highly oriented crystalline phase has a beneficial impact on the mechanical behavior of the material (Dairanieh et al., 1999; Rao and Rajagopal, 2001). Hence, most PET articles are manufactured this way (Boyce et al., 2000; Rao and Rajagopal, 2001; Makradi et al., 2005).

1.3 Contributions

Given the outline presented in the previous sections, this work aims to contribute to the development of computational tools for the multiscale modeling of heterogeneous materials, with a particular focus on semi-crystalline polymers. The main contributions of this work fall into two categories: (i) the formulation of variationally consistent mean-field homogenization models within the PMVP and its dual, and (ii) the review of constitutive models for semi-crystalline polymers and the formulation of new models based on the derived MFH models. These contributions are detailed in the following subsections.

1.3.1 Variationally consistent mean-field homogenization models

In this work, we present MFH in a rigorous and unified variational framework by embedding it within the PMVP and its dual, the Principle of Multiscale Complementary Virtual Power (PMCVP). The explicit consideration of kinematically admissible displacement fields for each material phase as a basis for the PMVP allows for the derivation of an alternative macroscopic stress-homogenization rule. In contrast to classical volume-averaging approaches, this rule does not reduce to a simple average of phase fields and, for elastic materials, ensures mechanical power equivalence across scales. Moreover, the models derived using this framework are guaranteed to satisfy angular momentum balance. The PMCVP provides a complementary variational formulation based on statically admissible stress fields, thereby extending the framework to stress-driven settings. Together, the PMVP and PMCVP enable the derivation of two hierarchies of nested models by systematically relaxing kinematic and static constraints. Based on kinematic constraints, we recover the classical strain-driven MFH model, a projected variant similar to the $\tilde{\boldsymbol{S}}$-inclusion model proposed by Lee et al. (1993b,a), and the Sachs model, which arises under minimal kinematic assumptions. From static constraints, we obtain the classical stress-driven MFH formulation, a projected variant linked to the $\tilde{\boldsymbol{D}}$-inclusion model also proposed by Lee et al. (1993b,a), and the Taylor model, associated with the least restrictive assumptions on stress potential fields. These formulations reinterpret and unify established mean-field models within a consistent variational framework, yielding generalized homogenization rules and providing a robust theoretical foundation for multiscale modeling of heterogeneous materials. The main contributions of this work on this theme can be summarized as follows:

- A systematic variational formulation of mean-field homogenization is established within the PMVP framework, encompassing a rigorous definition of admissible displacement fields, the construction of a nested model hierarchy, and the derivation of a generalized macroscopic stress-homogenization rule.

- The PMCVP is proposed as the dual counterpart to the PMVP, providing a variational foundation for treating statically admissible stress fields. This dual principle is yet to be explored in the literature to the best of the author's knowledge.
- The variational formulation of MFH models is pursued within the PMCVP setting through the appropriate definition of the admissible stress fields, yielding a hierarchy of stress-driven models and corresponding homogenization rules for the macroscopic deformation gradient.
- Numerical examples are provided to illustrate the predictions obtained with the derived MFH models, exploring their consistency regarding energetic equivalence and angular momentum conservation, employing constitutive models, ranging from hyperelasticity to plasticity, to describe the behavior of each material phase.

The contributions above are detailed in the following publication:

- Vila-Chã, José L. P., António M. Couto Carneiro, Bernardo P. Ferreira, and F. M. Andrade Pires. 2026. "Unifying mean-field models through the method of multiscale virtual power and its dual formulation." *Journal of the Mechanics and Physics of Solids* 215: 106724. `https://doi.org/10.1016/j.jmps.2026.106724`.

1.3.2 Constitutive modeling of semi-crystalline polymers

Despite the vast number of constitutive models available in the literature for semi-crystalline polymers, most of these models face significant challenges. Within this setting, some models

- fail to account for the full range of phenomena that are characteristic of polymer behavior,
- involve a large number of material parameters whose identification is not straightforward,
- pose difficulties in numerical implementation, and
- may have limitations in their range of applicability.

These constraints highlight the need for a comprehensive understanding of the various modeling techniques and their respective trade-offs.

This work aims to provide a thorough overview of the different modeling approaches and tools available to predict the thermomechanical behavior of thermoplastic polymers. It includes an in-depth analysis of the main phenomenological constitutive models for thermoplastics, in particular, semi-crystalline polymers, with a special focus on how the experimental evidence motivates the progression from thermoviscoelasticity to nonlinear thermoviscoplasticity. These models are also relevant in the context of mean-field homogenization, as they are employed to describe the behavior of each material phase in a semi-crystalline polymer. A theoretical outline for specializing the variationally consistent MFH models derived using the PMVP and PMCVP frameworks to the semi-crystalline polymer case, based on the modeling choices of Lee et al. (1993a,b), is also provided; a full numerical realization of this specialization was not pursued in the present work and is left as future work.

The contributions above are detailed in the following publication:

- Vila-Chã, José L. P., Francisca Carvalho Alves, Mohsen Mirkhalaf, and F. M. Andrade Pires. 2026. "A Comprehensive Review of Continuum Constitutive Models for

Thermoplastic Polymers." Preprint. engrXiv. https://doi.org/10.31224/6674.

1.3.3 Other contributions

In addition to the contributions detailed above, some of the research conducted by the author during the PhD program has been directed toward the development and assessment of numerical techniques for solving coupled thermomechanical problems. These efforts are not directly related to the work described in this thesis but are briefly summarized in the following paragraphs for completeness.

Having achieved an appropriate formulation of the thermomechanical problem, the FEM can be used to solve it. After spatial and temporal discretization, the thermomechanical problem is reduced to a system of coupled nonlinear algebraic equations on the mechanical variables (displacement) and thermal variables (temperatures). Generally speaking, the strategies typically employed to solve this problem can be classified into monolithic and partitioned approaches. The latter can be further divided into explicit (loosely or weakly coupled) and implicit (strongly coupled) schemes, depending on the type of coupling enforcement. The most common approach in the literature when employing implicit coupled partitioned schemes is to regard the problem as a fixed-point procedure, where acceleration may be employed for improved stability and efficiency. In the work developed by the author, the problem is regarded as a suitable nonlinear system of equations. This system is built using the single-field solvers, and its solution coincides with the solution to the discretized balance of momentum and energy equations. This minor change in perspective allows a more straightforward application of the diverse solution methods for systems of nonlinear equations such as the multisecant quasi-Newton methods, the Newton–Krylov methods, or the polynomial vector extrapolation techniques in cycling mode. These techniques are employed to solve three different problems, including thermoelastic and thermoplastic constitutive behaviors, as well as contact.

The contributions above are detailed in the following publication:

- Vila-Chã, José L.P., António M. Couto Carneiro, Bernardo P. Ferreira, and F.M. Andrade Pires. 2023. "A Numerical Assessment of Partitioned Implicit Methods for Thermomechanical Problems." *Computers & Structures* 277–278 (March): 106969. https://doi.org/10.1016/j.compstruc.2022.106969.

1.4 Computational framework

All the numerical simulations presented in this work were performed using a piece of software developed by the author in the context of his PhD program, housed at the Computational Multi-Scale Modeling of Solids and Structures (CM2S) (Figure 1.3) research group, at the Department of Mechanical Engineering, Faculty of Engineering of the University of Porto (FEUP). This software is written in the `Python` programming language, making extensive use of the `PyTorch` library for tensor operations and automatic differentiation, as well as the `NumPy` and `SciPy` libraries for numerical computing.

Figure 1.3: Logo of the Computational Multi-Scale Modeling of Solids and Structures (CM2S) research group.

1.5 Document structure

This section outlines the structure of this thesis, providing a brief description of each chapter's content. The chapters may be grouped into two main parts: Chapters 3 to 7 focus on the development of variationally consistent mean-field homogenization models, while Chapters 8 and 9 are dedicated to the constitutive modeling of semi-crystalline polymers. Finally, Chapter 10 summarizes the main conclusions and suggests directions for future research. Appendix A contains supplementary material on infinitesimal thermoviscoelasticity, while Appendices B to D contain additional derivations supporting the main text.

Chapter 2 - Thermomechanical problem
This chapter covers the concepts required to describe how a solid responds to thermal and mechanical loads under large deformations, including the conservation laws that guarantee mechanical equilibrium and energy conservation. Additionally, the application of thermodynamics with internal variables is discussed, along with the resulting inferences about the constitutive behavior of the solid material. Special attention is given to the stress-driven formulation of the thermomechanical and constitutive problems, which is less commonly found in the literature.

Chapter 3 - Principle of Multiscale Virtual Power and Principle of Multiscale Complementary Virtual Power

This chapter introduces the Principle of Multiscale Virtual Power (PMVP) and its dual, the Principle of Multiscale Complementary Virtual Power (PMCVP). These principles provide a variational framework for multiscale modeling, ensuring energetic consistency across scales. The PMVP is formulated based on kinematically admissible displacement fields, while the PMCVP is based on statically admissible stress fields. Together, they enable the systematic derivation of multiscale models that respect fundamental physical principles, such as balance of momentum and energy conservation.

Chapter 4 - Mean-field homogenization

This chapter presents the method of mean-field homogenization (MFH), a widely used technique for estimating the effective properties of heterogeneous materials. The single-inclusion problem is highlighted, as well as the interaction models employed to account

for the influence of materials on each other. The standard homogenization rules most often employed in the literature are also described.

Chapter 5 - Variationally consistent mean-field models

This chapter details the derivation of MFH models within the PMVP and PMCVP frameworks. Appropriate minimal kinematic and static constraints compatible with MFH are adopted to define admissible displacement and stress fields. Two hierarchies of nested models are then derived, as these constraints are systematically tightened. The classical Taylor and Sachs models are recovered as the most extreme cases in each hierarchy, along with projected variants similar to the $\tilde{\boldsymbol{S}}$-inclusion and $\tilde{\boldsymbol{D}}$-inclusion models proposed by Lee et al. (1993b,a).

Chapter 6 - Computational implementation

This chapter discusses the computational implementation of the variationally consistent mean-field models derived in Chapter 5. The inversion of the Piola–Kirchhoff stress-strain relations required by the models is addressed, along with the numerical algorithms employed to solve the resulting multiscale problems.

Chapter 7 - Numerical examples

Several numerical examples are presented to illustrate the performance and capabilities of the proposed models in predicting the behavior of heterogeneous materials.

Chapter 8 - Thermomechanical behavior of semi-crystalline polymers
This chapter outlines the thermomechanical response of semi-crystalline polymers. An account of their deformation mechanisms, experimental results of various mechanical experiments, and an appropriate discussion regarding their dependency on factors such as temperature, strain rate, or pressure are included. This chapter also contains the results of thermal analysis techniques, such as differential scanning calorimetry. An effort is made to provide relevant literature references where the experimental results can be found.

Chapter 9 - State of the art in thermomechanical semi-crystalline polymer modeling
The main goal of this chapter is to report on the state of the art in semi-crystalline polymer modeling. The departure point is infinitesimal thermoviscoelasticity. Nonlinear generalizations are considered by specifying nonlinear laws for the elastic and viscous elements in rheological models originating from infinitesimal viscoelasticity. These are the most commonly available models in the literature, and a detailed overview is provided in this chapter. Following that is a description of models that distinguish between the crystalline and amorphous phases while only considering bulk crystallinity and no additional geometrical information. Finally, multiscale models with micro- and mesostructure considerations are described.

Chapter 10 - Conclusion and Future Work

The final chapter summarizes the main conclusions drawn from the research presented in this thesis. It also outlines potential directions for future research, building upon the tools developed throughout the work.

Chapter 2

Continuum thermomechanics

This chapter presents a brief overview of the fundamental concepts and governing equations of continuum thermomechanics, which form the basis for the development of constitutive models for materials undergoing mechanical and thermal loads. Based on the works of Marsden and Hughes (1982), Holzapfel (2000) and de Souza Neto et al. (2008), it begins with the kinematics of finite deformation in Section 2.1 and proceeds to the strong forms of the balance laws and the associated entropy-production inequality in Section 2.3. Section 2.4 then develops the thermodynamically consistent constitutive framework in two complementary forms—the strain-driven Helmholtz formulation and the stress-driven Gibbs formulation of Section 2.4.1, while Sections 2.5.1, 2.6.2 and 2.6.3 close the chapter with the incremental form of the constitutive initial-value problem and the weak-form statements of the deformation- and stress-driven initial boundary-value problems.

2.1 Kinematics of deformation

Let a deformable body $\mathscr{B}$ occupy a simply connected open region Ω_0 of the tridimensional Euclidean space $\mathscr{E}$ with a regular boundary $\partial\Omega_0$ in its reference configuration. A smooth one-to-one function defines its motion $\boldsymbol{\varphi}\colon \Omega \times \mathbb{R} \to \mathscr{E}$, mapping each material particle of coordinates $\boldsymbol{X}$ in the reference configuration to its position $\boldsymbol{x}$ in the deformed configuration at time t. Accordingly, the displacement is defined as $\boldsymbol{u} \equiv \varphi(\boldsymbol{X}) - \boldsymbol{X} = \boldsymbol{x} - \boldsymbol{X}$, and the well-known deformation gradient is a second-order tensor defined as

$$\boldsymbol{F}(\boldsymbol{X}, t) \equiv \nabla_0 \boldsymbol{\varphi}(\boldsymbol{X}, t) = \nabla_0 \boldsymbol{u}(\boldsymbol{X}, t) + \boldsymbol{I}, \tag{2.1}$$

and its determinant, denoted as $J \equiv \det \boldsymbol{F} > 0$, represents the local unit volume change, where ∇_0 is the gradient operator with respect to the material coordinates $\boldsymbol{X}$.

The polar decomposition theorem yields two unique multiplicative decompositions of the deformation gradient as

$$\boldsymbol{F} = \boldsymbol{R}\boldsymbol{U} = \boldsymbol{V}\boldsymbol{R}, \tag{2.2}$$

where $\boldsymbol{R}$ is a proper orthogonal tensor representing a rigid body rotation, $\boldsymbol{U}$ is the right stretch tensor, and $\boldsymbol{V}$ is the left stretch tensor, the unique symmetric and positive definite square roots of the right and left Cauchy-Green deformation tensors, defined as

$$\boldsymbol{C} \equiv \boldsymbol{F}^T\boldsymbol{F} = \boldsymbol{U}^2, \quad \boldsymbol{B} \equiv \boldsymbol{F}\boldsymbol{F}^T = \boldsymbol{V}^2, \tag{2.3}$$

respectively. The principal stretches λ_i $(i = 1,2,3)$ are defined as the eigenvalues of both the right and left stretch tensors. A commonly used family of strain measures is the Seth-Hill family

of generalized strain tensors, defined as

$$\boldsymbol{E}^{(m)} \equiv \begin{cases} \frac{1}{2m}(\boldsymbol{C}^m - \boldsymbol{I}), & m \neq 0, \\ \frac{1}{2}\ln \boldsymbol{C}, & m = 0, \end{cases} \tag{2.4}$$

where m is a real number and $\boldsymbol{I}$ is the second-order identity tensor. The infinitesimal strain tensor $\boldsymbol{\varepsilon}$ is recovered as the first order approximation of $\boldsymbol{E}^{(m)}$, valid for small deformations,

$$\boldsymbol{\varepsilon} \equiv \frac{1}{2}(\nabla_0 \boldsymbol{u} + \nabla_0 \boldsymbol{u}^T). \tag{2.5}$$

Isochoric and volumetric versions of these strain measures are also commonly used in the modeling of incompressible or nearly incompressible materials, such as polymers, through a multiplicative decomposition of the deformation gradient into volumetric and isochoric parts as

$$\boldsymbol{F} = J^{1/3}\boldsymbol{F}_{\text{iso}}, \tag{2.6}$$

where $\boldsymbol{F}_{\text{iso}} \equiv J^{-1/3}\boldsymbol{F}$ is the isochoric part of the deformation gradient, satisfying $\det \boldsymbol{F}_{\text{iso}} = 1$.

Also relevant to the present work is the spatial velocity gradient

$$\boldsymbol{L} \equiv \dot{\boldsymbol{F}}\boldsymbol{F}^{-1}, \tag{2.7}$$

where $\dot{\boldsymbol{F}}$ denotes the time derivative of the deformation gradient. This tensor can be additively decomposed into its symmetric and skew-symmetric parts as

$$\boldsymbol{L} = \boldsymbol{D} + \boldsymbol{W}, \tag{2.8}$$

where $\boldsymbol{D} \equiv \frac{1}{2}(\boldsymbol{L} + \boldsymbol{L}^T)$ is the rate of deformation tensor and $\boldsymbol{W} \equiv \frac{1}{2}(\boldsymbol{L} - \boldsymbol{L}^T)$ is the spin tensor.

2.2 Stress measures

In continuum mechanics, several stress measures are used to describe the internal forces within a deformable body. The Cauchy stress tensor $\boldsymbol{\sigma}$ is the most commonly used stress measure, relating forces and areas in the current configuration, i.e.,

$$\boldsymbol{t} = \boldsymbol{\sigma}\boldsymbol{n}, \tag{2.9}$$

where $\boldsymbol{t}$ is the traction vector acting on a surface with normal vector $\boldsymbol{n}$ in the current configuration at some point $\boldsymbol{x} \in \partial\Omega$. However, for large deformations, it is often more convenient to use stress measures defined in the reference configuration. The first Piola-Kirchhoff stress tensor $\boldsymbol{P}$ relates forces in the current configuration to areas in the reference configuration, i.e.,

$$\boldsymbol{t}_0 = \boldsymbol{P}\boldsymbol{N}, \tag{2.10}$$

where $\boldsymbol{t}_0$ is the traction vector acting on a surface with normal vector $\boldsymbol{N}$ in the reference configuration at some point $\boldsymbol{X} \in \partial\Omega_0$, while the second Piola-Kirchhoff stress tensor $\boldsymbol{S}$ relates forces and areas both in the reference configuration. These stress measures are related through

$$\boldsymbol{P} = J\boldsymbol{\sigma}\boldsymbol{F}^{-T}, \quad \boldsymbol{S} = \boldsymbol{F}^{-1}\boldsymbol{P}. \tag{2.11}$$

Other stress measures include the Kirchhoff stress tensor $\boldsymbol{\tau} = J\boldsymbol{\sigma}$ and the Mandel stress tensor $\boldsymbol{M} = J\boldsymbol{F}^T\boldsymbol{\sigma}\boldsymbol{F}^{-T}$. We also introduce the generally non-symmetric Biot stress tensor,

$$\boldsymbol{T}_B = \boldsymbol{R}^T\boldsymbol{P}, \tag{2.12}$$

as yet another stress measure useful in finite deformation mechanics.

Each stress measure is paired with a specific strain measure, defining the work-conjugate pairs used in constitutive modeling. In effect, the mechanical power per unit reference volume can be expressed equivalently in terms of any of these stress–strain pairs as

$$\boldsymbol{P} : \dot{\boldsymbol{F}} = J(\boldsymbol{\sigma} : \boldsymbol{D}) = \operatorname{sym} \boldsymbol{T}_B : \dot{\boldsymbol{U}} = \boldsymbol{S} : \dot{\boldsymbol{E}}^{(1)} = \boldsymbol{\tau} : \boldsymbol{D} = (\boldsymbol{R}^T \boldsymbol{\tau} \boldsymbol{R}) : \dot{\boldsymbol{\varepsilon}}^{(0)} = \boldsymbol{M} : \dot{\boldsymbol{E}}^{(0)}, \tag{2.13}$$

where the colon operator $(\bullet) : (\bullet) \equiv \operatorname{tr}\left((\bullet)(\bullet)^T\right)$ denotes the double contraction between two second-order tensors, and $\boldsymbol{\varepsilon}^{(0)} \equiv \ln \boldsymbol{V}$ is the logarithmic or Hencky strain tensor.

When modeling constitutive behavior, it is common to consider the deviatoric and volumetric components of the stress tensors separately. The deviatoric part of a second-order tensor $\boldsymbol{A}$ is defined as

$$\boldsymbol{A}_{\text{dev}} \equiv \boldsymbol{A} - A_m \boldsymbol{I}, \tag{2.14}$$

where $A_m = \operatorname{tr} \boldsymbol{A}/3$ is the mean normal component and $\operatorname{tr}(\bullet)$ denotes the trace operator. p is the hydrostatic pressure, defined as $p \equiv -\sigma_m$.

2.3 Fundamental conservation principles

In continuum thermomechanics, there is a set of conservation principles and thermodynamic laws that, irrespective of the quantities used to describe the mechanical behavior of a body undergoing large deformations, must always be satisfied. These principles include the balance of momentum, the balance of moment of momentum, the balance of energy, and the entropy production inequality. When expressed in the material configuration and in their strong form, these principles are written as

$$\operatorname{div}_0 \boldsymbol{P} + \boldsymbol{b}_0 = \rho_0 \ddot{\boldsymbol{u}}, \quad \text{(balance of momentum)}; \tag{2.15}$$

$$\boldsymbol{P}\boldsymbol{F}^T = (\boldsymbol{P}\boldsymbol{F}^T)^T, \quad \text{(balance of moment of momentum)}; \tag{2.16}$$

$$\rho_0 \dot{e} = \boldsymbol{P} : \dot{\boldsymbol{F}} + \rho_0 r - \operatorname{div}_0 \boldsymbol{q}_0, \quad \text{(balance of energy)}; \tag{2.17}$$

$$\rho_0 \dot{s} + \operatorname{div}_0 \left[\frac{\boldsymbol{q}_0}{T} \right] - \frac{\rho_0 r}{T} \geq 0, \quad \text{(entropy production inequality)}, \tag{2.18}$$

where $\boldsymbol{b}_0$ is the body forces field , measured in force per unit reference volume; ρ_0 is the material density, measured in mass per unit reference volume; e is the internal energy per unit mass; r is the heat supply per unit mass; $\boldsymbol{q}_0$ is the heat flux vector, measured in heat power per unit reference surface; T is the absolute temperature; and s is specific entropy per unit mass.

Substituting the balance of energy (Equation (2.17)) into the entropy production inequality (Equation (2.18)) leads to the Clausius-Duhem inequality, expressed as

$$\rho_0(\dot{e} - T\dot{s}) - \boldsymbol{P} : \dot{\boldsymbol{F}} + \frac{1}{T} \boldsymbol{q}_0 \cdot \nabla_0 T \leq 0, \tag{2.19}$$

which is a more convenient form to impose the entropy production inequality when developing thermodynamically consistent constitutive models.

Remark 2.1 | Angular momentum balance and the Biot stress tensor

We highlight, in particular, that to satisfy the balance of angular momentum, the Biot stress tensor must fulfill the symmetry condition

$$\boldsymbol{T}_B \boldsymbol{U} = (\boldsymbol{T}_B \boldsymbol{U})^T, \tag{2.20}$$

as a direct consequence of Equation (2.16), the definition of the Biot stress tensor (Equation (2.12)) and the polar decomposition of the deformation gradient (Equation (2.2)). The angular momentum balance in Equation (2.20) can be rewritten as $\operatorname{skew}(\boldsymbol{T}_B\boldsymbol{U}) = \boldsymbol{0}$.

Looking at Equation (2.13), we can observe that only the symmetric part of the Biot stress tensor contributes to the mechanical power. In fact, the angular momentum balance provides an algebraic constraint that allows the skew part of the Biot stress to be expressed in terms of the symmetric part and the right stretch tensor. Splitting the Biot stress into its symmetric and skew parts, and using the symmetry of $\boldsymbol{U}$, the symmetry condition becomes

$$(\operatorname{sym}\boldsymbol{T}_B + \operatorname{skew}\boldsymbol{T}_B)\,\boldsymbol{U} = \boldsymbol{U}\,(\operatorname{sym}\boldsymbol{T}_B - \operatorname{skew}\boldsymbol{T}_B), \tag{2.21}$$

which rearranges to the Sylvester equation for the skew part

$$\operatorname{skew}\boldsymbol{T}_B\,\boldsymbol{U} + \boldsymbol{U}\operatorname{skew}\boldsymbol{T}_B \;=\; \boldsymbol{U}\operatorname{sym}\boldsymbol{T}_B - \operatorname{sym}\boldsymbol{T}_B\,\boldsymbol{U}. \tag{2.22}$$

Since the right-hand side depends only on $\operatorname{sym}\boldsymbol{T}_B$ and $\boldsymbol{U}$, the skew Biot stress is fully determined by the symmetric part together with the right stretch. Equation (2.22) has a unique solution for $\operatorname{skew}\boldsymbol{T}_B$ when $\boldsymbol{U}$ is positive definite (see, e.g., (Chillingworth et al., 1982, Proposition 3.3)).

2.3.1 Compatibility and the stress potential

Given the hypothesis established in Section 2.1, regarding the existence of a smooth one-to-one motion function $\boldsymbol{\varphi}$ defined in a simply connected domain, the deformation gradient automatically satisfies the compatibility condition (see (Ciarlet, 2013, Section 6.17) for details) expressed as

$$\operatorname{curl}_0\boldsymbol{F} = \operatorname{curl}_0(\nabla_0\boldsymbol{\varphi}) = \boldsymbol{O}, \tag{2.23}$$

where curl_0 is the curl operator with respect to the material coordinates (see Appendix B.1 for details on the definition of the curl operator). Thus, the motion function $\boldsymbol{\varphi}$, or equivalently the displacement field $\boldsymbol{u}$, can be interpreted as potentials that generate the deformation gradient field $\boldsymbol{F}$ through the relation $\boldsymbol{F} = \nabla_0\boldsymbol{\varphi} = \boldsymbol{I} + \nabla_0\boldsymbol{u}$.

Similarly, if we consider a quasi-static process, i.e., neglecting inertial effects, with no body forces, the balance of momentum (Equation (2.15)) reduces to

$$\operatorname{div}_0\boldsymbol{P} = \boldsymbol{0}, \tag{2.24}$$

and we can also consider the existence of a stress potential function $\boldsymbol{Z}$ that serves as a large deformation analogue of the classical Beltrami stress tensor (Gurtin, 1963; Sadd, 2005) such that $\boldsymbol{P} = \operatorname{curl}_0\boldsymbol{Z}$ satisfies the quasi-static balance of momentum automatically, i.e.,

$$\operatorname{div}_0\boldsymbol{P} = \operatorname{div}_0(\operatorname{curl}_0\boldsymbol{Z}) = \boldsymbol{0}. \tag{2.25}$$

2.4 Thermodynamically consistent constitutive modeling

Equations (2.15) to (2.18) do not constitute a well-posed problem, as they contain more unknowns than equations. The stresses, entropies and heat fluxes in the governing equations need to be connected with the deformations and temperatures via constitutive laws that represent the physical behavior of the material.

Thermodynamic determinism Following our physical intuition, it is standard to assume that the stress, entropy and heat flux at a given material point depend on the history of deformation and temperature at that same point. These assumptions, formalized as the axioms of *thermodynamic determinism* and *local action*, allow the constitutive equations to be expressed symbolically as functionals of the history of the deformation gradient and temperature. We write these functional dependencies as

$$\boldsymbol{P} = \mathscr{H}({}^t\boldsymbol{F}, {}^tT), \tag{2.26}$$

$$s = \mathscr{J}({}^t\boldsymbol{F}, {}^tT), \tag{2.27}$$

$$\boldsymbol{q}_0 = \mathscr{G}({}^t\boldsymbol{F}, {}^tT, {}^t\boldsymbol{g}_0), \tag{2.28}$$

where $\boldsymbol{g}_0 \equiv \nabla_0 T$ is the material gradient of the temperature and the notation ${}^t\boldsymbol{F}$, ${}^tT$ and ${}^t\boldsymbol{g}_0$ denote the history of deformation gradient, temperature, and temperature gradient up to time t, respectively.

However, such general functional dependencies are sometimes not practical for constitutive modeling, e.g., in the FEM context. A subset of models which satisfies thermodynamic determinism and which is more amenable to computational implementation is based on the concept of internal variables. For a so-called *simple material*, the thermodynamic state is assumed to be completely defined by the instantaneous values of a finite number of state variables, i.e., $\{\boldsymbol{F}, T, \boldsymbol{g}_0, \boldsymbol{\alpha}\}$, where $\boldsymbol{\alpha} \equiv \{\alpha_k\}$ is a set of internal variables, scalar or tensorial, associated with dissipative mechanisms. This approach is included within the so-called rational thermodynamics as developed by Truesdell, Noll, Coleman and others (Noll, 1958; Coleman and Noll, 1961; Coleman and Mizel, 1964). It is a framework broad enough to describe thermodynamically irreversible processes, i.e., processes involving dissipation, thus allowing the modeling of physical phenomena relevant in terms of engineering practice. A thorough review of the different approaches to the thermodynamics of irreversible processes can be found in Lavenda (1978) and Maugin (1999).

Accordingly, we rewrite Equations (2.26) to (2.28) as

$$\boldsymbol{P} = \boldsymbol{h}(\boldsymbol{F}, T, \boldsymbol{\alpha}), \tag{2.29}$$

$$s = j(\boldsymbol{F}, T, \boldsymbol{\alpha}), \tag{2.30}$$

$$\boldsymbol{q}_0 = \boldsymbol{k}(\boldsymbol{F}, T, \boldsymbol{g}_0, \boldsymbol{\alpha}), \tag{2.31}$$

and adopt appropriate evolution equations for the internal variables of the form

$$\dot{\boldsymbol{\alpha}} = \boldsymbol{f}(\boldsymbol{F}, T, \boldsymbol{g}_0, \boldsymbol{\alpha}). \tag{2.32}$$

The constitutive description of the material through the functions $\boldsymbol{h}$, j and $\boldsymbol{k}$ must be consistent with the principles established by Equations (2.15) to (2.18). In particular, to satisfy the balance of angular momentum, the first Piola–Kirchhoff stress tensor must fulfill the symmetry condition in Equation (2.16). Thus, we require the constitutive relation $\boldsymbol{h}$ to satisfy

$$\boldsymbol{h}(\boldsymbol{F}, T, \boldsymbol{\alpha})\boldsymbol{F}^T = \left(\boldsymbol{h}(\boldsymbol{F}, T, \boldsymbol{\alpha})\boldsymbol{F}^T\right)^T. \tag{2.33}$$

These constitutive laws are further constrained by the second law of thermodynamics, expressed in the form of the Clausius-Duhem inequality (Equation (2.19)). Assuming that there is a function ψ depending on the deformation gradient $\boldsymbol{F}$, temperature T, and internal variables $\boldsymbol{\alpha}$ describing the Helmholtz free energy, i.e.,

$$\psi(\boldsymbol{F}, T, \boldsymbol{\alpha}) \equiv e(\boldsymbol{F}, T, \boldsymbol{\alpha}) - Ts(\boldsymbol{F}, T, \boldsymbol{\alpha}), \tag{2.34}$$

the Clausius-Duhem inequality now reads

$$\rho_0(\dot{\psi} + \dot{T}s) - \boldsymbol{P} : \dot{\boldsymbol{F}} + \frac{1}{T}\boldsymbol{q}_0 \cdot \nabla_0 T \leq 0. \tag{2.35}$$

Substituting Equations (2.29) to (2.31) into Equation (2.35), writing the time-derivative of the free Helmholtz energy in full using the chain rule, i.e.,

$$\dot{\psi} = \frac{\partial \psi}{\partial \boldsymbol{F}} : \dot{\boldsymbol{F}} + \frac{\partial \psi}{\partial T}\dot{T} + \frac{\partial \psi}{\partial \boldsymbol{\alpha}} * \dot{\boldsymbol{\alpha}}, \tag{2.36}$$

and considering that the deformation gradient and temperature can vary independently, it follows that the constitutive equations for the stress and entropy must be of the form

$$\boldsymbol{P} = \boldsymbol{h}(\boldsymbol{F}, T, \boldsymbol{\alpha}) = \rho_0 \frac{\partial \psi}{\partial \boldsymbol{F}}, \tag{2.37}$$

$$s = j(\boldsymbol{F}, T, \boldsymbol{\alpha}) = -\frac{\partial \psi}{\partial T}, \tag{2.38}$$

and that the remaining terms in Equation (2.35) satisfy

$$\frac{1}{T}\boldsymbol{k}(\boldsymbol{F}, T, \boldsymbol{g}_0, \boldsymbol{\alpha}) \cdot \boldsymbol{g}_0 + \rho_0 \frac{\partial \psi}{\partial \boldsymbol{\alpha}} * \boldsymbol{f}(\boldsymbol{F}, T, \boldsymbol{g}_0, \boldsymbol{\alpha}) \leq 0, \tag{2.39}$$

where the operator $*$ denotes an appropriate tensorial contraction between the derivative of the Helmholtz free energy with respect to the internal variables and the evolution equations for the internal variables. This motivates the definition of the mechanical dissipation per unit reference volume as

$$\mathcal{D}_{\text{int}} \equiv \mathcal{A}_{\text{int}} * \dot{\boldsymbol{\alpha}} \geq 0,, \tag{2.40}$$

where the thermodynamic forces associated with the internal variables are defined as

$$\mathcal{A}_{\text{int}} = \rho_0 \frac{\partial \psi}{\partial \boldsymbol{\alpha}}, \tag{2.41}$$

and the heat flux vector must satisfy the classical Fourier inequality

$$\boldsymbol{k}(\boldsymbol{F}, T, \boldsymbol{g}_0, \boldsymbol{\alpha}) \cdot \boldsymbol{g}_0 \leq 0, \tag{2.42}$$

which states that the heat flux vector and the temperature gradient are always oriented in opposite directions.

Finally, combining the chain-rule expression for the time derivative of the Helmholtz free energy in Equation (2.36), and the definition of the internal dissipation in Equation (2.40), we obtain

$$\mathcal{D}_{\text{int}} = \boldsymbol{P} : \dot{\boldsymbol{F}} - \rho_0(\dot{\psi} + \dot{T}s), \tag{2.43}$$

as an alternative expression for the internal dissipation, where Equation (2.37) has been used.

The development of concrete models that are framed within such a constitutive theory can be achieved by postulating suitable functions for the Helmholtz free energy, or supplying directly the functions for the stress, entropy and heat and other ingredients, such as dissipation potentials and yield surfaces, and the evolution equations for the internal variables.

Material objectivity The constitutive description of the material's behavior is assumed to be independent of the spatial reference frame chosen, that is, $\boldsymbol{h}$, j and $\boldsymbol{k}$ must be objective or observer independent and thus for any proper orthogonal tensor $\boldsymbol{Q}$, satisfy

$$\boldsymbol{Q}\boldsymbol{P} = \boldsymbol{h}(\boldsymbol{Q}\boldsymbol{F}, T, \boldsymbol{Q} * \boldsymbol{\alpha}), \tag{2.44}$$

$$s = j(\boldsymbol{Q}\boldsymbol{F}, T, \boldsymbol{Q} * \boldsymbol{\alpha}), \tag{2.45}$$

$$\boldsymbol{q}_0 = \boldsymbol{k}(\boldsymbol{Q}\boldsymbol{F}, T, \boldsymbol{g}_0, \boldsymbol{Q} * \boldsymbol{\alpha}), \tag{2.46}$$

where we dropped the dependency on the coordinates $\boldsymbol{X}$ and the time t for the sake of compactness. Notice that the rotation $\boldsymbol{Q}$ acts on the first index of the second-order tensors $\boldsymbol{F}$ and $\boldsymbol{P}$, as these are two-point tensors, whose first index refers to the spatial configuration. This spatial rotation has no effect on the entropy and the temperature, which are scalar quantities and on the material gradient of temperature and the material heat flux vector, which are material vectors. The action of $\boldsymbol{Q}$ on the internal variables, denoted by $\boldsymbol{Q} * \boldsymbol{\alpha}$, is defined according to the tensorial nature of each internal variable. For instance, if an internal variable is a spatial second-order tensor, the action is given by $\boldsymbol{Q} * \boldsymbol{\alpha} = \boldsymbol{Q}\boldsymbol{\alpha}\boldsymbol{Q}^T$. For spatial vector-valued internal variables, the action is $\boldsymbol{Q} * \boldsymbol{\alpha} = \boldsymbol{Q}\boldsymbol{\alpha}$, and for scalar internal variables, it remains unchanged, i.e., $\boldsymbol{Q} * \alpha = \alpha$.

These requirements are automatically satisfied if $\boldsymbol{h}$ and j are derived from a free energy function ψ that is itself objective, i.e., satisfies $\psi(\boldsymbol{Q}\boldsymbol{F}, T, \boldsymbol{Q} * \boldsymbol{\alpha}) = \psi(\boldsymbol{F}, T, \boldsymbol{\alpha})$ for any proper orthogonal tensor $\boldsymbol{Q}$.

We highlight the Biot stress's relationship with the constitutive description relating the first Piola-Kirchhoff stress tensor and the deformation gradient, choosing $\boldsymbol{Q} = \boldsymbol{R}^T$ in Equation (2.44), which yields

$$\boldsymbol{T}_B = \boldsymbol{h}|_{\mathbb{S}^3_+}(\boldsymbol{U}, T, \boldsymbol{R}^T * \boldsymbol{\alpha}), \tag{2.47}$$

where we've used the definition of the Biot stress tensor (Equation (2.12)). Therefore, we conclude that the function $\boldsymbol{h}$ with its domain restricted to the positive definite symmetric tensors, $\mathbb{S}^3_+$, in its first argument maps the right stretch tensor to the Biot stress tensor.

Material symmetry The constitutive descriptions of a material must also respect its material symmetries, i.e., changes in material reference frame that belong to the symmetry group of the material do not affect the constitutive response. Therefore, for any symmetry transformation $\boldsymbol{Q}$ of the material, the constitutive equations must satisfy

$$\boldsymbol{P}\boldsymbol{Q} = \boldsymbol{h}(\boldsymbol{F}\boldsymbol{Q}, T, \boldsymbol{\alpha} * \boldsymbol{Q}), \tag{2.48}$$

$$s = j(\boldsymbol{F}\boldsymbol{Q}, T, \boldsymbol{\alpha} * \boldsymbol{Q}), \tag{2.49}$$

$$\boldsymbol{Q}^T\boldsymbol{q}_0 = \boldsymbol{k}(\boldsymbol{F}\boldsymbol{Q}, T, \boldsymbol{Q}^T\boldsymbol{g}_0, \boldsymbol{\alpha} * \boldsymbol{Q}), \tag{2.50}$$

where the action of $\boldsymbol{Q}$ on the internal variables, denoted by $\boldsymbol{\alpha} * \boldsymbol{Q}$, is defined according to the tensorial nature of each internal variable. For isotropic materials, the symmetry group contains all proper orthogonal transformations, i.e., $\boldsymbol{Q} \in \mathrm{SO}(3)$.

Remark 2.2 | The Biot stress tensor for isotropic materials is symmetric

The second Piola-Kirchhoff stress tensor $\boldsymbol{S} = \boldsymbol{F}^{-1}\boldsymbol{P}$ for an isotropic material is symmetric and coaxial, i.e., shares the same eigenvectors, with the right stretch $\boldsymbol{U}$ (Raoult, 2009). Since the second Piola-Kirchhoff stress tensor is related to the Biot stress tensor through $\boldsymbol{T}_B = \boldsymbol{U}\boldsymbol{S}$, the Biot stress tensor for an isotropic material must also be symmetric. This is not the case for anisotropic materials, where the Biot stress tensor can be non-symmetric, even though

the second Piola-Kirchhoff stress tensor is symmetric as required by the balance of angular momentum.

2.4.1 Stress-driven constitutive equations

In this work, particularly in the context of the Principle of Multiscale Complementary Virtual Power discussed in Chapter 3, we are required to consider the stress as the primary variable in the constitutive description of the material behavior. The constitutive behavior is still described using internal variables, but now the deformation gradient is expressed as a function of the first Piola-Kirchhoff stress tensor, temperature, and internal variables. We focus only on the stress-deformation constitutive equations, which we write as

$$\boldsymbol{F} = \boldsymbol{p}\left(\boldsymbol{P}, T, \boldsymbol{\alpha}\right), \tag{2.51}$$

because the entropy, heat flux, and evolution equations for the internal variables (Equations (2.30) to (2.32)) can be made to depend on the stress instead of the deformation simply by substituting Equation (2.51) for the deformation gradient in the corresponding expressions. Note that as written, Equation (2.51) is multivalued, as the deformation gradient is not a one-to-one function of the first Piola-Kirchhoff stress tensor. This is explored in more detail in this section.

Equation (2.51) is also required to be thermodynamically consistent, satisfying the principles established by Equations (2.15) to (2.18). In particular, to satisfy the balance of angular momentum, the first Piola–Kirchhoff stress tensor must fulfill the symmetry condition in Equation (2.16). Thus, we assume that the constitutive relation $\boldsymbol{p}$ is constructed such that

$$\boldsymbol{P}\boldsymbol{p}(\boldsymbol{P}, T, \boldsymbol{\alpha})^T = \left(\boldsymbol{P}\boldsymbol{p}(\boldsymbol{P}, T, \boldsymbol{\alpha})^T\right)^T. \tag{2.52}$$

To better appreciate the constraints imposed by the second law of thermodynamics on the stress-driven constitutive equations, it is worthwhile to rewrite the Clausius-Duhem inequality (Equation (2.19)) in terms of the Gibbs free energy. It is the Legendre-Fenchel transform of the Helmholtz free energy (see Ogden (1997, Section 5.4) for a discussion on the Legendre-Fenchel transform in the context of nonlinear elasticity and Rockafellar (1972) for a more general treatment in the context of convex analysis) defined as

$$g(\boldsymbol{P}, T, \boldsymbol{\alpha}) = \sup_{\boldsymbol{F}} \left[\frac{1}{\rho_0} \boldsymbol{P} : \boldsymbol{F} - \psi(\boldsymbol{F}, T, \boldsymbol{\alpha}) \right]. \tag{2.53}$$

If we assume that the Helmholtz free energy is differentiable everywhere as a function of the deformation gradient–but not necessarily convex–the supremum is attained at those $\boldsymbol{F}$ where

$$\boldsymbol{P} = \rho_0 \frac{\partial \psi}{\partial \boldsymbol{F}}, \tag{2.54}$$

which is precisely the constitutive equation for the stress in Equation (2.37). Without convexity of the Helmholtz free energy, the supremum is not attained at a unique deformation gradient, as there are multiple solutions due to the rotational invariance of the free energy.

This multiplicity of solutions can also be appreciated by considering the elasticity tensor, defined as

$$\mathbf{C} = \frac{\partial \boldsymbol{h}}{\partial \boldsymbol{F}}. \tag{2.55}$$

At configurations where $\boldsymbol{F}(0) \in \mathrm{SO}(3)$, i.e., when the deformation is a pure rotation and thus induces no stress, the range of $\mathbf{C}$ coincides with the space of symmetric tensors, while its kernel

coincides with the space of skew-symmetric tensors (Gurtin, 1981). This reflects the classical property that, in small-strain elasticity, the stress depends only on the symmetric part of the deformation gradient (the infinitesimal strain tensor), and is insensitive to the skew-symmetric part (the infinitesimal rotation tensor). As a consequence, $\mathbf{C}$ fails to be an isomorphism, and Equation (2.54) may admit multiple solutions (bifurcations) near such stress-free states. Indeed, as shown in Chillingworth et al. (1982, 1983), the number of bifurcation branches can be as high as forty, depending on the specific structure of the functions $\boldsymbol{h}$ and $\boldsymbol{P}$. This multiplicity of solutions highlights the non-uniqueness of the inverse constitutive relation in the vicinity of SO(3). Away from SO(3), we assume that the material models are constructed such that $\mathbf{C}$ is of full rank. This ensures local invertibility and rules out further bifurcation points in the stress–deformation map. Hence, provided that we select a suitable initial solution near the stress-free (trivial) states, the solution can be continued uniquely along a branch, yielding a locally one-to-one relationship between the stress and the deformation gradient.

Having selected an appropriate branch of the solution, we can now write the Gibbs free energy as

$$g(\boldsymbol{P}, T, \boldsymbol{\alpha}) \equiv \frac{1}{\rho_0}\boldsymbol{P} : \boldsymbol{F}(\boldsymbol{P}, T, \boldsymbol{\alpha}) - e(\boldsymbol{P}, T, \boldsymbol{\alpha}) + Ts(\boldsymbol{P}, T, \boldsymbol{\alpha}), \tag{2.56}$$

which depends on the first Piola-Kirchhoff stress tensor, temperature, and internal variables, where we used the definition of the Helmholtz free energy in Equation (2.34). This step is analogous to the one taken when introducing the Helmholtz free energy in Equation (2.34). The Clausius-Duhem inequality can now be expressed as

$$\rho_0(\dot{T}s - \dot{g}) + \boldsymbol{F} : \dot{\boldsymbol{P}} + \frac{1}{T}\boldsymbol{q}_0 \cdot \nabla_0 T \leq 0. \tag{2.57}$$

Substituting Equations (2.30), (2.31) and (2.51) into Equation (2.57), writing the time-derivative of the Gibbs free energy in full using the chain rule, i.e.,

$$\dot{g} = \frac{\partial g}{\partial \boldsymbol{P}} : \dot{\boldsymbol{P}} + \frac{\partial g}{\partial T}\dot{T} + \frac{\partial g}{\partial \boldsymbol{\alpha}} * \dot{\boldsymbol{\alpha}}, \tag{2.58}$$

and considering that the stress and temperature can vary independently, it follows that the constitutive equations for the deformation gradient and entropy must be of the form

$$\boldsymbol{F} = \boldsymbol{p}(\boldsymbol{P}, T, \boldsymbol{\alpha}) = \rho_0 \frac{\partial g}{\partial \boldsymbol{P}}, \tag{2.59}$$

$$s = j(\boldsymbol{P}, T, \boldsymbol{\alpha}) = \frac{\partial g}{\partial T}, \tag{2.60}$$

and that the remaining terms in Equation (2.57) satisfy

$$\frac{1}{T}\boldsymbol{k}(\boldsymbol{P}, T, \boldsymbol{g}_0, \boldsymbol{\alpha}) \cdot \boldsymbol{g}_0 + \rho_0 \frac{\partial g}{\partial \boldsymbol{\alpha}} * \boldsymbol{f}(\boldsymbol{P}, T, \boldsymbol{g}_0, \boldsymbol{\alpha}) \leq 0, \tag{2.61}$$

where we abused notation by using $\boldsymbol{k}$ and $\boldsymbol{f}$ to denote both the heat flux function and the evolution equations for the internal variables as a function of deformation gradient and stress, respectively. The internal dissipation per unit reference volume is now defined as

$$\mathcal{D}_{\text{int}} \equiv \rho_0 \frac{\partial g}{\partial \boldsymbol{\alpha}} * \dot{\boldsymbol{\alpha}} \geq 0, \tag{2.62}$$

which is equivalent to

$$\mathcal{D}_{\text{int}} = \rho_0(\dot{g} - \dot{T}s) - \boldsymbol{F} : \dot{\boldsymbol{P}}, \tag{2.63}$$

where Equation (2.59) has been used. Note that Equation (2.63) provides a physical interpretation for the term $\boldsymbol{F} : \dot{\boldsymbol{P}}$ as the isothermal Gibbs energy rate per unit reference volume. This mirrors the interpretation of the term $\boldsymbol{P} : \dot{\boldsymbol{F}}$ as the isothermal Helmholtz energy rate per unit reference volume in Equation (2.43), also often referred to as the mechanical power per unit reference volume. It also highlights the connection between the Gibbs free energy and the complementary strain energy, W_c, and between the Helmholtz free energy and the strain energy, W, as we now show. In isothermal, non-dissipative conditions, we have

$$\boldsymbol{P} : \boldsymbol{F} = \rho_0 g + \rho_0 \psi = W + W_c, \tag{2.64}$$

which can be graphically interpreted in one dimension as the area of the rectangle defined by the stress and deformation gradient in the stress–deformation space, decomposed into the area below the stress–deformation curve (the Helmholtz free energy) and the area above the curve (the Gibbs free energy), as illustrated in Figure 2.1. Thus, the Gibbs free energy is related to the complementary energy through the identity

$$\rho_0 g = W_c, \tag{2.65}$$

in isothermal, non-dissipative conditions.

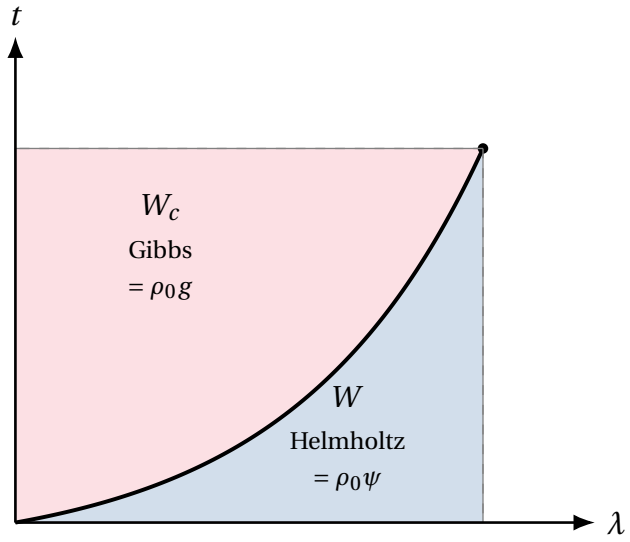

Figure 2.1: Graphical interpretation, for a one-dimensional non-dissipative isothermal response, of the decomposition of the total mechanical work per unit reference volume $t\lambda = W + W_c$ (the area of the rectangle) into the strain energy W (the Helmholtz free energy $\rho_0\psi$, the area below the stress–stretch curve) and the complementary strain energy W_c (the Gibbs free energy $\rho_0 g$, the area above the curve). Here, λ denotes the stretch and t the associated traction.

2.5 Thermomechanical constitutive initial value problem

Given the constitutive requirements described in Section 2.4, the use of a thermodynamically consistent constitutive model based on internal variables implies the solution of an initial value problem. More specifically, the strain-driven material thermomechanical constitutive initial value problem consists in finding the stress, heat flux, and internal variables as functions of time, given the history of deformation and temperature, along with the initial values of the internal variables. Thus, it can be stated as

Problem 2.1 | Strain-driven material thermomechanical constitutive initial value problem.

Given the initial values of the internal variables, $\boldsymbol{\alpha}(t_0)$, the history of the deformation gradient

$$\boldsymbol{F}(t), \quad t \in [t_0, t_{\text{end}}], \tag{2.66}$$

and the history of the temperature distribution and its gradient

$$T(t), \quad t \in [t_0, t_{\text{end}}], \tag{2.67}$$

$$\boldsymbol{g}_0(t), \quad t \in [t_0, t_{\text{end}}], \tag{2.68}$$

find the functions for $\boldsymbol{P}(t)$, $\boldsymbol{q}_0(t)$ and $\boldsymbol{\alpha}(t)$ such that the constitutive equations

$$\boldsymbol{P} = \boldsymbol{h}(\boldsymbol{F}, T, \boldsymbol{\alpha}), \tag{2.69}$$

$$s = j(\boldsymbol{F}, T, \boldsymbol{\alpha}), \tag{2.70}$$

$$\boldsymbol{q}_0 = \boldsymbol{k}(\boldsymbol{F}, T, \boldsymbol{g}_0, \boldsymbol{\alpha}), \tag{2.71}$$

$$\dot{\boldsymbol{\alpha}} = \boldsymbol{f}(\boldsymbol{F}, T, \boldsymbol{g}_0, \boldsymbol{\alpha}), \tag{2.72}$$

are satisfied for every $t \in [t_0, t_{\text{end}}]$.

Likewise, the material stress-driven thermomechanical constitutive initial value problem can be stated as

Problem 2.2 | Stress-driven material thermomechanical constitutive initial value problem.

Given the initial values of the internal variables, $\boldsymbol{\alpha}(t_0)$, the history of the first Piola-Kirchhoff stress tensor

$$\boldsymbol{P}(t), \quad t \in [t_0, t_{\text{end}}], \tag{2.73}$$

and the history of the temperature distribution and its gradient

$$T(t), \quad t \in [t_0, t_{\text{end}}], \tag{2.74}$$

$$\boldsymbol{g}_0(t), \quad t \in [t_0, t_{\text{end}}], \tag{2.75}$$

find the functions for $\boldsymbol{F}(t)$, $\boldsymbol{q}_0(t)$ and $\boldsymbol{\alpha}(t)$ such that the constitutive equations

$$\boldsymbol{F} = \boldsymbol{p}(\boldsymbol{P}, T, \boldsymbol{\alpha}), \tag{2.76}$$
$$s = j(\boldsymbol{P}, T, \boldsymbol{\alpha}), \tag{2.77}$$
$$\boldsymbol{q}_0 = \boldsymbol{k}(\boldsymbol{P}, T, \boldsymbol{g}_0, \boldsymbol{\alpha}), \tag{2.78}$$
$$\dot{\boldsymbol{\alpha}} = \boldsymbol{f}(\boldsymbol{P}, T, \boldsymbol{g}_0, \boldsymbol{\alpha}), \tag{2.79}$$

are satisfied for every $t \in [t_0, t_{\text{end}}]$.

2.5.1 Time discretization for the constitutive equations

A closed-form solution to the thermomechanical constitutive initial value problem (Problem 2.1 or Problem 2.2) is in general not available. Therefore, it is necessary to employ a suitable numerical approach to integrate the rate constitutive equations.

Attending to the strain-driven thermomechanical constitutive initial boundary value problem and considering the time increment $[t_n, t_{n+1}]$, this approach comprises the following requirements:

- **First Piola-Kirchhoff stress tensors.** Considering a time increment $[t_n, t_{n+1}]$ and given the set $\boldsymbol{\alpha}_n$ of internal variables at t_n, the deformation gradient $\boldsymbol{F}_{n+1}$ and the temperature distribution T_{n+1} at time t_{n+1} determine the first Piola-Kirchhoff stress tensor $\boldsymbol{P}_{n+1}$ uniquely as

$$\boldsymbol{P}_{n+1} = \hat{\boldsymbol{P}}(\boldsymbol{F}_{n+1}, T_{n+1}, \boldsymbol{\alpha}_n), \tag{2.80}$$

  where $\hat{\boldsymbol{P}}$ is the incremental constitutive function for the first Piola-Kirchhoff stress tensor.

- **Heat flux vector.** Considering a time increment $[t_n, t_{n+1}]$ and given the set $\boldsymbol{\alpha}_n$ of internal variables at t_n, the deformation gradient $\boldsymbol{F}_{n+1}$, temperature distribution T_{n+1} and its gradient $\boldsymbol{g}_{0,n+1}$ at time t_{n+1} determine the heat flux vector $\boldsymbol{q}_{0,n+1}$ uniquely as

$$\boldsymbol{q}_{0,n+1} = \hat{\boldsymbol{q}}_0(\boldsymbol{F}_{n+1}, T_{n+1}, \boldsymbol{g}_{0,n+1}, \boldsymbol{\alpha}_n), \tag{2.81}$$

  where $\hat{\boldsymbol{q}}_0$ is the incremental constitutive function for the heat flux vector.

- **Set of internal variables.** Assuming that the set of internal variables $\boldsymbol{\alpha}_n$ is known at t_n, the set of internal variables must be uniquely determined by the prescribed deformation gradient $\boldsymbol{F}_{n+1}$ and temperature distribution T_{n+1} prescribed at t_{n+1} as

$$\boldsymbol{\alpha}_{n+1} = \hat{\boldsymbol{\alpha}}(\boldsymbol{F}_{n+1}, T_{n+1}, \boldsymbol{\alpha}_n), \tag{2.82}$$

  where $\hat{\boldsymbol{\alpha}}$ is the incremental constitutive function for the set of internal variables.

Generally, the numerical constitutive laws are nonlinear and path-independent within one increment.

For the stress-driven thermomechanical constitutive initial boundary value problem, the time discretization is similar, with the difference that the first Piola-Kirchhoff stress tensor is known at t_{n+1} and the deformation gradient is to be determined. Thus, we require:

- **Deformation gradient.** Considering a time increment $[t_n, t_{n+1}]$ and given the set $\boldsymbol{\alpha}_n$ of internal variables at t_n, the first Piola-Kirchhoff stress tensor $\boldsymbol{P}_{n+1}$ and the temperature distribution T_{n+1} at time t_{n+1} determine the deformation gradient $\boldsymbol{F}_{n+1}$ uniquely as

$$\boldsymbol{F}_{n+1} = \hat{\boldsymbol{F}}(\boldsymbol{P}_{n+1}, T_{n+1}, \boldsymbol{\alpha}_n), \tag{2.83}$$

  where $\hat{\boldsymbol{F}}$ is the incremental constitutive function for the deformation gradient.

- **Heat flux vector.** Considering a time increment $[t_n, t_{n+1}]$ and given the set $\boldsymbol{\alpha}_n$ of internal variables at t_n, the first Piola-Kirchhoff stress tensor $\boldsymbol{P}_{n+1}$, temperature distribution T_{n+1} and its gradient $\boldsymbol{g}_{0,n+1}$ at time t_{n+1} determine the heat flux vector $\boldsymbol{q}_{0,n+1}$ uniquely as

$$\boldsymbol{q}_{0,n+1} = \hat{\boldsymbol{q}}_0(\boldsymbol{P}_{n+1}, T_{n+1}, \boldsymbol{g}_{0,n+1}, \boldsymbol{\alpha}_n), \tag{2.84}$$

  where $\hat{\boldsymbol{q}}_0$ is the incremental constitutive function for the heat flux vector.

- **Set of internal variables.** Assuming that the set of internal variables $\boldsymbol{\alpha}_n$ is known at t_n, the set of internal variables must be uniquely determined by the prescribed first Piola-Kirchhoff stress tensor $\boldsymbol{P}_{n+1}$ and temperature distribution T_{n+1} prescribed at t_{n+1} as

$$\boldsymbol{\alpha}_{n+1} = \hat{\boldsymbol{\alpha}}(\boldsymbol{P}_{n+1}, T_{n+1}, \boldsymbol{\alpha}_n), \tag{2.85}$$

  where $\hat{\boldsymbol{\alpha}}$ is the incremental constitutive function for the set of internal variables.

2.6 Thermomechanical initial boundary value problem

The strong equations that enforce the equilibrium of a body and the balance of energy can be written using the material description as

$$\rho_0 \ddot{\boldsymbol{u}} = \operatorname{div}_0 \boldsymbol{P} + \boldsymbol{b}_0, \quad \text{in } \Omega_0, \tag{2.86}$$

$$\rho_0 \dot{e} = \boldsymbol{P} : \dot{\boldsymbol{F}} + \rho_0 r - \operatorname{div}_0 \boldsymbol{q}_0, \quad \text{in } \Omega_0, \tag{2.87}$$

where we seek to find the displacement field $\boldsymbol{u}$ and the temperature field T in the reference configuration Ω_0, given appropriate initial and boundary conditions. When there are no body forces and inertial effects are negligible, an equivalent problem is to find the stress potential and the temperature field such that compatibility and the balance of energy are satisfied, i.e.,

$$\operatorname{curl}_0 \boldsymbol{F} = \boldsymbol{O}, \quad \text{in } \Omega_0, \tag{2.88}$$

$$\rho_0 \dot{e} = \boldsymbol{P} : \dot{\boldsymbol{F}} + \rho_0 r - \operatorname{div}_0 \boldsymbol{q}_0, \quad \text{in } \Omega_0, \tag{2.89}$$

since the balance of linear momentum is automatically satisfied (see Equation (2.25)).

Equations (2.87) and (2.89), however, are not the most common way to write the balance of energy in thermomechanics. Instead, it is customary to express the balance of energy in terms of the temperature rate, leading to the so-called heat conduction equation, as we show next. After introducing the heat conduction equation, we state the weak forms of both strain-driven and stress-driven thermomechanical initial boundary value problems.

2.6.1 Heat conduction equation

In the context of thermomechanics, the most common form of the energy balance equation (Equation (2.17)) is the heat conduction equation. Let $C_{\boldsymbol{F}}$ denote the specific heat at constant deformation, i.e., the amount of heat required to change a unit mass of a substance by one degree in temperature at fixed deformation, defined as

$$C_{\boldsymbol{F}} \equiv \frac{\partial e(\boldsymbol{F}, T, \boldsymbol{\alpha})}{\partial T}, \tag{2.90}$$

and the specific heat at constant stress, $C_{\boldsymbol{P}}$, defined as

$$C_{\boldsymbol{P}} \equiv \frac{\partial e(\boldsymbol{P}, T, \boldsymbol{\alpha})}{\partial T}, \tag{2.91}$$

where we incur a slight abuse of notation by using the same symbol e to denote the internal energy expressed as a function of deformation gradient and temperature, $e(\boldsymbol{F}, T, \boldsymbol{\alpha})$, or as a function of stress and temperature, $e(\boldsymbol{P}, T, \boldsymbol{\alpha})$. Given the relationship between the internal energy and the Helmholtz free energy (Equation (2.34)), the specific heat at constant deformation can be expressed as

$$C_{\boldsymbol{F}} = -T\frac{\partial^2 \psi}{\partial T^2}. \tag{2.92}$$

Likewise, using the relationship between the internal energy and the Gibbs free energy (Equation (2.56)), one can express the specific heat at constant stress as

$$C_{\boldsymbol{P}} = T\frac{\partial^2 g}{\partial T^2} + \boldsymbol{P} : \frac{\partial^2 g}{\partial \boldsymbol{P} \partial T}. \tag{2.93}$$

We deduce first the heat conduction equation in the strain-driven context. Taking the time derivative of Helmholtz's free energy (Equation (2.34)), we find

$$\dot{\psi} = \dot{e} - T\dot{s} - \dot{T}s. \tag{2.94}$$

Combining this expression with the chain rule for the entropy rate,

$$\dot{s} = \frac{\partial s}{\partial T}\dot{T} + \frac{\partial s}{\partial \boldsymbol{F}} : \dot{\boldsymbol{F}} + \frac{\partial s}{\partial \boldsymbol{\alpha}} * \dot{\boldsymbol{\alpha}}, \tag{2.95}$$

we can rewrite the balance of energy (Equation (2.87)) as

$$\rho_0(\dot{\psi} + \dot{T}s) + \rho_0 T\left(\frac{\partial s}{\partial T}\dot{T} + \frac{\partial s}{\partial \boldsymbol{F}} : \dot{\boldsymbol{F}} + \frac{\partial s}{\partial \boldsymbol{\alpha}} * \dot{\boldsymbol{\alpha}}\right) = \boldsymbol{P} : \dot{\boldsymbol{F}} + \rho_0 r - \operatorname{div}_0 \boldsymbol{q}_0. \tag{2.96}$$

Substituting in Equation (2.38) and rearranging terms yields

$$-\rho_0 T\frac{\partial^2 \psi}{\partial T^2}\dot{T} = \boldsymbol{P} : \dot{\boldsymbol{F}} - \rho_0(\dot{\psi} + \dot{T}s) - \rho_0 T\left(\frac{\partial^2 \psi}{\partial \boldsymbol{F}\partial T} : \dot{\boldsymbol{F}} + \frac{\partial^2 \psi}{\partial \boldsymbol{\alpha}\partial T} * \dot{\boldsymbol{\alpha}}\right) + \rho_0 r - \operatorname{div}_0 \boldsymbol{q}_0, \tag{2.97}$$

which motivates the introduction of the thermomechanical coupling term, $\mathcal{H}^{\text{ep}}$, as

$$\mathcal{H}^{\text{ep}} = -\rho_0 T\left(\frac{\partial^2 \psi}{\partial \boldsymbol{F}\partial T} : \dot{\boldsymbol{F}} + \frac{\partial^2 \psi}{\partial \boldsymbol{\alpha}\partial T} * \dot{\boldsymbol{\alpha}}\right). \tag{2.98}$$

Noting that the first two terms on the right-hand side are equal to the internal dissipation $\mathcal{D}_{\text{int}}$ (see Equation (2.43)) and the connection between the specific heat at constant deformation and Helmholtz's free energy (Equation (2.92)), the energy balance equation can be recast as

$$\rho_0 C_{\boldsymbol{F}} \dot{T} = \rho_0 r - \operatorname{div}_0 \boldsymbol{q}_0 + \mathcal{D}_{\text{int}} + \mathcal{H}^{\text{ep}}. \tag{2.99}$$

In the thermoelastic context, the thermomechanical coupling term specializes to

$$\mathcal{H}^{\text{e}} = -T\boldsymbol{\beta}_{\boldsymbol{P}} : \dot{\boldsymbol{F}}, \tag{2.100}$$

where $\boldsymbol{\beta}_{\boldsymbol{P}}$ is the thermal stress tensor, defined as

$$\frac{\partial^2 \psi}{\partial \boldsymbol{F} \partial T} = \frac{1}{\rho_0} \frac{\partial \boldsymbol{P}}{\partial T} = \frac{1}{\rho_0} \boldsymbol{\beta}_{\boldsymbol{P}}, \tag{2.101}$$

where we assume the necessary smoothness requirements to interchange the order of differentiation. The heat conduction equation in the thermoelastic context thus reads

$$\rho_0 C_{\boldsymbol{F}} \dot{T} = \rho_0 r - \operatorname{div}_0 \boldsymbol{q}_0 - T\boldsymbol{\beta}_{\boldsymbol{P}} : \dot{\boldsymbol{F}}. \tag{2.102}$$

Remark 2.3 | Thermomechanical coupling

The mechanical and thermal fields are coupled bidirectionally. More specifically:

- the temperature couples to the structural field via additional thermal stresses and possibly via temperature-dependent material parameters.
- the structure couples to the thermal field via coupling terms such as the internal dissipation $\mathcal{D}_{\text{int}}$ and the thermomechanical coupling term $\mathcal{H}^{\text{ep}}$. Furthermore, for finite deformation thermomechanical problems, where the initial domain Ω_0 deforms to Ω, so that $\Omega \neq \Omega_0$, and a Lagrangian formulation is used, the deformation enters the thermal field additionally due to the mapping of all quantities in the balance equations to the reference configuration.

A form of the heat conduction equation more suitable to a context where the stress is the independent variable can be derived similarly. Taking the time derivative of the Gibbs free energy (Equation (2.56)), we find

$$\dot{g} = \frac{1}{\rho_0} \dot{\boldsymbol{P}} : \boldsymbol{F} + \frac{1}{\rho_0} \boldsymbol{P} : \dot{\boldsymbol{F}} - \dot{e} + T\dot{s} + \dot{T}s. \tag{2.103}$$

Combining this expression with the chain rule for the entropy rate,

$$\dot{s} = \frac{\partial s}{\partial T} \dot{T} + \frac{\partial s}{\partial \boldsymbol{P}} : \dot{\boldsymbol{P}} + \frac{\partial s}{\partial \boldsymbol{\alpha}} * \dot{\boldsymbol{\alpha}}, \tag{2.104}$$

we can rewrite the balance of energy (Equation (2.89)) as

$$\rho_0 (\dot{T}s - \dot{g}) + \dot{\boldsymbol{P}} : \boldsymbol{F} + \boldsymbol{P} : \dot{\boldsymbol{F}} + \rho_0 T \left(\frac{\partial s}{\partial T} \dot{T} + \frac{\partial s}{\partial \boldsymbol{P}} : \dot{\boldsymbol{P}} + \frac{\partial s}{\partial \boldsymbol{\alpha}} * \dot{\boldsymbol{\alpha}} \right) = \boldsymbol{P} : \dot{\boldsymbol{F}} + \rho_0 r - \operatorname{div}_0 \boldsymbol{q}_0. \tag{2.105}$$

Substituting in Equation (2.60) concerning the relationship between the Gibbs free energy and the entropy, we find

$$\rho_0 (\dot{T}s - \dot{g}) + \dot{\boldsymbol{P}} : \boldsymbol{F} + \rho_0 T \left(\frac{\partial^2 g}{\partial T^2} \dot{T} + \frac{\partial^2 g}{\partial \boldsymbol{P} \partial T} : \dot{\boldsymbol{P}} + \frac{\partial^2 g}{\partial \boldsymbol{\alpha} \partial T} * \dot{\boldsymbol{\alpha}} \right) = \rho_0 r - \operatorname{div}_0 \boldsymbol{q}_0. \tag{2.106}$$

Rearranging terms yields

$$\rho_0\left(T\frac{\partial^2 g}{\partial T^2}+\boldsymbol{P}:\frac{\partial^2 g}{\partial T\partial \boldsymbol{P}}\right)\dot{T}-\rho_0\left(\boldsymbol{P}:\frac{\partial^2 g}{\partial T\partial \boldsymbol{P}}\right)\dot{T}=$$
$$\rho_0(\dot{g}-\dot{T}s)-\dot{\boldsymbol{P}}:\boldsymbol{F}-\rho_0\left(T\frac{\partial^2 g}{\partial \boldsymbol{P}\partial T}:\dot{\boldsymbol{P}}+\frac{\partial^2 g}{\partial T\partial \boldsymbol{\alpha}}*\dot{\boldsymbol{\alpha}}\right)+\rho_0 r-\mathrm{div}_0\,\boldsymbol{q}_0, \quad (2.107)$$

which motivates the introduction of the thermomechanical coupling term in the stress-driven formulation, $\mathcal{K}^{\mathrm{ep}}$, as

$$\mathcal{K}^{\mathrm{ep}}=-\rho_0\left(T\frac{\partial^2 g}{\partial \boldsymbol{P}\partial T}:\dot{\boldsymbol{P}}+\frac{\partial^2 g}{\partial T\partial \boldsymbol{\alpha}}*\dot{\boldsymbol{\alpha}}\right). \quad (2.108)$$

Noting that the first two terms on the right-hand side are equal to the internal dissipation $\mathcal{D}_{\mathrm{int}}$ (see Equation (2.63)) and the connection between the specific heat at constant stress and Gibbs free energy (Equation (2.93)), the energy balance equation can be recast as

$$(\rho_0 C_{\boldsymbol{P}}-\boldsymbol{P}:\boldsymbol{\alpha}_{\boldsymbol{F}})\dot{T}=\mathcal{D}_{\mathrm{int}}+\mathcal{K}^{\mathrm{ep}}+\rho_0 r-\mathrm{div}_0\,\boldsymbol{q}_0, \quad (2.109)$$

where we have introduced the thermal expansion tensor, $\boldsymbol{\alpha}_{\boldsymbol{F}}$, defined as

$$\boldsymbol{\alpha}_{\boldsymbol{F}}=\frac{\partial \boldsymbol{F}}{\partial T}=\rho_0\frac{\partial^2 g}{\partial \boldsymbol{P}\partial T}. \quad (2.110)$$

In the thermoelastic context, the stress-driven thermomechanical coupling term specializes to

$$\mathcal{K}^{\mathrm{e}}=-T\boldsymbol{\alpha}_{\boldsymbol{F}}:\dot{\boldsymbol{P}}, \quad (2.111)$$

yielding the classical form of the heat conduction equation in thermoelasticity

$$(\rho_0 C_{\boldsymbol{P}}-\boldsymbol{P}:\boldsymbol{\alpha}_{\boldsymbol{F}})\dot{T}=\rho_0 r-\mathrm{div}_0\,\boldsymbol{q}_0-T\boldsymbol{\alpha}_{\boldsymbol{F}}:\dot{\boldsymbol{P}}. \quad (2.112)$$

2.6.2 Thermomechanical initial boundary value problem

It is now possible to pose the thermomechanical constitutive initial value problem in its weak form. We begin with the strain-driven thermomechanical constitutive initial boundary value problem. To this end, we first introduce the appropriate boundary conditions. We consider that the boundary $\partial\Omega_0$ of the body $\mathscr{B}$ is divided into non-overlapping portions where either traction forces or displacements are prescribed for the mechanical field, and either heat flux or temperature are prescribed for the thermal field, i.e.,

- **Natural (or Neumann) boundary condition:**
  - **Mechanical field:** The boundary portion $\partial\Omega_{\mathrm{traction},0}$ of $\mathscr{B}$ is subjected to a prescribed history of traction forces, $\boldsymbol{t}_{\mathrm{presc},0}(\boldsymbol{X},t)$, $\boldsymbol{X}\in\partial\Omega_{\mathrm{traction},0}$, $t\in[t_0,t_{\mathrm{end}}]$,
  - **Thermal field:** The boundary portion $\partial\Omega_{\mathrm{heat},0}$ of $\mathscr{B}$ is subject to a prescribed history of heat flux, $h_{\mathrm{presc},0}(\boldsymbol{X},t)=\boldsymbol{q}_{\mathrm{presc},0}(\boldsymbol{X},t)\cdot\boldsymbol{N}(\boldsymbol{X})$, $\boldsymbol{X}\in\partial\Omega_{\mathrm{heat},0}$, $t\in[t_0,t_{\mathrm{end}}]$.
- **Essential (or Dirichlet) boundary condition:**

– **Mechanical field:** The boundary portion $\partial\Omega_{\text{motion},0}$ of $\mathscr{B}$ is subjected to a prescribed displacement field history, $\boldsymbol{u}_{\text{presc}}(\boldsymbol{X},t)$, such that

$$\boldsymbol{\varphi}(\boldsymbol{X},t) = \boldsymbol{X} + \boldsymbol{u}_{\text{presc}}(\boldsymbol{X},t), \quad \boldsymbol{X} \in \partial\Omega_{\text{motion, }0}, \quad t \in [t_0, t_{\text{end}}].$$

– **Thermal field:** The boundary portion $\partial\Omega_{\text{temperature},0}$ of $\mathscr{B}$ is subject to a prescribed temperature history, $T_{\text{presc}}(\boldsymbol{X},t)$, $\boldsymbol{X} \in \partial\Omega_{\text{temperature},0}$, $t \in [t_0, t_{\text{end}}]$.

It is also convenient to define the set of kinematically admissible displacements and admissible temperature distributions of $\mathscr{B}$ as the set of all sufficiently regular displacement and temperature functions that satisfy the corresponding essential boundary conditions, i.e.,

$$\mathscr{K}_u \equiv \left\{ \boldsymbol{u} : \Omega_0 \times \mathbb{R} \to \mathbb{R}^3 \mid \boldsymbol{u}(\boldsymbol{X},t) = \boldsymbol{u}_{\text{presc}}(\boldsymbol{X},t), \boldsymbol{X} \in \partial\Omega_{\text{motion},0}, \quad t \in [t_0, t_{\text{end}}] \right\}. \tag{2.113}$$

$$\mathscr{K}_T \equiv \left\{ T : \Omega_0 \times \mathbb{R} \to \mathbb{R} \mid T(\boldsymbol{X},t) = T_{\text{presc}}(\boldsymbol{X},t), \boldsymbol{X} \in \partial\Omega_{\text{temperature},0}, \quad t \in [t_0, t_{\text{end}}] \right\}. \tag{2.114}$$

So the weak form of the thermomechanical constitutive initial boundary value problem can be stated in a material description as follows

Problem 2.3 | Strain-driven material thermomechanical initial BVP.

Find a kinematically admissible displacement function, $\boldsymbol{u} \in \mathscr{K}_u$, and an admissible temperature distribution, $T \in \mathscr{K}_T$, such that for every $t \in [t_0, t_{\text{end}}]$, the body $\mathscr{B}$ is in mechanical and energetic equilibrium

$$\int_{\Omega_0} [\boldsymbol{P}(t) : \nabla_0 \boldsymbol{\eta} - (\boldsymbol{b}_0(t) - \rho_0 \ddot{\boldsymbol{u}}(t)) \cdot \boldsymbol{\eta}] \, \mathrm{d}v - \int_{\partial\Omega_0} \boldsymbol{t}_0(t) \cdot \boldsymbol{\eta} \, \mathrm{d}a = 0, \quad \forall \boldsymbol{\eta} \in \mathscr{V}_{u,0}, \tag{2.115}$$

$$\int_{\Omega_0} \left[\left(\rho_0 C_{\boldsymbol{F}}(t) \dot{T}(t) - \mathcal{D}_{\text{int}}(t) - \mathcal{H}^{\text{ep}}(t) - \rho_0 r(t) \right) \xi - \boldsymbol{k}(t) \cdot \nabla_0 \xi \right] \mathrm{d}v - \int_{\partial\Omega_0} h_0(t) \xi \, \mathrm{d}a = 0, \quad \forall \xi \in \mathscr{V}_{T,0}, \tag{2.116}$$

where the space of virtual displacements at time t is defined by

$$\mathscr{V}_{u,0} \equiv \left\{ \boldsymbol{\eta} : \Omega_0 \to \mathbb{R}^3 \mid \boldsymbol{\eta} = \boldsymbol{0} \quad \text{in} \quad \partial\Omega_{\text{motion},0} \right\}, \tag{2.117}$$

the space of virtual temperatures at time t is defined by

$$\mathscr{V}_{T,0} \equiv \left\{ \xi : \Omega_0 \to \mathbb{R} \mid \xi = 0 \quad \text{in} \quad \partial\Omega_{\text{temperature},0} \right\}, \tag{2.118}$$

and at each point of $\mathscr{B}$, the first Piola-Kirchhoff stress tensor is the solution of strain-driven material thermomechanical constitutive initial value problem (Problem 2.1).

Making use of the time discretization described in Section 2.5.1, one can state the weak form of the strain-driven material incremental thermomechanical initial boundary value problem in the material description as

Problem 2.4 | Strain-driven material incremental thermomechanical initial BVP.

Given the set of internal variables $\boldsymbol{\alpha}_n$ at t_n, the prescribed body and traction force fields $\boldsymbol{b}_{0,n+1}$ and $\boldsymbol{t}_{0,n+1}$, as well as the prescribed heat sources, r_{n+1} and heat fluxes, $h_{0,n+1}$, at t_{n+1}, find the kinematically admissible displacement field $\boldsymbol{u}_{n+1} \in \mathscr{K}_{u,n+1}$ and the admissible temperature distribution $T_{n+1} \in \mathscr{K}_{T,n+1}$ such that the body $\mathscr{B}$ is in mechanical and energetic equilibrium

$$\int_{\Omega_0} [\hat{\boldsymbol{P}}(\boldsymbol{F}(\boldsymbol{u}_{n+1}), T_{n+1}, \boldsymbol{\alpha}_n) : \nabla_0 \boldsymbol{\eta} - (\boldsymbol{b}_{0,n+1} - \rho_0 \ddot{\boldsymbol{u}}_{n+1}) \cdot \boldsymbol{\eta}] \, \mathrm{d}v - \int_{\partial\Omega_0} \boldsymbol{t}_{0,n+1} \cdot \boldsymbol{\eta} \, \mathrm{d}a = 0, \quad \forall \boldsymbol{\eta} \in \mathscr{V}_{u,n+1}, \tag{2.119}$$

$$\int_{\Omega_0} \left[\left(\rho_0 C_{\boldsymbol{F},n+1} \dot{T}_{n+1} - \mathcal{D}_{\mathrm{int},n+1} - \mathcal{H}^{\mathrm{ep}}_{n+1} - \rho_0 r_{n+1} \right) \xi - \hat{\boldsymbol{k}}(\boldsymbol{F}(\boldsymbol{u}_{n+1}), T_{n+1}, \boldsymbol{\alpha}_n) \cdot \nabla_0 \xi \right] \mathrm{d}v - \int_{\partial\Omega_0} h_{0,n+1} \xi \, \mathrm{d}a = 0, \quad \forall \xi \in \mathscr{V}_{T,n+1}, \tag{2.120}$$

where

$$\mathscr{K}_{u,n+1} \equiv \left\{ \boldsymbol{u}_{n+1} : \Omega_0 \to \mathbb{R}^3 \mid \boldsymbol{u}_{n+1}(\boldsymbol{X}) = \boldsymbol{u}_{\mathrm{presc},n+1}(\boldsymbol{X}),\ \boldsymbol{X} \in \partial\Omega_{\mathrm{motion},0} \right\}, \tag{2.121}$$

$$\mathscr{K}_{T,n+1} \equiv \left\{ T_{n+1} : \Omega_0 \to \mathbb{R} \mid T_{n+1}(\boldsymbol{X}) = T_{\mathrm{presc},n+1}(\boldsymbol{X}),\ \boldsymbol{X} \in \partial\Omega_{\mathrm{temperature},0} \right\}, \tag{2.122}$$

and

$$\boldsymbol{\alpha}_{n+1} = \hat{\boldsymbol{\alpha}}(\boldsymbol{F}(\boldsymbol{u}_{n+1}), T_{n+1}, \boldsymbol{\alpha}_n). \tag{2.123}$$

2.6.3 Stress-driven formulation

We now turn our attention to the stress-driven thermomechanical constitutive initial boundary value problem. Assume that the interior of the body was subjected to a prescribed history of heat sources, $r(\boldsymbol{X}, t)$, $t \in [t_0, t_{\mathrm{end}}]$, and to the following boundary conditions:

- **Natural (or Neumann) boundary condition:**
  - **Mechanical field:** The boundary portion $\partial\Omega_{\mathrm{motion},0}$ of $\mathscr{B}$ is subjected to a prescribed history of the boundary deformation measure $\boldsymbol{A}_{\mathrm{presc},0}(\boldsymbol{X}, t)$, where $\boldsymbol{A}_0 = \boldsymbol{N} \times \boldsymbol{F}$, $\boldsymbol{X} \in \partial\Omega_{\mathrm{motion},0}$, $t \in [t_0, t_{\mathrm{end}}]$,

- **Essential (or Dirichlet) boundary condition:**
  - **Mechanical field:** The boundary portion $\partial\Omega_{\mathrm{traction},0}$ of $\mathscr{B}$ is subjected to a prescribed stress potential field history, $\boldsymbol{Z}_{\mathrm{presc}}(\boldsymbol{X}, t)$.

It is also convenient to define the set of statically admissible stress potentials on $\mathscr{B}$ as the set of all sufficiently regular stress potentials that satisfy the corresponding essential boundary conditions

$$\mathscr{S}_Z \equiv \left\{ \boldsymbol{Z} : \Omega_0 \times \mathbb{R} \to \mathbb{R}^{3\times 3} \mid \boldsymbol{Z}(\boldsymbol{X},t) = \boldsymbol{Z}_{\text{presc}}(\boldsymbol{X},t),\ \boldsymbol{X} \in \partial\Omega_{\text{traction},0},\quad t \in [t_0, t_{\text{end}}] \right\}. \tag{2.124}$$

Given the less common nature of the stress-driven formulation, we provide some details on the derivation of the weak form of the compatibility condition, which is a key ingredient of the stress-driven thermomechanical constitutive initial boundary value problem. The strong form of the compatibility condition reads

$$\operatorname{curl}_0 \boldsymbol{F} = \boldsymbol{O}, \quad \text{in } \Omega_0. \tag{2.125}$$

Contracting this equation with an arbitrary second-order tensor field $\boldsymbol{\zeta}$ that vanishes on the portion of the boundary where stress potentials are prescribed, i.e., $\boldsymbol{\zeta} \in \mathscr{H}_{Z,0}$, such that

$$\mathscr{H}_{Z,0} \equiv \left\{ \boldsymbol{\zeta} : \Omega_0 \to \mathbb{R}^{3\times 3} \mid \boldsymbol{\zeta} = \boldsymbol{O} \quad \text{in} \quad \partial\Omega_{\text{traction},0} \right\}, \tag{2.126}$$

and integrating over the domain Ω_0, we obtain

$$\int_{\Omega_0} \boldsymbol{\zeta} : \operatorname{curl}_0 \boldsymbol{F}\ dv = 0, \quad \forall\, \boldsymbol{\zeta} \in \mathscr{H}_{Z,0}, \tag{2.127}$$

To obtain the weak form of the compatibility equation recall the following tensor identity

$$\operatorname{div}_0(\boldsymbol{A} \times \boldsymbol{B}) = \operatorname{curl}_0 \boldsymbol{A}\boldsymbol{B}^T - \boldsymbol{A}(\operatorname{curl}_0 \boldsymbol{B})^T, \tag{2.128}$$

where the divergence operator acts on the last leg of the third-order tensor $\boldsymbol{A} \times \boldsymbol{B}$, and $\boldsymbol{A}, \boldsymbol{B}$ are arbitrary second-order tensor fields.

To verify the identity, we use index notation and the recursive definition of the tensor cross-product (Equation (B.3)):

$$\begin{aligned}
(\operatorname{div}_0(\boldsymbol{A} \times \boldsymbol{B}))_{lm} &= (\varepsilon_{ijk} A_{li} B_{mj})_{,k} && (2.129)\\
&= \varepsilon_{ijk} A_{li,k} B_{mj} + \varepsilon_{ijk} A_{li} B_{mj,k} && (2.130)\\
&= \varepsilon_{kij} A_{li,k} B_{mj} - \varepsilon_{kji} A_{li} B_{mj,k} && (2.131)\\
&= (\operatorname{curl}_0 \boldsymbol{A})_{lj} B_{mj} - (\operatorname{curl}_0 \boldsymbol{B})_{mi} A_{li} && (2.132)\\
&= ((\operatorname{curl}_0 \boldsymbol{A})\boldsymbol{B}^T)_{lm} - (\boldsymbol{A}(\operatorname{curl}_0 \boldsymbol{B})^T)_{lm}. && (2.133)
\end{aligned}$$

Taking the trace of this identity, i.e, substituting m by l in the previous expressions, we obtain

$$\operatorname{tr}(\operatorname{div}_0(\boldsymbol{A} \times \boldsymbol{B})) = \operatorname{curl}_0 \boldsymbol{A} : \boldsymbol{B} - \boldsymbol{A} : \operatorname{curl}_0 \boldsymbol{B}. \tag{2.134}$$

Identifying $\boldsymbol{A}$ with $\boldsymbol{\zeta}$ and $\boldsymbol{B}$ with $\boldsymbol{F}$, we can now integrate this expression over the domain Ω_0, finding

$$\int_{\Omega_0} \operatorname{tr}(\operatorname{div}_0(\boldsymbol{\zeta} \times \boldsymbol{F}))\ dv = \int_{\Omega_0} \operatorname{curl}_0 \boldsymbol{\zeta} : \boldsymbol{F}\ dv - \int_{\Omega_0} \boldsymbol{\zeta} : \operatorname{curl}_0 \boldsymbol{F}\ dv. \tag{2.135}$$

Using the divergence theorem, the left-hand side can be converted into a surface integral. In index notation, it reads

$$\int_{\Omega_0} (\varepsilon_{ijk} \zeta_{li} F_{lj})_{,k}\ dv = \int_{\partial\Omega_0} \varepsilon_{ijk} \zeta_{li} F_{lj} N_k\ da. \tag{2.136}$$

Applying the definition of the cross product between a vector and a second-order tensor (Equation (B.3)), we can rewrite this as

$$\int_{\Omega_0} \operatorname{tr}(\operatorname{div}_0(\boldsymbol{\zeta} \times \boldsymbol{F})) = -\int_{\partial\Omega_0} \boldsymbol{\zeta} : (\boldsymbol{N} \times \boldsymbol{F})\ da. \tag{2.137}$$

Finally, combining the previous results, we obtain the integration by parts formula

$$\int_{\Omega_0} \boldsymbol{\zeta} : \operatorname{curl}_0 \boldsymbol{F} \, dv = \int_{\Omega_0} \operatorname{curl}_0 \boldsymbol{\zeta} : \boldsymbol{F} \, dv + \int_{\partial\Omega_0} \boldsymbol{\zeta} : (\boldsymbol{N} \times \boldsymbol{F}) \, da = 0. \tag{2.138}$$

From the boundary conditions introduced earlier, we identify

$$(\boldsymbol{N} \times \boldsymbol{F})(\boldsymbol{Y}, t) = \boldsymbol{A}_0(\boldsymbol{Y}, t), \quad \boldsymbol{Y} \in \partial\Omega_{\text{motion},0}, \tag{2.139}$$

yielding the final form of the weak compatibility condition

$$\int_{\Omega_0} \boldsymbol{\zeta} : \operatorname{curl}_0 \boldsymbol{F} \, dv = \int_{\Omega_0} \operatorname{curl}_0 \boldsymbol{\zeta} : \boldsymbol{F} \, dv + \int_{\partial\Omega_0} \boldsymbol{\zeta} : \boldsymbol{A}_0 \, da = 0, \tag{2.140}$$

In the context of standard solid mechanics, it is typically assumed that there are no incompatibilities, with the strain-driven formulation ensuring compatibility by construction. However, in the stress-driven formulation, compatibility must be explicitly enforced through the weak form derived above. For related discussions in the small-strain setting, we refer to the work of Eshelby (1956) on the continuum theory of lattice defects, where incompatibilities serve as a model for defect fields.

Finally, the weak form of the thermomechanical constitutive initial boundary value problem can be stated in a material description as follows

Problem 2.5 | Stress-driven material thermomechanical initial BVP.

Find a statically admissible stress potential function, $\boldsymbol{Z} \in \mathscr{S}_Z$, and an admissible temperature distribution, $T \in \mathscr{K}_T$, such that for every $t \in [t_0, t_{\text{end}}]$, the body $\mathscr{B}$ is compatible and in energetic equilibrium

$$\int_{\Omega_0} [\boldsymbol{F}(t) : \operatorname{curl}_0 \boldsymbol{\zeta}] \, \mathrm{d}v + \int_{\partial\Omega_0} \boldsymbol{A}_0(t) : \boldsymbol{\zeta} \, \mathrm{d}a = 0, \quad \forall \boldsymbol{\zeta} \in \mathscr{H}_{Z,0}, \tag{2.141}$$

$$\int_{\Omega_0} \Big[\Big((\rho_0 C_{\boldsymbol{P}}(t) - \operatorname{curl}_0 \boldsymbol{Z}(t) : \boldsymbol{\alpha}_{\boldsymbol{F}}(t)) \dot{T}(t) + T(t) \boldsymbol{\alpha}_{\boldsymbol{F}}(t) : \dot{\boldsymbol{P}}(t) - \mathcal{D}_{\text{int}}(t) - \mathcal{K}^{\text{ep}}(t) - \rho_0 r(t) \Big) \xi - \boldsymbol{k}(t) \cdot \nabla_0 \xi \Big] \, \mathrm{d}v - \int_{\partial\Omega_0} h_0(t) \xi \, \mathrm{d}a = 0, \quad \forall \xi \in \mathscr{V}_{T,0}, \tag{2.142}$$

where the space of virtual stress potentials at time t is defined by

$$\mathscr{H}_{Z,0} \equiv \left\{ \boldsymbol{\zeta} : \Omega_0 \to \mathbb{R}^{3\times 3} \mid \boldsymbol{\zeta} = \boldsymbol{O} \quad \text{in} \quad \partial\Omega_{\text{traction},0} \right\}, \tag{2.143}$$

the space of virtual temperatures at time t is defined by

$$\mathscr{V}_{T,0} \equiv \left\{ \xi : \Omega_0 \to \mathbb{R} \mid \xi = 0 \quad \text{in} \quad \partial\Omega_{\text{temperature},0} \right\}, \tag{2.144}$$

and at each point of $\mathscr{B}$, the deformation gradient tensor is the solution of material thermomechanical constitutive initial value problem (Problem 2.2).

Making use of the time discretization procedure described in Section 2.5.1, one can state the weak form of the stress-driven material incremental thermomechanical initial boundary value problem in the material description as

Problem 2.6 | Stress-driven material incremental thermomechanical initial BVP.

Given the set of internal variables $\boldsymbol{\alpha}_n$ at t_n, the prescribed field $\boldsymbol{A}_{0,n+1}$, as well as the prescribed heat sources, r_{n+1} and heat fluxes, $h_{0,n+1}$, at t_{n+1}, find the statically admissible stress potential field $\boldsymbol{Z}_{n+1} \in \mathscr{S}_{Z,n+1}$ and the admissible temperature distribution $T_{n+1} \in \mathscr{K}_{T,n+1}$ such that the body $\mathscr{B}$ is in mechanical and energetic equilibrium

$$\int_{\Omega_0} [\hat{\boldsymbol{F}}(\boldsymbol{P}(\boldsymbol{Z}_{n+1}), T_{n+1}, \boldsymbol{\alpha}_n) : \operatorname{curl}_0 \boldsymbol{\zeta}] \, \mathrm{d}v + \int_{\partial\Omega_0} \boldsymbol{A}_{0,n+1} : \boldsymbol{\zeta} \, \mathrm{d}a = 0, \quad \forall \boldsymbol{\zeta} \in \mathscr{H}_{Z,n+1}, \tag{2.145}$$

$$\begin{aligned} \int_{\Omega_0} \Big[\Big(& (\rho_0 C_{\boldsymbol{P},n+1} - \operatorname{curl}_0 \boldsymbol{Z}_{n+1} : \boldsymbol{\alpha}_{\boldsymbol{F},n+1}) \dot{T}_{n+1} \\ & + T_{n+1} \boldsymbol{\alpha}_{\boldsymbol{F},n+1} : \operatorname{curl}_0 \dot{\boldsymbol{Z}}_{n+1} - \mathcal{D}_{\mathrm{int},n+1} - \mathcal{K}^{\mathrm{ep}}_{n+1} - \rho_0 r_{n+1} \Big) \xi \\ & - \hat{\boldsymbol{k}}(\boldsymbol{P}(\boldsymbol{Z}_{n+1}), T_{n+1}, \boldsymbol{\alpha}_n) \cdot \nabla_0 \xi \Big] \, \mathrm{d}v - \int_{\partial\Omega_0} h_{0,n+1} \xi \, \mathrm{d}a = 0, \quad \forall \xi \in \mathscr{V}_{T,n+1}, \end{aligned} \tag{2.146}$$

where

$$\mathscr{S}_{Z,n+1} \equiv \left\{ \boldsymbol{Z}_{n+1} : \Omega_0 \to \mathbb{R}^{3\times 3} \mid \boldsymbol{Z}_{n+1}(\boldsymbol{X}) = \boldsymbol{Z}_{\mathrm{presc},n+1}(\boldsymbol{X}),\ \boldsymbol{X} \in \partial\Omega_{\mathrm{traction},0} \right\}, \tag{2.147}$$

$$\mathscr{K}_{T,n+1} \equiv \left\{ T_{n+1} : \Omega_0 \to \mathbb{R} \mid T_{n+1}(\boldsymbol{X}) = T_{\mathrm{presc},n+1}(\boldsymbol{X}),\ \boldsymbol{X} \in \partial\Omega_{\mathrm{temperature},0} \right\}. \tag{2.148}$$

and

$$\boldsymbol{\alpha}_{n+1} = \hat{\boldsymbol{\alpha}}(\boldsymbol{P}(\boldsymbol{Z}_{n+1}), T_{n+1}, \boldsymbol{\alpha}_n). \tag{2.149}$$

Page intentionally left blank.

Chapter 3

Principle of Multiscale Virtual Power and its dual

3.1 Principle of Multiscale Virtual Power

The following description of the PMVP is based on the works of de Souza Neto and Feijóo (2008); de Souza Neto et al. (2015); Blanco et al. (2016b).

Consider a body occupying a domain $\Omega_0 \subset \mathbb{R}^3$ in its reference configuration. Associated with each macroscopic material point $\boldsymbol{X} \in \Omega_0$, we assume the existence of a representative volume element (RVE), denoted by $\Omega_{0,\mu}$, whose characteristic length ℓ_μ is much smaller than the characteristic length of the macroscopic body, ℓ, i.e., $\ell_\mu \ll \ell$. To clearly distinguish between the macro- and microscales, we adopt the subscript μ for microscopic quantities, and denote macroscopic and microscopic material points by $\boldsymbol{X}$ and $\boldsymbol{Y}$, respectively.

3.1.1 Constitutive description at the microscale

At the microscale, we model the mechanical behavior of the material at point $\boldsymbol{Y}$ in $\Omega_{0,\mu}$ using the internal-variable description of Chapter 2.

3.1.2 Kinematical insertion

Consider an RVE associated with a macroscopic material point $\boldsymbol{X} \in \Omega_0$, subjected to a macroscopic deformation gradient $\boldsymbol{F}(\boldsymbol{X}, t)$. The procedure of *kinematical insertion* establishes a connection between macroscopic kinematical quantities and their microscopic counterparts.

We assume that all points within the RVE, $\boldsymbol{Y} \in \Omega_{0,\mu}$, undergo a linear displacement field $\boldsymbol{u}^{\text{lin}}$, defined as

$$\boldsymbol{u}^{\text{lin}} = \big(\boldsymbol{F}(\boldsymbol{X}, t) - \boldsymbol{I}\big)\,(\boldsymbol{Y} - \boldsymbol{Y}_0), \tag{3.1}$$

where $\boldsymbol{Y}_0$ denotes the centroid of the RVE domain $\Omega_{0,\mu}$, given by

$$\boldsymbol{Y}_0 = \frac{1}{|\Omega_{0,\mu}|}\int_{\Omega_{0,\mu}} \boldsymbol{Y}\, dv, \tag{3.2}$$

and $|\Omega_{0,\mu}|$ is the volume of the RVE.

To ensure local equilibrium, we superimpose a fluctuation field $\tilde{\boldsymbol{u}}_\mu$ onto the linear displacement. The total microscopic displacement field is then expressed as

$$\boldsymbol{u}_\mu(\boldsymbol{Y},t) = \boldsymbol{u}(\boldsymbol{X},t) + \big(\boldsymbol{F}(\boldsymbol{X},t) - \boldsymbol{I}\big)(\boldsymbol{Y}-\boldsymbol{Y}_0) + \tilde{\boldsymbol{u}}_\mu(\boldsymbol{Y},t), \tag{3.3}$$

where $\boldsymbol{u}(\boldsymbol{X},t)$ is the macroscopic displacement at the RVE center.

From this decomposition, the microscopic deformation gradient is obtained as

$$\boldsymbol{F}_\mu(\boldsymbol{Y}) = \boldsymbol{F} + \nabla_0 \tilde{\boldsymbol{u}}_\mu(\boldsymbol{Y}), \tag{3.4}$$

where, for brevity, the explicit dependence on $\boldsymbol{X}$ and t has been omitted. The operator ∇_0 denotes the gradient with respect to the reference configuration coordinates of the microscale.

Kinematical homogenization and admissibility

In addition to the previous kinematical assumptions, we postulate that the macroscopic displacement and deformation gradient are given by the volume averages of their microscopic counterparts. Accordingly, the homogenization rules are expressed as

$$\boldsymbol{u} = \frac{1}{|\Omega_{0,\mu}|}\int_{\Omega_{0,\mu}} \boldsymbol{u}_\mu \, dv, \tag{3.5}$$

and

$$\boldsymbol{F} = \frac{1}{|\Omega_{0,\mu}|}\int_{\Omega_{0,\mu}} \boldsymbol{F}_\mu \, dv. \tag{3.6}$$

The adoption of Equations (3.5) and (3.6) as homogenization relations imposes constraints on the microscopic displacement field. These admissibility conditions can be conveniently expressed in terms of the fluctuation field $\tilde{\boldsymbol{u}}_\mu$ as

$$\int_{\Omega_{0,\mu}} \tilde{\boldsymbol{u}}_\mu \, dv = \boldsymbol{0}, \tag{3.7}$$

and

$$\int_{\Omega_{0,\mu}} \nabla_0 \tilde{\boldsymbol{u}}_\mu \, dv = \boldsymbol{0}, \tag{3.8}$$

which follow from combining the homogenization rules in Equations (3.5) and (3.6) with the displacement and deformation gradient decompositions in Equations (3.3) and (3.4), respectively. In turn, the space of admissible fluctuation fields, denoted by $\tilde{\mathscr{K}}_\mu$, is the linear subspace of $\boldsymbol{H}^1(\Omega_{0,\mu})$ defined by

$$\tilde{\mathscr{K}}_\mu = \left\{ \boldsymbol{v} \in \boldsymbol{H}^1(\Omega_{0,\mu}) \;\middle|\; \int_{\Omega_{0,\mu}} \boldsymbol{v} \, dv = \boldsymbol{0}, \quad \int_{\Omega_{0,\mu}} \nabla_0 \boldsymbol{v} \, dv = \boldsymbol{0} \right\}, \tag{3.9}$$

where $\boldsymbol{H}^1(\Omega_{0,\mu})$ denotes the Sobolev space of vector-valued functions $\tilde{\boldsymbol{u}} : \Omega_{0,\mu} \to \mathbb{R}^3$ with square-integrable first derivatives. The corresponding space of virtual kinematically admissible fluctuation fields, $\tilde{\mathscr{V}}_\mu$, is defined as

$$\tilde{\mathscr{V}}_\mu = \left\{ \boldsymbol{v} = \boldsymbol{v}_1 - \boldsymbol{v}_2 \;\middle|\; \boldsymbol{v}_1, \boldsymbol{v}_2 \in \tilde{\mathscr{K}}_\mu \right\} = \tilde{\mathscr{K}}_\mu, \tag{3.10}$$

which coincides with $\tilde{\mathscr{K}}_\mu$ due to the linearity and homogeneity of the admissibility conditions.

3.1.3 Principle of Multiscale Virtual Power

The PMVP enforces energetic consistency between the macroscopic and microscopic scales, equating the pointwise macroscopic stress virtual power to the volume average of the microscopic stress virtual power. This principle serves as a variational counterpart to the Hill–Mandel condition of macro-homogeneity (de Souza Neto and Feijóo, 2008), and is expressed as

$$\boldsymbol{P} : \delta \boldsymbol{F} = \frac{1}{|\Omega_{0,\mu}|} \int_{\Omega_{0,\mu}} \boldsymbol{P}_\mu : \left(\delta \boldsymbol{F} + \nabla_0 \delta \tilde{\boldsymbol{u}}_\mu \right) d v, \tag{3.11}$$

for all virtual macroscopic deformation gradients $\delta \boldsymbol{F} \in \mathbb{R}^{3\times 3}$ and all virtual microscopic fluctuation fields $\delta \tilde{\boldsymbol{u}}_\mu \in \tilde{\mathscr{V}}_\mu$, ignoring body force contributions, from a purely constitutive perspective.

Stress homogenization and microscopic equilibrium

From the PMVP, we can derive the macroscopic stress-homogenization rule by setting $\delta \tilde{\boldsymbol{u}}_\mu = \boldsymbol{0}$ and allowing arbitrary variations $\delta \boldsymbol{F}$,

$$\boldsymbol{P} = \frac{1}{|\Omega_{0,\mu}|} \int_{\Omega_{0,\mu}} \boldsymbol{P}_\mu \, d v. \tag{3.12}$$

Conversely, by setting $\delta \boldsymbol{F} = \boldsymbol{0}$ and considering arbitrary admissible fluctuation fields $\delta \tilde{\boldsymbol{u}}_\mu \in \tilde{\mathscr{V}}_\mu$, we obtain the microscopic equilibrium condition

$$\int_{\Omega_{0,\mu}} \boldsymbol{P}_\mu : \nabla_0 \delta \tilde{\boldsymbol{u}}_\mu \, d v = 0, \quad \forall \delta \tilde{\boldsymbol{u}}_\mu \in \tilde{\mathscr{V}}_\mu. \tag{3.13}$$

3.1.4 Balance of angular momentum

The homogenized first Piola–Kirchhoff stress tensor computed from Equation (3.12) must satisfy the macroscopic balance of angular momentum. In this section, we show that the homogenization rule for the first Piola–Kirchhoff stress derived from the PMVP leads to a macroscopic stress–deformation relation that satisfies the balance of angular momentum. For an alternative derivation of this result, the reader is referred to de Souza Neto et al. (2015).

Since we require that the angular momentum balance holds at the microscopic scale, from Equation (2.16) we have that

$$\int_{\Omega_{0,\mu}} \boldsymbol{P}_\mu \boldsymbol{F}_\mu^T \, d v = \int_{\Omega_{0,\mu}} (\boldsymbol{P}_\mu \boldsymbol{F}_\mu^T)^T \, d v, \tag{3.14}$$

after integration over the RVE domain $\Omega_{0,\mu}$. Taking into account the decomposition of the microscopic deformation gradient into its macroscopic and fluctuating parts, we can write

$$\frac{1}{|\Omega_{0,\mu}|} \int_{\Omega_{0,\mu}} \boldsymbol{P}_\mu \boldsymbol{F}_\mu^T \, d v = \frac{1}{|\Omega_{0,\mu}|} \int_{\Omega_{0,\mu}} \boldsymbol{P}_\mu (\boldsymbol{F} + \nabla_0 \tilde{\boldsymbol{u}}_\mu)^T \, d v \tag{3.15}$$

$$= \boldsymbol{P}\boldsymbol{F}^T + \frac{1}{|\Omega_{0,\mu}|} \int_{\Omega_{0,\mu}} \boldsymbol{P}_\mu (\nabla_0 \tilde{\boldsymbol{u}}_\mu)^T \, d v. \tag{3.16}$$

Hence, if we show that the last term is equal to zero, we can conclude that $\boldsymbol{P}\boldsymbol{F}^T$ is symmetric, because if

$$\boldsymbol{P}\boldsymbol{F}^T = \frac{1}{|\Omega_{0,\mu}|} \int_{\Omega_{0,\mu}} \boldsymbol{P}_\mu \boldsymbol{F}_\mu^T \, d v, \tag{3.17}$$

then

$$\left(\boldsymbol{P}\boldsymbol{F}^T\right)^T = \left(\frac{1}{|\Omega_{0,\mu}|}\int_{\Omega_{0,\mu}} \boldsymbol{P}_\mu \boldsymbol{F}_\mu^T \, dv\right)^T \tag{3.18}$$

$$= \frac{1}{|\Omega_{0,\mu}|}\int_{\Omega_{0,\mu}} (\boldsymbol{P}_\mu \boldsymbol{F}_\mu^T)^T \, dv \tag{3.19}$$

$$= \frac{1}{|\Omega_{0,\mu}|}\int_{\Omega_{0,\mu}} \boldsymbol{P}_\mu \boldsymbol{F}_\mu^T \, dv \tag{3.20}$$

$$= \boldsymbol{P}\boldsymbol{F}^T, \tag{3.21}$$

and thus the macroscopic balance of angular momentum is satisfied.

To this end, we consider the weak equilibrium condition in Equation (3.13), and select a virtual variation $\delta\tilde{\boldsymbol{u}}_\mu = \boldsymbol{C}\tilde{\boldsymbol{u}}_\mu$, with $\boldsymbol{C}$ an arbitrary second-order tensor and $\tilde{\boldsymbol{u}}_\mu \in \tilde{\mathscr{K}}_\mu = \tilde{\mathscr{V}}_\mu$. To show that $\delta\tilde{\boldsymbol{u}}_\mu$ is an admissible variation, consider

$$\int_{\Omega_{0,\mu}} \boldsymbol{C}\tilde{\boldsymbol{u}}_\mu \, dv = \boldsymbol{C}\int_{\Omega_{0,\mu}} \tilde{\boldsymbol{u}}_\mu \, dv = \boldsymbol{0}, \tag{3.22}$$

and

$$\int_{\Omega_{0,\mu}} \nabla_0(\boldsymbol{C}\tilde{\boldsymbol{u}}_\mu) \, dv = \boldsymbol{C}\int_{\Omega_{0,\mu}} \nabla_0\tilde{\boldsymbol{u}}_\mu \, dv = \boldsymbol{0}, \tag{3.23}$$

since $\tilde{\boldsymbol{u}}_\mu \in \tilde{\mathscr{K}}_\mu = \tilde{\mathscr{V}}_\mu$. Then, we have from Equation (3.13) that

$$\int_{\Omega_{0,\mu}} \boldsymbol{P}_\mu : \nabla_0(\boldsymbol{C}\tilde{\boldsymbol{u}}_\mu) \, dv = 0, \tag{3.24}$$

which can be rearranged as

$$\int_{\Omega_{0,\mu}} \boldsymbol{P}_\mu(\nabla_0\tilde{\boldsymbol{u}}_\mu)^T \, dv : \boldsymbol{C} = 0, \tag{3.25}$$

and since $\boldsymbol{C}$ is arbitrary, we conclude that

$$\int_{\Omega_{0,\mu}} \boldsymbol{P}_\mu(\nabla_0\tilde{\boldsymbol{u}}_\mu)^T \, dv = \boldsymbol{0}. \tag{3.26}$$

In summary, it is shown that

$$\boldsymbol{P}\boldsymbol{F}^T = (\boldsymbol{P}\boldsymbol{F}^T)^T, \tag{3.27}$$

i.e., the macroscopic first Piola–Kirchhoff stress and deformation gradient satisfy the balance of angular momentum.

3.2 Principle of Multiscale Complementary Virtual Power

Complementary variational principles in single-scale finite elasticity have been the subject of several contributions in the literature. Among these, Zubov (1970) was perhaps the first to introduce a formulation in terms of a stress potential $\boldsymbol{Z}$ with $\boldsymbol{P} = \mathrm{curl}_0\,\boldsymbol{Z}$ (see Appendix B.1 for the definition of the curl operator), where $\boldsymbol{Z}$ is a second-order tensor field whose curl yields the first Piola–Kirchhoff stress tensor. This approach was later revisited by Koiter (1973, 1976), who clarified the stationary (rather than extremal) character of the principle in the geometrically nonlinear setting. In parallel, de Veubeke (1972) showed that the canonical principle cannot be

reduced to a pure complementary-energy principle, and proposed a formulation involving the rotation as an independent variable.

In this work, we extend the stress-driven complementary viewpoint to the multiscale setting by introducing the PMCVP, the variational dual of the PMVP, which takes the stress-potential fluctuation as the primary microscopic variable.

3.2.1 Constitutive description at the microscale

At the microscale, we model the mechanical behavior of the material at point $\boldsymbol{Y}$ in $\Omega_{0,\mu}$ using the internal-variable description of Chapter 2.

3.2.2 Static insertion

We revisit the RVE associated with a point $\boldsymbol{X}$ in the macroscopic domain Ω_0, subjected to a macroscopic first Piola–Kirchhoff stress tensor $\boldsymbol{P}(\boldsymbol{X},t)$. Following an approach analogous to that of Section 3.1.2, we decompose the microscopic stress potential into a macroscopic contribution and a fluctuation component

$$\boldsymbol{Z}_\mu(\boldsymbol{Y},t) = \boldsymbol{Z}(\boldsymbol{X},t) + \frac{1}{2}\boldsymbol{P}(\boldsymbol{X},t)\times(\boldsymbol{Y}-\boldsymbol{Y}_0) + \tilde{\boldsymbol{Z}}_\mu(\boldsymbol{Y},t). \tag{3.28}$$

See Appendix B.1 for the definition of the cross product between a second-order tensor and a vector. In turn, the macroscopic contribution is composed of a linear contribution

$$\boldsymbol{Z}^{\text{lin}} = \frac{1}{2}\boldsymbol{P}(\boldsymbol{X},t)\times(\boldsymbol{Y}-\boldsymbol{Y}_0), \tag{3.29}$$

where $\boldsymbol{Y}_0$ denotes the centroid of the RVE, and a constant contribution, the macroscopic stress potential at point $\boldsymbol{X}$, $\boldsymbol{Z}(\boldsymbol{X},t)$.

Taking the curl of Equation (3.28) yields the following expression for the microscopic first Piola–Kirchhoff stress tensor

$$\begin{aligned}
\boldsymbol{P}_\mu(\boldsymbol{Y},t) &= \operatorname{curl}_0 \boldsymbol{Z}_\mu(\boldsymbol{Y},t) && (3.30)\\
&= \operatorname{curl}_0 \boldsymbol{Z}(\boldsymbol{X},t) + \operatorname{curl}_0\left(\frac{1}{2}\boldsymbol{P}(\boldsymbol{X},t)\times(\boldsymbol{Y}-\boldsymbol{Y}_0)\right) + \operatorname{curl}_0 \tilde{\boldsymbol{Z}}_\mu(\boldsymbol{Y},t) && (3.31)\\
&= \boldsymbol{P}(\boldsymbol{X},t) + \operatorname{curl}_0 \tilde{\boldsymbol{Z}}_\mu(\boldsymbol{Y},t), && (3.32)
\end{aligned}$$

where we used

$$\operatorname{curl}_0 \boldsymbol{Z}^{\text{lin}} = \operatorname{curl}_0\left(\frac{1}{2}\boldsymbol{P}\times(\boldsymbol{Y}-\boldsymbol{Y}_0)\right) = \boldsymbol{P}. \tag{3.33}$$

See Appendix B.2 for the proof of this identity. Note that $\operatorname{div}_0 \boldsymbol{P}_\mu = \operatorname{div}_0(\boldsymbol{P} + \operatorname{curl}_0 \tilde{\boldsymbol{Z}}_\mu) = 0$, so the microscopic stresses are in equilibrium by construction.

Static homogenization and admissibility

In the context of static homogenization, we postulate that the macroscopic stress potential and stress tensors are given by the volume averages of their microscopic counterparts

$$\boldsymbol{Z} = \frac{1}{|\Omega_{0,\mu}|}\int_{\Omega_{0,\mu}} \boldsymbol{Z}_\mu \, dv, \tag{3.34}$$

$$\boldsymbol{P} = \frac{1}{|\Omega_{0,\mu}|} \int_{\Omega_{0,\mu}} \boldsymbol{P}_\mu \, dv. \tag{3.35}$$

Here, the stress-homogenization rule is introduced as a postulate. Equations (3.34) and (3.35) impose static constraints on the microscopic stress potential field, thus defining conditions for its admissibility. By employing the decomposition of the microscopic stress potential field in Equation (3.28), these constraints can be reformulated in terms of the fluctuation field $\tilde{\boldsymbol{Z}}_\mu$ as

$$\int_{\Omega_{0,\mu}} \tilde{\boldsymbol{Z}}_\mu \, dv = \boldsymbol{0}, \tag{3.36}$$

$$\int_{\Omega_{0,\mu}} \operatorname{curl}_0 \tilde{\boldsymbol{Z}}_\mu \, dv = \boldsymbol{0}. \tag{3.37}$$

We now define the space of admissible stress-potential fluctuations $\tilde{\mathscr{S}}_\mu$ as the set of fluctuation fields satisfying the static admissibility constraints

$$\tilde{\mathscr{S}}_\mu = \left\{ \boldsymbol{T} \in \mathbf{H}(\operatorname{curl}_0, \Omega_{0,\mu}) \;\middle|\; \int_{\Omega_{0,\mu}} \boldsymbol{T} \, dv = \boldsymbol{0}, \int_{\Omega_{0,\mu}} \operatorname{curl}_0 \boldsymbol{T} \, dv = \boldsymbol{0} \right\}, \tag{3.38}$$

where $\mathbf{H}(\operatorname{curl}_0, \Omega_{0,\mu})$ denotes the Sobolev space of second-order tensor fields with square-integrable curl.

The corresponding space of virtual statically admissible stress-potential fluctuations, $\tilde{\mathscr{H}}_\mu$, is defined as

$$\tilde{\mathscr{H}}_\mu = \left\{ \boldsymbol{T} = \boldsymbol{T}_1 - \boldsymbol{T}_2 \;\middle|\; \boldsymbol{T}_1, \boldsymbol{T}_2 \in \tilde{\mathscr{S}}_\mu \right\} = \tilde{\mathscr{S}}_\mu, \tag{3.39}$$

which coincides with $\tilde{\mathscr{S}}_\mu$ due to the linearity and homogeneity of the imposed static constraints.

3.2.3 Principle of Multiscale Complementary Virtual Power

The PMCVP, analogous to the PMVP, enforces energetic consistency between the macroscopic and microscopic scales. It constitutes a variational statement that is equivalent to the complementary Hill–Mandel condition of macro-homogeneity and is expressed as

$$\delta \boldsymbol{P} : \boldsymbol{F} = \frac{1}{|\Omega_{0,\mu}|} \int_{\Omega_{0,\mu}} (\delta \boldsymbol{P} + \operatorname{curl}_0 \delta \tilde{\boldsymbol{Z}}_\mu) : \boldsymbol{F}_\mu \, dv, \tag{3.40}$$

for all virtual macroscopic stress tensors $\delta \boldsymbol{P} \in \mathbb{R}^{3\times 3}$, and all virtual microscopic stress-potential fluctuation fields $\delta \tilde{\boldsymbol{Z}}_\mu \in \tilde{\mathscr{H}}_\mu$.

Deformation homogenization and microscopic compatibility

We derive the deformation homogenization rule from the PMCVP by setting $\delta \tilde{\boldsymbol{Z}}_\mu = \boldsymbol{0}$ and allowing arbitrary variations $\delta \boldsymbol{P}$, yielding

$$\boldsymbol{F} = \frac{1}{|\Omega_{0,\mu}|} \int_{\Omega_{0,\mu}} \boldsymbol{F}_\mu \, dv. \tag{3.41}$$

Conversely, by setting $\delta \boldsymbol{P} = \boldsymbol{0}$ and considering arbitrary statically admissible virtual stress-potential fluctuation fields $\delta \tilde{\boldsymbol{Z}}_\mu \in \tilde{\mathscr{H}}_\mu$, we obtain the microscopic compatibility equation

$$\int_{\Omega_{0,\mu}} \operatorname{curl}_0 \delta \tilde{\boldsymbol{Z}}_\mu : \boldsymbol{F}_\mu \, dv = 0, \quad \forall \delta \tilde{\boldsymbol{Z}}_\mu \in \tilde{\mathscr{H}}_\mu. \tag{3.42}$$

For further discussion on the interpretation of Equation (3.42), see Section 2.6.3.

3.2.4 Balance of angular momentum

In this section, we demonstrate that the macroscopic stress and deformation gradient tensors obtained from the homogenization rules in Equations (3.35) and (3.41), respectively, satisfy the macroscopic angular momentum balance.

Starting from the split of the microscopic stress tensor in Equation (3.30), we write

$$\begin{aligned}\frac{1}{|\Omega_{0,\mu}|}\int_{\Omega_{0,\mu}} \boldsymbol{P}_\mu \boldsymbol{F}_\mu^T \, d\upsilon &= \frac{1}{|\Omega_{0,\mu}|}\int_{\Omega_{0,\mu}} (\boldsymbol{P} + \operatorname{curl}_0 \tilde{\boldsymbol{Z}}_\mu)\boldsymbol{F}_\mu^T \, d\upsilon \\ &= \boldsymbol{P}\boldsymbol{F}^T + \frac{1}{|\Omega_{0,\mu}|}\int_{\Omega_{0,\mu}} \operatorname{curl}_0 \tilde{\boldsymbol{Z}}_\mu \boldsymbol{F}_\mu^T \, d\upsilon. \end{aligned} \tag{3.43}$$

Our objective is to show that the second term on the right-hand side vanishes. Note that any admissible fluctuation field $\tilde{\boldsymbol{Z}}_\mu \in \tilde{\mathscr{V}}_\mu$ also belongs to $\tilde{\mathscr{H}}_\mu$, the space of virtual stress-potential fluctuation fields. Therefore, the microscopic compatibility equation in Equation (3.42) applies.

However, while Equation (3.42) is expressed in terms of a double contraction, Equation (3.43) involves a matrix product. To bridge this gap, we consider an arbitrary constant second-order tensor $\boldsymbol{C}$, and observe that the field $\boldsymbol{C}^T\tilde{\boldsymbol{Z}}_\mu$ is also admissible

$$\int_{\Omega_{0,\mu}} \boldsymbol{C}^T \tilde{\boldsymbol{Z}}_\mu \, d\upsilon = \boldsymbol{C}^T \int_{\Omega_{0,\mu}} \tilde{\boldsymbol{Z}}_\mu \, d\upsilon = \boldsymbol{0}, \tag{3.44}$$

$$\int_{\Omega_{0,\mu}} \operatorname{curl}_0(\boldsymbol{C}^T \tilde{\boldsymbol{Z}}_\mu) \, d\upsilon = \boldsymbol{C}^T \int_{\Omega_{0,\mu}} \operatorname{curl}_0 \tilde{\boldsymbol{Z}}_\mu \, d\upsilon = \boldsymbol{0}. \tag{3.45}$$

Hence, $\boldsymbol{C}^T\tilde{\boldsymbol{Z}}_\mu \in \tilde{\mathscr{H}}_\mu$ and satisfies

$$\int_{\Omega_{0,\mu}} \operatorname{curl}_0(\boldsymbol{C}^T \tilde{\boldsymbol{Z}}_\mu) : \boldsymbol{F}_\mu \, d\upsilon = 0. \tag{3.46}$$

Since $\boldsymbol{C}$ is constant, we can write

$$\int_{\Omega_{0,\mu}} (\boldsymbol{C}^T \operatorname{curl}_0 \tilde{\boldsymbol{Z}}_\mu) : \boldsymbol{F}_\mu \, d\upsilon = 0. \tag{3.47}$$

Using the identity for arbitrary second-order tensors $\boldsymbol{A}, \boldsymbol{B}, \boldsymbol{D}$

$$(\boldsymbol{D}^T\boldsymbol{A}) : \boldsymbol{B} = \boldsymbol{D} : (\boldsymbol{A}\boldsymbol{B}^T),$$

we rewrite Equation (3.47) as

$$\boldsymbol{C} : \int_{\Omega_{0,\mu}} \operatorname{curl}_0 \tilde{\boldsymbol{Z}}_\mu \boldsymbol{F}_\mu^T \, d\upsilon = 0. \tag{3.48}$$

Since $\boldsymbol{C}$ is arbitrary, we conclude that

$$\int_{\Omega_{0,\mu}} \operatorname{curl}_0 \tilde{\boldsymbol{Z}}_\mu \boldsymbol{F}_\mu^T \, d\upsilon = \boldsymbol{0}. \tag{3.49}$$

Substituting back into Equation (3.43), we obtain

$$\boldsymbol{P}\boldsymbol{F}^T = \frac{1}{|\Omega_{0,\mu}|}\int_{\Omega_{0,\mu}} \boldsymbol{P}_\mu \boldsymbol{F}_\mu^T \, d\upsilon. \tag{3.50}$$

Finally, invoking the pointwise angular momentum balance condition at the microscale in Equation (2.52), we have

$$\boldsymbol{P}\boldsymbol{F}^T = \frac{1}{|\Omega_{0,\mu}|}\int_{\Omega_{0,\mu}} \boldsymbol{P}_\mu \boldsymbol{F}_\mu^T \, dv \tag{3.51}$$

$$= \frac{1}{|\Omega_{0,\mu}|}\int_{\Omega_{0,\mu}} (\boldsymbol{P}_\mu \boldsymbol{F}_\mu^T)^T \, dv \tag{3.52}$$

$$= \left(\frac{1}{|\Omega_{0,\mu}|}\int_{\Omega_{0,\mu}} \boldsymbol{P}_\mu \boldsymbol{F}_\mu^T \, dv\right)^T \tag{3.53}$$

$$= (\boldsymbol{P}\boldsymbol{F}^T)^T. \tag{3.54}$$

This confirms that the homogenized stress and deformation gradient satisfy the macroscopic angular momentum balance.

Table 3.1 summarizes the main equations of the PMVP and PMCVP, while also emphasizing their duality.

Table 3.1: Duality between the Principle of Multiscale Virtual Power (PMVP) and the Principle of Multiscale Complementary Virtual Power (PMCVP).

PMVP (Kinematic)	**PMCVP (Static)**
Kinematical insertion $\boldsymbol{u}_\mu(\boldsymbol{Y},t) = \boldsymbol{u}(\boldsymbol{X},t)$ $+\left(\boldsymbol{F}(\boldsymbol{X},t)-\boldsymbol{I}\right)(\boldsymbol{Y}-\boldsymbol{Y}_0)+\tilde{\boldsymbol{u}}_\mu(\boldsymbol{Y},t)$ $\boldsymbol{F}_\mu(\boldsymbol{Y},t) = \boldsymbol{F}(\boldsymbol{X},t)+\nabla_0\tilde{\boldsymbol{u}}_\mu(\boldsymbol{Y},t)$	Static insertion $\boldsymbol{Z}_\mu(\boldsymbol{Y},t) = \boldsymbol{Z}(\boldsymbol{X},t)$ $+\frac{1}{2}\boldsymbol{P}(\boldsymbol{X},t)\times(\boldsymbol{Y}-\boldsymbol{Y}_0)+\tilde{\boldsymbol{Z}}_\mu(\boldsymbol{Y},t)$ $\boldsymbol{P}_\mu(\boldsymbol{Y},t) = \boldsymbol{P}(\boldsymbol{X},t)+\operatorname{curl}_0\tilde{\boldsymbol{Z}}_\mu(\boldsymbol{Y},t)$
Kinematical homogenization $\boldsymbol{F} = \dfrac{1}{\lvert\Omega_{0,\mu}\rvert}\displaystyle\int_{\Omega_{0,\mu}}\boldsymbol{F}_\mu\,dv$	Static homogenization $\boldsymbol{P} = \dfrac{1}{\lvert\Omega_{0,\mu}\rvert}\displaystyle\int_{\Omega_{0,\mu}}\boldsymbol{P}_\mu\,dv$
Admissible displacement fluctuations $\tilde{\mathscr{K}}_\mu = \left\{\boldsymbol{v}\in\boldsymbol{H}^1(\Omega_{0,\mu}) \;\middle\vert\; \int_{\Omega_{0,\mu}}\boldsymbol{v}\,dv=\boldsymbol{0},\ \int_{\Omega_{0,\mu}}\nabla_0\boldsymbol{v}\,dv=\boldsymbol{0}\right\}$	Admissible stress-potential fluctuations $\tilde{\mathscr{S}}_\mu = \left\{\boldsymbol{T}\in\mathbf{H}(\operatorname{curl}_0,\Omega_{0,\mu}) \;\middle\vert\; \int_{\Omega_{0,\mu}}\boldsymbol{T}\,dv=\boldsymbol{0},\ \int_{\Omega_{0,\mu}}\operatorname{curl}_0\boldsymbol{T}\,dv=\boldsymbol{0}\right\}$
Principle of Multiscale Virtual Power $\boldsymbol{P}:\delta\boldsymbol{F} = \dfrac{1}{\lvert\Omega_{0,\mu}\rvert}\displaystyle\int_{\Omega_{0,\mu}}\boldsymbol{P}_\mu:\left(\delta\boldsymbol{F}+\nabla_0\delta\tilde{\boldsymbol{u}}_\mu\right)dv$	Principle of Multiscale Complementary Virtual Power $\delta\boldsymbol{P}:\boldsymbol{F} = \dfrac{1}{\lvert\Omega_{0,\mu}\rvert}\displaystyle\int_{\Omega_{0,\mu}}(\delta\boldsymbol{P}+\operatorname{curl}_0\delta\tilde{\boldsymbol{Z}}_\mu):\boldsymbol{F}_\mu\,dv$
Stress homogenization $\boldsymbol{P} = \dfrac{1}{\lvert\Omega_{0,\mu}\rvert}\displaystyle\int_{\Omega_{0,\mu}}\boldsymbol{P}_\mu\,dv$	Deformation homogenization $\boldsymbol{F} = \dfrac{1}{\lvert\Omega_{0,\mu}\rvert}\displaystyle\int_{\Omega_{0,\mu}}\boldsymbol{F}_\mu\,dv$
Microscopic equilibrium (weak form) $\displaystyle\int_{\Omega_{0,\mu}}\boldsymbol{P}_\mu:\nabla_0\delta\tilde{\boldsymbol{u}}_\mu\,dv=0,\quad\forall\delta\tilde{\boldsymbol{u}}_\mu\in\tilde{\mathscr{V}}_\mu$	Microscopic compatibility (weak form) $\displaystyle\int_{\Omega_{0,\mu}}\operatorname{curl}_0\delta\tilde{\boldsymbol{Z}}_\mu:\boldsymbol{F}_\mu\,dv=0,\quad\forall\delta\tilde{\boldsymbol{Z}}_\mu\in\tilde{\mathscr{K}}_\mu$

Page intentionally left blank.

Chapter 4

Mean-field homogenization

MFH is a widely used technique to estimate the effective response of composite materials without resorting to full-field simulations. It relies on the existence of an RVE and, in general, exploits idealized spatial arrangements of the different material phases. The main advantages of MFH are its computational efficiency and the relatively simple microstructural discretization it requires. The presentation provided in this chapter is loosely based on Ortolano et al. (2013).

To carry out the MFH procedure, consider decomposing the RVE, $\Omega_{0,\mu}$, into n_P distinct phases. These occupy the non-overlapping subdomains $\Omega^i_{0,\mu}$ for $i = 1,\dots,n_P$, such that

$$\Omega_{0,\mu} = \bigcup_{i=1}^{n_P} \Omega^i_{0,\mu}, \quad \Omega^i_{0,\mu} \cap \Omega^j_{0,\mu} = \emptyset \quad \text{for } i \neq j. \tag{4.1}$$

We assume that the boundaries of these subdomains are sufficiently smooth. If a matrix phase exists[1], it is denoted by the superscript $(\bullet)^m$ (see Figure 4.1). The volume fraction of the i-th phase is given by

$$\phi^i_{0,\mu} = \frac{|\Omega^i_{0,\mu}|}{|\Omega_{0,\mu}|}. \tag{4.2}$$

Unlike full-field homogenization, MFH operates with average quantities over each phase. Accordingly, we define the average deformation gradient and the average first Piola–Kirchhoff stress in phase i, $i = 1,\dots,n_P$, as

$$\boldsymbol{F}^i_\mu(t) = \frac{1}{|\Omega^i_{0,\mu}|} \int_{\Omega^i_{0,\mu}} \boldsymbol{F}_\mu(\boldsymbol{Y},t)\, dv, \tag{4.3}$$

$$\boldsymbol{P}^i_\mu(t) = \frac{1}{|\Omega^i_{0,\mu}|} \int_{\Omega^i_{0,\mu}} \boldsymbol{P}_\mu(\boldsymbol{Y},t)\, dv. \tag{4.4}$$

In particular, we restrict our attention to so-called *first-moment* MFH schemes, in which the primary microscopic variables are the first moments of the deformation and stress fields inside each phase, i.e., the phase-averaged deformation gradients and stresses, $\boldsymbol{F}^i_\mu$ and $\boldsymbol{P}^i_\mu$, respectively (see Remark 4.2 for a discussion of second-moment approaches).

To perform mean-field homogenization, the mechanical interaction among phases is approximated using an interaction model. For each phase (excluding the matrix, when present), a single-inclusion initial-value problem (IVP) is solved. In this problem, the inclusion is

[1] The formulation described here remains applicable to materials without a clearly defined matrix phase (e.g., polycrystals), with only minor modifications.

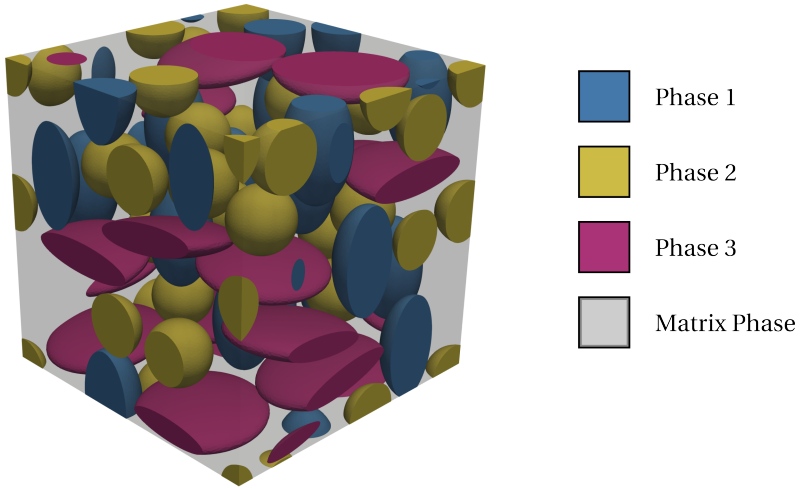

Figure 4.1: Illustration of the discretization of the RVE assumed in the mean-field homogenization procedure.

embedded in an unbounded, homogeneous, fictitious matrix that approximates the surrounding medium. The interaction with the remainder of the microstructure is then accounted for via the properties of this fictitious matrix and the loading conditions in the single-inclusion IVP.

4.1 Single-inclusion microscopic mechanical problems

This section provides a brief overview of the single-inclusion microscopic mechanical problems that underpin the various interaction models employed in the MFH framework. The solution to these problems is essential in the formulation of MFH and the use of different interaction models, as discussed in Section 4.2.

In a single-inclusion problem, we consider a two-phase composite material consisting of a single inclusion embedded within an infinite fictitious matrix. The inclusion represents one of the material phases present in the RVE, while the matrix serves as a homogenized representation of the remaining phases. Note that the fictitious matrix present in the single-inclusion problem does not necessarily coincide with the actual matrix phase of the RVE. Its material properties are chosen according to the interaction model being employed (see Section 4.2). In this work, however, the actual and fictitious matrix materials always share the same material properties—see the dilute interaction model and the Mori–Tanaka scheme (Table 4.1). In contrast, this equivalence would not hold in self-consistent schemes (Nemat-Nasser and Hori, 1993).

To ensure computational feasibility and efficiency, MFH is restricted to phase geometries that allow for simple solutions to the associated single-inclusion microscopic mechanical problems. In particular, the focus is on geometries that produce uniform deformation and stress fields within the inclusion, at least for small-strain linear elastic materials, such as ellipsoids and simple laminates.

The unbounded nature of the matrix renders the problem dependent on the average

deformation gradient and stress only. As a result, the governing problem is an IVP subject to suitable macroscopic loading conditions. These are imposed via the so-called *forcing macroscopic fields*, $\boldsymbol{F}^*$ and $\boldsymbol{P}^*$. Note that these are not necessarily the actual macroscopic fields $\boldsymbol{F}$ and $\boldsymbol{P}$, but rather are chosen according to the interaction model (see, e.g., Table 4.1) to drive the single-inclusion problems.

In a strain-driven setting, the single-inclusion problem associated with the i-th phase involves two phases: the i-th phase itself and an infinite fictitious matrix, denoted by the superscript $(\bullet)^{i,m,\mathrm{si}}$. The constitutive response of each phase is described via Equations (2.29) and (2.32), such that the stress tensors are functions of the respective deformation gradients, $\boldsymbol{F}_\mu^{i,\mathrm{si}}$ and $\boldsymbol{F}_\mu^{i,m,\mathrm{si}}$, and the internal variables, $\boldsymbol{\alpha}_\mu^{i,\mathrm{si}}$ and $\boldsymbol{\alpha}_\mu^{i,m,\mathrm{si}}$. Furthermore, the deformation gradient in the fictitious matrix, $\boldsymbol{F}_\mu^{i,m,\mathrm{si}}$, is expressed in terms of the inclusion's deformation gradient and the macroscopic forcing field $\boldsymbol{F}^*$, such that the volume-weighted average of the deformation gradients matches the prescribed macroscopic field

$$\boldsymbol{F}_\mu^{i,m,\mathrm{si}} = \frac{\boldsymbol{F}^* - \phi_{0,\mu}^i \boldsymbol{F}_\mu^{i,\mathrm{si}}}{\phi_{0,\mu}^{i,m,\mathrm{si}}}. \tag{4.5}$$

For a bounded inclusion such as an ellipsoid, $\phi_{0,\mu}^i = 0$ and $\phi_{0,\mu}^{i,m,\mathrm{si}} = 1$, yielding $\boldsymbol{F}_\mu^{i,m,\mathrm{si}} = \boldsymbol{F}^*$. In contrast, for unbounded inclusions such as in laminates, the appropriate volume fractions must be used in Equation (4.5) to recover the correct matrix deformation gradient. In a stress-driven setting, the single-inclusion problem is formulated analogously, with the stress in the inclusion and matrix phases denoted by $\boldsymbol{P}_\mu^{i,\mathrm{si}}$ and $\boldsymbol{P}_\mu^{i,m,\mathrm{si}}$, respectively.

We distinguish between two types of single-inclusion problems: those associated with simple laminates and those associated with ellipsoidal inclusions. The former are much simpler to solve, as the fields within each phase of the laminate are piecewise constant even in the nonlinear setting. For ellipsoidal inclusions, however, no exact solution is available in the nonlinear setting, and approximations must be employed to estimate the phase-averaged fields.

4.1.1 Simple laminates

As mentioned above, simple laminates are a special class of microstructures for which the deformation and stress fields are piecewise constant within each phase, regardless of the constitutive behavior. The single-inclusion problem associated with a simple laminate simplifies to the enforcement of equilibrium and compatibility across the interface between the two phases, which can be expressed as

$$\mathbf{P}_{N,\mu}^i : \boldsymbol{P}_\mu^{i,\mathrm{si}} = \mathbf{P}_{N,\mu}^i : \boldsymbol{P}_\mu^{i,m,\mathrm{si}}, \qquad \text{(equilibrium across the interface)} \tag{4.6}$$

$$\mathbf{P}_{T,\mu}^i : \boldsymbol{F}_\mu^{i,\mathrm{si}} = \mathbf{P}_{T,\mu}^i : \boldsymbol{F}_\mu^{i,m,\mathrm{si}}, \qquad \text{(compatibility along the interface)} \tag{4.7}$$

where $\mathbf{P}_{N,\mu}^i$ and $\mathbf{P}_{T,\mu}^i$ are the normal and tangential projection tensors associated with the lamination direction $\boldsymbol{N}_\mu^i$, defined as

$$\mathbf{P}_{N,\mu}^i : \boldsymbol{A} = \boldsymbol{A}\boldsymbol{N}_\mu^i, \quad \mathbf{P}_{T,\mu}^i : \boldsymbol{A} = \boldsymbol{A} - \mathbf{P}_{N,\mu}^i : \boldsymbol{A}, \quad \forall \boldsymbol{A} \in \mathbb{R}^{3\times 3}. \tag{4.8}$$

Since deformation and stress are constant within each phase of the laminate, these two equations are sufficient to enforce compatibility and equilibrium across the interface, thereby fully defining the microscopic mechanical IVP (Milton, 2004).

4.1.2 Ellipsoidal inclusions

For simple laminates, the single-inclusion problem admits an exact solution in which the fields within each phase are piecewise constant, irrespective of the constitutive laws employed. This is a direct consequence of the interface jump conditions and the translation invariance of the problem along the lamination plane (Milton, 2004). For ellipsoidal inclusions in small-strain linear elastic materials, Eshelby (1957) derived a closed-form solution for the interior fields, which are uniform and related to the far-field loading through the Eshelby tensor.

The extension of Eshelby's solution to nonlinear materials, whether hyperelastic at finite strain or dissipative, generally fails: the interior field is non-uniform, and no closed-form expression for the phase-averaged deformation gradient is available. The standard response in the MFH literature is to construct a *Linear Comparison Composite* (LCC), i.e., a fictitious linear composite whose phases have uniform moduli chosen to approximate the nonlinear behavior at the current loading state. The classical linear Eshelby solution is then applied to the LCC, yielding an estimate for the phase-averaged fields of the real nonlinear composite. The quality of this approximation depends on how the comparison moduli are defined—the so-called *linearization scheme*. In what follows, we summarize the principal first-moment linearization schemes available in the literature, all of which evaluate the comparison moduli at the *phase-averaged* fields (first statistical moments only). These schemes can be composed with any of the interaction models discussed in Section 4.2 to produce a complete MFH procedure.

Secant scheme. For each phase, the comparison moduli are defined as the *isotropic secant* moduli relating the current phase-averaged stress and strain through the origin. For J_2 plasticity, this amounts to replacing the phase elastic moduli with a reduced shear modulus that captures the chord slope of the current stress–strain response. The classical secant scheme is simple and naturally isotropic, avoiding the difficulties of anisotropic tangent operators in the Eshelby step, but it is restricted to *monotonic, proportional* loading paths since the secant relation presumes a single stress–strain direction. It also tends to produce overly stiff effective responses (Berveiller and Zaoui, 1978; Tandon and Weng, 1988). Wu, Noels, Adam and Doghri (2013) introduced a scheme that combines the load-path flexibility of incremental methods with the natural isotropy of secant methods.

Incremental tangent scheme. Introduced by Hill (1965a) in the context of polycrystal plasticity, this scheme uses the anisotropic tangent moduli of each phase, evaluated at the current phase-averaged state. Unlike the classical secant, the incremental tangent handles arbitrary loading paths, including cyclic and non-proportional ones. Its main drawback is that, for elastoplastic composites, it consistently over-predicts the effective stiffness. To mitigate the overstiffness of the incremental tangent scheme while retaining its flexibility across loading paths, several authors have proposed to project the anisotropic tangent onto the space of isotropic fourth-order tensors before using it in the Eshelby step (Doghri and Ouaar, 2003; Chaboche et al., 2005).

Affine scheme. Proposed by Masson, Bornert, Suquet and Zaoui (2000), the affine scheme linearizes each phase such that the stress obeys an affine law with respect to the strain. The affine law is defined by a tangent operator and a polarization stress chosen so that it passes through the current stress–strain point rather than through the origin. The affine scheme is generally softer and more accurate than the incremental tangent, handles cyclic loading naturally, and sits on firmer ground than the *ad hoc* isotropization of the tangent scheme. Pierard and Doghri (2006) refined the affine scheme with algorithmic improvements for

elasto-viscoplastic composites. Doghri, Adam and Bilger (2010) proposed an incremental variant.

4.1.3 Single-inclusion operator

We introduce the function $\mathscr{A}_\mu^{i,\mathrm{si}}$ that provides the inclusion's deformation gradient as a function of the loading conditions through the forcing deformation gradient, $\boldsymbol{F}^*$, and the internal variables, $\boldsymbol{\alpha}_\mu^{I,\mathrm{si}} = \{\boldsymbol{\alpha}_\mu^{i,\mathrm{si}}, \boldsymbol{\alpha}_\mu^{i,m,\mathrm{si}}\}$, associated with the single-inclusion problem,

$$\boldsymbol{F}_\mu^{i,\mathrm{si}} = \mathscr{A}_\mu^{i,\mathrm{si}}(\boldsymbol{F}^*, \boldsymbol{\alpha}_\mu^{I,\mathrm{si}}), \tag{4.9}$$

where we describe the constitutive behavior of each material phase by means of a formulation based on internal variables (see Chapter 2). This function is generally nonlinear, owing to both material and geometric nonlinearities. In a stress-driven setting, an analogous function $\mathscr{B}_\mu^{i,\mathrm{si}}$ can be defined to provide the inclusion's stress as a function of the applied stress field and internal variables

$$\boldsymbol{P}_\mu^{i,\mathrm{si}} = \mathscr{B}_\mu^{i,\mathrm{si}}(\boldsymbol{P}^*, \boldsymbol{\alpha}_\mu^{I,\mathrm{si}}). \tag{4.10}$$

For further details on specific models and solution strategies, see, for instance, Nemat-Nasser and Hori (1993) and Ortolano et al. (2013).

The equilibrium and compatibility equations for the single-inclusion problem can be implicitly written using a residual function $\mathscr{R}^{i,\mathrm{si}}$ as

$$\mathscr{R}^{i,\mathrm{si}}(\boldsymbol{F}_\mu^{i,\mathrm{si}}, \boldsymbol{P}_\mu^{i,\mathrm{si}}, \boldsymbol{F}_\mu^{i,m,\mathrm{si}}, \boldsymbol{P}_\mu^{i,m,\mathrm{si}}) = \boldsymbol{0}, \tag{4.11}$$

which depends on the average deformation gradients and stress tensors in each phase.

Substituting Equations (2.29) and (4.5) into Equation (4.11), the single-inclusion problem can be recast as

$$\mathscr{R}^{i,\mathrm{si}}(\boldsymbol{F}^*, \boldsymbol{F}_\mu^{i,\mathrm{si}}, \boldsymbol{\alpha}_\mu^{I,\mathrm{si}}) = \boldsymbol{0}, \tag{4.12}$$

where the set of internal variables $\boldsymbol{\alpha}_\mu^{I,\mathrm{si}} = \{\boldsymbol{\alpha}_\mu^{i,\mathrm{si}}, \boldsymbol{\alpha}_\mu^{i,m,\mathrm{si}}\}$ aggregates the state variables of both phases, with the superscript I indicating that this set corresponds to the single-inclusion problem for phase i. Applying the implicit function theorem (Garrity, 2002), we recover Equations (4.9) and (4.10), in which $\mathscr{A}_\mu^{i,\mathrm{si}}$ and $\mathscr{B}_\mu^{i,\mathrm{si}}$ represent the solutions to the corresponding single-inclusion IVPs.

Remark 4.1 | On the well-posedness of the single-inclusion operator

Equation (4.9) defines $\mathscr{A}_\mu^{i,\mathrm{si}}$ as the operator taking the forcing $\boldsymbol{F}^*$ and the phase-averaged internal variables $\boldsymbol{\alpha}_\mu^{I,\mathrm{si}}$ to the phase-averaged deformation gradient $\boldsymbol{F}_\mu^{i,\mathrm{si}}$ in the inclusion. In the stress-driven setting, $\mathscr{B}_\mu^{i,\mathrm{si}}$ is defined analogously, with the forcing field being the macroscopic stress $\boldsymbol{P}^*$ and the output being the phase-averaged stress $\boldsymbol{P}_\mu^{i,\mathrm{si}}$ in the inclusion. Since these operators are central pieces in the effort to integrate MFH into the PMVP and PMCVP variational frameworks, described in Chapter 5, it is important to clarify the sense in which they are well-defined.

1. In general, we cannot provide closed-form expressions for $\mathscr{A}_\mu^{i,\mathrm{si}}$ and $\mathscr{B}_\mu^{i,\mathrm{si}}$. For laminates, $\mathscr{A}_\mu^{i,\mathrm{si}}$ is defined implicitly through the interface compatibility condition in Equation (4.7), the traction equilibrium condition in Equation (4.6), and the phase constitutive laws. For ellipsoidal inclusions at finite strain, it is defined implicitly through an LCC problem.

2. No uniformity of fields within the inclusion is assumed. For laminates, uniformity is a consequence of translation invariance, not an assumption. For ellipsoidal inclusions at finite strain, interior fields are genuinely non-uniform, and MFH provides only an estimate of the phase-averaged fields. The classical Eshelby uniformity applies to the *LCC*, a linear approximation, and not to the actual nonlinear composite.

The single-inclusion operators $\mathscr{A}_\mu^{i,\mathrm{si}}$ and $\mathscr{B}_\mu^{i,\mathrm{si}}$ are useful objects in the formulation of MFH within the PMVP and PMCVP variational frameworks, as they provide a compact notation for the solution, i.e., the average deformation and stress, of the single-inclusion problems.

4.2 Interaction models

Assuming the IVPs described earlier can be efficiently solved for the microstructural phase geometries, we now turn to formulating the interaction models. These models provide estimates of the average deformation and stress fields in each phase, denoted by $\boldsymbol{F}_\mu^{i,\mathrm{mfh}}$ and $\boldsymbol{P}_\mu^{i,\mathrm{mfh}}$, respectively. These auxiliary quantities are later used in the homogenization procedures.

We assume the existence of a true matrix phase, indexed by m, and consider two types of macroscopic control: strain-driven and stress-driven. In the strain-driven setting, the interaction model must satisfy the self-consistency condition

$$\boldsymbol{F} = \langle \boldsymbol{F}_\mu^{i,\mathrm{mfh}} \rangle = \sum_{i=1}^{n_P} \phi_{0,\mu}^i \boldsymbol{F}_\mu^{i,\mathrm{mfh}}, \tag{4.13}$$

whereas in the stress-driven setting, the corresponding condition is

$$\boldsymbol{P} = \langle \boldsymbol{P}_\mu^{i,\mathrm{mfh}} \rangle = \sum_{i=1}^{n_P} \phi_{0,\mu}^i \boldsymbol{P}_\mu^{i,\mathrm{mfh}}. \tag{4.14}$$

We are particularly interested in the instantaneous strain and stress localization tensors implied by the interaction models, as these are required in the homogenization strategies discussed in Chapter 5.

Let $\mathscr{A}_\mu^{i,\mathrm{mfh}}$ be the function mapping the macroscopic deformation gradient $\boldsymbol{F}$ to the MFH average deformation in the i-th inclusion phase

$$\boldsymbol{F}_\mu^{i,\mathrm{mfh}} = \mathscr{A}_\mu^{i,\mathrm{mfh}}(\boldsymbol{F}, \boldsymbol{\alpha}_\mu^{\mathrm{mfh}}) = \mathscr{A}_\mu^{i,\mathrm{si}}\left(\boldsymbol{F}^*(\boldsymbol{F}, \boldsymbol{F}_\mu^{\mathrm{mfh}}, \boldsymbol{\alpha}_\mu^{\mathrm{mfh}}), \boldsymbol{\alpha}_\mu^{I,\mathrm{si}}\right), \tag{4.15}$$

where $\boldsymbol{\alpha}_\mu^{\mathrm{mfh}} = \{\boldsymbol{\alpha}_\mu^{I,\mathrm{si}}\}_{I=1}^{n_P}$ is the family of all internal variables from the single-inclusion problems and $\boldsymbol{F}_\mu^{\mathrm{mfh}} = \{\boldsymbol{F}_\mu^{i,\mathrm{mfh}}\}_{i=1}^{n_P}$ the family of all phase-averaged deformation gradients. We can also symbolically write

$$\dot{\boldsymbol{\alpha}}_\mu^{\mathrm{mfh}}(t) = \mathscr{D}_\mu^{\mathrm{mfh}}(\boldsymbol{F}(t), \boldsymbol{\alpha}_\mu^{\mathrm{mfh}}(t)), \tag{4.16}$$

describing the evolution of the internal variables in the MFH procedure.

The interaction model implicitly determines the properties of the fictitious unbounded phase and the loading conditions used in the inclusion problems. For the matrix phase, the auxiliary deformation gradient is obtained from the self-consistency condition in Equation (4.13)

$$\boldsymbol{F}_\mu^{m,\mathrm{mfh}} = \frac{1}{\phi_{0,\mu}^m}\left(\boldsymbol{F} - \sum_{\substack{i=1 \\ i\neq m}}^{n_P} \phi_{0,\mu}^i \boldsymbol{F}_\mu^{i,\mathrm{mfh}}\right). \tag{4.17}$$

The instantaneous strain localization tensor $\mathbf{A}_\mu^{i,\mathrm{mfh}}$ is then defined by

$$\mathbf{A}_\mu^{i,\mathrm{mfh}} = \frac{\partial \mathscr{A}_\mu^{i,\mathrm{mfh}}}{\partial \boldsymbol{F}}, \tag{4.18}$$

and for the matrix phase,

$$\mathbf{A}_\mu^{m,\mathrm{mfh}} = \frac{1}{\phi_{0,\mu}^m}\left(\mathbf{I} - \sum_{\substack{i=1\\ i\neq m}}^{n_P} \phi_{0,\mu}^i \mathbf{A}_\mu^{i,\mathrm{mfh}}\right). \tag{4.19}$$

It then follows from Equation (4.13) that the volume-weighted average of the strain localization tensors satisfies

$$\langle \mathbf{A}_\mu^{i,\mathrm{mfh}} \rangle = \mathbf{I}. \tag{4.20}$$

Analogously, let $\mathscr{B}_\mu^{i,\mathrm{mfh}}$ denote the interaction function that maps the macroscopic stress $\boldsymbol{P}$ to the auxiliary MFH average stress estimate in the i-th inclusion phase

$$\boldsymbol{P}_\mu^{i,\mathrm{mfh}} = \mathscr{B}_\mu^{i,\mathrm{mfh}}(\boldsymbol{P}, \boldsymbol{\alpha}_\mu^{\mathrm{mfh}}) = \mathscr{B}_\mu^{i,\mathrm{si}}\left(\boldsymbol{P}^*(\boldsymbol{P}, \boldsymbol{P}_\mu^{\mathrm{mfh}}, \boldsymbol{\alpha}_\mu^{\mathrm{mfh}}), \boldsymbol{\alpha}_\mu^{I,\mathrm{si}}\right). \tag{4.21}$$

where $\boldsymbol{P}_\mu^{\mathrm{mfh}} = \{\boldsymbol{P}_\mu^{i,\mathrm{mfh}}\}_{i=1}^{n_P}$ is the family of all phase-averaged stresses. The matrix stress follows similarly

$$\boldsymbol{P}_\mu^{m,\mathrm{mfh}} = \frac{1}{\phi_{0,\mu}^m}\left(\boldsymbol{P} - \sum_{\substack{i=1\\ i\neq m}}^{n_P} \phi_{0,\mu}^i \boldsymbol{P}_\mu^{i,\mathrm{mfh}}\right). \tag{4.22}$$

The stress localization tensor $\mathbf{B}_\mu^{i,\mathrm{mfh}}$ is defined by

$$\mathbf{B}_\mu^{i,\mathrm{mfh}} = \frac{\partial \mathscr{B}_\mu^{i,\mathrm{mfh}}}{\partial \boldsymbol{P}}, \tag{4.23}$$

and for the matrix,

$$\mathbf{B}_\mu^{m,\mathrm{mfh}} = \frac{1}{\phi_{0,\mu}^m}\left(\mathbf{I} - \sum_{\substack{i=1\\ i\neq m}}^{n_P} \phi_{0,\mu}^i \mathbf{B}_\mu^{i,\mathrm{mfh}}\right). \tag{4.24}$$

From Equation (4.14), it follows that

$$\langle \mathbf{B}_\mu^{i,\mathrm{mfh}} \rangle = \mathbf{I}. \tag{4.25}$$

Table 4.1 collects the $\mathscr{A}_\mu^{i,\mathrm{mfh}}$ and $\mathscr{B}_\mu^{i,\mathrm{mfh}}$ functions for some of the most common interaction models found in the literature. The most basic interaction model assumes that 'no interaction' occurs between the different phases. Under this assumption, the average fields within each phase are equal to the macroscopic fields applied to the overall material. These are the well-known Taylor and Sachs models (Taylor, 1938; Sachs, 1928) in the strain-driven and stress-driven settings, respectively. As an alternative, the dilute interaction model assumes that each inclusion phase interacts only with the matrix phase, thereby introducing a weak level of interaction. The fictitious matrix phase in the IVPs is assigned the same material properties as the composite's actual matrix. In this model, the forcing fields remain the macroscopic ones. The Mori–Tanaka model accounts for phase interactions in a yet more refined manner. As in the dilute model, the fictitious matrix phase in the IVPs is assigned the same material properties as the actual matrix. However, in contrast to the dilute model, the forcing fields are no longer the macroscopic ones but rather the average fields in the material's actual matrix.

Table 4.1: Summary of some of the interaction models found in the literature, where $\mathscr{A}_\mu^{i,\mathrm{si}}$ and $\mathscr{B}_\mu^{i,\mathrm{si}}$ are the functions yielding the average deformation gradient and stress in phase i computed from the corresponding single-inclusion problem. The material properties of the fictitious matrix phase in each single-inclusion IVP are assumed to be the same as those of the actual matrix phase.

Strain-driven	**Stress-driven**
No Interaction	
$\boldsymbol{F}_\mu^{i,\mathrm{mfh}} = \boldsymbol{F}$	$\boldsymbol{P}_\mu^{i,\mathrm{mfh}} = \boldsymbol{P}$
Dilute Interaction Model	
$\boldsymbol{F}_\mu^{i,\mathrm{mfh}} = \mathscr{A}_\mu^{i,\mathrm{si}}(\boldsymbol{F}, \boldsymbol{\alpha}_\mu^{I,\mathrm{si}})$	$\boldsymbol{P}_\mu^{i,\mathrm{mfh}} = \mathscr{B}_\mu^{i,\mathrm{si}}(\boldsymbol{P}, \boldsymbol{\alpha}_\mu^{I,\mathrm{si}})$
Mori–Tanaka Interaction Model	
$\boldsymbol{F}_\mu^{i,\mathrm{mfh}} = \mathscr{A}_\mu^{i,\mathrm{si}}(\boldsymbol{F}_\mu^{m,\mathrm{mfh}}, \boldsymbol{\alpha}_\mu^{I,\mathrm{si}})$	$\boldsymbol{P}_\mu^{i,\mathrm{mfh}} = \mathscr{B}_\mu^{i,\mathrm{si}}(\boldsymbol{P}_\mu^{m,\mathrm{mfh}}, \boldsymbol{\alpha}_\mu^{I,\mathrm{si}})$

Remark 4.2 | Beyond first moments: variational and second-moment approaches

All the schemes summarized above are *direct linearizations* based on first statistical moments: the comparison moduli are evaluated at the phase-averaged state, implicitly assuming that the fields and internal variables are uniform within each phase. A fundamentally different class of approaches defines the comparison moduli through optimization of a variational principle, and naturally incorporates *second statistical moments* of the fields within each phase (Castañeda, 1991; Ponte Castañeda, 2002; Ponte Castañeda and Suquet, 1997; Idiart and Castañeda, 2007). By accounting for intraphase field fluctuations, variational methods provide more accurate predictions for high-contrast composites and strongly nonlinear behaviors. Their extension to dissipative, history-dependent materials has been achieved through the incremental variational principles of Lahellec and Suquet (2007a,b) and Brassart et al. (2011, 2012), in which the time-discretized constitutive evolution is cast as a condensed incremental potential whose effective behavior is then estimated variationally.

A key structural difference from first-moment MFH is that in variational second-moment methods, the construction of the LCC and the specification of the interaction model are no longer independent: both emerge from a single optimization problem defined over the entire composite. This coupling, while producing more accurate estimates, complicates the clean modular separation between the single-inclusion problem and the interaction model that underpins first-moment MFH. The integration of such variational schemes into the PMVP/PMCVP framework—while preserving the consistency guarantees established in the present work—remains an open question, and constitutes a natural direction for future investigation.

4.3 Standard homogenization rules

Once the average fields in each phase have been found, the most commonly adopted approach in the literature for computing the macroscopic fields is to apply standard homogenization rules based on volume averaging (Ortolano et al., 2013; Nemat-Nasser and Hori, 1993). Specifically, in

the strain-driven case, the homogenized stress is obtained from

$$\boldsymbol{P} = \sum_{i=1}^{n_P} \phi_{0,\mu}^i \boldsymbol{P}_\mu^{i,\mathrm{mfh}} = \langle \boldsymbol{P}_\mu^{i,\mathrm{mfh}} \rangle, \tag{4.26}$$

and in the stress-driven case, the homogenized deformation gradient is found from

$$\boldsymbol{F} = \sum_{i=1}^{n_P} \phi_{0,\mu}^i \boldsymbol{F}_\mu^{i,\mathrm{mfh}} = \langle \boldsymbol{F}_\mu^{i,\mathrm{mfh}} \rangle. \tag{4.27}$$

4.4 Objectivity of the mean-field homogenization procedure

As for constitutive models (see Section 2.4), we require that the interaction models be objective, meaning that they remain invariant under superimposed rigid-body motions, in particular under superimposed rotations. This requirement stems from the natural physical expectation that the average deformation gradient and stress in each phase should not depend on the observer's frame of reference. For the strain-driven case, objectivity implies that for any proper orthogonal tensor $\boldsymbol{Q}$,

$$\mathscr{A}_\mu^{i,\mathrm{mfh}}(\boldsymbol{QF}, \boldsymbol{Q} * \boldsymbol{\alpha}_\mu^{\mathrm{mfh}}) = \boldsymbol{Q}\mathscr{A}_\mu^{i,\mathrm{mfh}}(\boldsymbol{F}, \boldsymbol{\alpha}_\mu^{\mathrm{mfh}}) = \boldsymbol{QF}_\mu^{i,\mathrm{mfh}}. \tag{4.28}$$

Similarly, for the stress-driven case,

$$\mathscr{B}_\mu^{i,\mathrm{mfh}}(\boldsymbol{QP}, \boldsymbol{Q} * \boldsymbol{\alpha}_\mu^{\mathrm{mfh}}) = \boldsymbol{Q}\mathscr{B}_\mu^{i,\mathrm{mfh}}(\boldsymbol{P}, \boldsymbol{\alpha}_\mu^{\mathrm{mfh}}) = \boldsymbol{QP}_\mu^{i,\mathrm{mfh}}. \tag{4.29}$$

These relationships, in turn, imply that for non-dissipative materials whose description eschews the use of internal variables, the localization tensors must satisfy

$$\mathsf{A}_\mu^{i,\mathrm{mfh}}(\boldsymbol{F}) : (\boldsymbol{WF}) = \boldsymbol{W}\mathscr{A}_\mu^{i,\mathrm{mfh}}(\boldsymbol{F}) = \boldsymbol{WF}_\mu^{i,\mathrm{mfh}}, \tag{4.30}$$

and

$$\mathsf{B}_\mu^{i,\mathrm{mfh}}(\boldsymbol{P}) : (\boldsymbol{WP}) = \boldsymbol{W}\mathscr{B}_\mu^{i,\mathrm{mfh}}(\boldsymbol{P}) = \boldsymbol{WP}_\mu^{i,\mathrm{mfh}}, \tag{4.31}$$

for any skew-symmetric tensor $\boldsymbol{W}$.

To derive these conditions, consider the definition of the strain localization tensor in Equation (4.18) as a derivative. Consider the perturbation of the macroscopic deformation gradient $\boldsymbol{F}$ by

$$\hat{\boldsymbol{F}} = e^{\boldsymbol{W}\epsilon}\boldsymbol{F}, \tag{4.32}$$

where ϵ is a small parameter. Note that $e^{\boldsymbol{W}\epsilon}$ is a proper orthogonal tensor for any value of ϵ since $\boldsymbol{W}$ is skew-symmetric (Stillwell, 2008).

Accordingly, we write by the chain rule

$$\mathsf{A}_\mu^{i,\mathrm{mfh}}(\boldsymbol{F}) : \left(\lim_{\epsilon \to 0} \frac{\hat{\boldsymbol{F}} - \boldsymbol{F}}{\epsilon} \right) = \lim_{\epsilon \to 0} \frac{\mathscr{A}_\mu^{i,\mathrm{mfh}}(\hat{\boldsymbol{F}}) - \mathscr{A}_\mu^{i,\mathrm{mfh}}(\boldsymbol{F})}{\epsilon}, \tag{4.33}$$

where

$$\hat{\boldsymbol{F}} - \boldsymbol{F} = e^{\boldsymbol{W}\epsilon}\boldsymbol{F} - \boldsymbol{F} \tag{4.34}$$

$$= (e^{\boldsymbol{W}\epsilon} - \boldsymbol{I})\boldsymbol{F}. \tag{4.35}$$

Working first on the left-hand side, we note that from the derivative of the exponential map, we have

$$\frac{d}{dt} e^{\boldsymbol{W}t} = \boldsymbol{W} e^{\boldsymbol{W}t}. \tag{4.36}$$

In particular, at $t = 0$, using the definition of the derivative, this implies

$$\lim_{\epsilon \to 0} \frac{e^{\boldsymbol{W}\epsilon} - \boldsymbol{I}}{\epsilon} = \boldsymbol{W}. \tag{4.37}$$

Thus, the left-hand side becomes

$$\mathbf{A}_{\mu}^{i,\mathrm{mfh}}(\boldsymbol{F}) : \left(\lim_{\epsilon \to 0} \frac{e^{\boldsymbol{W}\epsilon} - \boldsymbol{I}}{\epsilon} \boldsymbol{F} \right) = \mathbf{A}_{\mu}^{i,\mathrm{mfh}}(\boldsymbol{F}) : (\boldsymbol{W}\boldsymbol{F}). \tag{4.38}$$

Now, regarding the right-hand side, using the objectivity of the interaction model, we find

$$\mathscr{A}_{\mu}^{i,\mathrm{mfh}}(\hat{\boldsymbol{F}}) = \mathscr{A}_{\mu}^{i,\mathrm{mfh}}(e^{\boldsymbol{W}\epsilon}\boldsymbol{F}) \tag{4.39}$$

$$= e^{\boldsymbol{W}\epsilon} \mathscr{A}_{\mu}^{i,\mathrm{mfh}}(\boldsymbol{F}) \tag{4.40}$$

$$= e^{\boldsymbol{W}\epsilon} \boldsymbol{F}_{\mu}^{i,\mathrm{mfh}}, \tag{4.41}$$

where we have used the fact that $e^{\boldsymbol{W}\epsilon}$ is a proper orthogonal tensor. Substituting this result back into the definition of the strain localization tensor, we obtain

$$\mathbf{A}_{\mu}^{i,\mathrm{mfh}}(\boldsymbol{F}) : (\boldsymbol{W}\boldsymbol{F}) = \lim_{\epsilon \to 0} \frac{e^{\boldsymbol{W}\epsilon} \boldsymbol{F}_{\mu}^{i,\mathrm{mfh}} - \boldsymbol{F}_{\mu}^{i,\mathrm{mfh}}}{\epsilon} \tag{4.42}$$

$$= \lim_{\epsilon \to 0} \frac{(e^{\boldsymbol{W}\epsilon} - \boldsymbol{I})}{\epsilon} \boldsymbol{F}_{\mu}^{i,\mathrm{mfh}} \tag{4.43}$$

$$= \boldsymbol{W}\boldsymbol{F}_{\mu}^{i,\mathrm{mfh}}, \tag{4.44}$$

which confirms Equation (4.30).

The derivation for the stress localization tensor in Equation (4.31) is identical, and thus omitted for brevity.

Chapter 5

Variationally consistent mean-field models

This chapter presents one of the main contributions of this thesis: a novel framework to derive variationally consistent mean-field homogenization (MFH) models for heterogeneous materials based on the Principle of Multiscale Virtual Power (PMVP) introduced in Chapter 3.

5.1 The Principle of Multiscale Virtual Power and Mean-Field Homogenization

In this section, we introduce an alternative derivation of MFH rules grounded in the PMVP and its associated variational framework.

5.1.1 Incompatible displacements

To embed MFH within the PMVP framework and derive consistent stress homogenization relations, we first identify the appropriate functional spaces for the admissible displacement fluctuations. Let us define an auxiliary functional space $\tilde{\mathscr{U}}_\mu^i$ for each phase i, comprising displacement fields supported on $\Omega_{0,\mu}^i$ with square-integrable weak derivatives

$$\tilde{\mathscr{U}}_\mu^i = \left\{ \boldsymbol{v} \in \boldsymbol{H}^1(\Omega_{0,\mu}) \mid \boldsymbol{v}(\boldsymbol{Y}) = \boldsymbol{0} \quad \text{for } \boldsymbol{Y} \notin \Omega_{0,\mu}^i \right\}. \tag{5.1}$$

MFH provides estimates for the average deformation gradient in each phase, but these estimates generally correspond to incompatible displacement fields across the composite domain. As a result, interfacial displacement continuity cannot be assumed, though regularity within each phase must still be preserved. The admissible displacement fluctuation fields over the entire RVE are then drawn from the direct sum of these phase-wise spaces, subject to the constraint that the overall fluctuation has vanishing average gradient. This defines the minimal admissible space

$$\tilde{\mathscr{K}}_\mu^* = \left\{ \boldsymbol{v} \in \bigoplus_{i=1}^{n_P} \tilde{\mathscr{U}}_\mu^i \;\middle|\; \sum_{i=1}^{n_P} \int_{\Omega_{0,\mu}^i} \nabla_0 \boldsymbol{v} \, dv = \boldsymbol{0} \right\}. \tag{5.2}$$

In this setting, $\tilde{\mathscr{K}}_\mu^*$ includes displacement fields that are continuous within each phase but may exhibit discontinuities at phase interfaces.

Remark 5.1 | On admissibility constraints

Comparing Equation (5.2) with the fully compatible fluctuation space defined in Equation (3.9), we observe that the constraint on the volume-weighted average of displacement fluctuations has been relaxed. In the context of MFH without body or inertial forces, this simplification does not affect the results and yields a cleaner derivation. Accordingly, we adopt this less restrictive formulation throughout the remainder of the section.

Given the linearity of the kinematical constraints, the space of virtual admissible displacement fluctuations, denoted by $\tilde{\mathcal{V}}_\mu^*$, coincides with $\tilde{\mathscr{K}}_\mu^*$, i.e.,

$$\tilde{\mathcal{V}}_\mu^* = \tilde{\mathscr{K}}_\mu^*. \tag{5.3}$$

While $\tilde{\mathscr{K}}_\mu^*$ captures the general admissibility conditions under the PMVP, further constraints can be imposed. These constraints are constructed from the phase-averaged deformation gradients predicted by MFH and allow us to define nested subsets of admissible fluctuation fields. We begin with the most restrictive case.

5.1.2 Full Mean-Field Homogenization

To fully incorporate the MFH estimates, we require that the average deformation gradient in each phase matches the corresponding MFH prediction

$$\boldsymbol{F}_\mu^i = \boldsymbol{F}_\mu^{i,\mathrm{mfh}}, \quad i = 1,\dots,n_P. \tag{5.4}$$

Rewriting this constraint in terms of the displacement fluctuations, we take the average over each phase domain using Equation (3.4), producing

$$\boldsymbol{F}_\mu^i = \boldsymbol{F} + \frac{1}{|\Omega_{0,\mu}^i|}\int_{\Omega_{0,\mu}^i} \nabla_0 \tilde{\boldsymbol{u}}_\mu \, dv, \tag{5.5}$$

which, combined with Equation (5.4), yields

$$\int_{\Omega_{0,\mu}^i} \nabla_0 \tilde{\boldsymbol{u}}_\mu \, dv = |\Omega_{0,\mu}^i|(\boldsymbol{F}_\mu^{i,\mathrm{mfh}} - \boldsymbol{F}). \tag{5.6}$$

Note that, in general, $\boldsymbol{F}_\mu^{i,\mathrm{mfh}}$ depends nonlinearly on the macroscopic deformation and internal variables of the phase, i.e.,

$$\boldsymbol{F}_\mu^{i,\mathrm{mfh}} = \mathscr{A}_\mu^{i,\mathrm{mfh}}(\boldsymbol{F}, \boldsymbol{\alpha}_\mu^{\mathrm{mfh}}), \tag{5.7}$$

as detailed in Equation (4.15).

The set of admissible displacement fluctuations satisfying these phase-wise average constraints defines a subset of $\tilde{\mathscr{K}}_\mu^*$ and is given by

$$\tilde{\mathscr{K}}_{\mu,\mathrm{MFH}}(\boldsymbol{F}) = \left\{ \boldsymbol{v} \in \tilde{\mathscr{K}}_\mu^* \;\middle|\; \int_{\Omega_{0,\mu}^i} \nabla_0 \boldsymbol{v} \, dv = |\Omega_{0,\mu}^i|(\boldsymbol{F}_\mu^{i,\mathrm{mfh}} - \boldsymbol{F}),\ \forall i = 1,\dots,n_P \right\}. \tag{5.8}$$

This is not a linear subspace for each $\boldsymbol{F}$ since it does not, in general, contain the zero vector.

For internal consistency, we must ensure that $\tilde{\mathscr{K}}_{\mu,\mathrm{MFH}}(\boldsymbol{F}) \subseteq \tilde{\mathscr{K}}_\mu^*$. This holds provided the self-consistency condition is satisfied

$$\langle \boldsymbol{F}_\mu^{i,\mathrm{mfh}} \rangle = \boldsymbol{F}, \tag{5.9}$$

as seen by summing Equation (5.6) over all phases and rewriting the right-hand side in terms of volume fractions $\phi^i_{0,\mu}$.

The corresponding space of virtual admissible fluctuations is derived by linearizing Equation (5.6). In particular, we consider how a small perturbation in the macroscopic deformation gradient $\delta\boldsymbol{F}$ affects the phase-wise average deformation gradients $\boldsymbol{F}^{i,\mathrm{mfh}}_\mu$. Consider the linearization of Equations (4.15) and (4.16), along a given trajectory $(\boldsymbol{F}(t), \boldsymbol{\alpha}^{\mathrm{mfh}}_\mu(t))$, where momentarily we allow for time dependence to account for the evolution of internal variables. We have

$$\delta\dot{\boldsymbol{\alpha}}^{\mathrm{mfh}}_\mu(t) = \mathbf{D}^{\mathrm{mfh}}_\mu(t) : \delta\boldsymbol{F}(t) + \mathbb{D}^{\mathrm{mfh}}_\mu(t) : \delta\boldsymbol{\alpha}^{\mathrm{mfh}}_\mu(t), \tag{5.10}$$

$$\delta\boldsymbol{F}^{i,\mathrm{mfh}}_\mu(t) = \mathbf{A}^{i,\mathrm{mfh}}_\mu(t) : \delta\boldsymbol{F}(t) + \mathbb{A}^{i,\mathrm{mfh}}_\mu(t) : \delta\boldsymbol{\alpha}^{\mathrm{mfh}}_\mu(t), \tag{5.11}$$

where

$$\mathbf{D}^{\mathrm{mfh}}_\mu(t) = \frac{\partial\mathscr{D}^{\mathrm{mfh}}_\mu}{\partial\boldsymbol{F}}(\boldsymbol{F}(t), \boldsymbol{\alpha}^{\mathrm{mfh}}_\mu(t)), \quad \mathbb{D}^{\mathrm{mfh}}_\mu(t) = \frac{\partial\mathscr{D}^{\mathrm{mfh}}_\mu}{\partial\boldsymbol{\alpha}^{\mathrm{mfh}}}(\boldsymbol{F}(t), \boldsymbol{\alpha}^{\mathrm{mfh}}_\mu(t)), \tag{5.12}$$

$$\mathbf{A}^{i,\mathrm{mfh}}_\mu(t) = \frac{\partial\mathscr{A}^{i,\mathrm{mfh}}_\mu}{\partial\boldsymbol{F}}(\boldsymbol{F}(t), \boldsymbol{\alpha}^{\mathrm{mfh}}_\mu(t)), \quad \mathbb{A}^{i,\mathrm{mfh}}_\mu(t) = \frac{\partial\mathscr{A}^{i,\mathrm{mfh}}_\mu}{\partial\boldsymbol{\alpha}^{\mathrm{mfh}}}(\boldsymbol{F}(t), \boldsymbol{\alpha}^{\mathrm{mfh}}_\mu(t)). \tag{5.13}$$

Given that Equation (5.10) is a linear ODE, we can write its solution symbolically as (Beffa, 2023)

$$\delta\boldsymbol{\alpha}^{\mathrm{mfh}}_\mu(t) = \boldsymbol{\Phi}^{\mathrm{mfh}}_\mu(t, t_0) : \delta\boldsymbol{\alpha}^{\mathrm{mfh}}_\mu(t_0) + \int_{t_0}^{t} \boldsymbol{\Phi}^{\mathrm{mfh}}_\mu(t,\tau) : \mathbf{D}^{\mathrm{mfh}}_\mu(\tau) : \delta\boldsymbol{F}(\tau)\ d\tau, \tag{5.14}$$

where $\delta\boldsymbol{\alpha}^{\mathrm{mfh}}_\mu(t_0)$ is the initial perturbation of the internal variables at time t_0 that we set to zero moving forward, i.e., $\delta\boldsymbol{\alpha}^{\mathrm{mfh}}_\mu(t_0) = \mathbf{0}$, and $\boldsymbol{\Phi}^{\mathrm{mfh}}_\mu(t, t_0)$ is the state-transition operator associated with the homogeneous part of Equation (5.10).[1]

Thus, substituting into Equation (5.11), we obtain

$$\delta\boldsymbol{F}^{i,\mathrm{mfh}}_\mu(t) = \mathbf{A}^{i,\mathrm{mfh}}_\mu(t) : \delta\boldsymbol{F}(t) + \int_{t_0}^{t} \mathbb{A}^{i,\mathrm{mfh}}_\mu(t) : \boldsymbol{\Phi}^{\mathrm{mfh}}_\mu(t,\tau) : \mathbf{D}^{\mathrm{mfh}}_\mu(\tau) : \delta\boldsymbol{F}(\tau)\ d\tau. \tag{5.16}$$

Finally, we consider an instantaneous perturbation at time t since we are only considering spatial variations, i.e.,

$$\delta\boldsymbol{F}(\tau) = \begin{cases} \delta\boldsymbol{F}, & \tau = t \\ \mathbf{0}, & \tau \neq t \end{cases} \tag{5.17}$$

and find

$$\delta\boldsymbol{F}^{i,\mathrm{mfh}}_\mu(t) = \mathbf{A}^{i,\mathrm{mfh}}_\mu(t) : \delta\boldsymbol{F}, \tag{5.18}$$

since the integral term vanishes, given that the integrand is non-zero only at a single point[2]. This choice is particularly relevant for non-dissipative materials, where the internal variables do

[1] The state-transition operator describes how the state of a linear system changes over time, satisfying

$$\frac{\partial\boldsymbol{\Phi}^{\mathrm{mfh}}_\mu}{\partial t}(t, t_0) = \mathbb{D}^{\mathrm{mfh}}_\mu(t) : \boldsymbol{\Phi}^{\mathrm{mfh}}_\mu(t, t_0), \tag{5.15}$$

with the initial condition $\boldsymbol{\Phi}^{\mathrm{mfh}}_\mu(t_0, t_0) = \mathbf{I}$.

[2] Yet another way to arrive at the same conclusion is to consider a time discretized version of the constraint in Equation (5.6). We write

$$\boldsymbol{\alpha}^{\mathrm{mfh}}_{\mu,n+1} = \hat{\mathscr{D}}^{\mathrm{mfh}}_\mu(\boldsymbol{F}_{n+1}, \boldsymbol{\alpha}^{\mathrm{mfh}}_{\mu,n}),$$
$$\boldsymbol{F}^{i,\mathrm{mfh}}_{\mu,n+1} = \hat{\mathscr{A}}^{i,\mathrm{mfh}}_\mu(\boldsymbol{F}_{n+1}, \boldsymbol{\alpha}^{\mathrm{mfh}}_{\mu,n}),$$

where the $\hat{(\bullet)}$ denotes the time discretized version of $\bullet$. This implies that $\boldsymbol{F}^{i,\mathrm{mfh}}_{\mu,n+1}$ does not depend on $\boldsymbol{\alpha}^{\mathrm{mfh}}_{\mu,n+1}$ yielding a similar result as in the body of the text, with the localization tensor computed from the consistent stiffness tangent.

not evolve with time. Putting all this together, the linearization of Equation (5.6) reads

$$\int_{\Omega^i_{0,\mu}} \nabla_0 \delta\tilde{\boldsymbol{u}}_\mu \, dv = |\Omega^i_{0,\mu}|(\mathbf{A}^{i,\mathrm{mfh}}_\mu - \mathbf{I}) : \delta\boldsymbol{F}, \tag{5.19}$$

where $\mathbf{A}^{i,\mathrm{mfh}}_\mu$ is the instantaneous localization tensor (see Equation (4.18)). This defines the set of virtual displacement fluctuations as

$$\tilde{\mathscr{V}}_{\mu,\mathrm{MFH}}(\boldsymbol{F},\delta\boldsymbol{F}) = \left\{ \boldsymbol{v} \in \tilde{\mathscr{V}}^*_\mu \;\middle|\; \int_{\Omega^i_{0,\mu}} \nabla_0 \boldsymbol{v} \, dv = |\Omega^i_{0,\mu}|(\mathbf{A}^{i,\mathrm{mfh}}_\mu - \mathbf{I}) : \delta\boldsymbol{F},\ \forall i = 1,\dots,n_P \right\}. \tag{5.20}$$

Principle of Multiscale Virtual Power

To enforce the constraints on the space of virtual admissible displacement fields within the PMVP framework, we employ the method of Lagrange multipliers. Specifically, we introduce a set of second-order tensor-valued multipliers, denoted $\boldsymbol{\Omega}^i_\mu$ for $i = 1,\dots,n_P$, each having the dimensions of stress.

The extended variational statement of the Principle of Multiscale Virtual Power then reads

$$\begin{aligned} |\Omega_{0,\mu}|\boldsymbol{P} : \delta\boldsymbol{F} = \int_{\Omega_{0,\mu}} \boldsymbol{P}_\mu : (\nabla_0 \delta\tilde{\boldsymbol{u}}_\mu + \delta\boldsymbol{F}) \, dv \\ - \sum_{i=1}^{n_P} \boldsymbol{\Omega}^i_\mu : \left(\int_{\Omega^i_{0,\mu}} \nabla_0 \delta\tilde{\boldsymbol{u}}_\mu \, dv - |\Omega^i_{0,\mu}|(\mathbf{A}^{i,\mathrm{mfh}}_\mu - \mathbf{I}) : \delta\boldsymbol{F} \right) \\ - \sum_{i=1}^{n_P} \delta\boldsymbol{\Omega}^i_\mu : \left(\int_{\Omega^i_{0,\mu}} \nabla_0 \tilde{\boldsymbol{u}}_\mu \, dv - |\Omega^i_{0,\mu}|(\boldsymbol{F}^{i,\mathrm{mfh}}_\mu - \boldsymbol{F}) \right), \end{aligned} \tag{5.21}$$

where the last two terms enforce the kinematic constraints on the space of admissible fluctuation displacement fields. We now examine the consequences of this formulation under suitable choices of the variations.

Kinematical homogenization

We begin by setting all variations to zero except the variations of the Lagrange multipliers $\delta\boldsymbol{\Omega}^i_\mu$. This yields

$$\int_{\Omega^i_{0,\mu}} \nabla_0 \tilde{\boldsymbol{u}}_\mu \, dv = |\Omega^i_{0,\mu}|(\boldsymbol{F}^{i,\mathrm{mfh}}_\mu - \boldsymbol{F}), \quad i = 1,\dots,n_P. \tag{5.22}$$

These equations correspond precisely to the constraints introduced in Equation (5.6), and imply

$$\boldsymbol{F}^i_\mu = \boldsymbol{F}^{i,\mathrm{mfh}}_\mu, \quad i = 1,\dots,n_P. \tag{5.23}$$

Interpretation of the Lagrange multipliers

Next, we isolate the effect of the Lagrange multipliers by setting $\delta\boldsymbol{F} = \mathbf{0}$ and $\delta\boldsymbol{\Omega}^i_\mu = \mathbf{0}$ for all i. The PMVP then reduces to

$$\int_{\Omega_{0,\mu}} \boldsymbol{P}_\mu : \nabla_0 \delta\tilde{\boldsymbol{u}}_\mu \, dv - \sum_{i=1}^{n_P} \boldsymbol{\Omega}^i_\mu : \int_{\Omega^i_{0,\mu}} \nabla_0 \delta\tilde{\boldsymbol{u}}_\mu \, dv = 0. \tag{5.24}$$

To extract physical meaning from this condition, we choose test functions of the form

$$\delta\tilde{\boldsymbol{u}}_\mu(\boldsymbol{Y}) = \begin{cases} \boldsymbol{C}(\boldsymbol{Y}-\boldsymbol{Y}_0^i), & \boldsymbol{Y}\in\Omega_{0,\mu}^i \\ \boldsymbol{0}, & \text{otherwise} \end{cases} \tag{5.25}$$

where $\boldsymbol{C}$ is an arbitrary second-order tensor and $\boldsymbol{Y}_0^i$ is the centroid of phase i.

Substituting into Equation (5.24) and exploiting the arbitrariness of $\boldsymbol{C}$, we find

$$\boldsymbol{\Omega}_\mu^i = \frac{1}{|\Omega_{0,\mu}^i|}\int_{\Omega_{0,\mu}^i} \boldsymbol{P}_\mu \, dv = \boldsymbol{P}_\mu^i, \quad i=1,\dots,n_P. \tag{5.26}$$

Thus, each Lagrange multiplier $\boldsymbol{\Omega}_\mu^i$ corresponds to the average first Piola–Kirchhoff stress in phase i, as formally stated in

$$\boldsymbol{\Omega}_\mu^i = \boldsymbol{P}_\mu^i, \quad i=1,\dots,n_P. \tag{5.27}$$

Accordingly, we can rewrite Equation (5.24) as

$$\int_{\Omega_{0,\mu}} \boldsymbol{P}_\mu : \nabla_0\delta\tilde{\boldsymbol{u}}_\mu \, dv = \sum_{i=1}^{n_P} \boldsymbol{P}_\mu^i : \int_{\Omega_{0,\mu}^i} \nabla_0\delta\tilde{\boldsymbol{u}}_\mu \, dv. \tag{5.28}$$

Stress homogenization

Finally, we consider the variation with respect to $\delta\boldsymbol{F}$, while setting both $\delta\tilde{\boldsymbol{u}}_\mu$ and $\delta\boldsymbol{\Omega}_\mu^i$, $i=1,\dots,n_P$, to zero. Substituting into the PMVP, we obtain

$$|\Omega_{0,\mu}|\boldsymbol{P}:\delta\boldsymbol{F} = \int_{\Omega_{0,\mu}} \boldsymbol{P}_\mu \, dv : \delta\boldsymbol{F} - \sum_{i=1}^{n_P} \boldsymbol{\Omega}_\mu^i : \left(-|\Omega_{0,\mu}^i|(\mathbf{A}_\mu^{i,\mathrm{mfh}} - \mathbf{I}) : \delta\boldsymbol{F}\right). \tag{5.29}$$

Rearranging and substituting in Equation (5.27), we have

$$|\Omega_{0,\mu}|\boldsymbol{P}:\delta\boldsymbol{F} = \int_{\Omega_{0,\mu}} \boldsymbol{P}_\mu \, dv : \delta\boldsymbol{F} - \sum_{i=1}^{n_P} |\Omega_{0,\mu}^i|\boldsymbol{P}_\mu^i : \delta\boldsymbol{F} + \sum_{i=1}^{n_P} |\Omega_{0,\mu}^i|\boldsymbol{P}_\mu^i : \mathbf{A}_\mu^{i,\mathrm{mfh}} : \delta\boldsymbol{F}. \tag{5.30}$$

Noting that the first two terms on the right-hand side cancel due to the definition of the average phase stress (see Equation (4.4)), we arrive at

$$|\Omega_{0,\mu}|\boldsymbol{P}:\delta\boldsymbol{F} = \sum_{i=1}^{n_P} |\Omega_{0,\mu}^i|\boldsymbol{P}_\mu^i : \mathbf{A}_\mu^{i,\mathrm{mfh}} : \delta\boldsymbol{F}. \tag{5.31}$$

Dividing by the volume $|\Omega_{0,\mu}|$, and taking into account that $\delta\boldsymbol{F}$ is an arbitrary second-order tensor, we arrive at the stress homogenization rule

$$\boldsymbol{P} = \left\langle \boldsymbol{P}_\mu^i : \mathbf{A}_\mu^{i,\mathrm{mfh}} \right\rangle. \tag{5.32}$$

This result deviates from the conventional MFH stress homogenization formula, which typically assumes

$$\boldsymbol{P} = \langle \boldsymbol{P}_\mu^i \rangle.$$

Here, the macroscopic stress is not simply the volume average of the microscopic stresses but instead includes contributions from phase-dependent deformation localization tensors.

Remark 5.2 | Taylor model

If we further assume that the deformation gradient is identical across all phases, i.e., $\boldsymbol{F}_\mu^{i,\mathrm{mfh}} = \boldsymbol{F}$ for all i, then $\mathbf{A}_\mu^{i,\mathrm{mfh}} = \mathbf{I}$ and Equation (5.32) reduces to the classical volume average

$$\boldsymbol{P} = \langle \boldsymbol{P}_\mu^i \rangle.$$

This corresponds to the classical Taylor model, which assumes uniform strain throughout the microstructure and can be interpreted as a special case of the present variational framework under the 'no-interaction' rule (see Table 4.1).

Energetic consistency

Having established the stress homogenization relation in Equation (5.32), we now assess the energetic consistency of the proposed framework by comparing macroscopic and microscopic mechanical power.

Taking the double contraction of both sides of Equation (5.32) with the time derivative of the macroscopic deformation gradient, we obtain

$$\boldsymbol{P} : \dot{\boldsymbol{F}} = \left\langle \boldsymbol{P}_\mu^i : \mathbf{A}_\mu^{i,\mathrm{mfh}} \right\rangle : \dot{\boldsymbol{F}}. \tag{5.33}$$

Since $\dot{\boldsymbol{F}}$ is independent of the microscale coordinate $\boldsymbol{Y}$, it may be brought inside the volume average

$$\boldsymbol{P} : \dot{\boldsymbol{F}} = \left\langle \boldsymbol{P}_\mu^i : \mathbf{A}_\mu^{i,\mathrm{mfh}} : \dot{\boldsymbol{F}} \right\rangle. \tag{5.34}$$

We now relate the time derivative of the phase deformation gradient to its constitutive dependence on both macroscopic deformation and internal variables. Under the assumptions of the full MFH model (Equation (5.4)), and taking into account Equation (4.15), we have

$$\dot{\boldsymbol{F}}_\mu^i = \dot{\boldsymbol{F}}_\mu^{i,\mathrm{mfh}} = \mathbf{A}_\mu^{i,\mathrm{mfh}} : \dot{\boldsymbol{F}} + \mathbb{A}_\mu^{i,\mathrm{mfh}} : \dot{\boldsymbol{\alpha}}_\mu^{\mathrm{mfh}}, \tag{5.35}$$

where $\mathbf{A}_\mu^{i,\mathrm{mfh}}$ is defined as in Equation (4.18) and $\mathbb{A}_\mu^{i,\mathrm{mfh}}$ denotes the sensitivity of the local deformation to the internal variables, i.e.,

$$\mathbb{A}_\mu^{i,\mathrm{mfh}} = \frac{\partial \mathscr{A}_\mu^{i,\mathrm{mfh}}}{\partial \boldsymbol{\alpha}_\mu^{\mathrm{mfh}}}.$$

Substituting into Equation (5.34), we obtain

$$\begin{aligned} \boldsymbol{P} : \dot{\boldsymbol{F}} &= \left\langle \boldsymbol{P}_\mu^i : \left(\dot{\boldsymbol{F}}_\mu^i - \mathbb{A}_\mu^{i,\mathrm{mfh}} : \dot{\boldsymbol{\alpha}}_\mu^{\mathrm{mfh}} \right) \right\rangle && (5.36) \\ &= \left\langle \boldsymbol{P}_\mu^i : \dot{\boldsymbol{F}}_\mu^i \right\rangle - \left\langle \boldsymbol{P}_\mu^i : \mathbb{A}_\mu^{i,\mathrm{mfh}} : \dot{\boldsymbol{\alpha}}_\mu^{\mathrm{mfh}} \right\rangle. && (5.37) \end{aligned}$$

Thus, the macroscopic mechanical power decomposes into the average microscopic power minus a term involving the internal variables

$$\boldsymbol{P} : \dot{\boldsymbol{F}} = \left\langle \boldsymbol{P}_\mu^i : \dot{\boldsymbol{F}}_\mu^i \right\rangle - \left\langle \boldsymbol{P}_\mu^i : \mathbb{A}_\mu^{i,\mathrm{mfh}} : \dot{\boldsymbol{\alpha}}_\mu^{\mathrm{mfh}} \right\rangle. \tag{5.38}$$

This identity reveals important energetic implications. For elastic materials, i.e., those that do not require internal variables for their constitutive description, we recover an exact energetic equivalence

$$\boldsymbol{P} : \dot{\boldsymbol{F}} = \left\langle \boldsymbol{P}_\mu^i : \dot{\boldsymbol{F}}_\mu^i \right\rangle. \tag{5.39}$$

Such consistency is not, in general, ensured in traditional MFH models due to the inconsistent stress-homogenization rule.

In contrast, for dissipative materials governed by internal variables, this equality may not hold. Consider, for instance, a scenario where the macroscopic deformation gradient becomes stationary at some time t, i.e., $\dot{\boldsymbol{F}} = \boldsymbol{0}$. The macroscopic mechanical power vanishes, but the microscopic power becomes

$$\left\langle \boldsymbol{P}_\mu^i : \dot{\boldsymbol{F}}_\mu^i \right\rangle = \left\langle \boldsymbol{P}_\mu^i : \mathbb{A}_\mu^{i,\mathrm{mfh}} : \dot{\boldsymbol{\alpha}}_\mu^{\mathrm{mfh}} \right\rangle. \tag{5.40}$$

In this case, the microscopic power may remain non-zero due to the ongoing evolution of the internal variables. Since distinct single-inclusion problems govern these, their contributions may not cancel, leading to a residual microscopic dissipation that is not reflected at the macroscale.

This highlights a fundamental limitation of mean-field approaches: incompatibilities between localized evolution and global equilibrium can manifest as discrepancies in energy consistency, particularly in dissipative regimes. However, in the current approach, the energetic inconsistency follows immediately from the variational statement of the PMVP and is well-identified. This can enable strategic future modifications to mitigate this problem.

Angular momentum balance

We now show that angular momentum balance is satisfied by the homogenized stress obtained from Equation (5.32). To achieve this, consider a virtual variation of the form $\delta\boldsymbol{F} = \boldsymbol{W}\boldsymbol{F}$, with $\boldsymbol{W}$ skew-symmetric. Substituting into Equation (5.31), we have

$$|\Omega_{0,\mu}|\boldsymbol{P} : (\boldsymbol{W}\boldsymbol{F}) = \sum_{i=1}^{n_P} |\Omega_{0,\mu}|\boldsymbol{P}_\mu^i : \mathbf{A}_\mu^{i,\mathrm{mfh}} : (\boldsymbol{W}\boldsymbol{F}). \tag{5.41}$$

Using the objectivity condition for the localization tensors, again subject to the assumption that the materials are not dissipative (see Equation (4.30) in Section 4.4), we obtain

$$|\Omega_{0,\mu}|\boldsymbol{P} : (\boldsymbol{W}\boldsymbol{F}) = \sum_{i=1}^{n_P} |\Omega_{0,\mu}|\boldsymbol{P}_\mu^i : (\boldsymbol{W}\boldsymbol{F}_\mu^{i,\mathrm{mfh}}), \tag{5.42}$$

and thus

$$|\Omega_{0,\mu}|(\boldsymbol{P}\boldsymbol{F}^T) : \boldsymbol{W} = \sum_{i=1}^{n_P} |\Omega_{0,\mu}|(\boldsymbol{P}_\mu^i (\boldsymbol{F}_\mu^{i,\mathrm{mfh}})^T) : \boldsymbol{W}, \tag{5.43}$$

taking into account the relationship between the transpose of a matrix and the double contraction.

Noting that $\boldsymbol{F}_\mu^{i,\mathrm{mfh}} = \boldsymbol{F}_\mu^i$, $i = 1, \ldots, n_P$, from Equation (5.4), we find

$$|\Omega_{0,\mu}|(\boldsymbol{P}\boldsymbol{F}^T) : \boldsymbol{W} = \left(\sum_{i=1}^{n_P} |\Omega_{0,\mu}|\boldsymbol{P}_\mu^i (\boldsymbol{F}_\mu^i)^T \right) : \boldsymbol{W}, \tag{5.44}$$

and finally since $\boldsymbol{W}$ is an arbitrary skew-symmetric tensor, we conclude

$$\mathrm{skew}(\boldsymbol{P}\boldsymbol{F}^T) = \langle \mathrm{skew}(\boldsymbol{P}_\mu^i (\boldsymbol{F}_\mu^i)^T) \rangle. \tag{5.45}$$

To show that the right-hand side vanishes and consequently $\boldsymbol{P}\boldsymbol{F}^T = \mathrm{sym}(\boldsymbol{P}\boldsymbol{F}^T)$, we return to Equation (5.28) and consider variations of the form $\delta\tilde{\boldsymbol{u}}_\mu = \boldsymbol{C}\tilde{\boldsymbol{u}}_\mu$, where $\tilde{\boldsymbol{u}} \in \tilde{\mathscr{U}}_\mu^i$ (see Equation (5.1)), and $\boldsymbol{C}$ is an arbitrary second-order tensor. Note that since we are

employing the method of Lagrange multipliers, we are free to choose the virtual variations as needed. Substituting into Equation (5.28), we have

$$\int_{\Omega^i_{0,\mu}} \boldsymbol{P}_\mu : \nabla_0(\boldsymbol{C}\tilde{\boldsymbol{u}}_\mu)\,dv - \boldsymbol{P}^i_\mu : \int_{\Omega^i_{0,\mu}} \nabla_0(\boldsymbol{C}\tilde{\boldsymbol{u}}_\mu)\,dv = 0. \tag{5.46}$$

Noting that $\boldsymbol{C}$ is constant, and using the properties of the double contraction, we have

$$\left(\int_{\Omega^i_{0,\mu}} \boldsymbol{P}_\mu(\nabla_0\tilde{\boldsymbol{u}}_\mu)^T\,dv\right) : \boldsymbol{C} - \left(\boldsymbol{P}^i_\mu\left(\int_{\Omega^i_{0,\mu}} \nabla_0\tilde{\boldsymbol{u}}_\mu\,dv\right)^T\right) : \boldsymbol{C} = 0. \tag{5.47}$$

Since $\boldsymbol{C}$ is arbitrary, we find

$$\int_{\Omega^i_{0,\mu}} \boldsymbol{P}_\mu(\nabla_0\tilde{\boldsymbol{u}}_\mu)^T\,dv = \boldsymbol{P}^i_\mu\left(\int_{\Omega^i_{0,\mu}} \nabla_0\tilde{\boldsymbol{u}}_\mu\,dv\right)^T. \tag{5.48}$$

Adding $\int_{\Omega^i_{0,\mu}} \boldsymbol{P}_\mu\boldsymbol{F}^T\,dv$ to both sides and using Equation (5.5) yields

$$\int_{\Omega^i_{0,\mu}} \boldsymbol{P}_\mu\boldsymbol{F}^T_\mu\,dv = |\Omega^i_{0,\mu}|\boldsymbol{P}^i_\mu(\boldsymbol{F}^i_\mu)^T. \tag{5.49}$$

Finally, we take into account that the angular momentum balance holds at each microscopic point, and thus

$$\int_{\Omega^i_{0,\mu}} \boldsymbol{P}_\mu\boldsymbol{F}^T_\mu\,dv = \int_{\Omega^i_{0,\mu}} (\boldsymbol{P}_\mu\boldsymbol{F}^T_\mu)^T\,dv = \left(\int_{\Omega^i_{0,\mu}} \boldsymbol{F}_\mu\boldsymbol{P}^T_\mu\,dv\right)^T, \tag{5.50}$$

i.e., the integral is symmetric, implying that its skew-symmetric part vanishes, and therefore

$$\operatorname{skew}(\boldsymbol{P}^i_\mu\boldsymbol{F}^T_\mu) = \operatorname{skew}\left(\int_{\Omega^i_{0,\mu}} \boldsymbol{P}_\mu\boldsymbol{F}^T_\mu\,dv\right) = \boldsymbol{0}. \tag{5.51}$$

Substituting back in Equation (5.45), we finally obtain

$$\operatorname{skew}(\boldsymbol{P}\boldsymbol{F}^T) = \langle\operatorname{skew}(\boldsymbol{P}^i_\mu(\boldsymbol{F}^i_\mu)^T)\rangle = \boldsymbol{0}, \tag{5.52}$$

thus confirming that the angular momentum balance is also satisfied at the macroscale for the homogenized stress found.

5.1.3 Projected Mean-Field Homogenization

We now introduce another homogenization model based on MFH, in which the MFH estimates are enforced only along selected directions associated with the microstructural orientation of each phase. Accordingly, we refer to this approach as Projected Mean-Field Homogenization (PMFH). This approach is particularly suitable for anisotropic microstructures, such as laminates, where mechanical response is strongly direction-dependent. It is based on the models proposed by Lee et al. (1993b,a) for semi-crystalline polymers. We discuss the relationship between our formulation and these earlier models at the end of this section.

Let $\boldsymbol{N}^i_\mu$ be a characteristic direction associated with phase i, for instance, the normal to a laminar interface, with $i = 1,\ldots,n_P$. We constrain the right stretch tensor $\boldsymbol{U}^i_\mu$ corresponding to the average deformation gradient $\boldsymbol{F}^i_\mu$ in phase i to match its counterpart computed from the MFH estimate, $\boldsymbol{F}^{i,\mathrm{mfh}}_\mu$, in the $\boldsymbol{N}^i_\mu$ direction[3]. The polar rotation tensor $\boldsymbol{R}^i_\mu$ computed from $\boldsymbol{F}^i_\mu$ is

[3] A simpler model where we constrain only the normal projection of the deformation gradient, a linear constraint, was also explored; however, we found that it failed to satisfy basic constitutive axioms.

also constrained to match the one found from the MFH estimate. The remaining directions are left unconstrained except for minimal admissibility. These constraints can be expressed as

$$\mathbf{P}^i_{\mathbb{S}^3_N,\mu} : \boldsymbol{U}(\boldsymbol{F}^i_\mu) = \mathbf{P}^i_{\mathbb{S}^3_N,\mu} : \boldsymbol{U}(\boldsymbol{F}^{i,\mathrm{mfh}}_\mu), \qquad i = 1,\dots,n_P, \tag{5.53}$$

$$\boldsymbol{R}(\boldsymbol{F}^i_\mu) = \boldsymbol{R}(\boldsymbol{F}^{i,\mathrm{mfh}}_\mu), \qquad i = 1,\dots,n_P, \tag{5.54}$$

where the symmetric orthogonal projections onto normal and tangential components are defined as

$$\mathbf{P}^i_{\mathbb{S}^3_N,\mu} : \boldsymbol{A} = (\boldsymbol{A}\boldsymbol{N}^i_\mu)\otimes\boldsymbol{N}^i_\mu + \boldsymbol{N}^i_\mu\otimes(\boldsymbol{A}\boldsymbol{N}^i_\mu) - (\boldsymbol{N}^i_\mu\cdot\boldsymbol{A}\boldsymbol{N}^i_\mu)(\boldsymbol{N}^i_\mu\otimes\boldsymbol{N}^i_\mu), \tag{5.55}$$

$$\mathbf{P}^i_{\mathbb{S}^3_T,\mu} : \boldsymbol{A} = \boldsymbol{A} - \mathbf{P}^i_{\mathbb{S}^3_N,\mu} : \boldsymbol{A}, \tag{5.56}$$

for any second-order symmetric tensor $\boldsymbol{A}$, i.e., $\boldsymbol{A}\in\mathbb{S}^3$. The functions $\boldsymbol{U}:\mathbb{R}^{3\times3}\to\mathbb{S}^3_+$ and $\boldsymbol{R}:\mathbb{R}^{3\times3}\to\mathrm{SO}(3)$ extract the right stretch and rotation tensors from the polar decomposition of their argument, respectively (see Equation (2.2)).

For the matrix phase, denoted by index m, the MFH estimate for the corresponding right stretch can be either adopted or discarded. These two cases correspond to choosing $\mathbf{P}^m_{\mathbb{S}^3_N,\mu} = \mathbf{I}_S$ or $\mathbf{P}^m_{\mathbb{S}^3_N,\mu} = \mathbf{O}$, respectively.[4]

This leads to the following admissible set for the displacement fluctuations

$$\tilde{\mathscr{K}}_{\mu,\mathrm{PMFH}}(\boldsymbol{F}) = \Big\{\boldsymbol{v}\in\tilde{\mathscr{K}}^*_\mu \;\Big|\; \mathbf{P}^i_{\mathbb{S}^3_N,\mu} : \boldsymbol{U}(\boldsymbol{F}^i_\mu) = \mathbf{P}^i_{\mathbb{S}^3_N,\mu} : \boldsymbol{U}(\boldsymbol{F}^{i,\mathrm{mfh}}_\mu), \\ \boldsymbol{R}(\boldsymbol{F}^i_\mu) = \boldsymbol{R}(\boldsymbol{F}^{i,\mathrm{mfh}}_\mu),\ \forall i = 1,\dots,n_P\Big\}, \tag{5.57}$$

where the average deformation gradient in phase i can be expressed in terms of the displacement fluctuations and the macroscopic deformation gradient using Equation (5.5).

This functional set contains the fully constrained counterpart defined in Equation (5.8), i.e.,

$$\tilde{\mathscr{K}}_{\mu,\mathrm{MFH}}(\boldsymbol{F}) \subseteq \tilde{\mathscr{K}}_{\mu,\mathrm{PMFH}}(\boldsymbol{F}) \subseteq \tilde{\mathscr{K}}^*_\mu, \tag{5.58}$$

assuming that $\langle\boldsymbol{F}^{i,\mathrm{mfh}}_\mu\rangle = \boldsymbol{F}$ holds.

The corresponding space of virtual admissible displacement fields is given by

$$\tilde{\mathscr{V}}_{\mu,\mathrm{PMFH}}(\boldsymbol{F},\delta\boldsymbol{F}) = \Bigg\{\boldsymbol{v}\in\tilde{\mathscr{V}}^*_\mu \;\Bigg|\; \\ \mathbf{P}^i_{\mathbb{S}^3_N,\mu} : \frac{d\boldsymbol{U}}{d\boldsymbol{F}}(\boldsymbol{F}^i_\mu) : \int_{\Omega^i_{0,\mu}} \nabla_0\boldsymbol{v}\,dv = |\Omega^i_{0,\mu}|\,\mathbf{P}^i_{\mathbb{S}^3_N,\mu} : \left(\frac{d\boldsymbol{U}}{d\boldsymbol{F}}(\boldsymbol{F}^{i,\mathrm{mfh}}_\mu) : \mathbf{A}^{i,\mathrm{mfh}}_\mu - \frac{d\boldsymbol{U}}{d\boldsymbol{F}}(\boldsymbol{F}^i_\mu)\right) : \delta\boldsymbol{F}, \\ \frac{d\boldsymbol{R}}{d\boldsymbol{F}}(\boldsymbol{F}^i_\mu) : \int_{\Omega^i_{0,\mu}} \nabla_0\boldsymbol{v}\,dv = |\Omega^i_{0,\mu}|\left(\frac{d\boldsymbol{R}}{d\boldsymbol{F}}(\boldsymbol{F}^{i,\mathrm{mfh}}_\mu) : \mathbf{A}^{i,\mathrm{mfh}}_\mu - \frac{d\boldsymbol{R}}{d\boldsymbol{F}}(\boldsymbol{F}^i_\mu)\right) : \delta\boldsymbol{F},\ \forall i = 1,\dots,n_P\Bigg\}, \tag{5.59}$$

making use of the chain rule to linearize Equations (5.53) and (5.54) and reordering the terms appropriately.

[4] $\mathbf{I}_S$ is the symmetric identity operator, defined component-wise according to

$$(\mathbf{I}_S)_{ijkl} = \frac{1}{2}(\delta_{ik}\delta_{jl} + \delta_{il}\delta_{jk}).$$

To enforce the above constraints within the PMVP formulation, we employ Lagrange multipliers. One full second-order tensor $\boldsymbol{\Omega}_\mu$ enforces the minimal admissibility condition (Equation (5.2)); n_P multipliers $\boldsymbol{\Omega}^i_{N,\mu}$ enforce the phase-wise normal conditions. Each $\boldsymbol{\Omega}^i_{N,\mu}$ satisfies

$$\mathbf{P}^i_{\mathbb{S}^3_N,\mu} : \boldsymbol{\Omega}^i_{N,\mu} = \boldsymbol{\Omega}^i_{N,\mu} : \mathbf{P}^i_{\mathbb{S}^3_N,\mu} = \boldsymbol{\Omega}^i_{N,\mu} = \boldsymbol{a} \otimes \boldsymbol{N}^i_\mu + \boldsymbol{N}^i_\mu \otimes \boldsymbol{a} - (\boldsymbol{N}^i_\mu \cdot \boldsymbol{a}) \boldsymbol{N}^i_\mu \otimes \boldsymbol{N}^i_\mu, \tag{5.60}$$

for some material vector $\boldsymbol{a} \in \mathbb{R}^3$, thus containing only three independent components (except for the matrix, where full enforcement may be allowed, i.e., when $\mathbf{P}^i_{\mathbb{S}^3_N,\mu} = \mathbf{I}_S$). Similarly, n_P multipliers $\boldsymbol{\Omega}^i_{R,\mu}$ enforce the phase-wise rotational constraints. Each $\boldsymbol{\Omega}^i_{R,\mu}$ multiplier only contributes to the derivation that follows through $\text{skew}(\boldsymbol{R}^{i\,T}_\mu \boldsymbol{\Omega}^i_{R,\mu})$, and thus can be parameterized by three independent components.

Note that in this section we employ a Lagrange multiplier $\boldsymbol{\Omega}_\mu$ to enforce the minimal admissibility condition, whereas in Section 5.1.2 we do not. This is because, in the full MFH model, the constraints on all the phases as a whole automatically lead to a set of average deformation gradients that respect the minimal admissibility condition by virtue of the kinematic self-consistency requirement on the MFH procedure, i.e., $\langle \boldsymbol{F}^i_\mu \rangle = \langle \boldsymbol{F}^{i,\text{mfh}}_\mu \rangle = \boldsymbol{F}$, implying that $\tilde{\boldsymbol{u}}_\mu \in \tilde{\mathscr{K}}^*_\mu$. Here, the kinematic restrictions, along with the self-consistency requirement on the MFH procedure, do not suffice to guarantee minimal admissibility; thus, we need to enforce it explicitly via an appropriate Lagrange multiplier.

The resulting Principle of Multiscale Virtual Power is expressed as

$$\begin{aligned}
|\Omega_{0,\mu}| \boldsymbol{P} : \delta \boldsymbol{F} = \int_{\Omega_{0,\mu}} \boldsymbol{P}_\mu : (\nabla_0 \delta \tilde{\boldsymbol{u}}_\mu + \delta \boldsymbol{F}) \, dv \\
- \boldsymbol{\Omega}_\mu : \sum_{i=1}^{n_P} \int_{\Omega^i_{0,\mu}} \nabla_0 \delta \tilde{\boldsymbol{u}}_\mu \, dv - \delta \boldsymbol{\Omega}_\mu : \sum_{i=1}^{n_P} \int_{\Omega^i_{0,\mu}} \nabla_0 \tilde{\boldsymbol{u}}_\mu \, dv \\
- \sum_{i=1}^{n_P} \boldsymbol{\Omega}^i_{N,\mu} : \mathbf{P}^i_{\mathbb{S}^3_N,\mu} : \left(\frac{d\boldsymbol{U}}{d\boldsymbol{F}}(\boldsymbol{F}^i_\mu) : \int_{\Omega^i_{0,\mu}} \nabla_0 \delta \tilde{\boldsymbol{u}}_\mu \, dv - |\Omega^i_{0,\mu}| \left(\frac{d\boldsymbol{U}}{d\boldsymbol{F}}(\boldsymbol{F}^{i,\text{mfh}}_\mu) : \mathbf{A}^{i,\text{mfh}}_\mu - \frac{d\boldsymbol{U}}{d\boldsymbol{F}}(\boldsymbol{F}^i_\mu) \right) : \delta \boldsymbol{F} \right) \\
- \sum_{i=1}^{n_P} \delta \boldsymbol{\Omega}^i_{N,\mu} : \mathbf{P}^i_{\mathbb{S}^3_N,\mu} : \left(\boldsymbol{U}(\boldsymbol{F}^i_\mu) - \boldsymbol{U}(\boldsymbol{F}^{i,\text{mfh}}_\mu) \right) \\
- \sum_{i=1}^{n_P} \boldsymbol{\Omega}^i_{R,\mu} : \left(\frac{d\boldsymbol{R}}{d\boldsymbol{F}}(\boldsymbol{F}^i_\mu) : \int_{\Omega^i_{0,\mu}} \nabla_0 \delta \tilde{\boldsymbol{u}}_\mu \, dv - |\Omega^i_{0,\mu}| \left(\frac{d\boldsymbol{R}}{d\boldsymbol{F}}(\boldsymbol{F}^{i,\text{mfh}}_\mu) : \mathbf{A}^{i,\text{mfh}}_\mu - \frac{d\boldsymbol{R}}{d\boldsymbol{F}}(\boldsymbol{F}^i_\mu) \right) : \delta \boldsymbol{F} \right) \\
- \sum_{i=1}^{n_P} \delta \boldsymbol{\Omega}^i_{R,\mu} : \left(\boldsymbol{R}(\boldsymbol{F}^i_\mu) - \boldsymbol{R}(\boldsymbol{F}^{i,\text{mfh}}_\mu) \right).
\end{aligned} \tag{5.61}$$

Interpretation of the Lagrange multipliers

To interpret the Lagrange multipliers, we now fix $\delta \boldsymbol{F} = \boldsymbol{0}$, $\delta \boldsymbol{\Omega}^i_{N,\mu} = \boldsymbol{0}$ and $\delta \boldsymbol{\Omega}^i_{R,\mu} = \boldsymbol{0}$ for $i = 1, \ldots, n_P$, and $\delta \boldsymbol{\Omega}_\mu = \boldsymbol{0}$. The PMVP then reduces to

$$\begin{aligned}
\int_{\Omega_{0,\mu}} \boldsymbol{P}_\mu : \nabla_0 \delta \tilde{\boldsymbol{u}}_\mu \, dv - \boldsymbol{\Omega}_\mu : \sum_{i=1}^{n_P} \int_{\Omega^i_{0,\mu}} \nabla_0 \delta \tilde{\boldsymbol{u}}_\mu \, dv \\
- \sum_{i=1}^{n_P} \boldsymbol{\Omega}^i_{N,\mu} : \mathbf{P}^i_{\mathbb{S}^3_N,\mu} : \frac{d\boldsymbol{U}}{d\boldsymbol{F}}(\boldsymbol{F}^i_\mu) : \int_{\Omega^i_{0,\mu}} \nabla_0 \delta \tilde{\boldsymbol{u}}_\mu \, dv \\
- \sum_{i=1}^{n_P} \boldsymbol{\Omega}^i_{R,\mu} : \frac{d\boldsymbol{R}}{d\boldsymbol{F}}(\boldsymbol{F}^i_\mu) : \int_{\Omega^i_{0,\mu}} \nabla_0 \delta \tilde{\boldsymbol{u}}_\mu \, dv = 0.
\end{aligned} \tag{5.62}$$

Firstly, to find how the average first Piola–Kirchhoff stress in each phase is related to the Lagrange multipliers, let us consider a linear test function $\delta\tilde{\boldsymbol{u}}_\mu = \boldsymbol{C}(\boldsymbol{Y} - \boldsymbol{Y}_0^i)$ in phase i and zero elsewhere, where $\boldsymbol{C}$ is an arbitrary second-order tensor. Substituting into the above condition and exploiting the arbitrariness of $\boldsymbol{C}$, we find

$$\boldsymbol{P}_\mu^i = \boldsymbol{\Omega}_\mu + \boldsymbol{\Omega}_{N,\mu}^i : \mathsf{P}^i_{\mathbb{S}^3_N,\mu} : \frac{d\boldsymbol{U}}{d\boldsymbol{F}}(\boldsymbol{F}_\mu^i) + \boldsymbol{\Omega}_{R,\mu}^i : \frac{d\boldsymbol{R}}{d\boldsymbol{F}}(\boldsymbol{F}_\mu^i), \quad i = 1,\dots,n_P. \tag{5.63}$$

This relation connects the Lagrange multipliers to the average first Piola–Kirchhoff stress in each phase. It also allows us to rewrite Equation (5.62) as

$$\int_{\Omega_{0,\mu}} \boldsymbol{P}_\mu : \nabla_0 \delta\tilde{\boldsymbol{u}}_\mu \, dv = \sum_{i=1}^{n_P} \boldsymbol{P}_\mu^i : \int_{\Omega_{0,\mu}^i} \nabla_0 \delta\tilde{\boldsymbol{u}}_\mu \, dv. \tag{5.64}$$

Before proceeding with the choice of appropriate test functions to extract information about the Lagrange multipliers, note that

$$\frac{d\boldsymbol{U}}{d\boldsymbol{F}}(\boldsymbol{F}_\mu^i) : (\boldsymbol{R}_\mu^i \boldsymbol{S}) = \boldsymbol{S}, \quad \frac{d\boldsymbol{R}}{d\boldsymbol{F}}(\boldsymbol{F}_\mu^i) : (\boldsymbol{R}_\mu^i \boldsymbol{S}) = \boldsymbol{O}, \quad \forall \boldsymbol{S} \in \mathbb{S}^3, \tag{5.65}$$

$$\frac{d\boldsymbol{U}}{d\boldsymbol{F}}(\boldsymbol{F}_\mu^i) : (\boldsymbol{W}\boldsymbol{F}_\mu^i) = \boldsymbol{O}, \quad \frac{d\boldsymbol{R}}{d\boldsymbol{F}}(\boldsymbol{F}_\mu^i) : (\boldsymbol{W}\boldsymbol{F}_\mu^i) = \boldsymbol{W}\boldsymbol{R}_\mu^i, \quad \forall \boldsymbol{W} \in \mathfrak{so}(3), \tag{5.66}$$

as pointed out in (Chen and Wheeler, 1992, Equation (4)), where $\mathbb{S}^3$ and $\mathfrak{so}(3)$ denote the spaces of symmetric and skew-symmetric second-order tensors in three dimensions, respectively.

Accordingly, we choose a linear test function $\delta\tilde{\boldsymbol{u}}_\mu = \boldsymbol{R}_\mu^i \boldsymbol{S}(\boldsymbol{Y} - \boldsymbol{Y}_0^i)$ in phase i and zero elsewhere, where $\boldsymbol{S}$ is symmetric, and deduce that

$$\boldsymbol{P}_\mu^i : (\boldsymbol{R}_\mu^i \boldsymbol{S}) = \boldsymbol{\Omega}_\mu : (\boldsymbol{R}_\mu^i \boldsymbol{S}) + \boldsymbol{\Omega}_{N,\mu}^i : \boldsymbol{S}, \quad i = 1,\dots,n_P, \tag{5.67}$$

where we took into account that the derivative of the polar rotation is zero in the $\boldsymbol{R}_\mu^i \boldsymbol{S}$ direction and that the derivative of the right stretch in the same direction is $\boldsymbol{S}$ (Equation (5.65)). Using the properties of the double contraction operation, we rewrite Equation (5.67) as

$$(\boldsymbol{R}_\mu^i)^T \boldsymbol{P}_\mu^i : \boldsymbol{S} = (\boldsymbol{R}_\mu^i)^T \boldsymbol{\Omega}_\mu : \boldsymbol{S} + \boldsymbol{\Omega}_{N,\mu}^i : \boldsymbol{S}, \quad i = 1,\dots,n_P. \tag{5.68}$$

Since $\boldsymbol{S}$ is an arbitrary symmetric second-order tensor, we conclude that

$$\operatorname{sym} \boldsymbol{T}_{B,\mu}^i = \operatorname{sym}((\boldsymbol{R}_\mu^i)^T \boldsymbol{\Omega}_\mu) + \boldsymbol{\Omega}_{N,\mu}^i, \quad i = 1,\dots,n_P, \tag{5.69}$$

where we used the definition of the Biot stress tensor $\boldsymbol{T}_{B,\mu}^i = (\boldsymbol{R}_\mu^i)^T \boldsymbol{P}_\mu^i$. Finally, we consider the projection of the last equation onto the tangential direction using the symmetric orthogonal projection defined in Equation (5.55) and find

$$\mathsf{P}^i_{\mathbb{S}^3_T,\mu} : \boldsymbol{T}_{B,\mu}^i = \mathsf{P}^i_{\mathbb{S}^3_T,\mu} : ((\boldsymbol{R}_\mu^i)^T \boldsymbol{\Omega}_\mu), \quad i = 1,\dots,n_P. \tag{5.70}$$

To better elucidate the relationship between the Lagrange multipliers, we can also choose a linear test function $\delta\tilde{\boldsymbol{u}}_\mu = \boldsymbol{W}\boldsymbol{F}_\mu^i(\boldsymbol{Y} - \boldsymbol{Y}_0^i)$ in phase i and zero elsewhere, where $\boldsymbol{W}$ is skew-symmetric, and deduce that

$$\boldsymbol{P}_\mu^i : (\boldsymbol{W}\boldsymbol{F}_\mu^i) = \boldsymbol{\Omega}_\mu : (\boldsymbol{W}\boldsymbol{F}_\mu^i) + \boldsymbol{\Omega}_{R,\mu}^i : (\boldsymbol{W}\boldsymbol{R}_\mu^i), \quad i = 1,\dots,n_P, \tag{5.71}$$

where we took into account that the derivative of the right stretch is zero in the $\boldsymbol{W}\boldsymbol{F}_\mu^i$ direction and that the derivative of the polar rotation in the same direction is $\boldsymbol{W}\boldsymbol{R}_\mu^i$ (Equation (5.66)).

Using the fact that the polar rotation is orthogonal and employing the formula for the polar decomposition, we rewrite Equation (5.71) as

$$\boldsymbol{P}_\mu^i : (\boldsymbol{R}_\mu^i (\boldsymbol{R}_\mu^i)^T \boldsymbol{W} \boldsymbol{R}_\mu^i \boldsymbol{U}_\mu^i) = \boldsymbol{\Omega}_\mu : (\boldsymbol{R}_\mu^i (\boldsymbol{R}_\mu^i)^T \boldsymbol{W} \boldsymbol{R}_\mu^i \boldsymbol{U}_\mu^i) + \boldsymbol{\Omega}_{R,\mu}^i : (\boldsymbol{R}_\mu^i (\boldsymbol{R}_\mu^i)^T \boldsymbol{W} \boldsymbol{R}_\mu^i), \quad i = 1, \dots, n_P. \tag{5.72}$$

Using the properties of the double contraction operation and the fact that $\boldsymbol{U}_\mu^i$ is symmetric, we rewrite the above equation as

$$((\boldsymbol{R}_\mu^i)^T \boldsymbol{P}_\mu^i \boldsymbol{U}_\mu^i) : \boldsymbol{W}^* = ((\boldsymbol{R}_\mu^i)^T \boldsymbol{\Omega}_\mu \boldsymbol{U}_\mu^i) : \boldsymbol{W}^* + ((\boldsymbol{R}_\mu^i)^T \boldsymbol{\Omega}_{R,\mu}^i) : \boldsymbol{W}^*, \quad i = 1, \dots, n_P, \tag{5.73}$$

where we defined $\boldsymbol{W}^* = (\boldsymbol{R}_\mu^i)^T \boldsymbol{W} \boldsymbol{R}_\mu^i$, which is also skew-symmetric. Since $\boldsymbol{W}^*$ is an arbitrary skew-symmetric second-order tensor, we conclude that

$$\operatorname{skew}(\boldsymbol{T}_{B,\mu}^i \boldsymbol{U}_\mu^i) = \operatorname{skew}((\boldsymbol{R}_\mu^i)^T \boldsymbol{\Omega}_\mu \boldsymbol{U}_\mu^i) + \operatorname{skew}((\boldsymbol{R}_\mu^i)^T \boldsymbol{\Omega}_{R,\mu}^i), \quad i = 1, \dots, n_P, \tag{5.74}$$

where we used the definition of the Biot stress tensor (Equation (2.12)). Finally, notice that to satisfy the balance of angular momentum at each phase, $\operatorname{skew}(\boldsymbol{T}_{B,\mu}^i \boldsymbol{U}_\mu^i) = \boldsymbol{O}$, (Equation (C.40)) and thus

$$\operatorname{skew}((\boldsymbol{R}_\mu^i)^T \boldsymbol{\Omega}_{R,\mu}^i) = -\operatorname{skew}((\boldsymbol{R}_\mu^i)^T \boldsymbol{\Omega}_\mu \boldsymbol{U}_\mu^i), \quad i = 1, \dots, n_P. \tag{5.75}$$

Stress homogenization

To derive the homogenization rule for the macroscopic stress, we consider the variation where $\delta \tilde{\boldsymbol{u}}_\mu = \boldsymbol{0}$, $\delta \boldsymbol{\Omega}_\mu = \boldsymbol{0}$, $\delta \boldsymbol{\Omega}_{N,\mu}^i = \boldsymbol{0}$, $\delta \boldsymbol{\Omega}_{R,\mu}^i = \boldsymbol{0}$, $i = 1, \dots, n_P$. The resulting expression reads

$$\begin{aligned} |\Omega_{0,\mu}| \boldsymbol{P} : \delta \boldsymbol{F} = \int_{\Omega_{0,\mu}} \boldsymbol{P}_\mu : \delta \boldsymbol{F} \\ + \sum_{i=1}^{n_P} |\Omega_{0,\mu}^i| \boldsymbol{\Omega}_{N,\mu}^i : \mathbf{P}_{\mathbb{S}^3_N,\mu}^i : \left(\frac{d\boldsymbol{U}}{d\boldsymbol{F}} (\boldsymbol{F}_\mu^{i,\mathrm{mfh}}) : \mathbf{A}_\mu^{i,\mathrm{mfh}} - \frac{d\boldsymbol{U}}{d\boldsymbol{F}} (\boldsymbol{F}_\mu^i) \right) : \delta \boldsymbol{F} \\ + \sum_{i=1}^{n_P} |\Omega_{0,\mu}^i| \boldsymbol{\Omega}_{R,\mu}^i : \left(\frac{d\boldsymbol{R}}{d\boldsymbol{F}} (\boldsymbol{F}_\mu^{i,\mathrm{mfh}}) : \mathbf{A}_\mu^{i,\mathrm{mfh}} - \frac{d\boldsymbol{R}}{d\boldsymbol{F}} (\boldsymbol{F}_\mu^i) \right) : \delta \boldsymbol{F}. \end{aligned} \tag{5.76}$$

We can now work to obtain an expression for the macroscopic stress $\boldsymbol{P}$ in terms of the Lagrange multipliers and the MFH estimates. From the self-consistency condition imposed in Equation (4.20) on the MFH procedure and the fact that $\boldsymbol{\Omega}_\mu$ is a constant, we know that

$$\sum_{i=1}^{n_P} |\Omega_{0,\mu}^i| \boldsymbol{\Omega}_\mu : (\mathbf{A}_\mu^{i,\mathrm{mfh}} - \mathbf{I}) : \delta \boldsymbol{F} = \boldsymbol{0}, \tag{5.77}$$

and thus we can add this term to Equation (5.76) as follows

$$\begin{aligned} |\Omega_{0,\mu}| \boldsymbol{P} : \delta \boldsymbol{F} = \int_{\Omega_{0,\mu}} \boldsymbol{P}_\mu : \delta \boldsymbol{F} \\ + \sum_{i=1}^{n_P} |\Omega_{0,\mu}^i| \boldsymbol{\Omega}_{N,\mu}^i : \mathbf{P}_{\mathbb{S}^3_N,\mu}^i : \left(\frac{d\boldsymbol{U}}{d\boldsymbol{F}} (\boldsymbol{F}_\mu^{i,\mathrm{mfh}}) : \mathbf{A}_\mu^{i,\mathrm{mfh}} - \frac{d\boldsymbol{U}}{d\boldsymbol{F}} (\boldsymbol{F}_\mu^i) \right) : \delta \boldsymbol{F} \\ + \sum_{i=1}^{n_P} |\Omega_{0,\mu}^i| \boldsymbol{\Omega}_{R,\mu}^i : \left(\frac{d\boldsymbol{R}}{d\boldsymbol{F}} (\boldsymbol{F}_\mu^{i,\mathrm{mfh}}) : \mathbf{A}_\mu^{i,\mathrm{mfh}} - \frac{d\boldsymbol{R}}{d\boldsymbol{F}} (\boldsymbol{F}_\mu^i) \right) : \delta \boldsymbol{F} \\ + \sum_{i=1}^{n_P} |\Omega_{0,\mu}^i| \boldsymbol{\Omega}_\mu : (\mathbf{A}_\mu^{i,\mathrm{mfh}} - \mathbf{I}) : \delta \boldsymbol{F}. \end{aligned} \tag{5.78}$$

We can now rearrange terms to obtain

$$
\begin{aligned}
|\Omega_{0,\mu}|\boldsymbol{P}:\delta\boldsymbol{F} = &\sum_{i=1}^{n_P}|\Omega_{0,\mu}^i|\boldsymbol{P}_\mu^i:\delta\boldsymbol{F}\\
&-\sum_{i=1}^{n_P}|\Omega_{0,\mu}^i|\left(\boldsymbol{\Omega}_\mu+\boldsymbol{\Omega}_{N,\mu}^i:\mathbf{P}_{\mathbb{S}_N^3,\mu}^i:\frac{d\boldsymbol{U}}{d\boldsymbol{F}}(\boldsymbol{F}_\mu^i)+\boldsymbol{\Omega}_{R,\mu}^i:\frac{d\boldsymbol{R}}{d\boldsymbol{F}}(\boldsymbol{F}_\mu^i)\right):\delta\boldsymbol{F}\\
&+\sum_{i=1}^{n_P}|\Omega_{0,\mu}^i|\left(\boldsymbol{\Omega}_\mu+\boldsymbol{\Omega}_{N,\mu}^i:\mathbf{P}_{\mathbb{S}_N^3,\mu}^i:\frac{d\boldsymbol{U}}{d\boldsymbol{F}}(\boldsymbol{F}_\mu^{i,\mathrm{mfh}})+\boldsymbol{\Omega}_{R,\mu}^i:\frac{d\boldsymbol{R}}{d\boldsymbol{F}}(\boldsymbol{F}_\mu^{i,\mathrm{mfh}})\right):\mathbf{A}_\mu^{i,\mathrm{mfh}}:\delta\boldsymbol{F}. \qquad (5.79)
\end{aligned}
$$

Notice that the second term on the right-hand side is equal to the average stress in phase i per Equation (5.63), and thus cancels out with the first term. We then find

$$
\begin{aligned}
|\Omega_{0,\mu}|\boldsymbol{P}:\delta\boldsymbol{F} = &\\
&\sum_{i=1}^{n_P}|\Omega_{0,\mu}^i|\left(\boldsymbol{\Omega}_\mu+\boldsymbol{\Omega}_{N,\mu}^i:\mathbf{P}_{\mathbb{S}_N^3,\mu}^i:\frac{d\boldsymbol{U}}{d\boldsymbol{F}}(\boldsymbol{F}_\mu^{i,\mathrm{mfh}})+\boldsymbol{\Omega}_{R,\mu}^i:\frac{d\boldsymbol{R}}{d\boldsymbol{F}}(\boldsymbol{F}_\mu^{i,\mathrm{mfh}})\right):\mathbf{A}_\mu^{i,\mathrm{mfh}}:\delta\boldsymbol{F}, \qquad (5.80)
\end{aligned}
$$

which, taking into account that $\delta\boldsymbol{F}$ is arbitrary, leads to

$$
\boldsymbol{P}=\left\langle\left(\boldsymbol{\Omega}_\mu+\boldsymbol{\Omega}_{N,\mu}^i:\mathbf{P}_{\mathbb{S}_N^3,\mu}^i:\frac{d\boldsymbol{U}}{d\boldsymbol{F}}(\boldsymbol{F}_\mu^{i,\mathrm{mfh}})+\boldsymbol{\Omega}_{R,\mu}^i:\frac{d\boldsymbol{R}}{d\boldsymbol{F}}(\boldsymbol{F}_\mu^{i,\mathrm{mfh}})\right):\mathbf{A}_\mu^{i,\mathrm{mfh}}\right\rangle, \qquad (5.81)
$$

as the homogenization rule for the macroscopic stress. We write the last equation in shorthand as

$$
\boldsymbol{P}=\left\langle\boldsymbol{P}_\mu^{i,*}:\mathbf{A}_\mu^{i,\mathrm{mfh}}\right\rangle, \qquad (5.82)
$$

where

$$
\boldsymbol{P}_\mu^{i,*}=\boldsymbol{\Omega}_\mu+\boldsymbol{\Omega}_{N,\mu}^i:\frac{d\boldsymbol{U}}{d\boldsymbol{F}}(\boldsymbol{F}_\mu^{i,\mathrm{mfh}})+\boldsymbol{\Omega}_{R,\mu}^i:\frac{d\boldsymbol{R}}{d\boldsymbol{F}}(\boldsymbol{F}_\mu^{i,\mathrm{mfh}}), \qquad (5.83)
$$

can be interpreted as an effective first Piola–Kirchhoff stress in phase i.

To evaluate the terms involving the derivatives of the polar decomposition, we use the following expressions

$$
\begin{aligned}
\boldsymbol{\Omega}_{N,\mu}^i:\frac{d\boldsymbol{U}}{d\boldsymbol{F}}(\boldsymbol{F}_\mu^{i,\mathrm{mfh}}) &= \left(\frac{d\boldsymbol{U}}{d\boldsymbol{F}}(\boldsymbol{F}_\mu^{i,\mathrm{mfh}})\right)^T:\boldsymbol{\Omega}_{N,\mu}^i \qquad (5.84)\\
&= \boldsymbol{R}_\mu^i\boldsymbol{\Omega}_{N,\mu}^i-2(\det\boldsymbol{Y}_\mu^{i,\mathrm{mfh}})^{-1}\boldsymbol{R}_\mu^i\boldsymbol{Y}_\mu^{i,\mathrm{mfh}}\,\mathrm{skew}(\boldsymbol{\Omega}_{N,\mu}^i\boldsymbol{U}_\mu^{i,\mathrm{mfh}})\,\boldsymbol{Y}_\mu^{i,\mathrm{mfh}}, \qquad (5.85)
\end{aligned}
$$

and

$$
\begin{aligned}
\boldsymbol{\Omega}_{R,\mu}^i:\frac{d\boldsymbol{R}}{d\boldsymbol{F}}(\boldsymbol{F}_\mu^{i,\mathrm{mfh}}) &= \left(\frac{d\boldsymbol{R}}{d\boldsymbol{F}}(\boldsymbol{F}_\mu^{i,\mathrm{mfh}})\right)^T:\boldsymbol{\Omega}_{R,\mu}^i \qquad (5.86)\\
&= 2(\det\boldsymbol{Y}_\mu^{i,\mathrm{mfh}})^{-1}\boldsymbol{R}_\mu^i\boldsymbol{Y}_\mu^{i,\mathrm{mfh}}\,\mathrm{skew}((\boldsymbol{R}_\mu^i)^T\boldsymbol{\Omega}_{R,\mu}^i)\,\boldsymbol{Y}_\mu^{i,\mathrm{mfh}}, \qquad (5.87)
\end{aligned}
$$

derived in (Chen and Wheeler, 1992, Equation (10)), where

$$
\boldsymbol{Y}_\mu^{i,\mathrm{mfh}}=(\mathrm{tr}(\boldsymbol{U}_\mu^{i,\mathrm{mfh}}))\boldsymbol{I}-\boldsymbol{U}_\mu^{i,\mathrm{mfh}}. \qquad (5.88)
$$

In the expressions above we already took into account that $\boldsymbol{R}_\mu^i=\boldsymbol{R}_\mu^{i,\mathrm{mfh}}$.[5]

[5] To the best of the authors' knowledge, the factor 2 in the skew-symmetric terms is missing in (Chen and Wheeler, 1992, Equation (10)).

Accordingly, we can rewrite $\boldsymbol{P}_{\mu}^{i,*}$ as

$$\boldsymbol{P}_{\mu}^{i,*} = \boldsymbol{R}_{\mu}^{i}(\operatorname{sym}\boldsymbol{T}_{B,\mu}^{i,*} + \operatorname{skew}\boldsymbol{T}_{B,\mu}^{i,*}), \tag{5.89}$$

where

$$\operatorname{sym}\boldsymbol{T}_{B,\mu}^{i,*} = \operatorname{sym}((\boldsymbol{R}_{\mu}^{i})^{T}\boldsymbol{\Omega}_{\mu}) + \boldsymbol{\Omega}_{N,\mu}^{i}, \tag{5.90}$$

and

$$\begin{aligned}\operatorname{skew}\boldsymbol{T}_{B,\mu}^{i,*} = {}& \operatorname{skew}((\boldsymbol{R}_{\mu}^{i})^{T}\boldsymbol{\Omega}_{\mu}) \\ & + 2(\det\boldsymbol{Y}_{\mu}^{i,\mathrm{mfh}})^{-1}\boldsymbol{Y}_{\mu}^{i,\mathrm{mfh}}\operatorname{skew}((\boldsymbol{R}_{\mu}^{i})^{T}\boldsymbol{\Omega}_{R,\mu}^{i} - \boldsymbol{\Omega}_{N,\mu}^{i}\boldsymbol{U}_{\mu}^{i,\mathrm{mfh}})\boldsymbol{Y}_{\mu}^{i,\mathrm{mfh}}.\end{aligned} \tag{5.91}$$

Comparing with Equation (5.69), we conclude that the symmetric part of the effective Biot stress $\boldsymbol{T}_{B,\mu}^{i,*}$ is equal to the symmetric part of the actual Biot stress $\boldsymbol{T}_{B,\mu}^{i}$ in phase i, i.e.,

$$\operatorname{sym}\boldsymbol{T}_{B,\mu}^{i,*} = \operatorname{sym}\boldsymbol{T}_{B,\mu}^{i}. \tag{5.92}$$

In general, however, their skew-symmetric components differ.

The homogenization rule for the macroscopic stress obtained for this projected model (Equation (5.82)), bears similarities with the one obtained for the fully constrained model (Equation (5.32)). As before, the appearance of the localization tensors is one of the distinctions of this formulation with respect to the classical mean-field averaging through a simple volume average of the phase stresses. It is particularly relevant to ensuring the model's energetic consistency, as discussed below. In addition, the stress that enters our weighted average is not the average stress in each phase, but an appropriately computed effective stress. This stems from the nonlinearity of the kinematic constraints imposed on the PMVP. It is shown to be essential in ensuring that the macroscopic response satisfies angular momentum balance. Finally, note that the effective stress in each phase depends on the Lagrange multipliers, which are not known a priori, and must be computed as part of the solution of the model.

Remark 5.3 | The $\tilde{\boldsymbol{S}}$-Inclusion Model

The model described in this section is based on the $\tilde{\boldsymbol{S}}$-inclusion model proposed in Lee et al. (1993b,a). The original model employs a rate formulation relating the Cauchy stress tensor to the spatial velocity gradient, with the normal component of the rate of deformation set equal to its MFH counterpart. In particular, the MFH procedure selected by the authors equates the strain in each phase to the corresponding macroscopic quantity, i.e., assumes 'no interaction' between the phases. Here, we have rigorously derived a similar model from the variational structure of the PMVP, without any heuristic assumptions, under more general conditions that account for finite strain and other choices for the interaction model used in the MFH procedure.

Energetic consistency and balance of angular momentum

Employing similar derivations to those in Section 5.1.2, we can show that the projected MFH model derived in this section guarantees energetic consistency across scales for non-dissipative materials, and the corresponding stress homogenization rule satisfies the balance of angular momentum. See Appendix C.1.1 for the detailed derivation.

5.1.4 Sachs model

We show in the following that the model that coincides with the minimal admissible space $\tilde{\mathscr{K}}_\mu^*$ is the standard Sachs model, in which the average stress in each phase is assumed to equal the macroscopic stress. The functional space of admissible displacement fluctuations in this case is

$$\tilde{\mathscr{K}}_{\mu,\text{Sachs}} = \tilde{\mathscr{K}}_\mu^*, \tag{5.93}$$

and the corresponding space of virtual displacement fluctuations is

$$\tilde{\mathscr{V}}_{\mu,\text{Sachs}} = \tilde{\mathscr{V}}_\mu^*. \tag{5.94}$$

To enforce the minimal constraint implied by (5.2), we again use the method of Lagrange multipliers. Introducing a second-order tensor $\boldsymbol{\Omega}_\mu$, the Principle of Multiscale Virtual Power becomes

$$|\Omega_{0,\mu}|\boldsymbol{P}:\delta\boldsymbol{F} = \int_{\Omega_{0,\mu}} \boldsymbol{P}_\mu : (\nabla_0 \delta\tilde{\boldsymbol{u}}_\mu + \delta\boldsymbol{F})\, dv \\ - \boldsymbol{\Omega}_\mu : \sum_{i=1}^{n_P} \int_{\Omega_{0,\mu}^i} \nabla_0 \delta\tilde{\boldsymbol{u}}_\mu \, dv - \delta\boldsymbol{\Omega}_\mu : \sum_{i=1}^{n_P} \int_{\Omega_{0,\mu}^i} \nabla_0 \tilde{\boldsymbol{u}}_\mu \, dv. \tag{5.95}$$

Kinematical homogenization

By setting all variations to zero except for $\delta\boldsymbol{\Omega}_\mu$, we retrieve the enforced constraint

$$\sum_{i=1}^{n_P} \int_{\Omega_{0,\mu}^i} \nabla_0 \tilde{\boldsymbol{u}}_\mu \, dv = \boldsymbol{0}, \tag{5.96}$$

which is the minimal admissibility constraint.

Interpretation of the Lagrange multipliers

To interpret the Lagrange multiplier, we choose $\delta\boldsymbol{F} = \boldsymbol{0}$ and $\delta\boldsymbol{\Omega}_\mu = \boldsymbol{0}$. We then obtain

$$\int_{\Omega_{0,\mu}} \boldsymbol{P}_\mu : \nabla_0 \delta\tilde{\boldsymbol{u}}_\mu \, dv - \boldsymbol{\Omega}_\mu : \sum_{i=1}^{n_P} \int_{\Omega_{0,\mu}^i} \nabla_0 \delta\tilde{\boldsymbol{u}}_\mu \, dv = 0. \tag{5.97}$$

Using a linear test function $\delta\tilde{\boldsymbol{u}}_\mu = \boldsymbol{C}(\boldsymbol{Y} - \boldsymbol{Y}_0^i)$ in each phase, we deduce

$$\boldsymbol{\Omega}_\mu = \boldsymbol{P}_\mu^i, \quad i = 1, \dots, n_P, \tag{5.98}$$

which shows that the average stress is the same in all phases and equals the Lagrange multiplier.

Thus, substituting the Lagrange multiplier in the second term of Equation (5.97), we can write

$$\int_{\Omega_{0,\mu}} \boldsymbol{P}_\mu : \nabla_0 \delta\tilde{\boldsymbol{u}}_\mu \, dv = \sum_{i=1}^{n_P} \boldsymbol{P}_\mu^i : \int_{\Omega_{0,\mu}^i} \nabla_0 \delta\tilde{\boldsymbol{u}}_\mu \, dv. \tag{5.99}$$

Stress homogenization

Finally, setting $\delta\tilde{\boldsymbol{u}}_\mu = \boldsymbol{0}$ and $\delta\boldsymbol{\Omega}_\mu = \boldsymbol{0}$, we obtain

$$\boldsymbol{P} = \langle \boldsymbol{P}_\mu^i \rangle. \tag{5.100}$$

Thus, we recover $\boldsymbol{\Omega}_\mu = \boldsymbol{P}$, and the model enforces uniform average stress across all phases.

Remark 5.4 | Sachs model

This derivation recovers the classical Sachs model assumption that the stress is uniform across all phases and equal to the macroscopic stress. Importantly, this result is derived systematically from the variational principle, without ad hoc hypotheses.

Remark 5.5 | Consistency of the stress homogenization rule

Although the stress homogenization rule in Equation (5.100) appears distinct from those in Equation (5.32) and Equation (5.81), consistency can be shown under the assumptions of the Sachs model. Although not necessary for the derivation or use of the Sachs model, we can write the relationship between the average deformation gradient in each phase and the macroscopic deformation gradient symbolically as

$$\boldsymbol{F}_\mu^i = \mathscr{A}_\mu^i(\boldsymbol{F}, \boldsymbol{\alpha}_\mu^i). \tag{5.101}$$

The corresponding derivative with respect to the macroscopic deformation gradient can be written as

$$\mathbf{A}_\mu^i = \frac{\partial \mathscr{A}_\mu^i}{\partial \boldsymbol{F}}, \tag{5.102}$$

such that $\langle \mathbf{A}_\mu^i \rangle = \mathbf{I}$ per the minimal admissibility condition. Now, if all phases are subjected to the same stress, then

$$\begin{aligned} \langle \boldsymbol{P}_\mu^i : \mathbf{A}_\mu^i \rangle &= \langle \boldsymbol{P} : \mathbf{A}_\mu^i \rangle && (5.103)\\ &= \boldsymbol{P} : \langle \mathbf{A}_\mu^i \rangle && (5.104)\\ &= \boldsymbol{P} : \mathbf{I} && (5.105)\\ &= \boldsymbol{P}. && (5.106) \end{aligned}$$

Note that $\mathbf{A}_\mu^i$ replaces here its MFH counterpart, $\mathbf{A}_\mu^{i,\mathrm{mfh}}$, since for the Sachs model the MFH estimates are discarded.

Thus, we conclude that the homogenization rule found in Equations (5.32) and (5.81) is consistent for all the models considered, including the Sachs model.

Energetic consistency and balance of angular momentum

The Sachs model satisfies both energetic consistency across scales and the balance of angular momentum, as shown in Appendix C.1.2.

Box 5.1 summarizes the algorithm for the models formulated in Section 5.1 based on the PMVP.

Box 5.1: Algorithm for the models formulated in Section 5.1 based on the PMVP.

1. Given $\boldsymbol{F}$, compute from the strain-driven MFH procedure

$$\boldsymbol{F}_\mu^{i,\mathrm{mfh}},\ \boldsymbol{P}_\mu^{i,\mathrm{mfh}},\ \mathbf{A}_\mu^{i,\mathrm{mfh}},\quad i=1,\dots,n_P.$$

2. IF this is the full MFH model THEN

   (a) Set $\boldsymbol{F}_\mu^i=\boldsymbol{F}_\mu^{i,\mathrm{mfh}},\quad \boldsymbol{P}_\mu^i=\boldsymbol{P}_\mu^{i,\mathrm{mfh}},\quad i=1,\dots,n_P.$

   (b) Compute the homogenized stress as

$$\boldsymbol{P}=\langle \boldsymbol{P}_\mu^i:\mathbf{A}_\mu^{i,\mathrm{mfh}}\rangle.$$

   ELSE IF this is the projected MFH model THEN

   (a) Solve the nonlinear system of equations given by the kinematic homogenization condition

$$\boldsymbol{F}=\langle \boldsymbol{F}_\mu^i\rangle,$$

   for the unknown Lagrange multiplier $\boldsymbol{\Omega}_\mu$, adopting for each phase

$$\mathbf{P}^i_{\mathbb{S}^3_N,\mu}:\boldsymbol{U}_\mu^i=\mathbf{P}^i_{\mathbb{S}^3_N,\mu}:\boldsymbol{U}_\mu^{i,\mathrm{mfh}},\quad \boldsymbol{R}_\mu^i=\boldsymbol{R}_\mu^{i,\mathrm{mfh}},\quad \mathbf{P}^i_{\mathbb{S}^3_T,\mu}:\boldsymbol{T}^i_{B,\mu}=\mathbf{P}^i_{\mathbb{S}^3_T,\mu}:((\boldsymbol{R}_\mu^i)^T\boldsymbol{\Omega}_\mu).$$

   (b) Having found the Lagrange multiplier $\boldsymbol{\Omega}_\mu$, and computed the average stress and deformation gradient in each phase, $\boldsymbol{P}_\mu^i$ and $\boldsymbol{F}_\mu^i$, we can obtain the other Lagrange multipliers as

$$\boldsymbol{\Omega}^i_{N,\mu}=\mathrm{sym}(\boldsymbol{T}^i_{B,\mu}-(\boldsymbol{R}_\mu^i)^T\boldsymbol{\Omega}_\mu),\quad i=1,\dots,n_P,$$

   and

$$\mathrm{skew}((\boldsymbol{R}_\mu^i)^T\boldsymbol{\Omega}^i_{R,\mu})=-\mathrm{skew}((\boldsymbol{R}_\mu^i)^T\boldsymbol{\Omega}_\mu\boldsymbol{U}_\mu^i),\quad i=1,\dots,n_P.$$

   (c) Compute the effective stress in each phase as

$$\boldsymbol{P}_\mu^{i,*}=\boldsymbol{\Omega}_\mu+\boldsymbol{\Omega}^i_{N,\mu}:\frac{d\boldsymbol{U}}{d\boldsymbol{F}}(\boldsymbol{F}_\mu^{i,\mathrm{mfh}})+\boldsymbol{\Omega}^i_{R,\mu}:\frac{d\boldsymbol{R}}{d\boldsymbol{F}}(\boldsymbol{F}_\mu^{i,\mathrm{mfh}}),\quad i=1,\dots,n_P.$$

   (d) Compute the homogenized stress as

$$\boldsymbol{P}=\langle \boldsymbol{P}_\mu^{i,*}:\mathbf{A}_\mu^{i,\mathrm{mfh}}\rangle.$$

   ELSE IF this is the Sachs model THEN

   (a) Solve the nonlinear system of equations given by the kinematic homogenization condition

$$\boldsymbol{F}=\langle \boldsymbol{F}_\mu^i\rangle,$$

   for the unknown macroscopic stress $\boldsymbol{P}$ adopting for each phase

$$\boldsymbol{P}_\mu^i=\boldsymbol{P},\quad i=1,\dots,n_P.$$

5.2 The Principle of Multiscale Complementary Virtual Power and Mean-Field Homogenization

This section parallels the development presented in Section 5.1, but adopts the PMCVP as the variational framework. As before, the formulation is structured to accommodate the estimates derived from stress-driven MFH, but now emphasizes static admissibility. Given the clear parallels with the derivations in Section 5.1, we focus on the key differences and their implications and point the reader to Appendix C.2 for details on the derivations.

5.2.1 Non-equilibrium stresses

In contrast to the standard PMVP formulation, which allows for displacement incompatibilities, the PMCVP framework posits that interphase stresses may be out of equilibrium. This assumption is introduced explicitly to allow the incorporation of stress estimates from MFH procedures. Regularity within each phase is still enforced, but jumps in traction across interfaces are permitted.

Remark 5.6 | Incompatible Displacements and Non-equilibrium Stresses

In Section 5.1, phase incompatibilities in displacement are postulated, from which stress non-equilibrium followed as a consequence. Here, the logic is reversed: we postulate non-equilibrium stresses and deduce that displacements may be incompatible across phase boundaries, creating a clear parallel between the two sets of models, which mirror each other.

To formalize this, we define auxiliary functional spaces $\tilde{\mathscr{Z}}_\mu^i$ consisting of stress potential fields supported in phase i, with square-integrable curl

$$\tilde{\mathscr{Z}}_\mu^i = \left\{ \boldsymbol{T} \in \mathbf{H}(\mathrm{curl}_0, \Omega_{0,\mu}) \;\middle|\; \boldsymbol{T}(\boldsymbol{Y}) = \mathbf{0} \text{ for } \boldsymbol{Y} \notin \Omega_{0,\mu}^i \right\}. \tag{5.107}$$

The global space of admissible stress potential fluctuations is then the direct sum of these phase-wise spaces, further constrained to satisfy a global static admissibility condition

$$\tilde{\mathscr{S}}_\mu^* = \left\{ \boldsymbol{T} \in \bigoplus_{i=1}^{n_P} \tilde{\mathscr{Z}}_\mu^i \;\middle|\; \sum_{i=1}^{n_P} \int_{\Omega_{0,\mu}^i} \mathrm{curl}_0\, \boldsymbol{T}\, dv = \mathbf{0} \right\}. \tag{5.108}$$

Remark 5.7 | Comparison with full-field static admissibility

When comparing Equation (5.108) with the full-field admissibility condition (3.38), it is evident that we have relaxed the constraint on the volume average of the stress potential fluctuation. The relaxation introduces no essential loss of generality and permits a more streamlined derivation of the models.

Since the constraint set defined by Equation (5.108) is linear and homogeneous, the space of virtual stress potential fields, denoted $\tilde{\mathscr{H}}_\mu^*$, coincides with the admissible space itself, i.e.,

$$\tilde{\mathscr{H}}_\mu^* = \tilde{\mathscr{S}}_\mu^*. \tag{5.109}$$

The minimal space $\tilde{\mathscr{S}}_\mu^*$ contains a wide class of admissible stress potential fluctuations. However, it can be narrowed down using auxiliary estimates from the MFH scheme. In analogy

with the developments under PMVP, we now introduce additional constraints to define nested subsets of $\tilde{\mathscr{S}}_\mu^*$, corresponding to specific homogenization models. As with the kinematically based models, we begin with the most restrictive set of constraints, those that enforce the full MFH estimates in each phase, and then progressively relax them in later subsections.

5.2.2 Full Mean-Field Homogenization

As in the standard PMVP framework, our goal is to exploit the stress estimates provided by the MFH procedure. In this context, we adopt the hypothesis that the average stress in each phase coincides with its corresponding MFH estimate, i.e.,

$$\boldsymbol{P}_\mu^i = \boldsymbol{P}_\mu^{i,\mathrm{mfh}}. \tag{5.110}$$

Accordingly, we write the admissible set of stress potential fluctuations that satisfy this static hypothesis as

$$\tilde{\mathscr{S}}_{\mu,\mathrm{MFH}}(\boldsymbol{P}) = \left\{ \boldsymbol{T} \in \tilde{\mathscr{S}}_\mu^* \;\middle|\; \int_{\Omega_{0,\mu}^i} \mathrm{curl}_0\, \boldsymbol{T}\, dv = |\Omega_{0,\mu}^i| \left(\boldsymbol{P}_\mu^{i,\mathrm{mfh}} - \boldsymbol{P} \right),\ \forall i = 1,\dots,n_P \right\}. \tag{5.111}$$

To ensure $\tilde{\mathscr{S}}_{\mu,\mathrm{MFH}}(\boldsymbol{P}) \subseteq \tilde{\mathscr{S}}_\mu^*$, we must enforce the consistency condition $\langle \boldsymbol{P}_\mu^{i,\mathrm{mfh}} \rangle = \boldsymbol{P}$. Note also that $\tilde{\mathscr{S}}_{\mu,\mathrm{MFH}}(\boldsymbol{P})$ forms a subset rather than a subspace of the minimal admissible field space. The corresponding set of admissible virtual stress potential fields is found to be

$$\tilde{\mathscr{H}}_{\mu,\mathrm{MFH}}(\boldsymbol{P}, \delta\boldsymbol{P}) = \left\{ \boldsymbol{T} \in \tilde{\mathscr{H}}_\mu^* \;\middle|\; \int_{\Omega_{0,\mu}^i} \mathrm{curl}_0\, \boldsymbol{T}\, dv = |\Omega_{0,\mu}^i| \left(\mathbf{B}_\mu^{i,\mathrm{mfh}} - \mathbf{I} \right) : \delta\boldsymbol{P},\ \forall i = 1,\dots,n_P \right\}. \tag{5.112}$$

In an analogous way to the approach in Section 5.1.2, and as detailed in Appendix C.2.1, we employ the method of Lagrange multipliers to enforce $\tilde{\boldsymbol{Z}}_\mu \in \tilde{\mathscr{S}}_{\mu,\mathrm{MFH}}(\boldsymbol{P})$ within the PMCVP framework, and obtain as a consequence of our static hypotheses on the average stress in each phase, the homogenization rule for the macroscopic deformation gradient. It reads

$$\boldsymbol{F} = \left\langle \boldsymbol{F}_\mu^i : \mathbf{B}_\mu^{i,\mathrm{mfh}} \right\rangle. \tag{5.113}$$

This expression generalizes the classical MFH homogenization rule for the deformation gradient (cf. Equation (4.27)), as it accounts not only for phase volume fractions but also for the stress localization tensors. Notably, this expression mirrors the homogenization rule for stress (Equation (5.32)) obtained via the PMVP, thereby establishing a duality between stress and deformation gradients and their associated localization tensors.

Remark 5.8 | Sachs model

This model reduces to the classical Sachs model when $\boldsymbol{P}_\mu^{i,\mathrm{mfh}} = \boldsymbol{P}$ for all $i = 1,\dots,n_P$, i.e., when each phase is subject to the same average stress. This equality is equivalent to employing the no-interaction assumption described in Table 4.1. In that case, $\mathbf{B}_\mu^{i,\mathrm{mfh}} = \mathbf{I}$ and the homogenized deformation gradient becomes the volume-weighted average of the microscopic deformation gradients.

Employing similar derivations to those in Section 5.1.2, we can show that the full MFH model based on the PMCVP introduced in this section guarantees energetic consistency across scales

for non-dissipative materials, i.e., the macroscopic complementary power equals the volume average of the microscopic complementary power, or symbolically,

$$\dot{\boldsymbol{P}} : \boldsymbol{F} = \langle \dot{\boldsymbol{P}}^i_\mu : \boldsymbol{F}^i_\mu \rangle. \tag{5.114}$$

Moreover, the corresponding deformation gradient homogenization rule satisfies the balance of angular momentum. See Appendix C.2.1 for the detailed derivation.

5.2.3 Projected Mean-Field Homogenization

We turn now to projected models based on the PMCVP. To better motivate the static hypothesis adopted regarding the use of the MFH estimates, we highlight the analogy with the strain-driven models based on the original PMVP. While in Section 5.1.3 the normal component of the right stretch was retained from a strain-driven MFH procedure, here we analogously retain the tangential component of the Biot stress obtained from a stress-driven MFH procedure. We also adopt the polar rotation estimate from the MFH scheme. Effectively, for each phase, we impose

$$\mathbf{P}^i_{\mathbb{S}^3_T,\mu} : \boldsymbol{T}_B(\boldsymbol{P}^i_\mu) = \mathbf{P}^i_{\mathbb{S}^3_T,\mu} : \boldsymbol{T}_B(\boldsymbol{P}^{i,\mathrm{mfh}}_\mu), \quad i = 1,\dots,n_P, \tag{5.115}$$

$$\boldsymbol{R}(\boldsymbol{P}^i_\mu) = \boldsymbol{R}(\boldsymbol{P}^{i,\mathrm{mfh}}_\mu), \quad i = 1,\dots,n_P, \tag{5.116}$$

where $\boldsymbol{T}_B$ maps $\boldsymbol{P}^i_\mu$ to $(\boldsymbol{R}^i_\mu)^T \boldsymbol{P}^i_\mu$ and $\boldsymbol{R}(\boldsymbol{P}^i_\mu)$ is the polar rotation found from the deformation gradient corresponding to the stress $\boldsymbol{P}^i_\mu$, i.e., $\boldsymbol{F}^i_\mu = \boldsymbol{f}(\boldsymbol{P}^i_\mu, \boldsymbol{\alpha}^i_\mu)$ (see Equation (2.51)). For the matrix phase, one may choose either to enforce $\mathbf{P}^m_{\mathbb{S}^3,\mu} : \boldsymbol{T}^m_{B,\mu} = \mathbf{P}^m_{\mathbb{S}^3,\mu} : \boldsymbol{T}^{m,\mathrm{mfh}}_{B,\mu}$, or to leave it unconstrained. These choices may not yet be completely justified, however, in the following, we show that they lead to a straightforward model that mirrors the projected model based on the PMVP.

The set of admissible stress potential fluctuation fields corresponding to the static hypothesis chosen for the phases is given by

$$\tilde{\mathscr{S}}_{\mu,\mathrm{PMFH}}(\boldsymbol{P}) = \Big\{ \boldsymbol{T} \in \tilde{\mathscr{S}}^*_\mu \;\Big|\; \mathbf{P}^i_{\mathbb{S}^3_T,\mu} : \boldsymbol{T}_B(\boldsymbol{P}^i_\mu) = \mathbf{P}^i_{\mathbb{S}^3_T,\mu} : \boldsymbol{T}_B(\boldsymbol{P}^{i,\mathrm{mfh}}_\mu), \\ \boldsymbol{R}(\boldsymbol{P}^i_\mu) = \boldsymbol{R}(\boldsymbol{P}^{i,\mathrm{mfh}}_\mu), \quad \forall\, i = 1,\dots,n_P \Big\}. \tag{5.117}$$

Note that the average first Piola–Kirchhoff stress in each phase is a function of the stress potential fluctuation and the macroscopic stress, according to

$$\boldsymbol{P}^i_\mu = \boldsymbol{P} + \frac{1}{|\Omega^i_{0,\mu}|} \int_{\Omega^i_{0,\mu}} \mathrm{curl}_0\, \tilde{\boldsymbol{Z}}_\mu \, dv, \tag{5.118}$$

and that the auxiliary MFH estimate $\boldsymbol{P}^{i,\mathrm{mfh}}_\mu$ depends on the macroscopic stress $\boldsymbol{P}$, as well. This admissible set satisfies the nested inclusion

$$\tilde{\mathscr{S}}_{\mu,\mathrm{MFH}}(\boldsymbol{P}) \subseteq \tilde{\mathscr{S}}_{\mu,\mathrm{PMFH}}(\boldsymbol{P}) \subseteq \tilde{\mathscr{S}}^*_\mu, \tag{5.119}$$

provided that $\langle \boldsymbol{P}^{i,\mathrm{mfh}}_\mu \rangle = \boldsymbol{P}$ holds.

The corresponding space of admissible virtual stress potential fields is given by

$$\tilde{\mathscr{H}}_{\mu,\mathrm{PMFH}}(\boldsymbol{P},\delta\boldsymbol{P}) = \Big\{ \boldsymbol{T} \in \tilde{\mathscr{H}}_\mu^* \;\Big|\; \mathbf{P}^i_{\mathbb{S}^3_T,\mu} : \frac{d\boldsymbol{T}_B}{d\boldsymbol{P}}(\boldsymbol{P}^i_\mu) : \int_{\Omega^i_{0,\mu}} \mathrm{curl}_0\, \boldsymbol{T}\, dv = |\Omega^i_{0,\mu}| \mathbf{P}^i_{\mathbb{S}^3_T,\mu} : \left(\frac{d\boldsymbol{T}_B}{d\boldsymbol{P}}(\boldsymbol{P}^{i,\mathrm{mfh}}_\mu) : \mathbf{B}^{i,\mathrm{mfh}}_\mu - \frac{d\boldsymbol{T}_B}{d\boldsymbol{P}}(\boldsymbol{P}^i_\mu) \right) : \delta\boldsymbol{P}, \\ \frac{d\boldsymbol{R}}{d\boldsymbol{P}}(\boldsymbol{P}^i_\mu) : \int_{\Omega^i_{0,\mu}} \mathrm{curl}_0\, \boldsymbol{T}\, dv = |\Omega^i_{0,\mu}| \left(\frac{d\boldsymbol{R}}{d\boldsymbol{P}}(\boldsymbol{P}^{i,\mathrm{mfh}}_\mu) : \mathbf{B}^{i,\mathrm{mfh}}_\mu - \frac{d\boldsymbol{R}}{d\boldsymbol{P}}(\boldsymbol{P}^i_\mu) \right) : \delta\boldsymbol{P} \Big\}, \quad (5.120)$$

which is obtained using the chain rule and rearranging some of the terms.

To enforce these constraints within the PMCVP framework, we introduce Lagrange multipliers again. One multiplier, $\boldsymbol{\Gamma}_\mu$, enforces the minimal constraint for all phases, while n_P individual multipliers $\boldsymbol{\Gamma}^i_{T,\mu}$, $i = 1,\dots,n_P$, enforce the tangential constraints on the Biot stress tensor. The tangential multipliers satisfy

$$\mathbf{P}^i_{\mathbb{S}^3_T,\mu} : \boldsymbol{\Gamma}^i_{T,\mu} = \boldsymbol{\Gamma}^i_{T,\mu} : \mathbf{P}^i_{\mathbb{S}^3_T,\mu} = \boldsymbol{\Gamma}^i_{T,\mu}, \quad (5.121)$$

i.e., they possess only three independent components, except in the matrix phase, where $\boldsymbol{\Gamma}^m_{T,\mu}$ can have six independent components or none depending on the choice for $\mathbf{P}^m_{\mathbb{S}^3_T,\mu}$. Similarly, n_P multipliers $\boldsymbol{\Gamma}^i_{R,\mu}$, $i = 1,\dots,n_P$, enforce the constraints on the polar rotation. These multipliers enter the derivation below only through the quantity $\mathrm{skew}((\boldsymbol{R}^i_\mu)^T \boldsymbol{\Gamma}^i_{R,\mu})$, which is a skew-symmetric second-order tensor with three independent components.

The Principle of Multiscale Complementary Virtual Power then reads

$$|\Omega_{0,\mu}| \delta\boldsymbol{P} : \boldsymbol{F} = \int_{\Omega_{0,\mu}} (\mathrm{curl}_0\, \delta\tilde{\boldsymbol{Z}}_\mu + \delta\boldsymbol{P}) : \boldsymbol{F}_\mu\, dv \\ - \boldsymbol{\Gamma}_\mu : \sum_{i=1}^{n_P} \int_{\Omega^i_{0,\mu}} \mathrm{curl}_0\, \delta\tilde{\boldsymbol{Z}}_\mu\, dv - \delta\boldsymbol{\Gamma}_\mu : \sum_{i=1}^{n_P} \int_{\Omega^i_{0,\mu}} \mathrm{curl}_0\, \tilde{\boldsymbol{Z}}_\mu\, dv \\ - \sum_{i=1}^{n_P} \boldsymbol{\Gamma}^i_{T,\mu} : \mathbf{P}^i_{\mathbb{S}^3_T,\mu} : \left(\frac{d\boldsymbol{T}_B}{d\boldsymbol{P}}(\boldsymbol{P}^i_\mu) : \int_{\Omega^i_{0,\mu}} \mathrm{curl}_0\, \delta\tilde{\boldsymbol{Z}}_\mu\, dv - |\Omega^i_{0,\mu}| \left(\frac{d\boldsymbol{T}_B}{d\boldsymbol{P}}(\boldsymbol{P}^{i,\mathrm{mfh}}_\mu) : \mathbf{B}^{i,\mathrm{mfh}}_\mu - \frac{d\boldsymbol{T}_B}{d\boldsymbol{P}}(\boldsymbol{P}^i_\mu) \right) : \delta\boldsymbol{P} \right) \\ - \sum_{i=1}^{n_P} \delta\boldsymbol{\Gamma}^i_{T,\mu} : \mathbf{P}^i_{\mathbb{S}^3_T,\mu} : \left(\boldsymbol{T}_B(\boldsymbol{P}^i_\mu) - \boldsymbol{T}_B(\boldsymbol{P}^{i,\mathrm{mfh}}_\mu) \right) \\ - \sum_{i=1}^{n_P} \boldsymbol{\Gamma}^i_{R,\mu} : \left(\frac{d\boldsymbol{R}}{d\boldsymbol{P}}(\boldsymbol{P}^i_\mu) : \int_{\Omega^i_{0,\mu}} \mathrm{curl}_0\, \delta\tilde{\boldsymbol{Z}}_\mu\, dv - |\Omega^i_{0,\mu}| \left(\frac{d\boldsymbol{R}}{d\boldsymbol{P}}(\boldsymbol{P}^{i,\mathrm{mfh}}_\mu) : \mathbf{B}^{i,\mathrm{mfh}}_\mu - \frac{d\boldsymbol{R}}{d\boldsymbol{P}}(\boldsymbol{P}^i_\mu) \right) : \delta\boldsymbol{P} \right) \\ - \sum_{i=1}^{n_P} \delta\boldsymbol{\Gamma}^i_{R,\mu} : \left(\boldsymbol{R}(\boldsymbol{P}^i_\mu) - \boldsymbol{R}(\boldsymbol{P}^{i,\mathrm{mfh}}_\mu) \right). \quad (5.122)$$

Interpretation of the Lagrange multipliers

Letting $\delta\boldsymbol{P} = \mathbf{0}$, $\delta\boldsymbol{\Gamma}_\mu = \mathbf{0}$, $\delta\boldsymbol{\Gamma}^i_{T,\mu} = \mathbf{0}$ and $\delta\boldsymbol{\Gamma}^i_{R,\mu} = \mathbf{0}$ for all $i = 1,\dots,n_P$, we isolate the expression

$$\int_{\Omega_{0,\mu}} \mathrm{curl}_0\, \delta\tilde{\boldsymbol{Z}}_\mu : \boldsymbol{F}_\mu\, dv - \boldsymbol{\Gamma}_\mu : \sum_{i=1}^{n_P} \int_{\Omega^i_{0,\mu}} \mathrm{curl}_0\, \delta\tilde{\boldsymbol{Z}}_\mu\, dv \\ - \sum_{i=1}^{n_P} \boldsymbol{\Gamma}^i_{T,\mu} : \mathbf{P}^i_{\mathbb{S}^3_T,\mu} : \frac{d\boldsymbol{T}_B}{d\boldsymbol{P}}(\boldsymbol{P}^i_\mu) : \int_{\Omega^i_{0,\mu}} \mathrm{curl}_0\, \delta\tilde{\boldsymbol{Z}}_\mu\, dv \\ - \boldsymbol{\Gamma}^i_{R,\mu} : \frac{d\boldsymbol{R}}{d\boldsymbol{P}}(\boldsymbol{P}^i_\mu) : \int_{\Omega^i_{0,\mu}} \mathrm{curl}_0\, \delta\tilde{\boldsymbol{Z}}_\mu\, dv = 0. \quad (5.123)$$

Choosing $\delta\tilde{\boldsymbol{Z}}_\mu = \frac{1}{2}\boldsymbol{C}\times(\boldsymbol{Y}-\boldsymbol{Y}_0^i)$ for $\boldsymbol{Y}\in\Omega_{0,\mu}^i$ and zero elsewhere, with $\boldsymbol{C}$ an arbitrary constant second-order tensor, we obtain

$$\boldsymbol{F}_\mu^i = \boldsymbol{\Gamma}_\mu + \boldsymbol{\Gamma}_{T,\mu}^i : \mathbf{P}_{\mathbb{S}_T^3,\mu}^i : \frac{d\boldsymbol{T}_B}{d\boldsymbol{P}}(\boldsymbol{P}_\mu^i) + \boldsymbol{\Gamma}_{R,\mu}^i : \frac{d\boldsymbol{R}}{d\boldsymbol{P}}(\boldsymbol{P}_\mu^i), \quad i=1,\dots,n_P, \tag{5.124}$$

connecting the average deformation gradient in phase i to the Lagrange multipliers, here we used the symmetry and projection properties of $\mathbf{P}_{\mathbb{S}_T^3,\mu}^i$. We can also rewrite Equation (5.123) as

$$\int_{\Omega_{0,\mu}} \mathrm{curl}_0\,\delta\tilde{\boldsymbol{Z}}_\mu : \boldsymbol{F}_\mu\,dv = \sum_{i=1}^{n_P} \boldsymbol{F}_\mu^i : \int_{\Omega_{0,\mu}^i} \mathrm{curl}_0\,\delta\tilde{\boldsymbol{Z}}_\mu\,dv. \tag{5.125}$$

To proceed, we need the derivatives of the Biot stress and polar rotation with respect to the first Piola–Kirchhoff stress. Note, the Biot stress lives in a six-dimensional manifold $\mathcal{N}$, parameterized by the right stretch $\boldsymbol{U}$ through the material's constitutive model (Equation (2.47)), and not, in general, equal to $\mathbb{S}^3$. However, we can recover very similar results to those in Equation (5.65) for the derivatives of $\boldsymbol{U}$ with respect to $\boldsymbol{F}$, considering the directional derivatives along $\boldsymbol{R}_\mu^i\boldsymbol{S}$, where $\boldsymbol{S}\in T_{\boldsymbol{U}_\mu^i}\mathcal{N}_\mu^i \equiv \mathcal{V}_\mu^i$, instead of $\boldsymbol{S}\in\mathbb{S}^3$. From the derivations provided in Appendix D, we have

$$\frac{d\boldsymbol{T}_B}{d\boldsymbol{P}}(\boldsymbol{P}_\mu^i) : (\boldsymbol{R}_\mu^i\boldsymbol{S}) = \boldsymbol{S}, \quad \frac{d\boldsymbol{R}}{d\boldsymbol{P}}(\boldsymbol{P}_\mu^i) : (\boldsymbol{R}_\mu^i\boldsymbol{S}) = \boldsymbol{O}, \quad \forall\boldsymbol{S}\in\mathcal{V}_\mu^i, \tag{5.126}$$

when $\boldsymbol{P}_\mu^i \neq \boldsymbol{O}$.

We can now use these results to interpret the Lagrange multipliers in Equation (5.124). To this end, we select virtual stress potential fields of the form $\delta\tilde{\boldsymbol{Z}}_\mu = \frac{1}{2}(\boldsymbol{R}_\mu^i\boldsymbol{S})\times(\boldsymbol{Y}-\boldsymbol{Y}_0^i)$, where $\boldsymbol{S}\in\mathcal{V}_\mu^i$, recalling that $\mathrm{curl}(\frac{1}{2}(\boldsymbol{R}_\mu^i\boldsymbol{S})\times(\boldsymbol{Y}-\boldsymbol{Y}_0^i)) = \boldsymbol{R}_\mu^i\boldsymbol{S}$. Substituting into the PMCVP expression yields

$$\boldsymbol{F}_\mu^i : (\boldsymbol{R}_\mu^i\boldsymbol{S}) = \boldsymbol{\Gamma}_\mu : (\boldsymbol{R}_\mu^i\boldsymbol{S}) + \boldsymbol{\Gamma}_{T,\mu}^i : \mathbf{P}_{\mathbb{S}_T^3,\mu}^i : \frac{d\boldsymbol{T}_B}{d\boldsymbol{P}}(\boldsymbol{P}_\mu^i) : (\boldsymbol{R}_\mu^i\boldsymbol{S}) + \boldsymbol{\Gamma}_{R,\mu}^i : \frac{d\boldsymbol{R}}{d\boldsymbol{P}}(\boldsymbol{P}_\mu^i) : (\boldsymbol{R}_\mu^i\boldsymbol{S}). \tag{5.127}$$

Taking into account the expressions in Equation (5.126), we find

$$\boldsymbol{F}_\mu^i : (\boldsymbol{R}_\mu^i\boldsymbol{S}) = \boldsymbol{\Gamma}_\mu : (\boldsymbol{R}_\mu^i\boldsymbol{S}) + \boldsymbol{\Gamma}_{T,\mu}^i : \boldsymbol{S}, \tag{5.128}$$

using the properties of the double contraction, we conclude that

$$\boldsymbol{U}_\mu^i : \boldsymbol{S} = ((\boldsymbol{R}_\mu^i)^T\boldsymbol{\Gamma}_\mu) : \boldsymbol{S} + \boldsymbol{\Gamma}_{T,\mu}^i : \boldsymbol{S}. \tag{5.129}$$

Since $\boldsymbol{S}$ is an arbitrary tensor in $\mathcal{V}_\mu^i$, we obtain

$$\mathbf{P}_{\mathcal{V},\mu}^i : \boldsymbol{U}_\mu^i = \mathbf{P}_{\mathcal{V},\mu}^i : ((\boldsymbol{R}_\mu^i)^T\boldsymbol{\Gamma}_\mu) + \mathbf{P}_{\mathcal{V},\mu}^i : \boldsymbol{\Gamma}_{T,\mu}^i. \tag{5.130}$$

Motivated by the fact that $\boldsymbol{\Gamma}_{T,\mu}^i$ is in $\mathbb{S}_T^3$, given that it is the Lagrange multiplier enforcing the restriction concerning the projection of the Biot stresses onto this space (Equation (5.115)), we project onto an appropriate subspace of $(\mathbb{S}_T^3)^\perp$. Since we are dealing with projected models, in which we take into account the geometric directions $\boldsymbol{N}_\mu^i$, we try to draw an analogy with the corresponding models based on the PMVP. Consider the subspace

$$\mathbb{S}_T^3 = \{\boldsymbol{X}\in\mathbb{S}^3 \mid \boldsymbol{X}\boldsymbol{N} = \boldsymbol{0}\}, \tag{5.131}$$

for some normal direction $\boldsymbol{N}$. Then, $\mathbf{P}_{\mathbb{S}^3_T}$ defined in Equation (5.55) is the orthogonal projection onto this subspace, i.e., $\mathbf{P}_{\mathbb{S}^3_T} : \boldsymbol{Y} = \boldsymbol{Y}$ for $\boldsymbol{Y} \in \mathbb{S}^3_T$, and $\mathbf{P}_{\mathbb{S}^3_N}$ projects onto

$$\mathbb{S}^3_N = (\mathbb{S}^3_T)^\perp \cap \mathbb{S}^3. \tag{5.132}$$

Accordingly, we have written our kinematic hypothesis on the phases in the projected model described in Section 5.1.3 as

$$\mathbf{P}^i_{\mathbb{S}^3_N,\mu} : \boldsymbol{U}^i_\mu = \mathbf{P}^i_{\mathbb{S}^3_N,\mu} : \boldsymbol{U}^{i,\mathrm{mfh}}_\mu. \tag{5.133}$$

Moving to the projected models based on the PMCVP, we now consider

$$\mathcal{V}^i_{\mu,N} = (\mathbb{S}^3_T)^\perp \cap \mathcal{V}^i_\mu, \tag{5.134}$$

where $\mathcal{V}^i_\mu$ replaces $\mathbb{S}^3$ in Equation (5.132). Given that $\mathcal{V}^i_{\mu,N} \subset (\mathbb{S}^3_T)^\perp$ and $\boldsymbol{\Gamma}^i_{T,\mu} \in \mathbb{S}^3_T$, there are no components of $\boldsymbol{\Gamma}^i_{T,\mu}$ in $\mathcal{V}^i_{\mu,N}$, thus projecting Equation (5.130) onto $\mathcal{V}^i_{\mu,N}$ leads to

$$\mathbf{P}^i_{\mathcal{V}_N,\mu} : \boldsymbol{U}^i_\mu = \mathbf{P}^i_{\mathcal{V}_N,\mu} : ((\boldsymbol{R}^i_\mu)^T \boldsymbol{\Gamma}_\mu), \tag{5.135}$$

thereby removing $\boldsymbol{\Gamma}^i_{T,\mu}$ from our equation.

Note the similarities between Equation (5.135) and Equation (5.53). In fact, in the special case of isotropic phases, the Biot stress tensor is always symmetric (see Remark 2.2), thus $T_{\boldsymbol{U}^i_\mu}\mathcal{N}^i_\mu = \mathbb{S}^3$ and Equations (5.115) and (5.135) can be rewritten as

$$\mathbf{P}^i_{\mathbb{S}^3_N,\mu} : \boldsymbol{U}^i_\mu = \mathbf{P}^i_{\mathbb{S}^3_N,\mu} : ((\boldsymbol{R}^i_\mu)^T \boldsymbol{\Gamma}_\mu), \tag{5.136}$$

$$\mathbf{P}^i_{\mathbb{S}^3_T,\mu} : \boldsymbol{T}^i_{B,\mu} = \mathbf{P}^i_{\mathbb{S}^3_T,\mu} : \boldsymbol{T}^{i,\mathrm{mfh}}_{B,\mu}, \tag{5.137}$$

which are analogous to the expressions obtained for the right stretch tensor in Equation (5.53) and for the tangential projection of the Biot stress in Equation (5.70).

We now consider virtual stress-potential fields of the form $\delta\tilde{\boldsymbol{Z}}_\mu = \frac{1}{2}(\boldsymbol{W}\boldsymbol{P}^i_\mu) \times (\boldsymbol{Y} - \boldsymbol{Y}^i_0)$, where $\boldsymbol{W}$ is an arbitrary skew-symmetric second-order tensor. Substituting into Equation (5.122) yields, after some manipulations further detailed in Appendix C.2.2,

$$\mathrm{skew}((\boldsymbol{R}^i_\mu)^T \boldsymbol{\Gamma}^i_{R,\mu}) = -\mathrm{skew}((\boldsymbol{R}^i_\mu)^T \boldsymbol{\Gamma}_\mu (\boldsymbol{T}^i_{B,\mu})^T). \tag{5.138}$$

Deformation homogenization

We can now use the PMCVP to derive an expression for the homogenized deformation gradient. Setting $\delta\tilde{\boldsymbol{Z}}_\mu = \boldsymbol{0}$, $\delta\boldsymbol{\Gamma}_\mu = \boldsymbol{0}$, $\delta\boldsymbol{\Gamma}^i_{T,\mu} = \boldsymbol{0}$ and $\delta\boldsymbol{\Gamma}^i_{R,\mu} = \boldsymbol{0}$ for all i, after working through the derivation, we obtain

$$\boldsymbol{F} = \langle \boldsymbol{F}^{i,*}_\mu : \mathbf{B}^{i,\mathrm{mfh}}_\mu \rangle, \tag{5.139}$$

where the effective deformation gradient in each phase is

$$\boldsymbol{F}^{i,*}_\mu = \boldsymbol{\Gamma}_\mu + \boldsymbol{\Gamma}^i_{T,\mu} : \frac{d\boldsymbol{T}_B}{d\boldsymbol{P}}(\boldsymbol{P}^{i,\mathrm{mfh}}_\mu) + \boldsymbol{\Gamma}^i_{R,\mu} : \frac{d\boldsymbol{R}}{d\boldsymbol{P}}(\boldsymbol{P}^{i,\mathrm{mfh}}_\mu). \tag{5.140}$$

Note that the effective deformation gradient $\boldsymbol{F}^{i,*}_\mu$ is in general different from the actual deformation gradient $\boldsymbol{F}^i_\mu$.

Remark 5.9 | $\tilde{D}$-inclusion model

As for the projected model based on the standard PMVP, the projected model derived in this section, based on the PMCVP framework, is based on the rate-formulated $\tilde{\boldsymbol{D}}$-inclusion model introduced in Lee et al. (1993a,b), appropriately adapted to the present formulation. Another related model is presented in van Dommelen et al. (2003), where the authors also consider large deformations; however, it is important to emphasize that, in this work, the model arises naturally and rigorously from the PMCVP framework, without resorting to ad hoc hypotheses. This leads to differences in both the prescription for the normal component of the average right stretch tensor in each phase (Equation (5.135)) and the homogenization rule for the macroscopic deformation gradient (Equation (5.139)), both of which are consequences of using the PMCVP framework.

Energetic consistency and balance of angular momentum

Employing similar derivations to those in Section 5.1.2, we can show that the projected MFH model based on PMCVP derived in this section guarantees energetic consistency across scales for non-dissipative materials, and the corresponding deformation gradient homogenization rule satisfies the balance of angular momentum. See Appendix C.2.2 for the details.

5.2.4 Taylor's assumption

The model corresponding to the minimal space of admissible stress-potential fluctuations is the Taylor model. In this case, no constraints are imposed on the stress potential fields beyond static admissibility

$$\tilde{\mathscr{S}}_{\mu,\text{Taylor}} = \tilde{\mathscr{S}}_{\mu}^{*}. \tag{5.141}$$

Similarly, the associated space of virtual admissible stress potential fields is

$$\tilde{\mathscr{H}}_{\mu,\text{Taylor}} = \tilde{\mathscr{H}}_{\mu}^{*}. \tag{5.142}$$

These static hypotheses yield the Taylor model within the PMCVP framework, i.e., the average deformation gradient is uniform across all phases and equal to the macroscopic deformation gradient, or symbolically

$$\boldsymbol{F} = \boldsymbol{F}_{\mu}^{i}, \quad i = 1,\dots,n_P. \tag{5.143}$$

The Taylor model guarantees energetic consistency across scales, and the corresponding deformation gradient homogenization rule satisfies the balance of angular momentum. See Appendix C.2.3 for the detailed derivation.

Remark 5.10 | Taylor model

The Taylor model arises from the minimal admissible space for stress-potential fluctuations. It postulates that each phase deforms identically to the macroscopic material response. Importantly, this result is here derived systematically from the PMCVP framework, with no ad hoc hypotheses.

Remark 5.11 | Consistency of deformation homogenization rules

At first glance, the deformation homogenization rule of the Taylor model (Equation (5.143)) may appear distinct from the ones obtained in the full and projected mean-field models (Equations (5.113) and (5.139), respectively). Although not necessary for the derivation or use of the Taylor model, we can write the relationship between the average stress in each phase and the macroscopic stress symbolically as

$$\boldsymbol{P}_\mu^i = \mathscr{B}_\mu^i(\boldsymbol{P}, \boldsymbol{\alpha}_\mu^i). \tag{5.144}$$

The corresponding derivative with respect to the macroscopic stress can be written as

$$\mathbf{B}_\mu^i = \frac{\partial \mathscr{B}_\mu^i}{\partial \boldsymbol{P}}, \tag{5.145}$$

such that $\langle \mathbf{B}_\mu^i \rangle = \mathbf{I}$ per the minimal admissibility condition.

Recognizing that in the Taylor model $\boldsymbol{F}_\mu^i = \boldsymbol{F}$ for all i, we can write

$$\begin{aligned}
\left\langle \boldsymbol{F}_\mu^i : \mathbf{B}_\mu^i \right\rangle &= \left\langle \boldsymbol{F} : \mathbf{B}_\mu^i \right\rangle && \text{(by Eq. (5.143))} && (5.146)\\
&= \boldsymbol{F} : \left\langle \mathbf{B}_\mu^i \right\rangle && && (5.147)\\
&= \boldsymbol{F} : \mathbf{I} && \text{(by Eq. (4.25))} && (5.148)\\
&= \boldsymbol{F}. && && (5.149)
\end{aligned}$$

Hence, the homogenization rules derived from the PMCVP framework are consistent across all models. Note that $\mathbf{B}_\mu^i$ replaces here its MFH counterpart, $\mathbf{B}_\mu^{i,\mathrm{mfh}}$, since for the Taylor model the MFH estimates are discarded.

Remark 5.12 | Relationship between minimal and most constrained fluctuation fields

In the standard PMVP setting, the Sachs model corresponds to the minimal admissible displacement fluctuation space, whereas the Taylor model represents the most constrained case. When employing the PMCVP formulation, the relation is reversed: the minimal admissible stress potential space yields the Taylor model, and the most constrained formulation yields the Sachs model. This duality highlights the symmetry and flexibility of the PMCVP framework.

Remark 5.13 | Relationship with full-field models

We want to highlight the connection between the homogenization rules derived from the PMVP and PMCVP frameworks in the context of mean-field homogenization and those obtained in full-field homogenization. In particular, we focus on the apparent difference regarding the inclusion of the strain and stress localization tensors between the homogenization rules found for the first Piola–Kirchhoff stress and the deformation gradient in both frameworks.

In full-field homogenization, the microscopic fields are related to the macroscopic ones

through generally nonlinear operators, denoted by $\mathscr{A}_\mu$ and $\mathscr{B}_\mu$, such that

$$\boldsymbol{F}_\mu(\boldsymbol{Y}) = \mathscr{A}_\mu(\boldsymbol{Y}, \boldsymbol{F}), \tag{5.150}$$

and

$$\boldsymbol{P}_\mu(\boldsymbol{Y}) = \mathscr{B}_\mu(\boldsymbol{Y}, \boldsymbol{P}). \tag{5.151}$$

They symbolize the solution to the microscopic boundary-value problem for a given macroscopic deformation gradient $\boldsymbol{F}$ or first Piola–Kirchhoff stress $\boldsymbol{P}$. The notation choice here emphasizes that the operators play a similar role to $\mathscr{A}_\mu^{i,\mathrm{mfh}}$ and $\mathscr{B}_\mu^{i,\mathrm{mfh}}$ in the mean-field homogenization models, but they are potentially different from point to point.

The corresponding localization tensors are defined as

$$\mathbf{A}_\mu(\boldsymbol{Y}, \boldsymbol{F}) = \frac{\partial \mathscr{A}_\mu}{\partial \boldsymbol{F}}(\boldsymbol{Y}, \boldsymbol{F}), \tag{5.152}$$

and

$$\mathbf{B}_\mu(\boldsymbol{Y}, \boldsymbol{P}) = \frac{\partial \mathscr{B}_\mu}{\partial \boldsymbol{P}}(\boldsymbol{Y}, \boldsymbol{P}). \tag{5.153}$$

If we take the integral over the RVE of Equations (5.150) and (5.151), and take their derivatives with respect to $\boldsymbol{F}$ and $\boldsymbol{P}$, respectively, we obtain

$$\int_{\Omega_{0,\mu}} \mathbf{A}_\mu(\boldsymbol{Y})\, dv = \mathbf{I}, \tag{5.154}$$

and

$$\int_{\Omega_{0,\mu}} \mathbf{B}_\mu(\boldsymbol{Y})\, dv = \mathbf{I}. \tag{5.155}$$

Now, consider the variation $\nabla_0 \delta \tilde{\boldsymbol{u}}_\mu(\boldsymbol{Y}) = (\mathbf{A}_\mu(\boldsymbol{Y}) - \mathbf{I}) : \boldsymbol{C} \in \tilde{\mathscr{K}_\mu} = \tilde{\mathscr{V}_\mu}$ in Equation (3.13), with $\boldsymbol{C}$ an arbitrary second-order tensor. We find

$$\int_{\Omega_{0,\mu}} \boldsymbol{P}_\mu(\boldsymbol{Y}) : (\mathbf{A}_\mu(\boldsymbol{Y}) - \mathbf{I}) : \boldsymbol{C}\, dv = 0. \tag{5.156}$$

Rearranging, yields

$$\int_{\Omega_{0,\mu}} \boldsymbol{P}_\mu(\boldsymbol{Y}) : \mathbf{A}_\mu(\boldsymbol{Y}) dv : \boldsymbol{C} = \int_{\Omega_{0,\mu}} \boldsymbol{P}_\mu(\boldsymbol{Y})\, dv : \boldsymbol{C}, \tag{5.157}$$

taking into account that $\boldsymbol{C}$ is a constant. Finally, since $\boldsymbol{C}$ is arbitrary, we conclude that

$$\boldsymbol{P} = \int_{\Omega_{0,\mu}} \boldsymbol{P}_\mu(\boldsymbol{Y})\, dv = \int_{\Omega_{0,\mu}} \boldsymbol{P}_\mu(\boldsymbol{Y}) : \mathbf{A}_\mu(\boldsymbol{Y}) dv. \tag{5.158}$$

Therefore, we find that a homogenization rule for the first Piola–Kirchhoff stress, similar to that for mean-field homogenization models containing the strain localization tensor, also applies to full-field models; however, it simplifies to the classical volume average in that context.

A similar derivation can be performed in a driven context. Considering the variation $\text{curl}_0 \delta\tilde{\boldsymbol{Z}}_\mu(\boldsymbol{Y}) = (\mathbf{B}_\mu(\boldsymbol{Y}) - \mathbf{I}) : \boldsymbol{C} \in \tilde{\mathscr{S}}_\mu = \tilde{\mathscr{H}}_\mu$ in Equation (3.42), we obtain

$$\int_{\Omega_{0,\mu}} \boldsymbol{F}_\mu(\boldsymbol{Y}) : (\mathbf{B}_\mu(\boldsymbol{Y}) - \mathbf{I}) : \boldsymbol{C} \; dv = 0. \tag{5.159}$$

Rearranging, yields

$$\int_{\Omega_{0,\mu}} \boldsymbol{F}_\mu(\boldsymbol{Y}) : \mathbf{B}_\mu(\boldsymbol{Y}) dv : \boldsymbol{C} = \int_{\Omega_{0,\mu}} \boldsymbol{F}_\mu(\boldsymbol{Y}) \; dv : \boldsymbol{C}, \tag{5.160}$$

taking into account that $\boldsymbol{C}$ is a constant. Finally, since $\boldsymbol{C}$ is arbitrary, we conclude that

$$\boldsymbol{F} = \int_{\Omega_{0,\mu}} \boldsymbol{F}_\mu(\boldsymbol{Y}) \; dv = \int_{\Omega_{0,\mu}} \boldsymbol{F}_\mu(\boldsymbol{Y}) : \mathbf{B}_\mu(\boldsymbol{Y}) dv, \tag{5.161}$$

and thus we conclude that, for the displacement-driven context, this homogenization rule for the deformation gradient, identical to the one found for mean-field homogenization models (which contain the stress localization tensor), also applies to full-field models, simplifying, however, to the classical volume average in the full-field context.

Box 5.2 summarizes the algorithm for the models formulated in Section 5.2 based on the PMCVP.

Box 5.2: Algorithm for the models formulated in Section 5.2 based on the PMCVP.

1. Given $\boldsymbol{P}$, compute from the stress-driven MFH procedure

$$\boldsymbol{P}_\mu^{i,\mathrm{mfh}},\ \boldsymbol{F}_\mu^{i,\mathrm{mfh}},\ \mathbf{B}_\mu^{i,\mathrm{mfh}},\quad i=1,\dots,n_P.$$

2. IF this is the full MFH model THEN

   (a) Set $\boldsymbol{P}_\mu^i=\boldsymbol{P}_\mu^{i,\mathrm{mfh}},\quad \boldsymbol{F}_\mu^i=\boldsymbol{F}_\mu^{i,\mathrm{mfh}},\quad i=1,\dots,n_P.$

   (b) Compute the homogenized deformation gradient as

$$\boldsymbol{F}=\langle \boldsymbol{F}_\mu^i:\mathbf{B}_\mu^{i,\mathrm{mfh}}\rangle.$$

   ELSE IF this is the projected MFH model THEN

   (a) Solve the nonlinear system of equations given by the static homogenization condition

$$\boldsymbol{P}=\langle \boldsymbol{P}_\mu^i\rangle,$$

   for the unknown Lagrange multiplier $\boldsymbol{\Gamma}_\mu$, adopting for each phase

$$\mathbf{P}_{\mathcal{V}_N,\mu}^i:\boldsymbol{U}_\mu^i=\mathbf{P}_{\mathcal{V}_N,\mu}^i:((\boldsymbol{R}_\mu^i)^T\boldsymbol{\Gamma}_\mu),\quad \boldsymbol{R}_\mu^i=\boldsymbol{R}_\mu^{i,\mathrm{mfh}},\quad \mathbf{P}_{\mathbb{S}_T^3,\mu}^i:\boldsymbol{T}_{B,\mu}^i=\mathbf{P}_{\mathbb{S}_T^3,\mu}^i:\boldsymbol{T}_{B,\mu}^{i,\mathrm{mfh}}.$$

   (b) Having found the Lagrange multiplier $\boldsymbol{\Gamma}_\mu$, and computed the average stress and deformation gradient in each phase, $\boldsymbol{P}_\mu^i$ and $\boldsymbol{F}_\mu^i$, we can obtain the other Lagrange multipliers as

$$\boldsymbol{\Gamma}_{T,\mu}^i=\mathbf{P}_{\mathbb{S}_T^3,\mu}^i:(\boldsymbol{U}_\mu^i-(\boldsymbol{R}_\mu^i)^T\boldsymbol{\Gamma}_\mu),\quad i=1,\dots,n_P,$$

   and

$$\mathrm{skew}((\boldsymbol{R}_\mu^i)^T\boldsymbol{\Gamma}_{R,\mu}^i)=-\mathrm{skew}((\boldsymbol{R}_\mu^i)^T\boldsymbol{\Gamma}_\mu(\boldsymbol{T}_{B,\mu}^i)^T),\quad i=1,\dots,n_P.$$

   (c) Compute the effective deformation gradient in each phase as

$$\boldsymbol{F}_\mu^{i,*}=\boldsymbol{\Gamma}_\mu+\boldsymbol{\Gamma}_{T,\mu}^i:\frac{d\boldsymbol{T}_B}{d\boldsymbol{P}}(\boldsymbol{P}_\mu^{i,\mathrm{mfh}})+\boldsymbol{\Gamma}_{R,\mu}^i:\frac{d\boldsymbol{R}}{d\boldsymbol{P}}(\boldsymbol{P}_\mu^{i,\mathrm{mfh}}),\quad i=1,\dots,n_P.$$

   (d) Compute the homogenized deformation gradient as

$$\boldsymbol{F}=\langle \boldsymbol{F}_\mu^{i,*}:\mathbf{B}_\mu^{i,\mathrm{mfh}}\rangle.$$

   ELSE IF this is the Taylor model THEN

   (a) Solve the nonlinear system of equations given by the static homogenization condition

$$\boldsymbol{P}=\langle \boldsymbol{P}_\mu^i\rangle,$$

   for the unknown macroscopic deformation gradient $\boldsymbol{F}$ adopting for each phase

$$\boldsymbol{F}_\mu^i=\boldsymbol{F},\quad i=1,\dots,n_P.$$

Chapter 6

Computational implementation

The stress-driven variationally consistent mean-field models derived in the previous chapters rely on two operations whose straightforward implementation breaks down near the reference configuration: the pointwise inversion of the constitutive relation $\boldsymbol{P} = \boldsymbol{h}(\boldsymbol{F})$, required in the solution of stress-driven auxiliary problems, and the evaluation of the stress localization operator $\mathsf{B}_{\mu}^{i,\mathrm{mfh}}$, which inherits the same near-singular Jacobian along skew directions. This chapter describes the computational strategies adopted to restore robustness in both cases. Section 6.1 exploits the bifurcation structure of the inversion problem, following Chillingworth et al. (1982, 1983), to seed a least-squares Newton iteration near a bifurcation point where the Jacobian is ill-conditioned. Section 6.2 then reformulates the homogenization rule in a co-rotational form that replaces the full localization operator by a numerically better-behaved symmetrized counterpart, and closes the phase-level kinematic condition through a projector-free Newton solve that sidesteps the implicit stress-dependence of the tangent-space projector.

6.1 Inversion of Piola–Kirchhoff stress–strain relations

The stress-driven formulations developed in the previous chapters require, in particular in the MFH procedure, the pointwise inversion of the constitutive relation $\boldsymbol{P} = \boldsymbol{h}(\boldsymbol{F})$ to obtain the deformation gradient $\boldsymbol{F}$ corresponding to a given target stress $\boldsymbol{P}^{\star}$, that is,

$$\text{find } \boldsymbol{F} \in \mathrm{GL}^{+}(3) \quad \text{such that} \quad \boldsymbol{h}(\boldsymbol{F}) = \boldsymbol{P}^{\star}, \tag{6.1}$$

where $\boldsymbol{h}$ is the constitutive map of Equation (2.29) and $\mathrm{GL}^{+}(3)$ is the set of invertible 3×3 matrices with positive determinant. This section describes the algorithm that performs this inversion, the structural difficulties associated with it, and how they are circumvented in practice. Our main reference for this section is the work of Chillingworth et al. (1982, 1983), which provides a comprehensive analysis of the mathematical structure of the problem and its bifurcations, and whose insights are key to the design of a robust numerical algorithm.

6.1.1 Sources of non-uniqueness

The main source of ill-posedness of Equation (6.1) is the frame indifference of the constitutive law. The principle of material objectivity introduced in Equation (2.44) implies that, at zero load, every rigid rotation $\boldsymbol{Q} \in \mathrm{SO}(3)$ produces the same (vanishing) stress, $\boldsymbol{h}(\boldsymbol{Q}) = \boldsymbol{0}$. The pre-image of the reference stress is therefore the entire rotation group SO(3), not a single point. As the load is

turned on, this three-parameter family breaks into a finite (but generically non-trivial) number of branches. More precisely, the objectivity of the constitutive description implies that

$$\frac{d\boldsymbol{h}}{d\boldsymbol{F}}(\boldsymbol{F}) : (\boldsymbol{W}\boldsymbol{F}) = \boldsymbol{W}\boldsymbol{h}(\boldsymbol{F}) \quad \text{for all } \boldsymbol{W} \in \mathfrak{so}(3), \tag{6.2}$$

so the Jacobian's action along the $\boldsymbol{W}\boldsymbol{F}$ directions scales linearly with the load $\|\boldsymbol{P}^\star\|$, making the problem near-singular in the vicinity of the reference configuration and exactly singular at the stress-free states $\boldsymbol{F} \in \mathrm{SO}(3)$.

A naive Newton iteration applied directly to the residual $\boldsymbol{h}(\boldsymbol{F}) - \boldsymbol{P}^\star = \boldsymbol{0}$ will face extreme difficulties due to the near-singularity of the Jacobian in the vicinity of the reference configuration. This may lead to divergence of the iterates or convergence to an undesired branch due to very large steps in the rotation direction. One way to mitigate this issue is to use a least-squares solve to 'invert' the Jacobian, or equivalently, employ the pseudo-inverse, which regularizes the problem by effectively projecting the Newton step onto the subspace of non-singular directions. However, this approach alone is not sufficient to guarantee robustness, since in general we are not guaranteed a bifurcation point near the identity, requiring a finite rotation to be applied, which the deflated Jacobian cannot provide. Accordingly, we follow the lead of Chillingworth et al. (1982, 1983) and exploit the mathematical structure of the problem to select the first iterate of the inversion procedure near a bifurcation point, so that only very small rotations are required to reach the target load, and the least-squares solve is effective in regularizing the problem.

6.1.2 The Lyapunov–Schmidt reduction: decoupling stretch and rotation

Given the structure of the singular Jacobian, we can apply a Lyapunov–Schmidt reduction, exploiting the polar decomposition $\boldsymbol{F} = \boldsymbol{R}\boldsymbol{U}$ of Equation (2.2), to decouple the problem into a six-dimensional equation on the symmetric stretch $\boldsymbol{U}$ and a three-dimensional constraint on the rotation $\boldsymbol{R}$.

Substituting $\boldsymbol{F} = \boldsymbol{R}\boldsymbol{U}$ into Equation (6.1) and projecting onto sym and skew yields the equivalent system

$$\operatorname{sym}\boldsymbol{h}(\boldsymbol{U}) = \operatorname{sym}\big(\boldsymbol{R}^T\boldsymbol{P}^\star\big), \tag{6.3}$$

$$\operatorname{skew}\boldsymbol{h}(\boldsymbol{U}) = \operatorname{skew}\big(\boldsymbol{R}^T\boldsymbol{P}^\star\big). \tag{6.4}$$

The first equation (Equation (6.3)) is a six-dimensional nonlinear system which we assume has a full-rank Jacobian with respect to $\boldsymbol{U}$. As such we can invoke the implicit function theorem to solve for $\boldsymbol{U}$ as a function of $\boldsymbol{R}$ and $\boldsymbol{P}^\star$, $\boldsymbol{U}(\boldsymbol{R};\boldsymbol{P}^\star)$, and substitute into the second equation (Equation (6.4)) to obtain a three-dimensional constraint on $\boldsymbol{R}$ alone.

The symmetric block (Equation (6.3)) is a strain-driven Biot inversion: for any *fixed* rotation $\boldsymbol{R}$ the right-hand side is known, and the implicit function theorem guarantees a locally unique solution $\boldsymbol{U}(\boldsymbol{R};\boldsymbol{P}^\star)$ around $\boldsymbol{F} = \boldsymbol{I}$. This is solved in practice by a Newton–Raphson scheme on the six independent components of $\boldsymbol{U}$.

6.1.3 Recovering the rotation: orbit of the prescribed stress

It remains to determine $\boldsymbol{R}$ such that Equation (6.4) is satisfied. At leading order in $\|\boldsymbol{P}^\star\|$, the right stretch $\boldsymbol{U}(\boldsymbol{R};\boldsymbol{P}^\star)$ obtained from Equation (6.3) reduces to the identity and the skew constraint collapses to the kinematic condition

$$\operatorname{skew}\big(\boldsymbol{R}^T\boldsymbol{P}^\star\big) = \boldsymbol{0} \quad \text{or equivalently,} \quad \boldsymbol{R}^T\boldsymbol{P}^\star \in \mathbb{S}^3, \tag{6.5}$$

which selects the set of rotations that can play the role of polar factor of the unknown $\boldsymbol{F}$. Following Chillingworth et al. (1982, 1983), we call this set the *orbit* of $\boldsymbol{P}^\star$,

$$S_{\boldsymbol{P}^\star} := \left\{ \boldsymbol{R} \in \mathrm{SO}(3) \;\middle|\; \boldsymbol{R}^T \boldsymbol{P}^\star \in \mathbb{S}^3 \right\}. \tag{6.6}$$

Its topology depends only on the multiplicity pattern of the singular values of $\boldsymbol{P}^\star$ and falls into the five types collected in Table 6.1: four isolated rotations, two isolated rotations together with a circle, the real projective plane $\mathbb{RP}^2$, the union of two circles, and the full SO(3), respectively.

Table 6.1: Classification of the orbit $S_{\boldsymbol{P}^\star}$ as a function of the singular values $\sigma_1 \geq \sigma_2 \geq \sigma_3 \geq 0$ of the prescribed stress $\boldsymbol{P}^\star$, after Chillingworth et al. (1982).

Type	Singular values	Orbit $S_{\boldsymbol{P}^\star}$
0	three distinct, $\sigma_1 > \sigma_2 > \sigma_3 \geq 0$	four isolated points
1	two distinct, repeated value > 0	$\{\boldsymbol{R}_1, \boldsymbol{R}_2\} \cup S^1$
2	all equal, $\sigma_1 = \sigma_2 = \sigma_3 > 0$	$\mathbb{RP}^2$
3	rank one, $\sigma_1 > \sigma_2 = \sigma_3 = 0$	$S^1 \cup S^1$
4	$\boldsymbol{P}^\star = \boldsymbol{0}$	SO(3)

The full skew constraint (Equation (6.4)) restores the dependence on $\boldsymbol{U}(\boldsymbol{R}; \boldsymbol{P}^\star)$ and selects, on each connected component of $S_{\boldsymbol{P}^\star}$, a finite subset of rotations as the actual equilibria. In practice, we replace the constitutive response by its linearization at $\boldsymbol{F} = \boldsymbol{I}$ to obtain an analytical expression for the bifurcation equation that selects the branches, which is justified by the fact that we are interested in the small-load regime and that the branch selection is continuous in the load.

6.1.4 Practical algorithm and branch selection

The complete inversion strategy used in this work proceeds in three stages, summarized in Box 6.1: an orbit enumeration based on the classification of Table 6.1, an analytical bifurcation-point computation on each circle component, and a least-squares Newton iteration seeded from the bifurcation point closest to the identity.

Box 6.1: Stress-to-deformation inversion algorithm.

1. **Orbit enumeration.** Compute the singular value decomposition of $\boldsymbol{P}^\star$, classify according to Table 6.1, and generate one rotation seed per connected component of $S_{\boldsymbol{P}^\star}$.
2. **Bifurcation point computation.** On each circle component, the bifurcation equation is constructed analytically from $\boldsymbol{P}^\star$ and $\mathbf{C}^{-1}$, and its critical points are obtained.
3. **First iterate selection.** From the bifurcation points obtained in the previous step, the one closest to the identity is selected as the first iterate of the Newton procedure, which is then carried out with a least-squares solve to regularize the near-singularity of the Jacobian.

6.1.5 Limitations

The algorithm has one known limitation that should be kept in mind when interpreting its output: the analytical branch finder relies on the linearized compliance at $\boldsymbol{F} = \boldsymbol{I}$ and therefore

returns critical points of the bifurcation equation that agree with those of the full nonlinear problem only to leading order in $\|\boldsymbol{P}^\star\|$; at finite loads the branches are used as warm starts for the Newton iteration rather than as final equilibria.

6.2 Numerical solution of the variationally consistent MFH models

The least-squares (pseudo-inverse) Newton step that robustly handles the inversion problem of the previous section carries over to the evaluation of the stress localization operator $\mathbf{B}_\mu^{i,\mathrm{mfh}}$ defined in Equation (4.23), whose Jacobian is likewise near-singular along skew directions at small loads. In this section, we describe how to obtain the homogenization rule for the macroscopic right stretch tensor $\boldsymbol{U}$, which does not require the full stress localization operator, depending instead on a numerically better-behaved alternative.

Co-rotational test function. To achieve this, we introduce a co-rotational test function

$$\delta\boldsymbol{P} = \boldsymbol{R}\boldsymbol{S}, \tag{6.7}$$

with $\boldsymbol{S}$ a symmetric tensor, and $\boldsymbol{R}$ the macroscopic polar rotation.

Remark 6.1 | Directional derivatives of equivariant and invariant functions

We describe here two useful identities concerning the directional derivatives of *equivariant* and *invariant* functions, which are helpful in the derivations that follow. We first take an equivariant map $\mathscr{M}$, satisfying $\mathscr{M}(\boldsymbol{Q}\boldsymbol{F}) = \boldsymbol{Q}\mathscr{M}(\boldsymbol{F})$ for all $\boldsymbol{Q} \in \mathrm{SO}(3)$ (the constitutive map is a representative example). The directional derivative of $\mathscr{M}$ at $\boldsymbol{F}$ in the direction $\boldsymbol{Q}\boldsymbol{H}$ is given by

$$\frac{d\mathscr{M}}{d\boldsymbol{F}}(\boldsymbol{F}) : (\boldsymbol{Q}\boldsymbol{H}) = \lim_{\epsilon\to 0} \frac{\mathscr{M}(\boldsymbol{F}+\epsilon\boldsymbol{Q}\boldsymbol{H}) - \mathscr{M}(\boldsymbol{F})}{\epsilon}. \tag{6.8}$$

Note that we did not place any restriction on $\boldsymbol{H}$, so the direction of differentiation is arbitrary, except for the left multiplication by $\boldsymbol{Q}$. Using the rotational invariance of $\mathscr{M}$ we can rewrite the numerator as

$$\mathscr{M}(\boldsymbol{F}+\epsilon\boldsymbol{Q}\boldsymbol{H}) - \mathscr{M}(\boldsymbol{F}) = \boldsymbol{Q}(\mathscr{M}(\boldsymbol{Q}^T\boldsymbol{F}+\epsilon\boldsymbol{H}) - \mathscr{M}(\boldsymbol{Q}^T\boldsymbol{F})). \tag{6.9}$$

Since $\boldsymbol{Q}$ is independent of ϵ, we can pull it out of the limit, and the remaining limit is the directional derivative of $\mathscr{M}$ at $\boldsymbol{Q}^T\boldsymbol{F}$ in the direction $\boldsymbol{H}$, so we have the identity

$$\frac{d\mathscr{M}}{d\boldsymbol{F}}(\boldsymbol{F}) : (\boldsymbol{Q}\boldsymbol{H}) = \boldsymbol{Q}\left(\frac{d\mathscr{M}}{d\boldsymbol{F}}(\boldsymbol{Q}^T\boldsymbol{F}) : \boldsymbol{H}\right). \tag{6.10}$$

If we contract both sides with a tensor $\boldsymbol{G}$, we also conclude that

$$\boldsymbol{G} : \frac{d\mathscr{M}}{d\boldsymbol{F}}(\boldsymbol{F}) : (\boldsymbol{Q}\boldsymbol{H}) = (\boldsymbol{Q}^T\boldsymbol{G}) : \frac{d\mathscr{M}}{d\boldsymbol{F}}(\boldsymbol{Q}^T\boldsymbol{F}) : \boldsymbol{H}. \tag{6.11}$$

An analogous identity holds when $\mathscr{M}$ is instead *invariant*, i.e., $\mathscr{M}(\boldsymbol{Q}\boldsymbol{F}) = \mathscr{M}(\boldsymbol{F})$ for all $\boldsymbol{Q} \in \mathrm{SO}(3)$. Repeating the argument with $\mathscr{M}(\boldsymbol{F}+\epsilon\boldsymbol{Q}\boldsymbol{H}) = \mathscr{M}(\boldsymbol{Q}^T\boldsymbol{F}+\epsilon\boldsymbol{H})$—so that no factor of $\boldsymbol{Q}$

is pulled out front—yields

$$\boldsymbol{G} : \frac{d\mathcal{M}}{d\boldsymbol{F}}(\boldsymbol{F}) : (\boldsymbol{Q}\boldsymbol{H}) = \boldsymbol{G} : \frac{d\mathcal{M}}{d\boldsymbol{F}}(\boldsymbol{Q}^T\boldsymbol{F}) : \boldsymbol{H}, \tag{6.12}$$

i.e., the rotation is carried onto the argument alone, with no rotation left on the contracting tensor $\boldsymbol{G}$. In the sequel, the polar rotation $\boldsymbol{R}$ is equivariant, $\boldsymbol{R}(\boldsymbol{Q}\boldsymbol{P}) = \boldsymbol{Q}\boldsymbol{R}(\boldsymbol{P})$, so its derivative obeys Equation (6.11), whereas the Biot stress $\boldsymbol{T}_B$ is invariant, $\boldsymbol{T}_B(\boldsymbol{Q}\boldsymbol{P}) = \boldsymbol{T}_B(\boldsymbol{P})$, so its derivative obeys Equation (6.12).

6.2.1 Full MFH model

Focusing first on the full MFH model, we insert the co-rotational test function into the variational statement of Equation (C.56) to obtain

$$|\Omega_{0,\mu}|(\boldsymbol{R}\boldsymbol{S}) : \boldsymbol{F} = \int_{\Omega_{0,\mu}} (\boldsymbol{R}\boldsymbol{S}) : \boldsymbol{F}_\mu \, dv + \sum_{i=1}^{n_P} \boldsymbol{\Gamma}_\mu^i : |\Omega_{0,\mu}^i| \left(\mathbf{B}_\mu^{i,\mathrm{mfh}}(\boldsymbol{P}) - \mathbf{I} \right) : (\boldsymbol{R}\boldsymbol{S}). \tag{6.13}$$

Employing the properties of the double contraction operator and the directional derivative identity described above (Equation (6.11)), we can move the rotation from the test function to the remaining factors, to obtain

$$|\Omega_{0,\mu}|\boldsymbol{S} : (\boldsymbol{R}^T\boldsymbol{F}) = \sum_{i=1}^{n_P} |\Omega_{0,\mu}^i|\boldsymbol{S} : (\boldsymbol{R}^T\boldsymbol{F}_\mu^i) + \sum_{i=1}^{n_P} |\Omega_{0,\mu}^i|(\boldsymbol{R}^T\boldsymbol{\Gamma}_\mu^i) : \left(\mathbf{B}_\mu^{i,\mathrm{mfh}}(\boldsymbol{R}^T\boldsymbol{P}) - \mathbf{I} \right) : \boldsymbol{S}, \tag{6.14}$$

where we also employed the definition of the average deformation gradient in phase i (Equation (4.3)). Using the Biot-stress identity $\boldsymbol{R}^T\boldsymbol{P} = \boldsymbol{T}_B$ (Equation (2.12)), the argument of $\mathbf{B}_\mu^{i,\mathrm{mfh}}$ can be rewritten as $\boldsymbol{T}_B$, and taking into account that $\boldsymbol{\Gamma}_\mu^i$ is found to coincide with the volume-averaged deformation gradient in each phase, $\boldsymbol{F}_\mu^i$ (see Equation (C.61)), the term $\boldsymbol{S} : (\boldsymbol{R}^T\boldsymbol{F}_\mu^i)$ cancels against the $-\mathbf{I}$ contribution of the Lagrange-multiplier sum, leaving

$$|\Omega_{0,\mu}|\boldsymbol{S} : \boldsymbol{U} = \sum_{i=1}^{n_P} |\Omega_{0,\mu}^i|\boldsymbol{G}_\mu^i : \mathbf{B}_\mu^{i,\mathrm{mfh}}(\boldsymbol{T}_B) : \boldsymbol{S}, \tag{6.15}$$

where $\boldsymbol{G}_\mu^i = \boldsymbol{R}^T\boldsymbol{F}_\mu^i$ is the co-rotated deformation gradient in phase i.

Because $\boldsymbol{S}$ is restricted to the symmetric subspace $\mathbb{S}^3$, only the output-symmetric part of $\boldsymbol{G}_\mu^i : \mathbf{B}_\mu^{i,\mathrm{mfh}}$ is seen when pairing against $\boldsymbol{S}$; we therefore absorb this projection into the operator itself by introducing the symmetrized localization operator

$$\bar{\mathbf{B}}_\mu^{i,\mathrm{mfh}}(\boldsymbol{T}_B) = \mathbf{B}_\mu^{i,\mathrm{mfh}}(\boldsymbol{T}_B) : \mathbf{I}_S, \tag{6.16}$$

where $\mathbf{I}_S$ is the fourth-order symmetric identity (symmetrizing projector) defined in the footnote of Section 5.1.3. Finally, given that $\boldsymbol{S}$ is an arbitrary symmetric tensor, we find the homogenization rule for the macroscopic right stretch tensor $\boldsymbol{U}$, as

$$\boldsymbol{U} = \langle \boldsymbol{G}_\mu^i : \bar{\mathbf{B}}_\mu^{i,\mathrm{mfh}} \rangle, \tag{6.17}$$

where we took into account that $\boldsymbol{U}$ is symmetric and that the localization operator is symmetrized.

6.2.2 Projected MFH model

The same procedure is now applied to the projected MFH model, whose variational statement is given in Equation (C.96) and whose full (non-co-rotational) derivation is collected in Appendix C.2.2. Inserting the co-rotational test function $\delta \boldsymbol{P} = \boldsymbol{R}\boldsymbol{S}$, with $\boldsymbol{S} \in \mathbb{S}^3$, yields

$$
\begin{aligned}
|\Omega_{0,\mu}|(\boldsymbol{R}\boldsymbol{S}) : \boldsymbol{F} = &\int_{\Omega_{0,\mu}} (\boldsymbol{R}\boldsymbol{S}) : \boldsymbol{F}_\mu \, dv \\
&+ \sum_{i=1}^{n_P} |\Omega^i_{0,\mu}| \boldsymbol{\Gamma}^i_{T,\mu} : \mathbf{P}^i_{\mathbb{S}^3_T,\mu} : \left(\frac{d\boldsymbol{T}_B}{d\boldsymbol{P}}(\boldsymbol{P}^{i,\mathrm{mfh}}_\mu) : \mathbf{B}^{i,\mathrm{mfh}}_\mu(\boldsymbol{P}) - \frac{d\boldsymbol{T}_B}{d\boldsymbol{P}}(\boldsymbol{P}^i_\mu) \right) : (\boldsymbol{R}\boldsymbol{S}) \\
&+ \sum_{i=1}^{n_P} |\Omega^i_{0,\mu}| \boldsymbol{\Gamma}^i_{R,\mu} : \left(\frac{d\boldsymbol{R}}{d\boldsymbol{P}}(\boldsymbol{P}^{i,\mathrm{mfh}}_\mu) : \mathbf{B}^{i,\mathrm{mfh}}_\mu(\boldsymbol{P}) - \frac{d\boldsymbol{R}}{d\boldsymbol{P}}(\boldsymbol{P}^i_\mu) \right) : (\boldsymbol{R}\boldsymbol{S}). \quad (6.18)
\end{aligned}
$$

The maps $\boldsymbol{R}$ and $\boldsymbol{T}_B$ transform differently under a superposed rotation: $\boldsymbol{R}$ is *equivariant*, $\boldsymbol{R}(\boldsymbol{Q}\boldsymbol{P}) = \boldsymbol{Q}\boldsymbol{R}(\boldsymbol{P})$, whereas $\boldsymbol{T}_B$ is *invariant*, $\boldsymbol{T}_B(\boldsymbol{Q}\boldsymbol{P}) = \boldsymbol{T}_B(\boldsymbol{P})$ (cf. Section 4.4). Applying the equivariant identity Equation (6.11) to $d\boldsymbol{R}/d\boldsymbol{P}$ and the invariant identity Equation (6.12) to $d\boldsymbol{T}_B/d\boldsymbol{P}$, the macroscopic rotation is moved from the test function onto the remaining factors, onto both the argument and the multiplier for the equivariant $d\boldsymbol{R}/d\boldsymbol{P}$, but onto the argument alone for the invariant $d\boldsymbol{T}_B/d\boldsymbol{P}$. Introducing the co-rotated phase averages

$$
\boldsymbol{G}^i_\mu = \boldsymbol{R}^T \boldsymbol{F}^i_\mu, \qquad \boldsymbol{H}^i_\mu = \boldsymbol{R}^T \boldsymbol{P}^i_\mu, \tag{6.19}
$$

and their MFH counterparts $\boldsymbol{G}^{i,\mathrm{mfh}}_\mu$, $\boldsymbol{H}^{i,\mathrm{mfh}}_\mu = \mathscr{B}^{i,\mathrm{mfh}}_\mu(\boldsymbol{T}_B)$, together with the average deformation gradient definition (Equation (4.3)), Equation (6.18) becomes

$$
\begin{aligned}
|\Omega_{0,\mu}|\boldsymbol{S} : \boldsymbol{U} = &\sum_{i=1}^{n_P} |\Omega^i_{0,\mu}| \boldsymbol{S} : \boldsymbol{G}^i_\mu \\
&+ \sum_{i=1}^{n_P} |\Omega^i_{0,\mu}| \boldsymbol{\Gamma}^i_{T,\mu} : \mathbf{P}^i_{\mathbb{S}^3_T,\mu} : \left(\frac{d\boldsymbol{T}_B}{d\boldsymbol{P}}(\boldsymbol{H}^{i,\mathrm{mfh}}_\mu) : \mathbf{B}^{i,\mathrm{mfh}}_\mu(\boldsymbol{T}_B) - \frac{d\boldsymbol{T}_B}{d\boldsymbol{P}}(\boldsymbol{H}^i_\mu) \right) : \boldsymbol{S} \\
&+ \sum_{i=1}^{n_P} |\Omega^i_{0,\mu}| (\boldsymbol{R}^T \boldsymbol{\Gamma}^i_{R,\mu}) : \left(\frac{d\boldsymbol{R}}{d\boldsymbol{P}}(\boldsymbol{H}^{i,\mathrm{mfh}}_\mu) : \mathbf{B}^{i,\mathrm{mfh}}_\mu(\boldsymbol{T}_B) - \frac{d\boldsymbol{R}}{d\boldsymbol{P}}(\boldsymbol{H}^i_\mu) \right) : \boldsymbol{S}. \quad (6.20)
\end{aligned}
$$

The remaining term $\boldsymbol{S} : \boldsymbol{G}^i_\mu$ is treated through the co-rotation relation $\boldsymbol{G}^i_\mu : \boldsymbol{S} = \boldsymbol{F}^i_\mu : (\boldsymbol{R}\boldsymbol{S})$, which follows directly from $\boldsymbol{G}^i_\mu = \boldsymbol{R}^T \boldsymbol{F}^i_\mu$ and holds for every $\boldsymbol{S}$. Substituting the phase-average decomposition of $\boldsymbol{F}^i_\mu$ (Equation (5.124)) and applying, term by term, the directional-derivative identities to the $\boldsymbol{R}\boldsymbol{S}$ direction, the equivariant identity to $d\boldsymbol{R}/d\boldsymbol{P}$ and the invariant one to $d\boldsymbol{T}_B/d\boldsymbol{P}$, exactly as above, gives

$$
\boldsymbol{G}^i_\mu : \boldsymbol{S} = \left(\boldsymbol{R}^T \boldsymbol{\Gamma}_\mu + \boldsymbol{\Gamma}^i_{T,\mu} : \mathbf{P}^i_{\mathbb{S}^3_T,\mu} : \frac{d\boldsymbol{T}_B}{d\boldsymbol{P}}(\boldsymbol{H}^i_\mu) + (\boldsymbol{R}^T \boldsymbol{\Gamma}^i_{R,\mu}) : \frac{d\boldsymbol{R}}{d\boldsymbol{P}}(\boldsymbol{H}^i_\mu) \right) : \boldsymbol{S}, \tag{6.21}
$$

whose second and third terms cancel, respectively, the $-\frac{d\boldsymbol{T}_B}{d\boldsymbol{P}}(\boldsymbol{H}^i_\mu)$ and $-\frac{d\boldsymbol{R}}{d\boldsymbol{P}}(\boldsymbol{H}^i_\mu)$ contributions inside the Lagrange-multiplier brackets. Folding the remaining constant term $\boldsymbol{R}^T\boldsymbol{\Gamma}_\mu$ into the localization contraction by means of the average-consistency property $\langle \mathbf{B}^{i,\mathrm{mfh}}_\mu \rangle = \mathbf{I}$

(Equation (4.25)), we obtain

$$|\Omega_{0,\mu}|\boldsymbol{S}:\boldsymbol{U}=\sum_{i=1}^{n_P}|\Omega_{0,\mu}^i|\left(\boldsymbol{R}^T\boldsymbol{\Gamma}_\mu+\boldsymbol{\Gamma}_{T,\mu}^i:\mathbf{P}_{\mathbb{S}_T^3,\mu}^i:\frac{d\boldsymbol{T}_B}{d\boldsymbol{P}}(\boldsymbol{H}_\mu^{i,\mathrm{mfh}})\right.$$
$$\left.+(\boldsymbol{R}^T\boldsymbol{\Gamma}_{R,\mu}^i):\frac{d\boldsymbol{R}}{d\boldsymbol{P}}(\boldsymbol{H}_\mu^{i,\mathrm{mfh}})\right):\mathbf{B}_\mu^{i,\mathrm{mfh}}(\boldsymbol{T}_B):\boldsymbol{S}. \quad (6.22)$$

Defining the co-rotated effective phase deformation

$$\boldsymbol{G}_\mu^{i,*}=\boldsymbol{R}^T\boldsymbol{\Gamma}_\mu+\boldsymbol{\Gamma}_{T,\mu}^i:\mathbf{P}_{\mathbb{S}_T^3,\mu}^i:\frac{d\boldsymbol{T}_B}{d\boldsymbol{P}}(\boldsymbol{H}_\mu^{i,\mathrm{mfh}})+(\boldsymbol{R}^T\boldsymbol{\Gamma}_{R,\mu}^i):\frac{d\boldsymbol{R}}{d\boldsymbol{P}}(\boldsymbol{H}_\mu^{i,\mathrm{mfh}}), \quad (6.23)$$

the co-rotational counterpart of $\boldsymbol{F}_\mu^{i,*}$ of Equation (C.103), in the sense that $\boldsymbol{G}_\mu^{i,*}:\boldsymbol{S}=\boldsymbol{F}_\mu^{i,*}:(\boldsymbol{R}\boldsymbol{S})$ for arbitrary $\boldsymbol{S}\in\mathbb{S}^3$, the symmetrization argument of the full-MFH case applies unchanged and we arrive at the right-stretch homogenization rule

$$\boldsymbol{U}=\langle\boldsymbol{G}_\mu^{i,*}:\bar{\mathbf{B}}_\mu^{i,\mathrm{mfh}}\rangle, \quad (6.24)$$

which mirrors Equation (6.15): an average of co-rotated effective phase deformations, weighted by the symmetrized localization operator $\bar{\mathbf{B}}_\mu^{i,\mathrm{mfh}}$.

Note that in this $\boldsymbol{U}$-based implementation of the projected MFH model, the Lagrange multipliers $\boldsymbol{\Gamma}_\mu$ and $\boldsymbol{\Gamma}_{R,\mu}^i$ appear pre-multiplied by the transpose of the macroscopic rotation, $\boldsymbol{R}^T$, reflecting the equivariance of the polar rotation, whereas $\boldsymbol{\Gamma}_{T,\mu}^i$ enters directly, since $\boldsymbol{T}_B$ is rotationally invariant.

6.2.3 Phase-level projector-free reformulation

Another difficulty that must be tackled in the computational implementation of the projected MFH model is the presence of the projector $\mathbf{P}_{\mathcal{V}_{N,\mu}^i}^i$, which depends on the macroscopic Biot stress $\boldsymbol{T}_B$, and whose derivative with respect to $\boldsymbol{T}_B$ is not readily available. To circumvent this issue, we adopt a 'projector-free' approach. First, we note that an admissible Biot-stress variation, which we henceforth denote by $\boldsymbol{\Sigma}$, must be tangent to the constitutive manifold $\boldsymbol{T}_B=\boldsymbol{h}|_{\mathbb{S}_+^3}(\boldsymbol{U})$. More precisely, the Biot stress $\boldsymbol{T}_B$ is the image of the macroscopic right stretch $\boldsymbol{U}$ under the constitutive map of Equation (2.47), so admissible variations $\boldsymbol{\Sigma}$ must be tangent to the constitutive manifold $\mathcal{N}=\{(\boldsymbol{U},\boldsymbol{h}|_{\mathbb{S}_+^3}(\boldsymbol{U}))\mid\boldsymbol{U}\in\mathbb{S}_+^3\}$. With the Biot tangent stiffness

$$\mathbb{B}(\boldsymbol{U})=\frac{\partial\boldsymbol{h}|_{\mathbb{S}_+^3}}{\partial\boldsymbol{U}}(\boldsymbol{U}), \quad (6.25)$$

a linear map $\mathbb{S}^3\to\mathbb{R}^{3\times3}$ that is not major-symmetric in general (for anisotropic materials), every tangent variation admits the representation

$$\boldsymbol{\Sigma}=\mathbb{B}:\boldsymbol{S},\qquad\boldsymbol{S}\in\mathbb{S}^3. \quad (6.26)$$

At the phase level, we denote the Biot tangent stiffness evaluated at the phase stretch by $\mathbb{B}_\mu^i:=\mathbb{B}(\boldsymbol{U}_\mu^i)$.

Following the description in the previous subsection, Equation (5.127) must be rewritten as

$$\boldsymbol{U}_\mu^i:\boldsymbol{\Sigma}=((\boldsymbol{R}_\mu^i)^T\boldsymbol{\Gamma}_\mu):\boldsymbol{\Sigma}+\boldsymbol{\Gamma}_{T,\mu}^i:\frac{d\boldsymbol{T}_B}{d\boldsymbol{P}}(\boldsymbol{P}_\mu^{i,\mathrm{mfh}}):(\boldsymbol{R}_\mu^i\boldsymbol{\Sigma}),\qquad\forall\boldsymbol{\Sigma}\in\mathcal{V}_\mu^i, \quad (6.27)$$

Box 6.2: Phase-level projector-free reformulation: unknowns and residual.

Input. The Lagrange multiplier $\boldsymbol{\Gamma}_\mu$, entering as $(\boldsymbol{R}^i_\mu)^T\boldsymbol{\Gamma}_\mu$, and the MFH phase-wise Biot stress $\boldsymbol{T}^{i,\mathrm{mfh}}_{B,\mu}$.
Solve for the phase-wise right stretch $\boldsymbol{U}^i_\mu \in \mathbb{S}^3_+$ and the Lagrange multiplier $\boldsymbol{\Gamma}^i_{T,\mu} \in \mathbb{S}^3_T$ such that

$$\mathsf{P}^i_{\mathbb{S}^3_T,\mu} : \boldsymbol{h}|_{\mathbb{S}^3_+}(\boldsymbol{U}^i_\mu) - \mathsf{P}^i_{\mathbb{S}^3_T,\mu} : \boldsymbol{T}^{i,\mathrm{mfh}}_{B,\mu} = \boldsymbol{0}, \qquad \text{(3 equations)} \tag{6.32}$$

$$(\mathbb{B}^i_\mu)^T : \left(\boldsymbol{U}^i_\mu - (\boldsymbol{R}^i_\mu)^T\boldsymbol{\Gamma}_\mu - \boldsymbol{\Gamma}^i_{T,\mu}\right) = \boldsymbol{0}. \qquad \text{(6 equations)} \tag{6.33}$$

where the last term is obtained by inserting the admissible test direction $\boldsymbol{R}^i_\mu\boldsymbol{\Sigma}$ and applying the polar-decomposition derivative identity $\frac{d\boldsymbol{T}_B}{d\boldsymbol{P}}(\boldsymbol{P}) : (\boldsymbol{R}(\boldsymbol{P})\boldsymbol{\Sigma}) = \boldsymbol{\Sigma}$ (cf. Equation (5.65)) with $\boldsymbol{R}^i_\mu = \boldsymbol{R}(\boldsymbol{P}^{i,\mathrm{mfh}}_\mu)$,

$$\boldsymbol{\Gamma}^i_{T,\mu} : \frac{d\boldsymbol{T}_B}{d\boldsymbol{P}}(\boldsymbol{P}^{i,\mathrm{mfh}}_\mu) : (\boldsymbol{R}^i_\mu\boldsymbol{\Sigma}) = \boldsymbol{\Gamma}^i_{T,\mu} : \boldsymbol{\Sigma}. \tag{6.28}$$

Substituting this result into Equation (6.27) yields

$$\boldsymbol{U}^i_\mu : \boldsymbol{\Sigma} = ((\boldsymbol{R}^i_\mu)^T\boldsymbol{\Gamma}_\mu) : \boldsymbol{\Sigma} + \boldsymbol{\Gamma}^i_{T,\mu} : \boldsymbol{\Sigma}, \qquad \forall \boldsymbol{\Sigma} \in \mathcal{V}^i_\mu. \tag{6.29}$$

Substituting $\boldsymbol{\Sigma} = \mathbb{B}^i_\mu : \boldsymbol{S}$ into Equation (6.29) and rearranging gives

$$\left(\boldsymbol{U}^i_\mu - (\boldsymbol{R}^i_\mu)^T\boldsymbol{\Gamma}_\mu - \boldsymbol{\Gamma}^i_{T,\mu}\right) : \mathbb{B}^i_\mu : \boldsymbol{S} = 0, \qquad \forall \boldsymbol{S} \in \mathbb{S}^3. \tag{6.30}$$

Since $\boldsymbol{S}$ is arbitrary,

$$(\mathbb{B}^i_\mu)^T : \left(\boldsymbol{U}^i_\mu - (\boldsymbol{R}^i_\mu)^T\boldsymbol{\Gamma}_\mu - \boldsymbol{\Gamma}^i_{T,\mu}\right) = \boldsymbol{0}, \tag{6.31}$$

which is the projector-free reformulation of the kinematic closure condition.

Implementation. For each phase i, instead of solving for the missing components of the Biot stress and the right stretch (totaling 6 unknowns) and post-computing the Lagrange multiplier, we now solve jointly for the right stretch $\boldsymbol{U}^i_\mu$ and the Lagrange multiplier $\boldsymbol{\Gamma}^i_{T,\mu}$, totaling 9 unknowns. The advantage of this approach is that we do not need to deal with the projector $\mathsf{P}^i_{\mathcal{V}_{N,\mu}}$ directly.

Chapter 7

Numerical examples

This chapter illustrates the use of the PMVP and PMCVP-derived models introduced in Chapter 5 through several numerical examples. In particular, we highlight the models' energetic consistency across scales and the satisfaction of the angular-momentum balance when all the phases are non-dissipative. Dissipative constitutive models for each phase are also considered, and their effect on the energetic consistency across scales is discussed. This last set of constitutive models is considered in the small-strain regime only. All the models considered for the individual phases are isotropic.

7.1 Problem definition

The geometry of each inclusion phase is assumed to be a lamella, with the corresponding single-inclusion problem being the mechanical problem concerning a simple laminate. Equations (4.6) and (4.7) provide the corresponding IVP, while Table 7.1 summarizes the volume fraction and orientation of each lamella. Figure 7.1 illustrates in a schematic fashion the single-inclusion problem associated with each phase. We consider a composite material made up of seven phases embedded in a matrix, resulting in eight phases total. This composite material is not intended to represent any specific material, but rather to serve as a benchmark for the numerical examples. As such the volume fractions and orientations of the phases are chosen purely for illustrative purposes, in order to highlight the differences between the models derived in Chapter 5.

Table 7.1: Orientation and volume fractions of the phases in the composite used in the numerical examples.

Phase	$\phi^i_{0,\mu}$	$\boldsymbol{N}^i_\mu$		
0	0.0396	0.4472	−0.8944	0.0000
1	0.0396	0.5774	0.5774	0.5774
2	0.0396	−0.7071	0.7071	0.0000
3	0.0396	0.9479	0.3160	0.0395
4	0.0396	0.8944	0.4472	0.0000
5	0.0396	0.7220	0.3094	0.6189
6	0.0396	0.7715	0.6172	0.1543
m	0.7225		-	

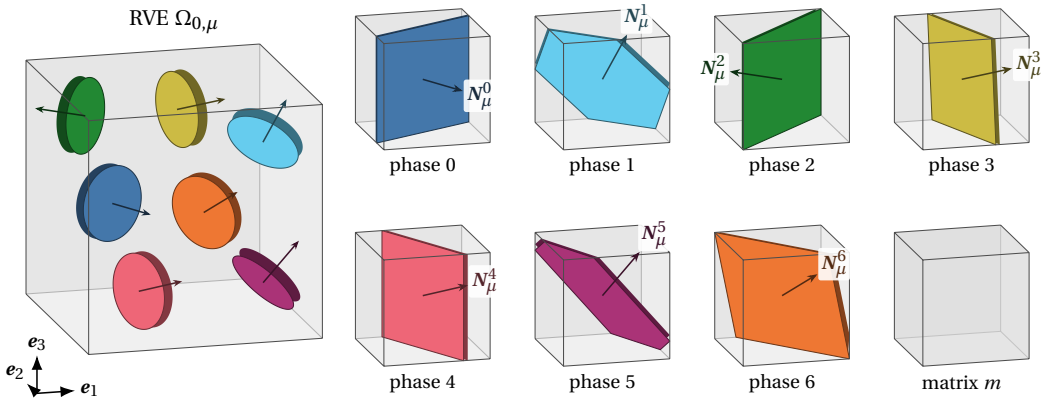

Figure 7.1: Composite material used in the numerical examples. Left: schematic of the RVE $\Omega_{0,\mu}$, with the seven lamellar inclusion phases embedded in the matrix phase m. Right: single-inclusion problem associated with each inclusion phase, namely a lamella with unit normal $\boldsymbol{N}_\mu^i$ (Table 7.1) embedded in the fictitious matrix.

We consider all the models derived in Sections 5.1 and 5.2, namely the full MFH, projected MFH, Sachs, and Taylor models based on the PMVP and PMCVP frameworks. We also consider their inconsistent counterparts, in which the homogenized stress or deformation gradient is computed using the classical volume-average homogenization rules, i.e., Equations (4.26) and (4.27), respectively. In the projected MFH models, we let the orthogonal projections $\mathbf{P}^m_{\mathbb{S}^3_N,\mu}$ and $\mathbf{P}^i_{\mathbb{S}^3_T,\mu}$ be $\mathbf{I}_S$ and $\mathbf{P}_{\mathbb{S}^3_T}$, respectively. Regarding the interaction models, we consider two: one with 'no interaction' between the phases, and the dilute interaction model (see Table 4.1). Concerning the constitutive descriptions of each of the phases, in Section 7.3 we adopt a hyperelastic model for each phase, while in Sections 7.4 and 7.5 we consider viscoelastic and von Mises plasticity models, respectively, for each phase.

7.2 Mechanical loading scheme

The mechanical loading for the strain-driven models based on the PMVP (Section 5.1) is also strain-driven, while for the stress-driven models based on the PMCVP (Section 5.2), it is stress-driven. This choice allows us to highlight the disagreements between the consistent and inconsistent versions of each model, since the difference between them lies only in the homogenized stress for the PMVP-based models and only in the homogenized deformation gradient for the PMCVP-based models.

The strain-driven loading scheme selected is an isochoric uniaxial tension loading scheme, defined through the macroscopic deformation gradient $\boldsymbol{F}(t)$ as follows

$$\boldsymbol{F}(t) = \begin{bmatrix} \lambda(t) & 0 & 0 \\ 0 & \frac{1}{\sqrt{\lambda(t)}} & 0 \\ 0 & 0 & \frac{1}{\sqrt{\lambda(t)}} \end{bmatrix}, \quad \text{with } \lambda(t) = \alpha t + 1. \tag{7.1}$$

The stress-driven loading scheme chosen is defined through the macroscopic first

Piola–Kirchhoff stress $\boldsymbol{P}(t)$ as follows

$$\boldsymbol{P}(t) = \nu(t) \begin{bmatrix} -0.5 & 0 & 0 \\ 0 & -0.25 & 0 \\ 0 & 0 & 3 \end{bmatrix}, \quad \text{with } \nu(t) = \beta t. \tag{7.2}$$

The choices for the loading rates α and β are specified in the respective sections below, as well as the time discretization adopted.

7.3 Hyperelastic material

In this section, each phase behaves as a compressible neo-Hookean material, with the strain energy density function given by

$$\psi^i_{\mu,\text{neo-Hookean}}(\boldsymbol{F}^i_\mu) = \frac{G^i}{2}(I_1 - 3 - 2\ln J^i_\mu) + \frac{\lambda^i}{2}(\ln J^i_\mu)^2, \tag{7.3}$$

where $I_1 = \text{tr}(\boldsymbol{F}^i_\mu(\boldsymbol{F}^i_\mu)^T)$, $J^i_\mu = \det(\boldsymbol{F}^i_\mu)$, and G^i and λ^i are the material constants coinciding with the Lamé parameters of phase i at infinitesimal strains. Note that the neo-Hookean material employed here is isotropic. These Lamé parameters are related to the Young's modulus E^i and Poisson's ratio ν^i of each phase through the following expressions

$$G^i = \frac{E^i}{2(1+\nu^i)}, \quad \lambda^i = \frac{E^i\nu^i}{(1+\nu^i)(1-2\nu^i)}. \tag{7.4}$$

Table 7.2: Elastic material properties of the phases in the composite used in the numerical examples.

Phase	E^i (Pa)	ν^i
0	0.7441	0.4662
1	1.2666	0.4443
2	1.9733	0.4170
3	2.8801	0.3855
4	3.9998	0.3514
5	5.3448	0.3165
6	6.9287	0.2822
m	34.9650	0.3320

7.3.1 Models based on the Principle of Multiscale Virtual Power

We consider first the models based on the PMVP. We impose an isochoric uniaxial strain-driven loading condition (Equation (7.1)). A time discretization with 40 increments is adopted, with $\Delta t = 2.5630 \times 10^{-7}$ s, resulting in a loading rate of $\alpha = 5.8540 \times 10^4\,\text{s}^{-1}$.

'No interaction' model

The first set of results concerns the models based on the PMVP, where the interaction model is 'no interaction', i.e., the average deformation gradient in each phase equals the macroscopic

deformation gradient. Since this interaction model implies $\mathbf{A}_{\mu}^{i,\mathrm{mfh}} = \mathbf{I}$, there is no distinction between the consistent and inconsistent full MFH models. Moreover, recalling Remark 5.2, we notice that in this case the full MFH model coincides with the Taylor model. Thus, we consider only the inconsistent version of the projected MFH model in addition to its consistent counterpart. Figure 7.2(a) shows the homogenized macroscopic first Piola–Kirchhoff stress components as a function of time. Figure 7.2(b) presents the excess angular momentum, defined as $\|\operatorname{skew}(\boldsymbol{P}\boldsymbol{F}^T)\|$, versus time, while Figure 7.2(c) shows the macroscopic power and average microscopic power versus time. The expected excess angular momentum computed from the homogenized response of each model is zero, indicating that the balance of angular momentum at the macroscale is satisfied. Equivalence between the macroscopic and average microscopic power, implying energetic consistency across scales, is also desired. In the figure, the model satisfies this requirement if the continuous line representing the macroscopic power threads the circular markers representing the average microscopic power.

We observe from Figure 7.2(a) that the diagonal components of the homogenized first Piola–Kirchhoff stress are identical between the Taylor model and both projected MFH models. Concerning the two projected MFH models, this is as expected, given that, from Equation (5.92), we know that the symmetric component of the homogenized Biot stress is the same for both models, with the skew part possibly differing. Since the polar rotation tensor is equal to the identity, i.e., $\boldsymbol{R} = \boldsymbol{I}$, only the symmetric part of the Biot stress contributes to the diagonal components of the first Piola–Kirchhoff stress; we conclude that these components must be identical for both models. The fact that the projected MFH models lead to the same diagonal components as the Taylor model is more surprising. This is not something to be expected in general. However, it may be a consequence of the particular constitutive description of the phases, as well as the mechanical loading considered here. Note also that the projected MFH models are both anisotropic, as seen in the off-diagonal components of the first Piola–Kirchhoff stress in Figure 7.2(a). In contrast, the Sachs and Taylor models are isotropic, given that the constitutive models of each of the phases are isotropic.

Given that mechanical loading is strain-driven and the models are based on the PMVP, the difference between the consistent and inconsistent projected MFH models lies only in the homogenized stress, with the average microscopic quantities being the same for both. We can confirm this from Figure 7.2(c), where we see that the average microscopic power is the same for both consistent and inconsistent models. Furthermore, recall from Equation (5.92) that only the skew part of the homogenized Biot stress may differ between the two models. Since only the symmetric part of the Biot stress contributes to the macroscopic power, i.e.,

$$\boldsymbol{P} : \dot{\boldsymbol{F}} = \operatorname{sym} \boldsymbol{T}_B : \dot{\boldsymbol{U}}, \tag{7.5}$$

we conclude that the macroscopic power must also be the same for both models. This is confirmed by Figure 7.2(c). However, even for this simple interaction model, the inconsistent model does not satisfy the balance of angular momentum, as seen in Figure 7.2(b). This defect is due to the differences in the skew part of the homogenized Biot stress of both models. More generally, we observe that the expected ordering of the power curves in Figure 7.2(c) is satisfied, with the Taylor model leading to the highest power, and the Sachs to the lowest.

Dilute interaction model

We now consider the same numerical experiment, except that the interaction model used in the MFH procedure is changed to the dilute interaction model. In this case, since the strain localization tensors will, in general, differ from the identity tensor, we consider the inconsistent versions of both the full and projected MFH models in addition to their consistent counterparts. Figure 7.3(a) shows the homogenized macroscopic first Piola–Kirchhoff stress components

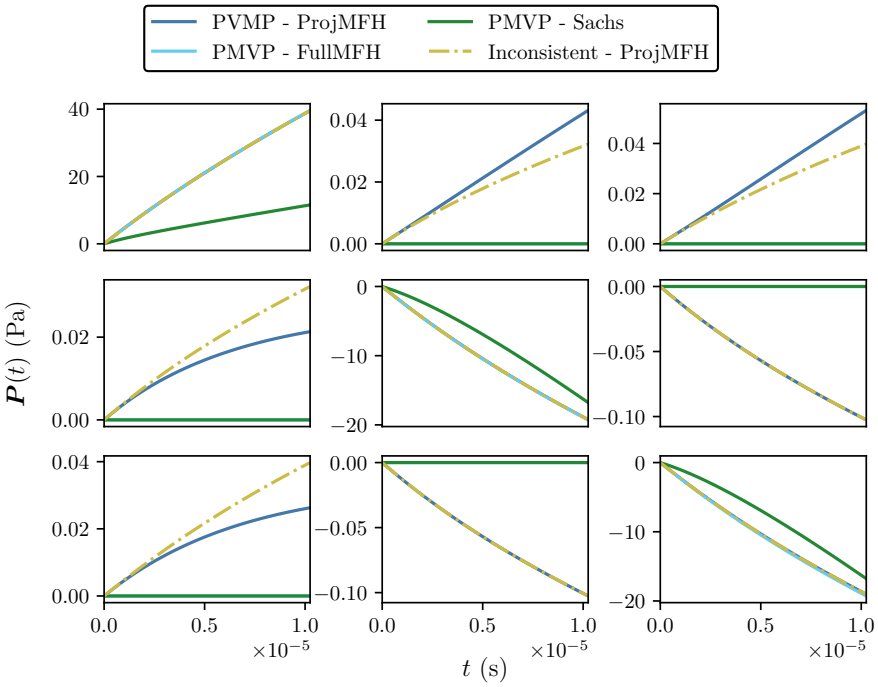

(a) Macroscopic first Piola–Kirchhoff stress components versus time.

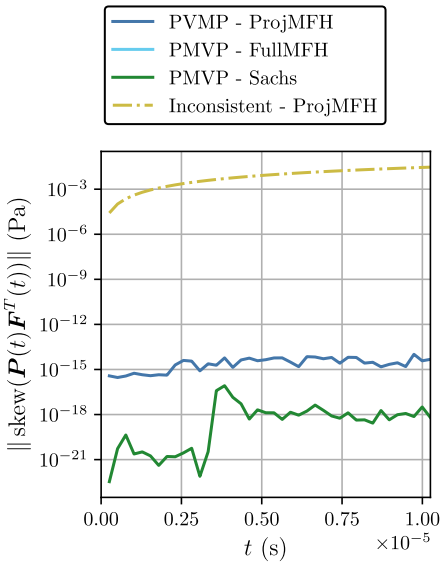

(b) Excess angular momentum versus time.

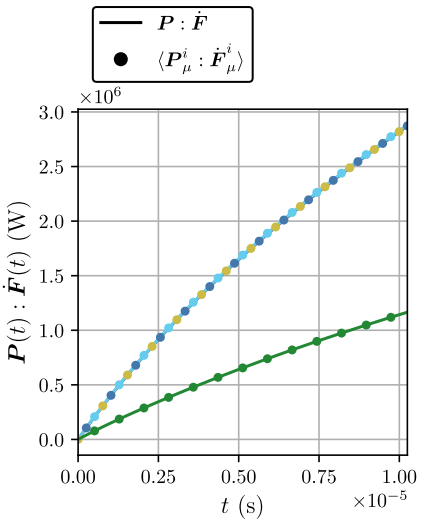

(c) Macroscopic power and average micro power versus time.

Figure 7.2: Macroscopic response for the strain-driven isochoric uniaxial loading case using the PMVP-based models and the 'no interaction' MFH model. (a) First Piola–Kirchhoff stress components, (b) excess angular momentum, (c) macroscopic and average microscopic power.

versus time. Figure 7.3(b) shows the excess angular momentum versus time, while Figure 7.3(c) shows the macroscopic power and average microscopic power versus time. Note again that since these models are based on the PMVP and the loading is strain-driven, the difference between the consistent and inconsistent models lies only in the homogenized stress, with the average microscopic quantities and the average microscopic power being the same for both.

All the components of the first Piola–Kirchhoff stress exhibit differences across the models, including the inconsistent ones, as seen in Figure 7.3(a). The response for all models, except the Sachs model, is anisotropic, as seen in the off-diagonal components of the first Piola–Kirchhoff stress. We note that the evolution of the P_{22} component of the first Piola–Kirchhoff stress for both consistent models displays some non-monotonicity, which is not observed in the inconsistent models. This behavior is likely a consequence of the geometric nonlinearities in the constitutive description of each phase, the relatively low number of phases considered, and the dilute interaction model employed here. Also, the compressible, anisotropic response may interact in a non-trivial way with the isochoric, uniaxial strain-driven loading condition considered here.

Despite this, we can confirm by looking at both Figure 7.3(b) and Figure 7.3(c) that the consistent models satisfy both the balance of angular momentum and energetic consistency, as expected. The same cannot be said for the inconsistent models, however. From Figure 7.3(b), we see that they do not satisfy the balance of angular momentum, with the excess angular momentum being non-zero, whereas for the consistent models it vanishes to machine precision. Moreover, from Figure 7.3(c), we see that the macroscopic power and average microscopic power do not coincide for both inconsistent models, indicating a lack of energetic consistency. In fact, the inconsistent models lead to negative power, which is non-physical. Finally, we observe that the expected ordering of the power curves in Figure 7.3(c) is again satisfied regarding the consistent models, with the full MFH model leading to the highest power, and the Sachs to the lowest, with the projected MFH model in between.

7.3.2 Models based on the Principle of Multiscale Complementary Virtual Power

We come now to the models based on the PMCVP. We impose stress-driven loading conditions, defined through the macroscopic first Piola–Kirchhoff stress $\boldsymbol{P}(t)$ as in Equation (7.2). A time discretization with 40 increments is adopted, with $\Delta t = 2.5000 \times 10^{-7}$ s, resulting in a loading rate of $\beta = 5.0000 \times 10^{-1}\,\mathrm{Pa\,s^{-1}}$.

'No interaction' model

The first set of results concerns the models based on the PMCVP, where the interaction model is 'no interaction', i.e., the average stress in each phase equals the macroscopic stress. Since this interaction model implies $\mathbf{B}_{\mu}^{i,\mathrm{mfh}} = \mathbf{I}$, there is no distinction between the consistent and inconsistent full MFH models. Thus, we consider only the inconsistent version of the projected MFH model in addition to the consistent one. Note also that from Remark 5.8, we see that in this case the full MFH model coincides with the Sachs model.

Regarding the numerical results obtained with these models, Figure 7.4(a) shows the homogenized macroscopic deformation gradient components as a function of time. Meanwhile, Figure 7.4(b) presents the excess angular momentum versus time, and Figure 7.4(c) shows the macroscopic complementary power and average microscopic complementary power, computed by subtracting the identity from the deformation gradient, versus time.

As with the results based on the PMVP with the 'no interaction' model, we observe from Figure 7.4(a) that the diagonal components of the homogenized deformation gradient are

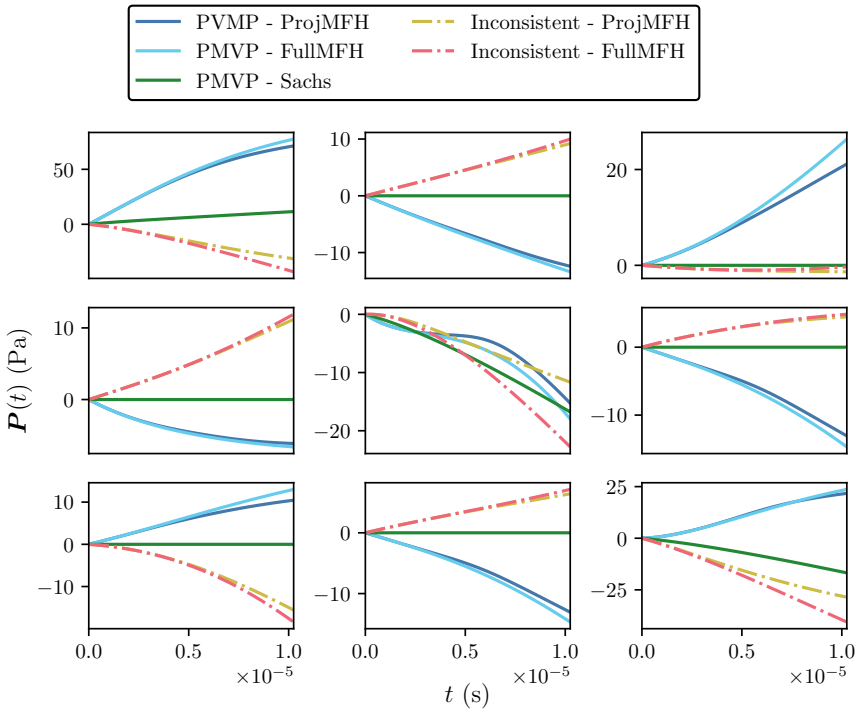

(a) Macroscopic first Piola–Kirchhoff stress components versus time.

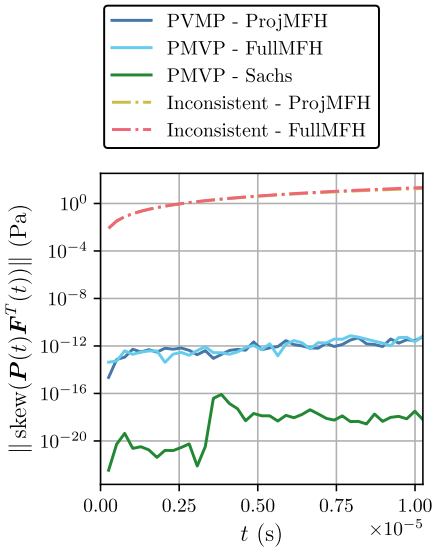

(b) Excess angular momentum versus time.

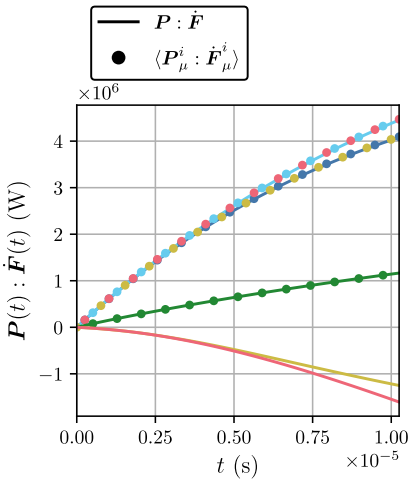

(c) Macroscopic power and average micro power versus time.

Figure 7.3: Macroscopic response for the strain-driven isochoric uniaxial loading case using the PMVP-based models and the dilute interaction MFH model. (a) First Piola–Kirchhoff stress components, (b) excess angular momentum, (c) macroscopic and average microscopic power.

identical between both projected MFH models. However, the full MFH/Sachs model now yields a different response from that of the projected models. We also note that the projected MFH models are both anisotropic, as seen in the off-diagonal components of the deformation gradient in Figure 7.4(a). In contrast, the full MFH/Sachs and Taylor models are isotropic, given that the constitutive models of each of the phases are isotropic.

Looking at Figure 7.4(c), we see that the average microscopic complementary power is the same for both consistent and inconsistent projected MFH models. Since these models are based on the PMCVP and the loading is stress-driven, the difference between the consistent and inconsistent models lies only in the homogenized deformation, with the average microscopic quantities and thus the average complementary power being the same for both consistent and inconsistent models. However, the inconsistent model does not satisfy the balance of angular momentum, as seen in Figure 7.4(b). Thus, similar conclusions to those drawn for the PMVP-based models with the 'no interaction' MFH model can be made here: even for this simple interaction model, the inconsistent model does not satisfy the angular momentum balance. In contrast, both models yield the same macroscopic complementary power and the same average microscopic complementary power. The expected ordering of the complementary power curves in Figure 7.4(c) is also satisfied, with the full MFH/Sachs model leading to the highest complementary power, and the Taylor to the lowest, with the projected MFH model in between.

Dilute interaction model

Finally, we repeat the same numerical experiment, except that the interaction model used in the MFH procedure is now the dilute interaction model. In this case, since the stress localization tensors will, in general, differ from the identity tensor, we consider the inconsistent versions of both the full and projected MFH models in addition to their consistent versions. Figure 7.5(a) shows the homogenized macroscopic deformation gradient components versus time. Now, all the components of the deformation gradient exhibit differences across the models, including the inconsistent ones, with all responses being anisotropic, as seen in the off-diagonal components of the deformation gradient, except for the Taylor model. We can confirm by looking at both Figure 7.5(b) and Figure 7.5(c) that the consistent models satisfy both the balance of angular momentum and energetic consistency, as expected. The same cannot be said for the inconsistent models, however. From Figure 7.5(b), we see that they do not satisfy the balance of angular momentum, as the excess angular momentum is non-zero for both inconsistent models. Moreover, from Figure 7.5(c), we see that the macroscopic complementary power and average microscopic complementary power do not coincide for both inconsistent models, indicating a lack of energetic consistency. Again, because these models are based on the PMCVP and the loading is stress-driven, the difference between the consistent and inconsistent models lies only in the homogenized deformation, with the average microscopic quantities being the same. Thus, the average complementary power is the same for both consistent and inconsistent models. The expected ordering of the complementary power curves in Figure 7.5(c) is again satisfied regarding the consistent models, with the full MFH model leading to the highest complementary power, and the Taylor to the lowest, with the projected MFH model in between.

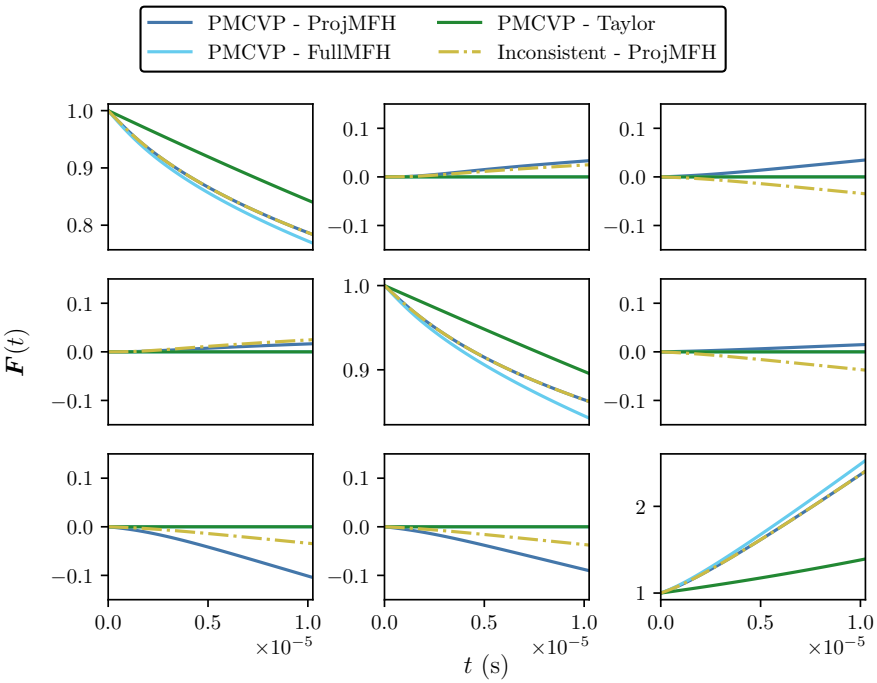

(a) Macroscopic deformation gradient components versus time.

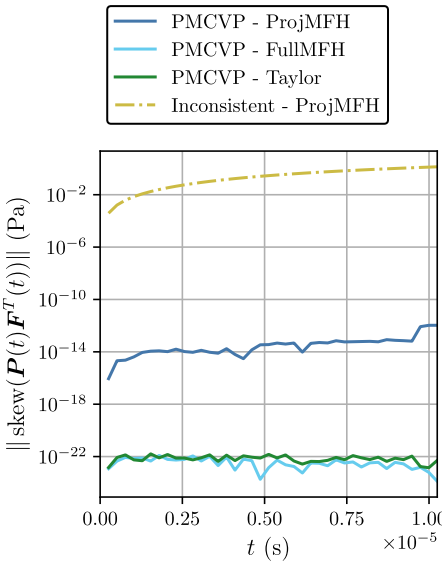

(b) Excess angular momentum versus time.

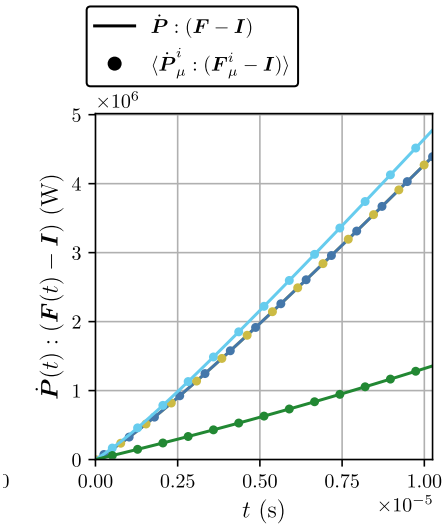

(c) Macroscopic complementary power and average micro complementary power versus time.

Figure 7.4: Macroscopic response for the stress-driven case using the PMCVP-based models and the 'no interaction' MFH model. (a) Deformation gradient components, (b) excess angular momentum, (c) macroscopic and average microscopic complementary power.

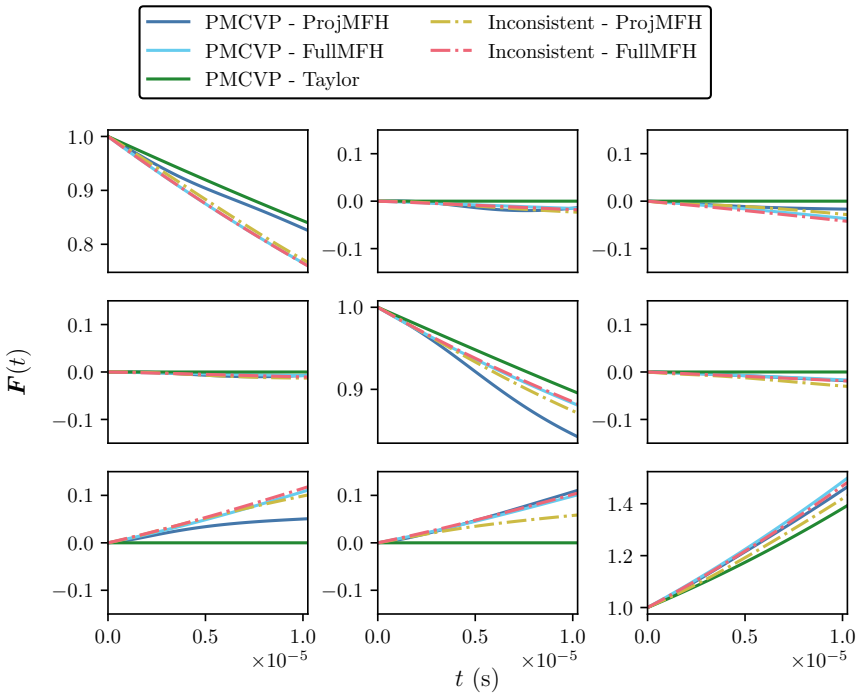

(a) Macroscopic deformation gradient components versus time.

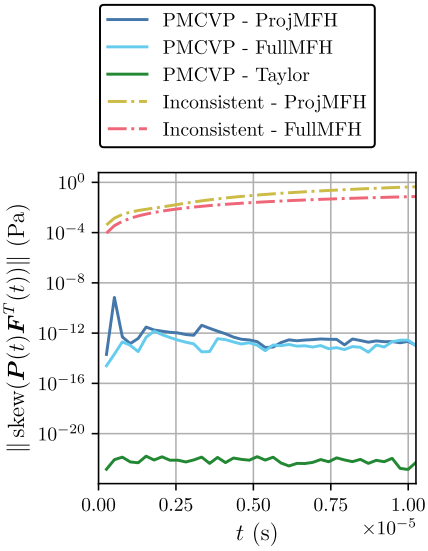

(b) Excess angular momentum versus time.

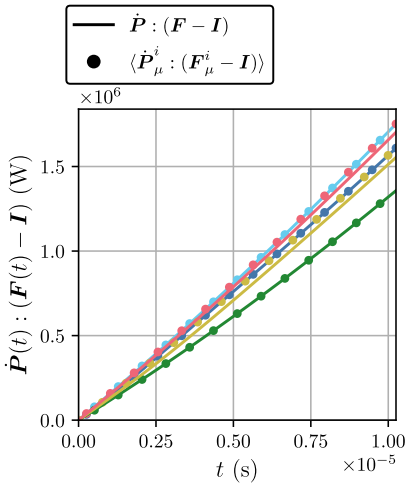

(c) Macroscopic complementary power and average micro complementary power versus time.

Figure 7.5: Macroscopic response for the stress-driven case using the PMCVP-based models and the dilute interaction MFH model. (a) Deformation gradient components, (b) excess angular momentum, (c) macroscopic and average microscopic complementary power.

7.4 Viscoelastic material

In this section, each phase behaves as a small-strain viscoelastic material, such that the strain energy function of each phase is given by

$$\psi^i_{\mu,\text{viscoelastic}}(\boldsymbol{\varepsilon}^i_\mu, \boldsymbol{\varepsilon}^{i,1}_\mu, \ldots, \boldsymbol{\varepsilon}^{i,n_\text{visc}}_\mu) = \frac{\kappa^i}{2}(\text{tr}\,\boldsymbol{\varepsilon}^i_\mu)^2 + G^i_\infty(\boldsymbol{\varepsilon}^i_{\mu,\text{dev}}) : (\boldsymbol{\varepsilon}^i_{\mu,\text{dev}}) + \sum_{m=1}^{n_\text{visc}} G^i_m \left(\boldsymbol{\varepsilon}^i_{\mu,\text{dev}} - \boldsymbol{\varepsilon}^{i,m}_{\mu,\text{dev}}\right) : \left(\boldsymbol{\varepsilon}^i_{\mu,\text{dev}} - \boldsymbol{\varepsilon}^{i,m}_{\mu,\text{dev}}\right), \quad (7.6)$$

where $\boldsymbol{\varepsilon}^i_\mu$ is the infinitesimal strain tensor in phase i, $\boldsymbol{\varepsilon}^{i,m}_\mu$ are the internal variables associated with the deviatoric viscoelastic response of phase i, κ^i is the bulk modulus of phase i, G^i_∞ is the long-term shear modulus of phase i, G^i_m are the shear moduli associated with the m-th Maxwell element of phase i, and n_visc is the number of Maxwell elements used to describe the viscoelastic behavior of each phase (see Figure 9.8). The evolution equations for the internal variables are given by

$$\dot{\boldsymbol{\varepsilon}}^{i,m}_{\mu,\text{dev}}(t) = \frac{1}{\theta^i_m}\left(\boldsymbol{\varepsilon}^i_{\mu,\text{dev}}(t) - \boldsymbol{\varepsilon}^{i,m}_{\mu,\text{dev}}(t)\right), \quad m = 1, \ldots, n_\text{visc}, \quad (7.7)$$

where θ^i_m is the relaxation time of the m-th Maxwell element of phase i. Table 7.3 summarizes the material properties of each phase.

Table 7.3: Viscoelastic material properties of the phases in the composite used in the numerical examples.

Phase	G^i_∞ (Pa)	κ^i (Pa)	G^i_1 (Pa)	θ^i_1 (s)	G^i_2 (Pa)	θ^i_2 (s)
0	0.1269					
1	0.2192					
2	0.3481					
3	0.5197	0.4367	0.2538	0.0010	-	-
4	0.7399					
5	1.0150					
6	1.3510					
m	4.3750	0.3320	8.7500	0.0020	13.1250	0.0100

7.4.1 Models based on the Principle of Multiscale Virtual Power

We consider first the models based on the PMVP. We impose an isochoric uniaxial strain-driven loading condition, defined through the small-strain approximation to the macroscopic deformation gradient $\boldsymbol{F}(t)$ in Equation (7.1). A time discretization with 40 increments is adopted, with $\Delta t = 1.2812 \times 10^{-3}$ s, resulting in a loading rate of $\alpha = 3.9024\,\text{s}^{-1}$.

Only the dilute interaction model is considered here, since the adoption of the small-strain approximation leads to the same results for both the consistent and inconsistent full and projected MFH models when using the 'no interaction' model.

Regarding the results of our numerical experiments, Figure 7.6 displays the homogenized macroscopic Cauchy stress components versus time (Figure 7.6(a)) and the macroscopic power and average microscopic power versus time (Figure 7.6(b)). From Figure 7.6(a) it is apparent

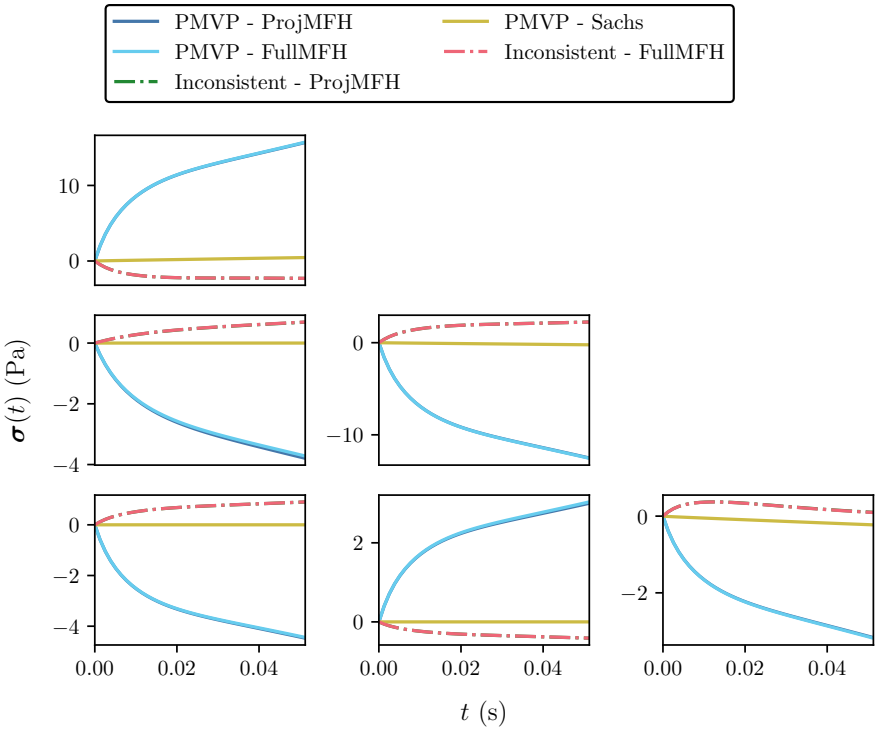

(a) Macroscopic Cauchy stress components versus time.

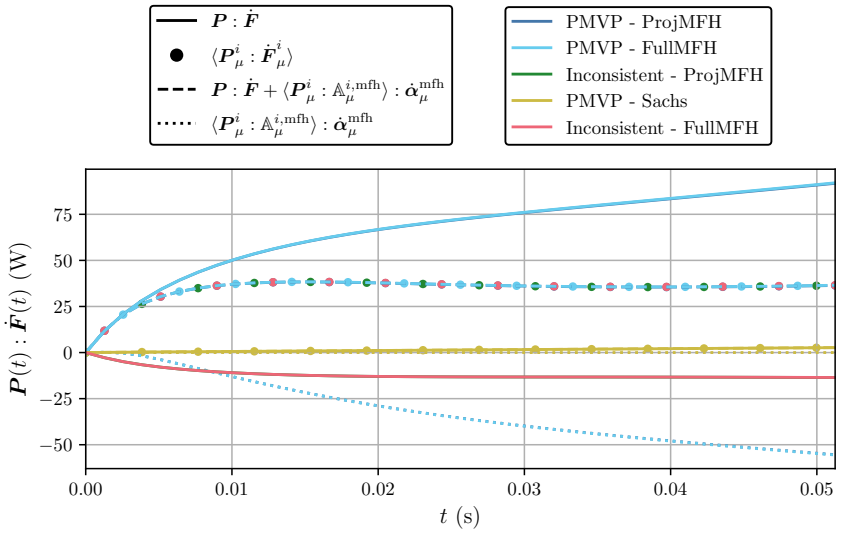

(b) Macroscopic power and average micro power versus time.

Figure 7.6: Macroscopic response for the strain-driven isochoric uniaxial loading case using the PMVP-based models and the 'dilute' MFH model. (a) Cauchy stress components, (b) macroscopic and average microscopic power.

that both consistent and inconsistent models lead to anisotropic responses, as seen in the off-diagonal components of the Cauchy stress, in contrast to the Sachs model, which leads to an isotropic response given the isotropic nature of each phase. The consistent and inconsistent versions of the full and projected MFH models are, however, substantially different from one another in the macroscopic stress predicted. The consistent models agree among themselves, as do the inconsistent ones, yet when the two groups are compared, we see that they lead to stress components with different signs. Given the loading scheme considered here, an isochoric uniaxial tension loading, the expected signs for the stress components are $\sigma_{11} > 0$, $\sigma_{22} < 0$, $\sigma_{33} < 0$, given the Poisson effect in the lateral directions. This is only satisfied by the consistent models, with the inconsistent models producing unexpected signs for all components. Finally, we note that the response predicted by the Sachs model is substantially more compliant than that of all other models.

From Figure 7.6(b), we confirm that the homogenization rule proposed does not lead to energetic consistency between scales in the case of materials described by internal variables, in this case, viscoelastic materials. In our example, the macroscopic power is always higher than the average microscopic power. This difference is also plotted in Figure 7.6(b), confirming that it can be computed as shown in Equation (5.38). That said, in the beginning of the simulation, while the response is mostly elastic, the difference between the macroscopic and average microscopic power is well accounted for using the homogenization rule proposed. The same cannot be said for the inconsistent models, which always lead to a substantial difference between the macroscopic and average microscopic power. In fact, in accordance with the signs observed for the corresponding macroscopic stress components, the inconsistent models lead to negative power, which is non-physical. Note, however, that the average microscopic power is the same for both consistent and inconsistent models, as expected given that these models are based on the PMVP and the loading is strain-driven.

7.4.2 Models based on the Principle of Multiscale Complementary Virtual Power

We turn now to the models based on the PMCVP. We impose a stress-driven loading condition, defined through the first Piola–Kirchhoff stress tensor $\boldsymbol{P}(t)$ in Equation (7.2), which is equal to the Cauchy stress tensor given the small-strain approximation adopted. A time discretization with 40 increments is used, with $\Delta t = 1.2813 \times 10^{-3}\,\mathrm{s}$, resulting in a loading rate of $\beta = 9.7561\,\mathrm{Pa\,s^{-1}}$.

Numerical results obtained are presented in Figure 7.7. Figure 7.7(a) displays the homogenized macroscopic infinitesimal strain tensor components versus time and Figure 7.7(b) the macroscopic complementary power and average microscopic complementary power versus time. From the plots in Figure 7.7(a), we conclude that both consistent and inconsistent models lead to approximately linear responses. They are anisotropic, as expected, given the non-zero off-diagonal components of the infinitesimal strain tensor, and the loading scheme considered. The response of the Taylor model is again isotropic, given the isotropic nature of each phase.

From Figure 7.7(b), we see that this loading scenario does not lead to a marked difference between the macroscopic complementary power and average microscopic complementary power for both consistent models, as well as the projected MFH inconsistent model. The same cannot be said for the full MFH inconsistent model, which leads to a substantial difference between the macroscopic and average microscopic complementary power. Given the approximately linear response observed, the expected ordering of the complementary power curves in Figure 7.7(b) is also satisfied, with the full MFH model leading to the highest complementary power, and the Taylor to the lowest, with the projected MFH model in between.

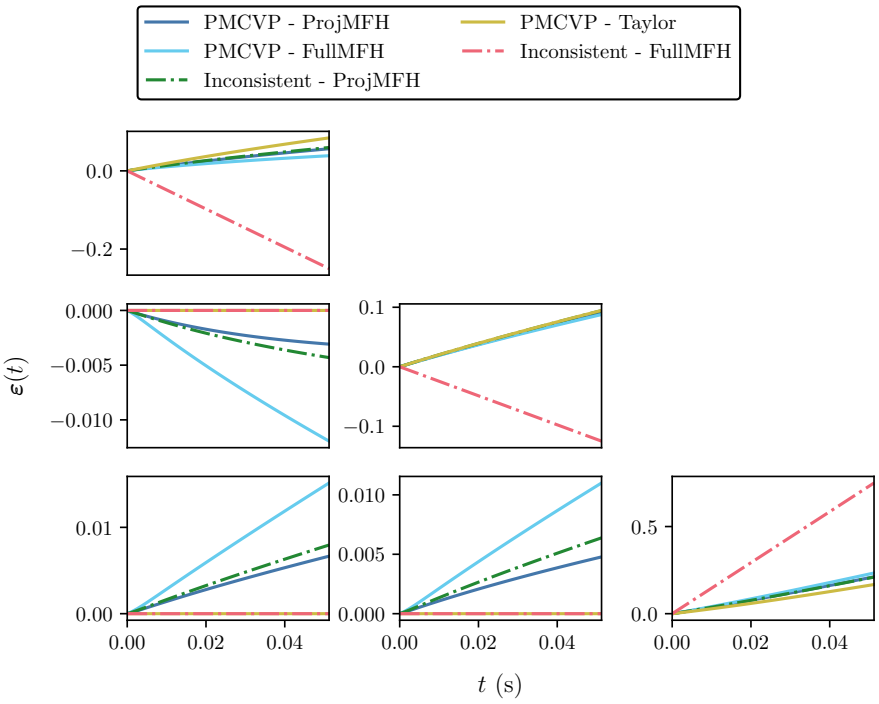

(a) Macroscopic infinitesimal strain tensor components versus time.

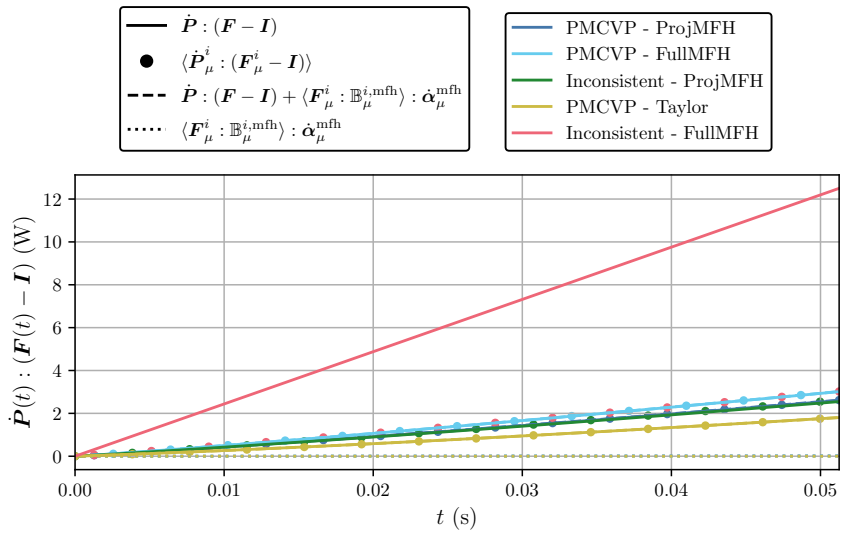

(b) Macroscopic complementary power and average micro complementary power versus time.

Figure 7.7: Macroscopic response for the stress-driven mixed loading case using the PMCVP-based models and the 'dilute' MFH model. (a) Infinitesimal strain tensor components, (b) macroscopic and average microscopic complementary power.

7.5 von Mises plastic material

This last section presents numerical results where the phases behave as small-strain von Mises plastic materials with no hardening. The Helmholtz free energy density function of each phase is given by

$$\psi^i_{\mu,\text{von Mises}}(\boldsymbol{\varepsilon}^i_\mu, \boldsymbol{\varepsilon}^{i,p}_{\mu,\text{dev}}) = \frac{\kappa^i}{2}(\text{tr}\,\boldsymbol{\varepsilon}^i_\mu)^2 + G^i(\boldsymbol{\varepsilon}^i_{\mu,\text{dev}} - \boldsymbol{\varepsilon}^{i,p}_{\mu,\text{dev}}) : (\boldsymbol{\varepsilon}^i_{\mu,\text{dev}} - \boldsymbol{\varepsilon}^{i,p}_{\mu,\text{dev}}), \tag{7.8}$$

where $\boldsymbol{\varepsilon}^i_\mu$ is the infinitesimal strain tensor in phase i, $\boldsymbol{\varepsilon}^{i,p}_{\mu,\text{dev}}$ is the plastic part of the deviatoric infinitesimal strain tensor in phase i, κ^i is the bulk modulus of phase i, and G^i is the shear modulus of phase i. The evolution equations for the plastic strain are given by

$$\dot{\boldsymbol{\varepsilon}}^{i,p}_{\mu,\text{dev}}(t) = \dot{\gamma}^i_\mu(t)\sqrt{\frac{3}{2}}\frac{\boldsymbol{\sigma}^i_{\mu,\text{dev}}(t)}{\|\boldsymbol{\sigma}^i_{\mu,\text{dev}}(t)\|}, \tag{7.9}$$

where $\dot{\gamma}^i_\mu(t)$ is the plastic multiplier in phase i at time t, and $\boldsymbol{\sigma}^i_{\mu,\text{dev}}$ is the deviatoric part of the Cauchy stress tensor in phase i. The plastic multiplier and Cauchy stress tensor in each phase must also satisfy the Kuhn–Tucker loading–unloading conditions

$$\dot{\gamma}^i_\mu(t) \geq 0, \quad \Phi^i_\mu(\boldsymbol{\sigma}^i_\mu) \leq 0, \quad \dot{\gamma}^i_\mu(t)\Phi^i_\mu(\boldsymbol{\sigma}^i_\mu) = 0, \tag{7.10}$$

where the yield function Φ^i_μ is defined as

$$\Phi^i_\mu(\boldsymbol{\sigma}^i_\mu) = \sqrt{\frac{3}{2}}\|\boldsymbol{\sigma}^i_{\mu,\text{dev}}\| - \sigma^i_Y, \tag{7.11}$$

with σ^i_Y being the yield stress of phase i. Table 7.4 summarizes the material properties of each phase in the composite.

Table 7.4: Elastoplastic material properties of the phases in the composite used in the numerical examples.

Phase	G^i (Pa)	κ^i (Pa)	σ^i_Y (Pa)
0	0.2538		
1	0.4385		
2	0.6963		
3	1.0394	0.4367	1.0e5
4	1.4799		
5	2.0300		
6	2.7019		
m	26.2500	0.3320	2.0

7.5.1 Models based on the Principle of Multiscale Virtual Power

We consider first the models based on the PMVP. We impose an isochoric uniaxial strain-driven loading condition, defined through the small-strain approximation of the macroscopic deformation gradient $\boldsymbol{F}(t)$ in Equation (7.1). A time discretization with 40 increments is adopted, with $\Delta t = 2.5125 \times 10^{-4}$ s, resulting in a loading rate of $\alpha = 5.9701\,\text{s}^{-1}$.

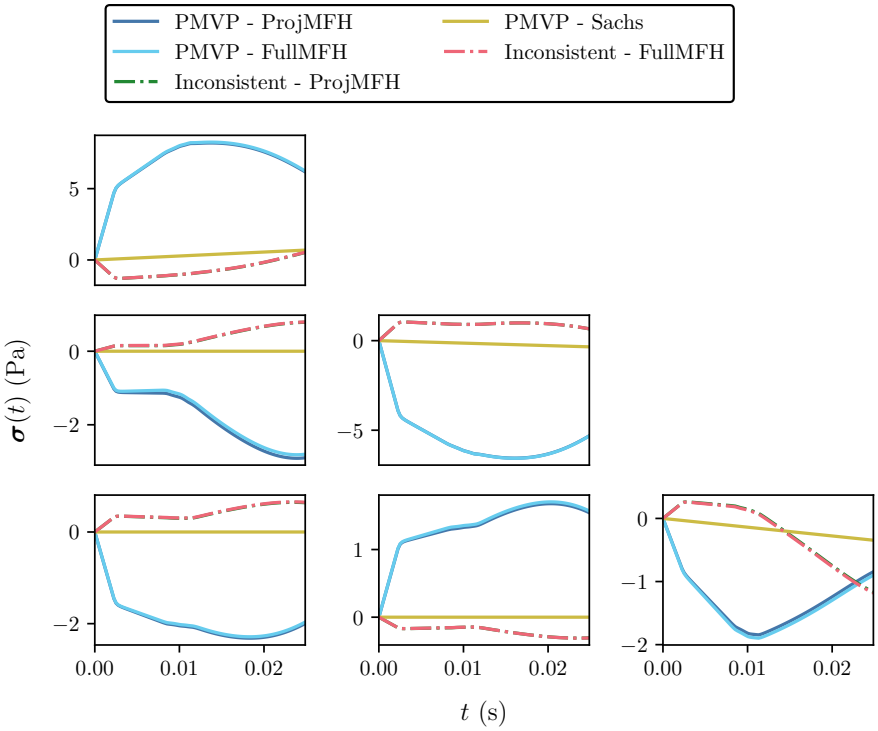

(a) Macroscopic Cauchy stress components versus time.

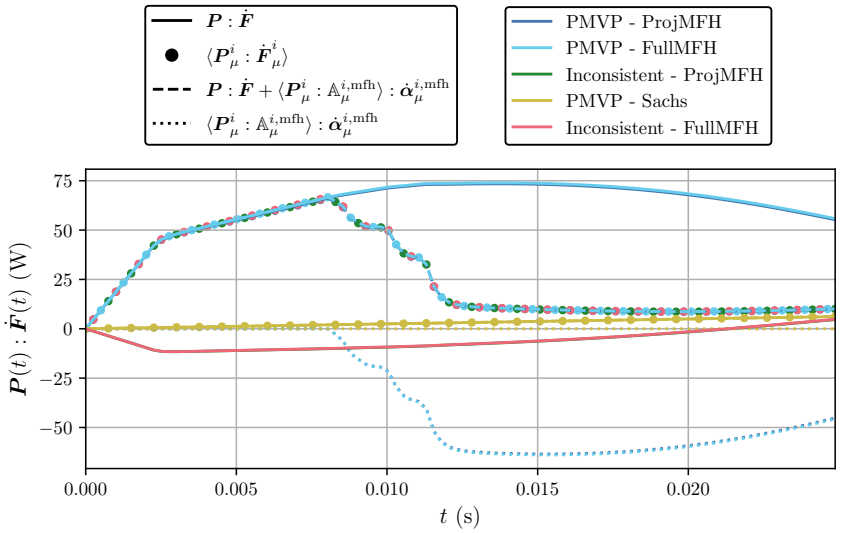

(b) Macroscopic power and average micro power versus time.

Figure 7.8: Macroscopic response for the strain-driven isochoric uniaxial loading case using the PMVP-based models and the 'dilute' MFH model. (a) Cauchy stress components, (b) macroscopic and average microscopic power.

Only the dilute interaction model is considered here, since the adoption of the small-strain approximation leads to the same results for both the consistent and inconsistent full and projected MFH models when using the 'no interaction' model.

Figure 7.8 displays the homogenized macroscopic Cauchy stress components versus time (Figure 7.8(a)) and the macroscopic power and average microscopic power versus time (Figure 7.8(b)). We can conclude from Figure 7.8(a) that both consistent and inconsistent models lead to anisotropic responses, as seen in the off-diagonal components of the Cauchy stress, which are more pronounced than those predicted by the Sachs model. From Figure 7.8(b), we confirm that the homogenization rule proposed does not lead to energetic consistency between scales in the case of materials described by internal variables, in this case, a perfectly plastic material, which is rate independent. In our example, the macroscopic power is always higher than the average microscopic power. This difference is also plotted in Figure 7.8(b), confirming that it can be computed as shown in Equation (5.38). That said, in the beginning of the simulation, while the response is elastic, the difference between the macroscopic and average microscopic power is well accounted for using the homogenization rule proposed. The same cannot be said for the inconsistent models, which always lead to a substantial difference between the macroscopic and average microscopic power.

7.5.2 Models based on the Principle of Multiscale Complementary Virtual Power

As in previous sections, the models based on the PMCVP are subjected to a stress-driven loading condition, defined through the first Piola–Kirchhoff stress tensor $\boldsymbol{P}(t)$ in Equation (7.2), which is equal to the Cauchy stress tensor given the small-strain approximation adopted. A time discretization with 40 increments is used, with $\Delta t = 2.5125 \times 10^{-4}\,\mathrm{s}$, resulting in a loading rate of $\beta = 9.9502\,\mathrm{Pa\,s^{-1}}$.

Figure 7.9 displays the homogenized macroscopic infinitesimal strain tensor components versus time (Figure 7.9(a)) and the macroscopic complementary power and average microscopic complementary power versus time (Figure 7.9(b)). We can conclude from Figure 7.9(a) that both consistent and inconsistent models lead to approximately linear anisotropic responses, as seen in the off-diagonal components of the infinitesimal strain tensor. From Figure 7.9(b), we see that this loading scenario does not lead to a marked difference between the macroscopic complementary power and average microscopic complementary power for both consistent models, as well as the projected MFH inconsistent model. The same cannot be said for the full MFH inconsistent model, which leads to a substantial difference between the macroscopic and average microscopic complementary power. Given the approximately linear response observed, the expected ordering of the complementary power curves in Figure 7.9(b) is also satisfied, with the full MFH model leading to the highest complementary power, and the Taylor to the lowest, with the projected MFH model in between.

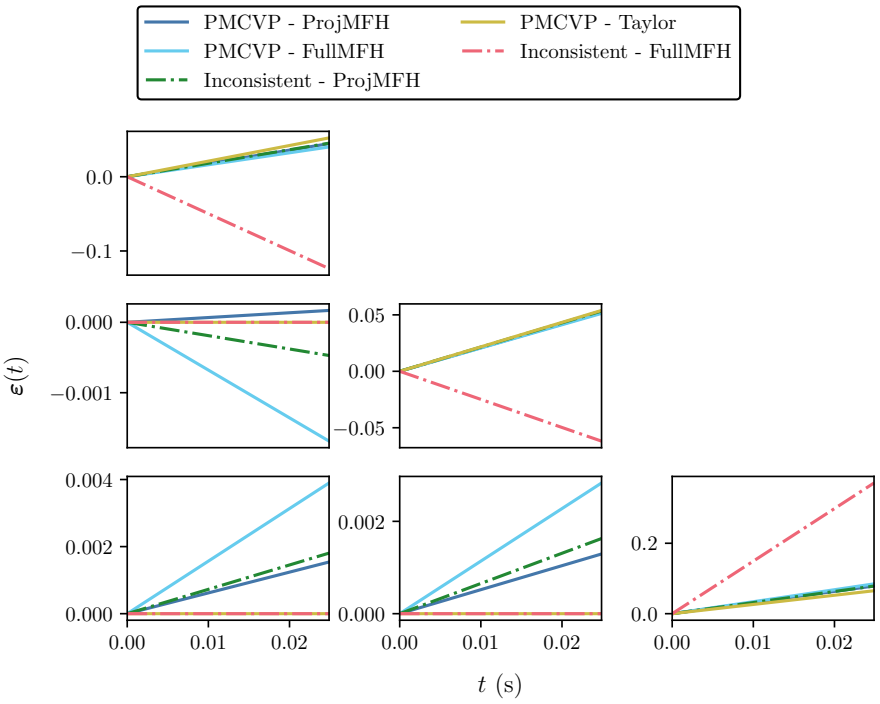

(a) Macroscopic infinitesimal strain tensor components versus time.

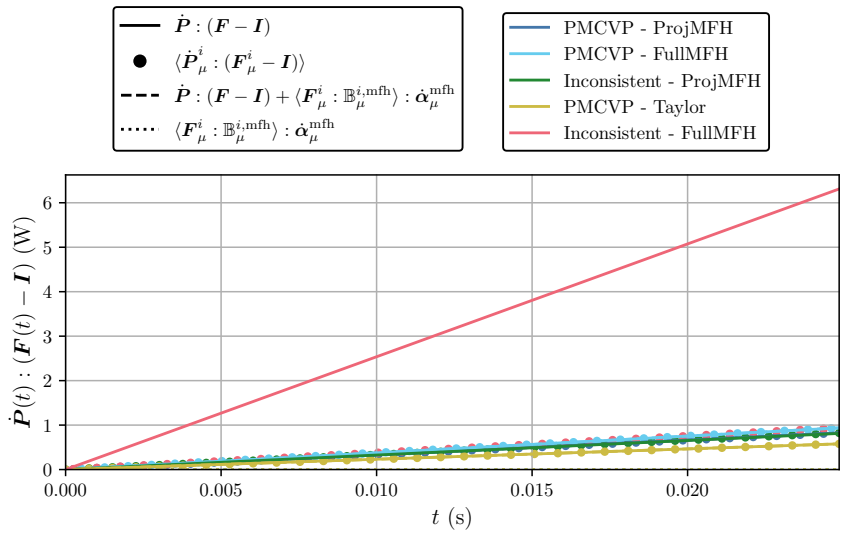

(b) Macroscopic complementary power and average micro complementary power versus time.

Figure 7.9: Macroscopic response for the stress-driven mixed loading case using the PMCVP-based models and the 'dilute' MFH model. (a) Infinitesimal strain components, (b) macroscopic and average microscopic complementary power.

Chapter 8

Thermomechanical behavior of semi-crystalline polymers

The goal of this chapter is to outline the thermomechanical response of semi-crystalline polymers. An account of their deformation mechanisms opens the chapter, followed by the experimental results of various mechanical experiments, such as constant strain rate, stress relaxation, and creep tests. A discussion regarding their dependency on factors such as temperature, strain rate, and pressure is also included. Closing the chapter are the results of thermal analysis techniques, such as differential scanning calorimetry. These experimental results establish the modeling requirements for semi-crystalline polymers, which are addressed in Chapter 9. To better understand how semi-crystalline polymers' thermomechanical behavior departs from linear thermoviscoelasticity, a brief review of this simpler behavior is provided in Appendix A.

8.1 Deformation mechanisms for semi-crystalline polymers

A deformation mechanism is a kinetic process occurring at the atomic, microscopic, or mesoscopic scale that is responsible for changes in a material's internal structure, shape, or volume, thus implying a characteristic deformation behavior, i.e., a constitutive relation between stress, strain, strain rate, and temperature (Frost and Ashby, 1982). According to Arzhakov (2019), it includes

1. molecular-kinetic aspects, such as the mutual torsional-vibrational and translational motions of microscopic kinetic units of various sizes,

2. structural aspects, such as the creation or annihilation of kinetic units or changes in the resistance to their motion,

where a kinetic unit is a structural element possessing vibrational and translational degrees of freedom. As a rule of thumb, the molecular-kinetic aspects by themselves describe a steady state, such that the stress and the temperature completely determine the strain rate and other variables describing the structure of the material. The structural aspects will lead to a transient behavior, meaning that the stress and the temperature will not be enough to determine the response of the material since the structure is also changing (Frost and Ashby, 1982).

One way to study the deformation mechanisms in a polymer is to consider its relaxation transitions. A relaxation transition is a change in the material's response to an external action caused by the mobility of a specific kinetic unit in a given temperature-time test mode. However, irreversible deformation or structural change is allowed (Arzhakov, 2019). The experimental approaches and techniques used to study relaxation phenomena are extremely diverse, including isochronal (considering the response at the same instant or frequency) and isothermal results from experiments such as thermomechanical analysis, differential scanning calorimetry (DSC) (reviewed in more detail below), dielectric and acoustic measurements, radiothermoluminescence, nuclear magnetic resonance, and several modifications of probing techniques (Ferry, 1980; Arzhakov, 2019).

Despite the partially ordered structure of the crystalline phase and the corresponding limitation of molecular mobility, the relaxation spectrum of a semi-crystalline polymer is generally richer than that of a glassy polymer. The kinetic units in the former can be made to correspond to features inside crystallites, in the intercrystalline amorphous region, or on the surface of the crystallites (Ferry, 1980; Arzhakov, 2019).

The assignment of a given relaxation transition to a deformation mechanism within a phase of the semi-crystalline polymer can be achieved in two ways: (i) by considering the same polymer at different degrees of crystallinity, lamellar thicknesses, defect content, cross-linking (Ferry, 1980); and (ii) by employing an etching procedure (Arzhakov, 2019). Hoffman and coworkers (Hoffman et al., 2007), when discussing the relaxation behavior of polychlorotrifluoroethylene (PCTFE) and polyethylene (PE) , describe deformation mechanisms such as the motion of chain folds coupled with interior chains and relaxation at chain-end induced row vacancies in chain-folded crystals. The relaxation behavior of semi-crystalline polymers is discussed later with thermomechanical experiments as a basis, both isothermal and isochronal. Some of the kinetic units involved in a semi-crystalline polymer's deformation mechanisms are (Arzhakov, 2019) (see Figure 8.1):

1. between the crystalline cores of the lamellae;
2. regular folds with suppressed mobility;
3. irregular loops;
4. folded tie-chains;
5. free ends of macromolecules coming out of lamellae;
6. slightly curved tie-chains;
7. folds the mobility of which is significantly limited by crystallites;
8. fully straightened tie-chains, the ends of which are fixed by neighboring lamellas.

Bowden and Young (1974) provide an early description of the deformation mechanisms in a semi-crystalline polymer not associated with relaxation transitions. These may include structural changes and lead to permanent deformation. Drozdov and coworkers (Drozdov et al., 2009) provide a fairly comprehensive list of such microstructural changes. In the amorphous phase, the orientation of macromolecules along the direction of maximum stress can be observed, as can changes in the concentration of entanglements between chains (junctions in the polymer network), and the formation and growth of micro-voids. In the crystalline phase, there can be formation and motion of dislocations in the crystallites, rotation and twist of lamellae in spherulites, fine (homogeneous shear of crystal blocks) and coarse (heterogeneous inter-lamellar sliding) slip of lamellar blocks and their fragmentation, micro-necking of

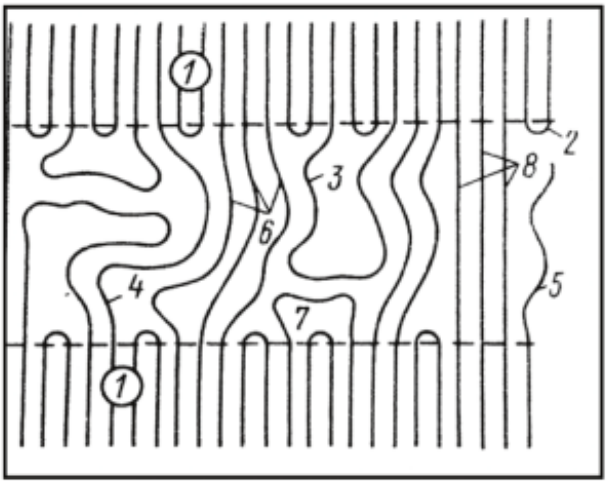

Figure 8.1: Schematic depiction of the kinetic units associated with relaxation transitions in lamellar PE. 1) between the crystalline cores of the lamellae; 2) regular folds with suppressed mobility; 3) irregular loops; 4) folded tie-chains; 5) free ends of macromolecules coming out of lamellas; 6) slightly curved tie-chains; 7) folds the mobility of which is significantly limited by crystallites; 8) fully straightened tie-chains, the ends of which are fixed by neighboring lamellas. Taken from Arzhakov (2019).

lamellae, rotation of lamellar stacks, or rearrangement of the spherulitic structure into a fibrillar structure, among others. At the interface between the amorphous and crystalline phases, phenomena such as chain slip through the crystals, sliding of tie chains and detachment of chain folds and loops from lamellar block surfaces, diffusion of micro-voids from the amorphous into the crystalline phase, and creation and annihilation of dislocations at lamellae surfaces can all be observed.

Based on several works, including Peterson (1966) and Lin and Argon (1994), Argon (2013) identifies three different intralamellar slip deformation mechanisms in semi-crystalline polymer crystallites: nucleation of a monolithic screw dislocation from the thin edge of the lamella into the (100) plane; nucleation of a screw dislocation half loop from the narrow edge; and nucleation of an edge-dislocation half loop from the large flat surface of the wide face of a lamella.

Relevant to the behavior of the amorphous phase, Boyce and coworkers (Boyce et al., 1988) mention that, for glassy polymers, flow is only observed after the segments of the polymer molecules undergo a sufficient rotation. This is followed by the molecular alignment of the polymer chains, resulting in entropy change and increased resistance to the loading.

The nature of the deformation associated with each of these mechanisms must be discussed, i.e., whether it is elastic or plastic, reversible or irreversible. After all, if they lead to flow, it may appear at first glance that the corresponding deformation is always permanent. Consider this simplified picture: the mechanisms are parallel combinations of dashpots and springs in series, as described in Keller and Pope (1971) (see Figure 8.2). The differences in the viscosities of the dashpots and the stiffnesses of the springs in this model allow for both permanent deformation and recovery (Fotheringham and Cherry, 1978). Some of the mechanisms may remain elastic, when the viscosity of the corresponding dashpot is very large, and even allow for complete recovery. Physically, it means that the kinetic units responsible for a given flow mechanism may be components of a composite overall structural element whose behavior remains elastic. Even intralamellar slip in the crystalline part of a semi-crystalline polymer can show some recovery

due to the polymer crystallite structure, e.g., when the slip planes cut across fold planes (Keller and Pope, 1971). The decomposition of deformation into reversible and irreversible parts is discussed based on mechanical experiments in Section 8.2.3.

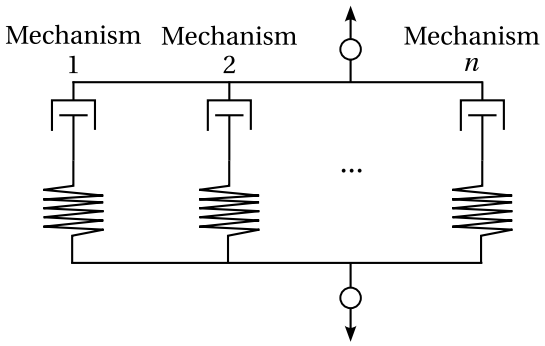

Figure 8.2: Simplified model of multiple deformation mechanisms as suggested in Keller and Pope (1971).

Regarding the modeling of the deformation behavior connected to each of these phenomena, some of them accept numerically feasible descriptions, e.g., the plastic flow rule corresponding to the nucleation of dislocations in the crystalline part of the polymer or the strain hardening due to the molecular alignment of the amorphous part of the polymer. However, there are some hurdles to the practical application of these models. Since semi-crystalline polymers are heterogeneous and hierarchical in structure, the descriptions of the deformation mechanisms may not be directly applicable to the bulk material. Also, the structure of the material changes with deformation, as does the relative importance of each mechanism in the overall deformation behavior. More details on some of these models are provided in Chapter 9.

To better understand how the micro- and mesostructure evolve with mechanical loading, consider the experimental results of Strobl and coworkers (Hiss et al., 1999; Hobeika et al., 2000; Hong et al., 2004a,b; Na et al., 2006). They consist of free shrinkage and step-cycle tests, as well as X-ray scattering experiments on deformed polyethylene samples with different degrees of crystallinity and molecular weight above the glass transition temperature. Distinct regimes in the deformation behavior of all the samples can be identified, with the transitions between them, denoted A through D, happening roughly at the same strain levels.

At small strains, below a true strain of approximately 0.025, deformation manifests itself mainly through the soft amorphous layers (Patlazhan and Remond, 2012). In fact, according to Nikolov and coworkers (Nikolov and Doghri, 2000; Nikolov et al., 2002), experiments show that interlamellar shear is the dominant deformation mode at small strains for PE. The onset of local flow processes (point A) at the end of the Hookean range through isolated slip processes begins at around a true strain of 0.025 (Hiss et al., 1999). Taking into account that local stresses in two-phase heterogeneous solids may strongly exceed the imposed stress, the plastic flow of crystal lamellae may appear locally at fairly low strains (Patlazhan and Remond, 2012). A collective onset of sliding processes among the crystal blocks composing the crystal lamellae determines the yield point (point B in Figure 8.3), at around a true strain of 0.1. The beginning of the disintegration of the crystal blocks, which is followed by fibril formation (point C in Figure 8.3), starts at around a strain of 0.6. Solid-state deformation of a semi-crystalline polymer normally results in the destruction of the crystallites belonging to the original morphology, followed by reordering to form new crystallites. Newly formed crystallites are themselves subject to disruption at higher orientation levels, being replaced by a fibrillar

morphology (Peacock, 2014). According to G'sell and Dahoun (1994), it is conceivable that the crystallites begin to undergo fragmentation and unfolding at strains between 0.5 and 1.0. Chain disentanglement (point D in Figure 8.3) happens at around a true strain of 1.

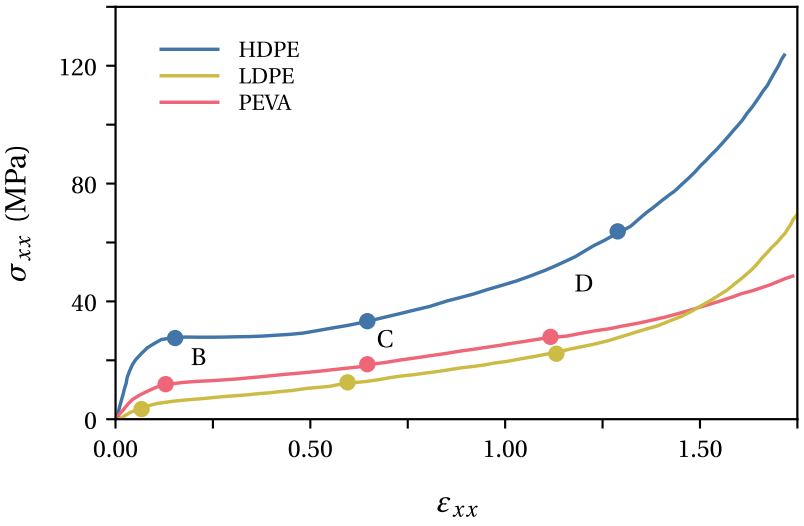

Figure 8.3: Locations of the transition points B-D along the stress–strain curve for HDPE, LDPE and PEVA. Adapted from Hiss et al. (1999).

8.2 Mechanical response of semi-crystalline polymers

The thermomechanical response of semi-crystalline polymers is reviewed in this section with the aim of identifying relevant features for constitutive modeling (see Chapter 9). There are several factors affecting the mechanical response of semi-crystalline polymers. Extrinsic factors, such as temperature, strain rate, hydrostatic pressure, and the chemical nature of the environment (e.g., the presence of water, oxygen, and organic solvents), are critical in describing the behavior of a polymer. Other relevant elements in the characterization of semi-crystalline polymers are intrinsic. Of crucial importance are the degree of crystallinity, lamellar thickness, type of mesoscopic structure, molecular weight, physical entanglement, cross-linking, and polymer aging (Ayoub et al., 2011; Şerban et al., 2013; Callister and Rethwisch, 2014; Cundiff et al., 2022).

Numerous experimental procedures provide information about a material's mechanical response. Constant strain rate tests are among the most relevant experiments for the characterization of semi-crystalline polymers, mainly through uniaxial loading experiments, whether tensile or compressive. Pure shear and torsion tests are also often employed. Stress relaxation, creep experiments, and dynamic mechanical analysis are useful tests as well, highlighting the time-dependent response of the material. The polymer's behavior upon unloading must also be considered, using step-cycle and free-shrinkage tests. The data from these last two experiments is critical in identifying irreversible deformation in semi-crystalline polymers, which is less easily defined at room temperature than in most metals. The impact of the previously mentioned factors, such as temperature, strain rate, and hydrostatic pressure, on the mechanical response of the polymer in each type of experiment is thoroughly discussed in the subsequent paragraphs.

8.2.1 Constant strain rate loading

The mechanical response of a semi-crystalline polymer in a constant strain rate experiment is determined by several factors. However, in the typical conditions of most applications, it exhibits the behavior of a plastic polymer. These polymers exhibit structural rigidity under load and are suitable for general-purpose applications. To be included in this material class, a polymer must possess a linear or branched structure. In addition, if amorphous, it must be used below its glass transition temperature, T_g, which is supposed to be in the range from 100 °C to 400 °C and much higher than its service temperature, T_{ser}. If semi-crystalline, the temperature should not exceed its melting temperature (Callister and Rethwisch, 2014; Arzhakov, 2019).

The stress–strain curves of different plastic polymers show some common features (see Figure 8.4). The material exhibits a relatively stiff initial response, followed by yielding. It must be stressed, however, that in most polymers, the development of permanent plastic strain is a continuous function of the applied strain, showing no discontinuity at the nominal stress drop or extrapolated yield point (Ward, 1971) (see Remark 8.1). After this transient behavior, there sometimes follows a steady state where the stress stabilizes, after which strain hardening begins, intensifying dramatically at large strains (Hiss et al., 1999; Callister and Rethwisch, 2014; Makradi et al., 2005).

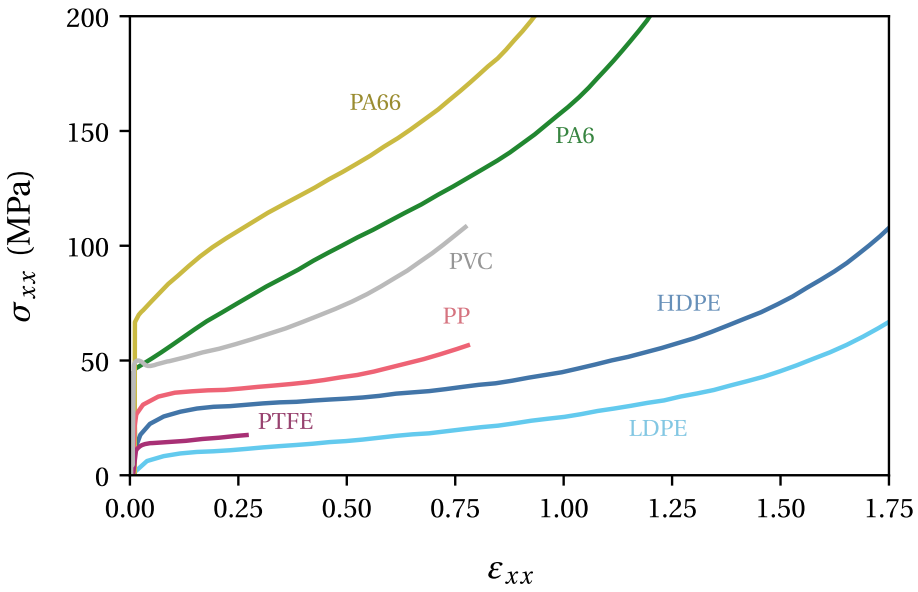

Figure 8.4: Stress–strain curves for different plastic polymers, including both glassy (PVC) and semi-crystalline (LDPE, HDPE, PTFE, PP, PA6, PA66) polymers in a constant strain rate uniaxial tension experiment. Adapted from G'Sell and Jonas (1981).

Remark 8.1 | Definition of yield in polymers

Yielding is commonly defined as the beginning of plastic flow. When modeling metals far from their melting temperature, it is commonly assumed that plastic flow only begins when a critical stress, the yield stress, is reached. Most polymers, on the other hand, may

flow, i.e., "yield," at any stress level. The initiation of plastic strain is mainly controlled by kinetic processes and appears to play no part in determining the yield stress of the material (Fotheringham and Cherry, 1978), commonly defined in one of three ways (Ward, 1971) (see Figure 8.5):

- the stress at the maximum observed load;
- the stress corresponding to the point of intersection of two tangent lines on the stress–strain curve;
- the stress obtained when offsetting the linear portion of the response by a pre-defined strain amount.

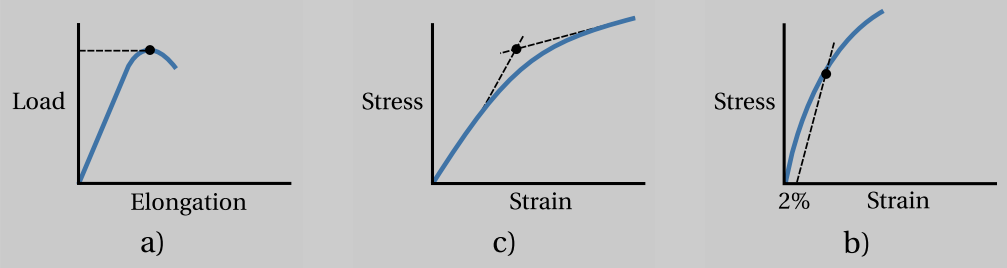

Figure 8.5: Yield criteria for polymers: a) stress at the maximum observed load; b) stress corresponding to the point of intersection of two tangent lines on the stress–strain curve; c) stress obtained when offsetting the linear portion of the response by a pre-defined strain amount.

Pre-yield and yield behavior Based on the description already given for the behavior of a plastic polymer, one should compare the stiffness and strength of polymers, particularly semi-crystalline polymers, relative to other materials. In general, the Young modulus of polymers ranges from 0.1 GPa to 10 GPa. The upper bound is the domain of resins, with thermoplastics, both glassy and semi-crystalline, rarely going over 2 GPa, which is relatively low compared with ceramics and metals, which boast Young moduli approximately 500 and 50 times larger, respectively. Their strength ranges from less than 10 MPa to approximately 100 MPa (see Table 8.1). In turn, some alloys reach tensile strengths above 1000 MPa, and some ceramics display compressive strengths as large as 10 000 MPa. That said, polymers possess densities around 1000 kg/m^3, making their specific stiffness and strength competitive with metals and well-suited for applications where weight reduction is paramount. Polymers are also distinguished by their relatively large yield strain, or the strain at which the materials cease to be linearly elastic, which ranges between 0.01 and 0.10, indicating an excellent capacity to store energy per unit weight (Ashby, 1999).

Table 8.1 displays the Young moduli and tensile strengths of semi-crystalline polymers ranging from commodity (HDPE and PP) to engineering grade (PA66 and PET), high performance (PPA), and ultra-high performance (PEEK) as supplied by a manufacturer (RTP Company, 2021). Glassy polymers of comparable stiffness and strength can be found, with PVC being suitable for commodity applications, ABS and PC being engineering grade, PSU being a high-performance glassy polymer, and PAI being an ultra-high-performance glassy polymer.

Regarding the response of a semi-crystalline polymer pre-yield, an increase in temperature will lead to a more compliant response and a lower yield strength, as shown in Figure 8.6 for nylon 101 (Khan and Farrokh, 2006), and in the results reported in Brown et al. (2007) and

Table 8.1: Young moduli and tensile strength of semi-crystalline polymers (RTP Company, 2021).

	HDPE	PP	PA66	PET	PPA	PEEK
Young modulus (MPa)	1241	1724	1793	1379	4137	3792
Tensile strength (MPa)	20	32	45	43	76	93

Hobeika et al. (2000) for PEs. In fact, temperature is possibly the single most influential parameter dictating a polymer's mechanical response. Some polymers may exhibit behaviors ranging from brittle fracture to necking or even homogeneous rupture during a uniaxial tension test depending on the temperature (Ward and Sweeney, 2004). Moreover, whether the polymer is below or above its glass transition temperature results in markedly different behaviors in the case of amorphous polymers (see Figure 8.6, adapted from Van Loock and Fleck (2018)). An amorphous polymer in its glassy state behaves as a plastic polymer, whereas in its rubbery state it has a much more compliant response that involves large deformations and a lack of a clear yield point. On the other hand, even if the temperature of a semi-crystalline polymer is much higher than its glass transition temperature, the crystalline phase causes the polymer's response to be qualitatively similar to that of a plastic polymer, although less stiff than it would be at a lower temperature (see Figure 8.6).

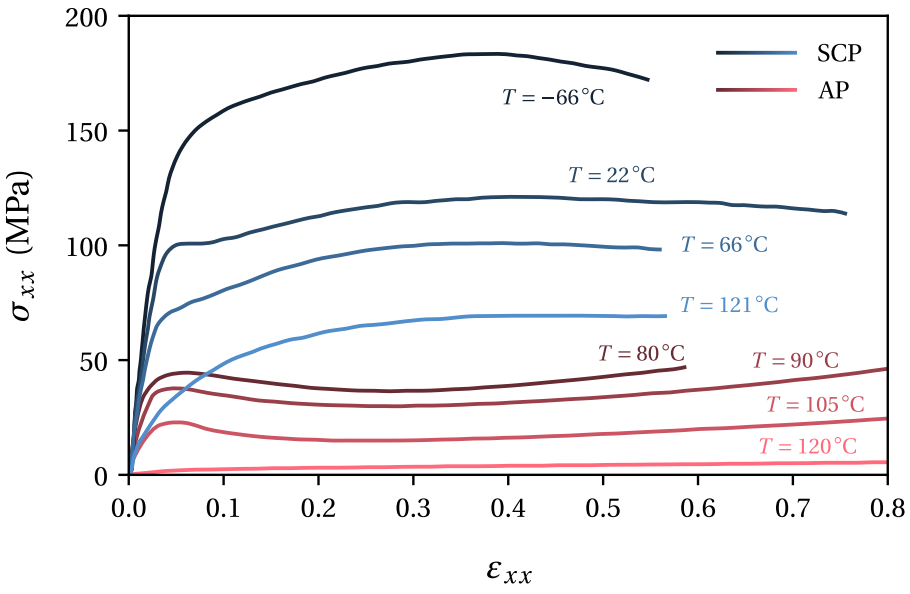

Figure 8.6: Stress–strain curves for a semi-crystalline polymer (SCP), nylon 101 (Khan and Farrokh, 2006), and an amorphous polymer (AP), poly(methyl methacrylate) (Van Loock and Fleck, 2018), above and below their glass transition temperatures, 60 °C and 118 °C, respectively.

The strain rate and the hydrostatic pressure have the opposite effect to that of temperature, such that their increase will lead to a stiffer response and higher yield stresses, as gathered from the results in Popelar et al. (1990) (uniaxial tension) and Truss et al. (1981) (torsion). More specifically, regarding the effect of the strain rate on the stress response, Walley and Field (1994) present experimental results for uniaxial compressive tests on a wide selection of polymers,

including semi-crystalline polymers. The HDPE samples display a linear relationship between the stress at different strain levels and the logarithm of the strain rate, while the PTFE's response shows a non-monotonic relationship between the same quantities, which is, however, broadly increasing. A linear relationship is found between the maximum stress and the logarithm of the strain rate for PEEK, until a critical strain rate is reached, followed by a decrease in the stress response. El-Qoubaa and Othman (2016) also provide an extensive set of results regarding the relationship between the strain rate, the temperature and the yield strength of PEEK. They find, however, that the yield stress of the polymer always increases with the strain rate, as shown in Figure 8.7.

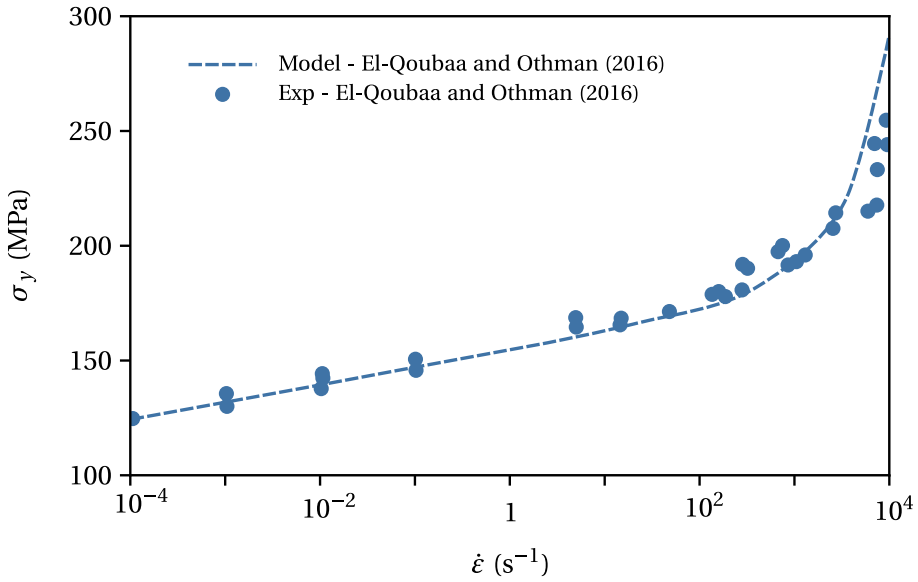

Figure 8.7: Yield stress, σ_y, as a function of the strain rate, $\dot{\varepsilon}$, for PEEK at room temperature. Model and experimental results are taken from El-Qoubaa and Othman (2016).

An increase in bulk crystallinity will lead to a stiffer response and increased strength, as evident in the results of Ayoub and coworkers (Ayoub et al., 2011) and Bedoui and coworkers (Bedoui et al., 2006) for polyethylenes with degrees of crystallinity by weight at room temperature ranging from 15 to 72% (see Figure 8.8(a)). However, the relationship between stiffness and crystallinity appears to be nonlinear. That said, Schrauwen and coworkers (Schrauwen et al., 2004) tests in uniaxial compression samples of both PET and PE containing more similar degrees of crystallinity among the samples, 0%, 21.7%, and 29.1% and 68.4%, 72.3%, and 76.6%, respectively, and no stiffness differences are observed. However, the yield strength increases noticeably (see Figure 8.8(b)). The results of Kurtz and coworkers (Kurtz et al., 2002) on UHMWPE also support a positive correlation between the degree of crystallinity and both stiffness and yield strength. The same authors (Kurtz et al., 1999, 2002) also explore the effect of cross-linking due to radiation combined with changes in crystallinity due to thermal treatments. A decrease in the elastic modulus and the yield stress with the irradiation dose and the temperature of the thermal treatment is reported.

Schrauwen and coworkers (Schrauwen et al., 2004) further report that the yield stress is proportional to the lamellar thickness. However, based on results for PE, Argon (2013) mentions that this linear dependence is only observed for lamellae of conventional thickness in the range

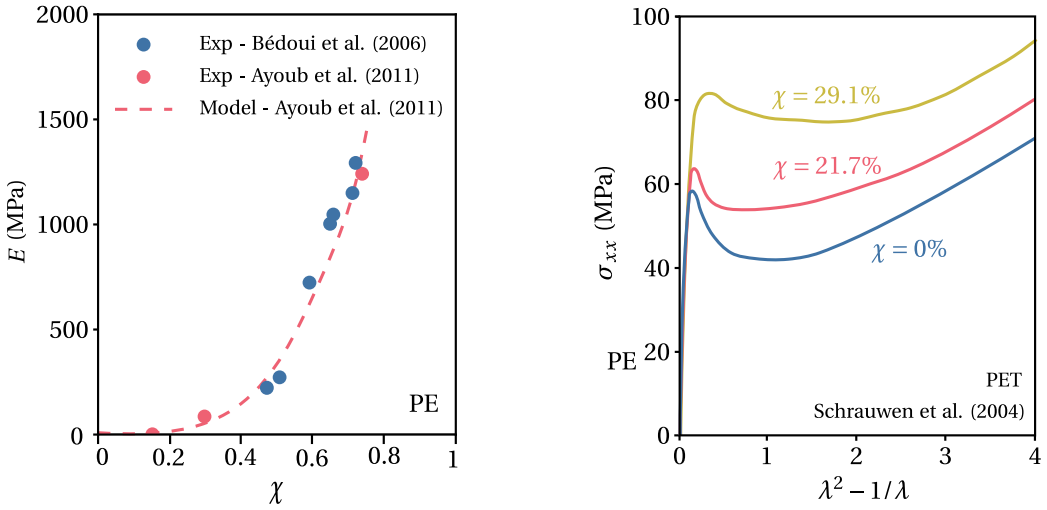

(a) (b)

Figure 8.8: Effect of the bulk crystallinity on (a) the Young modulus, E, and on the (b) yield strength of a semi-crystalline polymer.

of 10 nm to 15 nm. This dependence eventually breaks down, with the yield strength remaining constant for thicknesses from 20 nm to 170 nm. Also, for some polymers, an increase in molecular weight leads to an increase in tensile strength. This behavior is explained by an increase in chain entanglements with rising molecular weight (Callister and Rethwisch, 2014).

Regarding the effect of the mesostructure on the response of a semi-crystalline polymer, one can compare the behavior of isotropic (spherulitic) and oriented (fibrillar) PE when subject to uniaxial tension. As shown in Na et al. (2006), the latter possesses a higher yield strength and begins to strain harden immediately after yielding, while the former resists at approximately constant stress.

Finally, the critical strains at which the Hookean range ends, or yield is observed, are independent of the temperature and strain rate in the ranges considered by Hobeika and coworkers (Hobeika et al., 2000), i.e., 23 °C to 100 °C and $10^{-4}\,s^{-1}$ to $10^{-2}\,s^{-1}$, in PE and PEVA. In addition, both bulk crystallinity and molecular weight appear to have no impact on the location of these transition points.

Post-yield There may be some intrinsic strain softening after yielding, i.e., a decrease in stress with strain. The results in Schrauwen et al. (2004) show that after yield is reached, there is a sharp decrease in stress for completely amorphous PET above its glass transition temperature. The drop becomes broader and less pronounced as crystallinity increases to values of 21.7% and 29.1%. The same authors present PE results that show no strain softening for a degree of crystallinity of 76.6%. Minor strain softening is visible at lower crystallinity values for the same polymer. PP softens mildly as well, despite having a crystallinity of around 70% in the samples studied. These results were obtained under uniaxial compression. However, no softening is visible after yielding in the results of Truss and coworkers (Truss et al., 1981) obtained for PE in torsion. G'Sell and coworkers (G'Sell et al., 1983) present results of pure shear experiments in which HDPE exhibits mild strain softening at 23 °C while PP and PA66 show none.

The presence of strain softening can, nevertheless, change with the strain. G'Sell and Jonas

(1981) present experimental results where the strain rate alternates between $10^{-3}\,s^{-1}$ and $10^{-2}\,s^{-1}$. This makes possible the observation of stress transients at different strain levels, when the strain rate switches between the predetermined strain rates. An unusual behavior is detected in semi-crystalline polymers below the glass transition temperature, such that for lower strains, a "normal" transient, i.e., one corresponding to no strain softening, is observed, while at higher strains an "inverse" transient, i.e., one coinciding with strain softening, is detected. The latter type of transient is observable in glassy polymers when the same experiment is performed at any strain level. The results of Nanzai (1990) for poly(methyl methacrylate) (PMMA) support this claim regarding the transient behavior of glassy polymers. According to G'sell and Jonas (1979), an "inverse" transient happens when there are different conditions necessary for the initiation and propagation of yielding. Frost and Ashby (1982) mention that such transients are observed in "hard" materials, where dislocations are not readily available, such as lithium fluoride crystals (Gilman, 1959; Johnston, 1962) or diamond (Alexander and Haasen, 1969).

Despite the existence of intrinsic strain softening, its experimental observation is made difficult by two different phenomena: thermal softening and plastic instabilities. The results presented thus far were obtained at strain rates slow enough to allow for isothermal evolution. However, as the strain rate increases, a phenomenon known as "temperature softening" occurs, causing a similar decrease in stress with strain due to an increase in temperature. This rise in temperature is a result of the difficulty in offloading the heat generated by the plastic work in such a short period of time, making the process adiabatic. According to Furmanski and coworkers (Furmanski et al., 2013), this effect should be considered at strain rates greater than $0.01\,s^{-1}$ and strains greater than 15%. Cundiff and coworkers (Cundiff et al., 2022), for example, report uniaxial compressive tests for PA6 where temperature-induced strain softening may be observed.

Plastic instabilities, i.e., the growth of a locally thinned region in a material upon application of stresses, must also be considered when the intrinsic response of the material is sought. They are a function of the geometry and loading conditions of the loaded body, in addition to its intrinsic constitutive behavior (Ward and Sweeney, 2004). While uniaxial compressive loading of cylindrical specimens, generally, does not lead to heterogeneous deformation, this is not the case for uniaxial tension experiments, which often, but not always, lead to necking (see the comparison between isotropic and oriented PE in Na et al. (2006)), or simple shear experiments, which may lead to shear banding (G'Sell et al., 1983). There are, nonetheless, experimental methods that allow for the use of uniaxial tensile tests in the determination of intrinsic material behavior. The video-controlled technique in (G'Sell et al., 1992) is one example, as is the SE$\dot{E}$ method (Lauro et al., 2010; Balieu et al., 2015), which uses full-field data from digital image correlation measurements of heterogeneous displacement fields.

For a material whose stress response depends only on the current strain, a maximum in the nominal stress implies the formation of a neck (Ward and Sweeney, 2004). There are also other equivalent criteria, such as Considère's criterion for necking. Polymers, however, exhibit a strain rate dependence, and thus, because necking is associated with a local increase in strain rate, such a strong dependence can inhibit necking even when the nominal stress reaches a maximum. For these materials, the existence of a maximum in the nominal stress is only a necessary condition (Ward and Sweeney, 2004). In fact, according to Brooks and coworkers (Brooks et al., 1995), a double yield phenomenon is observed in polyethylenes ranging from LDPE to HDPE. Lucas and coworkers (Lucas et al., 1995) report similar results for linear polyethylenes and well-characterized ethylene copolymers of narrow molecular weight and composition distributions. Hao and coworkers (Hao et al., 2022b) mention that this phenomenon has also been observed in polyamide (PA), polytrimethyleneterephthalate (PTT), and polybutyleneterephthalate (PBT). The maximum force observed at the first yield point

under certain conditions is therefore associated with a homogeneous strain-softening process within the materials and not with the development of the neck (i.e., a geometrical instability), which occurs at the second yield point (see Figure 8.9). These experimental results make clear that such complex yielding processes are not always observed.

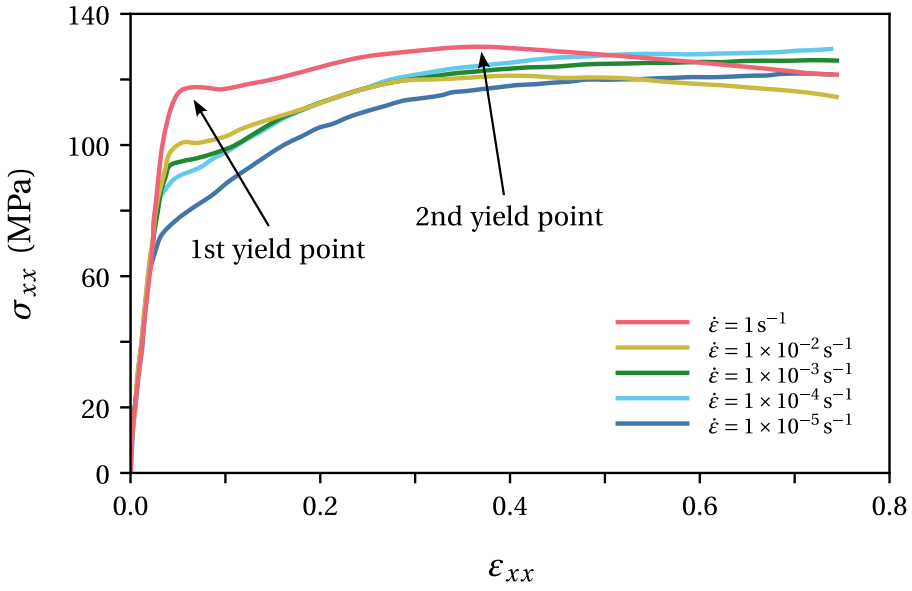

Figure 8.9: Stress–strain curve for nylon 101 exhibiting double yield. Adapted from Khan and Farrokh (2006).

Ye et al. (2015) report that for HDPE, even with measurements made on a relatively small strain rate range (smaller than 1 decade), the necking phenomenon depends on the strain rate. In particular, they found that the strain localization is more pronounced with higher strain rates near the yield point.

After necking occurs—usually at the maximum load, but not always, as in the case of the double yield—the material resists by reorienting the polymer chains so that the deformation is not limited to the necking zone, as in ductile materials (Callister and Rethwisch, 2014). As the specimen thins from the initial cross-section to the drawn cross-section, the shoulders of the neck propagate along the specimen—this phenomenon is called cold drawing (see Figure 8.10). The existence of a finite or natural draw ratio, i.e., a deformation corresponding to the stable propagation of the neck, is an important aspect of polymer deformation because a stabilized neck is not always formed (Ward and Sweeney, 2004). The neck's stable propagation occurs when the neck area has hardened sufficiently, allowing other sections of the specimen to meet the necking criteria. If this is the case, Considère's criterion for necking can be used to determine it.

Another important aspect regarding the plasticity of semi-crystalline polymers is that, in contrast to metals, permanent volumetric strains can be detected in addition to elasticity-related volumetric strains. These effects, found both in tension and compression, cannot be explained by Hooke's elasticity and correspond to an irreversible contraction or dilation of the material (Cangemi and Meimon, 2001; Polanco-Loria et al., 2010).

Cangemi and Meimon (2001) report the existence of plastic dilation in compression for semi-crystalline polymers. In contrast, glassy polymers show a very weak contraction. According to the same authors' results for PA11, the effect of plasticity on volumetric strain is felt when a

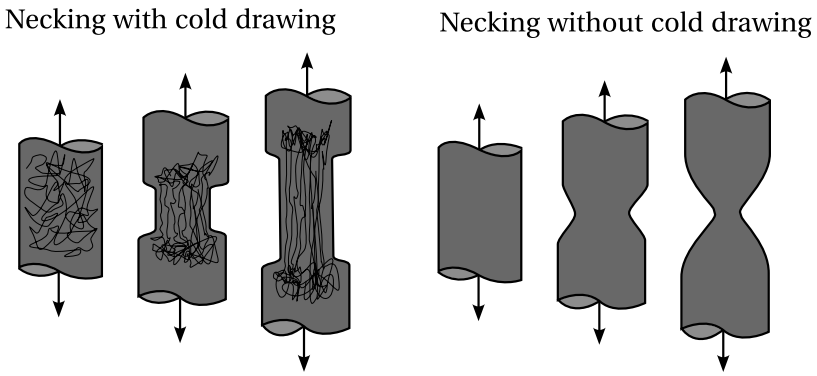

Figure 8.10: Schematic depiction of two tension experiments. One where there is the formation of a neck and stabilization, corresponding to cold drawing, and the other with neck formation but no neck stabilization, such that cold drawing is not observed.

strain of 0.03 is reached. Until then, the material contracts, after which a significant volume increase is observed. An increase in confining pressure was also investigated, and the authors discovered that it resulted in a qualitatively similar evolution of the volumetric strain, though it was more pronounced in magnitude, before attaining approximately the same value after a strain of 0.16 is reached. Tensile tests were also performed by the authors, during which the volume strain increased globally, due to the elastic response of the material. As the material approaches the plastic domain, the total volume strain is slightly reduced and then increases again at the end of the test. Qualitatively identical results were obtained by other authors for PA11 (Marchal, 1996).

Damage, or void growth, is one of the mechanisms responsible for these observations. However, according to Polanco-Loria and coworkers (Polanco-Loria et al., 2010), an increase in volume in semi-crystalline polymers may also be associated with crystalline deformation. This happens because the molecules are organized in a rather dense manner in the crystalline phase, and thus the specific volume is likely to increase when the crystalline lamellae break up. In fact, after a compression test in which the specimens showed net plastic expansion for the majority of the test, Kitagawa and Yoneyama (1988) made thin cuttings of semi-crystalline polymer samples (PP, POM, and PE) for observations in a polarized light microscope. No cracks or crazes were found. These observations highlight the peculiarity of plastic volume expansion in semi-crystalline polymers, which may be related to the complexity of their microstructures as well as their two-phase nature (Cangemi and Meimon, 2001).

Steady-state flow After the transient described above is cleared and before strain hardening starts to become noticeable, there may be a period of steady state flow, in which the polymer flows at a constant stress that is a function of the temperature and the strain rate. Both Kurtz and coworkers (Kurtz et al., 2002), for UHMWPE, and G'sell and Jonas (1979), for HDPE, found a reduced strain rate dependence coinciding with a small coefficient fitting a power-law relationship between the stress and the strain rate comparable to that of metals. The first authors point out, however, based on their results for UHMWPE, that the strain rate sensitivity increases significantly with temperature.

Strain hardening Semi-crystalline polymers, if ductile enough, will exhibit strain hardening, which can be quite dramatic at higher strains. Orientation hardening at large deformation due to molecular alignment is the main source of strain hardening (Ahzi et al., 2003). In addition to molecular alignment, crystal orientation may also contribute to the strain hardening observed in semi-crystalline polymers (Abdul-Hameed et al., 2014).

The results presented by G'Sell and Jonas (1981) at constant strain rate show that semi-crystalline polymers such as HDPE, LDPE, PA6 and PA66 exhibit marked strain hardening at 22 °C and a strain rate of $10^{-3}\,s^{-1}$. Based on the previously mentioned compressive tests, Schrauwen and coworkers (Schrauwen et al., 2004) conclude that crystallinity and lamellar thickness have no effect on the strain hardening of semi-crystalline polymers, in contrast with the melt cooling procedure and subsequent heat treatments. This implies that the amorphous phase is primarily responsible for the polymer's strain hardening behavior, with the density of entanglements being the primary determinant of hardening intensity (Argon, 2013).

Failure The maximum strain at rupture for semi-crystalline polymers can be very large, as evidenced by the results of G'Sell and coworkers (G'Sell and Jonas, 1981; G'Sell et al., 1983). HDPE can reach strains of more than 2 in tensile tests and more than 10 in shear tests. This is significantly greater than what glassy polymers like PVC and PC can achieve.

Experimental results Table 8.2 compiles a sample of the available experimental results in the literature concerning constant strain rate experiments on semi-crystalline polymers.

Table 8.2: Experimental results concerning constant strain rate experiments.

Author	Strain rate (s^{-1})	Temperature (°C)	Pressure (MPa)	Max strain	Loading mode	Material
G'Sell and Jonas (1981)	2×10^{-4} to 10^{-1}	22	Ambient	1.5 to 2	Uniaxial tension	HDPE
G'Sell and Jonas (1981)	10^{-3}	22	Ambient	1.7	Uniaxial tension	LDPE, HDPE, PA6, PA66, PTFE
Truss et al. (1981)	9×10^{-4}	20	10^{-1} to 4×10^{2}	0.16	Torsion	Rigidex
Popelar et al. (1990)	10^{-5} to 10^{-1}	23, 77	Ambient	0.25	Uniaxial tension	MDPE, HDPE
G'sell and Dahoun (1994)	5×10^{-4}	25	Ambient	2	Uniaxial tension	HDPE
Hiss et al. (1999)	10^{-4} to 10^{-2}	Room	Ambient	2	Uniaxial	HDPE
Hiss et al. (1999)	5×10^{-3}	Room	Ambient	1.75 to 2	Uniaxial tension	HDPE, LDPE, PEVA
Hobeika et al. (2000)	10^{-4} to 10^{-2}	23 to 110	Ambient	1.8	Uniaxial tension	HDPE, LDPE, PEVA
Beijer and Spoormaker (2000)	3×10^{-7} to 10^{-1}	43	Ambient	0.25	Uniaxial	HDPE
Schrauwen et al. (2004)	3×10^{-3}	Room	Ambient	0.9	Uniaxial compression	PE
Na et al. (2006)	10^{-3} to 10^{-2}	Room	Ambient	1	Uniaxial	Oriented HDPE
Drozdov (2007)	5×10^{-4} to 3×10^{-2}	Room	Ambient	0.2	Uniaxial tension	LDPE
Drozdov (2007)	5×10^{-4} to 10^{-1}	Room	Ambient	0.2	Uniaxial compression	LDPE
Brown et al. (2007)	10^{-4} to 3×10^{3}	−75 to 100	Ambient	0.5	Uniaxial compression	HDPE, PEX, UHMWPE
Ayoub et al. (2010)	5×10^{-4} to 10^{-2}	Room	Ambient	2.5	Uniaxial	HDPE
Zeng et al. (2010)	3×10^{-2} to 10^{-1}	90	Ambient	1.5	Uniaxial tension	PE, PA6
Ayoub et al. (2011)	10^{-4} to 10^{-2}	Ambient	Ambient	1.8	Uniaxial tension	PE copolymers
Furmanski et al. (2013)	10^{-3} to 1	−80 to 20	Ambient	0.6	Uniaxial compression	HDPE, UHMWPE
Bergström (2015)	2×10^{-3} to 10^{-2}	-	Ambient	0.5	Uniaxial tension	PTFE
Bergström (2015)	2×10^{-4} to 2×10^{-2}	-	Ambient	0.35	Uniaxial	HDPE
Arieby et al. (2017)	10^{-3}	Ambient	Ambient	1.6	Uniaxial tension	HDPE

8.2.2 Stress relaxation, creep, and dynamic mechanical analysis experiments

The stress relaxation, creep, and dynamic mechanical analysis experiments are all pertinent to characterize the time-dependent behavior of a material. In particular, semi-crystalline polymers exhibit a time-dependent behavior that sets them apart, for example, from metals at temperatures far below their melting point. This section will first focus on isothermal measurements, then on isochronal measurements.

The stress relaxation experiment involves applying a constant strain to the material, yielding its so-called relaxation modulus as the corresponding stress response. Polymeric systems, as a rule, display a decreasing relaxation modulus with time. A sharp drop is, however, not noticeable in highly crystalline and glassy polymers, which exhibit stress relaxation moduli on the order of GPa, as depicted in Figure 8.11(a). Semi-crystalline polymers with a lower crystalline content exhibit a primary viscoelastic transition from a glasslike to a leathery consistency as a decrease in the stiffness from the order of 10^9 Pa to 10^7 Pa, as shown in Figure 8.11(a). This is similar to the behavior of cross-linked amorphous polymers, since individual molecules may thread in and out of crystalline regions that act as multiple cross-links (Ferry, 1980; G'Sell and Jonas, 1981). See, for example, the results of Faucher (1959) comparing the relaxation behavior of amorphous and crystalline polypropylene.

This change in the material's response with time is commonly referred to as a transition from a glasslike to a rubberlike (or leatherlike, if a stiffer response is observed) behavior. However, it is a viscoelastic transition, not the transition verified at the glass transition temperature, in which the thermodynamic state of the material changes. The thermodynamic state of the material remains unchanged in this case, with this particular behavior traceable to the manner in which the kinetic units flow. Their flow can be described as a thermally activated process where the energetic barriers preventing their motion are cleared with the help of random thermal fluctuations. The kinetic units have to 'wait' until a large enough thermal variation puts them over the hump and they begin moving. Thus, for very short times, the response of the material will be stiffer, as the kinetic units do not have enough time to flow. As time goes on, more and more kinetic units will be able to move, leading to a softer response. Hence, in time-dependent materials, the ratio of the time it takes for a material to adjust to applied stresses or deformations, the relaxation time, t_c, to the characteristic time scale of an experiment (or a computer simulation), t_p, probing the response of the material is especially important. The Deborah number is the dimensionless quantity defined as this ratio, such that flow will happen when (Ward and Sweeney, 2004; Arzhakov, 2019)

$$\mathrm{De} = \frac{t_c}{t_p} \approx 1. \tag{8.1}$$

A constant stress is imposed in a creep experiment, for example, by dead-loading (Wilding and Ward, 1981), and an increase in strain is expected over time. This strain response is the so-called creep compliance of the material. Glassy polymers and highly crystalline polymers exhibit similar behaviors, with very slow increases in creep compliance with time at the longest times of observation, as do low crystallinity polymers and cross-linked polymers, which exhibit a viscoelastic transition via an increase in compliance as time progresses (Ferry, 1980) (see Figure 8.11(b)).

A dynamic mechanical analysis (DMA) employs either a strain- or stress-driven steady-state harmonic oscillation and records the corresponding stress or strain response, respectively. For a strain-driven experiment, the quantities of interest are the storage and loss moduli, defined as the stress response in phase and out of phase relative to the strain divided by the strain amplitude, and the loss tangent, which is the tangent of the phase shift between the strain and

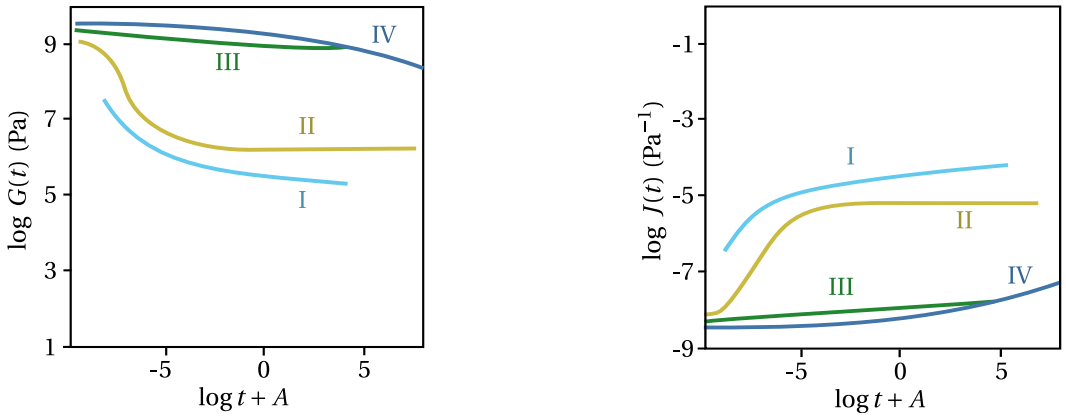

Figure 8.11: Typical viscoelastic properties of a very lightly cross-linked polymer (I), a slightly crystalline or lightly cross-linked polymer (II), a glassy polymer (III) and a highly crystalline polymer (IV): (a) relaxation modulus, G. (b) creep compliance, J. A is an appropriate horizontal shift constant. Adapted from Ferry (1980).

the stress. Loss and storage compliances can be defined in a similar way when considering a stress-driven experiment. Their physical interpretation is suggested by their respective names, as they are measures of the energy stored and lost per cycle. For a perfectly elastic material, one would expect no loss and, thus, for the stress and the strain to be in phase. On the other hand, a completely viscous material would exhibit a 90-degree phase shift, dissipating all the energy supplied to the system as heat. Depending on the frequency, a real material will exhibit an intermediate behavior. When $\omega t_c \approx 1$, i.e., $\mathrm{De} \approx 1$, for some deformation mechanism with a relaxation time of t_c, there will be an increase in the viscous character of the material, hence leading to a drop in the storage modulus, and maxima in loss modulus and loss tangent (often not exactly at the same frequency) (Ferry, 1980).

The storage modulus and compliance are approximately mirror images of the stress relaxation modulus and creep compliance, since a dynamic measurement at frequency ω is qualitatively equivalent to a transient one at $t = 1/\omega$. The glassy and crystalline polymers have values around 0.1 for the loss tangent and may present several maxima associated with various deformation mechanisms (Ferry, 1980). Most metallic alloys employed in engineering applications possess loss tangents one to two orders of magnitude smaller (Ashby, 1999). See Figure 8.12 for the loss and storage modulus of highly and lightly crystalline polymers.

Ferry (1980) collects some experimental results illustrating the nonlinear behavior of semi-crystalline polymers. See Appendix A for a more thorough discussion of the expected linear behavior for a time-dependent material. In a stress relaxation experiment, linear behavior implies coinciding curves when the relaxation modulus divided by the strain is plotted for different strain levels. However, for tensile stress relaxation of PE single crystal mats, the ratio of stress to strain decreases more rapidly with time at higher extensions, in the range of $\epsilon = 0.0003$ to 0.003; the degree of nonlinearity increases markedly with decreasing temperature in the range of 40 °C to 10 °C. Nonlinear creep recovery of polyethylene has also been reported. It is demonstrated that after a partial stress relaxation at constant strain for various times and strain magnitudes, recovery is much slower at large strains but somewhat faster for shorter durations of the initial strain. In this system, strains less than 0.01% appear to be required for a

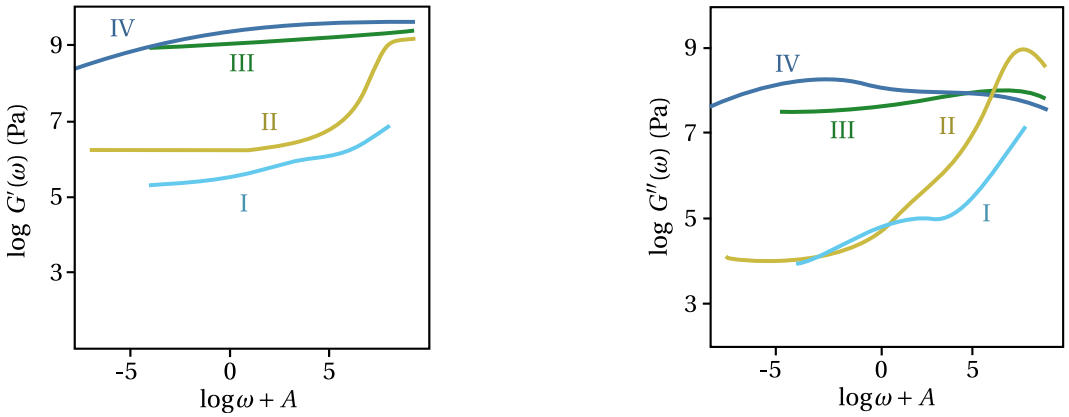

Figure 8.12: Typical viscoelastic properties of a very lightly cross-linked polymer (I), a slightly crystalline or lightly cross-linked polymer (II), a glassy polymer (III), and a highly crystalline polymer (IV): (a) storage modulus, G'. (b) loss modulus, G''. A is an appropriate horizontal shift constant. Adapted from Ferry (1980).

linear behavior. Nonlinear behavior when subject to sinusoidal deformations with large amplitudes has also been investigated. Finally, Ben Hadj Hamouda and coworkers (Ben Hadj Hamouda et al., 2007) report the existence of two regimes of creep deformation for medium-density ethylene-butene copolymers (MDPE).

Remark 8.2 | Types of nonlinear behavior

According to Malkin (1995), there are three types of nonlinearity in the constitutive response of a material.

1. *geometrical, stationary, or weak nonlinearity:* characterized by permanent material constants and unchanging relaxation properties. The neo-Hookean behavior of rubbers is one such example;
2. *physical, kinetic, or strong nonlinearity:* explained by changes in the inherent structure of a material due to deformation and characterized by changing material constants and relaxation properties with deformation. The hysteresis in repeated deformations of rubbers (the Mullins effect) and crystalline polymers are examples;
3. *phase, thermodynamic or rupture nonlinearity:* explained by phase or relaxation transitions induced by deformation and characterized by a change in the physical state of the material and radical changes in its relaxation spectrum. The transition of linear polymers from a rubbery to a glassy state is one example.

The results previously discussed were obtained at a constant temperature and are thus isothermal. By running tests at different temperatures it is often possible to extend the time/frequency range of the experimental results by employing the method of reduced variables, also known as the time-temperature superposition principle or the thermorheologically simple postulate (Ferry, 1980; Christensen, 2013). It consists of an appropriate horizontal and vertical shift of experimental results obtained at different

temperatures to construct a single isothermal master curve. A physical justification for the applicability of this procedure regarding the horizontal shift can be given in terms of the thermally activated processes that underlie the deformation mechanisms responsible for the relaxation transitions (Arzhakov, 2019). There are several models for the horizontal shift, perhaps the most well-known being the site model theory and the Williams, Landel, and Ferry (WLF) equation (Ward and Sweeney, 2004; Furmanski et al., 2013). A more detailed discussion of the available models is given in Section 9.1.1. A suitable vertical shift can be achieved through the multiplication by $T_0\rho_0/T\rho$, where the subscript 0 denotes a reference state and T and ρ are the temperature and density, respectively. Its use is justified due to the entropy-spring nature of the stored elastic energy in the flexible chain theory (Ferry, 1980). An application of the time-temperature superposition principle can be found in Popelar et al. (1990), where a master curve is built for polyethylene employing both horizontal and vertical shifts.

Isochronal results are obtained when the mechanical experiments described in this section are performed at different temperatures and plotted at the same time or frequency. These are, in fact, the most common type of available data on semi-crystalline polymers (Ferry, 1980). It should be noted that the system's structure changes with temperature, and thus an isothermal plot is, in some respects, more closely and simply related to the distribution of relaxation times than an isochronal plot (Hoffman et al., 2007). For example, there are relaxation behaviors that cannot be measured in low crystallinity samples of PCTFE, as it begins to crystallize before the corresponding temperature is reached (Hoffman et al., 2007).

Focus is given here to results obtained through DMA, although most observations apply to stress relaxation results as well as creep results. The most important information gathered from these experiments is the temperature of the relaxation transitions at a given frequency. Starting with low-crystallinity polymers helps clarify the discussion of relaxation transitions in semi-crystalline polymers. In fact, for a completely amorphous polymer glass, there will be two important transitions: the alpha and beta transitions. The alpha transition is tightly connected to the glass transition[1], and it is the main viscoelastic transition, while the beta transition is another transition generally happening at a lower temperature (Arzhakov, 2019). Which of these happens at higher temperatures may change at high enough frequencies (Matsuoka, 1996). According to Arzhakov (2019), the elementary kinetic unit responsible for these transitions is a macromolecule segment, with the beta transition being linked to the quasi-independent, localized displacement of the segments (intramolecule), and the alpha transition, to these quasi-independent modes acquiring a cooperative, correlated character (intermolecule) (Bershtein and Yegorov, 1985; Matsuoka, 1996). As the extent of crystallinity decreases and amorphous domains (large enough to allow configurational rearrangements of longer chain segments) appear in semi-crystalline polymers, the motions responsible for these two transitions gradually resemble those seen in the amorphous state in the transition zone of viscoelastic behavior (Ferry, 1980).

The previously used notation for alpha and beta transitions applies only to amorphous polymers. In general, semi-crystalline polymer transitions are also classified using the Greek alphabet, but without taking into account the character of the molecular motions corresponding to the transition or the phase in the polymer where it occurs. The transitions are named alphabetically, beginning with alpha in descending order of temperature, resulting in a sometimes confusing literature in which naming is not standardized. Here, the naming convention will follow the suggestion in Arzhakov (2019), using increasing Roman numerals for relaxations verified at increasing temperatures.

Starting at the lowest temperatures, increasing the crystal content of the polymer has little

[1]The glass transition is a thermodynamic transition that also implies a structural change in terms of a decrease in the free volume in addition to the cooperative motion of the polymer molecules associated with the alpha-viscoelastic transition (Arzhakov, 2019).

effect on the temperature at which Relaxation I is verified, resulting in similar loss moduli and loss tangent profiles. See the results:

- for PET (β relaxation) by Takayanagi presented in Ward and Sweeney (2004) with degrees of crystallinity of 5, 34 and 50%, corresponding to $-60\,^{\circ}$C at 138 Hz (see Figure 8.13(a));
- for PCTFE (γ relaxation) in McCrum (1962) with degrees of crystallinity of 27, 42 and 80%, corresponding to $-40\,^{\circ}$C at 1 Hz;
- for PE in Khanna et al. (1985) with degrees of crystallinity of ~45% (linear LDPE), ~48% (conventional LDPE) and ~67% (HDPE), corresponding to $-110\,^{\circ}$C at 1 Hz (see Figure 8.13(b));
- for PP in McCrum (1959) with different unspecified degrees of crystallinity, corresponding to $-30\,^{\circ}$C at 1 Hz.

However, the temperature at which the next transition, Relaxation II, is verified varies with crystallinity. See the shift to a higher temperature in the loss modulus, G'', of PET samples with increasing crystallinity in Figure 8.13(a). For the PE samples studied in Khanna et al. (1985), the temperature at which Relaxation II is observed varies between $-27\,^{\circ}$C and $-10\,^{\circ}$C. With increasing crystallinity, this relaxation becomes broader and less pronounced, eventually disappearing (see Figure 8.13). Relaxations I and II happen in the bulk amorphous phase of the semi-crystalline polymers, and the corresponding motions of the kinetic units are the ones responsible for the β and α transitions in the completely amorphous polymers. The disappearance of Relaxation II with the increase in crystallinity is tied to the shrinking of the amorphous domains, and the decrease in the number of longer kinetic units responsible for the relaxation. On the other hand, Relaxation I is connected to the motions of smaller kinetic units, like the β transition in the amorphous polymers, and hence are not affected in the same way by the increase in crystallinity.

The appearance and increase in the size of the crystalline phase will lead to the appearance of a third transition, Relaxation III, at higher temperatures. This transition is connected to motions on the surface of the crystal lamellae, and the temperature at which it is verified varies with their thickness (Khanna et al., 1985; Hoffman et al., 2007). Hoffman and coworkers (Hoffman et al., 2007) present a detailed model of the motions connected to each of the transitions in PCTFE and PE. Ward and Sweeney (2004) also provide an explanation based on the deformation mechanism available with increasing crystallinity for the "disappearance" of Relaxation II in PE.

According to Arzhakov (2019), by employing etching techniques that remove the amorphous phase, it can be gathered that the relaxation transitions described so far originate in kinetic units found in the amorphous phase of the polymer. There is, however, sometimes a fourth relaxation, connected to the kinetic units in the crystalline phase, which may imply the melting of some of the crystallites. This transition appears to be visible in the results of Panowicz and coworkers (Panowicz et al., 2021) for PET. It seems, however, not to be noticeable in the other experimental results mentioned so far. Hoffman and coworkers (Hoffman et al., 2007) also mention the existence of a cryogenic transition, present in some polymers, such as isotactic polypropylene (iPP).

As an example of a semi-crystalline polymer that does not fit exactly into the classification scheme just provided, see the results of McCrum (1959) for PTFE with crystallinities ranging from 48% to 92%. The relaxation observed at the lower temperatures ($\approx -100\,^{\circ}$C) disappears with the increase in crystallinity. In addition, there is a crystalline first-order transition ($\approx 25\,^{\circ}$C), corresponding to the change in the crystalline structure of the polymer, and a third relaxation at higher temperatures ($125\,^{\circ}$C) that merges with the second when the crystallinity increases.

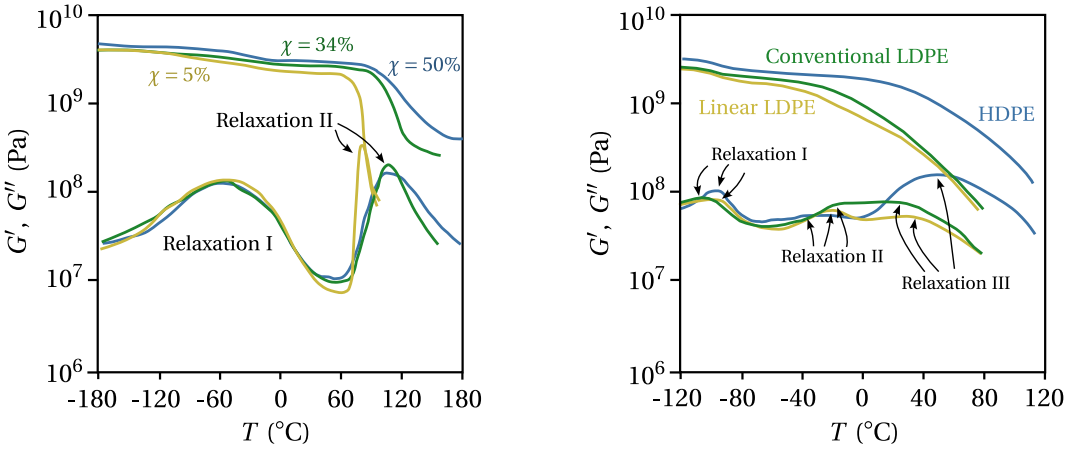

Figure 8.13: Dynamic mechanical analysis results for (a) PET with degrees of crystallinity of 5%, 34% and 50% at 138 Hz, obtained by Takayanagi (Ward and Sweeney, 2004), and for (b) PE samples, linear LDPE (~45%), conventional LDPE (~48%), and HDPE (~67%), at 1 Hz, obtained by Khanna et al. (1985).

According to Calleja and coworkers (Calleja et al., 2013), the two relaxations observed at the lowest and highest temperatures correspond to the relaxation of kinetic units in the amorphous phase of the polymer. The first is the "mobile amorphous fraction," which can relax at low temperatures, and the second is the "rigid amorphous fraction," which is composed of macromolecular segments found at the boundaries between crystalline and amorphous domains. Because of the close proximity of the crystallites, these macromolecular segments have more restricted mobility, and mechanical relaxation occurs at higher temperatures.

8.2.3 Reversible and irreversible deformation

The decomposition of the deformation of semi-crystalline polymers into elastic and plastic portions remains to be discussed. When applied to metals at temperatures far from their melting points, an elastic deformation pertains to the seemingly instantaneous part of the deformation that is recovered upon unloading. If the metal yields, there will be some plastic deformation that remains after unloading, which is irreversible. This decomposition is not as clear in the case of time-dependent materials, such as polymers, because there may be deformation that is not immediately recovered upon unloading but is recovered as time passes. It results in a definition of the irreversible part of the deformation, which is dependent on the observation time, i.e., some deformation may be irreversible during the experiment but potentially reversible if the observation were extended in time.

To clarify which part of the deformation is reversible and which is irreversible, the most useful mechanical experiments are the free shrinkage and step cycle tests. The former consists in straining the sample employing a constant strain rate, and releasing the load as some predefined strain is reached. The latter also begins as a constant strain rate experiment, but after a prescribed time interval has passed, the strain rate is reversed until the stress response reaches zero. Once it does, the strain rate is reversed again and enforced for the same time interval as before. The cycle is repeated until failure or a maximum strain is reached. During the unloading phases of an applied cyclic deformation process, the response is characterized by a nonlinear recovery driven by the release of stored internal energy (Bergström, 2002).

Strobl and coworkers (Hiss et al., 1999; Hobeika et al., 2000; Hong et al., 2004a,b; Na et al., 2006) performed a very detailed study on polyethylenes which includes the results of both free shrinkage and step cycle experiments. The decomposition of the constant strain rate stress–strain curve is based on the reversible and irreversible parts of the deformation as gathered from these experiments.

Consider the results of step-cycle experiments first. For strains less than 0.025, the polymer is perfectly elastic, and all deformation is immediately recovered. As the strain exceeds this limit, some deformation will not be recovered immediately. Once the strain reaches 0.1, the proportion of reversible strain increases relative to the irreversible strain. The former, on the other hand, plateaus once the strain exceeds 0.6 and begins to decrease once the strain reaches 1.

So far, only near-immediate recovery has been considered using data from step-cycle tests. To gain a better understanding of the reversible or irreversible deformation decomposition in semi-crystalline polymers, consider the results of free shrinkage experiments. In the results described in Hiss et al. (1999), where the deformation was observed for 10 minutes, the amount recovered for the same prestrain is greater than in a step-cycle experiment, as expected. Similarly, reversible deformation appears to peak around a strain of 0.6, with low-density polyethylene (LDPE) exhibiting a plateau until a strain of 1 is reached. A distinct plateau is not as visible in high-density polyethylene (HDPE) and poly(ethylene-co-vinyl acetate) (PEVA). However, above a strain of 0.6, all experiments show an increase in the amount of irreversible strain. Bartczak and coworkers (Bartczak et al., 1992) also report that HDPE samples deformed under uniaxial compression show large amounts of strain recovery upon releasing the load. The recovery is partly instantaneous and partly occurs over a period of a few hours (<24 h).

Finally, Hiss and coworkers (Hiss et al., 1999) report that increasing the temperature in a free shrinkage experiment allows for the recovery of more deformation. In fact, if the strain does not reach 1 and the temperature used is close to the melting point, almost all of the deformation is recovered. If the deformation exceeds 1, some permanent deformation will remain even after this treatment. Similarly, Arridge and coworkers (Arridge et al., 1977) report that ultra-oriented polyethylene fibers obtained by drawing to approximately 30 times their original length contract on heating to a length near the original. Furthermore, the same authors investigated the forces that cause this contractile behavior by monitoring the stress in the fiber while keeping its length constant. Between room temperature and 110 °C the stress decreases as the temperature rises, and this behavior is reversible. At 120 °C, there is an irreversible increase in stress, followed by a reversible linear dependence of stress on absolute temperature, indicating elastic entropic forces. Finally, there are two or three small irreversible stress jumps between 124 °C and 130 °C, as well as a large irreversible stress increase at around 132 °C, which corresponds to the region of large-scale retraction. As the fiber relaxes and eventually melts, there is a decay in the stress response. A fiber allowed to relax in this manner below the melting point differs from a drawn fiber in that it does not exhibit contractile behavior on subsequent heating over a similar temperature range. Furthermore, although the fiber has a lower tensile modulus after cooling, the modulus and density will rise to values close to their initial counterparts during storage.

8.3 Thermal analysis techniques

To fully characterize the thermomechanical behavior of semi-crystalline polymers, information about their thermal behavior must be gathered. This can be obtained from experiments such as dilatometry, differential scanning calorimetry, and laser flash tests (Blumm et al., 2010). The dilatometry experiment consists in tracking the change in length in a range of temperatures, furnishing the linear thermal expansion of the material. In principle, the glass transition can

be observed in these experiments as a change in the slope of the thermal expansion versus the temperature curve. This is not, however, the case for the results of Blumm and coworkers (Blumm et al., 2010) concerning PTFE. What is readily apparent in the results of the same author is the transition in the crystal structure of the polymer, visible as a step in the curve. The evolution of the linear thermal expansion coefficient in the remainder of the temperature range is approximately linear, ranging from $500 \times 10^{-6}\,\mathrm{K}^{-1}$ at $-100\,^{\circ}\mathrm{C}$ to $2000 \times 10^{-6}\,\mathrm{K}^{-1}$ at $100\,^{\circ}\mathrm{C}$.

The thermal expansion coefficient can also be found through pressure-volume-temperature (PVT) experiments, as shown in Olasz and Gudmundson (2005) for cross-linked polyethylene (XLPE). The sample is immersed in mercury and enclosed in a piezometer cell for the experiment. The cell is contained within a pressure vessel in which hydrostatic pressure can be applied. After reaching equilibrium at any constant temperature and pressure, the change in specific volume relative to a reference state is recorded. Measurements were performed from 10 MPa to 200 MPa, at 10 MPa increments, and at temperatures ranging from $25\,^{\circ}\mathrm{C}$ to $250\,^{\circ}\mathrm{C}$, at approximately $10\,^{\circ}\mathrm{C}$ increments. This allows the determination of the linear expansion coefficient and the bulk modulus as a function of the temperature. The values were found to range from around $300 \times 10^{-6}\,\mathrm{K}^{-1}$ at $50\,^{\circ}\mathrm{C}$ to $1300 \times 10^{-6}\,\mathrm{K}^{-1}$ at $130\,^{\circ}\mathrm{C}$. These values, like those reported above for PTFE, are an order of magnitude larger than those reported elsewhere for thermoplastics, in general, from $50 \times 10^{-6}\,\mathrm{K}^{-1}$ to $250 \times 10^{-6}\,\mathrm{K}^{-1}$ (Ashby, 1999). Leaving aside these differences, it is at least an order of magnitude larger than that of metals and ceramics. That said, in general, it does not often lead to thermal stresses, $\Delta\sigma = \alpha E \Delta T$, as large as in metals, since for polymers $\alpha E \approx 0.1\,\mathrm{MPa\,K}^{-1}$, while for metals $\alpha E \approx 1\,\mathrm{MPa\,K}^{-1}$ (Ashby, 1999).

Differential scanning calorimetry is an experimental method of thermal analysis that is widely used to study thermal transitions, i.e., solid–solid transitions as well as solid–liquid and various other transitions and reactions. The experiment is performed by supplying the necessary heat to a test sample as well as a calibrated sample so that a given temperature rate of change is achieved for both. Excluding the temperatures at which transitions happen, a material with a larger heat capacity will require more energy. If exothermic heat flow is considered, the glass transition will appear as a step, cold crystallization as a peak, and the melting of crystalline structures as a dip, with the heat capacity of the material being what is measured if these features are removed (Lukas and LeMaire, 2009).

Pope (1976) obtains three types of endotherms when studying the melting behavior of samples of oriented low-density polyethylene (LDPE) as a function of annealing temperature and time, subsequent heat treatment, and irradiation dose. These correspond to the primary melting of the lamellae, the melting of the reorganization products during the scan, and the melting of material crystallized during cooling from the original annealing temperature. The effect of ionizing radiation on the melting behavior of high-density and low-density polyethylene is also examined with data obtained by differential scanning calorimetry by Zoepfl and coworkers (Zoepfl et al., 1984). The data provided by Blumm and coworkers (Blumm et al., 2010) for PTFE makes apparent that the solid–solid transition occurs at $23.5\,^{\circ}\mathrm{C}$, connected to a change in the crystalline structure of the polymer, and that the melting of the crystalline phase occurs at $337.3\,^{\circ}\mathrm{C}$, both as peaks in the results. In the experimental results provided by Panowicz and coworkers (Panowicz et al., 2021) for PET in the form of exothermic heat flow, the glass transition is apparent as a step around $90\,^{\circ}\mathrm{C}$, and the melting of crystallites formed during secondary and primary crystallization as dips, the latter much larger than the former.

Regarding the experimental determination of the specific heat capacity of semi-crystalline polymers employing DSC, Blumm and coworkers (Blumm et al., 2010) report a value ranging from around $1000\,\mathrm{J\,kg}^{-1}\,\mathrm{K}^{-1}$ at $0\,^{\circ}\mathrm{C}$ to $1500\,\mathrm{J\,kg}^{-1}\,\mathrm{K}^{-1}$ at $300\,^{\circ}\mathrm{C}$ for PTFE. This agrees with the value of $\rho C_p \approx 3 \times 10^{6}\,\mathrm{J\,m}^{-3}\,\mathrm{K}^{-1}$, which according to Ashby (1999) is true for all solids, employing considerations from statistical mechanics.

Finally, Blumm and coworkers (Blumm et al., 2010) also supply the thermal diffusivity of

PTFE found by employing laser flash techniques. In addition to the change in the crystalline structure of the material already mentioned, the glass temperature is also detectable as a step. The values of the thermal diffusivity ranged from $0.24\,\mathrm{mm}^2/\mathrm{s}$ to $0.13\,\mathrm{mm}^2/\mathrm{s}$, between $-110\,^\circ\mathrm{C}$ and $140\,^\circ\mathrm{C}$. The authors combine the heat capacity, density, and thermal diffusivity measurements to compute the thermal conductivity of the polymer, which is approximately constant across the range of temperatures studied, $0.31\,\mathrm{W\,m^{-1}\,K^{-1}}$, except near the temperature at which the aforementioned solid–solid transition occurs. Both values of thermal diffusivity and conductivity for PTFE are in line with values reported in Ashby (1999) for other polymers and markedly lower than for ceramics and metals. Taking into account the relatively large values of the linear thermal expansion and the low thermal conductivity, polymers are more subject to heat distortion. This is because they combine a longer time to arrive at a uniform temperature with larger changes in size due to temperature differences when compared, for example, with metals.

Chapter 9

State of the art in thermomechanical semi-crystalline polymer modeling

The main goal of this chapter is to report on the semi-crystalline polymer modeling state of the art. The departure point is infinitesimal thermoviscoelasticity (reviewed in Appendix A), as it is one of the simplest models available to describe time-dependent materials. An exposition of its inadequacies in describing semi-crystalline polymers is supplied, motivating the introduction of more complex models. Nonlinear generalizations are considered by specifying nonlinear laws for the elastic and viscous elements in rheological models originating from infinitesimal viscoelasticity. Only properties of a homogenized single phase are taken into account in these models, employed chiefly in the description of plastic polymers. These are the most commonly available models in the literature, and a detailed overview is provided in this chapter. The caveats regarding the generalization to three dimensions and large deformations are explained, as well as how to introduce temperature into that description.

An account of microscopically informed models follows. Beginning with simple mean-field models which only consider bulk crystallinity, the discussion progresses to more complex models that account for morphological features such as spherulites and lamellae, including full-field models.

9.1 Phenomenological constitutive models

As described in more detail in Appendix A, infinitesimal viscoelasticity is a phenomenological model that describes some features of the time-dependent behavior of materials. It is often realized as a rheological model, where the material is represented by a combination of linear springs and dashpots. Despite its simplicity and ability to describe a wide range of material behaviors such as relaxation and creep, it has some significant limitations, in particular when applied to semi-crystalline polymers. The first among them is the use of infinitesimal strains in the constitutive description of the material. Semi-crystalline polymers, such as HDPE, can reach true strains exceeding 1.5 in axial tests, far surpassing what could be considered small deformations (G'Sell and Jonas, 1981). Furthermore, the Boltzmann superposition principle is frequently violated, and there is an energy exchange between the different relaxation modes, implying that the relaxation modulus depends on the strain, strain rate, and stress (Malkin and Isayev, 2017).

Semi-crystalline polymers exhibit nonlinear behavior that can be detected in a variety of mechanical experiments. References to experimental results depicting this behavior can be

found in Section 8.2.2. If we consider a set of constant-strain-rate experiments at different strain rates, a simple comparison between a linear response and possible nonlinear responses highlights some of the shortcomings of infinitesimal viscoelasticity. After sufficient time, a steady state is reached (see Equation (A.17)), and the stress predicted by an infinitesimal viscoelastic model is then either constant (liquid) or linear in the strain (solid). In either case, for a given strain, the stress varies linearly with the strain rate and is proportional to the relaxation time, corresponding to so-called Newtonian viscosity (Matsuoka, 1996) (see Figure 9.1(a)). Neither of these predictions is consistently observed in practice. For example, HDPE displays significant strain hardening that is nonlinear in the strain, i.e., the stiffness varies with the strain, as shown in the experimental results of G'Sell and Jonas (1981) (see Figure 9.1(b)). Moreover, the stress corresponding to the steady state as a function of the strain rate often follows a power law (see, e.g., G'sell and Jonas (1979)), coinciding with so-called non-Newtonian viscosity (see Figure 9.1(b)). In addition, Matsuoka (1996) emphasizes that the steady-state stress grows unbounded with the strain rate according to infinitesimal viscoelasticity, which is unphysical. Finally, some semi-crystalline polymers exhibit abrupt changes in flow behavior at a certain stress level, a behavior akin to yield in rate-independent plasticity (Bergström, 2015).

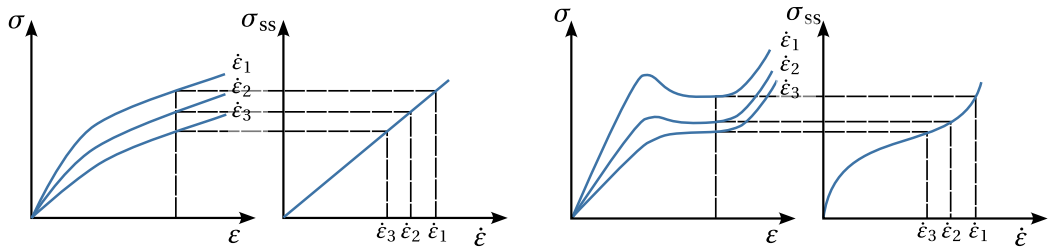

Figure 9.1: Stress–strain curve and steady-state stress–strain-rate curve for (a) an infinitesimal viscoelastic material (linear) and (b) a nonlinear material.

A viscoelastic constitutive model fit for large strains and capable of capturing the required nonlinear behaviors can often be achieved by specifying nonlinear laws for the behavior of the viscous and elastic elements in a rheological model. In what follows, well-established laws for both viscous and elastic elements are presented. The kinematic decomposition required to generate a large-strain three-dimensional model and the introduction of the temperature field are discussed. Finally, the most relevant models from the literature following this approach are presented.

These models are relevant in the modeling of semi-crystalline polymers, both when attempts are made to model the overall behavior of the material, disregarding its microstructure, and when they are used as the constitutive behavior of one of the phases in a multi-phase model.

9.1.1 Viscous elements or flow rules

In this section, we focus on the one-dimensional laws relating the strain rate $\dot{\gamma}$ to the applied stress τ. They are first collected in this simplified form for clarity, and later in the section, the different approaches for extending them to three dimensions are discussed.

As pointed out by Frost and Ashby (1982), plastic flow is a kinetic process. Therefore, the strength of a solid depends on both strain and strain rate, in addition to the temperature. This

observation runs counter to the valuable concept of yield strength, below which there is no flow and above which flow is fast. According to the same authors, this would only be strictly true at absolute zero. The corresponding theoretical flow stress is often called the mechanical threshold or athermal strength. Furthermore, flow below that mechanical threshold is due to thermally activated kinetic processes, i.e., their rate depends on the thermal fluctuations of the kinetic units. For the sake of completeness, it should be mentioned that there are kinetic processes that become relevant when the loading exceeds the mechanical threshold, coinciding with very high strain rates, and which do not necessitate thermal activation to occur (Kocks et al., 1975)[1]. These are beyond the scope of the present work.

To better understand how thermal fluctuations allow for flow, consider that, at a given temperature, the kinetic units of a solid material perform thermally driven oscillations of random magnitude near an equilibrium position. If the motion of the kinetic units coincides with their permanence near that equilibrium state, the behavior of the solid is elastic. On the other hand, flow happens when the energy, H_0, bounding the equilibrium state, is cleared. This energy is the energy of activation at 0 K, when no force is acting on the material (Kocks et al., 1975). Employing the Boltzmann distribution from statistical mechanics to calculate the probability of a thermal fluctuation providing enough energy to overcome the energy barrier, the rate of transition between states is given in the form of the Arrhenius equation, written in this context as

$$k = A \exp\left(-\frac{H_0}{k_B T}\right), \tag{9.1}$$

where k_B is Boltzmann's constant, A is the pre-exponential factor, H_0 is the height of the energy barrier. The pre-exponential term can be interpreted as the rate of attempts to move over the transition state (Atkins and de Paula, 2010). According to Kocks and coworkers (Kocks et al., 1975), it is related to one of two extreme frequencies: either the "atomic" frequency, i.e., the frequency of uncorrelated atomic motions, or the kinetic unit ground frequency, correlated with the overcoming of many obstacles at the same time. The inverse of this rate, i.e.,

$$\theta = \frac{1}{A} \exp\left(\frac{H_0}{k_B T}\right), \tag{9.2}$$

is the relaxation time of the process.

To include the effect of applying a stress, τ, to the material, consider firstly that it leads to a new equilibrium position for the kinetic unit (see Figure 9.2). Taking into account the work provided by the stress before flow happens, the total free energy necessary to overcome the obstacle, H_0, is now smaller and equal to ΔH. The free Gibbs energy, also known as free enthalpy, ΔG, is the missing portion of energy that a thermal oscillation must supply for flow to happen. It is, however, not equal to ΔH, since, during flow, the stress will supply further work, ΔW, which must be discounted from the total energy required to overcome the kinetic unit's obstacle to motion. Thus, $\Delta G = \Delta H - \Delta W$. Without factoring in the thermal fluctuations, the motion would occur only if the work supplied by the stress was larger than the energy barrier. Moreover, if the free energy of the kinetic unit is greater after crossing the barrier, the plastic work is not entirely dissipated, and some energy remains latent in the material, H_{stor}. On the other hand, the free enthalpy of the kinetic unit is always lower after crossing the barrier; otherwise, there would be no greater probability of crossing in one direction than the other (see Figure 9.2). For more details, see Kocks et al. (1975).

Following the procedure outlined by Eyring (1936), the shearing force acting on the system and its effect on the flow of the kinetic units can be considered. Its presence will lead to a

[1] In the context of polycrystalline materials, where slip is the primary deformation mechanism, thermally activated deformation below the mechanical threshold corresponds to so-called jerky glide and deformation above the mechanical threshold to continuous glide (Kocks et al., 1975).

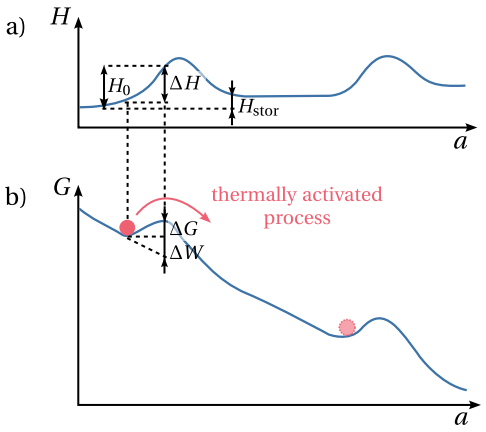

Figure 9.2: Transition of a kinetic unit between two states. a) Free energy, H, b) Free energy, G, where a is the area swept by the kinetic unit.

different rate of jumps in the forward and backward directions, which in energetic terms, means lowering the energy of the final state and increasing the energy of the initial state. Assuming similar activation volumes, and subtracting the rate of kinetic units moving against the shearing force from those moving along with the shearing force, τ, the strain rate obtained is

$$\dot{\gamma} = \dot{\gamma}_0 \exp\left(-\frac{\Delta H}{k_B T}\right) \sinh\left(\frac{\upsilon\tau}{k_B T}\right), \tag{9.3}$$

where υ is the so-called activation volume, and it can be identified with the product of the area swept out by the mobile unit in moving from one local free energy minimum to the next, and the resolved component of the distance moved by the kinetic unit in the direction of the applied stress.

According to the same author, $\upsilon\tau$ is much smaller than $k_B T$ in an ordinary flow. Thus, the expression for Newtonian viscous flow is recovered from Equation (9.3) as

$$\dot{\gamma} = \frac{\dot{\gamma}_0 \upsilon}{k_B T} \exp\left(-\frac{\Delta H}{k_B T}\right) \tau = \frac{1}{\eta}\tau, \tag{9.4}$$

where η is the viscosity, keeping only the first term in the Taylor expansion of the hyperbolic sine function. On the other hand, for plastic flow, where τ is large, the flow rule is

$$\dot{\gamma} = \dot{\gamma}_0 \exp\left(-\frac{\Delta H - \upsilon\tau}{k_B T}\right) = \dot{\gamma}_0 \exp\left(-\frac{\Delta G(\tau)}{k_B T}\right), \tag{9.5}$$

since $\sinh(x) \approx \frac{1}{2}\exp(x)$ for large x, implying a negligible rate in the backward direction, and where $\upsilon\tau$ is identified with the activation work such that $\Delta G = \Delta H - \upsilon\tau$. The contribution of the hydrostatic pressure can also be accounted for in this framework in a similar way to the shearing force, i.e.,

$$\dot{\gamma} = \dot{\gamma}_0 \exp\left(-\frac{\Delta H - \upsilon\tau + \Omega p}{k_B T}\right), \tag{9.6}$$

where Ω is the activation volume corresponding to the hydrostatic pressure. This relationship can be justified in terms of experimental results, where the stress response of polymers shows a pressure dependence, in part due to the low bulk moduli of polymers ($\approx$5 GPa, compared with

metals ≈100 GPa). Thus, a suitable expression for the effective stress on the kinetic units is a linear combination of shear stress and hydrostatic pressure, similar to the Mohr-Coulomb yield criterion (Ward and Sweeney, 2004). The expressions above show that higher shear stresses lead to higher flow rates, while higher hydrostatic pressures produce the reverse effect.

According to Fotheringham and Cherry (1978), the activation volumes in the forward and backward directions are not necessarily the same. However, note that this is irrelevant when describing plasticity, as only one activation volume must be considered. In fact, more general rate equations for thermally activated flow can be found in Brinkman and Schwarzl (1957) or Kocks et al. (1975).

The experimental determination of the parameters in these models is discussed, e.g., in Evans and Rawlings (1969), Conrad (1970) and Kocks et al. (1975), through the use of differential tests, changes of strain rate in a constant strain rate test, or stress level steps in a creep experiment.

Robertson (1966) presents an alternative to the Eyring model applicable to glassy polymers. The author considers a molecular model in which the shear-stress field is introduced as a bias on the rotational conformation of backbone bonds. The temperature at which the maximum fraction of flexed bonds is observed is estimated and inserted into the WLF equation to compute the corresponding viscosity, and hence the equation for the strain rate. Comparisons with results for PS and PMMA are provided. Duckett and coworkers (Duckett et al., 1970) also employ this model to fit the responses of PMMA and PET.

El-Qoubaa and Othman (2016) provide an implicit flow rule while seeking to model the yield stress of PEEK as a function of the strain rate and the temperature. The equation proposed is

$$\dot{\gamma} = \dot{\gamma}_0 \exp\left(\frac{\tau\, v(\dot{\gamma}, T)}{k_B T}\right), \tag{9.7}$$

where the activation volume, v, depends on the strain rate and the temperature according to

$$v(\dot{\gamma}, T) = v_0(T) \exp\left(-\sqrt{\frac{\dot{\gamma}}{\dot{\gamma}_c(T)}}\right), \tag{9.8}$$

$$v_0(T) = v_1 + v_2 \left(\frac{T}{T_g}\right)^n, \tag{9.9}$$

$$\dot{\gamma}_c(T) = \dot{\gamma}_1 \exp(qT), \tag{9.10}$$

T_g is the glass transition temperature, and $\dot{\gamma}_0$, v_1, v_2, n, $\dot{\gamma}_1$ and q are material constants. The authors find a good agreement between the model and experimental data.

The models described so far are often termed velocity-controlled, as they assume that yield (see Remark 8.1) will occur when the strain rate of the viscous element, identified with the movement of kinetic units, is equal to the impressed rate of deformation (Fotheringham and Cherry, 1978). These models can also be thought of as specifying that the presence of stress causes an increase in pre-existing flow processes in the material, such that the stress corresponding to their flow equals the loading stress (Ward and Sweeney, 2004).

Notice that despite mentioning the existence of deformation mechanisms corresponding to the motion of kinetic units, the models presented in the previous paragraphs do not attempt to model the specific physical events directly. Alternatively, in the case of nucleation-controlled models for polymer plastic flow, the free energy is directly modeled to determine the energy required in the nucleation and motion of the kinetic units (Fotheringham and Cherry, 1978; Ward and Sweeney, 2004).

Argon (1973) proposes a model for the plastic deformation of glassy polymers where the deformation mechanism is the buckling of the polymer chains via the action of a pair of opposed

kinks. The expression found for the free energy is

$$\Delta G(\tau) = \frac{3\pi G\omega^2 a^3}{16(1-\nu)}\left[1-\left(\frac{\tau}{\hat{\tau}}\right)^{5/6}\right], \tag{9.11}$$

where G and ν are the shear modulus and Poisson coefficient, respectively, $\hat{\tau}$ is the athermal strength defined as

$$\hat{\tau} = \frac{0.077G}{1-\nu}, \tag{9.12}$$

ω is the net angle of rotation of the molecular segment between the initial and activated configurations, and a is the mean molecular radius. The relationship between the athermal strength and the shear modulus in Equation (9.12) can be used to establish the temperature dependence of the athermal strength (Hao et al., 2022a). In the case of amorphous polymers, however, Ward and Sweeney (2004) mention that computer simulations of polymer chains at the atomic level on both glassy atactic polypropylene and polycarbonate did not yield a dominant deformation mechanism that should be the target of modeling.

Turning to semi-crystalline polymers, the picture changes in the sense that, as reviewed in the previous chapter (Chapter 8), the plastic behavior of the material is tightly linked to deformation mechanisms in the crystalline phase. There is extensive modeling of plastic behavior in polycrystalline solids with direct identification of the kinetic units as dislocations in the crystal[2]. According to Kocks, Argon and Ashby (1975), their motion can be modeled as in Equation (9.5), with the pre-exponential factor given by Equation (9.13), where

$$\dot{\gamma}_0 = b\rho_m L\nu_G, \tag{9.13}$$

where b is the Burgers vector[3] with dimensions of length, ρ_m is the mobile dislocation density with dimensions of dislocation length per unit volume, L the mean path of a mobile dislocation between inception and arrest at an obstacle and ν_G the frequency factor associated with the attempt rate of the nucleation process. At still moderate stresses, the average velocity is mainly controlled by thermally activated processes in which dislocations wait until a thermal fluctuation allows them to overcome the obstacle.

Argon (2013) presents the three relevant modes of dislocation nucleation in polymer lamellae as the nucleation of a monolithic straight screw-dislocation line from the edge of a lamella (mode A), nucleation of a screw-dislocation half loop from the narrow edge of a lamella (mode B), and nucleation of an edge-dislocation half loop from the wide face of a lamella (mode C). The respective free energies for each mode are

$$\Delta G_A(\tau) = \frac{\mu b^2}{4\pi}\ln\left(\frac{\hat{\tau}}{\tau}\right), \tag{9.14}$$

$$\Delta G_B(\tau) = \frac{\mu b^2}{4\pi}\frac{1-(\tau/\hat{\tau})^{2/3}}{(\tau/\hat{\tau})^{1.25}}, \tag{9.15}$$

$$\Delta G_C(\tau) = \frac{\mu b^3}{1-\nu}\frac{1-(\tau/\hat{\tau})^{1/3}}{(\tau/\hat{\tau})^{1.15}}. \tag{9.16}$$

The same author also presents expressions for the mobile dislocation density as

$$\rho_m = \frac{\chi pN\lambda}{\lambda\Lambda^2}, \tag{9.17}$$

[2]A dislocation loop can be defined as the demarcation line, in one slip plane, between an area that has slipped and a surrounding area that has not (Kocks et al., 1975).

[3]The Burgers vector is a vector that represents the magnitude and direction of the lattice distortion resulting from a dislocation in a crystal lattice.

where λ is the length of the dislocation produced, p the probability of a successful nucleation event at a site, χ is the degree of crystallinity, and $N = 2\Lambda/h$ is the number of possible nucleation sites in the representative volume $\lambda\Lambda^2$ allocated to a lamella, and h is the interplanar spacing. The mobile dislocation density, ρ_m, or the ideal shear force, $\hat{\tau}$, can also be taken as an internal variable and made to evolve according to a rate equation. See Klahn et al. (1970) and Kocks et al. (1975) for thorough discussions on modeling the deformation mechanisms in crystalline solids.

For an amorphous or semi-crystalline polymer, Equations (9.5) and (9.13) can still be employed, with a slightly different interpretation for the quantities involved and keeping in mind that the kinetic units are not as precisely defined as in the case of crystalline solids. Thus, the strain rate is still given by

$$\dot{\gamma} = b\rho_m \bar{v}_m, \tag{9.18}$$

i.e., by the product of the density of kinetic units responsible for the deformation, ρ_m, the amount of displacement per kinetic unit, b, and their average velocity, $\bar{v}_m$. This velocity is approximately given by

$$\bar{v}_m = L\nu_G \exp\left(-\frac{\Delta G(\tau)}{k_B T}\right), \tag{9.19}$$

where L is the mean free path of the kinetic unit, ν_G is the rate of attempts to move over the obstacle impeding its motion, and the Arrhenius term is the probability that the thermal fluctuations will supply the energy necessary to overcome the obstacle (G'Sell and Jonas, 1981; Gilman, 1992). Finally, one must keep in mind that both the nucleation and velocity-controlled models produce similar expressions, but their interpretations differ (Fotheringham and Cherry, 1978).

The motion of several different kinetic units contributes to the material's flow behavior, as discussed in Chapter 8. Ree and Eyring (1955) assume that they can be classified based on an average relaxation time that varies significantly between them. A single group is also composed of many kinetic units with different relaxation times, yet can be adequately described by an average value for the group. Assuming that each group behaves according to the previously described Eyring model, the shear stress is expressed as follows

$$\tau = \sum_{k=1}^{n} x_k \tau_k = \sum_{k=1}^{n} x_k \frac{k_B T}{v_k} \sinh^{-1}\left(\frac{\dot{\gamma}}{\dot{\gamma}_0} \exp\left(\frac{\Delta H}{k_B T}\right)\right), \tag{9.20}$$

where x_k is the area fraction swept by the kth kinetic unit during its movement.

Roetling mentions that the Ree-Eyring model with two flow groups describes the tensile yield strength of PMMA, below the glass transition temperature (Roetling, 1965), and isotactic polypropylene (iPP), above the glass transition temperature (Roetling, 1966), well in the strain rate range of $10^{-5}\,\mathrm{s}^{-1}$ to $1\,\mathrm{s}^{-1}$. The author suggests a connection between the α and β relaxation transitions and these two flow groups. Other authors have successfully captured the strain rate and temperature dependence of the yield strength of glassy polymers using the Ree-Eyring model and variations thereof (Bauwens et al., 1969; Bauwens, 1972; Bauwens-Crowet, 1973; Haussy et al., 1980).

Ree and Eyring's approach allows the inclusion of different deformation mechanisms in the model. In particular, Bauwens, Bauwens-Crowet and collaborators (Bauwens et al., 1969; Bauwens, 1972; Bauwens-Crowet, 1973) relate the two flow groups to the α and β relaxation processes, associating the former to the rotations of the main-chain segments of the polymer, and the latter to rotations of side groups. It can be interpreted as a rheological model in which parallel dashpots materialize distinct deformation mechanisms. Furthermore, using the fraction of area swept by each kinetic unit to weight their contribution to the total stress is analogous to popular approaches in semi-crystalline polymer modeling, where crystallinity is similarly incorporated (see Section 9.2.1).

As already noted, kinetic processes are cooperative, occurring only when several kinetic units act in unison. In fact, Cherry and Holmes (1969) mention that the fitted values to the activation volume in Eyring's model are too large to agree with their corresponding physical interpretation (see Equation (9.3).) As an alternative to the Ree-Eyring model with multiple flow groups, Fotheringham et al. (1976); Fotheringham and Cherry (1978) assume that n kinetic units, all following the Eyring model, are needed to substantiate a deformation mechanism. The expression found for the flow rate is

$$\dot{\gamma} = \dot{\gamma}_0 \sinh^n\left(\frac{v\tau}{2kT}\right)\exp\left(-\frac{n\Delta H}{kT}\right), \tag{9.21}$$

where the notation employed retains its meaning from the previous paragraphs, and a temperature below the glass transition temperature is assumed. Richeton and coworkers (Richeton et al., 2005, 2006, 2007b) seek to model the yield stress of amorphous polymers, extending the cooperative model to temperatures through the glass transition temperature. They achieve this by proposing

$$\dot{\gamma} = \dot{\gamma}_0 \exp\left(\frac{\ln 10 \cdot c_1^g (T - T_g)}{c_2^g + T - T_g}\right)\sinh^n\left(\frac{v\tau}{2kT}\right)\exp\left(-\frac{\Delta H}{kT_g}\right), \tag{9.22}$$

for temperatures above T_g, where c_1^g and c_2^g are the WLF parameters. These authors (Richeton et al., 2007a) also compare the models of Eyring (see Equation (9.3)), Argon (see Equation (9.11)), and their cooperative model in predicting the yield stress of PMMA and PC.

Other models, however, do not fit neatly into the scheme outlined above. Power laws are fairly common empirical laws for the flow rule (Brown and Ashby, 1980). They are given, for example, as (Bergström, 2015)

$$\dot{\gamma} = \dot{\gamma}_0 \left(\frac{\tau}{\hat{\tau}}\right)^m, \tag{9.23}$$

where m is a material parameter and $\hat{\tau}$ a reference stress. Perzyna (1963), e.g., proposes

$$\dot{\gamma} = \frac{1}{G}\left(\frac{\langle \tau - \hat{\tau} \rangle}{\hat{\tau}}\right)^{1/\epsilon}, \tag{9.24}$$

to describe the rate sensitivity of plastic materials, where $\langle \bullet \rangle$ denotes the ramp function, defined as $\langle x \rangle = (|x| + x)/2$, and G and ϵ are material parameters. Another law available for the strain rate is (Kelly and Gillis, 1974; Bodner and Partom, 1972)

$$\dot{\gamma} = \dot{\gamma}_0 \exp\left(-\left(\frac{\hat{\tau}}{\tau}\right)^n\right), \tag{9.25}$$

where n is a material parameter. According to Bodner and Partom (1972), this last set of laws is suggested by both direct measurements and theoretical considerations of the average velocity of mobile dislocations as a function of the applied stress in polycrystalline solids (see Equation (9.13)).

Yet another model available in the literature, based on reptation (Doi and Edwards, 1978), is described by Bergström and Boyce (1998, 2001). The flow is due in part to the Brownian motion of the polymer chains, in addition to thermally activated events, yielding the following flow rule

$$\dot{\gamma} = C_1 (\overline{\lambda} - 1)^{C_2} \left(\frac{\tau}{\hat{\tau}}\right)^m, \tag{9.26}$$

where $\overline{\lambda}$ is an effective stretch and C_1, C_2, m and $\hat{\tau}$ are material parameters. Bergström and Hilbert (2005) later extend this flow adding pressure sensitivity and temperature dependence, as

$$\dot{\gamma} = C_1(\overline{\lambda} - 1)^{C_2} \left(\frac{\tau}{\hat{\tau} + \alpha p} \right)^m \left(\frac{T}{\hat{T}} \right)^n, \tag{9.27}$$

where $\hat{T}$ is a reference temperature and n a material parameter.

Finally, in the same contribution (Bergström and Hilbert, 2005), the authors present yet another flow rule, now of the phenomenological type, given by

$$\dot{\gamma} = ab\left(\varepsilon - \varepsilon_0\right)^{b-1} \dot{\varepsilon} \tag{9.28}$$

where ε is an effective strain and $\dot{\varepsilon}$ its rate, $a > 0$, $b > 0$. The authors apply this flow rule paired with a yield criterion identical to the von Mises yield function.

According to de Souza Neto and coworkers (de Souza Neto et al., 2008), more flow rules can be generated by multiplying several simpler laws, including those already provided. For example, assuming that $\dot{\gamma}$ is a function of the stress, time, and temperature, one can write

$$\dot{\gamma} = \dot{\gamma}(\tau, t, T) = f_\sigma(\tau) f_t(t) f_T(T), \tag{9.29}$$

where f_σ, f_t and f_T are possibly experimentally defined functions.

Internal variables So far, all constitutive descriptions of the strain rate neglect the material's thermomechanical history. As discussed in more detail in Chapter 2, a set of appropriate internal variables is employed to capture the contribution of the material's history to its thermomechanical response (Kocks et al., 1975; Frost and Ashby, 1982). Thus, the implicit assumption so far is either that the structure remains constant during flow, ($\boldsymbol{\alpha} = \boldsymbol{\alpha}_0$), or that it has reached a steady state, ($\dot{\boldsymbol{\alpha}} =$ constant).

Either of these hypotheses is often unreasonable and fails to explain the nonlinear behavior of polymers. This shortcoming is evident in the ability to capture the shape of the transient during a constant-strain-rate test, whether the characteristic strain softening of many glassy polymers or the double yield of various semi-crystalline polymers. The most common targets of modeling are the athermal strength, $\hat{\tau}$, and the mobile dislocation density, ρ_m, (see Equations (9.12) and (9.13)).

Regarding the athermal strength $\hat{\tau}$, two natural assumptions are that it may depend on the plastic strain γ and time. Thus, by the chain rule, one finds

$$\dot{\hat{\tau}} = h\dot{\gamma} - r, \tag{9.30}$$

where $h \equiv \partial\hat{\tau}/\partial\gamma|_t$ corresponds to a hardening rate and $r \equiv -\partial\hat{\tau}/\partial t|_\gamma$ denotes a recovery or, in the case of polymers, also an aging rate. Hardening is expected if there is an increase in the number of obstacles to the motion of the kinetic unit (Kocks et al., 1975; Hasan and Boyce, 1995). The minus sign in the recovery/aging rate definition is introduced to enforce a decrease in the athermal strength connected to either recovery or aging. That said, Boyce and coworkers (Boyce et al., 1988) conclude that aging in PVC may increase its strength.

Bodner and Partom (1975) propose

$$\hat{\tau} = \hat{\tau}_1 + (\hat{\tau}_0 - \hat{\tau}_1) \exp\left(-\frac{m}{\hat{\tau}_0} w^p \right), \tag{9.31}$$

where $\hat{\tau}_0$ and $\hat{\tau}_1$ are the initial and final athermal strengths, respectively, and m is a material property. Compared with the original text, a multiplicative factor $((n+1)/n)^{1/n}$ is neglected as it

tends to 1 for large n. In the one-dimensional case, the plastic work, w^p, is defined as $\int \tau\dot{\gamma}\, dt$. The corresponding rate equation can be written as (Zaïri et al., 2007)

$$\dot{\hat{\tau}} = m\left(\frac{\hat{\tau}_1 - \hat{\tau}}{\hat{\tau}_0}\right)\dot{w}^p. \tag{9.32}$$

Zaïri and coworkers (Zaïri et al., 2007) propose similar rate equations for partial contributions, $\hat{\tau}^{(1)}$ and $\hat{\tau}^{(2)}$, to the athermal strength, $\hat{\tau}$, when modeling glassy polymers. The former concerns the hardening effect of the network alignment, such that the corresponding rate equation is defined as

$$\dot{\hat{\tau}}^{(1)} = m\left(\frac{\hat{\tau}^{(1)} - (1-\alpha)\hat{\tau}_0^{(1)}}{\hat{\tau}_0^{(1)}}\right)\dot{w}^p, \tag{9.33}$$

where m is a material parameter, $\hat{\tau}_0^{(1)}$ is the initial athermal strength and α a hardening parameter. In turn, the latter accounts for the effect of strain softening, with the corresponding rate equation given as

$$\dot{\hat{\tau}}^{(2)} = p\left(\frac{\hat{\tau}_1^{(2)} - \hat{\tau}^{(2)}}{\hat{\tau}_1^{(2)}}\right)\dot{w}^p, \tag{9.34}$$

where p is a material parameter and $\hat{\tau}_1^{(2)}$ is a final partial athermal strength, such that

$$\dot{\hat{\tau}} = \dot{\hat{\tau}}^{(1)} + \dot{\hat{\tau}}^{(2)}. \tag{9.35}$$

The solution to both equations can be found by substituting the appropriate values into Equation (9.32).

Note that the use of plastic work instead of the plastic strain in the definition of the rate equations just discussed is often equivalent. This is because the mapping between the two can be made one-to-one such that $\hat{\tau}(\gamma) = \tilde{\hat{\tau}}(w^p) \equiv \hat{\tau}(w^p(\gamma))$. See de Souza Neto et al. (2008) for the complete derivation.

Boyce, Parks and Argon (1988) propose an entirely similar rate equation for the athermal strength in a glassy polymer. The corresponding strain softening is described as

$$\dot{\hat{\tau}} = h\left(1 - \frac{\hat{\tau}}{\hat{\tau}_1\left(T,\dot{\gamma}\right)}\right)\dot{\gamma}, \tag{9.36}$$

employing, however, the strain rate as the 'driving force' behind its change. The initial structure is represented by the value of $\hat{\tau}$ at the upper yield point, $\hat{\tau}_0$, given by Equation (9.12), h is the slope of the yield drop with respect to the strain, $\hat{\tau}_1$ is the value of $\hat{\tau}$ reached at the steady state, i.e., the 'preferred' structure, and, as indicated, $\hat{\tau}_1$ may depend on temperature and strain rate. This choice for the rate equation of the athermal strength enables modeling the distinctive glassy polymer strain softening. They also account for pressure sensitivity by replacing $\hat{\tau}$ by $\hat{\tau} + \alpha p$, where α is a material parameter in Equation (9.11).

Hasan et al. (1993) propose the use of the softening parameter, D, that evolves to a saturation level, D_∞, according to an identical law, i.e.,

$$\dot{D} = h\left(1 - \frac{D}{D_\infty}\right)\dot{\gamma}, \tag{9.37}$$

where h is the softening slope. Subtracting D from the argument of the exponential function in Equation (9.3) allows the modeling of strain softening.

In their attempt to model semi-crystalline polymers, Ahzi and coworkers (Ahzi et al., 2003) propose

$$\dot{\hat{\tau}} = \frac{\hat{\tau}}{n}\left(\frac{\hat{\tau}_0}{\hat{\tau}}\right)^n \dot{\gamma}, \tag{9.38}$$

as the rate equation for the athermal strength $\hat{\tau}$, where $\hat{\tau}_0$ is the corresponding initial value and n is a hardening coefficient.

Seeking to model the effect of manufacturing-induced voids in polymer-based composites, Chowdhury and coworkers (Chowdhury et al., 2008) present an extension of Equation (9.36). It describes the transition from a pre-defined initial yield stress, $\hat{\tau}_0$, to a peak yield stress, $\hat{\tau}_1$, followed by strain softening to a saturated state, $\hat{\tau}_2$. The corresponding rate equation is

$$\dot{\hat{\tau}} = H_1(\gamma)\left(1-\frac{\hat{\tau}}{\hat{\tau}_1}\right)\dot{\gamma} + H_2(\gamma)\left(1-\frac{\hat{\tau}}{\hat{\tau}_2}\right)\dot{\gamma}, \tag{9.39}$$

with the smooth Heaviside-like functions H_i, $i = 1,2$ given by

$$H_1(\gamma) = -h_1\left(\tanh\left(\frac{\gamma-\gamma^p}{f\gamma^p}\right)-1\right); \quad H_2(\gamma) = h_2\left(\tanh\left(\frac{\gamma-\gamma^p}{f\gamma^p}\right)+1\right), \tag{9.40}$$

where h_1 and h_2 are the hardening (softening) parameters, f the smoothing factor and γ^p the plastic strain at the peak yielding point. This approach is also pursued by Hao and coworkers (Hao et al., 2022a), where a fourth athermal shear stress $\hat{\tau}_3$ is considered, connected to the yield of the crystalline phase in a semi-crystalline polymer. According to the authors, this property can depend on temperature, strain rate, crystallinity, and humidity. The rate equation for the athermal strength $\hat{\tau}$ is given similarly to Equation (9.39) as

$$\dot{\hat{\tau}} = H_1(\gamma)\left(1-\frac{\hat{\tau}}{\hat{\tau}_1}\right)\dot{\gamma} + H_2(\gamma)\left(1-\frac{\hat{\tau}}{\hat{\tau}_2}\right)\dot{\gamma} + H_3(\gamma)\left(1-\frac{\hat{\tau}}{\hat{\tau}_3}\right)\dot{\gamma}, \tag{9.41}$$

The corresponding smooth functions, H_i, $i = 1,2,3$, are given by

$$H_1(\gamma) = -h_1\left(\tanh\left(\frac{\gamma-\gamma^{p,1}}{f\gamma^{p,1}}\right)-1\right), \tag{9.42}$$

$$H_2(\gamma) = h_2\left(-\tanh\left(\frac{\gamma-\gamma^{p,1}}{f\gamma^{p,1}}\right)\tanh\left(\frac{\gamma-\gamma^{p,2}}{f\gamma^{p,2}}\right)+1\right), \tag{9.43}$$

$$H_3(\gamma) = h_3\left(\tanh\left(\frac{\gamma-\gamma^{p,2}}{f\gamma^{p,2}}\right)+1\right), \tag{9.44}$$

where h_1, h_2 and h_3 are the hardening (softening) parameters, f is the smoothing factor, (chosen as 0.3), $\gamma^{p,1}$ is the plastic strain at the peak yielding point, and $\gamma^{p,2}$ is the low yield point just before the yielding of the crystal structure takes place. This last parameter may depend on both the strain rate and the temperature, according to the authors.

In G'Sell and Jonas (1981), the authors discuss modeling the density of kinetic units instead of the strength of the obstacles impeding their motion. They aim to capture the strain softening/inverse transient in glassy polymers, also verified for semi-crystalline polymer at large strains. They propose that whenever a polymer experiences a strain rate increase or decrease, the density of kinetic units changes linearly over a particular strain interval until it reaches the new equilibrium value characteristic of the new strain rate.

Anand and Gurtin (2003) propose adding to the athermal strength $\hat{\tau}$ in the power law of Equation (9.23) a term αp to account for the influence of pressure, where α is a material parameter and p is the hydrostatic pressure. Additionally, they take η to be an internal variable in addition to the athermal strength $\hat{\tau}$ following an evolution law

$$\dot{\hat{\tau}} = h_0 \left(1 - \frac{\hat{\tau}}{\hat{\tau}^*(\eta)}\right)\dot{\gamma}, \tag{9.45}$$

$$\dot{\eta} = g_0 \left(\frac{\hat{\tau}}{\hat{\tau}_{cv}} - 1\right)\dot{\gamma}, \tag{9.46}$$

with

$$\hat{\tau}^*(\eta) = \hat{\tau}_{cv}(1 + b(\eta_{cv} - \eta)), \tag{9.47}$$

where h_0, g_0, b, $\hat{\tau}_{cv}$ and η_{cv} are material parameters. Note the similarities of Equation (9.45) with Equation (9.36). The authors point out that this differential system has a stable fixed point at $(\hat{\tau}, \eta) = (\hat{\tau}_{cv}, \eta_{cv})$, which corresponds to the steady-state flow condition. Moreover, the phase portrait of the system shows that for initial conditions $\hat{\tau} = \hat{\tau}_0$ and $\eta = 0$, with $\hat{\tau}_0 \leq \hat{\tau} \leq \hat{\tau}_{cv}(1 + b\eta_{cv})$, η increases monotonically to its equilibrium value η_{cv}, while $\hat{\tau}$ first increases to a peak value before decreasing to $\hat{\tau}_{cv}$, capturing the strain-softening behavior of glassy polymers.

Anand and coworkers (Anand et al., 2009; Ames et al., 2009) adopt an expression identical to Equation (9.21) describing a cooperative thermally activated motion, where the stress τ is replaced by an effective stress, τ_{eff}, defined as

$$\tau_{\text{eff}} = \tau - (\tau_1 + \tau_2 + \alpha_p p), \tag{9.48}$$

where τ_1 and τ_2 are internal variables with dimensions of stress, α_p is a material parameter and p is the hydrostatic pressure. Another dimensionless internal variable, η, is also introduced. According to the authors, the variables η and τ_1 are included in the model to capture the 'yield-peak' of glassy polymers. A key microstructural feature controlling the strain-softening associated with the 'yield-peak' is the deformation-induced disordering of glassy polymers. The variable η, a positive-valued dimensionless 'order'-parameter, is introduced to represent such deformation-induced disordering; and τ_1, a stress-dimensioned internal variable, represents the corresponding transient resistance to plastic flow accompanying the microstructural disordering. Their evolution equations are coupled similar to those in Equations (9.45) and (9.46). Their evolution is given by

$$\dot{\tau}_1 = h_1(\tau_1^*(\dot{\gamma}, T, \eta) - \tau_1)\dot{\gamma}, \tag{9.49}$$

$$\dot{\eta} = g_1(\eta^*(\dot{\gamma}, T) - \eta)\dot{\gamma}, \tag{9.50}$$

where h_1 and g_1 are material constants, and $\eta^*(\dot{\gamma}, T)$ and $\tau_1^*(\dot{\gamma}, T, \eta)$ are material parameter functions defined as

$$\eta^*(\dot{\gamma}, T) = \begin{cases} \eta_r \left(1 + \left(\dfrac{T_c - T}{k}\right)^r\right)\left(\dfrac{\dot{\gamma}}{\dot{\gamma}_r}\right)^s, & T < T_c, \\ 0, & T > T_c, \end{cases} \tag{9.51}$$

with

$$T_c = \begin{cases} T_g + n \ln\left(\dfrac{\dot{\gamma}}{\dot{\gamma}_r}\right), & \dot{\gamma} > \dot{\gamma}_r, \\ T_g, & \dot{\gamma} \leq \dot{\gamma}_r, \end{cases} \tag{9.52}$$

and

$$\tau_1^*(\dot{\gamma}, T, \eta) = b(\eta^*(\dot{\gamma}, T) - \eta). \tag{9.53}$$

In these expressions, η_r, k, r, s, n, b, and $\dot{\gamma}_r$ are material parameters, and T_g is the glass transition temperature.

The parameter τ_2, is another positive-valued stress-dimensioned internal variable, introduced to capture additional 'isotropic'-hardening aspects of the stress–strain response of these materials as the chains are pulled taut between entanglements at large strains. It evolves according to

$$\dot{\tau}_2 = h_2(\bar{\lambda} - 1)(\tau_2^*(T) - \tau_2)\dot{\gamma}, \tag{9.54}$$

where h_2 is a material constant, and $\tau_2^*(T)$ a material parameter function of the temperature, such that the resistance τ_2 increases and the material hardens as long as $\tau_2 < \tau_2^*(T)$. $\bar{\lambda}$ is the effective stretch computed from the strain associated with the viscous element described by this flow rule.

In an attempt to model the temperature and rate-dependent response of an incompressible semi-crystalline polymer, Okereke and Akpoyomare (2019) propose a flow rule

$$\dot{\gamma} = \frac{\tau}{\eta(\tau, p, T, T_f)} = \frac{\tau}{2G\theta(\tau, p, T, T_f)}, \tag{9.55}$$

where the relaxation time θ is given by

$$\theta(\tau, p, T, T_f) = a_T(T)a_S(T_f)a_\sigma(\tau, p, T)\theta_0^*, \tag{9.56}$$

with θ_0^* being a reference relaxation time. The influence of temperature is captured through the shift factor a_T as

$$a_T(T) = \exp\left(\frac{\Delta H}{R}\left(\frac{1}{T} - \frac{1}{T^*}\right)\right), \tag{9.57}$$

where R is the universal gas constant, and the superscript $*$ denotes a reference value. The effect of pressure and shear stress is taken into account through the shift factor a_σ as

$$a_\sigma(\tau, p, T) = \frac{v_s\tau}{2\sqrt{3}RT}\exp\left(-\frac{v_p p}{RT}\right)\left(\sinh\left(\frac{v_s\tau}{2\sqrt{3}RT}\right)\right)^{-1}, \tag{9.58}$$

where v_s and v_p are material parameters, according to Eyring's theory (see Equations (9.3) and (9.6)). The influence of the structure is taken into account through a fictive temperature, T_f, and the corresponding shift factor a_S is given by

$$a_S(T_f) = \exp\left(\frac{\Delta H}{R}\left(\frac{C}{T_f - T_\infty} - \frac{C}{T_f^* - T_\infty}\right)\right), \tag{9.59}$$

where C is the Cohen-Turnbull constant and T_∞ is the Vogel temperature. The rate equation for the fictive temperature is given by

$$\dot{T}_f = \frac{T - T_f}{a_S(T_f)a_T(T)\theta_0^*} + \frac{\kappa}{\sqrt{2}}\dot{\gamma}, \tag{9.60}$$

where κ is a material parameter. According to the authors, this choice of the rate equation for the fictive temperature incorporates significant post-yield strain-softening observed in high-rate compression of polypropylene into the model.

Generalization to three dimensions The models discussed so far concern one-dimensional flow, i.e., laws for the scalar strain rate $\dot{\gamma}$. For three-dimensional models capable of describing large deformations, it is necessary to provide a macroscopic flow rule, i.e., a law prescribing the spatial velocity gradient $\boldsymbol{L}$.

Consider the flow rule for the Newtonian fluid without the pressure term to see how this might be accomplished in the isotropic situation,

$$\boldsymbol{D} = \mathbf{S} : \boldsymbol{\sigma}, \quad \boldsymbol{W} = \mathbf{0}, \tag{9.61}$$

where $\mathbf{S}$ is the appropriate compliance tensor, defined as

$$\mathbf{S} = \frac{1}{2\eta}\left(\mathbf{I}_S - \frac{1}{3}\boldsymbol{I}\otimes\boldsymbol{I}\right) + \frac{1}{9\kappa}\boldsymbol{I}\otimes\boldsymbol{I}, \tag{9.62}$$

where η and κ are the dynamic and bulk viscosity, and $\mathbf{I}_S$ is the fourth-order symmetric identity tensor. Equation (9.61) can be rewritten as

$$\boldsymbol{D} = \frac{\|\boldsymbol{\sigma}_{\text{dev}}\|}{2\eta}\frac{\boldsymbol{\sigma}_{\text{dev}}}{\|\boldsymbol{\sigma}_{\text{dev}}\|} + \frac{\sigma_m}{3\kappa}\boldsymbol{I}. \tag{9.63}$$

To establish the connection with the one-dimensional flow rules already presented, consider a pure shear flow with a strain rate equal to $\dot{\gamma}$. The shear stress found from Equation (9.63) is

$$\tau = \eta\dot{\gamma}. \tag{9.64}$$

τ is identified with $\|\boldsymbol{\sigma}_{\text{dev}}\|$ to generalize from pure shear to a three-dimensional stress state. Some authors choose this quantity to be the octahedral shear stress, defined as $\tau_{\text{oct}} = \frac{1}{\sqrt{3}}\|\boldsymbol{\sigma}_{\text{dev}}\|$, instead (Okereke and Akpoyomare, 2019). Thus one can substitute $\|\boldsymbol{\sigma}_{\text{dev}}\|/\eta = \dot{\gamma}_{\text{dev}}$, and $\sigma_m/\kappa = \dot{\gamma}_{\text{vol}}$, found employing a similar logic, yielding

$$\boldsymbol{D} = \frac{\dot{\gamma}_{\text{dev}}}{2}\boldsymbol{N}_{\text{dev}} + \frac{\dot{\gamma}_{\text{vol}}}{3}\boldsymbol{N}_{\text{vol}}, \tag{9.65}$$

where

$$\boldsymbol{N}_{\text{dev}} = \frac{\boldsymbol{\sigma}_{\text{dev}}}{\|\boldsymbol{\sigma}_{\text{dev}}\|}, \quad \boldsymbol{N}_{\text{vol}} = \boldsymbol{I}, \tag{9.66}$$

Note that τ and p are computed from the Cauchy stress tensor, $\boldsymbol{\sigma}$, acting as the driving force on the viscous element. Other stress measures can also be employed, such as the Kirchhoff stress tensor, $\boldsymbol{\tau}$, or the Mandel stress tensor, $\boldsymbol{M}$ (Anand et al., 2009; Ames et al., 2009).

In the literature, there is not much focus on nonlinear laws for the volumetric strain rate, $\dot{\gamma}_{\text{vol}}$. When included, they are often chosen to coincide with the Newtonian fluid (see Equation (9.63)). Most often, the factors $1/2$ and $1/3$ in Equation (9.65) are neglected, perhaps because the flow rule contains a leading term that absorbs the missing elements during calibration.

When modeling the plastic flow in the crystalline phase of semi-crystalline polymers, crystal plasticity models are often employed (Lee et al., 1993a). In these models, the plastic deformation is assumed to occur by slip on a set of N crystallographic slip systems. The spatial velocity gradient is given by

$$\boldsymbol{L} = \sum_{i=1}^{N} \dot{\gamma}^{(i)}\boldsymbol{R}^{(i)}, \tag{9.67}$$

where $\dot{\gamma}^{(i)}$ is the shear rate on slip system i, and $\boldsymbol{R}^{(i)}$ is the Schmid tensor for slip system i defined as

$$\boldsymbol{R}^{(i)} = \boldsymbol{s}^{(i)}\otimes\boldsymbol{m}^{(i)}, \tag{9.68}$$

with $\boldsymbol{s}^{(i)}$ and $\boldsymbol{m}^{(i)}$ being the slip direction and slip plane normal, respectively. The shear rate is found from a flow rule such as Equation (9.23), using expressions for the activation energies such as those in Equations (9.14) to (9.16). Note that this flow rule leads in general to a non-symmetric velocity gradient, or equivalently, a non-zero spin tensor, $\boldsymbol{W} \neq \boldsymbol{0}$.

9.1.2 Yield criteria

The yield stress is not as clearly defined in polymers as in metals, even far below their melting points. This difficulty in defining yield stress arises because, for many polymers, flow is observed at all stress levels and does not occur at a characteristic yield stress. Notwithstanding, a yield criterion, Φ, can still be used to set the flow rule, defining the flow potential Ψ appropriately. Choosing the flow potential equal to the yield surface, associative plasticity, $\Psi = \Phi$, the flow direction is computed as

$$\boldsymbol{D} = \dot{\gamma}\boldsymbol{N} = \dot{\gamma}\frac{\partial \Phi}{\partial \boldsymbol{\sigma}}, \tag{9.69}$$

being perpendicular to the yield surface in the stress domain. The choice of $\dot{\gamma}$ in rate-independent plasticity is made to satisfy the loading-unloading conditions

$$\dot{\gamma} \geq 0, \quad \Phi(\boldsymbol{\sigma}, \mathcal{A}_{\text{int}}) \leq 0, \quad \Phi(\boldsymbol{\sigma}, \mathcal{A}_{\text{int}})\dot{\gamma} = 0, \tag{9.70}$$

where $\mathcal{A}_{\text{int}}$ is the set of thermodynamic conjugate forces to the internal variables. However, in the present context, an explicit expression for $\dot{\gamma}$, like the ones presented in Section 9.1.1, is the most common choice. Ghorbel (2008) provides a detailed description of the yield criteria employed to describe polymers. The most common criteria are the von Mises, Mohr-Coulomb, Drucker, and Raghava yield (Balieu et al., 2014) criteria.

9.1.3 Elastic elements or free energies

The elastic elements employed in the models under discussion typically fit into two classes: linear elasticity and rubber-like elasticity. The former is based on the energy for isotropic linear elasticity in small deformations, given by

$$\psi_{\text{lin}}(\boldsymbol{\varepsilon}) = \frac{1}{2}\boldsymbol{\varepsilon} : \mathbf{D} : \boldsymbol{\varepsilon}, \tag{9.71}$$

where $\mathbf{D}$ is the isotropic elastic modulus defined as

$$\mathbf{D} \equiv 2G\mathbf{I}_S + \left(K - \frac{2}{3}G\right)\boldsymbol{I} \otimes \boldsymbol{I}, \tag{9.72}$$

where G is the shear modulus, K is the bulk modulus, $\boldsymbol{I}$ is the second order identity tensor and $\mathbf{I}_S$ is the symmetric identity[4]. One way to extend this model to large deformations is to use finite-strain measures. In particular, one may employ logarithmic strains, $\boldsymbol{\varepsilon}^{(0)}$, finding the so-called Hencky model, whose free energy is given by

$$\psi_{\text{Hencky}}(\boldsymbol{\varepsilon}^{(0)}) = \frac{1}{2}\boldsymbol{\varepsilon}^{(0)} : \mathbf{D} : \boldsymbol{\varepsilon}^{(0)}, \tag{9.73}$$

or the Green-Lagrange strain tensor, $\boldsymbol{E}^{(1)}$, yielding the so-called Saint-Venant-Kirchhoff model, whose free energy is given by

$$\psi_{\text{SVK}}(\boldsymbol{E}^{(1)}) = \frac{1}{2}\boldsymbol{E}^{(1)} : \mathbf{D} : \boldsymbol{E}^{(1)}. \tag{9.74}$$

[4]The symmetric identity $\mathbf{I}_S$ is defined as $(\mathbf{I}_S)_{ijkl} = \frac{1}{2}(\delta_{ik}\delta_{jl} + \delta_{il}\delta_{jk})$ where δ_{ij} is the Kronecker delta, such that $\mathbf{I}_S : \boldsymbol{A} = \boldsymbol{A} : \mathbf{I}_S = \text{sym}(\boldsymbol{A})$, with $\boldsymbol{A}$ being a second order tensor.

The stress is then found from Equation (2.37). In modeling the intermolecular forces, generally connected with the initial stiffness of the polymer, these are the most common choices for elastic elements (Boyce et al., 1988; Anand and Gurtin, 2003).

In modeling the hardening or large-strain response of plastic polymers, models based on non-Gaussian statistical theory for rubber-like elasticity are the most common choice (Bergström, 2015). These models are based on the statistical mechanics of polymer chains, which consider the entropy change associated with the deformation of long-chain molecules. From an appropriate expression of the entropy as a function of the deformation, we can find the Helmholtz free energy, ψ, from Equation (2.34) and derive the constitutive relation from Equation (2.37). Assuming each chain has many links, $n \gg 1$, and that the end-to-end distance, r, is small compared to the contour length, $r \ll nl$, where l is the length of each link, yields the Gaussian chain model, i.e.,

$$s_{\text{Gaussian}}(\overline{\lambda}) = -\frac{3}{2} N k_B (\overline{\lambda})^2 + \text{const}, \tag{9.75}$$

where $\overline{\lambda}$ is the average chain stretch defined as $\overline{\lambda} = r/(\sqrt{n}l)$, where $\sqrt{n}l$ is the average end-to-end distance of the chain in the undeformed state, N is the number of chains per unit volume, and k_B is the Boltzmann constant.

When large deformations are being modeled, meaning that r is comparable to nl, non-Gaussian chain models must be employed. The corresponding entropy for a single chain is given by

$$s_{\text{Langevin}}\left(\overline{\lambda}\right) = N k_B \ln\left(\left(\frac{\sinh\beta}{\beta}\right)^n \exp\left(-\frac{\beta}{\lambda^{\text{lock}}}\right)\right), \tag{9.76}$$

where $\lambda^{\text{lock}} \equiv \sqrt{n}$, $\beta = \mathscr{L}^{-1}(\overline{\lambda}/\lambda^{\text{lock}})$, and the Langevin function is defined by

$$\mathscr{L}(\beta) = \coth\beta - \frac{1}{\beta}. \tag{9.77}$$

The choice of how the average chain stretch, $\overline{\lambda}$, depends on the deformation gradient varies between models. A three-chain model where a third of all the chains are assumed to be aligned with each of the principal stretches,

$$\overline{\lambda}(\boldsymbol{F}) = \lambda_i, \quad i = 1,2,3, \tag{9.78}$$

has been proposed by Wang and Guth (1952).

However, the most widely used model is the eight-chain model of Arruda and Boyce (1993); Arruda et al. (1995), which assumes that there are eight chains aligned with the diagonals of a unit cube in the principal stretch space. This implies that the average chain stretch is given by

$$\overline{\lambda}(\boldsymbol{F}) = \sqrt{\frac{\text{tr}(\boldsymbol{B})}{3}}, \tag{9.79}$$

where $\boldsymbol{B} = \boldsymbol{F}\boldsymbol{F}^T$ is the left Cauchy-Green deformation tensor. As the chain stretch hits its limiting value, this choice for functional dependency results in an asymptotically increasing stress. This same choice when applied to the Gaussian chain model in Equation (9.75) leads to the neo-Hookean model, valid for small to moderate deformations (Anand and Gurtin, 2003). These models can also compute $\bar{\lambda}$ from the isochoric component of the deformation gradient to account for the incompressibility of rubber-like materials. In general, the volumetric response is included in the internal energy (see Equation (2.34)) (Bergström, 2015).

Another alternative of the same type that takes more interactions between the polymer chains is presented by Edwards and Vilgis (1986), postulating the free energy as

$$\psi_{EV}(\lambda_1,\lambda_2,\lambda_3) = \frac{1}{2}N_c\left\{\frac{\Sigma_{i=1}^{3}\left(1-\alpha^2\right)\lambda_i^2}{1-\alpha^2\bar{Z}\lambda_i^2} - \log\left(1-\alpha^2\sum_{i=1}^{3}\lambda_i^2\right)\right\} + \\ + \frac{1}{2}N_s\left[\sum_{i=1}^{3}\left\{\frac{\lambda_i^2(1+\eta)\left(1-\alpha^2\right)}{\left(1+\eta\lambda_i^2\right)\left(1-\alpha^2\sum_i\lambda_i^2\right)} + \log\left(1+\eta\lambda_i^2\right)\right\} - \log\left(1-\alpha^2\Sigma\lambda_i^2\right)\right], \quad (9.80)$$

where λ_i are the principal stretches, α is a measure of the inextensibility and η of the slippage, N_c is the number of crosslinks and N_s the number of slip links. The stress is found from the constitutive relation in Equation (2.29).

9.1.4 Caveats regarding the generalization to three dimensions and large deformations

Before proceeding, some comments on developing a fully three-dimensional large-strain model from a one-dimensional rheological model are in order. When considering only infinitesimal strains, the strain applied to elements in series is added together, whereas elements in parallel are subjected to the same strain. For example, for the model in Figure 9.3, the strain across the elements on the first branch is decomposed additively, $\boldsymbol{\varepsilon} = \boldsymbol{\varepsilon}^e + \boldsymbol{\varepsilon}^p$, being the same across both branches. A suitable kinematic decomposition must be chosen to achieve an appropriate generalization to three dimensions and large deformations. The classical Lee multiplicative decomposition of the deformation gradient (Lee and Liu, 1967; Lee, 1969) is the most common choice,

$$\boldsymbol{F} = \boldsymbol{F}^e\boldsymbol{F}^p, \quad (9.81)$$

where $\boldsymbol{F}$ is the deformation gradient and superscripts e and p correspond to the elastic and plastic parts. In practice, elements in parallel will experience the same strain gradient, whereas elements in series will divide the deformation using a multiplicative decomposition. See Figure 9.3 for reference. Since, in general, the deformation gradients do not commute, the choice of order is relevant.

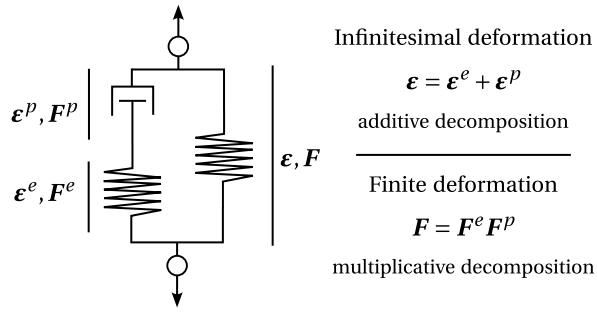

Figure 9.3: Additive and multiplicative strain decomposition corresponding to infinitesimal and finite deformations, respectively.

Focusing on a decomposition between an elastic, denoted here by e, and a viscous element, denoted here by p, the application of the decomposition in Equation (9.81) to the definition of

the spatial velocity gradient (see Section 2.1) yields

$$\boldsymbol{L} = \boldsymbol{L}^e + \boldsymbol{F}^e \boldsymbol{L}^p (\boldsymbol{F}^e)^{-1}, \tag{9.82}$$

where $\boldsymbol{L}^e$ and $\boldsymbol{L}^p$ are defined as

$$\boldsymbol{L}^e = \dot{\boldsymbol{F}}^e (\boldsymbol{F}^e)^{-1}, \tag{9.83}$$

$$\boldsymbol{L}^p = \dot{\boldsymbol{F}}^p (\boldsymbol{F}^p)^{-1}. \tag{9.84}$$

The deformation gradient may also be expressed as the product of the elastic stretch, the rotation, and the plastic stretch, as

$$\boldsymbol{F} = \boldsymbol{V}^e \boldsymbol{R} \boldsymbol{U}^p, \tag{9.85}$$

where $\boldsymbol{R} = \boldsymbol{R}^e \boldsymbol{R}^p$.

The constitutive description is most often supplied as a law for $\boldsymbol{D}^p$ and $\boldsymbol{W}^p$, where

$$\boldsymbol{D}^p = \mathrm{sym}(\boldsymbol{L}^p), \quad \boldsymbol{W}^p = \mathrm{skew}(\boldsymbol{L}^p). \tag{9.86}$$

A common approach is (de Souza Neto et al., 2008)

$$\bar{\boldsymbol{D}}^p \equiv (\boldsymbol{R}^e)^T \boldsymbol{D}^p \boldsymbol{R}^e = \dot{\gamma}_{\mathrm{dev}} \boldsymbol{N}_{\mathrm{dev}} + \dot{\gamma}_{\mathrm{vol}} \boldsymbol{N}_{\mathrm{vol}}, \tag{9.87}$$

$$\bar{\boldsymbol{W}}^p \equiv (\boldsymbol{R}^e)^T \boldsymbol{W}^p \boldsymbol{R}^e = \boldsymbol{0}, \tag{9.88}$$

with $\boldsymbol{R}^e$ defined by the polar decomposition theorem as $\boldsymbol{F}^e = \boldsymbol{R}^e \boldsymbol{U}^e$, where $\boldsymbol{N}_{\mathrm{dev}}$ and $\boldsymbol{N}_{\mathrm{vol}}$ are given by Equation (9.66) and $\dot{\gamma}_{\mathrm{dev}}$ is found from the laws described in Section 9.1.1. This yields the plastic spatial velocity gradient

$$\boldsymbol{L}^p = (\boldsymbol{R}^e)^T (\dot{\gamma}_{\mathrm{dev}} \boldsymbol{N}_{\mathrm{dev}} + \dot{\gamma}_{\mathrm{vol}} \boldsymbol{N}_{\mathrm{vol}}) \boldsymbol{R}^e, \tag{9.89}$$

and the elastic spatial velocity gradient

$$\boldsymbol{L}^e = \boldsymbol{L} - (\dot{\gamma}_{\mathrm{dev}} \boldsymbol{N}_{\mathrm{dev}} + \dot{\gamma}_{\mathrm{vol}} \boldsymbol{N}_{\mathrm{vol}}). \tag{9.90}$$

An alternative description can be given as

$$\frac{1}{2} \mathscr{L}_v \boldsymbol{b}^e = -(\dot{\gamma}_{\mathrm{dev}} \boldsymbol{N}_{\mathrm{dev}} + \dot{\gamma}_{\mathrm{vol}} \boldsymbol{N}_{\mathrm{vol}}) \boldsymbol{b}^e, \tag{9.91}$$

where $\mathscr{L}_v \boldsymbol{b}^e$ is the Lie derivative of $\boldsymbol{b}^e$ with respect to the velocity field $\boldsymbol{v}$, assuming isotropic plasticity. In particular, Reese and Govindjee (1998) explore isotropic finite viscoelasticity employing Newtonian viscous elements as given by Equation (9.61) and Equation (9.62). The same authors highlight that this approach implies truly finite viscoelasticity, i.e., valid for large deformations and large perturbations away from thermodynamic equilibrium. They point out that an intermediate description, allowing for large deformations but constrained to small deviations from thermodynamic equilibrium, is also possible. Thus linearizing Equation (9.91) yields

$$\dot{\boldsymbol{C}}^p = \frac{1}{\theta} (\boldsymbol{C} - \boldsymbol{C}^p), \tag{9.92}$$

where θ is a relaxation time. Note the similarities with Equation (A.14) describing the evolution of $\boldsymbol{\varepsilon}^p$ in infinitesimal viscoelasticity. Accordingly, the $\boldsymbol{C}^p$ is given by a convolution integral. This possibility had already been pointed out by Coleman and Noll (1961). A similar approach is pursued by Simo (1987), where the internal variables are the nonequilibrium forces acting on the different arms of the rheological model.

One can also prescribe a law for $\boldsymbol{D}^p$ directly (Boyce et al., 1988),

$$\boldsymbol{D}^p = \dot{\gamma}_{\text{dev}} \boldsymbol{N}_{\text{dev}} + \dot{\gamma}_{\text{vol}} \boldsymbol{N}_{\text{vol}}, \tag{9.93}$$

$$\boldsymbol{W}^p = \boldsymbol{W} - \mathscr{W} : (\boldsymbol{D} - \boldsymbol{D}^p), \tag{9.94}$$

where $\mathscr{W}$ is a fourth-order spin tensor whose full description is given by Onat (1987). This is necessary because the authors assumed that the rotation tensor, $\boldsymbol{R}$, is entirely plastic, i.e., $\boldsymbol{R} = \boldsymbol{R}^p$. As a consequence, the model attributes all rotation effects to plastic deformation. This results in a symmetric, and therefore unique, elastic deformation gradient, $\boldsymbol{F}^e = (\boldsymbol{F}^e)^T$. The spin tensor, $\boldsymbol{W}^p$, is thus required to sustain the adopted symmetry of $\boldsymbol{F}^e$.

Finally, we can also follow Bergström (Bergström, 2015)

$$\tilde{\boldsymbol{D}}^p \equiv \text{sym}((\boldsymbol{F}^e)^{-1} \boldsymbol{L}^p \boldsymbol{F}^e) = \dot{\gamma}_{\text{dev}} \boldsymbol{N}_{\text{dev}} + \dot{\gamma}_{\text{vol}} \boldsymbol{N}_{\text{vol}}, \tag{9.95}$$

$$\tilde{\boldsymbol{W}}^p \equiv \text{skew}((\boldsymbol{F}^e)^{-1} \boldsymbol{L}^p \boldsymbol{F}^e) = \boldsymbol{0}, \tag{9.96}$$

which is equivalent to Equation (9.87) if elastoplastic isotropy (de Souza Neto et al., 2008) is assumed.

Remark 9.1 | Rigid viscoplasticity

Some authors in the context of crystalline plasticity neglect the elastic deformation altogether, meaning that the deformation gradient and the stress are related directly by the flow rule. From a rheological point of view, this is equivalent to considering only viscous elements in the model. It leads to a rigid response when the flow rule is incapable of producing a given mode of deformation, e.g., volumetric compression in incompressible plasticity. In the case of polymer crystallites, another such constraint is the inextensibility in the direction of the polymer chains (Parks and Ahzi, 1990).

9.1.5 Inclusion of the thermal field

Including temperature-dependent material parameters is insufficient to account for the thermal field when using constitutive descriptions based on rheological models. The first missing feature of such a model is that a change in temperature with null stress would not lead to contraction or dilation. Similarly, a temperature change while preventing expansion/contraction would lead to zero stress. To fix this omission, an additional thermal configuration can be considered, e.g.,

$$\boldsymbol{F} = \boldsymbol{F}^{\text{mech}} \boldsymbol{F}^{\text{th}}, \tag{9.97}$$

where $\boldsymbol{F}^{\text{mech}}$ and $\boldsymbol{F}^{\text{th}}$ are the deformation gradients concerning only the mechanical and temperature fields, respectively. Note that the reverse order for the deformation gradients can be considered, as well as decompositions where the thermal deformation gradient is applied between elastic and plastic deformation gradients (Arruda et al., 1995).

When employing the models described so far, consider that an increase in the temperature with no mechanical loading applied leads to a null stress response from the 'mechanical part,' thus, its corresponding deformation gradient will be unitary, making the total deformation gradient equal to the thermal deformation gradient, $\boldsymbol{F} = \boldsymbol{F}^{\text{th}}$. Taking inspiration from isotropic infinitesimal thermoelasticity theory, we can write

$$\boldsymbol{\varepsilon}^{\text{th}} = \alpha_{\boldsymbol{\varepsilon}} \Delta T \boldsymbol{I}. \tag{9.98}$$

Lu and Pister (1975) suggest, however,

$$\boldsymbol{F}^{\text{th}} = v(T) \boldsymbol{I}, \tag{9.99}$$

where v is a scalar-valued function of temperature, reflecting intrinsic thermal expansion characteristics of the material of the body

$$v(T) = \exp\left[\int_{T_0}^{T} \alpha_{\boldsymbol{F}}(T^*)\, dT^*\right], \tag{9.100}$$

where α is the coefficient of thermal expansion, allowed to depend on the temperature. In particular, if $\alpha_{\boldsymbol{F}}$ is independent of temperature, Equation (9.100) reduces to

$$v(\Delta T) = \exp(\alpha_{\boldsymbol{F}} \Delta T). \tag{9.101}$$

Further, if the conditions for infinitesimal thermal strain are satisfied, i.e., $\alpha_{\boldsymbol{F}} \Delta T \ll 1$, we recover Equation (9.98).

Considering the energy balance equation (Equation (2.99)), the internal dissipation and the Gough-Joule effect still need to be added to the present analysis. In the one-dimensional rheological model, the dissipation is due to the linear dashpots,

$$\mathscr{D}^i_{\text{int}} = \sigma^i \dot{\gamma}^i, \tag{9.102}$$

where $\dot{\gamma}^i$ and σ^i are the strain rate and stress in the dashpot i. In three dimensions, this rationale yields

$$\mathscr{D}^i_{\text{int}} = \chi_{\text{d}} \boldsymbol{\sigma}_i : \boldsymbol{D}^i, \tag{9.103}$$

where $\boldsymbol{\sigma}^i$ is the Cauchy stress tensor across the ith viscous element and $\boldsymbol{D}^i$ the corresponding rate of deformation tensor. $\chi_{\text{d}} \in [0,1]$ is a constant dissipation factor, commonly chosen in the range $\chi_{\text{d}} \approx 0.85$ to 0.95 for metals (Simo and Miehe, 1992) and equal to 1 for polymers (Okereke and Akpoyomare, 2019; Hao et al., 2022b). The possibility of $\chi_{\text{d}} < 1$ materializes the fact that some plastic work may be stored in the material.

Concerning the temperature dependence of material parameters more broadly, several authors try to include it in their models, in general, through simple linear (Ferreira et al., 2023) or exponential dependencies (Arruda et al., 1995; Bergström and Hilbert, 2005).

Remark 9.2 | Single integral models

One approach that seeks to generalize the results of infinitesimal viscoelasticity is based on the integral constitutive equation for the stress as a function of the strain in Equation (A.1). These models include nonlinear phenomena while considering only small strains (Ward and Sweeney, 2004). For example, the model of Pipkin and Rogers is given by (Ward and Sweeney, 2004)

$$\sigma(t) = \int_{-\infty}^{t} R(t-\tau, \varepsilon(\tau)) \frac{\partial \varepsilon}{\partial \tau}\, d\tau, \tag{9.104}$$

where R is a nonlinear stress relaxation modulus depending on time and strain, incorporating nonlinear effects into the material's infinitesimal viscoelastic constitutive description.

A list of models of this type, including Leaderman, Pipkin and Rogers; Schapery; and Bernstein, Kearsley and Zapas (BKZ), can be found in Ward and Sweeney (2004) and Malkin and Isayev (2017). This class of models is not given much attention in this text since, due to their formulation in terms of convolution integrals with non-trivial kernels, they are not particularly appropriate for application in computational mechanics based on the FEM.

9.1.6 Classification according to the structure of the rheological models

Given that much of the models' ability to describe the experimental behavior of the polymers relies on the structural arrangement of the elements, i.e., whether elements are arranged in series or in parallel, we bin the different models according to a classification based on the underlying linear model. The next set of models generalizes various infinitesimal viscoelastic models by using the previously described nonlinear elements in the corresponding rheological models.

Generalization of the Maxwell model The Maxwell model is given as

$$\sigma + \frac{\eta}{E}\dot{\sigma} = \eta\dot{\varepsilon}, \tag{9.105}$$

corresponding to the rheological model in Figure 9.4. It is able to model stress relaxation and

Figure 9.4: Rheological model corresponding to the Maxwell model.

creep, but not time-dependent recovery. In a constant-strain experiment, it attains a plateau stress and only captures hardening through internal variables in the description of the flow rule.

An early improvement to describe the large-strain behavior of elastomers is presented by Smith (1962). The Bodner-Partom material model (Bodner and Partom, 1975) is another generalization of the same constitutive description. It can simulate the behavior of a visco-elastoplastic material under small strains and arbitrary loading history. The elastic element obeys Hooke's law, and the flow rule is given by Equations (9.25) and (9.93), with the athermal strength evolving according to Equation (9.32). The model can describe a rate-sensitive response and hardening. However, it cannot display strain recovery. Based on this work, the rate equations in Equation (9.35) for $\hat{\tau}$, in conjunction with a power law (see Equation (9.23)), have been used in models describing poly(methyl methacrylate) (PMMA), a glassy polymer, by Zaïri and coworkers (Zaïri et al., 2005, 2007, 2008), to describe HDPE by Zhang and Moore (1997), and to describe PC by Frank and Brockman (2001). It has also been used to model the behavior of metallic alloys at high temperatures (de Souza Neto et al., 2008).

In the same vein, Ben Hadj Hamouda and coworkers (Ben Hadj Hamouda et al., 2007) employ a Double Inelastic Deformation (DID) model—whose background is described in detail by Cailletaud and Saï (Cailletaud and Saï, 1995). Formulated in small strains, an additive split is assumed between a linear strain and two viscoplastic strains, corresponding to the deformation mechanisms in the amorphous and crystalline phases. Each viscoplastic strain follows a power law (see Equation (9.23)) with a von Mises yield criterion, accounting also for nonlinear kinematic hardening. The authors use it to model MDPE response in constant-strain-rate uniaxial tension experiments, as well as in stress-relaxation and dip tests. Balieu and coworkers (Balieu et al., 2014) also present a model that can be interpreted as a nonlinear Maxwell model. It is formulated using hypoelasticity, with the plastic flow rule deduced from Raghava's criterion, modified to include an isotropic damage variable representing micro-voids and micro-cracks developed in the material. The law for the strain rate is a power law (see Equation (9.23)), and the authors employ an integral-type nonlocal damage model to describe mineral-filled semi-crystalline polymers.

In the work developed by Doghri et al. (Miled et al., 2011; Krairi and Doghri, 2014; Gudimetla and Doghri, 2017; Krairi et al., 2019), a constitutive model that couples

viscoelasticity and viscoplasticity is also proposed. In their contributions, the elastic spring of the standard Maxwell model is replaced by a generalized Maxwell model, effectively allowing the modeling of viscoelasticity. The associated stress is expressed as a Boltzmann integral, and the viscoelastic relaxation moduli follow the general Prony series (Equation (A.13)). In Krairi and Doghri (2014), the viscoplastic response combines isotropic and nonlinear kinematic hardening. Moreover, a ductile damage evolution is implemented, with this variable linked to the viscoplastic strains. Krairi et al. (2019) extended the model proposed by Miled et al. (2011) by including the model into a thermomechanically coupled framework, such that it couples viscoelasticity and viscoplasticity under non-isothermal loading conditions.

Standard Linear Solid The following set of models is a generalization of the so-called standard linear solid model. In the context of infinitesimal viscoelasticity, it can be expressed in equivalent ways in its Maxwell or its Kelvin-Voigt representation, as shown in Figure 9.5 with the constitutive differential equations for the stress and the strain given as

$$\sigma + \frac{\eta}{E_2}\dot{\sigma} = E_1\varepsilon + \frac{\eta\left(E_1+E_2\right)}{E_2}\dot{\varepsilon}, \quad \text{(Maxwell representation)}, \tag{9.106}$$

$$\sigma + \frac{\eta}{E_1+E_2}\dot{\sigma} = \frac{E_1E_2}{E_1+E_2}\varepsilon + \frac{E_1\eta}{E_1+E_2}\dot{\varepsilon}, \quad \text{(Kelvin-Voigt representation)}, \tag{9.107}$$

where in both equations, the terms containing the strain, ε, are the stress response in equilibrium. For linear viscoelastic materials, both representations are equivalent. However, when nonlinear elements are introduced, the two representations generally yield different results. That said, these models can display stress relaxation with a plateau value, creep with a plateau strain, and time-dependent full recovery. In a constant-strain experiment, no steady-state stress is reached, allowing hardening even without internal variables beyond the viscous strain.

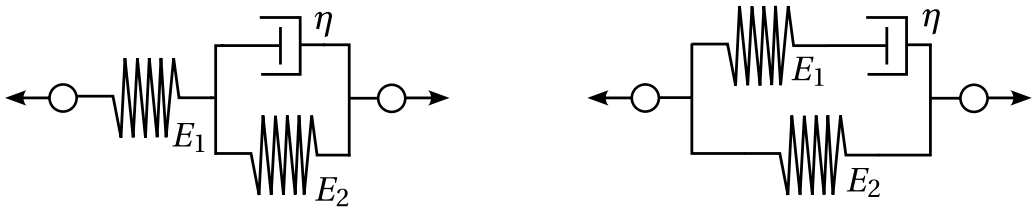

Figure 9.5: Rheological model for the standard linear solid: (a) Maxwell representation; (b) Voigt representation.

The viscoplasticity theory based on overstress (VBO) was introduced by Cernocky and Krempl (1980) and is based on the standard linear solid. The so-called overstress is the difference between the full stress and the equilibrium part, which is allowed to be a nonlinear function of the strain. Thus, Equations (9.106) and (9.107) can be written as

$$\sigma - f(\varepsilon) = M\dot{\varepsilon} - K\dot{\sigma}, \tag{9.108}$$

where f may be a nonlinear function of the strain, and M and K are general functions of the stress, the strain, and their derivatives. It has been used to successfully model metals (Liu and Krempl, 1979; Yao and Krempl, 1985) as well as polymers, such as polypropylene (Kitagawa et al., 1989), polyethylene (Kitagawa and Takagi, 1990), nylon 66, polyetherimide, poly(ether

ether ketone) (Krempl and Ho, 2000), and polyphenylene oxide (PPO) (Colak, 2005). More advanced versions of this approach include kinematic and isotropic hardening and strain softening through appropriate internal variables (Krempl and Ho, 2000; Ho and Krempl, 2002).

Polanco-Loria and coworkers (Polanco-Loria et al., 2010) present a generalization that allows for a hyperelastic-viscoplastic response due to intermolecular resistance and an entropic hyperelastic response due to molecular chain reorientation. The stress in the Maxwell branch is determined from an isotropic compressible Neo-Hookean material (see Equation (9.75)). At the same time, the flow in the dashpot is controlled by Raghava's yield criterion, which is pressure sensitive (see Section 9.1.2). A non-associative viscoplastic flow potential is employed, allowing for volumetric plastic strain. Finally, the eight-chain model provides the deviatoric part of the stress on the other branches, including a volumetric part similar to that shown in Equation (9.66) for the Neo-Hookean model. The authors validated their models against experimental results obtained for polypropylene samples.

That said, the most popular thermoplastic models are generalizations of the Voigt version of the standard solid. Halsey and coworkers (Halsey et al., 1945) present one of the earliest contributions considering an Eyring dashpot as the viscous element in an attempt to model the behavior of fibers. Likewise, Haward and Thackray (1968) proposed one of the first models for thermoplastic polymers below the glass transition temperature. The elastic element in the Maxwell branch is still a linear spring. However, the elastic element parallel to it is a Langevin spring, while the viscous element is an Eyring dashpot. The model is formulated assuming small strains and is restricted to one-dimensional loading.

Later, Boyce, Argon, and Parks (1988) generalized this model, now known as the BPA model, to three dimensions, among other additions. A multiplicative kinematic split between the elastic and inelastic deformation is enforced, as described in Section 9.1.4. The linear spring is generalized to three dimensions and large deformation using the Hencky model (see Equation (9.73)), with the shear and bulk moduli temperature-dependent. The thermally activated process is now nucleation controlled by employing the model proposed by Argon (1973) (see Equation (9.11)) with the addition that the athermal strength $\hat{\tau}_0$ is replaced by an internal variable, $\tilde{\tau}$, which is given by $\tilde{\tau} = \hat{\tau} + \alpha p$ and α is a material property. The rate equation for the athermal strength, $\hat{\tau}$, is chosen according to Equation (9.36), such that the distinctive strain softening of glassy polymers is captured. The model does not account for volumetric flow. Lastly, the three-chain model gives the stress in the other elastic element (see Equation (9.78)), responsible for the strain hardening. For other contributions exploring this model while employing different rubber-like elasticity models, see, e.g., Arruda and Boyce (1993); Arruda et al. (1995); Wu and Van Der Giessen (1993); Buckley and Jones (1995); Sweeney and Ward (1995). In fact, the most widely used model of this type is the so-called Arruda-Boyce model (Arruda and Boyce, 1993; Arruda et al., 1995), which employs an eight-chain model for the rubber-elastic element.

Arruda et al. (1995) extended the BPA model to the moderate strain rate domain, by considering a thermomechanical coupled framework with isotropic thermal expansion, and by incorporating an internal state variable associated with the temperature-evolution of the density of the weak entanglements. Bergström and Boyce (1998, 2000) also modified the BPA model to describe the response of elastomeric materials and filled elastomers. Their modification is based on a rheological decomposition into two parallel polymer networks: one capturing the equilibrium response, the branch containing the elastic spring, and the other describing the time-dependent deviation from equilibrium, the Maxwell branch. The flow rule adopted for the dashpot is given by Equation (9.26), inspired by the reptation theory of polymer dynamics (Doi and Edwards, 1978), with both elastic elements modeled employing the eight-chain model (see Equation (9.76)). The influence of filler particles is modeled by amplifying the scalar equivalent values of stretch and shear stress, effectively providing adjusted

measures of matrix stretch and matrix shear stress.

Also expanding on the BPA model (Boyce et al., 1988), Chowdhury and coworkers (Chowdhury et al., 2008) propose a very similar model in the context of manufacturing-induced voids in polymer-based composites, formulated, however, hypoelastically. The model was later validated on epoxy resins by Poulain and coworkers (Poulain et al., 2014). As in the BPA model, the athermal strength (Equation (9.11)) is taken as an internal variable following a different rate equation (Equation (9.39)). This choice allows a smoother strain softening. Also, the response of the rubber-elastic element is now a linear combination of the response obtained from a three-chain model (Equation (9.78)) and an eight-chain model (Equation (9.76)). Hao and coworkers (Hao et al., 2022a) propose a very similar model, where the rate equation for the athermal strength is given by Equation (9.41), rendering a model able to capture the double yield phenomenon in semi-crystalline polymers. The last authors also consider the thermomechanical aspects of polymer modeling, including self-heating, thermal softening, and temperature-dependent properties. They validate their model against experimental results obtained for epoxy, nylon101, and PA6.

Richeton and coworkers (Richeton et al., 2007b) also present a model based on the standard linear solid. Where the hardening spring is modeled employing the eight-chain model (see Equation (9.76)) and the flow rule is adopted as Equation (9.21) for flow below the glass transition temperature and Equation (9.22) above it. The authors compare their model against experimental results for PMMA and PC samples subject to compression tests at different strain rates and temperatures.

Employing a similar arrangement of rheological elements as the BPA model, Mirkhalaf et al. (2016) proposed a finite-strain elasto-viscoplastic constitutive model to predict the nonlinear behavior of amorphous polymers. Although the model operates within a finite-strain framework, it is implemented using a formulation based on the functional structure of the infinitesimal strain regime. Within this context, the state update procedure and the consistent tangent operator are pre- and post-processed by a purely kinematic finite-strain extension (De Souza Neto et al., 1994). Besides its simplicity, this type of extension preserves the most important properties of the infinitesimal strains formulation, namely volume-preserving plastic deformations and finite plastic incompressibility. In this context, instead of adopting the left Cauchy-Green strain tensor as the strain measure, the logarithmic strain tensor is used. It is worth highlighting that the use of the additive approximation of the logarithmic strains, also known as Green plasticity, significantly simplifies the computational implementation of this constitutive model. Moreover, this approximation is associated with a negligible error under moderately small elastic strains (Eterovic and Bathe, 1990). Note that an alternative formulation based on elastic corrector rates has been recently proposed (Latorre and Montáns, 2018; Zhang and Montáns, 2019; Zhang et al., 2021) to handle this additive update. In the work developed by Mirkhalaf et al. (2017), this model was further extended to capture the material's behavior under different triaxial states. Within this context, the strain-softening and strain-hardening constitutive laws have been modified to account for the stress triaxiality and the Lode angle.

Recently, the model proposed by Mirkhalaf et al. (2016) was extended to account for viscoelasticity Ferreira et al. (2023). In this context, the elastic spring parallel to the Maxwell branch is replaced by a generalized Maxwell model, where the shear relaxation modulus follows a Prony series as given in Equation (A.13). Since this falls under the umbrella of Finite Linear Viscoelasticity theory, which is based on a single stored energy (Simo, 1987; Simo and Hughes, 1998; Holzapfel, 2000), this choice alone does not lead to strain rate dependency. This is accounted for through the material parameters in the Prony series. As a result, the viscoelastic relaxation times are considered dependent on the strain rate, following the evolution law

introduced by Yu et al. (2014):

$$\theta_i(\dot{\varepsilon}^{\mathrm{eq}}) = \theta_{i,T}\,(\dot{\varepsilon}^{\mathrm{eq}})^{-\lambda_{g,i}}\,, \qquad i = 1, \ldots, n_{\mathrm{V}}\,, \tag{9.109}$$

where $\theta_{i,T}$ is constant, $\lambda_{g,i}$ represents the shear relaxation time strain rate sensitivity, and the spatial logarithmic equivalent strain rate is given by $\dot{\varepsilon}^{\mathrm{eq}} = \sqrt{\frac{2}{3}\dot{\overline{\|\boldsymbol{\varepsilon}\|}}}$, with $\dot{\overline{(\bullet)}}$ denoting the time derivative.

Holopainen et al. (2017); Holopainen and Barriere (2018) extended the BPA model to propose a thermodynamically consistent approach that describes the isothermal ductile fatigue damage in amorphous polymers. Wang et al. (2021) extended the effective temperature model proposed by Xiao and Nguyen (2015) to develop a large deformation model that accurately captures the temperature-dependent and strain rate-dependent post-yielding strain hardening behavior as well as the Bauschinger effect under reversed loading. In this model, the Eyring model is applied to characterize the temperature-dependence and strain rate-dependence of the viscous resistance to network deformation, and the Arruda-Boyce eight-chain model (Arruda and Boyce, 1993) is used to describe the internal energy associated with network deformation to account for the limiting stretch of the network structure.

Uchida et al. (2022) developed a viscoelastic viscoplastic model grounded in the physics of polymer chain deformation. Building on their earlier work (Uchida et al., 2019), they extended the model to incorporate the temperature- and strain rate-dependent mechanical behavior observed below the glass transition temperature.

Another significant contribution to the constitutive modeling of amorphous polymers was proposed by Leonov (1976), now based on the Maxwell representation of the standard linear solid. This model was later extended to a compressible version by Baaijens (1991), and later derived within a thermodynamically consistent framework by Tervoort et al. (1998). In addition, to capture the typical behavior of the post-yield region of amorphous polymers, namely the phenomenon of strain-softening and strain hardening, this model was extended by Timmermans and Govaert (1997; 2000), leading to the generalized compressible Leonov model, currently known as the Eindhoven Glassy Polymer (EGP) model.

Khaleghi et al. (2022) extended the EGP model with a thermodynamically consistent damage model based on the damage evolution law introduced by Lemaitre (2013). The Oxford Glass Rubber (OGR) model (Buckley and Jones, 1995) is structurally similar to the EGP model, but the resistance to entropy-elastic chain stretch is described by the Edwards-Vilgis free energy function (Edwards and Vilgis, 1986). In the work of van Breemen et al. (2011), the single-mode EGP model is extended to a multi-mode constitutive model. This extension assumes that the pre-yield response is governed by a spectrum of linear relaxation times, which shift to shorter timescales under the influence of applied stress.

Models originally developed for polymers have also been further extended and adapted for composite materials. For instance, in the work developed by Amiri-Rad et al. (2019), the EGP model is extended to establish an anisotropic viscoelastic viscoplastic macromechanical framework specifically tailored for short-fiber reinforced polymers, capturing the direction-dependent behavior introduced by fiber orientation. In a related effort, Nciri et al. (2018) proposed a continuum model for short-fiber-reinforced composites that incorporates viscoelastic and viscoplastic behavior of the amorphous polymer matrix, with particular emphasis on complex fiber orientation distributions and rate-dependent effects.

Although not explicitly making reference to a rheological model, Anand and Gurtin (2003) present a constitutive model for glassy polymers that can also be interpreted as a generalization of the standard linear solid in its Kelvin-Voigt representation. The elastic element in series is modeled employing the Saint-Venant-Kirchhoff model (see Equation (9.74)), while the flow rule is by a power law (Equation (9.23)), employing internal variables to capture strain softening

and hardening (see Equation (9.45)). The corresponding backstress is modeled for small to moderate strains employing a Neo-Hookean model (see Equation (9.75)), and a non-Gaussian network model (see Equation (9.76)) for large strains. The authors validate their model against experimental data in uniaxial compression for PC.

Some of the same authors (Anand et al., 2009; Ames et al., 2009) propose an improvement on this model, now with the rheological representation depicted in Figure 9.6. A flow rule based on the cooperative model (see Equation (9.21)) is now adopted for the viscous element, while the internal variables follow the evolution laws in Equation (9.49), capturing strain softening and hardening. Bouvard et al. (2013) proposed a finite-strain thermomechanical viscoplastic model with thermal expansion to predict the behavior of amorphous polymers. The model is derived adopting a formulation based on internal variables very similar to that of Anand and coworkers (Anand et al., 2009; Ames et al., 2009). This model was recently extended by Lan et al. (2022), by dividing the molecular entanglements into permanent entanglements and dynamic entanglements, as introduced by Jiang (2019); Jiang et al. (2020).

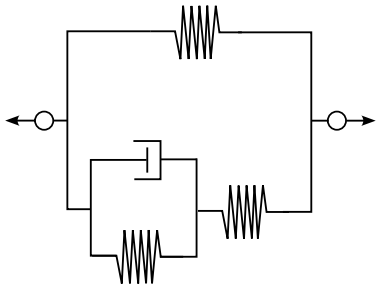

Figure 9.6: Rheological model for the Anand-Ames model (Anand et al., 2009; Ames et al., 2009).

Burgers material Another common material model in infinitesimal viscoelasticity is the so-called Burgers material, which incorporates viscous flow into the standard linear solid model. It also accepts two equivalent descriptions as

$$\sigma + \left(\frac{\eta_1}{E_1} + \frac{\eta_2}{E_2}\right)\dot{\sigma} + \frac{\eta_1\eta_2}{E_1E_2}\ddot{\sigma} = \left(\eta_1 + \eta_2\right)\dot{\varepsilon} + \frac{\eta_1\eta_2\left(E_1 + E_2\right)}{E_1E_2}\ddot{\varepsilon} \quad \text{(Maxwell representation)}, \tag{9.110}$$

$$\sigma + \left(\frac{\eta_1}{E_1} + \frac{\eta_2}{E_1} + \frac{\eta_2}{E_2}\right)\dot{\sigma} + \frac{\eta_1\eta_2}{E_1E_2}\ddot{\sigma} = \eta_2\dot{\varepsilon} + \frac{\eta_1\eta_2}{E_1}\ddot{\varepsilon} \quad \text{(Kelvin-Voigt representation)}, \tag{9.111}$$

in the context of small strains. See Figure 9.7 for the corresponding rheological models.

Bardenhagen and coworkers (Bardenhagen et al., 1997) propose a three-dimensional viscoplastic model for polymeric materials, which is a generalization of the Maxwell representation of the Burgers material. One of the branches is a three-dimensional, large-strain hypoelastic generalization of the Maxwell model. The other branch employs an associative hypoelastic elastoplastic model with the von Mises criterion as the yield criterion, including an isotropic hardening function. The authors provide a comparison with experimental results.

Boyce and coworkers (Boyce et al., 2000) also present a model generalizing the Maxwell representation of the Burgers material. One of the branches contains an elastic element following Hencky's model (see Equation (9.73)) and an Eyring dashpot, in the same way as the model already described in Boyce et al. (1988). In the other branch, the elastic element follows the eight-chain model (see Equation (9.76)), while the dashpot is similar to the Bergström-Boyce model (see Equation (9.26)). It is used by the authors to model poly(ethylene

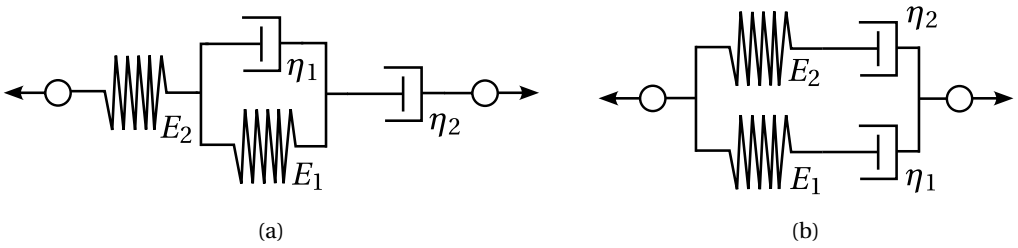

(a) (b)

Figure 9.7: Rheological model for the Burgers material. (a) Maxwell representation. (b) Voigt representation.

terephthalate) above the glass transition temperature, accounting for strain-induced crystallization. This is achieved by neglecting the last dashpot if the stretch is larger than a given value, which depends on the plastic strain rate and the temperature.

Kletschkowski and coworkers (Kletschkowski et al., 2002) present another description fitting into this class of material models. One of the Maxwell branches is made of a linear elastic spring, and its viscous element follows the cooperative model (see Equation (9.21)) for the strain rate. The other branch employs the endochronic viscoplasticity theory (Valanis, 1970). It resembles viscoelasticity with the caveat that time is replaced by an 'inner' time, a function of the strain, hence the name endochronic. The authors employ this model in the description of filled PTFE.

Pouriayevali and coworkers (Pouriayevali et al., 2013) present a constitutive model to describe the quasi-static and high strain rate, large deformation response of semi-crystalline polymers, which can be seen as a generalization of the Kelvin-Voigt representation of the Burgers material. The elastic elements are hyperelastic, and their stress response is obtained from Equation (2.29), given a suitable free energy potential. Regarding the viscous elements, element one obeys von Mises yield criterion with the strain rate also given by Equation (9.24), and the other obeys Newton's viscosity law (see Equation (9.61)), neglecting the volumetric contribution. The corresponding free energy, including the dependency on the temperature, is also supplied. The authors validate their model through comparisons with Nylon 6.

The dual network fluoropolymer model is presented in Bergström and Hilbert (2005) as an extension of the Bergström and Boyce (1998) and Arruda et al. (1995) models, generalizing the Kelvin-Voigt representation of the Burgers material. The Arruda-Boyce eight-chain model gives the response of both springs (see Equation (9.76)), with the response of the second element taken as a scalar factor $s^{(2)}$, a specified material parameter, times the expression employed to describe the response of the first evaluated according to the deformation gradient across element 2. The kinematic decomposition is as expected from the discussion in Sections 9.1.4 and 9.1.5, including a thermal deformation gradient. The rate equations for $\dot{\gamma}^{(1)}_{\text{dev}}$ and $\dot{\gamma}^{(1)}_{\text{vol}}$ in Equation (9.95) in the viscous element one are given similarly to the Bergström-Boyce model (see Equation (9.26)) multiplied by a power law, function of the stress and the temperature. The volumetric strain rate is given by Equation (9.63). The strain rate for the viscous element 2, $\dot{\gamma}^{(2)}_{\text{dev}}$, is given by Equation (9.28).

Generalized Maxwell model A generalized Maxwell model is one that contains n Maxwell branches in parallel. In addition, a single branch with only an elastic element may also be considered. See Figure 9.8 for the corresponding rheological model. This framework includes Maxwell representations for the standard linear solid model and the Burgers material. Models with more than two branches are considered in the following section.

Holmes and coworkers (Holmes et al., 2006) present a large-strain deformation

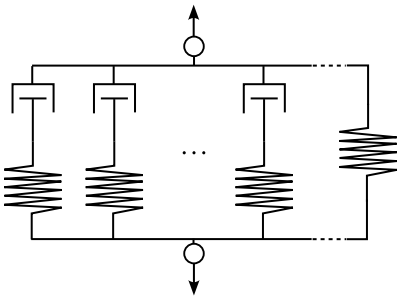

Figure 9.8: Rheological model for the generalized Maxwell model.

elasto-viscoplastic material model for modeling semi-crystalline polymers. According to the authors, each of the branches in the model coincides with a mode of deformation: elastic, viscoelastic, and viscoplastic. Each of the elastic elements' response follows from the free energy chosen and the constitutive relation in Equation (2.29). The authors suggest employing an Ogden free energy for the elastic and viscoelastic branches and a Saint Venant-Kirchhoff free energy (see Equation (9.74)) for the viscoplastic contribution. The flow rule adopted follows the work of Brusselle-Dupend and coworkers (Brusselle-Dupend et al., 2001, 2003) for semi-crystalline polypropylene, accounting for the inadequacies of the Eyring equation (see Equation (9.3)). Regarding the viscoplastic branch of the model, the strain rate is given by Equations (9.24) and (9.66).

Anand and Ames (2006) proposed a one-dimensional constitutive model to describe the localized viscoelastic viscoplastic mechanical response of amorphous polymers under micro-indentation. It considers several Voigt spring-damper units (a spring and a damper in parallel) in series. One of these units captures the macroscopic response, and the others model the microscopic response. There are also two extra springs, one in series with all the Voigt units and another in parallel with them, similar to the standard linear solid model. The flow rules selected for the viscous elements are of the power law type (see Equation (9.23)), with only the scalar internal variables related to the macroscopic response evolving according to Equation (9.49). Building directly on this thermodynamically consistent framework, Lele and Anand (2009) developed a strain-gradient framework to capture the behavior of isotropic viscoplastic materials undergoing large deformations. The theory incorporates strain gradients into the constitutive formulation, which allows for the modeling of size-dependent effects and localized deformation phenomena, such as those occurring in shear bands.

Regarding another model by some of the same authors (Anand et al., 2009; Ames et al., 2009), an extension was proposed by Srivastava et al. (2010) to accurately capture the mechanical response of amorphous polymers over a temperature range that includes the glass transition. They propose the addition of two Maxwell branches in parallel to capture the contribution of microscopic mechanisms, in addition to the appropriate temperature-dependent evolution laws for the internal variables, given the temperature range of interest. Wang et al. (2019) proposed a similar variation where new branches are added to capture the contributions of entangled chains and non-entangled chains to the intermolecular resistance to deformation.

Zeng and coworkers (Zeng et al., 2010) developed an elastoplastic constitutive model for semi-crystalline polymers under isothermal conditions between the glass transition temperature and the melting temperature under low-level strain rates, neglecting viscous effects. Each of the branches in the rheological model is based on physical considerations concerning the mesoscopic semi-crystalline structure. The foundational idea is a three-phase

morphology depending on the average distance between crystalline blocks. The interaction is modeled as elastoplastic with linear hardening when the distance is small. For medium distances, the behavior is elastoplastic with perfect plasticity, and for large distances, the material is modeled following the eight-chain model (see Equation (9.76)). The authors validate the model against the results of uniaxial and biaxial experiments on PA6 and PE at different strain rates. The model parameters are easily calibrated using these uniaxial stress–strain experimental curves.

The model developed by Bergström and Boyce (1998) based on the BPA model was later extended to the high-strain-rate domain by Mulliken and Boyce (2006); Mulliken (2006) by adding a new polymer network in parallel with the existing ones, enabling the model to capture the β-transition accurately. Subsequent modifications were introduced to enhance the model's predictive capability and broaden its applicability across different loading conditions and material behaviors — for instance, by introducing additional polymer networks, coupling the model with a thermo-mechanical adiabatic framework, and modifying the softening evolution laws of the polymer networks (Varghese and Batra, 2009; Safari et al., 2013; Wang et al., 2018; Johnsen et al., 2018). Inspired by the developments of Mulliken and Boyce (2006); Mulliken (2006), a finite-strain viscoelastic viscoplastic constitutive model is proposed by Carvalho Alves et al. (2023). This model extended the model in Ferreira et al. (2023) to predict the response of amorphous polymers across low and high strain rates by accounting for the distinct molecular processes that govern the material's mechanical behavior at these strain rates.

Okereke and Akpoyomare (2019) propose a model based on an elastic-viscoelastic-viscoplastic framework to predict the temperature and rate-dependent response of an incompressible semi-crystalline polymer. Three branches materialize it in a rheological model, two containing a viscous and an elastic element corresponding to the contribution of the mobile amorphous fraction, and the crystalline and rigid amorphous fractions, and another branch containing only an elastic element, representing the contribution of the entangled molecular network. The basis of this model is a one-process glass-rubber model for amorphous polymers (Buckley and Jones, 1995), adapted to the description of semi-crystalline polymers, which considers the α- and β-processes, making it a two-process model. The authors connect these processes to the glass transition of the rigid amorphous and the mobile amorphous phases, respectively. The flow rule for both branches containing the viscous elements is given according to Equation (9.66), where the volumetric contribution is neglected, and the deviatoric strain rate is given by Equation (9.55), capturing the significant post-yield strain-softening observed in high-rate compression of polypropylene. The elastic elements in the branches containing viscous elements follow the Saint-Venant-Kirchhoff model (see Equation (9.74)), while the other elastic element follows the Edwards-Vilgis model (see Equation (9.80)).

The three-network model is presented in Bergström (2015) and is very similar to the models already presented based on a generalized Maxwell model. The springs follow the Arruda-Boyce eight-chain model (see Equation (9.76)) and the dashpot power laws (similar to Equation (9.23)). The effective shear stress is taken as an internal variable with a corresponding rate equation. A linear dependence on temperature is also included for the stress response of the elastic elements. The same author also explores a parallel network model that adds more Maxwell branches, each following similar constitutive equations.

Hao and coworkers (Hao et al., 2022b) propose a model containing three branches to study the double yield phenomenon as well as the rate- and temperature-dependent thermomechanical response below the glass transition temperature of semi-crystalline polymers. The first branch contains an elastic element whose stress response follows Hencky's model (see Equation (9.73)). The corresponding viscous element obeys Equations (9.3) and (9.11) following the work of Boyce and coworkers (Boyce et al., 1988). The athermal

strength is taken as an internal variable, and its rate equation is shown in Equation (9.39), following Chowdhury and coworkers (Chowdhury et al., 2008). The behavior of the elastoplastic branch coincides with rate-independent plasticity, and it is made up of an elastic element, also following Hencky's model (see Equation (9.73)), and a viscous element respecting a paraboloidal yield criterion. The yield criterion describing the yielding in the crystalline region is similar to the Drucker-Prager yield criterion with the strain rate/plastic multiplier $\dot{\gamma}$ found by taking into account the Kuhn-Tucker's loading-unloading consistency conditions. The same law as Chowdhury and coworkers (Chowdhury et al., 2008) is adopted for the rubber-like elastic responsible for the hardening response, combining a three-chain model (see Equation (9.78)) and an eight-chain model (see Equation (9.76)).

The hybrid model has been developed to model UHMWPE (Bergström, 2002; Bergström et al., 2003) and employs the rheological model shown in Figure 9.9. The spring E is linear, following the Hencky model (Equation (9.73)), springs A and B follow the Arruda-Boyce eight-chain model (Equation (9.76)), employing the same expression except for a multiplicative constant s_B. This constant is treated in the model as an internal variable that evolves according to an equation similar to Equation (9.32). The rate of viscoplastic flow in element P, $\dot{\gamma}^p$, is given by a power law (Equation (9.23)), as is the flow rate in element B.

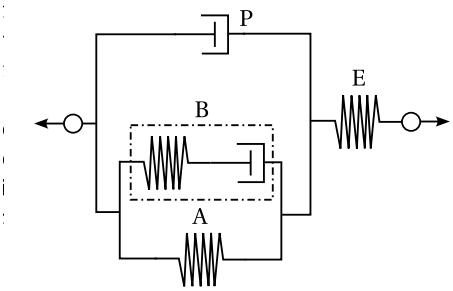

Figure 9.9: Rheological model for the Hybrid model (Bergström, 2002; Bergström et al., 2003).

9.2 Micromechanical models

The contribution of microscopic features such as bulk crystallinity and crystalline orientation to the overall response is usually captured through computational homogenization using either mean-field homogenization or full-field homogenization. For a brief overview on computational homogenization, see Section 1.2.1, while for more details on mean-field, see Chapter 4.

This section draws on the review by Mirkhalaf and Vadizadeh (2024).

9.2.1 Mean-field homogenization models

The simplest mean-field homogenization models used to describe semi-crystalline polymers are those based on the Voigt/Taylor and Reuss/Sachs mixture rules, where no particular microstructural geometry is considered beyond the volume fraction of the crystalline and amorphous phases (Ward and Sweeney, 2004). They also favor the use of isotropic constitutive models to describe the behavior of each phase. These two rules can be conceptualized as parallel and series arrangements of the two phases, respectively, since the Taylor model assumes that both phases experience the same strain, while the Sachs model assumes that both

phases experience the same stress. When the phases are assumed elastic, they provide upper and lower bounds for the overall stiffness of the semi-crystalline polymer (Nemat-Nasser and Hori, 1993).

The work of Takayanagi and coworkers (Takayanagi et al., 1964) is perhaps the earliest to consider such an approach to model semi-crystalline polymers. However, the mixture rule employed is neither purely the Taylor nor the Sachs mixture rule since a minimal geometric consideration is included regarding the distribution of the two phases. In their model, the amorphous phase is kept at the corner of the volume element, with dimensions φ and λ, as depicted in Figure 9.10. The quantity $\varphi\lambda$ is equal to the volume fraction of amorphous polymer, supplying an extra degree of freedom that can be correlated to the distribution of one phase in the other. A more homogeneous distribution of the amorphous phase leads to similar values for φ and λ, while inhomogeneities in either direction favor one or the other parameter. In Takayanagi et al. (1967), the authors employ similar techniques to model drawn samples of polyethylene (PE) and isotactic polypropylene (iPP), among other crystalline polymers.

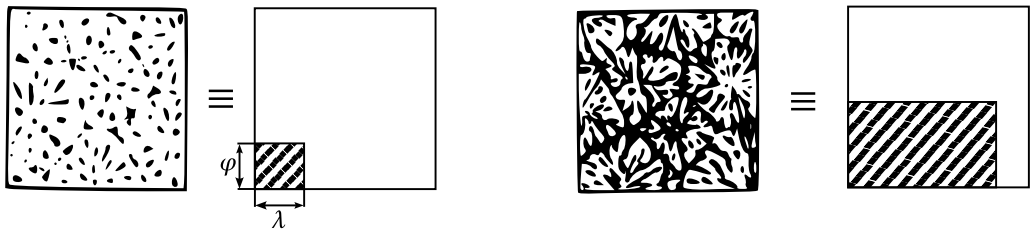

Figure 9.10: Mixture model of Takayanagi and coworkers (Takayanagi et al., 1964) for semi-crystalline polymers with crystallinities of about (a) 90% and (b) 50%, and their equivalent models. The black area denotes the non-crystalline region. Adapted from Takayanagi et al. (1964).

The model by Rao and Rajagopal (2001) considers the bulk crystallinity of semi-crystalline polymer through a Taylor-Voigt mixture rule. The amorphous phase is modeled employing a two process model, where one of them is characterized by a nonlinear viscosity, while the other is linear, as a function of the corresponding strain rate measure. They both depend nonlinearly on the bulk crystallinity, however. The elastic response coincides with an incompressible Neo-Hookean model (see Equation (9.75)). The crystalline phase is modeled taking into account the possibility of crystallization during deformation. The corresponding free energy depends both on the invariants of the average deformation gradient in the crystalline phase, as well as on invariants computed taking into account the orientation of the amorphous phase induced by the deformation.

Ahzi and coworkers (Ahzi et al., 2003) model PET at large strains, including strain-induced polymer crystallization above the glass transition temperature. The model is based on Boyce et al. (2000), considering two distinct resistances, an intermolecular (A) and network resistance (B). As in the base model, the network stress is captured by the Arruda-Boyce eight-chain model (see Equation (9.76)), and the viscous element follows the Bergström-Boyce model (see Equation (9.26)). The intermolecular resistance, however, is treated in a composite framework where the crystalline and amorphous phases are considered as two separate resistances coupled through either a Taylor or a Sachs-like mixture rule, which yield upper and lower bounds for the stiffness, respectively. The elastic elements corresponding to the crystalline and amorphous phases follow the Hencky model (see Equation (9.73)), and the

viscous elements follow a model similar to the one proposed by Argon (see Equation (9.11)), where the athermal strength s_i in each phase evolves according to Equation (9.38).

Regarding applying the mixture rules to the intermolecular resistance, contributions come from the crystalline part, denoted by c, and the amorphous part, a, of the semi-crystalline polymer. These are combined according to the degree of crystallinity, χ, in two ways (see Figure 9.11):

- in parallel, such that the gradient acting in each element is equal and the Cauchy stress is supplied by
$$\boldsymbol{\sigma}_A = \chi \boldsymbol{\sigma}_A^c + (1-\chi)\boldsymbol{\sigma}_A^a; \tag{9.112}$$
- in series, such that the stress acting on both elements is the same and the plastic rate of deformation is given by
$$\boldsymbol{D}_A^p = \chi \boldsymbol{D}_A^{p,\,c} + (1-\chi)\boldsymbol{D}_A^{p,\,a}. \tag{9.113}$$

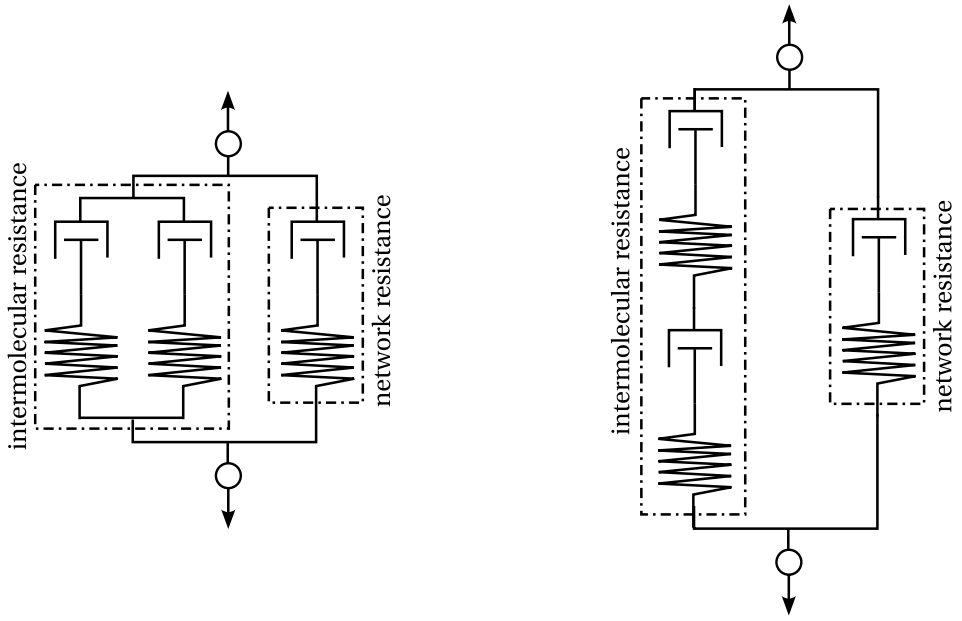

(a) (b)

Figure 9.11: Mixture models considered by Ahzi and coworkers (Ahzi et al., 2003): (a) Parallel arrangement; (b) Series arrangement.

The crystallization rate is expressed following a non-isothermal phenomenological expression based on the modified Avrami equation

$$\dot{\chi} = \chi_\infty \frac{\dot{\varepsilon}_{\text{eq}}}{\dot{\varepsilon}_{\text{ref}}} m K_{\text{av}}(T)(-\ln(1-y))^{(m-1)/m}(1-y)\exp\left(\xi \frac{\text{tr}\boldsymbol{\sigma}}{G_{\text{comp}}}\right), \tag{9.114}$$

where χ_∞ is the maximum degree of crystallinity, m is the Avrami exponent, ξ is a dimensionless model parameter, G_{comp} is the composite bulk modulus, $\dot{\varepsilon}_{\text{eq}}$ is the applied equivalent strain rate and $\dot{\varepsilon}_{\text{ref}}$ is taken as the maximum strain rate for which experimental results are available for the

calibration of the model parameters. K_{av} is the transformation rate function, which is defined in the case of PET as

$$K_{\text{av}}(T) = 1.47 \times 10^{-3} \left[\frac{4\pi \text{Nu}}{3\chi_\infty} \right]^{1/3} \exp\left[-\left(\frac{T-141}{47.33} \right) \right] \quad (\text{s}^{-1},\ T \text{ in } ^\circ\text{C}), \tag{9.115}$$

with Nu the number density of nuclei initially present within the amorphous phase.

Strobl and coworkers (Hong et al., 2004a,b; Na et al., 2006) propose a somewhat similar description for PE. They also consider two branches in a rheological model. The first is a Maxwell branch with a linear spring and an Eyring dashpot in series. The second is found through a Voigt mixture rule between rubber elastic and elastoplastic elements. Extensive experimental results on PEVA and PE support these choices.

Makradi and coworkers (Makradi et al., 2005) extend this model by considering a self-consistent approach based on the Eshelby result. It amounts to the use of a Maxwell branch as the intermolecular resistance, where the properties of the elastic and viscous elements are appropriate equivalent properties. The stress corresponding to the intermolecular resistance is thus given according to the Hencky model (see Equation (9.73)), with the isotropic elastic modulus $\mathbf{D}$ following the self-consistent method proposed by Hill (1965b). The flow rule for the viscous element is given by Equation (9.66), neglecting the volumetric part. The strain rate, $\dot{\gamma}_{\text{dev}}$, is defined as an average strain rate, $\dot{\bar{\gamma}}$, according to

$$\dot{\bar{\gamma}} = \frac{1}{V} \int_V \dot{\gamma}\, dV = \frac{1}{V} \sum_i V_i \dot{\gamma}_i, \tag{9.116}$$

where

$$\dot{\gamma}_i = \frac{1}{V_i} \int_{V_i} \dot{\gamma}\, dV_i, \tag{9.117}$$

with V_i denoting the volume of the ith phase and V representing the total volume. For each phase, the flow rule is also given by Equation (9.66), neglecting the volumetric part, with the strain rate in each phase following a power law (see Equation (9.23)). Thus, the average strain rate is also described by a power law, with an average strength $\bar{s}$. It can be shown, taking into account Eshelby's results for an ellipsoidal inclusion, that

$$\frac{\dot{\gamma}_i}{\dot{\bar{\gamma}}} = \frac{5}{3} - \frac{2}{3} \frac{s_i}{\bar{s}} \left(\frac{\dot{\gamma}_i}{\dot{\bar{\gamma}}} \right)^{1/n}, \tag{9.118}$$

which, combined with Equation (9.116) and the corresponding power law, yields the average strain rate. The authors employ the same description for the evolution of the crystallinity as Ahzi et al. (2003), in addition to Flory's theory, to predict the onset of crystallization as a function of the processing temperature and the extension of the polymer molecules. Later Regrain and coworkers (Regrain et al., 2009) extended the DID models to semi-crystalline models, employing a self-consistent scheme to consider the contribution of both phases.

A contribution that takes a different approach is that of Gueguen and coworkers (Gueguen et al., 2008). They focus only on modeling the yield behavior of semi-crystalline polymers, selecting a one-dimensional flow rule of the cooperative type (Equation (9.21)). The bulk crystallinity is included in the model through the use of a Taylor and Sachs-like mixture rule to compute the effective activation volume and activation energy that appear in the flow rule.

Dusunceli and Colak (2008) extend the viscoplasticity theory based on overstress (VBO) to include crystallinity. This is achieved by describing both phases employing the VBO model and considering their contributions using a Voigt or a Reuss mixture rule. The authors validate their model using polyethylenes (UHMWPE and XLPE) and PTFE.

Ayoub and coworkers (Ayoub et al., 2010, 2011) present a model very similar to Ahzi et al. (2003) and Boyce et al. (2000) to describe the mechanical behavior of HDPE. The inelastic mechanisms involve two parallel elements: a visco-hyperelastic network resistance acting in parallel with a viscoelastic–viscoplastic intermolecular resistance where the amorphous and crystalline phases are explicitly taken into consideration. The semi-crystalline polymer is considered as a two-phase composite similar to what has already been described. In the first contribution, both the crystalline and amorphous resistances are modeled employing the VBO model. Their contributions to the intermolecular resistance are incorporated through a Voigt mixture rule (see Equation (9.112)). In the second contribution, the elastic and viscous elements in crystalline and amorphous resistances are modeled employing Hencky's model (see Equation (9.73)) and a simplified version of Argon's model (see Equation (9.11)). They employ a modified Voigt mixture rule, where the contributions to the intermolecular resistance coming from the crystalline and amorphous phases are combined through

$$\boldsymbol{\sigma}_A = \chi^\beta \boldsymbol{\sigma}_c + (1-\chi)^\beta \boldsymbol{\sigma}_a, \tag{9.119}$$

where β is an appropriate exponent. Such an exponent is found from a fit of the Young's modulus as a function of the degree of crystallinity, as shown in Figure 8.8(a). When compared with the experimental results obtained for polyethylene samples containing degrees of crystallinity between 15% and 72%, the model can accurately capture the change in response with crystallinity before the strain hardening becomes evident. Different material parameters for each crystallinity are needed to capture the strain hardening at large strains (> 1). A similar model can be found in Abdul-Hameed et al. (2014), where the major difference is the substitution of the Maxwell branch in the network resistance for two branches, one corresponding to the amorphous contribution and the other to the crystalline contribution. They are combined as shown in Equation (9.119). This constitutive model attempts to generalize strain hardening behavior across different degrees of crystallinity, so that the same material parameters are used for all degrees of crystallinity. Very recently, Cundiff and coworkers (Cundiff et al., 2022) proposed another model where the inclusion of the crystallinity is achieved through the modified Voigt mixture rule (see Equation (9.119)). Regarding the constitutive description of each phase, it employs much of the same laws found in Ahzi et al. (2003) and Chowdhury et al. (2008). It describes strain rate crystallization through a rate equation similar to Equation (9.114).

Lastly, the two-phase model of Cangemi and Meimon for semi-crystalline polymers (Cangemi and Meimon, 2001) achieves the inclusion of the bulk crystallinity into the description of a semi-crystalline polymer in a different way. It is based on the continuum mixture theory such that according to the microstructure of semi-crystalline polymers, the free amorphous phase is assumed comparable to a fluid which saturates the complementary space to that of the solid structure, the crystalline phase plus the rigid amorphous phase.

The models described next include the crystalline orientation distribution into the description of the semi-crystalline polymer, instead of incorporating the bulk crystallinity. The earliest contributions in this direction are those of Parks and Ahzi (1990) and Ahzi and coworkers (Ahzi et al., 1994). Each lamella is treated as a grain in a polycrystalline aggregate, such that the amorphous regions are not explicitly modeled. This modeling option is justified by the high degree of crystallinity of the polymers studied (HDPE). The overall response is obtained through an appropriate mean-field homogenization scheme that takes into account the inability of a polymer crystallite to sustain shear such that there is extension along the chain direction. Each crystallite is modeled as a rigid rate-dependent viscoplastic crystal, following Equation (9.67), where the shear rate corresponding to each slip system is given by a power law (see Equation (9.23)). Hardening is not accounted for in their description given the thinness of the lamellae. The authors predict the evolution of texture and the macroscopic

stress–strain response. One more work in the same vein is that of Chen and coworkers (Chen et al., 1996).

Another approach is that of G'Sell, Dahoun, and coworkers (Dahoun et al., 1991). The constitutive description of each lamella follows a very similar rigid-viscoplastic crystal model as in Parks and Ahzi (1990), with the amorphous regions not explicitly modeled. The main difference is the interaction law employed to relate the microscopic and macroscopic fields. It is based on a local-global interaction model established for polycrystalline metal (Molinari et al., 1987), which also considers the kinematically indeterminate component of the stress in a rigid-viscoplastic crystal due to the locally inextensible direction. They consider a fully crystalline HDPE and make predictions regarding the large deformation texture and the macroscopic stress–strain response. Some of the same authors (G'sell and Dahoun, 1994; Dahoun et al., 1995) in an attempt to capture the contribution of the amorphous regions in the semi-crystalline polymer employ a Taylor mixture model to combine the contributions from the amorphous (rubber-like) and the crystalline (viscoplastic) portions of the polymer. They assume a temperature above the glass transition temperature and attempt to describe HDPE and PEEK subject to uniaxial tension and pure shear. The response of the amorphous portion of the polymer is given according to the elastic rubber model in Wu and Van Der Giessen (1993).

Another set of mean-field homogenization models for semi-crystalline polymers can be identified which attempts to incorporate both the bulk crystallinity and the crystalline orientation distribution into the constitutive description of semi-crystalline polymers, in addition to the orientation of the lamellae. Lee and coworkers (Lee et al., 1993a,b; Argon, 1997) propose a micromechanical model for semi-crystalline polymers based on a two-phase laminar composite approach. Each lamella is treated as a two-phase composite inclusion, where the crystalline phase is modeled as a power law rigid-viscoplastic crystal, following Equation (9.67), and the amorphous phase is also modeled as a power law rigid-viscoplastic material (Equation (9.65)) with a rubber-like backstress, following the eight-chain model (see Equation (9.76)). The overall response is obtained through interaction laws similar to the projected MFH models described in Sections 5.1.3 and 5.2.3.

Nikolov, Lebensohn and Raabe (2006) adopt a similar model, however the flow rule for the amorphous phase is not isotropic and it is related instead to an appropriate projection onto the corresponding lamella's normal plane. The hardening induced by the rubber-like backstress is also modified to account for coarse slip. The interaction law employed is based on the self-consistent scheme for polycrystalline metals already alluded to, proposed by Molinari and Ortiz (1987). Agoras and Ponte Castañeda (Agoras and Castañeda, 2012), based on their previous work (Agoras, 2010), propose yet another model where the description of the phases is also achieved through a rigid-viscoplastic law, but the interaction law employed is based on the variational approach denominated as the 'linear comparison composite method'.

Some studies focus solely on capturing the elastic response of semi-crystalline polymers through micromechanical modeling, employing several two-phase mean-field homogenization schemes (Guan and Pitchumani, 2004; Bedoui et al., 2006). Sedighiamiri et al. (2010); Gueguen et al. (2010); Ghazavizadeh et al. (2013) are examples of attempts to include the rigid-amorphous interphase that exists between the crystalline and amorphous phases in semi-crystalline polymers in a three-phase micromechanical model to predict the elastic response of semi-crystalline polymers. Other contributions extend the previous two-phase micromechanical models to include elasto-viscoplastic behavior in the amorphous and crystalline phases. One such example is the contribution of van Dommelen and coworkers (van Dommelen et al., 2003), where the authors propose the necessary adaptations to elastoplasticity of the projected interaction laws proposed in (Lee et al., 1993a,b). The work of Sedighiamiri and colleagues (Sedighiamiri et al., 2011, 2012, 2014) advances in the direction of more sophisticated nonlinear laws for the strain rates proposing the use of the Eyring model

(see Equation (9.3)) for both the amorphous and crystalline phases as an alternative to the power law (see Equation (9.23)). Mirkhalaf et al. (2019) follows this trend proposing a two-process flow of the Eyring type for the crystalline phase.

The variationally consistent projected MFH framework developed in Chapter 5 and explored numerically in Chapter 7 offers a natural setting in which this family of models can be revisited. A full specialization to the semi-crystalline polymer case would model the material as an aggregate composed of an amorphous matrix and many lamella-shaped crystalline inclusions with randomly oriented normals. The corresponding single-inclusion problem would reduce to a simple laminate problem. The crystalline phase would be described by the crystal-plasticity flow rule of Equation (9.67), and the amorphous phase by the deviatoric-volumetric flow rule of Equation (9.65) with the eight-chain rubber backstress of Equation (9.76). This model would be in the spirit of the models proposed by Lee and coworkers (Lee et al., 1993a,b) and van Dommelen and coworkers (van Dommelen et al., 2003), while being based on the variationally consistent MFH framework developed in the present work. A numerical realization of this specialization was not pursued here and is left as future work.

9.2.2 Full-field homogenization models

Despite the very high geometrical complexity of semi-crystalline polymers, evident in Figure 1.2(a), where the size of a single spherulite is typically on the order of micrometers and the thickness of the crystalline lamella on the order of nanometers, full-field homogenization models have also been proposed to describe their mechanical behavior. Doyle (2000) developed a finite element model whose basis is the composite inclusion to predict the elastic response of PE. Another contribution is that of van Dommelen and coworkers (van Dommelen et al., 2003), who developed a finite element micromechanical model to study the elasto-viscoplastic response of spherulitic PE. Alternatively, Uchida and coworkers (Tomita and Uchida, 2005; Uchida et al., 2010; Uchida and Tada, 2013) developed a large deformation finite element homogenization model of spherulitic HDPE. According to the authors, mean-field models are suitable when the macroscopic response and texture evolution are required. Meanwhile, the full-field models are appropriate when strain and stress distributions in the spherulite are required. Regarding the size of the representative domain, Teixeira-Pinto and coworkers (Teixeira-Pinto et al., 2016) claim that it significantly exceeds the size of a single spherulite. Some other FE-based contributions include those of Popa and coworkers (Popa et al., 2014) and Oktay and Gürses (Oktay and Gürses, 2015). Beyond the FE-based approaches, FFT-based full-field models have also been employed for semi-crystalline polymers (Bahloul et al., 2021).

Chapter 10

Conclusion and future work

10.1 Conclusions

The main goal of this work is twofold. First, we aim to contribute to the numerical tools available for the modeling of heterogeneous materials, and second, to apply these tools to the specific case of semi-crystalline polymers. Important steps are taken in this work toward both objectives.

In this work, we formulate MFH in a unified variational framework by embedding it within the PMVP and its dual, the PMCVP. After outlining both principles in the context of full-field homogenization, we emphasize their duality, pairing kinematic admissibility, displacement fluctuations, and stress homogenization in PMVP with static admissibility, stress-potential fields, and deformation gradient homogenization in PMCVP. We present the corresponding homogenization rules, along with the weak forms of the microscopic equilibrium and compatibility equations. Notably, the PMCVP remains largely unexplored in the literature; to address this, we provide a brief discussion regarding the weak form of the compatibility equation that follows from this principle, and a derivation showing that the homogenization rule for the deformation gradient leads to a macroscopic stress–deformation relation that respects the balance of angular momentum.

A concise formulation of MFH is provided, highlighting the role of single-inclusion problems and interaction models. The deformation and stress localization tensors are introduced as relevant quantities that are later used in linking microscopic and macroscopic fields within the PMVP and PMCVP frameworks, respectively. To embed MFH within PMVP, we introduce a minimal space of kinematically admissible displacement fluctuations, regular within each phase but potentially discontinuous across interfaces, subject to a vanishing volume-weighted average gradient. This construction enables a hierarchy of models: from the classical MFH formulation (fully constrained), to a projected variant generalizing the $\tilde{\boldsymbol{S}}$-inclusion model of Lee et al. (1993b,a), and finally the Sachs model, based on the least constrained space of admissible displacement fluctuations. These models are nested by construction, as highlighted in Figure 10.1, mirroring the hierarchy of boundary conditions in full-field PMVP applications (de Souza Neto et al., 2015). A key result is that the macroscopic stress is not given by the classical volume average but by a generalized expression involving deformation localization tensors. This rule emerges naturally from the PMVP postulates, without relying on ad hoc hypotheses. It guarantees mechanical power equivalence at micro and macro scales in elastic materials, but this equivalence generally breaks down in dissipative settings—highlighting the limitations of classical averaging schemes.

The dual development under the PMCVP follows an analogous path. We define a minimal space of statically admissible stress-potential fluctuations, regular within phases but potentially

discontinuous across interfaces, constrained by a vanishing volume-averaged curl. This inversion of roles allows for a complementary hierarchy of models: from the classical stress-driven MFH, to a projected variant related to the $\tilde{\boldsymbol{D}}$-inclusion model proposed by Lee et al. (1993b,a), and finally the Taylor model, based on the least constrained space. These models also form a nested structure and yield a non-classical deformation gradient homogenization rule that now features stress localization tensors.

The numerical results presented illustrate the performance of the various MFH models derived from both PMVP and PMCVP frameworks, for different loading conditions and interaction models. In particular, they highlight the importance of using consistent homogenization rules derived from variational principles to ensure angular-momentum balance and energetic consistency across scales.

In summary, the PMVP and PMCVP offer a systematic, variationally consistent, and dual foundation for MFH models. Their structure reinforces the symmetry between the roles of the stress and deformation localization tensors as mediators of the scale transition. The resulting homogenization rules are physically grounded, extensible to complex microstructures and nonlinear behavior, and they unify classical mean-field models within a robust multiscale framework.

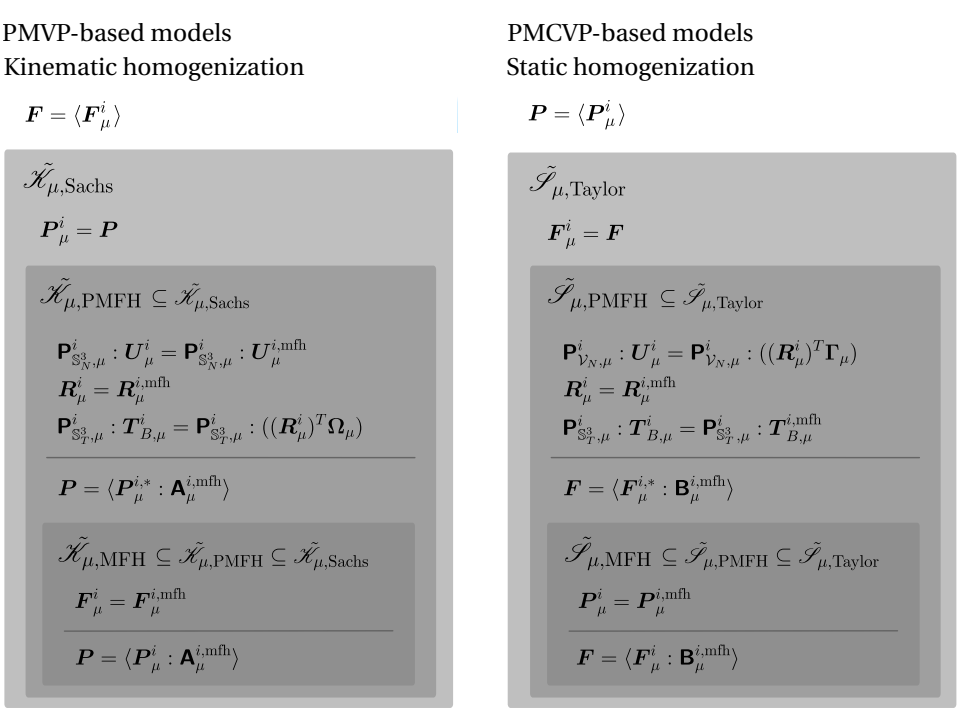

Figure 10.1: The sets of admissible displacement and stress-potential fluctuations in the various models considered are organized as nested subsets of the minimal admissible space, exhibiting a parallel structure. Likewise, the corresponding stress and deformation homogenization rules mirror each other, highlighting the duality between the kinematically and statically driven formulations.

Regarding the specific case of semi-crystalline polymers, we provide a comprehensive overview of their thermomechanical behavior and the state of the art in constitutive modeling. A thorough description of the mechanical response of semi-crystalline polymers is given, covering various experimental observations such as yield behavior, strain hardening, and the

influence of temperature, strain rate, and crystallinity. It is primarily based on this class of materials' response to various mechanical experiments, ranging from constant-strain-rate experiments to stress relaxation, creep, and dynamic mechanical analysis. Semi-crystalline polymers, in constant-strain-rate experiments, typically exhibit a response that consists of a linear stress–strain relationship followed by yield. A steady state is sometimes observed, followed by intense strain hardening at large strains. Regarding the influence of temperature on the behavior of this class of polymers, an increase in temperature leads to lower stiffness and yield strength. However, unlike glassy polymers, they retain usable structural properties even after the glass transition temperature is crossed. Common semi-crystalline polymers employed in commodity uses are HDPE and PP, while PA, PET, PPA, and PEEK satisfy the requirements of increasingly demanding engineering applications. The strain rate and the pressure exert the opposite effect to that of temperature on the stiffness and strength of semi-crystalline polymers. Furthermore, the yield phenomenon in semi-crystalline polymers is neither rate-independent nor linear with the strain rate, requiring appropriate nonlinear modeling.

Concerning the influence of bulk crystallinity and lamellar thickness, an increase in the former implies a nonlinear increase in stiffness and strength. In contrast, an increase in the latter results in a linear increase in strength for moderate thicknesses, but stagnates for thicker lamellae. Semi-crystalline polymers also have a double yield, which means that, as the strain increases, there are two distinct yield stresses. Semi-crystalline polymers may also exhibit thermal softening, in which higher strain rates cause significant heat production and temperature increases, softening the material. Furthermore, cold drawing is common, as observed when a neck develops in a uniaxial tensile test and the specimen thins in that region until the natural draw ratio is achieved. After that, the material in the neck has hardened sufficiently so that the thinned region travels across the specimen rather than continuing to thin until failure. Semi-crystalline polymer strain-hardening behavior is also similar to rubber elasticity.

In terms of the semi-crystalline polymer response to dynamic mechanical analysis, polymers with high crystallinity do not show a significant drop in storage modulus as frequency decreases in isothermal results. When the degree of crystallinity is low, a clear viscoelastic transition from glassy to leathery is observed. In isochronal results, one can observe the various relaxations present in semi-crystalline polymers. Relaxation I is visible at all crystallinity levels at lower temperatures, while relaxations II and III are more easily detectable at lower and higher crystallinities, respectively.

Finally, the thermal properties of semi-crystalline polymers are similar to those of other polymers in that they have a relatively large linear expansion coefficient and low thermal conductivity and diffusivity. This raises concerns about heat distortion when using semi-crystalline polymers in engineering applications and difficulties in tuning some manufacturing processes. On the other hand, they display a desirable behavior with respect to thermal shocks, despite the large linear thermal expansion coefficient, due to the relatively low Young's modulus.

With these experimental observations as a basis, an extensive overview of the state of the art in semi-crystalline polymer modeling is provided, emphasizing the rheological analogy and highlighting how the introduction of nonlinear viscous and elastic elements captures the complex behavior of these materials. Particular attention is given to these phenomenological models owing to their importance both in the direct modeling of semi-crystalline polymers and as the constitutive descriptions for the phases when computational homogenization is employed. Micromechanical models based on mean-field homogenization are also discussed, with a focus on their ability to capture the influence of microstructural features on the macroscopic response.

Finally, a theoretical outline of a constitutive model for semi-crystalline polymers based on

the work of Lee et al. (1993a,b) and van Dommelen et al. (2003), formulated within the MFH framework developed in this work, is provided; a full numerical realization was not pursued here and is left as future work.

10.2 Future research and challenges

Building on the research efforts already made in this work to establish a robust variational framework for MFH and its application to semi-crystalline polymers, we identify several avenues for future research and challenges that remain to be addressed. These include:

- **Energy consistency in dissipative settings:** Further investigation is needed to develop homogenization rules that ensure energy consistency across scales in materials exhibiting significant dissipation. This may involve exploring alternative variational principles or incorporating additional constraints into the MFH framework.
- **Comparison with full-field methods:** A systematic comparison between the MFH models derived from PMVP and PMCVP and full-field homogenization methods (e.g., FFT-based or finite-element-based approaches) would provide valuable insights into their accuracy and computational efficiency across various microstructures and loading conditions.
- **Mean-field thermomechanical homogenization:** Extending PMVP and PMCVP to fully coupled thermomechanical problems within the MFH context is a promising direction. This would involve formulating appropriate admissible spaces for thermal fields and deriving consistent homogenization rules that account for thermal effects.
- **Thermomechanical modeling of semi-crystalline polymers:** Developing constitutive models for semi-crystalline polymers within the MFH framework developed in this work, including the thermal field, is a natural next step. This would allow for a more accurate representation of the complex interplay between mechanical and thermal responses in these materials.

Bibliography

H. Abdul-Hameed, T. Messager, G. Ayoub, F. Zaïri, M. Naït-Abdelaziz, Z. Qu, and F. Zaïri. A two-phase hyperelastic-viscoplastic constitutive model for semi-crystalline polymers: Application to polyethylene materials with a variable range of crystal fractions. *Journal of the Mechanical Behavior of Biomedical Materials*, 37:323–332, September 2014. ISSN 17516161. doi: 10.1016/j.jmbbm.2014.04.016. URL https://linkinghub.elsevier.com/retrieve/pii/S1751616114001258.

Jacob Aboudi. Micromechanical Analysis of Composites by the Method of Cells. *Applied Mechanics Reviews*, 42(7):193–221, July 1989. ISSN 0003-6900. doi: 10.1115/1.3152428. URL https://doi.org/10.1115/1.3152428.

M. Agoras and P. Ponte Castañeda. Multi-scale homogenization-based modeling of semi-crystalline polymers. *Philosophical Magazine*, 92(8):925–958, March 2012. ISSN 1478-6435. doi: 10.1080/14786435.2011.637982.

Michalis Agoras. *On Macroscopic Constitutive Relations and Microstructure Evolution in Multi-Scale Viscoplastic Composites*. PhD thesis, University of Pennsylvania, 2010.

S. Ahzi, B. J. Lee, and R. J. Asaro. Plasticity and anisotropy evolution in crystalline polymers. *Materials Science and Engineering: A*, 189(1):35–44, December 1994. ISSN 0921-5093. doi: 10.1016/0921-5093(94)90399-9.

S. Ahzi, A. Makradi, R.V. Gregory, and D.D. Edie. Modeling of deformation behavior and strain-induced crystallization in poly(ethylene terephthalate) above the glass transition temperature. *Mechanics of Materials*, 35(12):1139–1148, December 2003. ISSN 01676636. doi: 10.1016/S0167-6636(03)00004-8. URL https://linkinghub.elsevier.com/retrieve/pii/S0167663603000048. tex.ids= ahziModelingDeformationBehavior2003a.

Ryan Alberdi, Guodong Zhang, and Kapil Khandelwal. A framework for implementation of RVE-based multiscale models in computational homogenization using isogeometric analysis. *International Journal for Numerical Methods in Engineering*, 114(9):1018–1051, 2018. ISSN 1097-0207. doi: 10.1002/nme.5775.

H. Alexander and P. Haasen. Dislocations and Plastic Flow in the Diamond Structure. In Frederick Seitz, David Turnbull, and Henry Ehrenreich, editors, *Solid State Physics*, volume 22, pages 27–158. Academic Press, January 1969. doi: 10.1016/S0081-1947(08)60031-4. URL https://www.sciencedirect.com/science/article/pii/S0081194708600314.

Nicoli M. Ames, Vikas Srivastava, Shawn A. Chester, and Lallit Anand. A thermo-mechanically coupled theory for large deformations of amorphous polymers. Part II: Applications. *International Journal of Plasticity*, 25(8):1495–1539, August 2009. ISSN 07496419. doi:

10.1016/j.ijplas.2008.11.005. URL https://linkinghub.elsevier.com/retrieve/pii/S074964190800171X.

A. Amiri-Rad, L.V. Pastukhov, L.E. Govaert, and J.A.W. van Dommelen. An anisotropic viscoelastic-viscoplastic model for short-fiber composites. *Mechanics of Materials*, 137:103141, 2019. ISSN 0167-6636. doi: https://doi.org/10.1016/j.mechmat.2019.103141. URL https://www.sciencedirect.com/science/article/pii/S0167663619301693.

L. Anand and N.M. Ames. On modeling the micro-indentation response of an amorphous polymer. *International Journal of Plasticity*, 22(6):1123–1170, 2006. ISSN 0749-6419. doi: https://doi.org/10.1016/j.ijplas.2005.07.006. URL https://www.sciencedirect.com/science/article/pii/S0749641905001415.

Lallit Anand and Morton E. Gurtin. A theory of amorphous solids undergoing large deformations, with application to polymeric glasses. *International Journal of Solids and Structures*, 40(6):1465–1487, March 2003. ISSN 00207683. doi: 10.1016/S0020-7683(02)00651-0. URL https://linkinghub.elsevier.com/retrieve/pii/S0020768302006510.

Lallit Anand, Nicoli M. Ames, Vikas Srivastava, and Shawn A. Chester. A thermo-mechanically coupled theory for large deformations of amorphous polymers. Part I: Formulation. *International Journal of Plasticity*, 25(8):1474–1494, August 2009. ISSN 07496419. doi: 10.1016/j.ijplas.2008.11.004. URL https://linkinghub.elsevier.com/retrieve/pii/S0749641908001708.

Franklin R. Anderson. Morphology of Isothermally Bulk-Crystallized Linear Polyethylene. *Journal of Applied Physics*, 35(1):64–70, January 1964. ISSN 0021-8979, 1089-7550. doi: 10.1063/1.1713100. URL http://aip.scitation.org/doi/10.1063/1.1713100.

Reinaldo A. Anonis, Javier L. Mroginski, and Pablo J. Sánchez. Multiscale formulation for materials composed by a saturated porous matrix and solid inclusions. *Computer Methods in Applied Mechanics and Engineering*, 429:117162, September 2024. ISSN 0045-7825. doi: 10.1016/j.cma.2024.117162.

A. S. Argon. A theory for the low-temperature plastic deformation of glassy polymers. *Philosophical Magazine*, 28(4):839–865, October 1973. ISSN 0031-8086. doi: 10.1080/14786437308220987. URL http://www.tandfonline.com/doi/abs/10.1080/14786437308220987.

Ali Argon. *The Physics of Deformation and Fracture of Polymers*. Cambridge University Press, 2013. ISBN 978-0-521-82184-1.

A.S. Argon. Morphological mechanisms and kinetics of large-strain plastic deformation and evolution of texture in semicrystalline polymers. *Journal of Computer-Aided Materials Design*, 4(2):75–98, 1997. ISSN 09281045. doi: 10.1023/A:1008608517177. URL http://link.springer.com/10.1023/A:1008608517177.

Rida B. Arieby, Kaïs Mrabet, Osama A. Terfas, Cédric Laurent, and Rachid Rahouadj. Anisotropic mechanical behavior of semi-crystalline polymers: Characterization and modeling of non-monotonic loading including damage. *Journal of Applied Polymer Science*, 134(7), 2017. ISSN 1097-4628. doi: 10.1002/app.44468. URL https://onlinelibrary.wiley.com/doi/abs/10.1002/app.44468. _eprint: https://onlinelibrary.wiley.com/doi/pdf/10.1002/app.44468.

R. G. C. Arridge, P. J. Barham, and A. Keller. Self-hardening of highly oriented polyethylene. *Journal of Polymer Science: Polymer Physics Edition*, 15(3):389–401, March 1977. ISSN 00981273, 15429385. doi: 10.1002/pol.1977.180150301. URL https://onlinelibrary.wiley.com/doi/10.1002/pol.1977.180150301.

Ellen M. Arruda and Mary C. Boyce. Evolution of plastic anisotropy in amorphous polymers during finite straining. *International Journal of Plasticity*, 9(6):697–720, January 1993. ISSN 0749-6419. doi: 10.1016/0749-6419(93)90034-N. URL https://www.sciencedirect.com/science/article/pii/074964199390034N.

Ellen M. Arruda, Mary C. Boyce, and R. Jayachandran. Effects of strain rate, temperature and thermomechanical coupling on the finite strain deformation of glassy polymers. *Mechanics of Materials*, 19(2-3):193–212, January 1995. ISSN 01676636. doi: 10.1016/0167-6636(94)00034-E. URL https://linkinghub.elsevier.com/retrieve/pii/016766369400034E. tex.ids= arrudaEffectsStrainRate1995a.

Maxim Arzhakov. *Relaxation in Physical and Mechanical Behavior of Polymers*. CRC Press, 1 edition, January 2019. ISBN 978-0-429-24452-0. doi: 10.1201/9780429244520. URL https://www.taylorfrancis.com/books/9780429521263.

M. F. Ashby. *Materials selection in mechanical design*. Butterworth-Heinemann, Oxford, OX ; Boston, MA, 2nd ed edition, 1999. ISBN 978-0-7506-4357-3.

P. Atkins and J. de Paula. *Atkins' physical chemistry*. OUP Oxford, 2010. ISBN 978-0-19-954337-3. URL https://books.google.pt/books?id=BV6cAQAAQBAJ. tex.lccn: 2010286938.

G. Ayoub, F. Zaïri, M. Naït-Abdelaziz, and J.M. Gloaguen. Modelling large deformation behaviour under loading–unloading of semicrystalline polymers: Application to a high density polyethylene. *International Journal of Plasticity*, 26(3):329–347, March 2010. ISSN 07496419. doi: 10.1016/j.ijplas.2009.07.005. URL https://linkinghub.elsevier.com/retrieve/pii/S0749641909000928. tex.ids= ayoubModellingLargeDeformation2010a.

G. Ayoub, F. Zaïri, C. Fréderix, J.M. Gloaguen, M. Naït-Abdelaziz, R. Seguela, and J.M. Lefebvre. Effects of crystal content on the mechanical behaviour of polyethylene under finite strains: Experiments and constitutive modelling. *International Journal of Plasticity*, 27(4):492–511, April 2011. ISSN 07496419. doi: 10.1016/j.ijplas.2010.07.005. URL https://linkinghub.elsevier.com/retrieve/pii/S0749641910000963.

F. Baaijens. Calculation of residual stresses in injection molded products. *Rheologica Acta*, 30: 284–299, 1991.

Amine Bahloul, Issam Doghri, and Laurent Adam. Linking a phase field model for polymer crystallization to full-field micromechanical simulations of semi-crystalline polymers. *Computational Materials Science*, 199:110685, November 2021. ISSN 0927-0256. doi: 10.1016/j.commatsci.2021.110685.

R. Balieu, F. Lauro, B. Bennani, T. Matsumoto, and E. Mottola. Non-associated viscoplasticity coupled with an integral-type nonlocal damage model for mineral filled semi-crystalline polymers. *Computers & Structures*, 134:18–31, April 2014. ISSN 00457949. doi: 10.1016/j.compstruc.2013.12.006. URL https://linkinghub.elsevier.com/retrieve/pii/S0045794913003386.

R. Balieu, F. Lauro, B. Bennani, G. Haugou, F. Chaari, T. Matsumoto, and E. Mottola. Damage at high strain rates in semi-crystalline polymers. *International Journal of Impact Engineering*, 76:1–8, February 2015. ISSN 0734743X. doi: 10.1016/j.ijimpeng.2014.08.013. URL https://linkinghub.elsevier.com/retrieve/pii/S0734743X14001924.

S.G. Bardenhagen, M.G. Stout, and G.T. Gray. Three-dimensional, finite deformation, viscoplastic constitutive models for polymeric materials. *Mechanics of Materials*, 25(4):235–253, May 1997. ISSN 01676636. doi: 10.1016/S0167-6636(97)00007-0. URL https://linkinghub.elsevier.com/retrieve/pii/S0167663697000070.

Z. Bartczak, R. E. Cohen, and A. S. Argon. Evolution of the crystalline texture of high-density polyethylene during uniaxial compression. *Macromolecules*, 25(18):4692–4704, August 1992. ISSN 0024-9297, 1520-5835. doi: 10.1021/ma00044a034. URL https://pubs.acs.org/doi/abs/10.1021/ma00044a034.

J. C. Bauwens. Relation between the compression yield stress and the mechanical loss peak of bisphenol-A-polycarbonate in the ? transition range. *Journal of Materials Science*, 7(5):577–584, May 1972. ISSN 0022-2461, 1573-4803. doi: 10.1007/BF00761956. URL http://link.springer.com/10.1007/BF00761956. tex.ids= bauwensRelationCompressionYield1972.

J. C. Bauwens, C. Bauwens-Crowet, and G. Homès. Tensile yield-stress behavior of poly(vinyl chloride) and polycarbonate in the glass transition region. *Journal of Polymer Science Part A-2: Polymer Physics*, 7(10):1745–1754, October 1969. ISSN 04492978, 15429377. doi: 10.1002/pol.1969.160071010. URL https://onlinelibrary.wiley.com/doi/10.1002/pol.1969.160071010.

C. Bauwens-Crowet. The compression yield behaviour of polymethyl methacrylate over a wide range of temperatures and strain-rates. *Journal of Materials Science*, 8(7):968–979, July 1973. ISSN 0022-2461, 1573-4803. doi: 10.1007/BF00756628. URL http://link.springer.com/10.1007/BF00756628.

F Bedoui, J Diani, G Regnier, and W Seiler. Micromechanical modeling of isotropic elastic behavior of semicrystalline polymers. *Acta Materialia*, 54(6):1513–1523, April 2006. ISSN 13596454. doi: 10.1016/j.actamat.2005.11.028. URL https://linkinghub.elsevier.com/retrieve/pii/S1359645405006920.

F. Beffa. *Weakly Nonlinear Systems: With Applications in Communications Systems*. Understanding Complex Systems. Springer Nature Switzerland, 2023. ISBN 978-3-031-40681-2. URL https://books.google.pt/books?id=dp3fEAAAQBAJ.

J.G.J Beijer and J.L Spoormaker. Modelling of creep behaviour in injection-moulded HDPE. *Polymer*, 41(14):5443–5449, June 2000. ISSN 00323861. doi: 10.1016/S0032-3861(99)00753-3. URL https://linkinghub.elsevier.com/retrieve/pii/S0032386199007533.

H. Ben Hadj Hamouda, L. Laiarinandrasana, and R. Piques. Viscoplastic behaviour of a medium density polyethylene (MDPE): Constitutive equations based on double nonlinear deformation model. *International Journal of Plasticity*, 23(8):1307–1327, August 2007. ISSN 07496419. doi: 10.1016/j.ijplas.2006.11.007. URL https://linkinghub.elsevier.com/retrieve/pii/S0749641906001586.

Y. Benveniste. A new approach to the application of Mori-Tanaka's theory in composite materials. *Mechanics of Materials*, 6(2):147–157, June 1987. ISSN 0167-6636. doi: 10.1016/0167-6636(87)90005-6. URL https://www.sciencedirect.com/science/article/pii/0167663687900056.

J Bergström. Constitutive modeling of ultra-high molecular weight polyethylene under large-deformation and cyclic loading conditions. *Biomaterials*, 23(11):2329–2343, June 2002. ISSN 01429612. doi: 10.1016/S0142-9612(01)00367-2. URL https://linkinghub.elsevier.com/retrieve/pii/S0142961201003672.

J.S. Bergström. *Mechanics of Solid Polymers : Theory and Computational Modeling*. Plastics Design Library. Elsevier Science, 2015. ISBN 978-0-323-32296-6. URL https://books.google.pt/books?id=DfucBAAAQBAJ.

J.S. Bergström and Mary C. Boyce. Constitutive modeling of the large strain time-dependent behavior of elastomers. *Journal of the Mechanics and Physics of Solids*, 46(5):931–954, May 1998. ISSN 00225096. doi: 10.1016/S0022-5096(97)00075-6. URL https://linkinghub.elsevier.com/retrieve/pii/S0022509697000756.

J.S. Bergström and M.C. Boyce. Large strain time-dependent behaviour of filled elastomers. *Mechanics of Materials*, 32:627–644, 11 2000. doi: 10.1016/S0167-6636(00)00028-4.

J.S. Bergström and M.C. Boyce. Constitutive modeling of the time-dependent and cyclic loading of elastomers and application to soft biological tissues. *Mechanics of Materials*, 33(9):523–530, September 2001. ISSN 01676636. doi: 10.1016/S0167-6636(01)00070-9. URL https://linkinghub.elsevier.com/retrieve/pii/S0167663601000709. tex.ids= bergstromConstitutiveModelingTimedependent2001a.

J.S. Bergström and L.B. Hilbert. A constitutive model for predicting the large deformation thermomechanical behavior of fluoropolymers. *Mechanics of Materials*, 37(8):899–913, August 2005. ISSN 01676636. doi: 10.1016/j.mechmat.2004.09.002. URL https://linkinghub.elsevier.com/retrieve/pii/S0167663604001310.

Jörgen S. Bergström, C.M. Rimnac, and S.M. Kurtz. Prediction of multiaxial mechanical behavior for conventional and highly crosslinked UHMWPE using a hybrid constitutive model. *Biomaterials*, 24(8):1365–1380, April 2003. ISSN 01429612. doi: 10.1016/S0142-9612(02)00514-8. URL https://linkinghub.elsevier.com/retrieve/pii/S0142961202005148.

V.A Bershtein and V.M Yegorov. General mechanism of the beta transition in polymers. *Polymer Science U.S.S.R.*, 27(11):2743–2757, January 1985. ISSN 00323950. doi: 10.1016/0032-3950(85)90477-0. URL https://linkinghub.elsevier.com/retrieve/pii/0032395085904770.

M. Berveiller and A. Zaoui. An extension of the self-consistent scheme to plastically-flowing polycrystals. *Journal of the Mechanics and Physics of Solids*, 26(5-6):325–344, October 1978. ISSN 00225096. doi: 10.1016/0022-5096(78)90003-0.

P. J. Blanco, P. J. Sánchez, E. A. de Souza Neto, and R. A. Feijóo. The method of multiscale virtual power for the derivation of a second order mechanical model. *Mechanics of Materials*, 99:53–67, August 2016a. ISSN 0167-6636. doi: 10.1016/j.mechmat.2016.05.003.

P. J. Blanco, A. Clausse, and R. A. Feijóo. Homogenization of the Navier-Stokes equations by means of the Multi-scale Virtual Power Principle. *Computer Methods in Applied Mechanics and Engineering*, 315:760–779, March 2017. ISSN 0045-7825. doi: 10.1016/j.cma.2016.11.022.

P. J. Blanco, P. J. Sánchez, F. F. Rocha, S. Toro, and R. A. Feijóo. A consistent multiscale mechanical formulation for media with randomly distributed voids. *International Journal of Solids and Structures*, 283:112494, November 2023. ISSN 0020-7683. doi: 10.1016/j.ijsolstr.2023.112494.

Pablo J. Blanco and Sebastián M. Giusti. Thermomechanical Multiscale Constitutive Modeling: Accounting for Microstructural Thermal Effects. *Journal of Elasticity*, 115(1):27–46, March 2014. ISSN 1573-2681. doi: 10.1007/s10659-013-9445-2.

Pablo J Blanco, Pablo J Sánchez, Eduardo Alberto de Souza Neto, and Raúl A Feijóo. Variational foundations and generalized unified theory of RVE-based multiscale models. *Archives of Computational Methods in Engineering*, 23(2):191–253, 2016b.

J. Blumm, A. Lindemann, M. Meyer, and C. Strasser. Characterization of PTFE Using Advanced Thermal Analysis Techniques. *International Journal of Thermophysics*, 31(10):1919–1927, October 2010. ISSN 1572-9567. doi: 10.1007/s10765-008-0512-z. URL https://doi.org/10.1007/s10765-008-0512-z.

S. R. Bodner and Y. Partom. A Large Deformation Elastic-Viscoplastic Analysis of a Thick-Walled Spherical Shell. *Journal of Applied Mechanics*, 39(3):751–757, September 1972. ISSN 0021-8936. doi: 10.1115/1.3422784.

S. R. Bodner and Y. Partom. Constitutive Equations for Elastic-Viscoplastic Strain-Hardening Materials. *Journal of Applied Mechanics*, 42(2):385–389, June 1975. ISSN 0021-8936. doi: 10.1115/1.3423586.

J.L. Bouvard, D.K. Francis, M.A. Tschopp, E.B. Marin, D.J. Bammann, and M.F. Horstemeyer. An internal state variable material model for predicting the time, thermomechanical, and stress state dependence of amorphous glassy polymers under large deformation. *International Journal of Plasticity*, 42:168–193, 2013. ISSN 0749-6419. doi: 10.1016/j.ijplas.2012.10.005.

P. B. Bowden and R. J. Young. Deformation mechanisms in crystalline polymers. *Journal of Materials Science*, 9(12):2034–2051, December 1974. ISSN 0022-2461, 1573-4803. doi: 10.1007/BF00540553. URL http://link.springer.com/10.1007/BF00540553.

Mary C. Boyce, David M. Parks, and Ali S. Argon. Large inelastic deformation of glassy polymers. part I: rate dependent constitutive model. *Mechanics of Materials*, 7(1):15–33, September 1988. ISSN 01676636. doi: 10.1016/0167-6636(88)90003-8. URL https://linkinghub.elsevier.com/retrieve/pii/0167663688900038.

M.C. Boyce, S. Socrate, and P.G. Llana. Constitutive model for the finite deformation stress–strain behavior of poly(ethylene terephthalate) above the glass transition. *Polymer*, 41(6):2183–2201, March 2000. ISSN 00323861. doi: 10.1016/S0032-3861(99)00406-1. URL https://linkinghub.elsevier.com/retrieve/pii/S0032386199004061.

L. Brassart, L. Stainier, I. Doghri, and L. Delannay. A variational formulation for the incremental homogenization of elasto-plastic composites. *Journal of the Mechanics and Physics of Solids*, 59(12):2455–2475, December 2011. ISSN 00225096. doi: 10.1016/j.jmps.2011.09.004. URL https://linkinghub.elsevier.com/retrieve/pii/S0022509611001712.

L. Brassart, L. Stainier, I. Doghri, and L. Delannay. Homogenization of elasto-(visco) plastic composites based on an incremental variational principle. *International Journal of Plasticity*, 36:86–112, September 2012. ISSN 07496419. doi: 10.1016/j.ijplas.2012.03.010. URL https://linkinghub.elsevier.com/retrieve/pii/S0749641912000502.

H. C. Brinkman and F. Schwarzl. A mechanical and thermodynamical theory of non-linear relaxation behaviour of solids. *Discussions of the Faraday Society*, 23:11, 1957. ISSN 0366-9033. doi: 10.1039/df9572300011. URL http://xlink.rsc.org/?DOI=df9572300011.

N. W. J. Brooks, R. A. Duckett, and I. M. Ward. Modeling of double yield points in polyethylene: Temperature and strain-rate dependence. *Journal of Rheology*, 39(2):425–436, March 1995. ISSN 0148-6055, 1520-8516. doi: 10.1122/1.550705. URL http://sor.scitation.org/doi/10.1122/1.550705.

A. M. Brown and M. F. Ashby. On the power-law creep equation. *Scripta Metallurgica*, 14(12): 1297–1302, December 1980. ISSN 0036-9748. doi: 10.1016/0036-9748(80)90182-9. URL https://www.sciencedirect.com/science/article/pii/0036974880901829.

E. N. Brown, R. B. Willms, G. T. Gray, P. J. Rae, C. M. Cady, K. S. Vecchio, J. Flowers, and M. Y. Martinez. Influence of Molecular Conformation on the Constitutive Response of Polyethylene: A Comparison of HDPE, UHMWPE, and PEX. *Experimental Mechanics*, 47(3):381–393, June 2007. ISSN 0014-4851, 1741-2765. doi: 10.1007/s11340-007-9045-9. URL https://link.springer.com/10.1007/s11340-007-9045-9.

N. Brusselle-Dupend, D. Lai, X. Feaugas, M. Guigon, and M. Clavel. Mechanical behavior of a semicrystalline polymer before necking. Part 1: Characterization of uniaxial behavior. *Polymer Engineering & Science*, 41(1):66–76, 2001. ISSN 1548-2634. doi: 10.1002/pen.10709.

N. Brusselle-Dupend, D. Lai, X. Feaugas, M. Guigon, and M. Clavel. Mechanical behavior of a semicrystalline polymer before necking. Part II: Modeling of uniaxial behavior. *Polymer Engineering & Science*, 43(2):501–518, 2003. ISSN 1548-2634. doi: 10.1002/pen.10041.

C. P. Buckley and D. C. Jones. Glass-rubber constitutive model for amorphous polymers near the glass transition. *Polymer*, 36(17):3301–3312, January 1995. ISSN 0032-3861. doi: 10.1016/0032-3861(95)99429-X. URL https://www.sciencedirect.com/science/article/pii/003238619599429X.

G. Cailletaud and K. Saï. Study of plastic/viscoplastic models with various inelastic mechanisms. *International Journal of Plasticity*, 11(8):991–1005, January 1995. ISSN 07496419. doi: 10.1016/S0749-6419(95)00040-2. URL https://linkinghub.elsevier.com/retrieve/pii/S0749641995000402.

Gérard Calleja, Alex Jourdan, Bruno Ameduri, and Jean-Pierre Habas. Where is the glass transition temperature of poly(tetrafluoroethylene)? A new approach by dynamic rheometry and mechanical tests. *European Polymer Journal*, 49(8):2214–2222, August 2013. ISSN 0014-3057. doi: 10.1016/j.eurpolymj.2013.04.028. URL https://www.sciencedirect.com/science/article/pii/S0014305713002164.

W.D. Callister and D.G. Rethwisch. *Materials science and engineering*. Wiley, 2014. ISBN 978-1-118-31922-2. URL https://books.google.pt/books?id=99UeMAEACAAJ.

L. Cangemi and Y. Meimon. A Two-Phase Model for the Mechanical Behavior of Semicrystalline Polymers. *Oil & Gas Science and Technology*, 56(6):555–580, November 2001. ISSN 1294-4475. doi: 10.2516/ogst:2001045. URL http://ogst.ifpenergiesnouvelles.fr/10.2516/ogst:2001045. tex.ids= cangemiTwoPhaseModelMechanical2001a.

A. Francisca Carvalho Alves, Bernardo P. Ferreira, and F.M. Andrade Pires. A constitutive model for amorphous thermoplastics from low to high strain rates: Formulation and computational aspects. *International Journal of Plasticity*, 169:103712, 2023. ISSN 0749-6419. doi: https://doi.org/10.1016/j.ijplas.2023.103712. URL https://www.sciencedirect.com/science/article/pii/S0749641923001961.

P.Ponte Castañeda. The effective mechanical properties of nonlinear isotropic composites. *Journal of the Mechanics and Physics of Solids*, 39(1):45–71, 1991. ISSN 00225096. doi: 10.1016/0022-5096(91)90030-R. URL https://linkinghub.elsevier.com/retrieve/pii/002250969190030R.

E. P. Cernocky and E. Krempl. A theory of viscoplasticity based on infinitesimal total strain. *Acta Mechanica*, 36(3):263–289, September 1980. ISSN 1619-6937. doi: 10.1007/BF01214636.

J Chaboche, P Kanoute, and A Roos. On the capabilities of mean-field approaches for the description of plasticity in metal matrix composites. *International Journal of Plasticity*, 21 (7):1409–1434, July 2005. ISSN 07496419. doi: 10.1016/j.ijplas.2004.07.001.

M. X. Chen, Q. S. Zheng, and W. Yang. A micromechanical model of texture induced orthotropy in planar crystalline polymers. *Journal of the Mechanics and Physics of Solids*, 44(2):157–178, February 1996. ISSN 0022-5096. doi: 10.1016/0022-5096(95)00076-3.

Yi-chao Chen and Lewis Wheeler. Derivatives of the stretch and rotation tensors. *Journal of Elasticity*, 32:175–182, 1992.

B. W. Cherry and C. M. Holmes. Yield of adhesive joints. *Journal of Physics D: Applied Physics*, 2 (6):821, June 1969. ISSN 0022-3727. doi: 10.1088/0022-3727/2/6/307. URL https://dx.doi.org/10.1088/0022-3727/2/6/307.

D. R. J. Chillingworth, J. E. Marsden, and Y. H. Wan. Symmetry and Bifurcation in Three-Dimensional Elasticity, Part I. *Arch. Rational Mech. Anal.*, 80(4):295–331, 1982. ISSN 0003-9527, 1432-0673. doi: 10.1007/BF00253119. URL http://link.springer.com/10.1007/BF00253119.

D. R. J. Chillingworth, J. E. Marsden, and Y. H. Wan. Symmetry and Bifurcation in Three-Dimensional Elasticity. Part II. *Arch. Rational Mech. Anal.*, 83(4):363–395, 1983. ISSN 0003-9527, 1432-0673. doi: 10.1007/BF00963840. URL http://link.springer.com/10.1007/BF00963840.

K. A. Chowdhury, R. Talreja, and A. A. Benzerga. Effects of Manufacturing-Induced Voids on Local Failure in Polymer-Based Composites. *Journal of Engineering Materials and Technology*, 130(2), March 2008. ISSN 0094-4289. doi: 10.1115/1.2841529.

R. M. Christensen and K. H. Lo. Solutions for effective shear properties in three phase sphere and cylinder models. *Journal of the Mechanics and Physics of Solids*, 27(4):315–330, August 1979. ISSN 0022-5096. doi: 10.1016/0022-5096(79)90032-2. URL https://www.sciencedirect.com/science/article/pii/0022509679900322.

R.M. Christensen. *Theory of viscoelasticity*. Dover civil and mechanical engineering. Dover Publications, 2nd edition edition, 2013. ISBN 978-0-486-31896-7. URL https://books.google.pt/books?id=h7TDAgAAQBAJ.

M. Ciampa, M. Franciosi, and M. Poletti. Linear Differential Equations and Related Continuous LTI Systems. *Circuits, Systems, and Signal Processing*, 38(10):4465–4503, October 2019. ISSN 1531-5878. doi: 10.1007/s00034-019-01080-7. URL https://doi.org/10.1007/s00034-019-01080-7.

Philippe G. Ciarlet. *Linear and Nonlinear Functional Analysis with Applications*. Applied mathematics. Society for Industrial and Applied Mathematics (SIAM), Philadelphia, PA, 2013. ISBN 978-1-61197-258-0. Number: 130.

O Colak. Modeling deformation behavior of polymers with viscoplasticity theory based on overstress. *International Journal of Plasticity*, 21(1):145–160, January 2005. ISSN 07496419. doi: 10.1016/j.ijplas.2004.04.004. URL https://linkinghub.elsevier.com/retrieve/pii/S074964190400049X.

Bernard D. Coleman and Victor J. Mizel. Existence of Caloric Equations of State in Thermodynamics. *The Journal of Chemical Physics*, 40(4):1116–1125, February 1964. ISSN 0021-9606, 1089-7690. doi: 10.1063/1.1725257. URL http://aip.scitation.org/doi/10.1063/1.1725257. tex.ids= colemanExistenceCaloricEquations1964a publisher: American Institute of Physics.

Bernard D. Coleman and Walter Noll. Foundations of Linear Viscoelasticity. *Reviews of Modern Physics*, 33(2):239–249, April 1961. doi: 10.1103/RevModPhys.33.239. URL https://link.aps.org/doi/10.1103/RevModPhys.33.239. Publisher: American Physical Society.

H. Conrad. The athermal component of the flow stress in crystalline solids. *Materials Science and Engineering*, 6(4):265–273, October 1970. ISSN 00255416. doi: 10.1016/0025-5416(70)90054-6. URL https://linkinghub.elsevier.com/retrieve/pii/0025541670900546.

K.N. Cundiff, G. Ayoub, and A.A. Benzerga. Modeling the viscoplastic behavior of a semicrystalline polymer. *International Journal of Solids and Structures*, 254-255:111920, November 2022. ISSN 00207683. doi: 10.1016/j.ijsolstr.2022.111920. URL https://linkinghub.elsevier.com/retrieve/pii/S0020768322003778.

A. Dahoun, G. R. Canova, A. Molinari, M. J. Philippe, and Ch. G/sell. The Modelling of Large Strain Textures and Stress-Strain Relations of Polyethylene. *Texture, Stress, and Microstructure*, 14(1):736469, 1991. ISSN 1687-5400. doi: 10.1155/TSM.14-18.347.

A. Dahoun, M. Aboulfaraj, C. G'Sell, A. Molinari, and G. R. Canova. Plastic behavior and deformation textures of poly(etherether ketone) under uniaxial tension and simple shear. *Polymer Engineering and Science*, 35(4):317–330, February 1995. ISSN 0032-3888, 1548-2634. doi: 10.1002/pen.760350406. URL https://onlinelibrary.wiley.com/doi/10.1002/pen.760350406.

I. S. Dairanieh, A. J. Mchugh, and A. K. Doufas. A Phenomenological Model for Flow-Induced Crystallization. *Journal of Reinforced Plastics and Composites*, 18(5):464–471, March 1999. ISSN 0731-6844, 1530-7964. doi: 10.1177/073168449901800506. URL http://journals.sagepub.com/doi/10.1177/073168449901800506.

Misael Dalbosco, Thiago A. Carniel, Eduardo A. Fancello, and Gerhard A. Holzapfel. Multiscale numerical analyses of arterial tissue with embedded elements in the finite strain regime. *Computer Methods in Applied Mechanics and Engineering*, 381:113844, August 2021. ISSN 0045-7825. doi: 10.1016/j.cma.2021.113844.

EA de Souza Neto and RA Feijóo. On the equivalence between spatial and material volume averaging of stress in large strain multi-scale solid constitutive models. *Mechanics of materials*, 40(10):803–811, 2008. Publisher: Elsevier.

E.A. De Souza Neto, Djordje Perić, and D.R.J. Owen. A model for elastoplastic damage at finite strains: Algorithmicissues and applications. *Engineering Computations*, 11(3):257–281, January 1994. ISSN 0264-4401. doi: 10.1108/02644409410799272.

E.A. de Souza Neto, D. Peric, and D.R.J. Owen. *Computational Methods for Plasticity: Theory and Applications*. Wiley, 2008. ISBN 978-0-470-69452-7. URL https://books.google.pt/books?id=cBrQmlQW8YAC.

Eduardo Alberto de Souza Neto, Pablo Javier Blanco, Pablo Javier Sánchez, and Raúl Antonino Feijóo. An RVE-based multiscale theory of solids with micro-scale inertia and body force effects. *Mechanics of Materials*, 80:136–144, 2015. doi: 10.1016/j.mechmat.2014.10.007. tex.ids= desouzanetoRVEbasedMultiscaleTheory2015a publisher: Elsevier.

B. Fraeijs de Veubeke. A new variational principle for finite elastic displacements. *International Journal of Engineering Science*, 10(9):745–763, September 1972. ISSN 0020-7225. doi: 10.1016/0020-7225(72)90079-1. URL https://www.sciencedirect.com/science/article/pii/0020722572900791.

I. Doghri and A. Ouaar. Homogenization of two-phase elasto-plastic composite materials and structures. *International Journal of Solids and Structures*, 40(7):1681–1712, April 2003. ISSN 00207683. doi: 10.1016/S0020-7683(03)00013-1.

I. Doghri, L. Adam, and N. Bilger. Mean-field homogenization of elasto-viscoplastic composites based on a general incrementally affine linearization method. *International Journal of Plasticity*, 26(2):219–238, February 2010. ISSN 07496419. doi: 10.1016/j.ijplas.2009.06.003.

Masao Doi and S. F. Edwards. Dynamics of concentrated polymer systems. Part 1.—Brownian motion in the equilibrium state. *J. Chem. Soc., Faraday Trans. 2*, 74(0):1789–1801, 1978. ISSN 0300-9238. doi: 10.1039/F29787401789. URL http://xlink.rsc.org/?DOI=F29787401789.

Wanderson F. dos Santos, Igor A. Rodrigues Lopes, Francisco M. Andrade Pires, and Sergio P. B. Proença. Second-order multi-scale modelling of natural and architected materials in the presence of voids: Formulation and numerical implementation. *Computer Methods in Applied Mechanics and Engineering*, 416:116374, November 2023. ISSN 0045-7825. doi: 10.1016/j.cma.2023.116374.

Wanderson F. dos Santos, Igor A. Rodrigues Lopes, Francisco M. Andrade Pires, and Sergio P. B. Proença. Exploring novel mechanical metamaterials: Unravelling deformation mode coupling and size effects through second-order computational homogenisation. *International Journal of Solids and Structures*, 292:112724, April 2024. ISSN 0020-7683. doi: 10.1016/j.ijsolstr.2024.112724.

Michael J. Doyle. On the effect of crystallinity on the elastic properties of semicrystalline polyethylene. *Polymer Engineering & Science*, 40(2):330–335, 2000. ISSN 1548-2634. doi: 10.1002/pen.11166.

A. D. Drozdov. Finite viscoelasticity and viscoplasticity of semicrystalline polymers. *Continuum Mechanics and Thermodynamics*, 19(1-2):111–132, June 2007. ISSN 0935-1175, 1432-0959. doi: 10.1007/s00161-007-0049-6. URL http://link.springer.com/10.1007/s00161-007-0049-6.

A.D. Drozdov, A.-L. Høg Lejre, and J. deC. Christiansen. Viscoelasticity, viscoplasticity, and creep failure of polypropylene/clay nanocomposites. *Composites Science and Technology*, 69(15-16):2596–2603, December 2009. ISSN 02663538. doi: 10.1016/j.compscitech.2009.07.018. URL https://linkinghub.elsevier.com/retrieve/pii/S0266353809002917.

R. A. Duckett, S. Rabinowitz, and I. M. Ward. The strain-rate, temperature and pressure dependence of yield of isotropic poly(methylmethacrylate) and poly(ethylene terephthalate). *Journal of Materials Science*, 5(10):909–915, October 1970. ISSN 0022-2461, 1573-4803. doi: 10.1007/BF00574864. URL http://link.springer.com/10.1007/BF00574864.

Necmi Dusunceli and Ozgen U. Colak. Modelling effects of degree of crystallinity on mechanical behavior of semicrystalline polymers. *International Journal of Plasticity*, 24(7):1224–1242, July 2008. ISSN 07496419. doi: 10.1016/j.ijplas.2007.09.003. URL https://linkinghub.elsevier.com/retrieve/pii/S0749641907001258.

George J. Dvorak. Transformation field analysis of inelastic composite materials. *Proceedings of the Royal Society of London. Series A: Mathematical and Physical Sciences*, 437(1900):311–327, May 1992. ISSN 0962-8444, 2053-9177. doi: 10.1098/rspa.1992.0063. URL https://royalsocietypublishing.org/doi/10.1098/rspa.1992.0063.

S. F. Edwards and Th. Vilgis. The effect of entanglements in rubber elasticity. *Polymer*, 27(4):483–492, April 1986. ISSN 0032-3861. doi: 10.1016/0032-3861(86)90231-4.

Zakaria El-Qoubaa and Ramzi Othman. Strain rate sensitivity of polyetheretherketone's compressive yield stress at low and high temperatures. *Mechanics of Materials*, 95:15–27, April 2016. ISSN 01676636. doi: 10.1016/j.mechmat.2015.12.008. URL https://linkinghub.elsevier.com/retrieve/pii/S0167663615002793.

J. D. Eshelby. The continuum theory of lattice defects. *Solid State Physics*, 3:79–144, 1956.

John Douglas Eshelby. The determination of the elastic field of an ellipsoidal inclusion, and related problems. *Proceedings of the Royal Society of London. Series A. Mathematical and Physical Sciences*, 241(1226):376–396, 1957. doi: 10.1098/rspa.1957.0133.

Adrian Luis Eterovic and Klaus-Jürgen Bathe. A hyperelastic-based large strain elasto-plastic constitutive formulation with combined isotropic-kinematic hardening using the logarithmic stress and strain measures. *International Journal for Numerical Methods in Engineering*, 30(6):1099–1114, 1990. doi: https://doi.org/10.1002/nme.1620300602. URL https://onlinelibrary.wiley.com/doi/abs/10.1002/nme.1620300602.

A. G. Evans and R. D. Rawlings. The Thermally Activated Deformation of Crystalline Materials. *physica status solidi (b)*, 34(1):9–31, 1969. ISSN 03701972, 15213951. doi: 10.1002/pssb.19690340102. URL https://onlinelibrary.wiley.com/doi/10.1002/pssb.19690340102.

David J Eyre and Graeme W Milton. A fast numerical scheme for computing the response of composites using grid refinement. *The European Physical Journal Applied Physics*, 6(1):41–47, 1999. Publisher: EDP Sciences.

Henry Eyring. Viscosity, Plasticity, and Diffusion as Examples of Absolute Reaction Rates. *The Journal of Chemical Physics*, 4(4):283–291, April 1936. ISSN 0021-9606, 1089-7690. doi: 10.1063/1.1749836. URL http://aip.scitation.org/doi/10.1063/1.1749836.

S. Fakirov and B. Krasteva. On the Glass Transition Temperature of Polyethylene as Revealed by Microhardness Measurements. *Journal of Macromolecular Science, Part B*, 39(2):297–301, March 2000. ISSN 0022-2348, 1525-609X. doi: 10.1081/MB-100100386. URL https://www.tandfonline.com/doi/full/10.1081/MB-100100386.

Joseph A. Faucher. Viscoelastic Behavior of Polyethylene and Polypropylene. *Transactions of the Society of Rheology*, 3(1):81–93, March 1959. ISSN 0038-0032. doi: 10.1122/1.548844. URL https://sor.scitation.org/doi/abs/10.1122/1.548844. Publisher: The Society of Rheology.

Bernardo P. Ferreira, A. Francisca Carvalho Alves, and F.M. Andrade Pires. An efficient finite strain constitutive model for amorphous thermoplastics: Fully implicit computational implementation and optimization-based parameter calibration. *Computers & Structures*, 281: 107007, 2023. ISSN 0045-7949. doi: https://doi.org/10.1016/j.compstruc.2023.107007. URL https://www.sciencedirect.com/science/article/pii/S0045794923000378.

Ferry. *Viscoelastic Properties of Polymers*. Wiley, 1980.

Frédéric Feyel. *Application du calcul parallèle aux modèles à grand nombre de variables internes*. These de doctorat, ENSMP, January 1998. URL https://theses.fr/1998ENMP0864.

Frédéric Feyel. A multilevel finite element method (FE2) to describe the response of highly non-linear structures using generalized continua. *Computer Methods in Applied Mechanics and Engineering*, 192(28):3233–3244, July 2003. ISSN 0045-7825. doi: 10.1016/S0045-7825(03)00348-7. URL https://www.sciencedirect.com/science/article/pii/S0045782503003487.

Frédéric Feyel and Jean-Louis Chaboche. FE2 multiscale approach for modelling the elastoviscoplastic behaviour of long fibre SiC/Ti composite materials. *Computer Methods in Applied Mechanics and Engineering*, 183(3):309–330, March 2000. ISSN 0045-7825. doi: 10.1016/S0045-7825(99)00224-8. URL https://www.sciencedirect.com/science/article/pii/S0045782599002248.

D. G. Fotheringham and B. W. Cherry. The role of recovery forces in the deformation of linear polyethylene. *Journal of Materials Science*, 13(5):951–964, May 1978. ISSN 0022-2461, 1573-4803. doi: 10.1007/BF00544690. URL http://link.springer.com/10.1007/BF00544690.

David Fotheringham, B. W. Cherry, and C. Bauwens-Crowet. Comment on "the compression yield behaviour of polymethyl methacrylate over a wide range of temperatures and strain-rates". *Journal of Materials Science*, 11(7):1368–1371, July 1976. ISSN 1573-4803. doi: 10.1007/BF00545162.

Geoffrey J Frank and Robert A Brockman. A viscoelastic–viscoplastic constitutive model for glassy polymers. *International Journal of Solids and Structures*, 38(30):5149–5164, July 2001. ISSN 0020-7683. doi: 10.1016/S0020-7683(00)00339-5.

H. J. Frost and M. F. Ashby. *Deformation-mechanism Maps: The Plasticity and Creep of Metals and Ceramics*. Elsevier Science Limited, 1982. ISBN 978-0-08-029337-0. Google-Books-ID: s9BRAAAAMAAJ.

Jevan Furmanski, Carl M. Cady, and Eric N. Brown. Time–temperature equivalence and adiabatic heating at large strains in high density polyethylene and ultrahigh molecular weight polyethylene. *Polymer*, 54(1):381–390, January 2013. ISSN 00323861. doi: 10.1016/j.polymer.2012.11.010. URL https://linkinghub.elsevier.com/retrieve/pii/S003238611200938X.

D. Garcia-Gonzalez, A. Rusinek, T. Jankowiak, and A. Arias. Mechanical impact behavior of polyether–ether–ketone (PEEK). *Composite Structures*, 124:88–99, June 2015. ISSN 02638223. doi: 10.1016/j.compstruct.2014.12.061. URL https://linkinghub.elsevier.com/retrieve/pii/S0263822314007272.

Thomas A. Garrity. *All the Mathematics You Missed: But Need to Know for Graduate School*. Cambridge University Press, Cambridge, UK, 2002. ISBN 0-521-79285-1. Includes bibliographical references and index.

Akbar Ghazavizadeh, Gregory C. Rutledge, Ali A. Atai, Saïd Ahzi, Yves Rémond, and Nasser Soltani. Micromechanical characterization of the interphase layer in semi-crystalline polyethylene. *Journal of Polymer Science Part B: Polymer Physics*, 51(16):1228–1243, 2013. ISSN 1099-0488. doi: 10.1002/polb.23319.

Elhem Ghorbel. A viscoplastic constitutive model for polymeric materials. *International Journal of Plasticity*, 24(11):2032–2058, November 2008. ISSN 07496419. doi: 10.1016/j.ijplas.2008.01.003. URL https://linkinghub.elsevier.com/retrieve/pii/S0749641908000119. tex.ids= ghorbelViscoplasticConstitutiveModel2008a.

J. J. Gilman. Dislocation Sources in Crystals. *Journal of Applied Physics*, 30(10):1584–1594, October 1959. ISSN 0021-8979, 1089-7550. doi: 10.1063/1.1735005. URL http://aip.scitation.org/doi/10.1063/1.1735005.

John J. Gilman. THE PLASTIC WAVE MYTH. In S. C. Schmidt, R. D. Dick, J. W. Forbes, and D. G. Tasker, editors, *Shock Compression of Condensed Matter–1991*, pages 387–389. Elsevier, Amsterdam, January 1992. ISBN 978-0-444-89732-9. doi: 10.1016/B978-0-444-89732-9.50087-X.

L. Govaert, Peter Timmermans, and W. Brekelmans. The Influence of Intrinsic Strain Softening on Strain Localization in Polycarbonate: Modeling and Experimental Validation. *Journal of Engineering Materials and Technology-transactions of The Asme - J. Eng. Mater. Technol.*, 122, April 2000. doi: 10.1115/1.482784.

C. G'sell and A. Dahoun. Evolution of microstructure in semi-crystalline polymers under large plastic deformation. *Materials Science and Engineering: A*, 175(1-2):183–199, February 1994. ISSN 09215093. doi: 10.1016/0921-5093(94)91058-8. URL https://linkinghub.elsevier.com/retrieve/pii/0921509394910588.

C. G'sell and J. J. Jonas. Determination of the plastic behaviour of solid polymers at constant true strain rate. *Journal of Materials Science*, 14(3):583–591, March 1979. ISSN 1573-4803. doi: 10.1007/BF00772717. URL https://doi.org/10.1007/BF00772717.

C. G'Sell and J. J. Jonas. Yield and transient effects during the plastic deformation of solid polymers. *Journal of Materials Science*, 16(7):1956–1974, July 1981. ISSN 0022-2461, 1573-4803. doi: 10.1007/BF00540644. URL http://link.springer.com/10.1007/BF00540644.

C. G'Sell, J. M. Hiver, A. Dahoun, and A. Souahi. Video-controlled tensile testing of polymers and metals beyond the necking point. *Journal of Materials Science*, 27(18):5031–5039, September 1992. ISSN 1573-4803. doi: 10.1007/BF01105270.

Christian G'Sell, Serge Boni, and Suresh Shrivastava. Application of the plane simple shear test for determination of the plastic behaviour of solid polymers at large strains. *Journal of Materials Science*, 18(3):903–918, March 1983. ISSN 1573-4803. doi: 10.1007/BF00745590. URL https://doi.org/10.1007/BF00745590.

X. Guan and R. Pitchumani. A micromechanical model for the elastic properties of semicrystalline thermoplastic polymers. *Polymer Engineering and Science*, 44(3):433–451, March 2004. ISSN 0032-3888, 1548-2634. doi: 10.1002/pen.20039. URL https://onlinelibrary.wiley.com/doi/10.1002/pen.20039.

Muralidhar Reddy Gudimetla and Issam Doghri. A finite strain thermodynamically-based constitutive framework coupling viscoelasticity and viscoplasticity with application to glassy polymers. *International Journal of Plasticity*, 98:197–216, 2017. ISSN 0749-6419. doi: https:

//doi.org/10.1016/j.ijplas.2017.08.001. URL https://www.sciencedirect.com/science/article/pii/S0749641917301286.

José Miranda Guedes and Noboru Kikuchi. Preprocessing and postprocessing for materials based on the homogenization method with adaptive finite element methods. *Computer Methods in Applied Mechanics and Engineering*, 83(2):143–198, October 1990. ISSN 0045-7825. doi: 10.1016/0045-7825(90)90148-F. URL https://www.sciencedirect.com/science/article/pii/004578259090148F.

O. Gueguen, J. Richeton, S. Ahzi, and A. Makradi. Micromechanically based formulation of the cooperative model for the yield behavior of semi-crystalline polymers. *Acta Materialia*, 56(7):1650–1655, April 2008. ISSN 1359-6454. doi: 10.1016/j.actamat.2007.12.015.

O. Gueguen, S. Ahzi, A. Makradi, and S. Belouettar. A new three-phase model to estimate the effective elastic properties of semi-crystalline polymers: Application to PET. *Mechanics of Materials*, 42(1):1–10, January 2010. ISSN 0167-6636. doi: 10.1016/j.mechmat.2009.04.012.

M. E. Gurtin. A Generalization of the Beltrami Stress Functions in Continuum Mechanics. *Archive for Rational Mechanics and Analysis*, 13(1):321–329, December 1963. ISSN 0003-9527, 1432-0673. doi: 10.1007/BF01262700. URL http://link.springer.com/10.1007/BF01262700.

Morton E. Gurtin. *An Introduction to Continuum Mechanics*, volume 158 of *Mathematics in Science and Engineering*. Academic Press, 1981. ISBN 0-12-309750-9.

George Halsey, Howard J. White, and Henry Eyring. Mechanical Properties of Textiles, I. *Textile Research Journal*, 15(9):295–311, September 1945. ISSN 0040-5175, 1746-7748. doi: 10.1177/004051754501500901. URL http://journals.sagepub.com/doi/10.1177/004051754501500901.

P. Hao, Z. Dai, V. Laheri, and F. A. Gilabert. A unified amorphous–crystalline viscoplastic hardening law for non-isothermal modelling of thermoplastics and thermosets. *International Journal of Plasticity*, 159:103469, December 2022a. ISSN 0749-6419. doi: 10.1016/j.ijplas.2022.103469. URL https://www.sciencedirect.com/science/article/pii/S0749641922002479. tex.ids= haoUnifiedAmorphousCrystalline2022a.

P. Hao, V. Laheri, Z. Dai, and F.A. Gilabert. A rate-dependent constitutive model predicting the double yield phenomenon, self-heating and thermal softening in semi-crystalline polymers. *International Journal of Plasticity*, 153:103233, June 2022b. ISSN 07496419. doi: 10.1016/j.ijplas.2022.103233. URL https://linkinghub.elsevier.com/retrieve/pii/S0749641922000201.

O. A. Hasan and M. C. Boyce. A constitutive model for the nonlinear viscoelastic viscoplastic behavior of glassy polymers. *Polymer Engineering & Science*, 35(4):331–344, 1995. ISSN 1548-2634. doi: 10.1002/pen.760350407.

O. A. Hasan, M. C. Boyce, X. S. Li, and S. Berko. An investigation of the yield and postyield behavior and corresponding structure of poly(methyl methacrylate). *Journal of Polymer Science Part B: Polymer Physics*, 31(2):185–197, 1993. ISSN 1099-0488. doi: 10.1002/polb.1993.090310207.

J. Haussy, J. P. Cavrot, B. Escaig, and J. M. Lefebvre. Thermodynamic analysis of the plastic deformation of glassy poly(methyl methacrylate). *Journal of Polymer Science: Polymer Physics Edition*, 18(2):311–325, February 1980. ISSN 00981273, 15429385. doi: 10.1002/pol.1980.180180214. URL https://onlinelibrary.wiley.com/doi/10.1002/pol.1980.180180214.

R. N. Haward and G. Thackray. The use of a mathematical model to describe isothermal stress-strain curves in glassy thermoplastics. *Proceedings of the Royal Society of London. Series A. Mathematical and Physical Sciences*, 302(1471):453–472, January 1968. ISSN 0080-4630, 2053-9169. doi: 10.1098/rspa.1968.0029. URL https://royalsocietypublishing.org/doi/10.1098/rspa.1968.0029.

R. Hill. Continuum micro-mechanics of elastoplastic polycrystals. *Journal of the Mechanics and Physics of Solids*, 13(2):89–101, April 1965a. ISSN 00225096. doi: 10.1016/0022-5096(65)90023-2. URL https://linkinghub.elsevier.com/retrieve/pii/0022509665900232.

R. Hill. A self-consistent mechanics of composite materials. *Journal of the Mechanics and Physics of Solids*, 13(4):213–222, August 1965b. ISSN 00225096. doi: 10.1016/0022-5096(65)90010-4. URL https://linkinghub.elsevier.com/retrieve/pii/0022509665900104.

Rodney Hill. On constitutive macro-variables for heterogeneous solids at finite strain. *Proceedings of the Royal Society of London. A. Mathematical and Physical Sciences*, 326(1565):131–147, January 1997. doi: 10.1098/rspa.1972.0001. URL https://royalsocietypublishing.org/doi/abs/10.1098/rspa.1972.0001. Publisher: Royal Society.

R. Hiss, S. Hobeika, C. Lynn, and G. Strobl. Network Stretching, Slip Processes, and Fragmentation of Crystallites during Uniaxial Drawing of Polyethylene and Related Copolymers. A Comparative Study. *Macromolecules*, 32(13):4390–4403, June 1999. ISSN 0024-9297. doi: 10.1021/ma981776b. URL https://doi.org/10.1021/ma981776b. Publisher: American Chemical Society.

K. Ho and E. Krempl. Extension of the viscoplasticity theory based on overstress (VBO) to capture non-standard rate dependence in solids. *International Journal of Plasticity*, 18(7):851–872, July 2002. ISSN 07496419. doi: 10.1016/S0749-6419(01)00011-0. URL https://linkinghub.elsevier.com/retrieve/pii/S0749641901000110.

S. Hobeika, Y. Men, and G. Strobl. Temperature and Strain Rate Independence of Critical Strains in Polyethylene and Poly(ethylene-co-vinyl acetate). *Macromolecules*, 33(5):1827–1833, March 2000. ISSN 0024-9297. doi: 10.1021/ma9910484. URL https://doi.org/10.1021/ma9910484. Publisher: American Chemical Society.

John D. Hoffman, G. Williams, and E. Passaglia. Analysis of the alpha, beta, and gamma relaxations in polychlorotrifluoroethylene and polyethylene: Dielectric and mechanical properties. *Journal of Polymer Science Part C: Polymer Symposia*, 14(1):173–235, March 2007. ISSN 04492994, 19353065. doi: 10.1002/polc.5070140116. URL https://onlinelibrary.wiley.com/doi/10.1002/polc.5070140116.

D. W. Holmes, J. G. Loughran, and H. Suehrcke. Constitutive model for large strain deformation of semicrystalline polymers. *Mechanics of Time-Dependent Materials*, 10(4):281–313, December 2006. ISSN 1385-2000, 1573-2738. doi: 10.1007/s11043-007-9023-8. URL https://link.springer.com/10.1007/s11043-007-9023-8.

Sami Holopainen and Thierry Barriere. Modeling of mechanical behavior of amorphous solids undergoing fatigue loadings, with application to polymers. *Computers & Structures*, 199:57–73, 2018. ISSN 0045-7949. doi: https://doi.org/10.1016/j.compstruc.2018.01.010. URL https://www.sciencedirect.com/science/article/pii/S0045794917312221.

Sami Holopainen, Thierry Barriere, Gang Cheng, and Reijo Kouhia. Continuum approach for modeling fatigue in amorphous glassy polymers. applications to the investigation of damage-ratcheting interaction in polycarbonate. *International Journal of Plasticity*, 91:109–133, 2017. ISSN 0749-6419. doi: https://doi.org/10.1016/j.ijplas.2016.12.001. URL https://www.sciencedirect.com/science/article/pii/S0749641916303242.

Gerhard A. Holzapfel. *Nonlinear Solid Mechanics: A Continuum Approach for Engineering*. Wiley, April 2000. ISBN 978-0-471-82319-3.

K. Hong, A. Rastogi, and G. Strobl. A Model Treating Tensile Deformation of Semicrystalline Polymers: Quasi-Static Stress-Strain Relationship and Viscous Stress Determined for a Sample of Polyethylene. *Macromolecules*, 37(26):10165–10173, December 2004a. ISSN 0024-9297. doi: 10.1021/ma049174h. URL https://doi.org/10.1021/ma049174h. tex.ids= hongModelTreatingTensile2004a publisher: American Chemical Society.

K. Hong, A. Rastogi, and G. Strobl. Model Treatment of Tensile Deformation of Semicrystalline Polymers: Static Elastic Moduli and Creep Parameters Derived for a Sample of Polyethylene. *Macromolecules*, 37(26):10174–10179, 2004b. ISSN 0024-9297. doi: 10.1021/ma049172x. URL https://doi.org/10.1021/ma049172x.

Muneo Hori and Sia Nemat-Nasser. Universal bounds for effective piezoelectric moduli. *Mechanics of Materials*, 30(1):1–19, September 1998. ISSN 0167-6636. doi: 10.1016/S0167-6636(98)00029-5. URL https://www.sciencedirect.com/science/article/pii/S0167663698000295.

M.F. Horstemeyer and P. Wang. Cradle-to-grave simulation-based design incorporating multiscale microstructure-property modeling: Reinvigorating design with science. *Journal of Computer-Aided Materials Design*, 10(1):13–34, 2003. ISSN 0928-1045. doi: 10.1023/B:JCAD.0000024171.13480.24.

Y. Huang, K. X. Hu, X. Wei, and A. Chandra. A generalized self-consistent mechanics method for composite materials with multiphase inclusions. *Journal of the Mechanics and Physics of Solids*, 42(3):491–504, March 1994. ISSN 0022-5096. doi: 10.1016/0022-5096(94)90028-0. URL https://www.sciencedirect.com/science/article/pii/0022509694900280.

John Woodside Hutchinson and Robert Hill. Bounds and self-consistent estimates for creep of polycrystalline materials. *Proceedings of the Royal Society of London. A. Mathematical and Physical Sciences*, 348(1652):101–127, January 1997. doi: 10.1098/rspa.1976.0027. URL https://royalsocietypublishing.org/doi/abs/10.1098/rspa.1976.0027. Publisher: Royal Society.

Martín I Idiart and Pedro Ponte Castañeda. Field statistics in nonlinear composites. I. Theory. *Proceedings of the Royal Society A: Mathematical, Physical and Engineering Sciences*, 463(2077):183–202, January 2007. ISSN 1364-5021, 1471-2946. doi: 10.1098/rspa.2006.1756. URL https://royalsocietypublishing.org/doi/10.1098/rspa.2006.1756.

Chengkai Jiang. Finite deformation constitutive model for macro-yield behavior of amorphous glassy polymers with a molecular entanglement-based internal-state variable. *International Journal of Mechanical Sciences*, 161-162:105064, 08 2019. doi: 10.1016/j.ijmecsci.2019.105064.

Chengkai Jiang, Zhongmeng Zhu, Jianwei Zhang, and Zhuoran YANG. Constitutive modeling of the rate- and temperature-dependent macro-yield behavior of amorphous glassy polymers. *International Journal of Mechanical Sciences*, 179:105653, 04 2020. doi: 10.1016/j.ijmecsci.2020.105653.

Joakim Johnsen, Arild Clausen, Frode Grytten, Ahmed Benallal, and Odd Hopperstad. A thermo-elasto-viscoplastic constitutive model for polymers. *Journal of the Mechanics and Physics of Solids*, 124, 11 2018. doi: 10.1016/j.jmps.2018.11.018.

W. G. Johnston. Yield Points and Delay Times in Single Crystals. *Journal of Applied Physics*, 33 (9):2716–2730, September 1962. ISSN 0021-8979, 1089-7550. doi: 10.1063/1.1702538. URL http://aip.scitation.org/doi/10.1063/1.1702538.

Lionel Jolly. *Analyse de la microstructure du polyamide 11 par diffusion des rayons X : application à une déformation uniaxiale*. phdthesis, Université Paul Verlaine - Metz, January 2000. URL https://hal.univ-lorraine.fr/tel-01748942.

A. Keller and D. P. Pope. Identification of structural processes in deformation of oriented polyethylene. *Journal of Materials Science*, 6(6):453–478, June 1971. ISSN 0022-2461, 1573-4803. doi: 10.1007/BF00550302. URL http://link.springer.com/10.1007/BF00550302.

James M. Kelly and Peter P. Gillis. The influence of a limiting dislocation flux on the mechanical response of polycrystalline metals. *International Journal of Solids and Structures*, 10(1):45–59, January 1974. ISSN 0020-7683. doi: 10.1016/0020-7683(74)90100-0.

E H Kerner. The Elastic and Thermo-elastic Properties of Composite Media. *Proceedings of the Physical Society. Section B*, 69(8):808–813, August 1956. ISSN 0370-1301. doi: 10.1088/0370-1301/69/8/305. URL https://iopscience.iop.org/article/10.1088/0370-1301/69/8/305.

Hassan Khaleghi, Ahmad Amiri-Rad, and Mohammad Mashayekhi. A thermodynamically consistent continuum damage model for time-dependent failure of thermoplastic polymers. *International Journal of Plasticity*, 154:103278, 2022. ISSN 0749-6419. doi: https://doi.org/10.1016/j.ijplas.2022.103278. URL https://www.sciencedirect.com/science/article/pii/S0749641922000614.

A Khan and B Farrokh. Thermo-mechanical response of nylon 101 under uniaxial and multi-axial loadings: Part I, Experimental results over wide ranges of temperatures and strain rates. *International Journal of Plasticity*, 22(8):1506–1529, August 2006. ISSN 07496419. doi: 10.1016/j.ijplas.2005.10.001.

Yash P. Khanna, Edith A. Turi, Thomas J. Taylor, Virgil V. Vickroy, and Richard F. Abbott. Dynamic mechanical relaxations in polyethylene. *Macromolecules*, 18(6):1302–1309, June 1985. ISSN 0024-9297, 1520-5835. doi: 10.1021/ma00148a045. URL https://pubs.acs.org/doi/abs/10.1021/ma00148a045.

F. Khoury and E. Passaglia. The Morphology of Crystalline Synthetic Polymers. In N. B. Hannay, editor, *Treatise on Solid State Chemistry*, pages 335–496. Springer US, Boston, MA, 1976. ISBN 978-1-4684-2666-3 978-1-4684-2664-9. doi: 10.1007/978-1-4684-2664-9_6. URL http://link.springer.com/10.1007/978-1-4684-2664-9_6. tex.ids= khouryMorphologyCrystallineSynthetic1976a.

Masayoshi Kitagawa and Hideyuki Takagi. Nonlinear constitutive equation for polyethylene under combined tension and torsion. *Journal of Polymer Science Part B: Polymer Physics*, 28 (11):1943–1953, 1990. ISSN 1099-0488. doi: 10.1002/polb.1990.090281105.

Masayoshi Kitagawa and Takeshi Yoneyama. Plastic dilatation due to compression in polymer solids. *Journal of Polymer Science Part C: Polymer Letters*, 26(4): 207–212, 1988. ISSN 1543-0472. doi: 10.1002/pol.1988.140260407. URL https:

//onlinelibrary.wiley.com/doi/abs/10.1002/pol.1988.140260407. _eprint: https://onlinelibrary.wiley.com/doi/pdf/10.1002/pol.1988.140260407.

Masayoshi Kitagawa, Tatsuya Mori, and Tomohiko Matsutani. Rate-dependent nonlinear constitutive equation of polypropylene. *Journal of Polymer Science Part B: Polymer Physics*, 27 (1):85–95, 1989. ISSN 1099-0488. doi: 10.1002/polb.1989.090270106.

Dale Klahn, Amiya K Mukherjee, and John E Dorn. Strain-rate Effects. In *Proceedings of the 2nd International Conference on the Strength of Metals and Alloys*. California Univ., Berkeley. Lawrence Radiation Lab., 1970. Keynote paper. Also issued as Lawrence Radiation Laboratory Report UCRL-20320, University of California, Berkeley. AEC Contract No. W-7405-eng-48.

Thomas Kletschkowski, Uwe Schomburg, and Albrecht Bertram. Endochronic viscoplastic material models for filled PTFE. *Mechanics of Materials*, 34(12):795–808, December 2002. ISSN 0167-6636. doi: 10.1016/S0167-6636(02)00197-7. URL https://www.sciencedirect.com/science/article/pii/S0167663602001977.

U.F. Kocks, A.S. Argon, and M.F. Ashby. *Thermodynamics and kinetics of slip*. Progress in materials science. Pergamon Press, 1975. ISBN 978-0-08-017964-3. URL https://books.google.pt/books?id=B0AkMgEACAAJ. tex.lccn: 75012519.

W. T. Koiter. On the Principle of Stationary Complementary Energy in the Nonlinear Theory of Elasticity. *SIAM Journal on Applied Mathematics*, 25(3):424–434, November 1973. ISSN 0036-1399, 1095-712X. doi: 10.1137/0125043. URL http://epubs.siam.org/doi/10.1137/0125043.

Warner T. Koiter. On the Complementary Energy Theorem in Non-Linear Elasticity Theory. In Gaetano Fichera, editor, *Trends in applications of pure mathematics to mechanics*, volume 2 of *Monographs and studies in mathematics*, pages 207–232. Pitman Publishing, London, 1976. ISBN 0-273-00129-9.

A. Krairi, I. Doghri, J. Schalnat, G. Robert, and W. Van Paepegem. Thermo-mechanical coupling of a viscoelastic-viscoplastic model for thermoplastic polymers: Thermodynamical derivation and experimental assessment. *International Journal of Plasticity*, 115:154–177, 2019. ISSN 0749-6419. doi: https://doi.org/10.1016/j.ijplas.2018.11.016. URL https://www.sciencedirect.com/science/article/pii/S0749641918304522.

Anouar Krairi and Issam Doghri. A thermodynamically-based constitutive model for thermoplastic polymers coupling viscoelasticity, viscoplasticity and ductile damage. *International Journal of Plasticity*, 60:163–181, 2014. ISSN 0749-6419. doi: https://doi.org/10.1016/j.ijplas.2014.04.010. URL https://www.sciencedirect.com/science/article/pii/S074964191400093X.

Erhard Krempl and Kwangsoo Ho. An overstress model for solid polymer deformation behavior applied to Nylon 66. *ASTM special technical publication*, 1357:118–140, 2000.

Ekkehart Kröner. Berechnung der elastischen Konstanten des Vielkristalls aus den Konstanten des Einkristalls. *Zeitschrift für Physik*, 151(4):504–518, August 1958. ISSN 0044-3328. doi: 10.1007/BF01337948. URL https://doi.org/10.1007/BF01337948.

S. M. Kurtz, C. W. Jewett, J. R. Foulds, and A. A. Edidin. A miniature specimen mechanical testing technique scaled to articulating surface of polyethylene components for total joint arthroplasty. *Journal of Biomedical Materials Research*, 48(1):75–81, 1999. ISSN 1097-4636. doi: 10.1002/(SICI)1097-4636(1999)48:1<75::AID-

JBM13>3.0.CO;2-H. URL https://onlinelibrary.wiley.com/doi/abs/10.1002/%28SICI%291097-4636%281999%2948%3A1%3C75%3A%3AAID-JBM13%3E3.0.CO%3B2-H. _eprint: https://onlinelibrary.wiley.com/doi/pdf/10.1002/%28SICI%291097-4636%281999%2948%3A1%3C75%3A%3AAID-JBM13%3E3.0.CO%3B2-H.

S.M Kurtz, M.L Villarraga, M.P Herr, J.S Bergström, C.M Rimnac, and A.A Edidin. Thermomechanical behavior of virgin and highly crosslinked ultra-high molecular weight polyethylene used in total joint replacements. *Biomaterials*, 23(17):3681–3697, September 2002. ISSN 01429612. doi: 10.1016/S0142-9612(02)00102-3. URL https://linkinghub.elsevier.com/retrieve/pii/S0142961202001023.

Noël Lahellec and Pierre Suquet. On the effective behavior of nonlinear inelastic composites: I. Incremental variational principles. *Journal of the Mechanics and Physics of Solids*, 55(9):1932–1963, September 2007a. ISSN 00225096. doi: 10.1016/j.jmps.2007.02.003. URL https://linkinghub.elsevier.com/retrieve/pii/S0022509607000312.

Noël Lahellec and Pierre Suquet. On the effective behavior of nonlinear inelastic composites: II. A second-order procedure. *Journal of the Mechanics and Physics of Solids*, 55(9):1964–1992, September 2007b. ISSN 00225096. doi: 10.1016/j.jmps.2007.02.004. URL https://linkinghub.elsevier.com/retrieve/pii/S0022509607000324.

Tianxiang Lan, Yaodong Jiang, and Peidong Wu. A thermodynamically-based constitutive theory for amorphous glassy polymers at finite deformations. *International Journal of Plasticity*, 158:103415, 2022. ISSN 0749-6419. doi: https://doi.org/10.1016/j.ijplas.2022.103415. URL https://www.sciencedirect.com/science/article/pii/S0749641922001930.

Marcos Latorre and Francisco J. Montáns. A new class of plastic flow evolution equations for anisotropic multiplicative elastoplasticity based on the notion of a corrector elastic strain rate. *Applied Mathematical Modelling*, 55:716–740, 2018. ISSN 0307-904X. doi: https://doi.org/10.1016/j.apm.2017.11.003. URL https://www.sciencedirect.com/science/article/pii/S0307904X17306947.

F. Lauro, B. Bennani, D. Morin, and A. F. Epee. The SEÈ method for determination of behaviour laws for strain rate dependent material: Application to polymer material. *International Journal of Impact Engineering*, 37(6):715–722, June 2010. ISSN 0734-743X. doi: 10.1016/j.ijimpeng.2009.11.007.

B.H. Lavenda. *Thermodynamics of irreversible processes*. Wiley, 1978. ISBN 978-0-470-98898-5. URL https://books.google.pt/books?id=FjW2AAAAIAAJ. tex.lccn: 76022604.

B. J. Lee, D. M. Parks, and S. Ahzi. Micromechanical modeling of large plastic deformation and texture evolution in semi-crystalline polymers. *Journal of the Mechanics and Physics of Solids*, 41(10):1651–1687, 1993a. ISSN 00225096. doi: 10.1016/0022-5096(93)90018-B. URL https://linkinghub.elsevier.com/retrieve/pii/002250969390018B.

B.J Lee, A.S Argon, D.M Parks, S Ahzi, and Z Bartczak. Simulation of large strain plastic deformation and texture evolution in high density polyethylene. *Polymer*, 34(17):3555–3575, September 1993b. ISSN 00323861. doi: 10.1016/0032-3861(93)90039-D. URL https://linkinghub.elsevier.com/retrieve/pii/003238619390039D.

E. H. Lee. Elastic-Plastic Deformation at Finite Strains. *Journal of Applied Mechanics*, 36(1):1–6, March 1969. ISSN 0021-8936. doi: 10.1115/1.3564580.

E. H. Lee and D. T. Liu. Finite-Strain Elastic—Plastic Theory with Application to Plane-Wave Analysis. *Journal of Applied Physics*, 38(1):19–27, January 1967. ISSN 0021-8979. doi: 10.1063/1.1708953.

Suvrat P. Lele and Lallit Anand. A large-deformation strain-gradient theory for isotropic viscoplastic materials. *International Journal of Plasticity*, 25(3):420–453, 2009. ISSN 0749-6419. URL https://www.sciencedirect.com/science/article/pii/S0749641908000624.

Jean Lemaitre. *A Course on Damage Mechanics*. Springer Science & Business Media, 2013. ISBN 9783642182556. doi: 10.1007/978-3-642-18255-6.

A. I. Leonov. Nonequilibrium thermodynamics and rheology of viscoelastic polymer media. *Rheologica Acta*, 15(2):85–98, February 1976. ISSN 0035-4511, 1435-1528. doi: 10.1007/BF01517499. URL http://link.springer.com/10.1007/BF01517499.

L. Lin and A. S. Argon. Rate Mechanism of Plasticity in the Crystalline Component of Semicrystalline Nylon 6. *Macromolecules*, 27(23):6903–6914, November 1994. ISSN 0024-9297, 1520-5835. doi: 10.1021/ma00101a031. URL https://pubs.acs.org/doi/abs/10.1021/ma00101a031.

M. C. M. Liu and E. Krempl. A uniaxial viscoplastic model based on total strain and overstress. *Journal of the Mechanics and Physics of Solids*, 27(5):377–391, December 1979. ISSN 0022-5096. doi: 10.1016/0022-5096(79)90021-8.

S. C. H. Lu and K. S. Pister. Decomposition of deformation and representation of the free energy function for isotropic thermoelastic solids. *International Journal of Solids and Structures*, 11(7):927–934, July 1975. ISSN 0020-7683. doi: 10.1016/0020-7683(75)90015-3.

J. C. Lucas, M. D. Failla, F. L. Smith, L. Mandelkern, and Andrew J. Peacock. The double yield in the tensile deformation of the polyethylenes. *Polymer Engineering and Science*, 35(13):1117–1123, July 1995. ISSN 0032-3888, 1548-2634. doi: 10.1002/pen.760351308. URL https://onlinelibrary.wiley.com/doi/10.1002/pen.760351308.

Kevin Lukas and Peter K. LeMaire. Differential scanning calorimetry: Fundamental overview. *Resonance*, 14(8):807–817, August 2009. ISSN 0971-8044, 0973-712X. doi: 10.1007/s12045-009-0076-7. URL http://link.springer.com/10.1007/s12045-009-0076-7.

H. A. Luo and G. J. Weng. On Eshelby's inclusion problem in a three-phase spherically concentric solid, and a modification of Mori-Tanaka's method. *Mechanics of Materials*, 6(4):347–361, December 1987. ISSN 0167-6636. doi: 10.1016/0167-6636(87)90032-9. URL https://www.sciencedirect.com/science/article/pii/0167663687900329.

A. Makradi, S. Ahzi, R.V. Gregory, and D.D. Edie. A two-phase self-consistent model for the deformation and phase transformation behavior of polymers above the glass transition temperature: application to PET. *International Journal of Plasticity*, 21(4):741–758, April 2005. ISSN 07496419. doi: 10.1016/j.ijplas.2004.04.012. URL https://linkinghub.elsevier.com/retrieve/pii/S0749641904000816.

A. IA Malkin and Avraam I. Isayev. *Rheology: concepts methods, and applications*. ChemTec Publishing, Toronto, 3rd edition edition, 2017. ISBN 978-1-927885-21-5. OCLC: ocn963393005.

Alexander Ya. Malkin. Non-linearity in rheology —an essay of classification. *Rheologica Acta*, 34(1):27–39, January 1995. ISSN 1435-1528. doi: 10.1007/BF00396052. URL https://doi.org/10.1007/BF00396052.

Leo Mandelkern. Crystalline polymer: Some reminiscences over the years. *Thermochimica Acta*, 442(1):31–34, March 2006. ISSN 0040-6031. doi: 10.1016/j.tca.2005.11.016. URL https://www.sciencedirect.com/science/article/pii/S0040603105005599.

Karine Marchal. *Influence du chemin de chargement sur le comportement du polyamide 11 autour de la transition vitreuse*. These de doctorat, Poitiers, January 1996. URL https://www.theses.fr/1996POIT2373.

Jerrold E. Marsden and Thomas J. R. Hughes. *Mathematical Foundations of Elasticity*, volume 1. Prentice Hall, 1982. ISBN 978-0-486-67865-8.

R. Masson, M. Bornert, P. Suquet, and A. Zaoui. An affine formulation for the prediction of the effective properties of nonlinear composites and polycrystals. *Journal of the Mechanics and Physics of Solids*, 48(6-7):1203–1227, June 2000. ISSN 00225096. doi: 10.1016/S0022-5096(99)00071-X.

Karel Matouš, Marc G. D. Geers, Varvara G. Kouznetsova, and Andrew Gillman. A review of predictive nonlinear theories for multiscale modeling of heterogeneous materials. *Journal of Computational Physics*, 330:192–220, February 2017. ISSN 0021-9991. doi: 10.1016/j.jcp.2016.10.070. URL https://www.sciencedirect.com/science/article/pii/S0021999116305782.

S. Matsuoka. Thermodynamic theory of viscoelasticity. *Journal of Thermal Analysis*, 46(3-4):985–1010, March 1996. ISSN 0368-4466, 1572-8943. doi: 10.1007/BF01983616. URL http://link.springer.com/10.1007/BF01983616.

G. A. Maugin. *The Thermomechanics of Nonlinear Irreversible Behaviours*, volume 27 of *World Scientific Series on Nonlinear Science, Series A*. World Scientific, 1999. ISBN 981-02-3375-2.

N. G. McCrum. A study of internal friction in copolymers of tetrafluoroethylene and hexafluoropropylene. *Die Makromolekulare Chemie*, 34(1):50–66, 1959. ISSN 0025-116X. doi: 10.1002/macp.1959.020340103. URL https://onlinelibrary.wiley.com/doi/abs/10.1002/macp.1959.020340103. _eprint: https://onlinelibrary.wiley.com/doi/pdf/10.1002/macp.1959.020340103.

N. G. McCrum. The variation of internal friction in polychlorotrifluoroethylene with density and temperature. *Journal of Polymer Science*, 60(169):S3–S5, 1962. ISSN 1542-6238. doi: 10.1002/pol.1962.1206016907. URL https://onlinelibrary.wiley.com/doi/abs/10.1002/pol.1962.1206016907. _eprint: https://onlinelibrary.wiley.com/doi/pdf/10.1002/pol.1962.1206016907.

R. McLaughlin. A study of the differential scheme for composite materials. *International Journal of Engineering Science*, 15(4):237–244, January 1977. ISSN 0020-7225. doi: 10.1016/0020-7225(77)90058-1. URL https://www.sciencedirect.com/science/article/pii/0020722577900581.

JC Michel, H Moulinec, and Pierre Suquet. A computational method based on augmented Lagrangians and fast Fourier transforms for composites with high contrast. *CMES(Computer Modelling in Engineering & Sciences)*, 1(2):79–88, 2000.

B. Miled, I. Doghri, and L. Delannay. Coupled viscoelastic–viscoplastic modeling of homogeneous and isotropic polymers: Numerical algorithm and analytical solutions. *Computer Methods in Applied Mechanics and Engineering*, 200(47):3381–3394, 2011. ISSN 0045-7825. doi: https://doi.org/10.1016/j.cma.2011.08.015. URL https://www.sciencedirect.com/science/article/pii/S0045782511002702.

Graeme W. Milton. *The Theory of Composites*, volume 1 of *Cambridge Monographs on Applied and Computational Mathematics*. Cambridge University Press, July 2004. ISBN 0-511-04092-X.

Mohsen Mirkhalaf and Rahele Vadizadeh. Micro-mechanical modeling of semi-crystalline polymers: A review. *International Journal of Solids and Structures*, 290:112691, March 2024. ISSN 0020-7683. doi: 10.1016/j.ijsolstr.2024.112691.

Mohsen Mirkhalaf, Johannes A. W. van Dommelen, Leon E. Govaert, Jevan Furmanski, and Marc G. D. Geers. Micromechanical modeling of anisotropic behavior of oriented semicrystalline polymers. *Journal of Polymer Science Part B: Polymer Physics*, 57(7):378–391, 2019. ISSN 1099-0488. doi: 10.1002/polb.24791.

S. M. Mirkhalaf, F. M. Andrade Pires, and R. Simoes. An elasto-viscoplastic constitutive model for polymers at finite strains: Formulation and computational aspects. *Computers & Structures*, 166:60–74, April 2016. ISSN 0045-7949. doi: 10.1016/j.compstruc.2016.01.002.

S.M. Mirkhalaf, F.M. Andrade Pires, and Ricardo Simoes. Modelling of the post yield response of amorphous polymers under different stress states. *International Journal of Plasticity*, 88: 159–187, January 2017. ISSN 07496419. doi: 10.1016/j.ijplas.2016.10.008.

A Molinari and M Ortiz. Global viscoelastic behavior of heterogeneous thermoelastic materials. *International journal of solids and structures*, 23(9):1285–1300, 1987.

A. Molinari, G. R. Canova, and S. Ahzi. A self consistent approach of the large deformation polycrystal viscoplasticity. *Acta Metallurgica*, 35(12):2983–2994, December 1987. ISSN 0001-6160. doi: 10.1016/0001-6160(87)90297-5.

T Mori and K Tanaka. Average stress in matrix and average elastic energy of materials with misfitting inclusions. *Acta Metallurgica*, 21(5):571–574, May 1973. ISSN 0001-6160. doi: 10.1016/0001-6160(73)90064-3. URL `https://www.sciencedirect.com/science/article/pii/0001616073900643`.

Hervé Moulinec and Pierre Suquet. A numerical method for computing the overall response of nonlinear composites with complex microstructure. *Computer methods in applied mechanics and engineering*, 157(1-2):69–94, 1998. Publisher: Elsevier.

A. Mulliken. *Mechanics of Amorphous Polymers and Polymer Nanocomposites during High Rate Deformation*. PhD Thesis, Massachusetts Institute of Technology, 2006.

A. D. Mulliken and M. C. Boyce. Mechanics of the rate-dependent elastic–plastic deformation of glassy polymers from low to high strain rates. *International Journal of Solids and Structures*, 43 (5):1331–1356, March 2006. ISSN 0020-7683. doi: 10.1016/j.ijsolstr.2005.04.016. URL `10.1016/j.ijsolstr.2005.04.016`.

Bing Na, Qin Zhang, Qiang Fu, Yongfeng Men, Ke Hong, and Gert Strobl. Viscous-Force-Dominated Tensile Deformation Behavior of Oriented Polyethylene. *Macromolecules*, 39(7): 2584–2591, April 2006. ISSN 0024-9297. doi: 10.1021/ma052496g. URL `https://doi.org/10.1021/ma052496g`. Publisher: American Chemical Society.

Yukuo Nanzai. Transition mechanism from elastic deformation to plastic flow in poly(methyl methacrylate). *Polymer Engineering and Science*, 30(2):96–107, January 1990. ISSN 0032-3888, 1548-2634. doi: 10.1002/pen.760300206. URL `https://onlinelibrary.wiley.com/doi/10.1002/pen.760300206`.

Mariem Nciri, Delphine Notta-Cuvier, Franck Lauro, Fahmi Chaari, Yamen Maalej, and Bassem Zouari. Viscoelastic-viscoplastic model for short-fibre-reinforced composites with complex fibre orientation. *Mechanics of Advanced Materials and Structures*, 26, 01 2018. doi: 10.1080/15376494.2018.1430264.

S. Nemat-Nasser and M. Hori. *Micromechanics: Overall Properties of Heterogeneous Materials*. Number v. 37 in North-Holland Series in Applied Mathematics and Mechanics. North-Holland, Amsterdam ; New York, 1993. ISBN 978-0-444-89881-4.

S Nikolov and I Doghri. A micro/macro constitutive model for the small-deformation behavior of polyethylene. *Polymer*, 41(5):1883–1891, March 2000. ISSN 00323861. doi: 10.1016/S0032-3861(99)00330-4. URL https://linkinghub.elsevier.com/retrieve/pii/S0032386199003304.

S. Nikolov, I. Doghri, O. Pierard, L. Zealouk, and A. Goldberg. Multi-scale constitutive modeling of the small deformations of semi-crystalline polymers. *Journal of the Mechanics and Physics of Solids*, 50(11):2275–2302, November 2002. ISSN 00225096. doi: 10.1016/S0022-5096(02)00036-4. URL https://linkinghub.elsevier.com/retrieve/pii/S0022509602000364.

S Nikolov, R Lebensohn, and D Raabe. Self-consistent modeling of large plastic deformation, texture and morphology evolution in semi-crystalline polymers. *Journal of the Mechanics and Physics of Solids*, 54(7):1350–1375, July 2006. ISSN 00225096. doi: 10.1016/j.jmps.2006.01.008.

Walter Noll. A mathematical theory of the mechanical behavior of continuous media. *Archive for Rational Mechanics and Analysis*, 2(1):197–226, January 1958. ISSN 1432-0673. doi: 10.1007/BF00277929. URL https://doi.org/10.1007/BF00277929.

A. N. Norris. A differential scheme for the effective moduli of composites. *Mechanics of Materials*, 4(1):1–16, March 1985. ISSN 0167-6636. doi: 10.1016/0167-6636(85)90002-X. URL https://www.sciencedirect.com/science/article/pii/016766368590002X.

R. W. Ogden. On the overall moduli of non-linear elastic composite materials. *Journal of the Mechanics and Physics of Solids*, 22(6):541–553, December 1974. ISSN 0022-5096. doi: 10.1016/0022-5096(74)90033-7. URL https://www.sciencedirect.com/science/article/pii/0022509674900337.

Ray W. Ogden. *Non-Linear Elastic Deformations*. Dover books on physics. Dover Publ, Mineola, NY, 1. publ., unabridged and corr. republ edition, 1997. ISBN 978-0-486-69648-5.

Michael I. Okereke and Ambrose I. Akpoyomare. Two-process constitutive model for semicrystalline polymers across a wide range of strain rates. *Polymer*, 183:121818, November 2019. ISSN 00323861. doi: 10.1016/j.polymer.2019.121818. URL https://linkinghub.elsevier.com/retrieve/pii/S0032386119308249.

H. Emre Oktay and Ercan Gürses. Modeling of spherulite microstructures in semicrystalline polymers. *Mechanics of Materials*, 90:83–101, November 2015. ISSN 0167-6636. doi: 10.1016/j.mechmat.2015.04.010.

L. Olasz and P. Gudmundson. Viscoelastic Model of Cross-Linked Polyethylene Including Effects of Temperature and Crystallinity. *Mechanics of Time-Dependent Materials*, 9(4):23–44, December 2005. ISSN 1385-2000, 1573-2738. doi: 10.1007/s11043-005-9002-x. URL http://link.springer.com/10.1007/s11043-005-9002-x.

Gregory B. Olson. Designing a New Material World. *Science*, 288(5468):993–998, May 2000. ISSN 0036-8075, 1095-9203. doi: 10.1126/science.288.5468.993.

E. T. Onat. Representation of elastic-plastic behavior in the presence of finite deformations and anisotropy. *International Journal of Plasticity*, 1987.

J. M. Ortolano, J. A. Hernández, and J. Oliver. A Comparative Study on Homogenization Strategies for Multi-Scale Analysis of Materials. Monograph 135, CIMNE, Barcelona, Spain, 2013.

Fermin Otero, Sergio Oller, and Xavier Martinez. Multiscale Computational Homogenization: Review and Proposal of a New Enhanced-First-Order Method. *Archives of Computational Methods in Engineering*, 25(2):479–505, April 2018. ISSN 1886-1784. doi: 10.1007/s11831-016-9205-0.

M. Paley and J. Aboudi. Micromechanical analysis of composites by the generalized cells model. *Mechanics of Materials*, 14(2):127–139, December 1992. ISSN 0167-6636. doi: 10.1016/0167-6636(92)90010-B. URL https://www.sciencedirect.com/science/article/pii/016766369290010B.

Robert Panowicz, Marcin Konarzewski, Tomasz Durejko, Mateusz Szala, Magdalena Łazińska, Magdalena Czerwińska, and Piotr Prasuła. Properties of Polyethylene Terephthalate (PET) after Thermo-Oxidative Aging. *Materials*, 14(14):3833, January 2021. ISSN 1996-1944. doi: 10.3390/ma14143833. URL https://www.mdpi.com/1996-1944/14/14/3833. Number: 14 Publisher: Multidisciplinary Digital Publishing Institute.

G. Papanicolau, A. Bensoussan, and J.-L. Lions. *Asymptotic Analysis for Periodic Structures*. Elsevier, January 1978. ISBN 978-0-08-087526-2.

D. M. Parks and S. Ahzi. Polycrystalline plastic deformation and texture evolution for crystals lacking five independent slip systems. *Journal of the Mechanics and Physics of Solids*, 38(5):701–724, January 1990. ISSN 0022-5096. doi: 10.1016/0022-5096(90)90029-4.

Stanislav Patlazhan and Yves Remond. Structural mechanics of semicrystalline polymers prior to the yield point: a review. *Journal of Materials Science*, 47(19):6749–6767, October 2012. ISSN 0022-2461, 1573-4803. doi: 10.1007/s10853-012-6620-y. URL http://link.springer.com/10.1007/s10853-012-6620-y.

Andrew Peacock. *Handbook of Polyethylene: Structures: Properties, and Applications*. CRC Press, Boca Raton, April 2014. ISBN 978-0-429-18077-4. doi: 10.1201/9781482295467.

P. Perzyna. The constitutive equations for rate sensitive plastic materials. *Quarterly of Applied Mathematics*, 20(4):321–332, 1963. ISSN 0033-569X, 1552-4485. doi: 10.1090/qam/144536.

A. Peterlin. Molecular model of drawing polyethylene and polypropylene. *Journal of Materials Science*, 6(6):490–508, June 1971. ISSN 1573-4803. doi: 10.1007/BF00550305. URL https://doi.org/10.1007/BF00550305.

James M. Peterson. Thermal Initiation of Screw Dislocations in Polymer Crystal Platelets. *Journal of Applied Physics*, 37(11):4047–4050, October 1966. ISSN 0021-8979. doi: 10.1063/1.1707973. URL https://aip.scitation.org/doi/abs/10.1063/1.1707973. Publisher: American Institute of Physics.

O Pierard and I Doghri. An enhanced affine formulation and the corresponding numerical algorithms for the mean-field homogenization of elasto-viscoplastic composites. *International Journal of Plasticity*, 22(1):131–157, January 2006. ISSN 07496419. doi: 10.1016/j.ijplas.2005.04.001.

Mario Polanco-Loria, Arild H. Clausen, Torodd Berstad, and Odd Sture Hopperstad. Constitutive model for thermoplastics with structural applications. *International Journal of Impact Engineering*, 37(12):1207–1219, December 2010. ISSN 0734743X. doi: 10.1016/j.ijimpeng.2010.06.006. URL https://linkinghub.elsevier.com/retrieve/pii/S0734743X10001065.

P. Ponte Castañeda and P. Suquet. Nonlinear Composites. In *Advances in Applied Mechanics*, volume 34, pages 171–302. Elsevier, 1997. ISBN 978-0-12-002034-8. doi: 10.1016/S0065-2156(08)70321-1. URL https://linkinghub.elsevier.com/retrieve/pii/S0065215608703211.

P. Ponte Castañeda, John Raymond Willis, and Anthony James Merrill Spencer. On the overall properties of nonlinearly viscous composites. *Proceedings of the Royal Society of London. A. Mathematical and Physical Sciences*, 416(1850):217–244, January 1997. doi: 10.1098/rspa.1988.0035. URL https://royalsocietypublishing.org/doi/abs/10.1098/rspa.1988.0035. Publisher: Royal Society.

Pedro Ponte Castañeda. Second-order homogenization estimates for nonlinear composites incorporating field fluctuations: I—theory. *Journal of the Mechanics and Physics of Solids*, 50(4):737–757, April 2002. ISSN 00225096. doi: 10.1016/S0022-5096(01)00099-0. URL https://linkinghub.elsevier.com/retrieve/pii/S0022509601000990.

C. M. Popa, R. Fleischhauer, K. Schneider, and M. Kaliske. Formulation and implementation of a constitutive model for semicrystalline polymers. *International Journal of Plasticity*, 61:128–156, October 2014. ISSN 0749-6419. doi: 10.1016/j.ijplas.2014.05.010.

D. P. Pope. Characterization of oriented low-density polyethylene samples by differential scanning calorimetry. *Journal of Polymer Science: Polymer Physics Edition*, 14(5):811–820, 1976. ISSN 1542-9385. doi: 10.1002/pol.1976.180140504. URL https://onlinelibrary.wiley.com/doi/abs/10.1002/pol.1976.180140504. _eprint: https://onlinelibrary.wiley.com/doi/pdf/10.1002/pol.1976.180140504.

C. F. Popelar, C. H. Popelar, and V. H. Kenner. Viscoelastic material characterization and modeling for polyethylene. *Polymer Engineering and Science*, 30(10):577–586, May 1990. ISSN 0032-3888, 1548-2634. doi: 10.1002/pen.760301004. URL https://onlinelibrary.wiley.com/doi/10.1002/pen.760301004.

X. Poulain, A. A. Benzerga, and R. K. Goldberg. Finite-strain elasto-viscoplastic behavior of an epoxy resin: Experiments and modeling in the glassy regime. *International Journal of Plasticity*, 62:138–161, November 2014. ISSN 0749-6419. doi: 10.1016/j.ijplas.2014.07.002.

H. Pouriayevali, S. Arabnejad, Y.B. Guo, and V.P.W. Shim. A constitutive description of the rate-sensitive response of semi-crystalline polymers. *International Journal of Impact Engineering*, 62:35–47, December 2013. ISSN 0734743X. doi: 10.1016/j.ijimpeng.2013.05.002. URL https://linkinghub.elsevier.com/retrieve/pii/S0734743X13001085.

Precedence Research. Polymers Market (By Product; By Material; By Application; By Process) - Global Industry Analysis, Size, Share, Growth, Trends, Regional Outlook, and Forecast 2022-2030. Technical report, Precedence Research, 2022.

P.J. Rae, E.N. Brown, and E.B. Orler. The mechanical properties of poly(ether-ether-ketone) (PEEK) with emphasis on the large compressive strain response. *Polymer*, 48(2):598–615, January 2007. ISSN 00323861. doi: 10.1016/j.polymer.2006.11.032. URL https://linkinghub.elsevier.com/retrieve/pii/S0032386106012742.

I.J. Rao and K.R. Rajagopal. A study of strain-induced crystallization of polymers. *International Journal of Solids and Structures*, 38(6-7):1149–1167, February 2001. ISSN 00207683. doi: 10.1016/S0020-7683(00)00079-2. URL https://linkinghub.elsevier.com/retrieve/pii/S0020768300000792.

Annie Raoult. Symmetry groups in nonlinear elasticity: An exercise in vintage mathematics. *Communications on Pure & Applied Analysis*, 8(1):435–456, 2009. ISSN 1553-5258. doi: 10.3934/cpaa.2009.8.435.

Taikyue Ree and Henry Eyring. Theory of Non-Newtonian Flow. I. Solid Plastic System. *Journal of Applied Physics*, 26(7):793–800, July 1955. ISSN 0021-8979, 1089-7550. doi: 10.1063/1.1722098. URL http://aip.scitation.org/doi/10.1063/1.1722098.

Stefanie Reese and Sanjay Govindjee. A theory of finite viscoelasticity and numerical aspects. *International Journal of Solids and Structures*, 35(26-27):3455–3482, September 1998. ISSN 00207683. doi: 10.1016/S0020-7683(97)00217-5. URL https://linkinghub.elsevier.com/retrieve/pii/S0020768397002175.

Cedric Regrain, Lucien Laiarinandrasana, Sophie Toillon, and Kacem Saï. Multi-mechanism models for semi-crystalline polymer: Constitutive relations and finite element implementation. *International Journal of Plasticity*, 25(7):1253–1279, July 2009. ISSN 07496419. doi: 10.1016/j.ijplas.2008.09.010. URL https://linkinghub.elsevier.com/retrieve/pii/S0749641908001496.

A. Reuss. Berechnung der Fließgrenze von Mischkristallen auf Grund der Plastizitätsbedingung für Einkristalle . *ZAMM - Journal of Applied Mathematics and Mechanics / Zeitschrift für Angewandte Mathematik und Mechanik*, 9(1):49–58, January 1929. ISSN 0044-2267, 1521-4001. doi: 10.1002/zamm.19290090104.

J. Richeton, S. Ahzi, L. Daridon, and Y. Rémond. A formulation of the cooperative model for the yield stress of amorphous polymers for a wide range of strain rates and temperatures. *Polymer*, 46(16):6035–6043, July 2005. ISSN 00323861. doi: 10.1016/j.polymer.2005.05.079. URL https://linkinghub.elsevier.com/retrieve/pii/S0032386105006865.

J. Richeton, S. Ahzi, K. S. Vecchio, F. C. Jiang, and R. R. Adharapurapu. Influence of temperature and strain rate on the mechanical behavior of three amorphous polymers: Characterization and modeling of the compressive yield stress. *International Journal of Solids and Structures*, 43(7):2318–2335, 2006. ISSN 0020-7683. doi: 10.1016/j.ijsolstr.2005.06.040. URL https://www.sciencedirect.com/science/article/pii/S0020768305003677.

J. Richeton, S. Ahzi, and L. Daridon. Thermodynamic investigation of yield-stress models for amorphous polymers. *Philosophical Magazine*, 87(24):3629–3643, August 2007a. ISSN 1478-6435, 1478-6443. doi: 10.1080/14786430701381162. URL http://www.tandfonline.com/doi/abs/10.1080/14786430701381162.

J. Richeton, S. Ahzi, K. S. Vecchio, F. C. Jiang, and A. Makradi. Modeling and validation of the large deformation inelastic response of amorphous polymers over a wide range of temperatures and strain rates. *International Journal of Solids and Structures*, 44(24):7938–7954, 2007b. ISSN 0020-7683. doi: 10.1016/j.ijsolstr.2007.05.018. URL https://www.sciencedirect.com/science/article/pii/S0020768307002296.

Richard E. Robertson. Theory for the Plasticity of Glassy Polymers. *The Journal of Chemical Physics*, 44(10):3950–3956, May 1966. ISSN 0021-9606. doi: 10.1063/1.1726558. URL https:

//aip.scitation.org/doi/abs/10.1063/1.1726558. Publisher: American Institute of Physics.

D. Roca, D. Yago, J. Cante, O. Lloberas-Valls, and J. Oliver. Computational design of locally resonant acoustic metamaterials. *Computer Methods in Applied Mechanics and Engineering*, 345:161–182, March 2019. ISSN 0045-7825. doi: 10.1016/j.cma.2018.10.037.

Felipe Figueredo Rocha, Pablo Javier Blanco, Pablo Javier Sánchez, and Raúl Antonino Feijóo. Multi-scale modelling of arterial tissue: Linking networks of fibres to continua. *Computer Methods in Applied Mechanics and Engineering*, 341:740–787, November 2018. ISSN 0045-7825. doi: 10.1016/j.cma.2018.06.031.

Ralph Tyrrell Rockafellar. *Convex Analysis*. Number 28 in Princeton Mathematical Series. Princeton university press, 1972. ISBN 978-0-691-08069-7.

Igor A. Rodrigues Lopes and Francisco M. Andrade Pires. An assessment of multi-scale models based on second-order computational homogenisation. *Computers & Structures*, 259:106679, January 2022. ISSN 0045-7949. doi: 10.1016/j.compstruc.2021.106679.

J.A Roetling. Yield stress behaviour of poly(ethyl methacrylate) in the glass transition region. *Polymer*, 6(11):615–619, November 1965. ISSN 00323861. doi: 10.1016/0032-3861(65)90056-X. URL https://linkinghub.elsevier.com/retrieve/pii/003238616590056X.

J.A Roetling. Yield stress behaviour of isotactic polypropylene. *Polymer*, 7(7):303–306, July 1966. ISSN 00323861. doi: 10.1016/0032-3861(66)90025-5. URL https://linkinghub.elsevier.com/retrieve/pii/0032386166900255.

RTP Company. Product Guide | RTP Company, February 2021.

G. Sachs. Zur Ableitung Einer Fliessbedingung. *Z. Ver, Dtsch. Ing.*, 72:734–736, 1928. URL https://cir.nii.ac.jp/crid/1572824498935759488.

Martin H. Sadd. *Elasticity*. Elsevier, 2005. ISBN 978-0-12-605811-6. doi: 10.1016/B978-0-12-605811-6.X5000-3. URL https://linkinghub.elsevier.com/retrieve/pii/B9780126058116X50003.

Keivan H. Safari, Jamal Zamani, Fernando J. Ferreira, and Rui M. Guedes. Constitutive modeling of polycarbonate during high strain rate deformation. *Polymer Engineering & Science*, 53(4):752–761, 2013. doi: https://doi.org/10.1002/pen.23315.

Enrique Sanchez-Palencia. Comportements local et macroscopique d'un type de milieux physiques heterogenes. *International Journal of Engineering Science*, 12(4):331–351, April 1974. ISSN 0020-7225. doi: 10.1016/0020-7225(74)90062-7. URL https://www.sciencedirect.com/science/article/pii/0020722574900627.

Bernard A. G. Schrauwen, Roel P. M. Janssen, Leon E. Govaert, and Han E. H. Meijer. Intrinsic Deformation Behavior of Semicrystalline Polymers. *Macromolecules*, 37(16):6069–6078, August 2004. ISSN 0024-9297. doi: 10.1021/ma035279t. URL https://doi.org/10.1021/ma035279t. tex.ids= schrauwenIntrinsicDeformationBehavior2004a publisher: American Chemical Society.

A. Sedighiamiri, T. B. Van Erp, G. W. M. Peters, L. E. Govaert, and J. a. W. van Dommelen. Micromechanical modeling of the elastic properties of semicrystalline polymers: A three-phase approach. *Journal of Polymer Science Part B: Polymer Physics*, 48(20):2173–2184, 2010. ISSN 1099-0488. doi: 10.1002/polb.22099.

A. Sedighiamiri, L. E. Govaert, and J. a. W. van Dommelen. Micromechanical modeling of the deformation kinetics of semicrystalline polymers. *Journal of Polymer Science Part B: Polymer Physics*, 49(18):1297–1310, 2011. ISSN 1099-0488. doi: 10.1002/polb.22297.

A. Sedighiamiri, D. J. A. Senden, D. Tranchida, L. E. Govaert, and J. A. W. van Dommelen. A micromechanical study on the deformation kinetics of oriented semicrystalline polymers. *Computational Materials Science*, 82:415–426, February 2014. ISSN 0927-0256. doi: 10.1016/j.commatsci.2013.09.068.

Amin Sedighiamiri, Leon E. Govaert, Marc J.W. Kanters, and Johannes A.W. van Dommelen. Micromechanics of semicrystalline polymers: Yield kinetics and long-term failure. *Journal of Polymer Science Part B: Polymer Physics*, 50(24):1664–1679, 2012. ISSN 1099-0488. doi: 10.1002/polb.23136.

Modesar Shakoor and Chung Hae Park. Computational homogenization of unsteady flows with obstacles. *International Journal for Numerical Methods in Fluids*, 95(4):499–527, 2023. ISSN 1097-0363. doi: 10.1002/fld.5158.

J. C. Simo and T. J. R. Hughes. *Computational Inelasticity*. Interdisciplinary Applied Mathematics. Springer-Verlag, New York, 1998. ISBN 978-0-387-97520-7. doi: 10.1007/b98904.

J. C. Simo and C. Miehe. Associative coupled thermoplasticity at finite strains: Formulation, numerical analysis and implementation. *Computer Methods in Applied Mechanics and Engineering*, 98(1):41–104, July 1992. ISSN 0045-7825. doi: 10.1016/0045-7825(92)90170-O.

J.C. Simo. On a fully three-dimensional finite-strain viscoelastic damage model: Formulation and computational aspects. *Computer Methods in Applied Mechanics and Engineering*, 60(2):153–173, February 1987. ISSN 00457825. doi: 10.1016/0045-7825(87)90107-1. URL `https://linkinghub.elsevier.com/retrieve/pii/0045782587901071`.

Thor L. Smith. Nonlinear Viscoelastic Response of Amorphous Elastomers to Constant Strain Rates. *Transactions of the Society of Rheology*, 6(1):61–80, March 1962. ISSN 0038-0032. doi: 10.1122/1.548933.

Vikas Srivastava, Shawn A. Chester, Nicoli M. Ames, and Lallit Anand. A thermo-mechanically-coupled large-deformation theory for amorphous polymers in a temperature range which spans their glass transition. *International Journal of Plasticity*, 26(8):1138–1182, 2010. ISSN 0749-6419. doi: https://doi.org/10.1016/j.ijplas.2010.01.004. URL `https://www.sciencedirect.com/science/article/pii/S0749641910000057`. Special Issue In Honor of Lallit Anand.

J. Stillwell. *Naive Lie Theory*. Undergraduate Texts in Mathematics. Springer New York, 2008. ISBN 978-0-387-78215-7. URL `https://books.google.pt/books?id=SuR5OAgxyDIC`.

J. Storm, D. Supriatna, and M. Kaliske. The concept of representative crack elements for phase-field fracture: Anisotropic elasticity and thermo-elasticity. *International Journal for Numerical Methods in Engineering*, 121(5):779–805, March 2020. ISSN 0029-5981. doi: 10.1002/nme.6244.

J. Storm, B. Yin, and M. Kaliske. The concept of Representative Crack Elements (RCE) for phase-field fracture: Transient thermo-mechanics. *Computational Mechanics*, 69(5):1165–1176, May 2022. ISSN 1432-0924. doi: 10.1007/s00466-021-02135-w.

J. Sweeney and I. M. Ward. Rate dependent and network phenomena in the multiaxial drawing of poly(vinyl chloride). *Polymer*, 36(2):299–308, January 1995. ISSN 0032-3861. doi: 10.1016/0032-3861(95)91317-Z. URL https://www.sciencedirect.com/science/article/pii/003238619591317Z.

Motowo Takayanagi, Shinsaku Uemura, and Shunsuke Minami. Application of equivalent model method to dynamic rheo-optical properties of crystalline polymer. *Journal of Polymer Science Part C: Polymer Symposia*, 5(1):113–122, 1964. ISSN 1935-3065. doi: 10.1002/polc.5070050111. URL https://onlinelibrary.wiley.com/doi/abs/10.1002/polc.5070050111. _eprint: https://onlinelibrary.wiley.com/doi/pdf/10.1002/polc.5070050111.

Motowo Takayanagi, Kiyohisa Imada, and Tisato Kajiyama. Mechanical properties and fine structure of drawn polymers. *Journal of Polymer Science Part C: Polymer Symposia*, 15(1):263–281, January 1967. ISSN 1935-3065. doi: https://doi.org/10.1002/polc.5070150118. URL https://onlinelibrary.wiley.com/doi/abs/10.1002/polc.5070150118. Publisher: John Wiley & Sons, Ltd.

Erik Tamsen and Daniel Balzani. A general, implicit, finite-strain FE^{2}framework for the simulation of dynamic problems on two scales. *Computational Mechanics*, 67(5):1375–1394, May 2021. ISSN 1432-0924. doi: 10.1007/s00466-021-01993-8.

G. P. Tandon and G. J. Weng. A theory of particle-reinforced plasticity. *Journal of Applied Mechanics*, 55(1):126–135, March 1988. ISSN 0021-8936, 1528-9036. doi: 10.1115/1.3173618.

G. I. Taylor. Plastic Strain in Metals. *Journal of the Institute of Metals*, 62:307–324, 1938. URL https://cir.nii.ac.jp/crid/1571135650487126144.

Jose Teixeira-Pinto, Carole Nadot-Martin, Fabienne Touchard, Mikaël Gueguen, and Sylvie Castagnet. Towards the size estimation of a Representative Elementary Domain in semi-crystalline polymers. *Mechanics of Materials*, 95:116–124, April 2016. ISSN 01676636. doi: 10.1016/j.mechmat.2016.01.003. URL https://linkinghub.elsevier.com/retrieve/pii/S0167663616000041.

T.A. Tervoort, R.J.M. Smit, W.A.M. Brekelmans, and L.E. Govaert. A constitutive equation for the elasto-viscoplastic deformation of glassy polymers. *Mechanics of Time-Dependent Materials*, 1(3):269–291, 1998. ISSN 1385-2000. doi: 10.1023/A:1009720708029.

J. L. M. Thiesen, B. Klahr, T. A. Carniel, G. A. Holzapfel, P. J. Blanco, and E. A. Fancello. Second-order computational homogenization for bridging poromechanical scales under large deformations. *Computer Methods in Applied Mechanics and Engineering*, 433:117481, January 2025. ISSN 0045-7825. doi: 10.1016/j.cma.2024.117481.

P. H. M. Timmermans. *Evaluation of a Constitutive Model for Solid Polymeric Materials: Model Selection and Parameter Quantification*. PhD thesis, Eindhoven University of Technology, 1997.

Yoshihiro Tomita and Makoto Uchida. Computational characterization of micro- to mesoscopic deformation behavior of semicrystalline polymers. *International Journal of Mechanical Sciences*, 47(4):687–700, April 2005. ISSN 0020-7403. doi: 10.1016/j.ijmecsci.2004.10.011.

S. Toro, P. J. Sánchez, P. J. Blanco, E. A. de Souza Neto, A. E. Huespe, and R. A. Feijóo. Multiscale formulation for material failure accounting for cohesive cracks at the macro and micro scales. *International Journal of Plasticity*, 76:75–110, January 2016a. ISSN 0749-6419. doi: 10.1016/j.ijplas.2015.07.001.

S. Toro, P. J. Sánchez, J. M. Podestá, P. J. Blanco, A. E. Huespe, and R. A. Feijóo. Cohesive surface model for fracture based on a two-scale formulation: Computational implementation aspects. *Computational Mechanics*, 58(4):549–585, October 2016b. ISSN 1432-0924. doi: 10.1007/s00466-016-1306-y.

R. W. Truss, R. A. Duckett, and I. M. Ward. Effect of hydrostatic pressure on the yield and fracture of polyethylene in torsion. *Journal of Materials Science*, 16(6):1689–1699, June 1981. ISSN 1573-4803. doi: 10.1007/BF02396889. URL https://doi.org/10.1007/BF02396889.

Makoto Uchida and Naoya Tada. Micro-, meso- to macroscopic modeling of deformation behavior of semi-crystalline polymer. *International Journal of Plasticity*, 49:164–184, October 2013. ISSN 07496419. doi: 10.1016/j.ijplas.2013.03.007. URL https://linkinghub.elsevier.com/retrieve/pii/S0749641913000776.

Makoto Uchida, Tsuruyo Tokuda, and Naoya Tada. Finite element simulation of deformation behavior of semi-crystalline polymers with multi-spherulitic mesostructure. *International Journal of Mechanical Sciences*, 52(2):158–167, February 2010. ISSN 0020-7403. doi: 10.1016/j.ijmecsci.2009.09.002.

Makoto Uchida, Ryohei Wakuda, and Yoshihisa Kaneko. Evaluation and modeling of mechanical behaviors of thermosetting polymer under monotonic and cyclic tensile tests. *Polymer*, 174:130–142, 2019. ISSN 0032-3861. doi: https://doi.org/10.1016/j.polymer.2019.04.064. URL https://www.sciencedirect.com/science/article/pii/S003238611930391X.

Makoto Uchida, Kouhei Kamimura, Toyoshi Yoshida, and Yoshihisa Kaneko. Viscoelastic-viscoplastic modeling of epoxy based on transient network theory. *International Journal of Plasticity*, 153:103262, 2022. ISSN 0749-6419. doi: https://doi.org/10.1016/j.ijplas.2022.103262. URL https://www.sciencedirect.com/science/article/pii/S0749641922000456.

K. C. Valanis. A Theory of Viscoplasticity without a Yield Surface. Part 1. General Theory. Technical report, Iowa State University, Engineering Research Institute, 1970.

L.C.A. van Breemen, E.T.J. Klompen, L.E. Govaert, and H.E.H. Meijer. Extending the egp constitutive model for polymer glasses to multiple relaxation times. *Journal of the Mechanics and Physics of Solids*, 59(10):2191–2207, 2011. ISSN 0022-5096. doi: https://doi.org/10.1016/j.jmps.2011.05.001. URL https://www.sciencedirect.com/science/article/pii/S0022509611000925.

J van Dommelen, D Parks, M Boyce, W Brekelmans, and F Baaijens. Micromechanical modeling of the elasto-viscoplastic behavior of semi-crystalline polymers. *Journal of the Mechanics and Physics of Solids*, 51(3):519–541, March 2003. ISSN 00225096. doi: 10.1016/S0022-5096(02)00063-7. URL https://linkinghub.elsevier.com/retrieve/pii/S0022509602000637.

J. A. W. van Dommelen, D. M. Parks, M. C. Boyce, W. A. M. Brekelmans, and F. P. T. Baaijens. Micromechanical modeling of intraspherulitic deformation of semicrystalline polymers. *Polymer*, 44(19):6089–6101, September 2003. ISSN 0032-3861. doi: 10.1016/S0032-3861(03)00558-5.

Frederik Van Loock and Norman Fleck. Deformation and failure maps for PMMA in uniaxial tension. *Polymer*, 148, June 2018. doi: 10.1016/j.polymer.2018.06.027.

A.G. Varghese and R.C. Batra. Constitutive equations for thermomechanical deformations of glassy polymers. *International Journal of Solids and Structures*, 46(22):4079–4094, 2009. ISSN 0020-7683. doi: https://doi.org/10.1016/j.ijsolstr.2009.08.006.

M. Vieira de Carvalho, I. A. Rodrigues Lopes, and F. M. Andrade Pires. A multi-scale formulation for polycrystalline materials accounting for cohesive micro-cracks: Homogenisation of the traction-separation law. *International Journal of Plasticity*, page 103780, October 2023. ISSN 0749-6419. doi: 10.1016/j.ijplas.2023.103780.

W. Voigt. Ueber die Beziehung zwischen den beiden Elasticitätsconstanten isotroper Körper. *Annalen der Physik*, 274(12):573–587, January 1889. ISSN 0003-3804, 1521-3889. doi: 10.1002/andp.18892741206.

S.M. Walley and J.E. Field. Strain rate sensitivity of polymers in compression from low to high rates. *DYMAT*, Journal 1:211–227, 1994.

L. J. Walpole. On the overall elastic moduli of composite materials. *Journal of the Mechanics and Physics of Solids*, 17(4):235–251, September 1969. ISSN 0022-5096. doi: 10.1016/0022-5096(69)90014-3. URL https://www.sciencedirect.com/science/article/pii/0022509669900143.

Haitao Wang, Yun Zhang, Zhigao Huang, Zhongbin Tang, Yanpei Wang, and Huamin Zhou. Establishment and comparison of four constitutive relationships of pc/abs from low to high uniaxial strain rates. *Mechanics of Time-Dependent Materials*, 22, 11 2018. doi: 10.1007/s11043-017-9367-7.

J. Wang, L.F. Peng, Y.J. Deng, X.M. Lai, M.W. Fu, and J. Ni. A finite strain thermodynamically-based constitutive modeling and analysis of viscoelastic-viscoplastic deformation behavior of glassy polymers. *International Journal of Plasticity*, 122:135–163, 2019. ISSN 0749-6419. doi: https://doi.org/10.1016/j.ijplas.2019.06.013. URL https://www.sciencedirect.com/science/article/pii/S0749641919301317.

Ming Chen Wang and Eugene Guth. Statistical Theory of Networks of Non-Gaussian Flexible Chains. *The Journal of Chemical Physics*, 20(7):1144–1157, July 1952. ISSN 0021-9606. doi: 10.1063/1.1700682.

Zheliang Wang, Jingkai Guo, Jonathan E. Seppala, and Thao D. Nguyen. Extending the effective temperature model to the large strain hardening behavior of glassy polymers. *Journal of the Mechanics and Physics of Solids*, 146:104175, 2021. ISSN 0022-5096. doi: https://doi.org/10.1016/j.jmps.2020.104175. URL https://www.sciencedirect.com/science/article/pii/S0022509620304051.

I. M. Ward. Review: The yield behaviour of polymers. *Journal of Materials Science*, 6(11):1397–1417, November 1971. ISSN 0022-2461, 1573-4803. doi: 10.1007/BF00549685. URL http://link.springer.com/10.1007/BF00549685.

I. M. Ward and J. Sweeney. *An introduction to the mechanical properties of solid polymers*. Wiley, Chichester, West Sussex, England, 2nd ed edition, 2004. ISBN 978-0-471-49625-0 978-0-471-49626-7.

M.A. Wilding and I.M. Ward. Creep and recovery of ultra high modulus polyethylene. *Polymer*, 22(7):870–876, July 1981. ISSN 00323861. doi: 10.1016/0032-3861(81)90259-7. URL https://linkinghub.elsevier.com/retrieve/pii/0032386181902597.

J. R. Willis. Bounds and self-consistent estimates for the overall properties of anisotropic composites. *Journal of the Mechanics and Physics of Solids*, 25(3):185–202, June 1977. ISSN 0022-5096. doi: 10.1016/0022-5096(77)90022-9. URL https://www.sciencedirect.com/science/article/pii/0022509677900229.

J. R. Willis. Variational Estimates for the Overall Response of an Inhomogeneous Nonlinear Dielectric. In J. L. Ericksen, David Kinderlehrer, Robert Kohn, and J.-L. Lions, editors, *Homogenization and Effective Moduli of Materials and Media*, pages 247–263, New York, NY, 1986. Springer. ISBN 978-1-4613-8646-9. doi: 10.1007/978-1-4613-8646-9_12.

L. Wu, L. Noels, L. Adam, and I. Doghri. A combined incremental-secant mean-field homogenization scheme with per-phase residual strains for elasto-plastic composites. *International Journal of Plasticity*, 51:80–102, December 2013. ISSN 07496419. doi: 10.1016/j.ijplas.2013.06.006.

P. D. Wu and E. Van Der Giessen. On improved network models for rubber elasticity and their applications to orientation hardening in glassy polymers. *Journal of the Mechanics and Physics of Solids*, 41(3):427–456, March 1993. ISSN 0022-5096. doi: 10.1016/0022-5096(93)90043-F. URL https://www.sciencedirect.com/science/article/pii/002250969390043F.

Rui Xiao and Thao D. Nguyen. An effective temperature theory for the nonequilibrium behavior of amorphous polymers. *Journal of the Mechanics and Physics of Solids*, 82:62–81, 2015. ISSN 0022-5096. doi: https://doi.org/10.1016/j.jmps.2015.05.021. URL https://www.sciencedirect.com/science/article/pii/S0022509615001325.

D. Yao and E. Krempl. Viscoplasticity theory based on overstress. The prediction of monotonic and cyclic proportional and nonproportional loading paths of an aluminum alloy. *International Journal of Plasticity*, 1(3):259–274, January 1985. ISSN 0749-6419. doi: 10.1016/0749-6419(85)90007-5. URL https://www.sciencedirect.com/science/article/pii/0749641985900075.

J. Ye, S. André, and L. Farge. Kinematic study of necking in a semi-crystalline polymer through 3D Digital Image Correlation. *International Journal of Solids and Structures*, 59:58–72, May 2015. ISSN 00207683. doi: 10.1016/j.ijsolstr.2015.01.009. URL https://linkinghub.elsevier.com/retrieve/pii/S0020768315000116.

Peng Yu, Xiaohu Yao, Qiang Han, Shuguang Zang, and Yabei Gu. A visco-elastoplastic constitutive model for large deformation response of polycarbonate over a wide range of strain rates and temperatures. *Polymer*, 55(25):6577–6593, December 2014. ISSN 0032-3861. doi: 10.1016/j.polymer.2014.09.071.

F. Zaïri, M. Naït-Abdelaziz, J.M. Gloaguen, and J.M. Lefebvre. Modelling of the elasto-viscoplastic damage behaviour of glassy polymers. *International Journal of Plasticity*, 24(6):945–965, June 2008. ISSN 07496419. doi: 10.1016/j.ijplas.2007.08.001. URL https://linkinghub.elsevier.com/retrieve/pii/S074964190700112X.

Fahmi Zaïri, Krzysztof Woznica, and Moussa Naït-Abdelaziz. Phenomenological nonlinear modelling of glassy polymers. *Comptes Rendus Mécanique*, 333(4):359–364, April 2005. ISSN 16310721. doi: 10.1016/j.crme.2005.02.003. URL https://linkinghub.elsevier.com/retrieve/pii/S1631072105000380.

Fahmi Zaïri, Moussa Naït-Abdelaziz, Krzysztof Woznica, and Jean-Michel Gloaguen. Elasto-viscoplastic constitutive equations for the description of glassy polymers behavior at constant strain rate. *Journal of Engineering Materials and Technology*, 129(1):29–35, January 2007. ISSN 0094-4289, 1528-8889. doi: 10.1115/1.2400256. URL https://asmedigitalcollection.asme.org/materialstechnology/article/129/1/29/464906/Elastoviscoplastic-constitutive-equations-for-the.

Fanfei Zeng, Philippe Le Grognec, Marie-France Lacrampe, and Patricia Krawczak. A constitutive model for semi-crystalline polymers at high temperature and finite plastic strain: Application to PA6 and PE biaxial stretching. *Mechanics of Materials*, 42(7):686–697, July 2010. ISSN 01676636. doi: 10.1016/j.mechmat.2010.04.006. URL https://linkinghub.elsevier.com/retrieve/pii/S0167663610000530.

Chuntao Zhang and Ian D. Moore. Nonlinear mechanical response of high density polyethylene. Part II: Uniaxial constitutive modeling. *Polymer Engineering & Science*, 37(2):414–420, February 1997. ISSN 0032-3888, 1548-2634. doi: 10.1002/pen.11684. URL https://onlinelibrary.wiley.com/doi/10.1002/pen.11684.

Meijuan Zhang and Francisco J. Montáns. A simple formulation for large-strain cyclic hyperelasto-plasticity using elastic correctors. theory and algorithmic implementation. *International Journal of Plasticity*, 113:185–217, 2019. ISSN 0749-6419. doi: https://doi.org/10.1016/j.ijplas.2018.09.013. URL https://www.sciencedirect.com/science/article/pii/S0749641918303061.

Meijuan Zhang, K. Nguyen, Javier Segurado, and Francisco J. Montáns. A multiplicative finite strain crystal plasticity formulation based on additive elastic corrector rates: Theory and numerical implementation. *International Journal of Plasticity*, 137:102899, 2021. ISSN 0749-6419. doi: https://doi.org/10.1016/j.ijplas.2020.102899. URL https://www.sciencedirect.com/science/article/pii/S0749641920307440.

Qamer Zia, Daniela Mileva, and René Androsch. Rigid Amorphous Fraction in Isotactic Polypropylene. *Macromolecules*, 41(21):8095–8102, November 2008. ISSN 0024-9297, 1520-5835. doi: 10.1021/ma801455m. URL https://pubs.acs.org/doi/10.1021/ma801455m.

F. J. Zoepfl, V. Marković, and Joseph Silverman. Differential scanning calorimetry studies of irradiated polyethylene: I. Melting temperatures and fusion endotherms. *Journal of Polymer Science: Polymer Chemistry Edition*, 22(9):2017–2032, 1984. ISSN 1542-9369. doi: 10.1002/pol.1984.170220907. URL https://onlinelibrary.wiley.com/doi/abs/10.1002/pol.1984.170220907. _eprint: https://onlinelibrary.wiley.com/doi/pdf/10.1002/pol.1984.170220907.

L. M. Zubov. The Stationary Principle of Complementary Work in Nonlinear Theory of Elasticity. *Journal of Applied Mathematics and Mechanics*, 34(2):228–232, January 1970. ISSN 0021-8928. doi: 10.1016/0021-8928(70)90136-X. URL https://www.sciencedirect.com/science/article/pii/002189287090136X.

Dan Andrei Şerban, Glenn Weber, Liviu Marşavina, Vadim V. Silberschmidt, and Werner Hufenbach. Tensile properties of semi-crystalline thermoplastic polymers: Effects of temperature and strain rates. *Polymer Testing*, 32(2):413–425, April 2013. ISSN 01429418. doi: 10.1016/j.polymertesting.2012.12.002. URL https://linkinghub.elsevier.com/retrieve/pii/S0142941812002346.

Page intentionally left blank.

Appendix A

Infinitesimal thermoviscoelasticity and Fourier's law

Given the modeling objectives specified in Chapter 9, infinitesimal viscoelasticity presents itself as a satisfactory starting point. Depending on the model, it can capture strain recovery, creep, stress relaxation, and the transient behavior under monotonic loading—these are essential features to describe the mechanical behavior of a semi-crystalline polymer.

A.1 Infinitesimal thermoviscoelasticity

Infinitesimal thermoviscoelasticity, as presented in Christensen (2013), assumes that strains, $\boldsymbol{\varepsilon}$, are small, as well as the temperature difference with respect to some reference temperature, $\Delta T = T - T_0$. This implies a small perturbation away from thermodynamic equilibrium. The constitutive relations found concerning stress and entropy, coinciding with the description of a linear time-invariant (LTI) system, are

$$\boldsymbol{\sigma}(t) = \int_{-\infty}^{t} \mathbf{G}(t-\tau) : \frac{\partial \boldsymbol{\varepsilon}}{\partial \tau} d\tau - \int_{-\infty}^{t} \boldsymbol{\beta}(t-\tau) \frac{\partial \Delta T(\tau)}{\partial \tau} d\tau, \tag{A.1}$$

$$\rho s(t) = \int_{-\infty}^{t} \boldsymbol{\beta}(t-\tau) : \frac{\partial \boldsymbol{\varepsilon}}{\partial \tau} d\tau + \int_{-\infty}^{t} m(t-\tau) \frac{\partial \Delta T(\tau)}{\partial \tau} d\tau, \tag{A.2}$$

assuming a quadratic free energy (Christensen, 2013) [1], where $\mathbf{G}$ denotes the time-dependent fourth-order relaxation modulus tensor, $\boldsymbol{\beta}$ is the time-dependent second-order thermal stress

[1] Employing the Stone–Weierstrass and Riesz representation theorems, the expression found for the free energy, discarding third-order effects, is

$$\begin{aligned}\rho\psi(t) = \int_{-\infty}^{t} \boldsymbol{D}(t-\tau) : \frac{\partial \boldsymbol{\varepsilon}(\tau)}{\partial \tau} d\tau + \int_{-\infty}^{t} \delta(t-\tau) \frac{\partial \Delta T(\tau)}{\partial \tau} d\tau \\ + \frac{1}{2} \int_{-\infty}^{t} \int_{-\infty}^{t} \frac{\partial \boldsymbol{\varepsilon}(\eta)}{\partial \eta} : \mathbf{G}(t-\tau, t-\eta) : \frac{\partial \boldsymbol{\varepsilon}(\tau)}{\partial \tau} d\tau d\eta \\ - \int_{-\infty}^{t} \int_{-\infty}^{t} \boldsymbol{\beta}(t-\tau, t-\eta) : \frac{\partial \boldsymbol{\varepsilon}(\tau)}{\partial \tau} \frac{\partial \Delta T(\eta)}{\partial \eta} d\tau d\eta \\ - \frac{1}{2} \int_{-\infty}^{t} \int_{-\infty}^{t} m(t-\tau, t-\eta) \frac{\partial \Delta T(\tau)}{\partial \tau} \frac{\partial \Delta T(\eta)}{\partial \eta} d\tau d\eta,\end{aligned} \tag{A.3}$$

where $\boldsymbol{D}$, δ, $\boldsymbol{G}$, $\boldsymbol{\beta}$ and m are appropriate functions describing material properties. In particular, the last three quantities are the counterparts in infinitesimal thermoviscoelasticity to the stiffness tensor, the coefficient of thermal stress, and a constant related to the specific heat at constant deformation, respectively, in infinitesimal thermoelasticity.

coefficient tensor, and m is a time-dependent material property related to the specific heat at constant deformation, i.e., $C_{\boldsymbol{F}} = Tm$. The constitutive equations above are linear in the sense that they satisfy the principle of superposition, i.e., the response to a sum of inputs is the sum of the responses to each individual input (see Figure A.1). In the context of viscoelasticity, this principle is called the Boltzmann–Volterra superposition principle (Ward and Sweeney, 2004). This is intrinsically connected to the fact that as a material property, the relaxation modulus is only a function of time and not of strain, strain rate or stress.

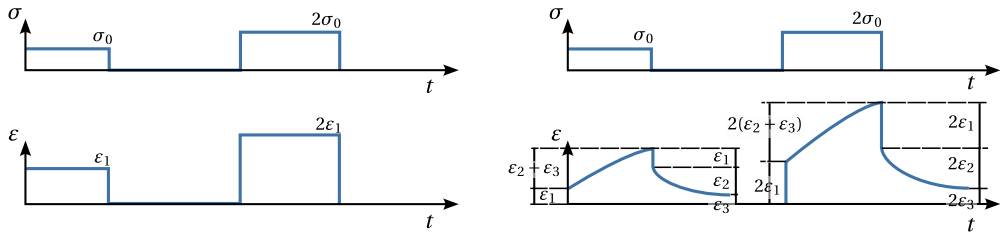

Figure A.1: Stress-driven linear response of (a) an elastic, and (b) a viscoelastic material. Adapted from Ward and Sweeney (2004).

The strain–stress relationship may also be expressed employing the stress as the independent variable, leading to the so-called creep compliance formulation, as

$$\boldsymbol{\varepsilon}(t) = \int_{-\infty}^{t} \mathbf{J}(t-\tau) : \frac{\partial \boldsymbol{\sigma}(\tau)}{\partial \tau}\, d\tau + \int_{-\infty}^{t} \boldsymbol{\alpha}(t-\tau) \frac{\partial \Delta T(\tau)}{\partial \tau} d\tau, \tag{A.4}$$

where $\mathbf{J}$ is the creep compliance of the material and $\boldsymbol{\alpha}$ is the thermal expansion coefficient tensor. Regarding dissipation, its magnitude is of second order and, as such, can be discarded in this infinitesimal theory.

These descriptions are equivalent to a system of linear ordinary differential equations governing the evolution of the internal variables[2]. Thus, Equation (A.1) is the solution of the system of equations

$$\dot{\boldsymbol{\alpha}}(t) = \mathbf{D} : \boldsymbol{\sigma}(t) + \boldsymbol{\varphi} \Delta T(t) + \mathbb{D} : \boldsymbol{\alpha}(t), \tag{A.5}$$

$$\boldsymbol{\sigma}(t) = \mathbf{G} : \boldsymbol{\varepsilon}(t) + \boldsymbol{\beta} \Delta T(t) + \mathbb{G} : \boldsymbol{\alpha}(t), \tag{A.6}$$

$$s(t) = \boldsymbol{\beta} : \boldsymbol{\varepsilon}(t) + m \Delta T(t) + \mathbb{B} : \boldsymbol{\alpha}(t), \tag{A.7}$$

where the matrices in the equations above are related to those in Equations (2.31) and (2.32) through

$$\mathbf{D} = \frac{\partial \boldsymbol{f}}{\partial \boldsymbol{F}}(\boldsymbol{I}, T, \boldsymbol{\alpha}_0), \quad \boldsymbol{\varphi} = \frac{\partial \boldsymbol{f}}{\partial T}(\boldsymbol{I}, T, \boldsymbol{\alpha}_0), \quad \mathbb{D} = \frac{\partial \boldsymbol{f}}{\partial \boldsymbol{\alpha}}(\boldsymbol{I}, T, \boldsymbol{\alpha}_0), \tag{A.8}$$

$$\mathbf{C} = \frac{\partial \boldsymbol{h}}{\partial \boldsymbol{F}}(\boldsymbol{I}, T, \boldsymbol{\alpha}_0), \quad \boldsymbol{\beta} = \frac{\partial \boldsymbol{h}}{\partial T}(\boldsymbol{I}, T, \boldsymbol{\alpha}_0), \quad \mathbb{G} = \frac{\partial \boldsymbol{h}}{\partial \boldsymbol{\alpha}}(\boldsymbol{I}, T, \boldsymbol{\alpha}_0), \tag{A.9}$$

$$\boldsymbol{\beta} = \frac{\partial j}{\partial \boldsymbol{F}}(\boldsymbol{I}, T, \boldsymbol{\alpha}_0), \quad m = \frac{\partial s}{\partial T}(\boldsymbol{I}, T, \boldsymbol{\alpha}_0), \quad \mathbb{B} = \frac{\partial s}{\partial \boldsymbol{\alpha}}(\boldsymbol{I}, T, \boldsymbol{\alpha}_0), \tag{A.10}$$

[2]The convolution and the internal variables formulation are equivalent when the relaxation modulus is chosen as a Prony series, i.e., as a sum of exponential functions. See Equation (A.13).

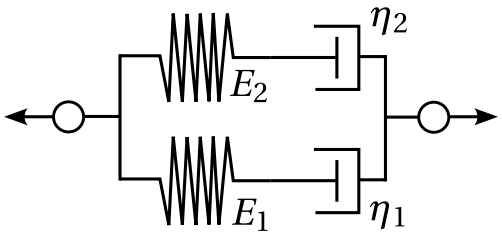

Figure A.2: Rheological model for the Burgers material (Maxwell representation).

Often, these can be identified with the behavior of linear rheological models, which provide a visual counterpart and help in the interpretation of the model. These are one-dimensional mechanical models containing diverse arrangements of linear springs and dashpots. For an in-depth discussion on the connection between LTIs and ordinary differential equations, see Ciampa et al. (2019).

There are other equivalent representations of the time-dependent material properties. In particular, when the loading is periodic, it is common to express the constitutive equations in the frequency domain, leading to the complex modulus representation (Ward and Sweeney, 2004). The storage modulus, $\mathbf{G}'$, and the loss modulus, $\mathbf{G}''$, represent the elastic and viscous behavior of the material, respectively. They are defined as the real and imaginary parts of the complex modulus, $\mathbf{G}^*$, given by

$$\mathbf{G}^*(\omega) = \mathbf{G}'(\omega) + i\mathbf{G}''(\omega), \tag{A.11}$$

where ω is the angular frequency of the loading. The loss factor, δ, is the phase shift between the strain loading and the stress response.

To better show what is the typical behavior of a viscoelastic material, we consider a so-called one-dimensional Burgers material, whose relaxation modulus, G, is given by (Malkin and Isayev, 2017)

$$G(t) = G_1 e^{-t/\theta_1} + G_2 e^{-t/\theta_2}, \tag{A.12}$$

where $\theta_i = \eta_i / G_i$ is the i-th relaxation time. See Figure A.2 for the corresponding rheological model, which consists of two Maxwell elements (spring and dashpot in series) in parallel. If a spring in parallel is added to the Burgers model, and more Maxwell branches are considered, the so-called generalized Maxwell model is obtained. A representation of its relaxation modulus is given by the so-called Prony series (Christensen, 2013; Ward and Sweeney, 2004), expressed as

$$G(t) = G_\infty + \sum_{i=1}^{n_\mathrm{V}} G_i e^{-t/\theta_i}, \tag{A.13}$$

where G_∞ is the long-term modulus, G_i are the moduli of each Maxwell element, θ_i are the corresponding relaxation times, and n_V is the number of Maxwell elements in the model.

Also, for a Burgers material, an equivalent description can be established as

$$\dot{\varepsilon}_1^p(t) = \frac{1}{\theta_1}(\varepsilon(t) - \varepsilon_1^p(t)), \tag{A.14}$$

$$\dot{\varepsilon}_2^p(t) = \frac{1}{\theta_2}(\varepsilon(t) - \varepsilon_2^p(t)), \tag{A.15}$$

$$\sigma(t) = G_1(\varepsilon(t) - \varepsilon_1^p(t)) + G_2(\varepsilon(t) - \varepsilon_2^p(t)), \tag{A.16}$$

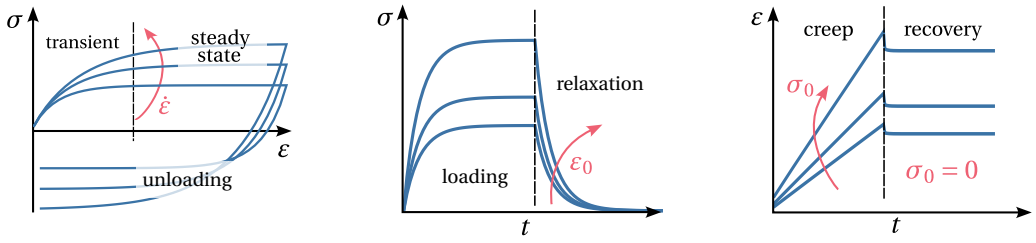

Figure A.3: Schematic response of the Burgers material in (a) a constant strain rate experiment followed by unloading at the same strain rate, (b) a stress relaxation experiment and a (c) creep experiment with recovery.

where ε_i^p is the strain in the i-th dashpot, $i = 1,2$, the internal variables of the constitutive model. In a set of constant-strain-rate experiments at different strain rates, their evolution can be tied to transient effects, such as the ones observed at the beginning of the monotonic loading at a constant strain rate in the case of a Burgers material (see Figure A.3(a)). At some point (see Figure 9.1(a)), a steady state will be reached, ($\dot{\boldsymbol{\alpha}} =$ constant), and the corresponding response of the Burgers material model is constant. Furthermore, for a given strain, the steady-state stress varies linearly with the strain rate and is proportional to the relaxation time, corresponding to so-called Newtonian viscosity (Matsuoka, 1996) (see Figure 9.1(a)). An infinitesimal viscoelastic material will not show strain-rate dependence in the steady-state stress–strain curve, or be able to capture different transient effects at different strain rates, as shown in Figure 9.1(b).

Figures A.3(b) and A.3(c) illustrate the response of the Burgers material to a constant strain and constant stress, respectively, followed by release illustrating the ability of the model to capture the phenomena of stress relaxation, creep, and recovery. The expected linear behavior in a stress relaxation experiment is to obtain the same stress response up to a multiplicative constant, which is the initial strain. Likewise, in a creep experiment, the strain response divided by the stress is equal for experiments at different stress levels. Both of these facts are not always observed in practice.

Note that the response of this very simple model is already quite rich, indicating that the choice in the arrangement of springs and dashpots in the rheological model is crucial to capture the relevant physics of the material under study, even before considering nonlinear effects (compare the two hypothetical responses shown in Figure 9.1). As such, a grouping of nonlinear models based on different arrangements of springs and dashpots is pursued in Section 9.1. Also note that in addition to being independent of the deformation, the thermomechanical properties in infinitesimal viscoelasticity are also independent of temperature. This is not the case in practice, where the relaxation modulus and creep compliance are highly dependent on temperature, as discussed in Section 8.2.2.

Chapter 8 aims to show that experimentally these linear assumptions are frequently violated. These results can now be discussed in light of the expected linear behavior, highlighting the necessary nonlinear additions for a more accurate constitutive model. The advances in that direction suggested in the literature are reviewed in Section 9.1.

In general, the relaxation modulus can also be written as (Malkin and Isayev, 2017)

$$G(t) = G_\infty + \varphi(t), \tag{A.17}$$

where G_∞ is the equilibrium modulus and φ is the relaxation function. Taking into account its physical meaning, the latter must be a decreasing function of time tending to zero as $t \to \infty$.

The functions of such type can always be presented by the following integral

$$\varphi(t) = \int_0^\infty H(\theta) e^{-t/\theta} \, d\theta, \tag{A.18}$$

where θ denotes the relaxation time, and H is a function of the distribution of the relaxation times, the so-called relaxation time spectrum.

A.2 Fourier's law

Regarding the constitutive model for the heat flux (Equation (2.31)), the second law of thermodynamics essentially requires the heat flow to occur in the opposite direction of the temperature gradient (Equation (2.42)). The Fourier heat conduction law for isotropic conduction in the deformed volume is one of the simplest and most popular alternatives, defining the heat flux as

$$\boldsymbol{q}_0 = -k_0 \boldsymbol{C}^{-1} \boldsymbol{g}_0, \tag{A.19}$$

where $k_0 > 0$ is the thermal conductivity.

Page intentionally left blank.

Appendix B

Topics in tensor calculus

B.1 Notation

Before proceeding, we introduce some notation used throughout the text, particularly concerning cross products and curl operations in the reference configuration.

The cross product between two three-dimensional vectors $\boldsymbol{a}$ and $\boldsymbol{b}$ is denoted by $\boldsymbol{a}\times\boldsymbol{b}$ and defined as

$$\boldsymbol{a}\times\boldsymbol{b}=\varepsilon_{ijk}a_i b_j \boldsymbol{e}_k, \tag{B.1}$$

where ε_{ijk} is the Levi-Civita symbol, and $\boldsymbol{e}_k$ is the k-th canonical basis vector in $\mathbb{R}^3$, with $k=1,2,3$.

Similarly, the curl of a vector field $\boldsymbol{v}$ defined on the reference domain $\Omega_{0,\mu}$ is denoted by $\operatorname{curl}_0\boldsymbol{v}$ and is given by

$$\operatorname{curl}_0\boldsymbol{v}=\varepsilon_{ijk}v_{j,i}\boldsymbol{e}_k, \tag{B.2}$$

where $v_{j,i}$ denotes the partial derivative of the j-th component of $\boldsymbol{v}$ with respect to the i-th reference coordinate.

The cross product between a vector and a second-order tensor is defined recursively through the relation

$$\boldsymbol{a}\times(\boldsymbol{C}^T\boldsymbol{b})=(\boldsymbol{a}\times\boldsymbol{C})^T\boldsymbol{b}, \tag{B.3}$$

where $\boldsymbol{a}$ and $\boldsymbol{b}$ are vectors, and $\boldsymbol{C}$ is a second-order tensor. In index notation, Equation (B.3) becomes

$$\varepsilon_{ijk}a_i C_{lj}b_l\boldsymbol{e}_k=\boldsymbol{b}\cdot(\varepsilon_{ijk}a_i C_{lj}\boldsymbol{e}_l\otimes\boldsymbol{e}_k), \tag{B.4}$$

where $\otimes$ denotes the dyadic product, such that $(\boldsymbol{a}\otimes\boldsymbol{b})_{ij}=a_i b_j$.

In analogy with the anti-commutative property of the vector cross product, i.e.,

$$\boldsymbol{a}\times\boldsymbol{b}=-\boldsymbol{b}\times\boldsymbol{a}, \tag{B.5}$$

we define the cross product of a second-order tensor with a vector as

$$\boldsymbol{C}\times\boldsymbol{a}=-\boldsymbol{a}\times\boldsymbol{C}. \tag{B.6}$$

The curl of a second-order tensor field $\boldsymbol{C}$ defined on $\Omega_{0,\mu}$ is denoted by $\operatorname{curl}_0\boldsymbol{C}$ and is defined analogously via the relation

$$\operatorname{curl}_0(\boldsymbol{C}^T\boldsymbol{a})=(\operatorname{curl}_0\boldsymbol{C})^T\boldsymbol{a}, \tag{B.7}$$

for any constant vector field $\boldsymbol{a}$ defined on $\Omega_{0,\mu}$. In component form, this reads

$$\varepsilon_{ijk}C_{lj,i}a_l\boldsymbol{e}_k=\boldsymbol{a}\cdot(\varepsilon_{ijk}C_{lj,i}\boldsymbol{e}_l\otimes\boldsymbol{e}_k). \tag{B.8}$$

Remark 2.1 | Why the transposes?

The transposes in Equations (B.3) and (B.7) may at first appear to complicate the definitions unnecessarily. However, they are essential to ensure that the operations apply to the second index of the second-order tensor, in alignment with common conventions in continuum mechanics.

This is analogous to the definition of the divergence of a second-order tensor field, which is typically taken with respect to the second index. The divergence operation is defined recursively by

$$\operatorname{div}_0(\boldsymbol{C}^T\boldsymbol{b}) = (\operatorname{div}_0\boldsymbol{C})^T\boldsymbol{b} = \boldsymbol{b}\cdot\operatorname{div}_0\boldsymbol{C},$$

for any constant vector $\boldsymbol{b}$. In index notation, this leads to

$$(C_{ij}b_i)_{,j} = C_{ij,j}b_i,$$

and therefore,

$$(\operatorname{div}_0\boldsymbol{C})_i = C_{ij,j},$$

as expected.

B.2 Tensor calculus identities

In this section, we derive two useful tensor calculus identities that are used in the main text.

First, we show that

$$\operatorname{curl}_0(\boldsymbol{Y}\times\boldsymbol{a}) = -2\boldsymbol{a}, \tag{B.9}$$

where $\boldsymbol{a}$ is a constant vector field, and $\boldsymbol{Y}$ is the microscopic position vector. In index notation

$$\operatorname{curl}_0(\boldsymbol{Y}\times\boldsymbol{a})_m = \varepsilon_{lkm}(\varepsilon_{ijk}Y_ia_j)_{,l}$$

Expanding this, we find

$$\begin{aligned}
\varepsilon_{lkm}(\varepsilon_{ijk}Y_ia_j)_{,l} &= \varepsilon_{lkm}\varepsilon_{ijk}a_jY_{i,l} && (\boldsymbol{a}\text{ constant})\\
&= \varepsilon_{lkm}\varepsilon_{ijk}a_j\delta_{il} && (\boldsymbol{Y}\text{ linear})\\
&= \varepsilon_{lkm}\varepsilon_{ljk}a_j && (\text{Kronecker delta property})\\
&= -\varepsilon_{mkl}\varepsilon_{jkl}a_j && (\text{Levi-Civita index swap})\\
&= -2\delta_{mj}a_j && (\text{Levi-Civita contraction})\\
&= -2a_m,
\end{aligned}$$

as required.

The second identity we need is

$$\boldsymbol{P} = \frac{1}{2}\operatorname{curl}_0\left(\boldsymbol{P}\times(\boldsymbol{Y}-\boldsymbol{Y}_0)\right). \tag{B.10}$$

We employ the recursive definition of the curl operator (Equation (B.7)) and the definition of the

cross product (Equation (B.3)), as well as Equation (B.9), as follows

$$\begin{aligned}
\operatorname{curl}_0\left(\frac{1}{2}\boldsymbol{P}\times(\boldsymbol{Y}-\boldsymbol{Y}_0)\right)^T\boldsymbol{c} &= -\frac{1}{2}\operatorname{curl}_0\left((\boldsymbol{Y}-\boldsymbol{Y}_0)\times\boldsymbol{P}\right)^T\boldsymbol{c} && \text{(Eq. (B.6))} && \text{(B.11)}\\
&= -\frac{1}{2}\operatorname{curl}_0\left(((\boldsymbol{Y}-\boldsymbol{Y}_0)\times\boldsymbol{P})^T\boldsymbol{c}\right) && \text{(Eq. (B.7))} && \text{(B.12)}\\
&= -\frac{1}{2}\operatorname{curl}_0\left((\boldsymbol{Y}-\boldsymbol{Y}_0)\times\boldsymbol{P}^T\boldsymbol{c}\right) && \text{(Eq. (B.3))} && \text{(B.13)}\\
&= -\frac{1}{2}(-2\boldsymbol{P}^T\boldsymbol{c}) && \text{(Eq. (B.9))} && \text{(B.14)}\\
&= \boldsymbol{P}^T\boldsymbol{c}. && && \text{(B.15)}
\end{aligned}$$

Since this holds for any constant vector $\boldsymbol{c}$, we confirm Equation (B.10).

Page intentionally left blank.

Appendix C

Further derivations regarding MFH models based on the PMVP and PMCVP

C.1 Detailed derivations regarding models based on the Principle of Multiscale Virtual Power

This section collects some of the detailed derivations regarding the models based on the PMVP that were omitted in the main text for brevity.

C.1.1 Projected Mean-Field Homogenization Model

This section provides the detailed derivation of the energetic consistency of the PMVP-based projected MFH model introduced in Section 5.1.3. It also details the derivation concerning the satisfaction of the macroscopic angular momentum balance condition.

Energetic consistency

We intend to show now that the stress-homogenization rule in Equation (5.82) implies consistency between the macroscopic and microscopic power. Accordingly, we consider the macroscopic power, writing

$$\boldsymbol{P} : \dot{\boldsymbol{F}} = \left\langle \boldsymbol{P}_{\mu}^{i,*} : \mathbf{A}_{\mu}^{i,\mathrm{mfh}} \right\rangle : \dot{\boldsymbol{F}}. \tag{C.1}$$

We then expand the right-hand side as

$$\boldsymbol{P}:\dot{\boldsymbol{F}} = \left\langle \left(\boldsymbol{\Omega}_\mu + \boldsymbol{\Omega}^i_{N,\mu} : \mathbf{P}^i_{N,\mu} : \frac{d\boldsymbol{U}}{d\boldsymbol{F}}(\boldsymbol{F}^{i,\mathrm{mfh}}_\mu) + \boldsymbol{\Omega}^i_{R,\mu} : \frac{d\boldsymbol{R}}{d\boldsymbol{F}}(\boldsymbol{F}^{i,\mathrm{mfh}}_\mu) \right) : \mathbf{A}^{i,\mathrm{mfh}}_\mu \right\rangle : \dot{\boldsymbol{F}} \tag{C.2}$$

$$= \left\langle \left(\boldsymbol{\Omega}_\mu + \boldsymbol{\Omega}^i_{N,\mu} : \mathbf{P}^i_{N,\mu} : \frac{d\boldsymbol{U}}{d\boldsymbol{F}}(\boldsymbol{F}^{i,\mathrm{mfh}}_\mu) + \boldsymbol{\Omega}^i_{R,\mu} : \frac{d\boldsymbol{R}}{d\boldsymbol{F}}(\boldsymbol{F}^{i,\mathrm{mfh}}_\mu) \right) : \mathbf{A}^{i,\mathrm{mfh}}_\mu : \dot{\boldsymbol{F}} \right\rangle \tag{C.3}$$

$$= \left\langle \left(\boldsymbol{\Omega}_\mu + \boldsymbol{\Omega}^i_{N,\mu} : \mathbf{P}^i_{N,\mu} : \frac{d\boldsymbol{U}}{d\boldsymbol{F}}(\boldsymbol{F}^{i,\mathrm{mfh}}_\mu) + \boldsymbol{\Omega}^i_{R,\mu} : \frac{d\boldsymbol{R}}{d\boldsymbol{F}}(\boldsymbol{F}^{i,\mathrm{mfh}}_\mu) \right) : \dot{\boldsymbol{F}}^{i,\mathrm{mfh}}_\mu \right\rangle \tag{C.4}$$

$$= \left\langle \boldsymbol{\Omega}_\mu : \dot{\boldsymbol{F}}^{i,\mathrm{mfh}}_\mu + \boldsymbol{\Omega}^i_{N,\mu} : \mathbf{P}^i_{N,\mu} : \frac{d\boldsymbol{U}}{d\boldsymbol{F}}(\boldsymbol{F}^{i,\mathrm{mfh}}_\mu) : \dot{\boldsymbol{F}}^{i,\mathrm{mfh}}_\mu + \boldsymbol{\Omega}^i_{R,\mu} : \frac{d\boldsymbol{R}}{d\boldsymbol{F}}(\boldsymbol{F}^{i,\mathrm{mfh}}_\mu) : \dot{\boldsymbol{F}}^{i,\mathrm{mfh}}_\mu \right\rangle, \tag{C.5}$$

where we used the expression for the effective stress found in Equation (5.83) and the relationship between the strain rate in phase i in the auxiliary problem and the macroscopic strain rate through Equation (4.18). We also assume that there are no internal variables in the constitutive description of the material phases, i.e., when dealing with elastic materials. They would be accounted for similarly as in the fully constrained case (see Section 5.1.2).

We take in turn each of the three terms corresponding to phase i in Equation (C.5). First, note that the Lagrange multiplier $\boldsymbol{\Omega}_\mu$ is a constant, and can be factored out of the volume-weighted average. Combining this with the self-consistency condition imposed on the MFH procedure, we write

$$\left\langle \boldsymbol{\Omega}_\mu : \dot{\boldsymbol{F}}^{i,\mathrm{mfh}}_\mu \right\rangle = \boldsymbol{\Omega}_\mu : \left\langle \dot{\boldsymbol{F}}^{i,\mathrm{mfh}}_\mu \right\rangle \tag{C.6}$$

$$= \boldsymbol{\Omega}_\mu : \dot{\boldsymbol{F}} \tag{C.7}$$

$$= \boldsymbol{\Omega}_\mu : \left\langle \dot{\boldsymbol{F}}^i_\mu \right\rangle \tag{C.8}$$

$$= \left\langle \boldsymbol{\Omega}_\mu : \dot{\boldsymbol{F}}^i_\mu \right\rangle. \tag{C.9}$$

Next, taking the time derivative of the constraint imposed in Equation (5.53), we find

$$\mathbf{P}^i_{N,\mu} : \dot{\boldsymbol{U}}^{i,\mathrm{mfh}}_\mu = \mathbf{P}^i_{N,\mu} : \frac{d\boldsymbol{U}}{d\boldsymbol{F}}(\boldsymbol{F}^{i,\mathrm{mfh}}_\mu) : \dot{\boldsymbol{F}}^{i,\mathrm{mfh}}_\mu \tag{C.10}$$

$$= \mathbf{P}^i_{N,\mu} : \frac{d\boldsymbol{U}}{d\boldsymbol{F}}(\boldsymbol{F}^{i,\mathrm{mfh}}_\mu) : \boldsymbol{A}^{i,\mathrm{mfh}}_\mu : \dot{\boldsymbol{F}} \tag{C.11}$$

$$= \mathbf{P}^i_{N,\mu} : \frac{d\boldsymbol{U}}{d\boldsymbol{F}}(\boldsymbol{F}^i_\mu) : \dot{\boldsymbol{F}} \tag{C.12}$$

$$= \mathbf{P}^i_{N,\mu} : \dot{\boldsymbol{U}}^i_\mu, \tag{C.13}$$

employing the chain rule. Likewise, taking the time derivative of the constraint imposed in Equation (5.54), we obtain

$$\dot{\boldsymbol{R}}^{i,\mathrm{mfh}}_\mu = \frac{d\boldsymbol{R}}{d\boldsymbol{F}}(\boldsymbol{F}^{i,\mathrm{mfh}}_\mu) : \dot{\boldsymbol{F}}^{i,\mathrm{mfh}}_\mu \tag{C.14}$$

$$= \frac{d\boldsymbol{R}}{d\boldsymbol{F}}(\boldsymbol{F}^i_\mu) : \dot{\boldsymbol{F}} \tag{C.15}$$

$$= \dot{\boldsymbol{R}}^i_\mu. \tag{C.16}$$

Using these results, we can rewrite Equation (C.5) as

$$\boldsymbol{P}:\dot{\boldsymbol{F}} = \left\langle \boldsymbol{\Omega}_\mu : \dot{\boldsymbol{F}}^i_\mu + \boldsymbol{\Omega}^i_{N,\mu} : \dot{\boldsymbol{U}}^i_\mu + \boldsymbol{\Omega}^i_{R,\mu} : \dot{\boldsymbol{R}}^i_\mu \right\rangle \tag{C.17}$$

$$= \left\langle \boldsymbol{\Omega}_\mu : \dot{\boldsymbol{F}}^i_\mu + \boldsymbol{\Omega}^i_{N,\mu} : \mathbf{P}^i_{N,\mu} : \frac{d\boldsymbol{U}}{d\boldsymbol{F}}(\boldsymbol{F}^i_\mu) : \dot{\boldsymbol{F}}^i_\mu + \boldsymbol{\Omega}^i_{R,\mu} : \frac{d\boldsymbol{R}}{d\boldsymbol{F}}(\boldsymbol{F}^i_\mu) : \dot{\boldsymbol{F}}^i_\mu \right\rangle \tag{C.18}$$

$$= \left\langle \left(\boldsymbol{\Omega}_\mu + \boldsymbol{\Omega}^i_{N,\mu} : \mathbf{P}^i_{N,\mu} : \frac{d\boldsymbol{U}}{d\boldsymbol{F}}(\boldsymbol{F}^i_\mu) + \boldsymbol{\Omega}^i_{R,\mu} : \frac{d\boldsymbol{R}}{d\boldsymbol{F}}(\boldsymbol{F}^i_\mu) \right) : \dot{\boldsymbol{F}}^i_\mu \right\rangle \tag{C.19}$$

$$= \left\langle \boldsymbol{P}^i_\mu : \dot{\boldsymbol{F}}^i_\mu \right\rangle, \tag{C.20}$$

concluding that the macroscopic power is equal to the volume-weighted average of the microscopic powers in each phase, as desired.

Balance of angular momentum

We consider now the implications of the stress-homogenization rule for the balance of angular momentum at the macroscale. As for the full MFH-PMVP model, we consider a virtual variation of the deformation gradient of the form $\delta\boldsymbol{F} = \boldsymbol{W}\boldsymbol{F}$, with $\boldsymbol{W}$ skew-symmetric. Substituting this expression into Equation (5.80), we find

$$|\Omega_{0,\mu}|\boldsymbol{P} : \boldsymbol{W}\boldsymbol{F} = \sum_{i=1}^{n_P} |\Omega^i_{0,\mu}| \boldsymbol{P}^{i,*}_\mu : \mathbf{A}^{i,\mathrm{mfh}}_\mu : \boldsymbol{W}\boldsymbol{F}. \tag{C.21}$$

Taking into account the objectivity properties of the strain localization tensor (see Equation (4.30)), we can write

$$|\Omega_{0,\mu}|\boldsymbol{P} : \boldsymbol{W}\boldsymbol{F} = \sum_{i=1}^{n_P} |\Omega^i_{0,\mu}| \boldsymbol{P}^{i,*}_\mu : \boldsymbol{W}\boldsymbol{F}^{i,\mathrm{mfh}}_\mu. \tag{C.22}$$

Substituting the expression for the effective stress in Equation (5.83), we obtain

$$|\Omega_{0,\mu}|\boldsymbol{P} : \boldsymbol{W}\boldsymbol{F} = \sum_{i=1}^{n_P} |\Omega^i_{0,\mu}| \left(\boldsymbol{\Omega}_\mu + \boldsymbol{\Omega}^i_{N,\mu} : \mathbf{P}^i_{N,\mu} : \frac{d\boldsymbol{U}}{d\boldsymbol{F}}(\boldsymbol{F}^{i,\mathrm{mfh}}_\mu) + \boldsymbol{\Omega}^i_{R,\mu} : \frac{d\boldsymbol{R}}{d\boldsymbol{F}}(\boldsymbol{F}^{i,\mathrm{mfh}}_\mu) \right) : \boldsymbol{W}\boldsymbol{F}^{i,\mathrm{mfh}}_\mu, \tag{C.23}$$

and rearranging terms, we have

$$\sum_{i=1}^{n_P} |\Omega^i_{0,\mu}| \Big(\boldsymbol{\Omega}_\mu : \boldsymbol{W}\boldsymbol{F}^{i,\mathrm{mfh}}_\mu + \boldsymbol{\Omega}^i_{N,\mu} : \mathbf{P}^i_{N,\mu} : \frac{d\boldsymbol{U}}{d\boldsymbol{F}}(\boldsymbol{F}^{i,\mathrm{mfh}}_\mu) : \boldsymbol{W}\boldsymbol{F}^{i,\mathrm{mfh}}_\mu + \boldsymbol{\Omega}^i_{R,\mu} : \frac{d\boldsymbol{R}}{d\boldsymbol{F}}(\boldsymbol{F}^{i,\mathrm{mfh}}_\mu) : \boldsymbol{W}\boldsymbol{F}^{i,\mathrm{mfh}}_\mu \Big). \tag{C.24}$$

Let us consider for each phase i each of the three terms in the summation above. For the first term, since both $\boldsymbol{\Omega}_\mu$ and $\boldsymbol{W}$ are constant, we can factor them out of the summation and use the self-consistency condition imposed on the MFH procedure to write

$$\sum_{i=1}^{n_P} |\Omega^i_{0,\mu}| \boldsymbol{\Omega}_\mu : \boldsymbol{W}\boldsymbol{F}^{i,\mathrm{mfh}}_\mu = \boldsymbol{\Omega}_\mu : \boldsymbol{W} \sum_{i=1}^{n_P} |\Omega^i_{0,\mu}| \boldsymbol{F}^{i,\mathrm{mfh}}_\mu, \tag{C.25}$$

$$= |\Omega_{0,\mu}| \boldsymbol{\Omega}_\mu : \boldsymbol{W}\boldsymbol{F}, \tag{C.26}$$

$$= \sum_{i=1}^{n_P} |\Omega^i_{0,\mu}| \boldsymbol{\Omega}_\mu : \boldsymbol{W}\boldsymbol{F}^i_\mu. \tag{C.27}$$

Regarding the second term, the derivative of the right stretch with respect to the deformation gradient at $\boldsymbol{F}_\mu^{i,\mathrm{mfh}}$ in the $\boldsymbol{W}\boldsymbol{F}_\mu^{i,\mathrm{mfh}}$ direction is zero, according to Equation (5.66). This is also the case for the derivative of the right stretch with respect to the deformation gradient at $\boldsymbol{F}_\mu^i$ in the $\boldsymbol{W}\boldsymbol{F}_\mu^i$ direction. Thus, we can replace one term with the other. Finally, for the third term, we have

$$\frac{d\boldsymbol{R}}{d\boldsymbol{F}}(\boldsymbol{F}_\mu^{i,\mathrm{mfh}}) : \boldsymbol{W}\boldsymbol{F}_\mu^{i,\mathrm{mfh}} = \boldsymbol{W}\boldsymbol{R}_\mu^{i,\mathrm{mfh}}, \tag{C.28}$$

$$= \boldsymbol{W}\boldsymbol{R}_\mu^i, \tag{C.29}$$

$$= \frac{d\boldsymbol{R}}{d\boldsymbol{F}}(\boldsymbol{F}_\mu^i) : \boldsymbol{W}\boldsymbol{F}_\mu^i. \tag{C.30}$$

Accordingly, we can rewrite the summation as

$$\sum_{i=1}^{n_P} |\Omega_{0,\mu}^i| \left(\boldsymbol{\Omega}_\mu : \boldsymbol{W}\boldsymbol{F}_\mu^i + \boldsymbol{\Omega}_{N,\mu}^i : \mathbf{P}_{N,\mu}^i : \frac{d\boldsymbol{U}}{d\boldsymbol{F}}(\boldsymbol{F}_\mu^i) : \boldsymbol{W}\boldsymbol{F}_\mu^i + \boldsymbol{\Omega}_{R,\mu}^i : \frac{d\boldsymbol{R}}{d\boldsymbol{F}}(\boldsymbol{F}_\mu^i) : \boldsymbol{W}\boldsymbol{F}_\mu^i \right) \tag{C.31}$$

Thus, we have

$$|\Omega_{0,\mu}|\boldsymbol{P} : \boldsymbol{W}\boldsymbol{F} = \sum_{i=1}^{n_P} |\Omega_{0,\mu}^i| \left(\boldsymbol{\Omega}_\mu + \boldsymbol{\Omega}_{N,\mu}^i : \mathbf{P}_{N,\mu}^i : \frac{d\boldsymbol{U}}{d\boldsymbol{F}}(\boldsymbol{F}_\mu^i) + \boldsymbol{\Omega}_{R,\mu}^i : \frac{d\boldsymbol{R}}{d\boldsymbol{F}}(\boldsymbol{F}_\mu^i) \right) : \boldsymbol{W}\boldsymbol{F}_\mu^i, \tag{C.32}$$

factoring out $\boldsymbol{W}\boldsymbol{F}_\mu^i$. From Equation (5.63), we recognize the term in parentheses as the average stress in each phase i, and thus we can write

$$|\Omega_{0,\mu}|\boldsymbol{P} : \boldsymbol{W}\boldsymbol{F} = \sum_{i=1}^{n_P} |\Omega_{0,\mu}^i| \boldsymbol{P}_\mu^i : \boldsymbol{W}\boldsymbol{F}_\mu^i. \tag{C.33}$$

Using the properties of the double contraction, we have

$$|\Omega_{0,\mu}|\boldsymbol{P}\boldsymbol{F}^T : \boldsymbol{W} = \sum_{i=1}^{n_P} |\Omega_{0,\mu}^i| \boldsymbol{P}_\mu^i (\boldsymbol{F}_\mu^i)^T : \boldsymbol{W} \tag{C.34}$$

Since $\boldsymbol{W}$ is an arbitrary skew-symmetric tensor, we obtain

$$\mathrm{skew}(\boldsymbol{P}\boldsymbol{F}^T) = \langle \mathrm{skew}(\boldsymbol{P}_\mu^i (\boldsymbol{F}_\mu^i)^T) \rangle. \tag{C.35}$$

Since Equation (5.64) is equal to Equation (5.28), the steps taken in the derivation of the balance of angular momentum for the fully constrained MFH-PMVP model (see Section 5.1.2) can be followed verbatim, leading to the same conclusion, namely that

$$\mathrm{skew}(\boldsymbol{P}\boldsymbol{F}^T) = \boldsymbol{0}, \tag{C.36}$$

and thus the macroscopic balance of angular momentum is satisfied. Note also that from Equation (5.51), we can write

$$\mathrm{skew}(\boldsymbol{P}_\mu^i (\boldsymbol{F}_\mu^i)^T) = \mathrm{skew}(\boldsymbol{R}_\mu^i \boldsymbol{T}_{B,\mu}^i \boldsymbol{U}_\mu^i (\boldsymbol{R}_\mu^i)^T), \tag{C.37}$$

$$= \boldsymbol{R}_\mu^i \, \mathrm{skew}(\boldsymbol{T}_{B,\mu}^i \boldsymbol{U}_\mu^i) (\boldsymbol{R}_\mu^i)^T, \tag{C.38}$$

and thus from

$$\mathrm{skew}(\boldsymbol{P}_\mu^i (\boldsymbol{F}_\mu^i)^T) = \boldsymbol{0}, \tag{C.39}$$

we can also conclude that

$$\mathrm{skew}(\boldsymbol{T}_{B,\mu}^i \boldsymbol{U}_\mu^i) = \boldsymbol{0}, \tag{C.40}$$

which is the local balance of angular momentum in each phase i.

C.1.2 Sachs model

This section provides the detailed derivation of the energetic consistency of the PMVP-based Sachs model introduced in Section 5.1.4. It also details the derivation concerning the satisfaction of the macroscopic angular momentum balance condition.

Energetic consistency and balance of angular momentum

The considerations regarding energetic consistency and the balance of angular momentum for the Sachs model are similar to those presented for the fully constrained MFH-PMVP and projected MFH-PMVP models. For energetic consistency, the derivation simplifies considerably, and we can directly write

$$\boldsymbol{P} : \dot{\boldsymbol{F}} = \boldsymbol{P} : \langle \dot{\boldsymbol{F}}^i_\mu \rangle \tag{C.41}$$

$$= \langle \boldsymbol{P} : \dot{\boldsymbol{F}}^i_\mu \rangle \tag{C.42}$$

$$= \langle \boldsymbol{P}^i_\mu : \dot{\boldsymbol{F}}^i_\mu \rangle. \tag{C.43}$$

The balance of angular momentum can be derived similarly, starting from the PMVP in Equation (5.95). Considering a virtual variation of the deformation gradient of the form $\delta\boldsymbol{P} = \boldsymbol{W}\boldsymbol{P}$, with $\boldsymbol{W}$ skew-symmetric, and $\delta\tilde{\boldsymbol{Z}}$ and $\delta\boldsymbol{\Omega}_\mu$ equal to zero, we find that

$$\boldsymbol{P} : \boldsymbol{W}\boldsymbol{F} = \boldsymbol{P} : \boldsymbol{W}\langle \boldsymbol{F}^i_\mu \rangle \tag{C.44}$$

$$= \langle \boldsymbol{P} : \boldsymbol{W}\boldsymbol{F}^i_\mu \rangle \tag{C.45}$$

$$= \langle \boldsymbol{P}^i_\mu : \boldsymbol{W}\boldsymbol{F}^i_\mu \rangle \tag{C.46}$$

$$= \langle \boldsymbol{P}^i_\mu (\boldsymbol{F}^i_\mu)^T \rangle : \boldsymbol{W}, \tag{C.47}$$

leading to

$$\mathrm{skew}(\boldsymbol{P}\boldsymbol{F}^T) = \langle \mathrm{skew}(\boldsymbol{P}^i_\mu (\boldsymbol{F}^i_\mu)^T) \rangle. \tag{C.48}$$

As for the full-MFH and projected-MFH, Equation (5.99) allows us to conclude that (see Section 5.1.2 for the derivation)

$$\mathrm{skew}(\boldsymbol{P}^i_\mu (\boldsymbol{F}^i_\mu)^T) = \boldsymbol{0}, \tag{C.49}$$

leading to the same conclusion, namely that

$$\mathrm{skew}(\boldsymbol{P}\boldsymbol{F}^T) = \boldsymbol{0}, \tag{C.50}$$

and thus the macroscopic balance of angular momentum is satisfied.

C.2 Detailed derivations regarding models based on the Principle of Multiscale Complementary Virtual Power

This section collects some of the detailed derivations regarding the models based on the PMCVP that were omitted in the main text for brevity.

C.2.1 Full Mean-Field Homogenization

This section provides the detailed derivation of the PMCVP-based full MFH model introduced in Section 5.2.2. As in the standard PMVP framework, our goal is to exploit the stress estimates

provided by the MFH procedure fully. In this context, we adopt the hypothesis that the average stress in each phase coincides with its corresponding MFH estimate, i.e.,

$$\boldsymbol{P}_\mu^i = \boldsymbol{P}_\mu^{i,\mathrm{mfh}}. \tag{C.51}$$

This condition can be equivalently expressed in terms of the stress potential fluctuations

$$\int_{\Omega_{0,\mu}^i} \operatorname{curl}_0 \tilde{\boldsymbol{Z}}_\mu \, dv = |\Omega_{0,\mu}^i| \left(\boldsymbol{P}_\mu^{i,\mathrm{mfh}} - \boldsymbol{P} \right), \tag{C.52}$$

since

$$\boldsymbol{P}_\mu^i = \boldsymbol{P} + \frac{1}{|\Omega_{0,\mu}^i|} \int_{\Omega_{0,\mu}^i} \operatorname{curl}_0 \tilde{\boldsymbol{Z}}_\mu \, dv, \tag{C.53}$$

found by integrating Equation (3.28) over phase i. This relation is nonlinear in the macroscopic stress $\boldsymbol{P}$ due to the dependency of $\boldsymbol{P}_\mu^{i,\mathrm{mfh}}$ on it, i.e., $\boldsymbol{P}_\mu^{i,\mathrm{mfh}} = \mathscr{B}_\mu^{i,\mathrm{mfh}}(\boldsymbol{P}, \boldsymbol{\alpha}_\mu^{\mathrm{mfh}})$ (see Equation (4.21)).

Accordingly, we define the admissible set of stress potential fluctuations that satisfy the MFH hypothesis

$$\tilde{\mathscr{S}}_{\mu,\mathrm{MFH}}(\boldsymbol{P}) = \left\{ \boldsymbol{T} \in \tilde{\mathscr{S}}_\mu^* \;\middle|\; \int_{\Omega_{0,\mu}^i} \operatorname{curl}_0 \boldsymbol{T} \, dv = |\Omega_{0,\mu}^i| \left(\boldsymbol{P}_\mu^{i,\mathrm{mfh}} - \boldsymbol{P} \right), \; \forall i = 1, \ldots, n_P \right\}. \tag{C.54}$$

To ensure $\tilde{\mathscr{S}}_{\mu,\mathrm{MFH}}(\boldsymbol{P}) \subseteq \tilde{\mathscr{S}}_\mu^*$, we must enforce the consistency condition $\langle \boldsymbol{P}_\mu^{i,\mathrm{mfh}} \rangle = \boldsymbol{P}$. It is important to note that $\tilde{\mathscr{S}}_{\mu,\mathrm{MFH}}(\boldsymbol{P})$ forms a subset rather than a subspace of the minimal admissible field space.

The corresponding set of admissible virtual stress potential fields is defined as

$$\tilde{\mathscr{H}}_{\mu,\mathrm{MFH}}(\boldsymbol{P}, \delta\boldsymbol{P}) = \left\{ \boldsymbol{T} \in \tilde{\mathscr{H}}_\mu^* \;\middle|\; \int_{\Omega_{0,\mu}^i} \operatorname{curl}_0 \boldsymbol{T} \, dv = |\Omega_{0,\mu}^i| \left(\mathbf{B}_\mu^{i,\mathrm{mfh}} - \mathbf{I} \right) : \delta\boldsymbol{P}, \; \forall i = 1, \ldots, n_P \right\}. \tag{C.55}$$

As in the PMVP approach, we enforce these constraints via Lagrange multipliers $\boldsymbol{\Gamma}_\mu^i$, $i = 1, \ldots, n_P$, which are dimensionless second-order tensors. The Principle of Multiscale Complementary Virtual Power thus reads

$$\begin{aligned} |\Omega_{0,\mu}| \delta\boldsymbol{P} : \boldsymbol{F} = \int_{\Omega_{0,\mu}} \left(\operatorname{curl}_0 \delta\tilde{\boldsymbol{Z}}_\mu + \delta\boldsymbol{P} \right) : \boldsymbol{F}_\mu \, dv \\ - \sum_{i=1}^{n_P} \boldsymbol{\Gamma}_\mu^i : \left(\int_{\Omega_{0,\mu}^i} \operatorname{curl}_0 \delta\tilde{\boldsymbol{Z}}_\mu \, dv - |\Omega_{0,\mu}^i| \left(\mathbf{B}_\mu^{i,\mathrm{mfh}} - \mathbf{I} \right) : \delta\boldsymbol{P} \right) \\ - \sum_{i=1}^{n_P} \delta\boldsymbol{\Gamma}_\mu^i : \left(\int_{\Omega_{0,\mu}^i} \operatorname{curl}_0 \tilde{\boldsymbol{Z}}_\mu \, dv - |\Omega_{0,\mu}^i| \left(\boldsymbol{P}_\mu^{i,\mathrm{mfh}} - \boldsymbol{P} \right) \right). \end{aligned} \tag{C.56}$$

Static homogenization

Taking variations only with respect to $\delta\boldsymbol{\Gamma}_\mu^i$, we recover the static constraints

$$\int_{\Omega_{0,\mu}^i} \operatorname{curl}_0 \tilde{\boldsymbol{Z}}_\mu \, dv = |\Omega_{0,\mu}^i| \left(\boldsymbol{P}_\mu^{i,\mathrm{mfh}} - \boldsymbol{P} \right), \quad i = 1, \ldots, n_P, \tag{C.57}$$

which, as expected, correspond to enforcing

$$\boldsymbol{P}_\mu^i = \boldsymbol{P}_\mu^{i,\mathrm{mfh}}, \quad i = 1, \ldots, n_P. \tag{C.58}$$

Interpretation of the Lagrange multipliers

To interpret the multipliers, we set $\delta \boldsymbol{P} = \boldsymbol{0}$ and $\delta \boldsymbol{\Gamma}_\mu^i = \boldsymbol{0}$ in the virtual power expression, yielding

$$\int_{\Omega_{0,\mu}} \operatorname{curl}_0 \delta \tilde{\boldsymbol{Z}}_\mu : \boldsymbol{F}_\mu \, dv - \sum_{i=1}^{n_P} \boldsymbol{\Gamma}_\mu^i : \int_{\Omega_{0,\mu}^i} \operatorname{curl}_0 \delta \tilde{\boldsymbol{Z}}_\mu \, dv = \boldsymbol{0}. \tag{C.59}$$

To extract phase-specific information, we select variations of the form $\delta \tilde{\boldsymbol{Z}}_\mu = \frac{1}{2} \boldsymbol{C} \times (\boldsymbol{Y} - \boldsymbol{Y}_0^i)$ in $\Omega_{0,\mu}^i$, and zero elsewhere, with $\boldsymbol{C}$ an arbitrary constant second-order tensor. Substituting into Equation (C.59) gives

$$\int_{\Omega_{0,\mu}^i} \boldsymbol{C} : \boldsymbol{F}_\mu \, dv - \boldsymbol{\Gamma}_\mu^i : \int_{\Omega_{0,\mu}^i} \boldsymbol{C} \, dv = \boldsymbol{0}. \tag{C.60}$$

Since $\boldsymbol{C}$ is arbitrary, we conclude

$$\boldsymbol{\Gamma}_\mu^i = \boldsymbol{F}_\mu^i, \quad i = 1, \ldots, n_P, \tag{C.61}$$

where $\boldsymbol{F}_\mu^i$ is the average deformation gradient in phase i. Thus, the Lagrange multipliers $\boldsymbol{\Gamma}_\mu^i$ represent the mean deformation gradients within each phase. We can also rewrite Equation (C.59), as

$$\int_{\Omega_{0,\mu}} \operatorname{curl}_0 \delta \tilde{\boldsymbol{Z}}_\mu : \boldsymbol{F}_\mu \, dv = \sum_{i=1}^{n_P} \boldsymbol{F}_\mu^i : \int_{\Omega_{0,\mu}^i} \operatorname{curl}_0 \delta \tilde{\boldsymbol{Z}}_\mu \, dv, \tag{C.62}$$

which will be helpful in further derivations.

Deformation homogenization

Finally, setting $\delta \tilde{\boldsymbol{Z}}_\mu = \boldsymbol{0}$ and $\delta \boldsymbol{\Gamma}_\mu^i = \boldsymbol{0}$ for all $i = 1, \ldots, n_P$, the virtual power principle reduces to

$$|\Omega_{0,\mu}| \delta \boldsymbol{P} : \boldsymbol{F} = \sum_{i=1}^{n_P} \left(|\Omega_{0,\mu}^i| \delta \boldsymbol{P} : \boldsymbol{F}_\mu^i + |\Omega_{0,\mu}^i| \boldsymbol{\Gamma}_\mu^i : (\mathbf{B}_\mu^{i,\mathrm{mfh}} - \mathbf{I}) : \delta \boldsymbol{P} \right). \tag{C.63}$$

Substituting the identity $\boldsymbol{\Gamma}_\mu^i = \boldsymbol{F}_\mu^i$, we obtain

$$|\Omega_{0,\mu}| \delta \boldsymbol{P} : \boldsymbol{F} = \sum_{i=1}^{n_P} \left(|\Omega_{0,\mu}^i| \delta \boldsymbol{P} : \boldsymbol{F}_\mu^i + |\Omega_{0,\mu}^i| \boldsymbol{F}_\mu^i : (\mathbf{B}_\mu^{i,\mathrm{mfh}} - \mathbf{I}) : \delta \boldsymbol{P} \right), \tag{C.64}$$

which simplifies, by grouping terms and exploiting the symmetry of the double contraction, to

$$|\Omega_{0,\mu}| \delta \boldsymbol{P} : \boldsymbol{F} = \sum_{i=1}^{n_P} |\Omega_{0,\mu}^i| \boldsymbol{F}_\mu^i : \mathbf{B}_\mu^{i,\mathrm{mfh}} : \delta \boldsymbol{P}. \tag{C.65}$$

Thus, the homogenized deformation gradient is given by

$$\boldsymbol{F} = \left\langle \boldsymbol{F}_\mu^i : \mathbf{B}_\mu^{i,\mathrm{mfh}} \right\rangle. \tag{C.66}$$

Energetic considerations

The energetic consistency of the MFH-PMCVP models can be verified in a manner analogous to that used for the PMVP-based models. For these stress-driven models, we focus on the complementary power, and using a similar approach as in Section 5.1.2, we find

$$\begin{aligned}
\boldsymbol{F} : \dot{\boldsymbol{P}} &= \langle \boldsymbol{F}_\mu^i : \mathbf{B}_\mu^{i,\mathrm{mfh}} \rangle : \dot{\boldsymbol{P}} && \text{by Eq. (C.66)} && \text{(C.67)}\\
&= \langle \boldsymbol{F}_\mu^i : \mathbf{B}_\mu^{i,\mathrm{mfh}} : \dot{\boldsymbol{P}} \rangle && \dot{\boldsymbol{P}} \text{ is spatially constant} && \text{(C.68)}\\
&= \langle \boldsymbol{F}_\mu^i : \dot{\boldsymbol{P}}_\mu^{i,\mathrm{mfh}} \rangle && \text{by Eq. (4.23)} && \text{(C.69)}\\
&= \langle \boldsymbol{F}_\mu^i : \dot{\boldsymbol{P}}_\mu^{i} \rangle && \text{by Eq. (C.51),} && \text{(C.70)}
\end{aligned}$$

where we assume that the material is elastic, such that its constitutive description does not depend on internal variables. The presence of internal variables is dealt with identically to what is done in Section 5.1.2, for the full-MFH PMVP-based model.

Angular momentum balance

To achieve this we consider $\delta \boldsymbol{P} = \boldsymbol{W}\boldsymbol{P}$ in Equation (C.65) yielding

$$\begin{aligned}
\boldsymbol{F} : \boldsymbol{W}\boldsymbol{P} &= \langle \boldsymbol{F}_\mu^i : \mathbf{B}_\mu^{i,\mathrm{mfh}} \rangle : \boldsymbol{W}\boldsymbol{P}, && \text{(C.71)}\\
&= \langle \boldsymbol{F}_\mu^i : \mathbf{B}_\mu^{i,\mathrm{mfh}} : \boldsymbol{W}\boldsymbol{P} \rangle. && \text{(C.72)}
\end{aligned}$$

From the objectivity requirements of the MFH procedure (Equation (4.31)), we conclude that

$$\langle \boldsymbol{F}_\mu^i : \mathbf{B}_\mu^{i,\mathrm{mfh}} : \boldsymbol{W}\boldsymbol{P} \rangle = \langle \boldsymbol{F}_\mu^i : \boldsymbol{W}\boldsymbol{P}_\mu^{i,\mathrm{mfh}} \rangle. \tag{C.73}$$

Also, from the hypotheses underlying the full-MFH model (Equation (C.51)), we find

$$\langle \boldsymbol{F}_\mu^i : \boldsymbol{W}\boldsymbol{P}_\mu^{i,\mathrm{mfh}} \rangle = \langle \boldsymbol{F}_\mu^i : \boldsymbol{W}\boldsymbol{P}_\mu^{i} \rangle, \tag{C.74}$$

and from the properties of the double contraction operations, combining the previous equations, we can write

$$\boldsymbol{F}\boldsymbol{P}^T : \boldsymbol{W} = \langle \boldsymbol{F}_\mu^i (\boldsymbol{P}_\mu^i)^T \rangle : \boldsymbol{W}. \tag{C.75}$$

Finally, since $\boldsymbol{W}$ is an arbitrary skew-symmetric tensor, we conclude that

$$\mathrm{skew}(\boldsymbol{F}\boldsymbol{P}^T) = \langle \mathrm{skew}(\boldsymbol{F}_\mu^i (\boldsymbol{P}_\mu^i)^T) \rangle. \tag{C.76}$$

To show that the right-hand side of this equation is zero, we use Equation (C.59), choosing as the test function $\delta \tilde{\boldsymbol{Z}}_\mu = \boldsymbol{C}\tilde{\boldsymbol{Z}}_\mu$ with $\boldsymbol{C}$ an arbitrary constant second-order tensor and $\tilde{\boldsymbol{Z}}_\mu \in \mathscr{Z}_\mu^i$ (see Equation (5.107)), yielding

$$\int_{\Omega_{\mu,0}^i} \mathrm{curl}_0(\boldsymbol{C}\tilde{\boldsymbol{Z}}_\mu) : \boldsymbol{F}_\mu \, dv = \boldsymbol{F}_\mu^i : \int_{\Omega_{\mu,0}^i} \mathrm{curl}_0(\boldsymbol{C}\tilde{\boldsymbol{Z}}_\mu) \, dv. \tag{C.77}$$

Taking into account that $\boldsymbol{C}$ is a constant tensor, we can rewrite the previous equation as

$$\int_{\Omega_{\mu,0}^i} \boldsymbol{F}_\mu (\mathrm{curl}_0 \tilde{\boldsymbol{Z}}_\mu)^T \, dv = \boldsymbol{F}_\mu^i \left(\int_{\Omega_{\mu,0}^i} \mathrm{curl}_0 \tilde{\boldsymbol{Z}}_\mu \, dv \right)^T, \tag{C.78}$$

and adding $\int_{\Omega^i_{\mu,0}} \boldsymbol{F}_\mu \boldsymbol{P}^T \, dv$ to both sides, we obtain

$$\int_{\Omega^i_{\mu,0}} \boldsymbol{F}_\mu \boldsymbol{P}_\mu^T \, dv = |\Omega^i_{\mu,0}| \boldsymbol{F}^i_\mu (\boldsymbol{P}^i_\mu)^T, \tag{C.79}$$

where we used Equation (C.53). We finally take into account that at each microscopic point $\boldsymbol{F}_\mu \boldsymbol{P}_\mu^T$ is symmetric, due to the balance of angular momentum at the microscale (Equation (2.52)), and thus

$$\operatorname{skew}\left(\int_{\Omega^i_{\mu,0}} \boldsymbol{F}_\mu \boldsymbol{P}_\mu^T \, dv \right) = |\Omega^i_{\mu,0}| \operatorname{skew}(\boldsymbol{F}^i_\mu (\boldsymbol{P}^i_\mu)^T) = \boldsymbol{0}. \tag{C.80}$$

Substituting into Equation (C.76), we conclude that the macroscopic balance of angular momentum is satisfied, i.e.,

$$\operatorname{skew}(\boldsymbol{F}\boldsymbol{P}^T) = \langle \operatorname{skew}(\boldsymbol{F}^i_\mu (\boldsymbol{P}^i_\mu)^T) \rangle = \boldsymbol{0}, \tag{C.81}$$

as desired.

C.2.2 Projected Mean-Field Homogenization

In the projected MFH model based on PMCVP, our static hypotheses on the phases are to retain the appropriate tangential component of the Biot stress obtained from a stress-driven MFH procedure. We also adopt the polar rotation estimate from the MFH scheme, imposing for each phase

$$\mathbf{P}^i_{\mathbb{S}^3_T,\mu} : \boldsymbol{T}_B(\boldsymbol{P}^i_\mu) = \mathbf{P}^i_{\mathbb{S}^3_T,\mu} : \boldsymbol{T}_B(\boldsymbol{P}^{i,\mathrm{mfh}}_\mu), \quad i = 1, \dots, n_P, \tag{C.82}$$

$$\boldsymbol{R}(\boldsymbol{P}^i_\mu) = \boldsymbol{R}(\boldsymbol{P}^{i,\mathrm{mfh}}_\mu), \quad i = 1, \dots, n_P, \tag{C.83}$$

where $\boldsymbol{T}_B$ maps $\boldsymbol{P}^i_\mu$ to $(\boldsymbol{R}^i_\mu)^T \boldsymbol{P}^i_\mu$ and $\boldsymbol{R}(\boldsymbol{P}^i_\mu)$ is the polar rotation found from the deformation gradient corresponding to the stress $\boldsymbol{P}^i_\mu$, i.e., $\boldsymbol{F}^i_\mu = \boldsymbol{f}(\boldsymbol{P}^i_\mu, \boldsymbol{\alpha}^i_\mu)$ (see Equation (2.51)). For the matrix phase, one may choose either to enforce $\mathbf{P}^m_{\mathbb{S}^3,\mu} : \boldsymbol{T}^m_{B,\mu} = \mathbf{P}^m_{\mathbb{S}^3,\mu} : \boldsymbol{T}^{m,\mathrm{mfh}}_{B,\mu}$, or to leave it unconstrained.

The set of admissible stress potential fluctuation fields corresponding to the static hypothesis chosen for the phases is given by

$$\begin{aligned} \tilde{\mathscr{S}}_{\mu,\mathrm{PMFH}}(\boldsymbol{P}) = \Big\{ \boldsymbol{T} \in \tilde{\mathscr{S}}^*_\mu \;\Big|\; & \mathbf{P}^i_{\mathbb{S}^3_T,\mu} : \boldsymbol{T}_B(\boldsymbol{P}^i_\mu) = \mathbf{P}^i_{\mathbb{S}^3_T,\mu} : \boldsymbol{T}_B(\boldsymbol{P}^{i,\mathrm{mfh}}_\mu), \\ & \boldsymbol{R}(\boldsymbol{P}^i_\mu) = \boldsymbol{R}(\boldsymbol{P}^{i,\mathrm{mfh}}_\mu), \quad \forall i = 1, \dots, n_P \Big\}. \end{aligned} \tag{C.84}$$

Note that the average first Piola–Kirchhoff stress in each phase is a function of the stress potential fluctuation and the macroscopic stress, according to

$$\boldsymbol{P}^i_\mu = \boldsymbol{P} + \frac{1}{|\Omega^i_{0,\mu}|} \int_{\Omega^i_{0,\mu}} \operatorname{curl}_0 \tilde{\boldsymbol{Z}}_\mu \, dv, \tag{C.85}$$

and that the auxiliary MFH estimate $\boldsymbol{P}^{i,\mathrm{mfh}}_\mu$ depends on the macroscopic stress $\boldsymbol{P}$, as well.

This admissible set satisfies the nested inclusion

$$\tilde{\mathscr{S}}_{\mu,\mathrm{MFH}}(\boldsymbol{P}) \subseteq \tilde{\mathscr{S}}_{\mu,\mathrm{PMFH}}(\boldsymbol{P}) \subseteq \tilde{\mathscr{S}}^*_\mu, \tag{C.86}$$

provided that $\langle \boldsymbol{P}_\mu^{i,\mathrm{mfh}} \rangle = \boldsymbol{P}$ holds.

The corresponding space of admissible virtual stress potential fields is given by

$$\begin{aligned}\tilde{\mathscr{H}}_{\mu,\mathrm{PMFH}}(\boldsymbol{P},\delta\boldsymbol{P}) = \Big\{ \boldsymbol{T} \in \tilde{\mathscr{H}}_\mu^* \;\Big|\; & \mathbf{P}^i_{\mathbb{S}^3_T,\mu} : \frac{d\boldsymbol{T}_B}{d\boldsymbol{P}}(\boldsymbol{P}_\mu^i) : \int_{\Omega^i_{0,\mu}} \mathrm{curl}_0\, \boldsymbol{T}\, dv = |\Omega^i_{0,\mu}| \mathbf{P}^i_{\mathbb{S}^3_T,\mu} : \left(\frac{d\boldsymbol{T}_B}{d\boldsymbol{P}}(\boldsymbol{P}_\mu^{i,\mathrm{mfh}}) : \mathbf{B}_\mu^{i,\mathrm{mfh}} - \frac{d\boldsymbol{T}_B}{d\boldsymbol{P}}(\boldsymbol{P}_\mu^i) \right) : \delta\boldsymbol{P}, \\ & \frac{d\boldsymbol{R}}{d\boldsymbol{P}}(\boldsymbol{P}_\mu^i) : \int_{\Omega^i_{0,\mu}} \mathrm{curl}_0\, \boldsymbol{T}\, dv = |\Omega^i_{0,\mu}| \left(\frac{d\boldsymbol{R}}{d\boldsymbol{P}}(\boldsymbol{P}_\mu^{i,\mathrm{mfh}}) : \mathbf{B}_\mu^{i,\mathrm{mfh}} - \frac{d\boldsymbol{R}}{d\boldsymbol{P}}(\boldsymbol{P}_\mu^i) \right) : \delta\boldsymbol{P} \Big\}, \end{aligned} \tag{C.87}$$

which is obtained using the chain rule and rearranging some of the terms.

To enforce these constraints within the PMCVP framework, we introduce Lagrange multipliers again. One multiplier, $\boldsymbol{\Gamma}_\mu$, enforces the minimal constraint for all phases, while n_P individual multipliers $\boldsymbol{\Gamma}^i_{T,\mu}$, $i = 1,\dots,n_P$, enforce the tangential constraints on the Biot stress tensor. The tangential multipliers satisfy

$$\mathbf{P}^i_{\mathbb{S}^3_T,\mu} : \boldsymbol{\Gamma}^i_{T,\mu} = \boldsymbol{\Gamma}^i_{T,\mu} : \mathbf{P}^i_{\mathbb{S}^3_T,\mu} = \boldsymbol{\Gamma}^i_{T,\mu}, \tag{C.88}$$

i.e., they possess only three independent components, except in the matrix phase, where $\boldsymbol{\Gamma}^m_{T,\mu}$ can have six independent components or none depending on the choice for $\mathbf{P}^m_{\mathbb{S}^3_T,\mu}$. Similarly, n_P multipliers $\boldsymbol{\Gamma}^i_{R,\mu}$, $i = 1,\dots,n_P$, enforce the constraints on the polar rotation. These multipliers enter the derivation below only through the quantity $\mathrm{skew}((\boldsymbol{R}^i_\mu)^T \boldsymbol{\Gamma}^i_{R,\mu})$, which is a skew-symmetric second-order tensor with three independent components.

The Multiscale Complementary Virtual Power Principle then reads

$$\begin{aligned} |\Omega_{0,\mu}| \delta\boldsymbol{P} : \boldsymbol{F} = & \int_{\Omega_{0,\mu}} (\mathrm{curl}_0\, \delta\tilde{\boldsymbol{Z}}_\mu + \delta\boldsymbol{P}) : \boldsymbol{F}_\mu\, dv \\ & - \boldsymbol{\Gamma}_\mu : \sum_{i=1}^{n_P} \int_{\Omega^i_{0,\mu}} \mathrm{curl}_0\, \delta\tilde{\boldsymbol{Z}}_\mu\, dv - \delta\boldsymbol{\Gamma}_\mu : \sum_{i=1}^{n_P} \int_{\Omega^i_{0,\mu}} \mathrm{curl}_0\, \tilde{\boldsymbol{Z}}_\mu\, dv \\ - \sum_{i=1}^{n_P} \boldsymbol{\Gamma}^i_{T,\mu} : \mathbf{P}^i_{\mathbb{S}^3_T,\mu} : & \left(\frac{d\boldsymbol{T}_B}{d\boldsymbol{P}}(\boldsymbol{P}_\mu^i) : \int_{\Omega^i_{0,\mu}} \mathrm{curl}_0\, \delta\tilde{\boldsymbol{Z}}_\mu\, dv - |\Omega^i_{0,\mu}| \left(\frac{d\boldsymbol{T}_B}{d\boldsymbol{P}}(\boldsymbol{P}_\mu^{i,\mathrm{mfh}}) : \mathbf{B}_\mu^{i,\mathrm{mfh}} - \frac{d\boldsymbol{T}_B}{d\boldsymbol{P}}(\boldsymbol{P}_\mu^i) \right) : \delta\boldsymbol{P} \right) \\ & - \sum_{i=1}^{n_P} \delta\boldsymbol{\Gamma}^i_{T,\mu} : \mathbf{P}^i_{\mathbb{S}^3_T,\mu} : \left(\boldsymbol{T}_B(\boldsymbol{P}_\mu^i) - \boldsymbol{T}_B(\boldsymbol{P}_\mu^{i,\mathrm{mfh}}) \right) \\ - \sum_{i=1}^{n_P} \boldsymbol{\Gamma}^i_{R,\mu} : & \left(\frac{d\boldsymbol{R}}{d\boldsymbol{P}}(\boldsymbol{P}_\mu^i) : \int_{\Omega^i_{0,\mu}} \mathrm{curl}_0\, \delta\tilde{\boldsymbol{Z}}_\mu\, dv - |\Omega^i_{0,\mu}| \left(\frac{d\boldsymbol{R}}{d\boldsymbol{P}}(\boldsymbol{P}_\mu^{i,\mathrm{mfh}}) : \mathbf{B}_\mu^{i,\mathrm{mfh}} - \frac{d\boldsymbol{R}}{d\boldsymbol{P}}(\boldsymbol{P}_\mu^i) \right) : \delta\boldsymbol{P} \right) \\ & - \sum_{i=1}^{n_P} \delta\boldsymbol{\Gamma}^i_{R,\mu} : \left(\boldsymbol{R}(\boldsymbol{P}_\mu^i) - \boldsymbol{R}(\boldsymbol{P}_\mu^{i,\mathrm{mfh}}) \right). \end{aligned} \tag{C.89}$$

Interpretation of the Lagrange multipliers

The derivation leading to the interpretation of the multipliers $\boldsymbol{\Gamma}_\mu$ and $\boldsymbol{\Gamma}^i_{T,\mu}$, $i = 1,\dots,n_P$, is provided in the main text (Section 5.2.3). Here, we focus on the derivation leading to the interpretation of the multipliers $\boldsymbol{\Gamma}^i_{R,\mu}$, $i = 1,\dots,n_P$ (Equation (5.138)). To proceed, we need the derivatives of the Biot stress and polar rotation with respect to the first Piola–Kirchhoff stress. From the derivations provided in Appendix D, we have

$$\frac{d\boldsymbol{T}_B}{d\boldsymbol{P}}(\boldsymbol{P}_\mu^i) : (\boldsymbol{W}\boldsymbol{P}_\mu^i) = \boldsymbol{O}, \quad \frac{d\boldsymbol{R}}{d\boldsymbol{P}}(\boldsymbol{P}_\mu^i) : (\boldsymbol{W}\boldsymbol{P}_\mu^i) = \boldsymbol{W}\boldsymbol{R}_\mu^i, \quad \forall \boldsymbol{W} \in \mathfrak{so}(3), \tag{C.90}$$

when $\boldsymbol{P}_\mu^i \neq \boldsymbol{O}$. We can now use these when considering the virtual stress potential fields of the form $\delta\tilde{\boldsymbol{Z}}_\mu = \frac{1}{2}(\boldsymbol{W}\boldsymbol{P}_\mu^i) \times (\boldsymbol{Y} - \boldsymbol{Y}_0^i)$, where $\boldsymbol{W}$ is an arbitrary skew-symmetric second-order tensor. When applied to the PMCVP, this choice yields

$$\boldsymbol{F}_\mu^i : (\boldsymbol{W}\boldsymbol{P}_\mu^i) = \boldsymbol{\Gamma}_\mu : (\boldsymbol{W}\boldsymbol{P}_\mu^i) + \boldsymbol{\Gamma}_{T,\mu}^i : \frac{d\boldsymbol{T}_B}{d\boldsymbol{P}}(\boldsymbol{P}_\mu^i) : (\boldsymbol{W}\boldsymbol{P}_\mu^i) + \boldsymbol{\Gamma}_{R,\mu}^i : \frac{d\boldsymbol{R}}{d\boldsymbol{P}}(\boldsymbol{P}_\mu^i) : (\boldsymbol{W}\boldsymbol{P}_\mu^i). \tag{C.91}$$

Using the expressions in Equation (C.90), using the fact that $\boldsymbol{R}_\mu^i$ is orthogonal, and the properties of the double contraction, we can rewrite this last expression as

$$\begin{aligned}((\boldsymbol{R}_\mu^i)^T \boldsymbol{F}_\mu^i (\boldsymbol{T}_{B,\mu}^i)^T) : ((\boldsymbol{R}_\mu^i)^T \boldsymbol{W} \boldsymbol{R}_\mu^i) = \\ ((\boldsymbol{R}_\mu^i)^T \boldsymbol{\Gamma}_\mu (\boldsymbol{T}_{B,\mu}^i)^T) : ((\boldsymbol{R}_\mu^i)^T \boldsymbol{W} \boldsymbol{R}_\mu^i) + ((\boldsymbol{R}_\mu^i)^T \boldsymbol{\Gamma}_{R,\mu}^i) : ((\boldsymbol{R}_\mu^i)^T \boldsymbol{W} \boldsymbol{R}_\mu^i).\end{aligned} \tag{C.92}$$

Defining the skew-symmetric tensor $\boldsymbol{W}^* = (\boldsymbol{R}_\mu^i)^T \boldsymbol{W} \boldsymbol{R}_\mu^i$ and recalling the definition of the right stretch tensor, we obtain

$$(\boldsymbol{U}_\mu^i (\boldsymbol{T}_{B,\mu}^i)^T) : \boldsymbol{W}^* = (\boldsymbol{R}_\mu^{i\,T} \boldsymbol{\Gamma}_\mu \boldsymbol{T}_{B,\mu}^{i\,T}) : \boldsymbol{W}^* + (\boldsymbol{R}_\mu^{i\,T} \boldsymbol{\Gamma}_{R,\mu}^i) : \boldsymbol{W}^*. \tag{C.93}$$

Since $\boldsymbol{W}^*$ is an arbitrary skew-symmetric second-order tensor, we conclude that

$$\operatorname{skew}(\boldsymbol{U}_\mu^i (\boldsymbol{T}_{B,\mu}^i)^T) = \operatorname{skew}((\boldsymbol{R}_\mu^i)^T \boldsymbol{\Gamma}_\mu (\boldsymbol{T}_{B,\mu}^i)^T) + \operatorname{skew}((\boldsymbol{R}_\mu^i)^T \boldsymbol{\Gamma}_{R,\mu}^i). \tag{C.94}$$

Finally, we take into account that for the constitutive description of the i-th phase to satisfy the angular momentum balance, we must have $\boldsymbol{T}_{B,\mu}^i \boldsymbol{U}_\mu^i$ symmetric (Equation (C.126)), and thus the left-hand side vanishes, yielding

$$\operatorname{skew}((\boldsymbol{R}_\mu^i)^T \boldsymbol{\Gamma}_{R,\mu}^i) = -\operatorname{skew}((\boldsymbol{R}_\mu^i)^T \boldsymbol{\Gamma}_\mu (\boldsymbol{T}_{B,\mu}^i)^T). \tag{C.95}$$

Deformation homogenization

To derive an expression for the homogenized deformation gradient from the PMCVP, set $\delta\tilde{\boldsymbol{Z}}_\mu = \boldsymbol{0}$, $\delta\boldsymbol{\Gamma}_\mu = \boldsymbol{0}$, $\delta\boldsymbol{\Gamma}_{T,\mu}^i = \boldsymbol{0}$ and $\delta\boldsymbol{\Gamma}_{R,\mu}^i = \boldsymbol{0}$ for all i. This choice for the virtual fields leads to

$$\begin{aligned}|\Omega_{0,\mu}| \delta\boldsymbol{P} : \boldsymbol{F} = \int_{\Omega_{0,\mu}} \delta\boldsymbol{P}_\mu : \boldsymbol{F} \\ + \sum_{i=1}^{n_P} |\Omega_{0,\mu}^i| \boldsymbol{\Gamma}_{T,\mu}^i : \mathbf{P}_{\mathbb{S}_T^3,\mu}^i : \left(\frac{d\boldsymbol{T}_B}{d\boldsymbol{P}}(\boldsymbol{P}_\mu^{i,\mathrm{mfh}}) : \mathbf{B}_\mu^{i,\mathrm{mfh}} - \frac{d\boldsymbol{T}_B}{d\boldsymbol{P}}(\boldsymbol{P}_\mu^i) \right) : \delta\boldsymbol{P} \\ + \sum_{i=1}^{n_P} |\Omega_{0,\mu}^i| \boldsymbol{\Gamma}_{R,\mu}^i : \left(\frac{d\boldsymbol{R}}{d\boldsymbol{P}}(\boldsymbol{P}_\mu^{i,\mathrm{mfh}}) : \mathbf{B}_\mu^{i,\mathrm{mfh}} - \frac{d\boldsymbol{R}}{d\boldsymbol{P}}(\boldsymbol{P}_\mu^i) \right) : \delta\boldsymbol{P}.\end{aligned} \tag{C.96}$$

From the self-consistency condition in Equation (4.25) imposed on the MFH procedure, we have that

$$\sum_{i=1}^{n_P} |\Omega_{0,\mu}| \boldsymbol{\Gamma}_\mu : (\mathbf{B}_\mu^{i,\mathrm{mfh}} - \mathbf{I}) : \delta\boldsymbol{P} = 0. \tag{C.97}$$

Adding this expression to the previous one, we obtain

$$
\begin{aligned}
|\Omega_{0,\mu}|\delta\boldsymbol{P}:\boldsymbol{F} = \int_{\Omega_{0,\mu}} \delta\boldsymbol{P}_\mu : \boldsymbol{F} \\
&+ \sum_{i=1}^{n_P} |\Omega^i_{0,\mu}| \boldsymbol{\Gamma}^i_{T,\mu} : \mathbf{P}^i_{\mathbb{S}^3_T,\mu} : \left(\frac{d\boldsymbol{T}_B}{d\boldsymbol{P}}(\boldsymbol{P}^{i,\mathrm{mfh}}_\mu) : \mathbf{B}^{i,\mathrm{mfh}}_\mu - \frac{d\boldsymbol{T}_B}{d\boldsymbol{P}}(\boldsymbol{P}^i_\mu) \right) : \delta\boldsymbol{P} \\
&+ \sum_{i=1}^{n_P} |\Omega^i_{0,\mu}| \boldsymbol{\Gamma}^i_{R,\mu} : \left(\frac{d\boldsymbol{R}}{d\boldsymbol{P}}(\boldsymbol{P}^{i,\mathrm{mfh}}_\mu) : \mathbf{B}^{i,\mathrm{mfh}}_\mu - \frac{d\boldsymbol{R}}{d\boldsymbol{P}}(\boldsymbol{P}^i_\mu) \right) : \delta\boldsymbol{P} \\
&+ \sum_{i=1}^{n_P} |\Omega^i_{0,\mu}| \boldsymbol{\Gamma}_\mu : (\mathbf{B}^{i,\mathrm{mfh}}_\mu - \mathbf{I}) : \delta\boldsymbol{P}. \qquad \text{(C.98)}
\end{aligned}
$$

We can now rearrange the last equation, yielding

$$
\begin{aligned}
|\Omega_{0,\mu}|\delta\boldsymbol{P}:\boldsymbol{F} = \sum_{i=1}^{n_P} |\Omega^i_{0,\mu}| \boldsymbol{F}^i_\mu : \delta\boldsymbol{P} \\
&- \sum_{i=1}^{n_P} |\Omega^i_{0,\mu}| \left(\boldsymbol{\Gamma}_\mu + \boldsymbol{\Gamma}^i_{T,\mu} : \mathbf{P}^i_{\mathbb{S}^3_T,\mu} : \frac{d\boldsymbol{T}_B}{d\boldsymbol{P}}(\boldsymbol{P}^i_\mu) + \boldsymbol{\Gamma}^i_{R,\mu} : \frac{d\boldsymbol{R}}{d\boldsymbol{P}}(\boldsymbol{P}^i_\mu) \right) : \delta\boldsymbol{P} \\
&+ \sum_{i=1}^{n_P} |\Omega^i_{0,\mu}| \left(\boldsymbol{\Gamma}_\mu + \boldsymbol{\Gamma}^i_{T,\mu} : \mathbf{P}^i_{\mathbb{S}^3_T,\mu} : \frac{d\boldsymbol{T}_B}{d\boldsymbol{P}}(\boldsymbol{P}^{i,\mathrm{mfh}}_\mu) + \boldsymbol{\Gamma}^i_{R,\mu} : \frac{d\boldsymbol{R}}{d\boldsymbol{P}}(\boldsymbol{P}^{i,\mathrm{mfh}}_\mu) \right) : \mathbf{B}^{i,\mathrm{mfh}}_\mu : \delta\boldsymbol{P}. \qquad \text{(C.99)}
\end{aligned}
$$

Taking into account the relationship between the average deformation gradient in each phase and the Lagrange multipliers in Equation (5.124), the first two terms in the right-hand side cancel out, leaving

$$
\begin{aligned}
|\Omega_{0,\mu}|\boldsymbol{F}:\delta\boldsymbol{P} = \\
&\sum_{i=1}^{n_P} |\Omega^i_{0,\mu}| \left(\boldsymbol{\Gamma}_\mu + \boldsymbol{\Gamma}^i_{T,\mu} : \frac{d\boldsymbol{T}_B}{d\boldsymbol{P}}(\boldsymbol{P}^{i,\mathrm{mfh}}_\mu) + \boldsymbol{\Gamma}^i_{R,\mu} : \frac{d\boldsymbol{R}}{d\boldsymbol{P}}(\boldsymbol{P}^{i,\mathrm{mfh}}_\mu) \right) : \mathbf{B}^{i,\mathrm{mfh}}_\mu : \delta\boldsymbol{P}, \qquad \text{(C.100)}
\end{aligned}
$$

which, taking into account that $\delta\boldsymbol{P}$ is arbitrary, leads to

$$
\boldsymbol{F} = \left\langle \left(\boldsymbol{\Gamma}_\mu + \boldsymbol{\Gamma}^i_{T,\mu} : \frac{d\boldsymbol{T}_B}{d\boldsymbol{P}}(\boldsymbol{P}^{i,\mathrm{mfh}}_\mu) + \boldsymbol{\Gamma}^i_{R,\mu} : \frac{d\boldsymbol{R}}{d\boldsymbol{P}}(\boldsymbol{P}^{i,\mathrm{mfh}}_\mu) \right) : \mathbf{B}^{i,\mathrm{mfh}}_\mu \right\rangle, \qquad \text{(C.101)}
$$

as the homogenization rule for the macroscopic deformation gradient. As for the projected model based on the standard PMVP, we can write this expression in shorthand as

$$
\boldsymbol{F} = \langle \boldsymbol{F}^{i,*}_\mu : \mathbf{B}^{i,\mathrm{mfh}}_\mu \rangle, \qquad \text{(C.102)}
$$

where the effective deformation gradient in each phase is defined as

$$
\boldsymbol{F}^{i,*}_\mu = \boldsymbol{\Gamma}_\mu + \boldsymbol{\Gamma}^i_{T,\mu} : \frac{d\boldsymbol{T}_B}{d\boldsymbol{P}}(\boldsymbol{P}^{i,\mathrm{mfh}}_\mu) + \boldsymbol{\Gamma}^i_{R,\mu} : \frac{d\boldsymbol{R}}{d\boldsymbol{P}}(\boldsymbol{P}^{i,\mathrm{mfh}}_\mu). \qquad \text{(C.103)}
$$

Note that the effective deformation gradient $\boldsymbol{F}^{i,*}_\mu$ is in general different from the actual deformation gradient $\boldsymbol{F}^i_\mu$.

The explicit expressions for the transpose of the derivatives of the Biot stress and polar rotation with respect to the first Piola–Kirchhoff stress needed to compute the homogenized deformation gradient are provided in Appendix D.

Energetic considerations

Employing a derivation similar to that in Appendix C.1.1, we can show that the model satisfies the following energetic consistency condition

$$\boldsymbol{F}:\dot{\boldsymbol{P}} = \langle \boldsymbol{F}_\mu^{i,*} : \mathbf{B}_\mu^{i,\mathrm{mfh}} \rangle : \dot{\boldsymbol{P}} \tag{C.104}$$

$$= \langle \boldsymbol{F}_\mu^{i,*} : \mathbf{B}_\mu^{i,\mathrm{mfh}} : \dot{\boldsymbol{P}} \rangle \tag{C.105}$$

$$= \langle \boldsymbol{F}_\mu^{i,*} : \dot{\boldsymbol{P}}_\mu^{i,\mathrm{mfh}} \rangle, \tag{C.106}$$

where we assumed that the materials are elastic, removing the dependence on the internal variables for clarity. They can be accounted for similarly as in Section 5.1.2. Using the definition of the effective deformation gradient in Equation (5.140), we can rewrite this expression as

$$\langle \boldsymbol{F}_\mu^{i,*} : \dot{\boldsymbol{P}}_\mu^{i} \rangle = \left\langle \left(\boldsymbol{\Gamma}_\mu + \boldsymbol{\Gamma}_{T,\mu}^{i} : \frac{d\boldsymbol{T}_B^{\mathrm{sym}}}{d\boldsymbol{P}}(\boldsymbol{P}_\mu^{i,\mathrm{mfh}}) + \boldsymbol{\Gamma}_{R,\mu}^{i} : \frac{d\boldsymbol{R}}{d\boldsymbol{P}}(\boldsymbol{P}_\mu^{i,\mathrm{mfh}}) \right) : \dot{\boldsymbol{P}}_\mu^{i,\mathrm{mfh}} \right\rangle. \tag{C.107}$$

Note that since $\boldsymbol{\Gamma}_\mu$ is a constant second-order tensor, we have

$$\langle \boldsymbol{\Gamma}_\mu : \dot{\boldsymbol{P}}_\mu^{i,\mathrm{mfh}} \rangle = \boldsymbol{\Gamma}_\mu : \langle \dot{\boldsymbol{P}}_\mu^{i,\mathrm{mfh}} \rangle \tag{C.108}$$

$$= \boldsymbol{\Gamma}_\mu : \dot{\boldsymbol{P}} \tag{C.109}$$

$$= \boldsymbol{\Gamma}_\mu : \langle \dot{\boldsymbol{P}}_\mu^{i} \rangle \tag{C.110}$$

$$= \langle \boldsymbol{\Gamma}_\mu : \dot{\boldsymbol{P}}_\mu^{i} \rangle. \tag{C.111}$$

Thus, taking the time derivative of Equations (5.115) and (5.116), we can rewrite Equation (C.107) as

$$\langle \boldsymbol{F}_\mu^{i,*} : \dot{\boldsymbol{P}}_\mu^{i} \rangle = \left\langle \left(\boldsymbol{\Gamma}_\mu + \boldsymbol{\Gamma}_{T,\mu}^{i} : \frac{d\boldsymbol{T}_B^{\mathrm{sym}}}{d\boldsymbol{P}}(\boldsymbol{P}_\mu^{i}) + \boldsymbol{\Gamma}_{R,\mu}^{i} : \frac{d\boldsymbol{R}}{d\boldsymbol{P}}(\boldsymbol{P}_\mu^{i}) \right) : \dot{\boldsymbol{P}}_\mu^{i} \right\rangle. \tag{C.112}$$

Noting that the quantity in parentheses is equal to the deformation gradient in each phase (see Equation (5.124)), we conclude that the macroscopic complementary power is equal to the volume average of its microscopic counterpart, i.e.,

$$\boldsymbol{F}:\dot{\boldsymbol{P}} = \langle \boldsymbol{F}_\mu^{i} : \dot{\boldsymbol{P}}_\mu^{i} \rangle. \tag{C.113}$$

Angular momentum balance

To prove that the homogenized deformation gradient satisfies the balance of angular momentum at the macroscale, we consider a virtual stress variation of the form $\delta\boldsymbol{P} = \boldsymbol{W}\boldsymbol{P}$, with $\boldsymbol{W}$ skew-

symmetric. Substituting this expression into Equation (C.100), we find

$$|\Omega_{0,\mu}|\boldsymbol{F}:\boldsymbol{W}\boldsymbol{P} = \sum_{i=1}^{n_P} |\Omega^i_{0,\mu}|\boldsymbol{F}^{i,*}_{\mu}:\mathbf{B}^{i,\mathrm{mfh}}_{\mu}:\boldsymbol{W}\boldsymbol{P} \tag{C.114}$$

$$= \sum_{i=1}^{n_P} |\Omega^i_{0,\mu}|\boldsymbol{F}^{i,*}_{\mu}:\boldsymbol{W}\boldsymbol{P}^{i,\mathrm{mfh}}_{\mu} \tag{C.115}$$

$$= \sum_{i=1}^{n_P} |\Omega^i_{0,\mu}|\left(\boldsymbol{\Gamma}_{\mu} + \boldsymbol{\Gamma}^i_{T,\mu}:\frac{d\boldsymbol{T}^{\mathrm{sym}}_B}{d\boldsymbol{P}}(\boldsymbol{P}^{i,\mathrm{mfh}}_{\mu}) + \boldsymbol{\Gamma}^i_{R,\mu}:\frac{d\boldsymbol{R}}{d\boldsymbol{P}}(\boldsymbol{P}^{i,\mathrm{mfh}}_{\mu})\right):\boldsymbol{W}\boldsymbol{P}^{i,\mathrm{mfh}}_{\mu} \tag{C.116}$$

$$= \sum_{i=1}^{n_P} |\Omega^i_{0,\mu}|\Bigg(\boldsymbol{\Gamma}_{\mu}:\boldsymbol{W}\boldsymbol{P}^{i,\mathrm{mfh}}_{\mu} + \boldsymbol{\Gamma}^i_{T,\mu}:\frac{d\boldsymbol{T}^{\mathrm{sym}}_B}{d\boldsymbol{P}}(\boldsymbol{P}^{i,\mathrm{mfh}}_{\mu}):\boldsymbol{W}\boldsymbol{P}^{i,\mathrm{mfh}}_{\mu} + \boldsymbol{\Gamma}^i_{R,\mu}:\frac{d\boldsymbol{R}}{d\boldsymbol{P}}(\boldsymbol{P}^{i,\mathrm{mfh}}_{\mu}):\boldsymbol{W}\boldsymbol{P}^{i,\mathrm{mfh}}_{\mu}\Bigg). \tag{C.117}$$

Given the derivatives of the Biot stress and the polar rotation with respect to the first Piola–Kirchhoff stress tensor in Equations (5.126) and (C.90), and the static hypothesis in Equations (C.82) and (C.83), we can, after some algebraic manipulation, rewrite the previous expression as

$$|\Omega_{0,\mu}|\boldsymbol{F}:\boldsymbol{W}\boldsymbol{P} = \sum_{i=1}^{n_P} |\Omega^i_{0,\mu}|\left(\boldsymbol{\Gamma}_{\mu} + \boldsymbol{\Gamma}^i_{T,\mu}:\frac{d\boldsymbol{T}^{\mathrm{sym}}_B}{d\boldsymbol{P}}(\boldsymbol{P}^{i}_{\mu}) + \boldsymbol{\Gamma}^i_{R,\mu}:\frac{d\boldsymbol{R}}{d\boldsymbol{P}}(\boldsymbol{P}^{i}_{\mu})\right):\boldsymbol{W}\boldsymbol{P}^{i}_{\mu}. \tag{C.118}$$

Noting that the quantity in parentheses is equal to the deformation gradient in each phase (see Equation (5.124)), we write

$$|\Omega_{0,\mu}|\boldsymbol{F}:\boldsymbol{W}\boldsymbol{P} = \sum_{i=1}^{n_P} |\Omega^i_{0,\mu}|\boldsymbol{F}^{i}_{\mu}:\boldsymbol{W}\boldsymbol{P}^{i}_{\mu}, \tag{C.119}$$

or, equivalently,

$$|\Omega_{0,\mu}|\boldsymbol{F}\boldsymbol{P}^T:\boldsymbol{W} = \sum_{i=1}^{n_P} |\Omega^i_{0,\mu}|\boldsymbol{F}^{i}_{\mu}(\boldsymbol{P}^{i}_{\mu})^T:\boldsymbol{W}. \tag{C.120}$$

Finally, since $\boldsymbol{W}$ is an arbitrary skew-symmetric second-order tensor, we conclude that

$$\mathrm{skew}(\boldsymbol{F}\boldsymbol{P}^T) = \langle \mathrm{skew}(\boldsymbol{F}^{i}_{\mu}(\boldsymbol{P}^{i}_{\mu})^T)\rangle \tag{C.121}$$

Since Equation (5.125) is equal to Equation (C.62), the steps taken in the derivation of the balance of angular momentum for the fully constrained MFH-PMCVP model (see Appendix C.2.1) can be followed verbatim, leading to the same conclusion, namely that

$$\mathrm{skew}(\boldsymbol{F}\boldsymbol{P}^T) = \mathbf{0}, \tag{C.122}$$

and thus the macroscopic balance of angular momentum is satisfied. Note also that from Equation (C.80), we can write

$$\mathrm{skew}(\boldsymbol{P}^{i}_{\mu}(\boldsymbol{F}^{i}_{\mu})^T) = \mathrm{skew}(\boldsymbol{R}^{i}_{\mu}\boldsymbol{T}^{i}_{B,\mu}\boldsymbol{U}^{i}_{\mu}(\boldsymbol{R}^{i}_{\mu})^T), \tag{C.123}$$

$$= \boldsymbol{R}^{i}_{\mu}\,\mathrm{skew}(\boldsymbol{T}^{i}_{B,\mu}\boldsymbol{U}^{i}_{\mu})(\boldsymbol{R}^{i}_{\mu})^T, \tag{C.124}$$

and thus from

$$\mathrm{skew}(\boldsymbol{P}^{i}_{\mu}(\boldsymbol{F}^{i}_{\mu})^T) = \mathbf{0}, \tag{C.125}$$

we can also conclude that

$$\mathrm{skew}(\boldsymbol{T}^{i}_{B,\mu}\boldsymbol{U}^{i}_{\mu}) = \mathbf{0}, \tag{C.126}$$

which is the local balance of angular momentum in each phase i.

C.2.3 Taylor's assumption

The model corresponding to the minimal space of admissible stress-potential fluctuations is the Taylor model. In this case, no constraints are imposed on the stress potential fields beyond static admissibility

$$\tilde{\mathscr{S}}_{\mu,\text{Taylor}} = \tilde{\mathscr{S}}_{\mu}^{*}. \tag{C.127}$$

Similarly, the associated space of virtual admissible stress potential fields is

$$\tilde{\mathscr{H}}_{\mu,\text{Taylor}} = \tilde{\mathscr{H}}_{\mu}^{*}. \tag{C.128}$$

As before, we enforce static admissibility using a Lagrange multiplier, denoted by $\boldsymbol{\Gamma}_\mu$, which is a second-order dimensionless tensor. The Principle of Multiscale Complementary Virtual Power becomes

$$\begin{aligned}|\Omega_{0,\mu}|\delta\boldsymbol{P}:\boldsymbol{F} = \int_{\Omega_{0,\mu}} \left(\delta\boldsymbol{P} + \operatorname{curl}_0 \delta\tilde{\boldsymbol{Z}}_\mu\right):\boldsymbol{F}_\mu \, dv \\ -\boldsymbol{\Gamma}_\mu : \sum_{i=1}^{n_P} \int_{\Omega_{0,\mu}^i} \operatorname{curl}_0 \delta\tilde{\boldsymbol{Z}}_\mu \, dv - \delta\boldsymbol{\Gamma}_\mu : \sum_{i=1}^{n_P} \int_{\Omega_{0,\mu}^i} \operatorname{curl}_0 \tilde{\boldsymbol{Z}}_\mu \, dv.\end{aligned} \tag{C.129}$$

Static homogenization

By setting all variations to zero except for $\delta\boldsymbol{\Gamma}_\mu$, we enforce the admissibility condition

$$\sum_{i=1}^{n_P} \int_{\Omega_{0,\mu}^i} \operatorname{curl}_0 \tilde{\boldsymbol{Z}}_\mu \, dv = \boldsymbol{0}. \tag{C.130}$$

Interpretation of the Lagrange multipliers

To interpret $\boldsymbol{\Gamma}_\mu$, we set $\delta\boldsymbol{P} = \boldsymbol{0}$ and $\delta\boldsymbol{\Gamma}_\mu = \boldsymbol{0}$ in the virtual power expression, yielding

$$\int_{\Omega_{0,\mu}} \operatorname{curl}_0 \delta\tilde{\boldsymbol{Z}}_\mu : \boldsymbol{F}_\mu \, dv - \boldsymbol{\Gamma}_\mu : \sum_{i=1}^{n_P} \int_{\Omega_{0,\mu}^i} \operatorname{curl}_0 \delta\tilde{\boldsymbol{Z}}_\mu \, dv = 0. \tag{C.131}$$

We now select $\delta\tilde{\boldsymbol{Z}}_\mu(\boldsymbol{Y}) = \dfrac{1}{2}\boldsymbol{C} \times (\boldsymbol{Y} - \boldsymbol{Y}_0^i)$ for $\boldsymbol{Y} \in \Omega_{0,\mu}^i$, and zero otherwise, for an arbitrary second-order tensor $\boldsymbol{C}$, and each $i = 1, \ldots, n_P$ individually. Then

$$\boldsymbol{\Gamma}_\mu = \frac{1}{|\Omega_{0,\mu}^i|} \int_{\Omega_{0,\mu}^i} \boldsymbol{F}_\mu \, dv = \boldsymbol{F}_\mu^i, \quad i = 1, \ldots, n_P, \tag{C.132}$$

which implies that the average deformation gradient in all phases is the same. Thus, we can write

$$\int_{\Omega_{0,\mu}} \operatorname{curl}_0 \delta\tilde{\boldsymbol{Z}}_\mu : \boldsymbol{F}_\mu \, dv - \sum_{i=1}^{n_P} \boldsymbol{F}_\mu^i : \int_{\Omega_{0,\mu}^i} \operatorname{curl}_0 \delta\tilde{\boldsymbol{Z}}_\mu \, dv = 0, \tag{C.133}$$

to use in the subsequent derivations.

Deformation homogenization

Taking $\delta\tilde{\boldsymbol{Z}}_\mu = \boldsymbol{0}$ and $\delta\boldsymbol{\Gamma}_\mu = \boldsymbol{0}$, we obtain

$$\boldsymbol{F} = \langle \boldsymbol{F}_\mu^i \rangle. \tag{C.134}$$

Combining this with Equation (C.132), we conclude

$$\boldsymbol{F} = \boldsymbol{\Gamma}_\mu = \boldsymbol{F}_\mu^i, \quad i = 1, \dots, n_P. \tag{C.135}$$

Therefore, in the Taylor model, the average deformation gradient is uniform across all phases and equal to the macroscopic deformation gradient.

Energetic consistency and balance of angular momentum

The considerations regarding energetic consistency and the balance of angular momentum for the Taylor model are similar to those presented for the fully constrained MFH-PMCVP and projected MFH-PMCVP models. For energetic consistency, the derivation simplifies considerably, and we can directly write

$$\begin{aligned} \boldsymbol{F} : \dot{\boldsymbol{P}} &= \boldsymbol{F} : \langle \dot{\boldsymbol{P}}_\mu^i \rangle, && \text{(C.136)} \\ &= \langle \boldsymbol{F} : \dot{\boldsymbol{P}}_\mu^i \rangle, && \text{(C.137)} \\ &= \langle \boldsymbol{F}_\mu^i : \dot{\boldsymbol{P}}_\mu^i \rangle. && \text{(C.138)} \end{aligned}$$

The balance of angular momentum can be derived similarly, starting from the PMCVP in Equation (C.129). Considering a virtual variation of the deformation gradient of the form $\delta \boldsymbol{P} = \boldsymbol{W}\boldsymbol{P}$, with $\boldsymbol{W}$ skew-symmetric, and $\delta \tilde{\boldsymbol{Z}}_\mu$ and $\delta \boldsymbol{\Gamma}_\mu$ equal to zero, we find that

$$\begin{aligned} \boldsymbol{F} : \boldsymbol{W}\boldsymbol{P} &= \boldsymbol{F} : \boldsymbol{W} \langle \boldsymbol{P}_\mu^i \rangle, && \text{(C.139)} \\ &= \langle \boldsymbol{F} : \boldsymbol{W}\boldsymbol{P}_\mu^i \rangle, && \text{(C.140)} \\ &= \langle \boldsymbol{F}_\mu^i : \boldsymbol{W}\boldsymbol{P}_\mu^i \rangle, && \text{(C.141)} \\ &= \langle \boldsymbol{F}_\mu^i (\boldsymbol{P}_\mu^i)^T \rangle : \boldsymbol{W}, && \text{(C.142)} \end{aligned}$$

leading to

$$\operatorname{skew}(\boldsymbol{F}\boldsymbol{P}^T) = \langle \operatorname{skew}(\boldsymbol{F}_\mu^i (\boldsymbol{P}_\mu^i)^T) \rangle. \tag{C.143}$$

As for the full-MFH and projected-MFH, Equation (C.133) allows us to conclude that (see Appendix C.2.1 for the derivation)

$$\operatorname{skew}(\boldsymbol{F}_\mu^i (\boldsymbol{P}_\mu^i)^T) = \boldsymbol{0}, \tag{C.144}$$

leading to the same conclusion, namely that

$$\operatorname{skew}(\boldsymbol{F}\boldsymbol{P}^T) = \boldsymbol{0}, \tag{C.145}$$

and thus the macroscopic balance of angular momentum is satisfied.

Appendix D

Derivatives of the Biot stress and the polar rotation with respect to the first Piola–Kirchhoff stress

In this contribution, we employ the derivatives of the Biot stress and polar rotation with respect to the first Piola–Kirchhoff stress. We are particularly interested in their derivative along specific directions. This derivation is adapted from Chen and Wheeler (1992), where the authors extracted the derivatives of the right stretch and polar rotation with respect to the deformation gradient. To motivate this choice, we first note that the Biot stress lives in a manifold $\mathcal{N}$ that can be parameterized by the right stretch through the relation

$$\boldsymbol{T}_B = \boldsymbol{h}|_{\mathbb{S}^3_+}(\boldsymbol{U}). \tag{D.1}$$

Employing the Taylor expansion of this function around a given right stretch tensor $\boldsymbol{U}$, we find

$$\boldsymbol{h}|_{\mathbb{S}^3_+}(\boldsymbol{U}+\epsilon\boldsymbol{S}) = \boldsymbol{h}|_{\mathbb{S}^3_+}(\boldsymbol{U}) + \epsilon\frac{d\boldsymbol{h}|_{\mathbb{S}^3_+}}{d\boldsymbol{U}}(\boldsymbol{U}) : \boldsymbol{S} + O(\epsilon^2) \tag{D.2}$$

$$= \boldsymbol{T}_B + \epsilon\boldsymbol{\Sigma} + O(\epsilon^2), \tag{D.3}$$

where $\boldsymbol{S}$ is symmetric second order tensor, i.e., $\boldsymbol{S} \in \mathbb{S}^3$, and $\boldsymbol{\Sigma}$ is a second-order tensor in $T_{\boldsymbol{U}}\mathcal{N}$, since $\dfrac{d\boldsymbol{h}|_{\mathbb{S}^3_+}}{d\boldsymbol{U}}(\boldsymbol{U})$ takes elements of $\mathbb{S}^3$ to $T_{\boldsymbol{U}}\mathcal{N}$. Accordingly, we seek to find the derivatives of $\boldsymbol{T}_B$ and $\boldsymbol{R}$ with respect to $\boldsymbol{P}$ along the direction $\boldsymbol{R\Sigma}$, where $\boldsymbol{\Sigma} \in T_{\boldsymbol{U}}\mathcal{N}$, i.e.,

$$\frac{d\boldsymbol{T}_B}{d\boldsymbol{P}}(\boldsymbol{P}) : (\boldsymbol{R\Sigma}), \quad \text{and} \quad \frac{d\boldsymbol{R}}{d\boldsymbol{P}}(\boldsymbol{P}) : (\boldsymbol{R\Sigma}). \tag{D.4}$$

We are also interested in the same derivatives along $\boldsymbol{WP}$, with $\boldsymbol{W} \in \mathfrak{so}(3)$, i.e., we want to find

$$\frac{d\boldsymbol{T}_B}{d\boldsymbol{P}}(\boldsymbol{P}) : (\boldsymbol{WP}), \quad \text{and} \quad \frac{d\boldsymbol{R}}{d\boldsymbol{P}}(\boldsymbol{P}) : (\boldsymbol{WP}). \tag{D.5}$$

Regarding the first pair of derivatives, we start from the definition of the derivative of $\boldsymbol{T}_B$ with respect to $\boldsymbol{P}$ along the direction $\boldsymbol{R\Sigma}$, i.e.,

$$\frac{d\boldsymbol{T}_B}{d\boldsymbol{P}}(\boldsymbol{P}) : (\boldsymbol{R\Sigma}) = \lim_{\epsilon\to 0}\frac{\boldsymbol{T}_B(\hat{\boldsymbol{P}}) - \boldsymbol{T}_B(\boldsymbol{P})}{\epsilon}, \tag{D.6}$$

where

$$\hat{\boldsymbol{P}} = \boldsymbol{P} + \epsilon \boldsymbol{R}\boldsymbol{\Sigma} \tag{D.7}$$

$$= \boldsymbol{R}(\boldsymbol{T}_B + \epsilon \boldsymbol{\Sigma}) \tag{D.8}$$

$$= \boldsymbol{R}\boldsymbol{h}|_{\mathbb{S}^3_+}(\boldsymbol{U} + \epsilon \boldsymbol{S}) + O(\epsilon^2). \tag{D.9}$$

Thus, to second order in ϵ, there is a right stretch tensor $\hat{\boldsymbol{U}} = \boldsymbol{U} + \epsilon \boldsymbol{S}$ such that

$$\boldsymbol{T}_B(\hat{\boldsymbol{P}}) = \boldsymbol{h}|_{\mathbb{S}^3_+}(\boldsymbol{U} + \epsilon \boldsymbol{S}) + O(\epsilon^2) = \boldsymbol{T}_B + \epsilon \boldsymbol{\Sigma} + O(\epsilon^2), \tag{D.10}$$

and thus

$$\boldsymbol{T}_B(\hat{\boldsymbol{P}}) - \boldsymbol{T}_B(\boldsymbol{P}) = \epsilon \boldsymbol{\Sigma} + O(\epsilon^2), \tag{D.11}$$

which leads to

$$\frac{d\boldsymbol{T}_B}{d\boldsymbol{P}}(\boldsymbol{P}) : (\boldsymbol{R}\boldsymbol{\Sigma}) = \boldsymbol{\Sigma}, \tag{D.12}$$

as ϵ tends to zero.

Concerning the derivative of the polar rotation with respect to the first Piola–Kirchhoff stress along the direction $\boldsymbol{R}\boldsymbol{\Sigma}$, we start from its definition

$$\frac{d\boldsymbol{R}}{d\boldsymbol{P}}(\boldsymbol{P}) : (\boldsymbol{R}\boldsymbol{\Sigma}) = \lim_{\epsilon \to 0} \frac{\boldsymbol{R}(\hat{\boldsymbol{P}}) - \boldsymbol{R}(\boldsymbol{P})}{\epsilon}. \tag{D.13}$$

Using the same reasoning as before, from Equation (D.8), we note that to second order in ϵ, there is a right stretch tensor $\hat{\boldsymbol{U}} = \boldsymbol{U} + \epsilon \boldsymbol{S}$ such that

$$\boldsymbol{R}(\hat{\boldsymbol{P}}) = \boldsymbol{R} + O(\epsilon^2), \tag{D.14}$$

and thus

$$\boldsymbol{R}(\hat{\boldsymbol{P}}) - \boldsymbol{R}(\boldsymbol{P}) = O(\epsilon^2). \tag{D.15}$$

This leads to

$$\frac{d\boldsymbol{R}}{d\boldsymbol{P}}(\boldsymbol{P}) : (\boldsymbol{R}\boldsymbol{\Sigma}) = \boldsymbol{O}, \tag{D.16}$$

as $\epsilon \to 0$.

Regarding the second pair of derivatives, we consider the Biot stress tensor computed at $e^{\boldsymbol{W}\eta}\boldsymbol{P}$. Note that $e^{\boldsymbol{W}\eta}$ is a proper orthogonal tensor for any scalar parameter η, since $\boldsymbol{W}$ is skew-symmetric, and that taking the derivative with respect to the scalar parameter η leads to

$$\frac{de^{\boldsymbol{W}\eta}}{d\eta}\boldsymbol{P} = \boldsymbol{W}e^{\boldsymbol{W}\eta}\boldsymbol{P}. \tag{D.17}$$

In particular, at $\eta = 0$, we have that

$$\left.\frac{de^{\boldsymbol{W}\eta}}{d\eta}\boldsymbol{P}\right|_{\eta=0} = \boldsymbol{W}\boldsymbol{P}. \tag{D.18}$$

Thus, by the chain rule, we have that

$$\frac{d\boldsymbol{T}_B}{d\boldsymbol{P}}(e^{\boldsymbol{W}\eta}\boldsymbol{P}) : \left(\frac{de^{\boldsymbol{W}\eta}}{d\eta}\boldsymbol{P}\right) = \frac{d\boldsymbol{T}_B}{d\boldsymbol{P}}(e^{\boldsymbol{W}\eta}\boldsymbol{P}) : (\boldsymbol{W}e^{\boldsymbol{W}\eta}\boldsymbol{P}). \tag{D.19}$$

From the definition of the derivative, we write that

$$\frac{d\boldsymbol{T}_B}{d\boldsymbol{P}}(e^{\boldsymbol{W}\eta}\boldsymbol{P}) : (\boldsymbol{W}e^{\boldsymbol{W}\eta}\boldsymbol{P}) = \lim_{\epsilon \to 0} \frac{\boldsymbol{T}_B(e^{\boldsymbol{W}(\eta+\epsilon)}\boldsymbol{P}) - \boldsymbol{T}_B(e^{\boldsymbol{W}\eta}\boldsymbol{P})}{\epsilon}. \tag{D.20}$$

Now, we choose $\eta = 0$, leading to

$$\frac{d\boldsymbol{T}_B}{d\boldsymbol{P}}(\boldsymbol{P}) : (\boldsymbol{W}\boldsymbol{P}) = \lim_{\epsilon \to 0} \frac{\boldsymbol{T}_B(e^{\boldsymbol{W}\epsilon}\boldsymbol{P}) - \boldsymbol{T}_B(\boldsymbol{P})}{\epsilon}. \tag{D.21}$$

From the properties of the Biot stress and $e^{\boldsymbol{W}\epsilon} \in SO(3)$, we find

$$\frac{d\boldsymbol{T}_B}{d\boldsymbol{P}}(\boldsymbol{P}) : (\boldsymbol{W}\boldsymbol{P}) = \lim_{\epsilon \to 0} \frac{\boldsymbol{T}_B(e^{\boldsymbol{W}\epsilon}\boldsymbol{P}) - \boldsymbol{T}_B(\boldsymbol{P})}{\epsilon}, \tag{D.22}$$

$$= \lim_{\epsilon \to 0} \frac{\boldsymbol{T}_B(\boldsymbol{P}) - \boldsymbol{T}_B(\boldsymbol{P})}{\epsilon}, \tag{D.23}$$

$$= \boldsymbol{O}, \tag{D.24}$$

leading to

$$\frac{d\boldsymbol{T}_B}{d\boldsymbol{P}}(\boldsymbol{P}) : (\boldsymbol{W}\boldsymbol{P}) = \boldsymbol{O}. \tag{D.25}$$

Moving to the derivative of the polar rotation with respect to the first Piola–Kirchhoff stress along the direction $\boldsymbol{W}\boldsymbol{P}$, we consider the polar rotation computed from $e^{\boldsymbol{W}\eta}\boldsymbol{P}$. Again, by the chain rule, after some manipulations similar to those above, we have that

$$\frac{d\boldsymbol{R}}{d\boldsymbol{P}}(\boldsymbol{P}) : (\boldsymbol{W}\boldsymbol{P}) = \lim_{\epsilon \to 0} \frac{\boldsymbol{R}(e^{\boldsymbol{W}\epsilon}\boldsymbol{P}) - \boldsymbol{R}(\boldsymbol{P})}{\epsilon}. \tag{D.26}$$

From the properties of the polar decomposition, we find that

$$\frac{d\boldsymbol{R}}{d\boldsymbol{P}}(\boldsymbol{P}) : (\boldsymbol{W}\boldsymbol{P}) = \lim_{\epsilon \to 0} \frac{e^{\boldsymbol{W}\epsilon}\boldsymbol{R}(\boldsymbol{P}) - \boldsymbol{R}(\boldsymbol{P})}{\epsilon}, \tag{D.27}$$

$$= \lim_{\epsilon \to 0} \frac{e^{\boldsymbol{W}\epsilon} - \boldsymbol{I}}{\epsilon}\boldsymbol{R}(\boldsymbol{P}), \tag{D.28}$$

$$= \boldsymbol{W}\boldsymbol{R}. \tag{D.29}$$

To compute the directional derivative of the Biot stress and polar rotation with respect to the first Piola–Kirchhoff stress along arbitrary directions, we need to show that any second-order tensor $\boldsymbol{L}$ can be uniquely written as

$$\boldsymbol{L} = \boldsymbol{R}\boldsymbol{\Sigma} + \boldsymbol{W}\boldsymbol{P}, \tag{D.30}$$

with $\boldsymbol{\Sigma} \in T_{\boldsymbol{U}}\mathcal{N}$ and $\boldsymbol{W} \in \mathfrak{so}(3)$, i.e., it remains to show that

$$\boldsymbol{R}T_{\boldsymbol{U}}\mathcal{N} \oplus \mathfrak{so}(3)\boldsymbol{P} = \mathbb{R}^{3\times 3}, \tag{D.31}$$

where

$$\boldsymbol{R}T_{\boldsymbol{U}}\mathcal{N} = \{\boldsymbol{R}\boldsymbol{\Sigma} \,|\, \boldsymbol{\Sigma} \in T_{\boldsymbol{U}}\mathcal{N}\}, \tag{D.32}$$

and

$$\mathfrak{so}(3)\boldsymbol{P} = \{\boldsymbol{W}\boldsymbol{P} \,|\, \boldsymbol{W} \in \mathfrak{so}(3)\}. \tag{D.33}$$

We restrict ourselves to the isotropic case, where $\mathcal{N}$ is the manifold of symmetric second-order tensors, i.e., $\mathcal{N} = \mathbb{S}^3$. In this case, we have that $T_{\boldsymbol{U}}\mathcal{N} = \mathbb{S}^3$. Starting from an arbitrary second-order tensor $\boldsymbol{L}$, we seek to find $\boldsymbol{\Sigma} \in \mathbb{S}^3$ and $\boldsymbol{W} \in \mathfrak{so}(3)$ such that

$$\boldsymbol{L} = \boldsymbol{R}\boldsymbol{\Sigma} + \boldsymbol{W}\boldsymbol{P}. \tag{D.34}$$

Multiplying by $\boldsymbol{R}^T$ from the left, we find

$$\boldsymbol{\Sigma} = \boldsymbol{R}^T\boldsymbol{L} - \boldsymbol{R}^T\boldsymbol{W}\boldsymbol{P}, \tag{D.35}$$

or, equivalently, applying the definition of the Biot stress (Equation (2.12)),

$$\boldsymbol{\Sigma} = \boldsymbol{R}^T \boldsymbol{L} - \boldsymbol{R}^T \boldsymbol{W} \boldsymbol{R} \boldsymbol{T}_B. \tag{D.36}$$

Defining $\boldsymbol{W}^* = \boldsymbol{R}^T \boldsymbol{W} \boldsymbol{R}$, we can rewrite this expression as

$$\boldsymbol{\Sigma} = \boldsymbol{R}^T \boldsymbol{L} - \boldsymbol{W}^* \boldsymbol{T}_B. \tag{D.37}$$

Noting that $\boldsymbol{\Sigma}$ is symmetric, we take the skew part of this equation, leading to

$$\operatorname{skew}(\boldsymbol{R}^T \boldsymbol{L}) = \operatorname{skew}(\boldsymbol{W}^* \boldsymbol{T}_B), \tag{D.38}$$

$$= \boldsymbol{W}^* \boldsymbol{T}_B + \boldsymbol{T}_B \boldsymbol{W}^* \tag{D.39}$$

where we used the fact that $\boldsymbol{T}_B$ is symmetric and $\boldsymbol{W}^*$ is skew-symmetric.

From (Chillingworth et al., 1982, Proposition 3.3.) we have that this equation has a unique skew solution $\boldsymbol{W}^*$ provided that $\operatorname{trace}(\boldsymbol{T}_B)$ is not an eigenvalue of $\boldsymbol{T}_B$. Thus, in this text, we restrict ourselves to this case. A finer analysis is required for the general case, which is beyond the scope of this contribution.